N° d'ordre : 368

CENTRALE LILLE

THESE

Présentée en vue
d'obtenir le grade de

DOCTEUR

En

Spécialité : Génie Electrique

Par

Emile Devillers

DOCTORAT DELIVRE PAR CENTRALE LILLE

Titre de la thèse :

Modélisation électromagnétique appliquée à la détermination des harmoniques de forces radiale et tangentielle dans les machines électriques en exploitant l'approche des sous-domaines

Soutenue le jeudi 13 décembre 2018 devant le jury d'examen :

Président	Vincent LANFRANCHI	Pr, Roberval - UTC
Rapporteur	Georges BARAKAT	Pr, GREAH - Univ. du Havre
Rapporteur	Yvan LEFEVRE	CR CNRS - HDR, Laplace - Toulouse INP
Examinateur	Imen ABDENNADHER	MCF HDR, RELEV - Univ. de Sfax, Tunisie
Directeur de thèse	Michel HECQUET	Pr, L2EP - Centrale Lille
Directeur de thèse	Jean-Philippe LECOINTE	Pr, LSEE - Univ. d'Artois
Encadrant	Thierry LUBIN	MCF HDR, GREEN - Univ. de Lorraine
Encadrant	Jean LE BESNERAIS	Dr Ing., EOMYS ENGINEERING

Thèse préparée dans le Laboratoire L2EP
Ecole Doctorale SPI 072

Contents

Remerciements

Je tiens avant tout à remercier profondément l'ensemble des encadrants et des collègues en entreprise et au laboratoire, qui ont chacun contribué à la réussite de cette thèse d'un point de vue technique et humain. Tout ce travail réalisé durant ces trois années aurait été certainement bien moins abouti et plaisant sans la formidable équipe avec laquelle j'ai eu la chance d'évoluer. Merci !

Je remercie naturellement Jean, à l'origine de ce projet de thèse en entreprise, de m'avoir fait confiance tout au long de la thèse, de m'avoir donné le temps de me consacrer entièrement à la thèse lorsque ce fut nécessaire, et surtout de m'avoir constamment challengé au travers de tes précieuses recommandations pour améliorer la qualité du travail produit. Je poursuis l'aventure à Eomys avec enthousiasme, au regard des nombreux projets très intéressants en cours.

Je remercie vivement Michel de m'avoir soutenu et guidé durant ces trois années côté L2EP. J'insiste sur la chance d'avoir pu profiter de toutes tes qualités d'encadrement, à la fois en termes d'expertise scientifique et de management de doctorants. Merci pour ta disponibilité, ta réactivité et ta gentillesse sans faille, et de m'avoir permis de participer à tant de congrès, synonymes de nouvelles rencontres et de beaux voyages.

Je remercie Jean-Philippe pour ton suivi durant ces trois années, pour les conseils et l'aide scientifique et technique que tu as régulièrement apporté malgré le fait que je n'ai pu venir au LSEE aussi souvent qu'il avait été prévu. Je te remercie en particulier pour ta très précieuse contribution à la conception du banc d'essai, dont les objectifs scientifiques iront bien au-delà du cadre de cette thèse.

Je remercie Thierry d'avoir accepté de joindre le projet de thèse un semestre après qu'elle ait débutée. Tu m'as donné les outils appropriés pour que la partie mathématique de cette thèse se transforme progressivement en terrain de jeu. Tu m'as également aidé à disposer du recul nécessaire à la bonne utilisation de ces modèles au regard de leurs atouts et de leurs faiblesses.

Je remercie ensuite tous les membres du jury de thèse. Tout d'abord, merci au Pr. Georges Barakat et au Dr. Yvan Lefèvre d'avoir accepté de rapporter mon manuscrit, et pour leurs appréciations et remarques toujours juste et constructives dans leur rapport et lors de la soutenance. Je remercie également Pr. Vincent Lanfranchi d'avoir présidé et examiné la soutenance, et Dr. Imen Abdennadher d'avoir accepté d'examiner la soutenance à distance, malgré les inconvénients de la téléconférence.

Mes remerciements vont ensuite à tous les collègues d'Eomys avec qui j'ai travaillé durant ces trois années, avec une mention spéciale à Pierre qui m'a entre autres initié à

un grand nombre de concepts et bonnes pratiques informatiques sous l'œil bienveillant de Jenkins, à Raphaël qui, en outre ses qualités à pouvoir te conseiller sur n'importe quel sujet, devient de facto notre pilier en R&D avec son sujet de thèse qui en vaut trois, à Karine et Paul qui ont mis le pied à l'étrier dès leur arrivée spécialement pour m'aider à obtenir les résultats des chapitres 4 et 5.

Merci également à tous mes collègues du L2ep, à mes co-bureaux et amis Ghislain et Patricio qui ont égayé bons nombres de moments, à Xavier et Simon pour leur disponibilité et leur aide précieuse dans la conception du banc d'essai et du capteur d'entrefer, et à la joyeuse bande des doctorants du L2ep et du LSEE.

Je remercie enfin ma famille qui m'a soutenu durant toute ma scolarité et a fortiori durant cette thèse, en particulier ma compagne, mes parents, mon frère et ma belle-famille. Une pensée également à mes amis, en particulier ceux du disque rond et ceux pourvus de corne et de crinière rose, qui se reconnaîtront.

Introduction

Noise sources in electrical machines

The presence of electrical machines in our everyday life has permanently grown in line with the need of electrified automatic systems. Nowadays, electrical machines are used in a wide range of applications, including transport, industry, energy production and household applications. Over the past decades, progress in electrical machines design mainly focused on improving their energy efficiency and compactness regarding cost and global environmental constraints. Furthermore, since electrical machines have been increasingly working close to people, their acoustic noise has recently become an additional key aspect.

Most of electric motors generate audible noise during operation. Some of them are quite silent while others can turn into very noisy devices. Following EOMYS experience, the Sound Pressure Level (SPL) of electrical machines at 1 m can vary from 70 to 125 dBA. Despite the increasing amount of electrical machines in our environment, noise concern is not systematically included in the design process. However, it is already necessary in some applications, such as home-automation or transportation in which noise concern is referred as Noise, Vibrations, and Harshness (NVH). Accounting for NVH criterion during design process requires Computer Aided Engineering (CAE) tools adapted to the current context of the increasing use of electrical machines in a growing range of applications.

Noise and vibrations generation patterns are quite complex in electric motors. Noise is generated by the movement of air particles, called vibrations, which are initially produced by external excitations and propagate through the air in form of sound waves at audible frequencies. There are mainly three types of noise in electrical machines:

— Aerodynamic noise, for example emitted by cooling fans, where fan blades typically excite air particles at blade passing frequency;

— Mechanical noise, for example emitted by both mechanical bearings and reducer, where friction between moving parts create noise and vibrations;

— Electromagnetic noise, referred as Electromagnetic Noise, Vibrations and Harshness (e-NVH), which is caused by the presence of variable electromagnetic fields inside electrical machines. These variable electromagnetic fields enable to produce torque and rotating motion, which are the main machine functions. However, they are also source of parasitic electromagnetic forces, for example at slot passing frequencies, which induce vibrations in the machine structure and potentially acoustic noise in the audible frequencies.

In summary, the scientific study of noise generation in electrical machines belongs to many fields of research, including acoustics, mechanics and electromagnetics, and is often referred as "noise and vibrations study", "NVH study" or "vibroacoustic study". This thesis exclusively focuses on the study of electromagnetic noise (e-NVH study) in

radial flux machines.

e-NVH is characterized by a strongly harmonic content, with a discrete set of excitation frequencies. Depending on machine applications, it can result in low frequency ("humming noise"), and/or at high frequency ("whining noise"). Besides, electromagnetic excitations can resonate with the machine structure if they excite its natural frequencies. In case of resonance, noise and vibration level is largely amplified and electromagnetic noise may be louder than aerodynamic and mechanical noise. The e-NVH study of electrical machines is required for the following reasons:

— Electromagnetic noise is generally source of discomfort to people staying close to electrical machines, due to the tonal property which becomes quickly irritating.

— Electromagnetic noise may be a health concern in industrial environments, where operators daily work close to loud electrical machines.

— Vibrations may compromise people and devices safety by causing mechanical fatigue, resulting in electrical machine operating lifetime reduction and maintenance cost increase.

Therefore, standard requirements IEEE and IEC (such as IEC61672-1 [2013]) limit noise and vibrations level of electrical machines. Recent machines must meet additional constraints in specific applications. For instance in electric vehicles, the emitted noise has to further meet with sound "pleasantness" requirements, based on psychoacoustic metrics. In critical applications such as scientific research or military, the aim is to cancel or reduce as much as possible the vibroacoustic signature, for example to avoid disturbing scientific experiments or being detected.

Electromagnetic and NVH design interactions

Noise and vibrations criteria are also relevant to help choosing between designs which seem equivalent prior to vibroacoustic analysis. In fact, several machine designs can be found for a same application if classical electromechanical performance is considered, such as speed, power-to-weight/volume ratios, efficiency etc. Vibroacoustic properties significantly vary among machine topologies. For example, the Sound Power Level (SWL) emitted by Squirrel Cage Induction Machines (SCIMs) can vary from ±20 dB depending on the number of poles and the number of stator and rotor slots combination [Le Besnerais et al., 2009a]. Vibroacoustic properties also strongly depend on the specified application (low/high speed, fixed/variable speed).

Furthermore, fulfilling NVH requirements may not be in agreement with actual economic and size constraints. Manufacturers tend to reduce both amount and grade of material required to mass-produce electrical machines. Machines structures may be consequently more deformable and less balanced due to less strict manufacturing tolerances. Besides, higher power density also means stronger stress due to electromagnetic field. Therefore, current electrical machines are more likely to emit louder noise.

The design challenge lies in finding the best compromise between all of these constraints by integrating electromagnetic and vibroacoustic simulations at each design stage of electrical machines. These simulations should first rely on fast and accurate modeling techniques, which enable to explore and sort as many topologies as possible without significantly slowing early design stages. Then, more finely detailed simulations are run to validate design evolution. Finally, vibroacoustic simulation should provide a

comprehensive understanding of e-NVH origins, which then enables to include reduction techniques while preserving as much as possible electromagnetic performances.

In summary, the study of e-NVH in electrical machines is an essential industrial research matter, for the challenges presented previously. Moreover, it is a scientific research topic in itself, involving complex aspects inherent to multi-physics modeling and simulation.

Industrial background

The context of this thesis contains both industrial and scientific sides. This thesis is actually an industrial PhD thesis which takes part of the internal research program of EOMYS ENGINEERING, a research and development company specialized in the vibroacoustic study of electrical machines. For five years now, EOMYS has provided technical consulting services to electrical machines designers and manufacturers facing vibroacoustic issues. Besides, the company develops and commercializes its own software solution MANATEE [MANATEE, 2018], a simulation environment dedicated to the fast and accurate prediction of electromagnetic noise and vibrations in electrical machines.

The first studies describing and explaining the main physical concepts, as it is still addressed nowadays, were published in the early 1950's [Alger, 1953; Jordan, 1950]. From this date, there have been many studies in this research field. Therefore, physical understanding of noise and vibrations generation process in electrical machines has certainly increased over the past decades [Timar, 1989; Gieras et al., 2006]. However, e-NVH modeling still faces numerous scientific and technological barriers which are actively investigated for the following reasons.

First of all, the global environmental constraints has led to the development of new electrical machines, with better energy efficiency and power density, and to re-design existing machines with low efficiency. This technological progress has introduced new machine topologies (e.g. new winding patterns such as concentrated windings, new laminations shapes such as flux barriers), new materials (e.g. permanent magnets, grain-oriented electrical steel) and new control strategies thanks to power electronics. This progress in terms of energy consumption and compactness has brought new challenges in the e-NVH design of electrical machines. In particular, the massive use of electronic variable speed drive has globally increased the contribution of e-NVH to the overall emitted noise level. Including these new technologies requires to understand and model new physical phenomena. It also leads to question and remove modeling assumptions that were fulfilled before but are no longer valid for new topologies.

Besides, the apparition of new applications, especially in automotive sector, has considerably tightened constraints in terms of low noise and vibrations level, speed range, compactness etc. Rushing towards any slight noise reduction demands to evaluate every potential source that may exist in the machine, including malfunctions, manufacturing tolerances etc. It also adds more complexity in both physical understanding and simulation modeling.

Then, several challenges remain even for old topologies of electrical machines, especially for re-design purposes, and two problems are particularly addressed in this thesis:

1. The contribution of the circumferential (i.e. tangential in 2D) magnetic field to radial forces applying on the structure is still under investigation, so as the contribution of circumferential forces to the radial vibration level of the structure.

2. The slotting modulation effect, which appears in recent machine topologies having close poles and slot numbers, implies that force harmonics with high wavenumber can resonate with structural modes of low circumferential order due to spatial aliasing. This new phenomenon is naturally little investigated and not considered in most of e-NVHs studies.

Finally, e-NVH simulation capacities are still limited by the current computing power. Even if it is possible to include all electromagnetic and vibroacoustic aspects in a simulation model, such simulation is barely feasible in terms of computation time and memory limitations. It would take weeks even on computing cluster. The full simulation is obviously not suitable yet for early design purpose. Therefore, a large variety of fast and accurate electromagnetic and vibroacoustic models have been developed to include the e-NVH criterion at each design stage. A benchmark study can be relevant to validate and classify the different modeling techniques, but it does not exist yet.

Thesis objectives and outlines

The first contribution of this thesis is the development of the SubDomain Method (SDM) to compute the electromagnetic excitations in large variety of electrical machines with an interesting compromise between accuracy and computation time. The second contribution is the design of an experimental test rig which enables to highlight noise and vibrations phenomenon, with a particular noisy machine (a Surface Permanent Magnet Synchronous Machine (SPMSM) $12s10p$, i.e. with 12 stators slots and 10 poles). Furthermore, the test rig aims at investigating circumferential effects and slotting modulation effect, and discussing on the necessity or not to include them in the e-NVH study.

Chapter 1 deals with the main physical aspects and challenges in the comprehension of e-NVH generation in electrical machines, including the origins of electromagnetic excitations and their interaction with the structure, and the main low-noise design rules. The studied topologies are essentially radial flux machines used in automotive applications (Electric Vehicles (EVs)/Hybrid Electric Vehicles (HEVs)), including SCIMs, Interior Permanent Magnet Synchronous Machines (IPMSMs) and SPMSMs, in particular the SPMSM $12s10p$ prototype designed during this thesis.

Chapter 2 presents the main challenges in terms of e-NVH modeling and simulation, based on a state of the art on simulation workflow, and on the different electromagnetic and mechanical models used in e-NVH studies. The aim is to improve or develop new models that can be integrated in the design process of electrical machines. In particular, the electromagnetic semi-analytical SubDomain Method (SDM) is chosen to be developed during this thesis, and implemented in MANATEE in order to compute the airgap magnetic stress distribution in a large variety of electrical machines.

Chapter 3 deeply develops the SDM theory in both mathematical and physical aspects, based on the Analytical Resolution of Maxwell Equations (ARME) using functional analysis. The aim is to propose a framework dedicated to the subdomain modeling of a large variety of electrical machines, and extend the existing models in order to account for the main sources of electromagnetic excitations.

Chapter 4 proposes a methodology to build subdomain models from the theory developed in Chapter 3. One subdomain model of SPMSM assuming tooth finite permeability and one SCIM model are developed and integrated in MANATEE. The simulation results are validated with Finite-Element Analysis (FEA), and the relevancy of the SDM regarding other models for the fast and accurate prediction of noise and vibrations is further discussed.

Chapter 5 details the objectives and the design of SPMSM $12s10p$ prototype, which is a common topology used in EVs/HEVs, e.g. as electric pump (generally not as traction machine). The whole test rig including sensors is designed to illustrate and investigate the e-NVH open questions presented in Chapter 1. It also aims at benchmarking the different multi-physics simulation approaches presented in Chapter 2, including SDM, and publicly share experimental and benchmark results.

Chapter 1

Physical origins of e-NVH in electrical machines

Contents

1.1 Introduction

1.1.1 Outlines

The physical process of electromagnetic force generation in electrical machines can be illustrated based on a simple experiment detailed in Subsection 1.1.2. This experiment shows that there is a quadratic relationship between electromagnetic flux and force quantities in both time and spatial domains. In particular, a single rotating flux wave, or flux harmonic, generates a local force density per unit surface area called magnetic stress, which can be decomposed into a static stress and a rotating stress wave, or stress harmonic, at twice the frequency and wavenumber of the flux wave.

In the real case of electrical machines, the electromagnetic flux contains many harmonics from various origins, which combine themselves to create stress waves following the quadratic relationship. The main harmonic sources are detailed in Subsection 1.2, based on the literature and illustrated for the SPMSM prototype designed for the experimental test rig.

Then, the physical nature of the magnetic stress is discussed in Subsection 1.3. Stress harmonics are called Maxwell stress harmonics, and are concentrated at the interface between airgap and magnetic circuit. The quadratic relationship between flux and stress is extended to the real case of electrical machines.

As shown by the qualitative experiment in Subsection 1.1.2, the magnetic stress deforms the structure and may cause vibrations and airborne noise. Besides, a mechanical resonance effect may exist between magnetic stress and structural modes, which has not been illustrated by the qualitative experiment. Interaction between magnetic stress and structure including the resonance effect is further studied in Subsection 1.4. Then, the acoustic noise generation is briefly discussed in Subsection 1.5.

Finally, knowing the origins of Maxwell stress harmonics, reduction and cancellation techniques can be applied to damp or remove both excitation and structural response. Subsection 1.6 proposes a short state of the art about e-NVH reduction techniques in electrical machines, in order to include them in the e-NVH simulation workflow, and according to the fact that the test rig designed during this thesis also aims at illustrating the main noise mitigation techniques.

1.1.2 A simple experiment to illustrate the generation of electromagnetic excitations in electrical machines

The experiment developed in this subsection provides a qualitative illustration of the interaction between electromagnetic excitations generated by two rotating permanent magnets and a flexible steel tube. Magnets represent the rotor of an electrical machine and the steel tube represents a slotless stator. The experimental setup is described in Figure 1.1. The two permanent magnets, with a north pole in red and a south pole in blue, are mounted on a rotating shaft and put inside the flexible steel tube. The air volume between magnets and tube is called airgap. Shaft, magnets, airgap and steel tube constitutes the magnetic circuit of the experiment.

The two permanent magnets create a magnetic field which generates a magnetic flux in the magnetic circuit, as it is illustrated in Figure 1.2b. In magnetic circuits, magnetic field is to flux what voltage is to current in electric circuits. Furthermore, the reluctance property qualifies the magnetic circuit ability to resist or not to magnetic flux passage, similarly to resistance for current in electric circuits. Magnetic flux always follows the

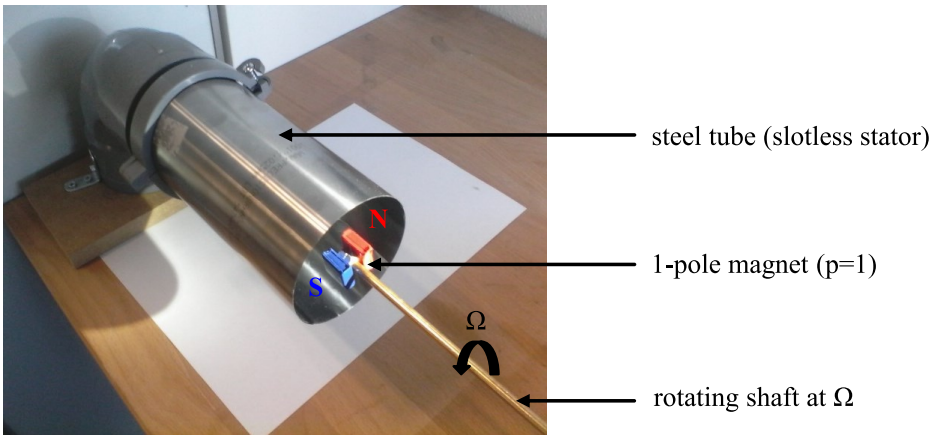

Figure 1.1 – Experimental setup to illustrate the interaction between electromagnetic field and ferromagnetic structure [Eomys Engineering, 2017].

path of least magnetic reluctance to minimize the energy required to travel.

The background color indicates the intensity of local magnetic flux density, which is maximum for yellow and minimum for blue, green being between yellow and blue. The black lines, called flux lines, indicate local flux density direction. Flux density is positive when it is oriented from south pole to north pole and negative otherwise. Flux lines are both along radial and circumferential direction in the airgap (see Appendix A.1 for radial and circumferential definitions). Besides, flux lines radially penetrate into the steel tube, and they circulate in the tube in the circumferential direction.

Even if some flux lines loop in the airgap, most of them are attracted and channeled inside the steel tube, and areas subject to the largest magnetic intensity (in yellow and green) are the permanent magnets and the steel tube. This channeling effect is due to the ferromagnetic properties of steel. Soft ferromagnetic materials concentrate external magnetic flux lines and therefore amplify their magnetic intensity, because their reluctance is far smaller than air reluctance. Soft ferromagnetic materials also adapt their polarity to the polarity of the external field source. As observed in Figure 1.2b, north and south magnets have respectively created a south pole and a north pole in the steel tube, so that magnetic flux circulates from south to north indeed.

This experiment aims at showing that the magnetic flux resulting from the two permanent magnets deflects the steel tube, as it can be seen in Figure 1.2a. Therefore, the magnetic flux creates magnetic excitations which are responsible for the tube deflection. In fact, magnetic poles with opposite polarities attract themselves, while magnetic poles with same polarities repulse themselves.

The deflection is almost only in radial direction, meaning that magnetic attraction and repulsion is also in the radial direction. Therefore, the local magnetic force, called magnetic stress and noted σ, is created by the radial flux which penetrate radially into the tube, and is concentrated at the interface between airgap and tube. When rotating the permanent magnets, tube polarity follows the magnetic excitation, so as the deflection shape. Furthermore, tube deflection is maximal where there are many flux lines entering in the tube.

If magnets are moving, both magnetic field and flux created by the magnets vary over time and space. Physically speaking, the two rotating magnets create an electromagnetic field wave **H** which propagates in the airgap over time and space. An electromagnetic

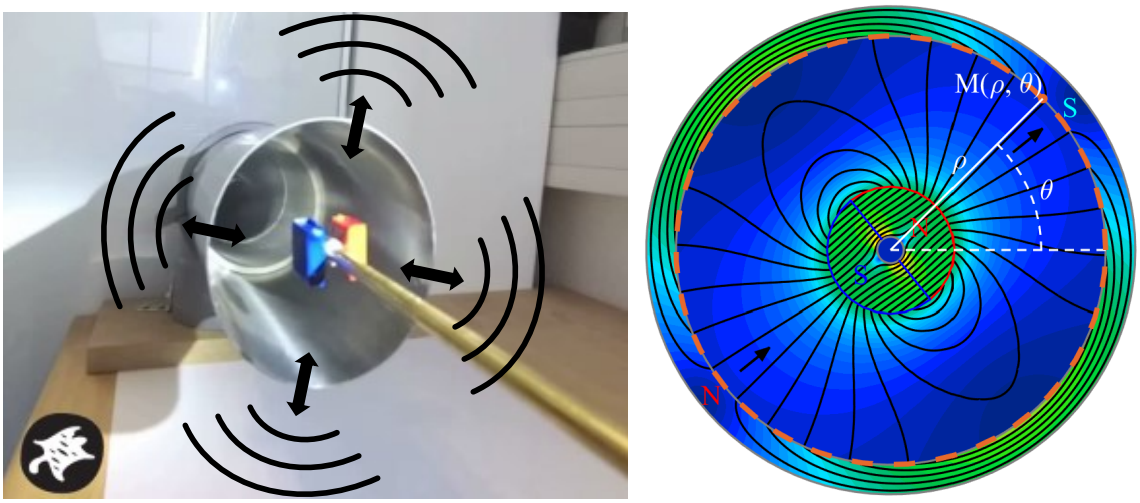

(a) Experimental deflection

(b) Simulated electromagnetic field

Figure 1.2 – Experimental illustration of deflection created by rotating magnetic field [Eomys Engineering, 2017].

wave is characterized by a time frequency f and a spatial wavenumber r, which indicates the number of maximums or minimums in the waveform, respectively in time and space domains. This field wave **H** generates a flux density wave **B** in the magnetic circuit at the electrical frequency f and wavenumber r.

In this experiment, the wavenumber of the generated wave is one ($r = 1$) because the spatial waveform has one maximum and one minimum along the airgap. The maximum is reached in front of the north magnetic pole and the minimum is reached in front of the south pole. In fact, a magnetic source of one pole pair ($p = 1$, one south and one north) naturally creates a wavenumber $r = 1$. Besides, the electrical frequency is $f = \Omega/2\pi$.

Then, it is interesting to compare the flux density waveform and the spatial deformation caused by this flux density. It is assumed that the steel tube mechanical behavior is linear, meaning that its deformation is proportional to the excitation which created it. In real machines, this assumption is verified in electrical machines where the displacement magnitude is barely visible as it does not exceed the micrometer scale.

Figure 1.2 shows that the stator spatial deformation has two minimums and two maximums. It means that the magnetic stress σ has also two minimums and two maximums, which is twice more than the waveform of the flux density generated by the two permanent magnets. This phenomenon is explained by the fact that each magnet creates an opposite pole in the slotless tube, as seen in Figure 1.2b. This is how the magnetic flux minimizes reluctance of its paths, by taking the shortest trajectory to cross the airgap (maximum reluctance) and loop in the steel tube (minimum reluctance). As opposite magnetic poles attract themselves, the magnetic stress is necessary maximal in front of each magnet and is minimal between each magnet. In other terms, the wavenumber of the stress wave is the number of magnetic poles $r' = 2p$, meaning twice the number of pole pairs which is the wavenumber of the field wave $r = p$. In fact, the radial stress σ_ρ is proportional to the square of the normal flux density B_ρ at the interface between airgap and steel tube:

$$\sigma_\rho \propto B_\rho^2 \tag{1.1}$$

This is a quadratic relationship which can be illustrated based on a simple mathe-

matical model. In terms of maths, the electromagnetic flux wave is represented by a sinusoidal function depending on time t and angle θ:

$$B_\rho(t,\theta) = B_1 \cos(\Omega t - \theta) \tag{1.2}$$

where B_1 is the flux density magnitude which depends on ρ. Physically speaking, B_ρ is a rotating flux density wave. In terms of maths, it is rather called a flux density harmonic over time and space. Therefore, the resulting stress σ_ρ generated by B_ρ at the interface between airgap and steel tube is written:

$$\sigma_\rho(t,\theta) \propto B_\rho^2(t,\theta) = B_1^2 \cos^2(\Omega t - \theta) \tag{1.3}$$

This stress wave can be decomposed into two distinct components using trigonometric transformation formula:

$$\sigma_\rho(t,\theta) = \sigma_0 + \sigma_2 \cos(2\Omega t - 2\theta) \tag{1.4}$$

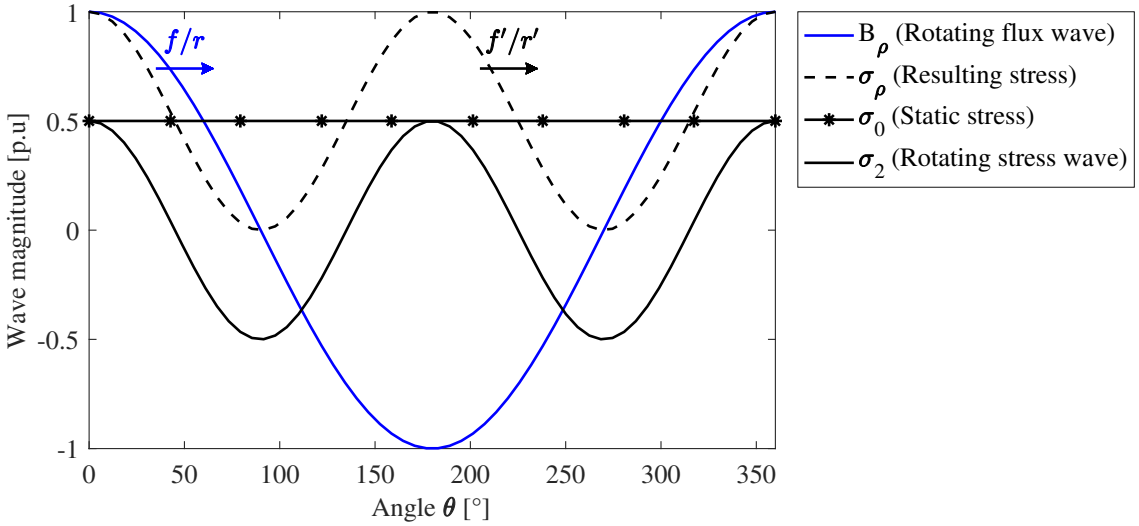

Figure 1.3 – Magnetic stress decomposition into two stress components (obtained from Equations (1.2)-(1.4)).

Therefore, the stress created by the electromagnetic wave is the sum of a static stress and a rotating stress wave. Flux density and stress components are represented in Figure 1.3. The rotating stress wave generated by the flux wave is illustrated in Figure 1.4.

This rotating stress wave, also called stress harmonic, is characterized by its frequency $f' = \Omega/\pi$ and its wavenumber $r' = 2r = 2$. The quadratic relationship was expected concerning flux and stress wavenumber but the mathematical model also shows that it concerns electrical frequencies. Flux and stress waves have therefore the same mechanical rotating speed:

$$\frac{f'}{r'} = \frac{2f}{2r} = \frac{f}{r} \tag{1.5}$$

The rotating stress harmonic, noted $(2f, 2)$, is responsible for the rotating deflection of the steel tube, which may generate radial vibrations waves in the air and radiate acoustic airborne noise. On the contrary, the static stress cannot produce noise and vibrations, as it does not transmit any motion to surrounding air particles.

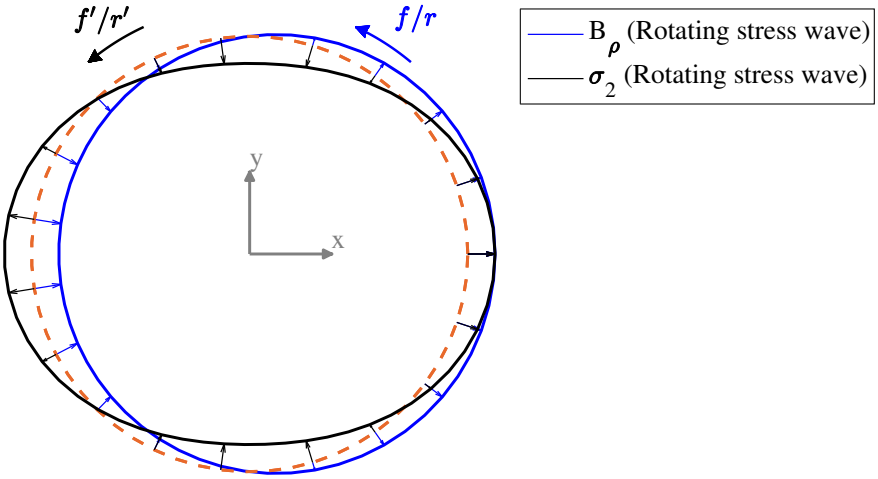

Figure 1.4 – Magnetic flux density and stress waves on the orange circle represented in Figure 1.2b (obtained from Equations (1.3)-(1.4)).

1.2 Origins of electromagnetic field harmonics

1.2.1 Torque generation principle

The presence of several electromagnetic fields inside electrical machines is linked to the basic principle of electromechanical conversion, which consists in using electromagnetic fields to create torque and rotating motion. Electromagnetic torque generation relies on two electromagnetic principles which have been already presented in the simple experiment 1.1.2. First, the attraction and repulsion property of stator and rotor magnetic poles results in the synchronous torque. Secondly, the fact that magnetic flux always follows the path of least reluctance generates reluctant torque.

Synchronous torque is obtained from the simultaneous attraction of stator and rotor opposite poles and repulsion of same polarities. Rotating motion is preserved if stator and rotor poles synchronously alternate between north and south poles, so that electromagnetic torque is always created. Therefore, synchronous torque generation requires the presence of both stator and rotor electromagnetic fields, as in Induction Machines (IMs), Permanent Magnet Synchronous Machines (PMSMs), Wound Rotor Synchronous Machines (WRSMs) and Direct Current Machines (DCMs). Certain topologies only work with synchronous torque, such as the SPMSM prototype represented in Figure 1.5.

Besides, reluctant torque generation does not require dual field machines. In topologies working on reluctant torque, such as Switched Reluctance Machines (SRMs) and Synchro-Reluctant Machines (SynRMs), only the stator is equipped with electromagnetic field. sources, i.e. windings. The ferromagnetic rotor is magnetized from the stator sources, on the same principle that steel tube is magnetized by the rotor permanent magnets in the simple experiment 1.1.2.

To create motion based on least reluctance principle, the rotor structure contains several air pockets (simple slots in SRMs, flux barriers in SynRMs) which periodically increase the magnetic circuit reluctance. Therefore, the stator flux crosses the airgap, loops in the rotor and crosses back to the stator where rotor reluctance is minimal. However, as the stator flux is rotating, the minimal flux path changes at every position, meaning that the rotor has no other choice but to mechanically follow the stator flux to ensure the

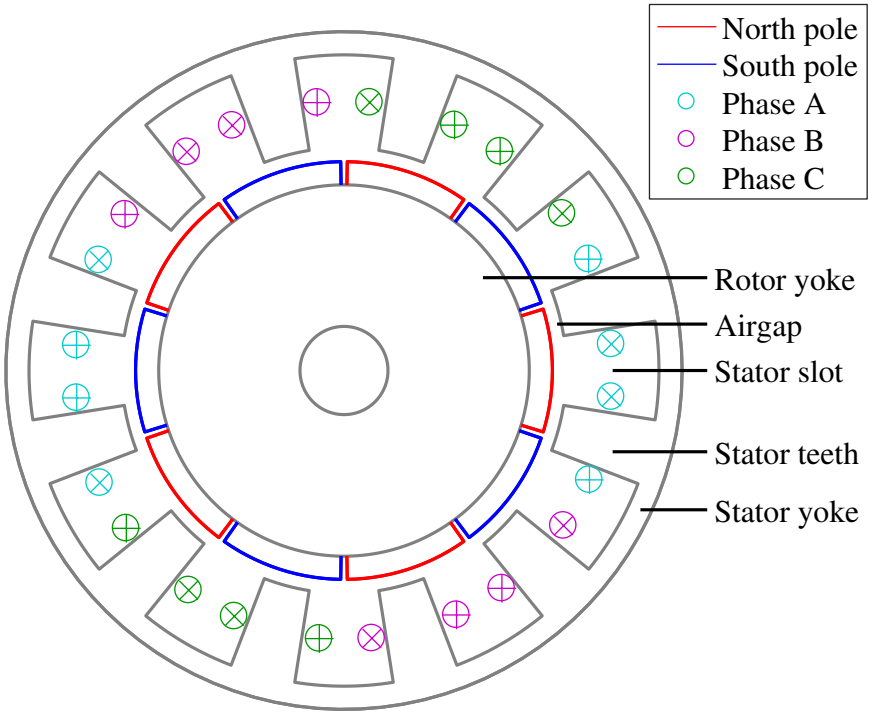

Figure 1.5 – Topology of machine prototype $12s10p$ with stator and rotor electromagnetic sources.

principle of least reluctance. In certain topologies such as IPMSMs and WRSMs, synchronous and reluctant torques both contribute to global torque generation.

Therefore, the main topologies studied in this thesis (SCIM, SPMSM, IPMSM, and WRSM) have rotor and stator field sources. In dual field machines, the overall electromagnetic field $\mathbf{H}$ can be written:

$$\mathbf{H} = \mathbf{H}_S + \mathbf{H}_R \tag{1.6}$$

where $\mathbf{H}_S$ and $\mathbf{H}_R$ are stator and rotor fields.

Stator and rotor rotating fields are illustrated on respectively Figure 1.6a and 1.6b for the machine prototype. On Figure 1.6a, the stator current distribution is indicated by the color inside the coils: red means maximum positive current value, blue means minimum negative, and white means zero. Both fields are synchronous and phase shifted of ninety electrical degrees, which enables to produce the maximum synchronous torque for a given current supply in SPMSMs. This phase angle between stator and rotor fields is called current angle and is noted ϕ_0, with $\phi_0 = (\mathbf{H}_R, \mathbf{H}_S)$.

However, field superposition may not guarantee the linear superposition of flux density $\mathbf{B}$ everywhere. Linear superposition is always true in paramagnetic materials such as air (a fortiori in the airgap), copper, aluminum, and in non-saturated ferromagnetic materials, such as:

$$\mathbf{B} = \mathbf{B}_S + \mathbf{B}_R \tag{1.7}$$

The relation between magnetic field and flux density becomes non-linear in case of magnetic saturation, and stator and rotor flux densities influence each other.

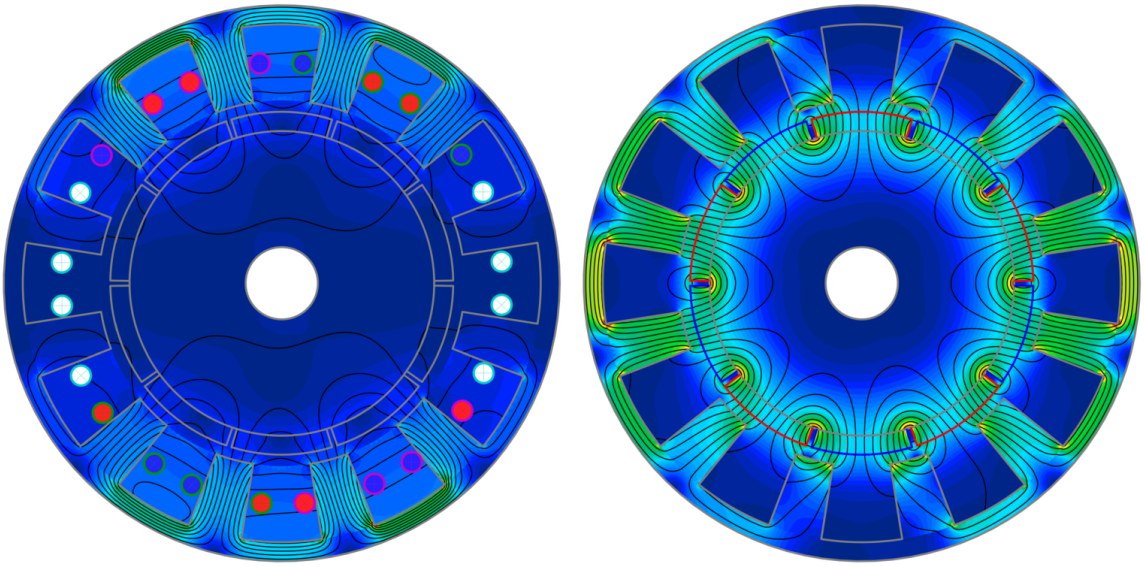

(a) Only stator source ($\phi_0 = 90°$) (b) Only rotor source

Figure 1.6 – Flux lines generated by stator and rotor electromagnetic sources over an electrical period, obtained with SDM [MANATEE, 2018].

In conclusion, the harmonic content of the electromagnetic field results from the superposition of rotor and stator harmonic contents. The contribution of stator and rotor fields depends on the operating torque, i.e. on the machine load state [Zhu et al., 2005; Pellerey et al., 2010; Valavi et al., 2015]. Rotor and stator field harmonics which have the same frequency and wavenumbers may add or subtract depending on their magnitude and phase. In other terms, load state modulates the harmonics magnitude of the global electromagnetic field **H**.

Load modulation effect is illustrated for machine prototype in Figure 1.7. It can be seen that field harmonics vary along the practical ϕ_0 range, which is here $[-90°;90°]$. In particular, field harmonics of wavenumbers $r = 5$ and $r = 7$ are strongly influenced by synchronous torque production.

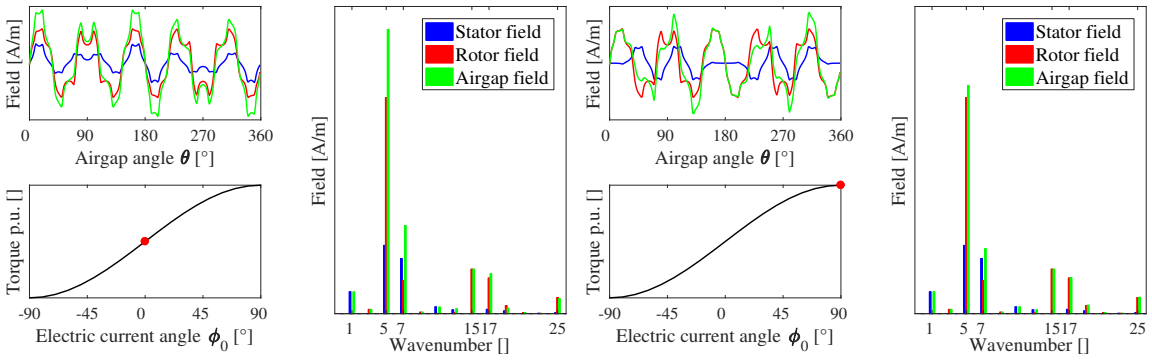

(a) Current angle $\phi_0 = 0°$ (b) Current angle $\phi_0 = 90°$

Figure 1.7 – Interaction of stator and rotor fields in function of current angle ϕ_0 for SPMSM $12s10p$ (obtained with SDM [MANATEE, 2018]).

1.2.2 Review of harmonic sources in electromagnetic field

Time and space harmonic content of electromagnetic field mainly depends on the technology used to generate stator and rotor variable fields. At the stator side, field is generally created by multiphase windings fed by Alternating Current (AC) in Synchronous Machines (SMs) and IMs, and by Direct Current (DC) in DCMs. In case of dual field machine, the rotor field is created by:

— permanent magnets in PMSMs and BrushLess Direct Current (BLDC) Machines;

— DC windings in WRSMs and DCMs;

— AC windings in IMs;

In the present SPMSM example, the stator winding is a three-phase all teeth wound concentrated winding commonly used in PMSMs. The stator winding is distributed in the twelve slots of the stator lamination, which is made of electrical steel. The permanent magnets are tile shaped, diametrically magnetized, and glued on the rotor surface. The rotor is a plain steel cylinder. A twelve stator slots and ten poles SPMSM is generally noted SPMSM $12s10p$. The harmonic content of another PMSM $12s10p$ is given in Dajaku and Gerling [2009]; Zou et al. [2017].

There are many references providing field harmonics sources existing in healthy and faulty SM and IM [Le Besnerais et al., 2013a,b; Hannon et al., 2016]. The first origin of time and space harmonics in the electromagnetic field generally comes from the non-sinusoidal distribution of windings and permanents magnets in the airgap. These harmonics are commonly called MagnetoMotive Force (MMF) harmonics. Their frequency and wavenumber depend on topology parameters: number of pole pairs p, number of phases q, number of stator and rotor slots Z_s and Z_r, etc.

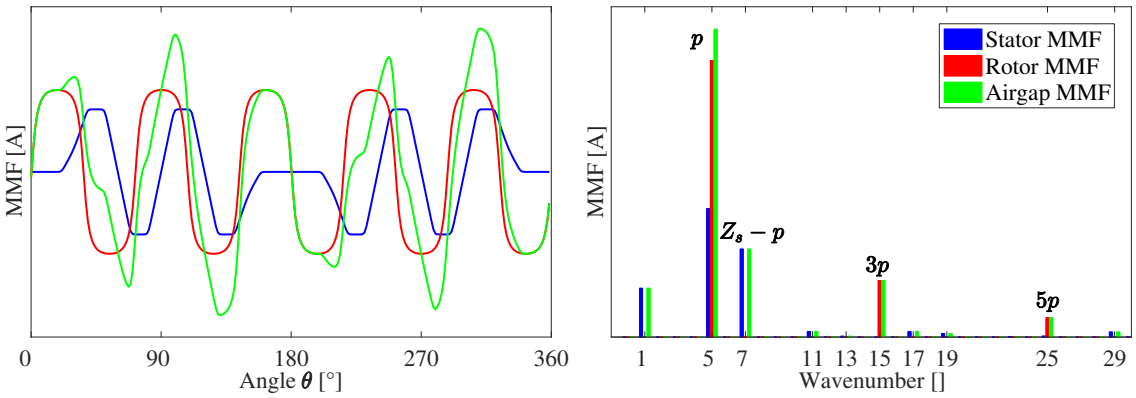

(a) Stator and rotor MMF waveforms

(b) Spatial harmonic content of MMFs waveforms

Figure 1.8 – Harmonic content due to stator and rotor MMFs for SPMSM $12s10p$ (obtained with SDM [MANATEE, 2018]).

Stator and rotor MagnetoMotive Forces (MMFs) waveforms and harmonic content are illustrated in Figure 1.8a for the case of machine prototype. The fundamental flux density wave is at $r = p = 5$ and is both generated by stator and rotor MMFs. The fundamental magnitude is not the algebraic sum of the stator and rotor contribution because of phase interference due to load state. As said before, stator and rotor fields are phase shifted of ninety electrical degrees. Furthermore, it can be seen in Figure 1.6a that stator MMF harmonics do not rotate necessarily in the same directions. For example, stator MMF harmonics of wavenumber $r = 1$, existing in the stator MMF harmonic content in

Figure 1.8b, rotates in the opposite direction of the stator fundamental at $r = p = 5$. On the contrary, rotor MMF harmonics rotate all together in the same direction.

Besides, windings and magnets are often placed in stator and rotor slots, between stator and rotor teeth. These slots modify the electromagnetic field lines in the airgap as the field is channeled by the teeth, which are ferromagnetic. These harmonics are usually called slotting harmonics or permeance harmonics. They also depend on the main topology parameters.

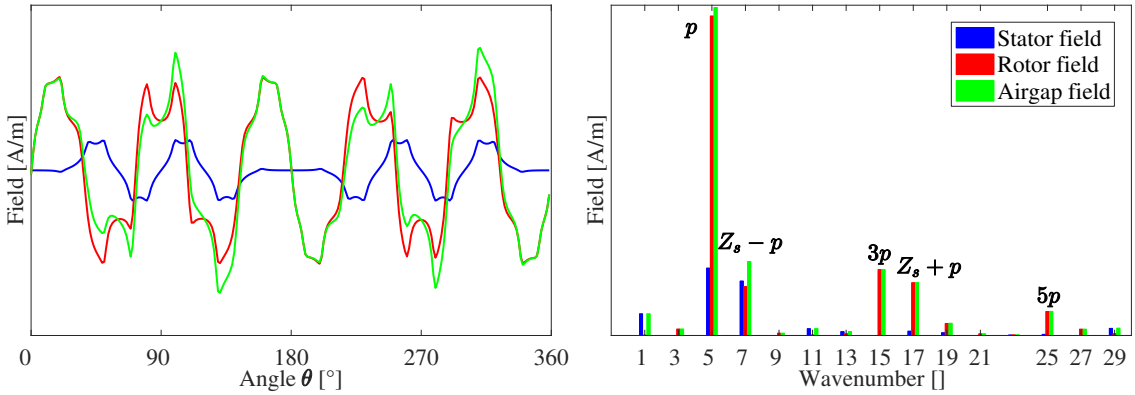

(a) Stator and rotor field waveforms

(b) Spatial harmonic content of magnetic field

Figure 1.9 – Field harmonic content due to stator and rotor MMFs and slotting effect for SPMSM $12s10p$ (obtained with SDM [MANATEE, 2018]).

Slotting modulation effect is shown in Figure 1.9a for the machine prototype. In front of a stator slot, the flux density created by permanent magnets significantly decreases. Compared with Figure 1.8b, two rotor fields components have appeared at $r = 7 = Z_s - p$ and $r = 17 = Z_s + p$. These new harmonics are due to the modulation of rotor MMF fundamental at $r = p$ with the first stator permeance harmonic at $r = Z_s$.

Power supply introduces rotor and stator current time harmonics in rotor and stator MMFs. For example, it includes switching harmonics due to power electronics, such as Pulse Width Modulation (PWM) converter [Le Besnerais et al., 2010a], or current control hysteresis [dos Santos et al., 2014]. In particular, PWM harmonics can be at high frequencies, and influence the average stress which applies on the structure, called force ripple or pulsating force. Force ripple increase is illustrated in Figure 1.10 for different PWM strategies, compared to the case without PWM (i.e. the "resistive load" case in black).

The local saturation of ferromagnetic materials is an additional source of field harmonics [Le Besnerais et al., 2009b]. From the physical point of view, saturation can be seen as a fictitious airgap length variation which introduces saturation harmonics in the airgap magnetic field of induction machines [Nandi, 2004].

Fault and dysfunctions are also source of additional harmonic content. They include unbalanced magnetization, static and dynamic eccentricities [Frauman et al., 2007], faulty or broken conductor/phase [Roubache et al., 2016], etc., which introduce asymmetry in the field distribution. Faults also include any variations of airgap length due to manufacturing tolerances of stator/rotor laminations [Le Besnerais, 2015a] and magnets [Eklund and Eriksson, 2016]. These faults modulate the existing harmonics or generate new harmonics in the electromagnetic field.

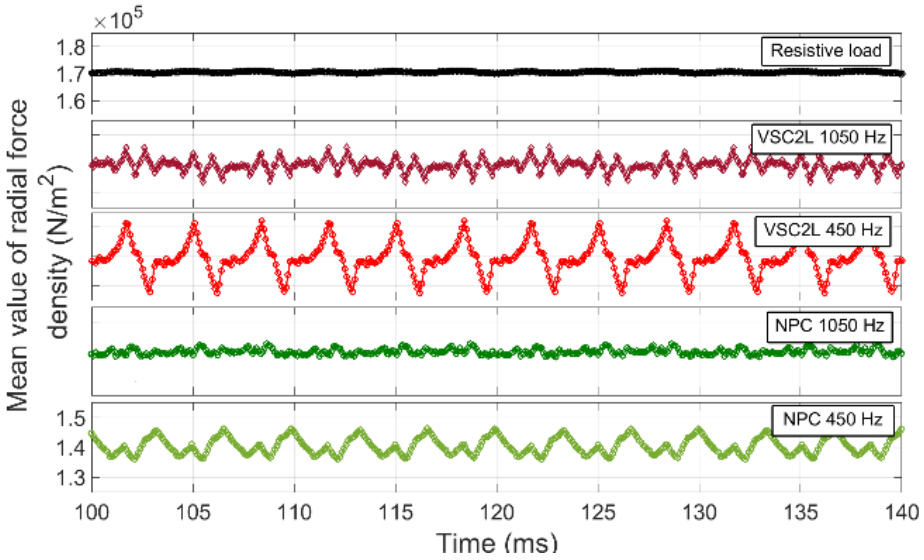

Figure 1.10 – Effect of PWM on force ripple for different PWM strategies for a low-speed generator (from Valavi et al. [2018])

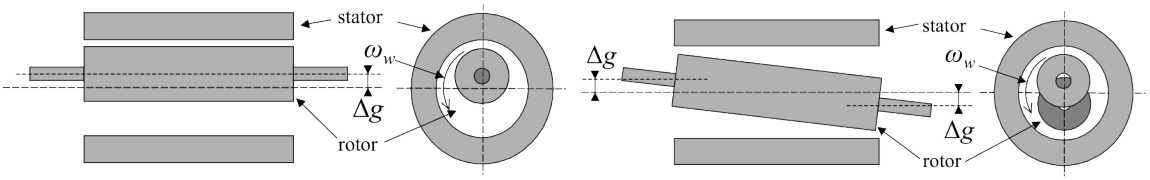

(a) Cylindrical whirling motion

(b) Conical whirling motion

Figure 1.11 – Static and dynamic 3D eccentricities of rotor motions (from Tenhunen [2003])

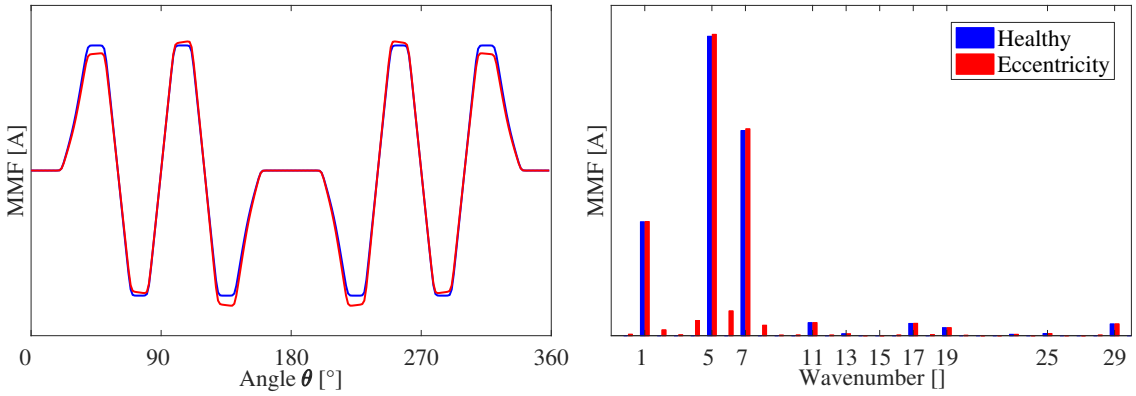

(a) Stator MMF with and without eccentricity

(b) Spatial harmonic content

Figure 1.12 – Harmonic content modulation of stator MMF due to rotor dynamic eccentricity (10%) for SPMSM $12s10p$ (obtained with SDM [MANATEE, 2018]).

Moreover, rotor slotting and rotor MMF harmonics induce new frequency content in the stator currents [Joksimovic et al., 2011; Lin et al., 2016]. Any asymmetries or airgap length variations presented above also create new harmonics in the stator current [Riley et al., 1999; Nandi et al., 2005]. Therefore, vibrations due to these induced stator current harmonics are generally investigated to develop condition monitoring and fault diagnosis of electrical machines [Riley et al., 1999; Nandi et al., 2005]. These new current harmonics create new field harmonics in opposition to the phenomena which created them (from Lenz's law). Accounting for this secondary induction phenomenon requires a strong coupling between electrical and electromagnetic module [dos Santos et al., 2014].

Besides, aliasing effect is potentially responsible for new harmonic content in stator and rotor induced currents, if the number of rotor and stator slots is lower than twice the airgap field wavenumber. Aliasing appears for example in the rotor induced current spectrum of SCIMs if the number of rotor bars is lesser than twice the wavenumber of the field [Guldemir, 1999]. Aliasing effect also depends on winding architecture.

Finally, 3D effects including skewing [Blum et al., 2014], end-effects (e.g. due to end-windings), axial eccentricities (conical/whirling motion) [Dorrell, 2011] are source of new field harmonics in the axial direction and causes a variation of radial and circumferential electromagnetic fields, meaning new wavenumbers in axial direction (see Subsection 1.3.2). 3D eccentricities are illustrated in Figure 1.11.

In conclusion, all of these field harmonics can potentially combine themselves and create parasitic magnetic stress harmonics which apply on machine structure.

1.3 Nature of electromagnetic excitations in electrical machines

1.3.1 Predominance of Maxwell stress

Except in electrostatic machines, electromagnetic excitations in electrical machines are mostly due to magnetic field and not to electric field. In fact, electric field can be neglected compared to magnetic field, as there are no electrostatic sources and no voltage gradient except in the conductors. Consequently, electric excitations are not considered and only magnetic ones are studied.

These magnetic excitations can have different natures which coexist in the machine. As seen in the simple experiment (Subsection 1.1.2), the electromagnetic field generates stress waves applying on the magnetic circuit surface, which then create a structural deflection. This stress is called Maxwell stress and is mostly concentrated at the interface between air and ferromagnetic parts. Maxwell stress deforms the magnetic circuit to globally minimize the airgap length and decrease the airgap reluctance.

Besides, the electromagnetic field may directly create a structural deflection due to material properties of ferromagnetic parts. This phenomenon, named magnetostriction, creates local stress inside machine structure, which is called magnetostrictive stress [Melkebeek et al., 2007].

Finally, Lorentz forces, also called Laplace forces, apply on an electric conductor fed by a current and plunged in an external magnetic flux density. They are usually distin-

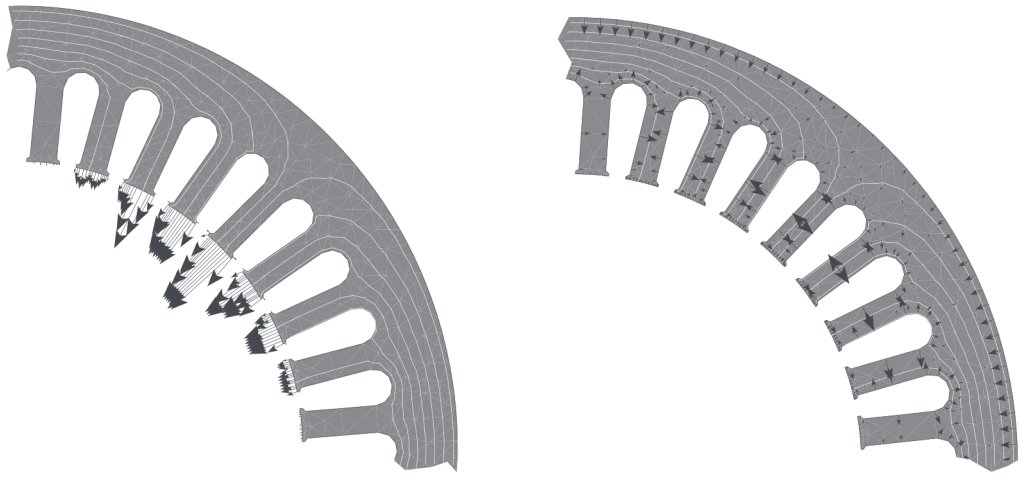

(a) Maxwell forces (b) Magnetostrictive forces

Figure 1.13 – Maxwell versus magnetostrictive forces distribution from Melkebeek et al. [2007]

guished from Maxwell and magnetostrictive stress but they are in fact included in the formulation of Maxwell stress [Bekemans, 2006]. As a consequence, only Maxwell and magnetostrictive stress are considered in slotted machines. Their contribution to noise and vibrations remains uncertain. The magnetic stress distribution in a slotted stator is illustrated in Figure 1.13 for both cases. Magnetostriction deforms the structure similarly to Maxwell stress and therefore both always interfere in electrical machines. Melkebeek et al. [2007]; Kuroishi and Saito [2018] show that magnetostriction and Maxwell stress excite the same structural modes of the machine. Depending on the topology, they can add up or subtract regarding their phase [Shahaj and Garvey, 2011]. In Wu et al. [2018], magnetostriction contribution is responsible for 8% of the vibration level.

In fact, both phenomena are quadratic effects of the magnetic field and therefore happens at the same frequencies [Låftman, 1998]. Magnetostriction contribution is more important at $2f_s$, meaning twice the fundamental electric frequency of stator currents f_s. However, most of the studies consider that Maxwell stress excitations are preponderant in electrical machines due to the airgap presence, which concentrates the electromagnetic energy. From EOMYS experience on more than fifty studied machines, magnetostriction has never been the root cause of electric machine e-NVH issues.

1.3.2 Characterization of Maxwell stress harmonics

In the simple experiment 1.1.2, the electromagnetic field propagating in the airgap is restricted to radial and circumferential directions. However, even in radial flux machines, it may also propagate in the axial direction, due to 3D effects presented in Subsection 1.2.2. Therefore, the 3D electromagnetic field creates Maxwell stress in the three directions. Beside radial stress, circumferential and axial stresses also apply on the electrical machine structure and may influence noise and vibrations [Garvey and Le Flem, 1999]. This interaction is further explained in Subsection 1.4.

In classical references, Maxwell stress is generally estimated on a cylindrical surface inside the airgap, or on a circular path inside the airgap if the stress is assumed to be invariant in the axial direction [Timar, 1989; Gieras et al., 2006]. Computation of Maxwell stress applying on the structure is detailed in Subsection 2.4.1. The 3D magnetic stress distribution in the airgap no longer depends on the radial variable ρ, since the radius is necessary the one of the airgap cylindrical surface chosen for the computation. There-

fore, the three stress components only depend on time t, circumferential θ and axial z variables. Mathematically speaking, the 3D airgap stress distribution is formulated as a 3D vector, such as:

$$\sigma(t,\theta,z) = \sigma_\rho \mathbf{e}_\rho + \sigma_\theta \mathbf{e}_\theta + \sigma_z \mathbf{e}_z \tag{1.8}$$

Radial and circumferential stress distributions σ_ρ are illustrated for SPMSM $12s10p$ in Figure 1.14, due to the interaction of stator and rotor fields shifted of ninety degrees. The airgap cylinder on which magnetic stress is computed is represented in black dotted lines. It can be seen that the average stress, i.e. the resultant force, is oriented towards machine center. It means that Maxwell stress attracts the stator structure and globally tends to reduce airgap length, as it was the case in the simple experiment 1.1.2. In Figure 1.14, the Maxwell stress distribution is invariant over axial direction because there is no skew and end-effects are neglected.

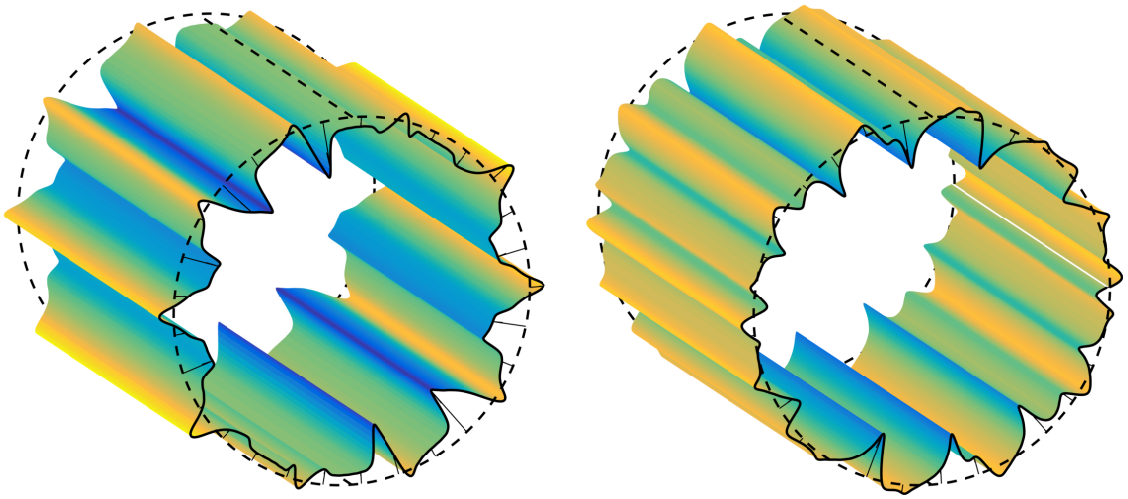

(a) Radial stress (b) Circumferential stress

Figure 1.14 – 3D stress distributions for SPMSM $12s10p$ (obtained with SDM and MST computed in the middle of the airgap [MANATEE, 2018]).

The 3D airgap stress distribution is decomposed into a sum of stress harmonics as it has been done in the simple experiment. Harmonic decomposition is obtained from 3D Fourier expansion [Meessen, 2012]. In reality, magnetic stress distribution is not periodic in axial direction, hence it is symmetrized at $z = \mathrm{L}_s$ so that magnetic stress becomes $2\mathrm{L}_\mathrm{S}$-periodic, i.e. twice the machine axial length L_S. The 3D airgap stress distribution is then a linear superposition of stress harmonics propagating in radial, circumferential and axial directions. These stress waves, or stress harmonics, are characterized by the frequency and wavenumber terminology introduced in the simple experiment 1.1.2. In electrical machines, the frequency is generally linked to the stator current supply frequency f_s. Therefore, the frequency order k is introduced such as $f = kf_s$. Values taken by k depend on the machine type and power supply [Alger, 1953; Timar, 1989]. A stress wave of triplet (k,r,l) can be modeled by the following sinusoidal function:

$$\sigma_x(t,\theta,z) = \sigma_x^{krl} \cos\left(2\pi k f_s t - r\theta + \pi l \frac{z}{\mathrm{L}_s} + \phi_x^{krl}\right)\mathbf{e}_x \tag{1.9}$$

where $x \in \{\rho;\theta;z\}$, r is the circumferential wavenumber, l is the axial wavenumber, L_S is the stator axial length, and σ_x^{krl} and ϕ_x^{krl} are the magnitude and phase angle of the stress harmonic along direction x.

Examples of radial, circumferential and axial stress waves are illustrated in Figure 1.15 for several triplets (k,r,l). It is worth mentioning that the three stress components contain the same frequencies and wavenumbers [Le Besnerais, 2015b; Zou et al., 2017]. Besides, particular triplet values are usually distinguished in e-NVH studies.

First, the circumferential force of triplet $(k=0,r=0,l=0)$, meaning the constant and uniform circumferential stress applying on the structure, is proportional to the electromagnetic torque. Radial stress waves with triplet $(k=0,r,l)$ are steady components which constantly stress the structure. These harmonics do not cause vibrations or airborne noise. However, this pre-stress may have an effect on modal behavior since it has for example an influence on Young elastic modulus [Millithaler, 2013].

Stress harmonics $(k,r=0,l=0)$, with zero circumferential wavenumber, are standing waves which are uniform along the airgap, and are therefore called pulsating harmonics. Pulsating harmonics of circumferential force are proportional to torque ripple. By extension, radial force ripple stands for harmonic of radial stress with triplet $(k,r=0,l=0)$. Torque and radial force ripples are often referred as global forces [Zou et al., 2017].

Radial stress harmonics with wavenumber $(k,r=1,l=0)$ are called Unbalanced Magnetic Pull (UMP) [Wu et al., 2010]. They are due to circumferential asymmetries in the airgap, such as asymmetric windings, eccentricity, uneven magnetization etc.

Axial stress harmonics with wavenumber $(k,r=0,l=0)$ and $(k,r=0,l=1)$ are called Unbalanced Magnetic Force (UMF) [Kim et al., 2012]. They result from axial asymmetries in the airgap, also due to eccentricity, uneven magnetization, skewing [Dorrell, 2011; Kang et al., 2017] etc.

Finally, the other stress harmonics with triplet $(k\neq 0,r\neq 0,l)$ are referred as rotating waves.

1.3.3 Physical origins of Maxwell stress harmonics

Previous Subsections 1.3.1 and 1.3.2 have shown that electromagnetic excitations are Maxwell stress harmonics mainly located at the interface between airgap and ferromagnetic parts. These Maxwell stress harmonics are rotating stress waves described by their frequency order, and spatial and axial wavenumbers (k,r,l). Besides, it has been shown in the simple experiment 1.1.2 that stress harmonics are quadratically dependent on field harmonics. Finally, the airgap electromagnetic field can be decomposed into the superposition of a stator and a rotor field (cf. Subsection 1.2.1).

The quadratic relationship developed in the simple experiment 1.1.2 for a single field wave interacting with itself can be extended to the general case of a stress harmonic created by the interaction of two distinct field harmonics, hence results either from the interaction of two stator flux harmonics, or two rotor flux harmonics, or one of each [Zhu, 1991]:

$$\sigma \propto \mathrm{B}_1\mathrm{B}_2\cos\left(2\pi k_1 f_s t - r_1\theta + \pi l_1\frac{z}{\mathrm{L}_s} + \phi_1\right)\cos\left(2\pi k_2 f_s t - r_2\theta + \pi l_2\frac{z}{\mathrm{L}_s} + \phi_2\right) \tag{1.10}$$

where $\mathrm{B}_1 = \mathrm{B}_{\mathrm{X}_1}^{k_1 r_1 l_1}$, $\mathrm{B}_2 = \mathrm{B}_{\mathrm{X}_2}^{k_2 r_2 l_2}$, $\phi_1 = \phi_{\mathrm{X}_1}^{k_1 r_1 l_1}$, $\phi_2 = \phi_{\mathrm{X}_2}^{k_2 r_2 l_2}$, with $(\mathrm{X}_1,\mathrm{X}_2) \in \{(\mathrm{S},\mathrm{S});\ (\mathrm{S},\mathrm{R});$

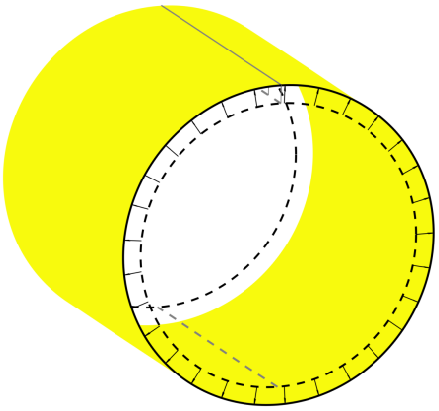

(a) Radial stress wave $(1,0,0)$

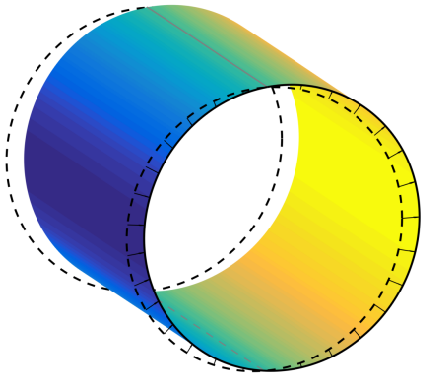

(b) Radial stress wave $(1,1,0)$

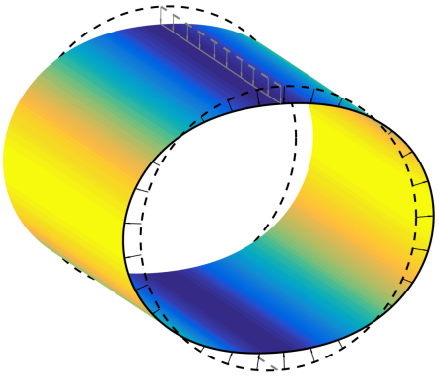

(c) Radial stress wave $(1,2,0)$

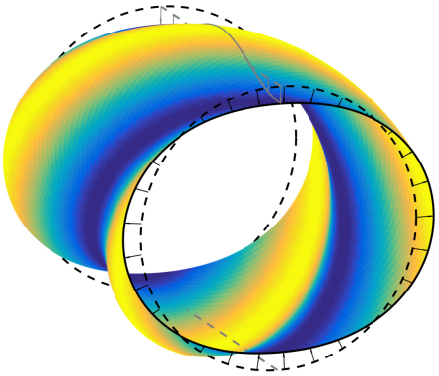

(d) Radial stress wave $(1,2,1)$

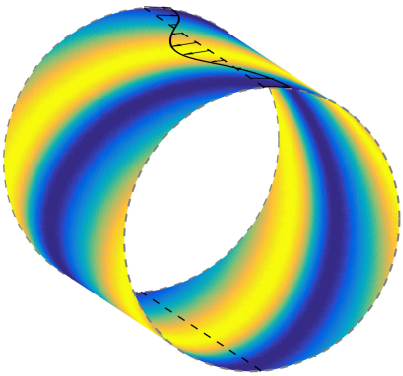

(e) Circumferential stress wave $(1,2,1)$

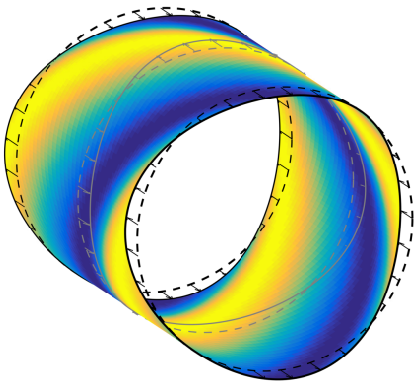

(f) Axial stress wave $(1,2,1)$

Figure 1.15 – Rotating stress wave waves in the airgap for different triplets (k,r,l) (obtained from Equation (1.9)).

(R,R); (R,S)}.

From trigonometric transformation formula, Equation (1.10) yields:

$$\sigma \propto \frac{B_1 B_2}{2}\Big[\cos\big(2\pi(k_1-k_2)f_s t-(r_1-r_2)\theta+\pi(l_1-l_2)\frac{z}{L_s}+\phi_1-\phi_2\big) + \cos\big(2\pi(k_1+k_2)f_s t-(r_1+r_2)\theta+\pi(l_1+l_2)\frac{z}{L_s}+\phi_1+\phi_2\big)\Big] \tag{1.11}$$

Equation (1.11) represents the quadratic relationship between harmonic contents of airgap field and stress. It shows that each couple of field harmonics generates two stress harmonics of frequency $k_1 f_s \pm k_2 f_s$ and wavenumbers $r_1 \pm r_2$, $l_1 \pm l_2$.

Therefore, the operator $\star$ is introduced to shorten the quadratic relationship (1.11) [Le Besnerais et al., 2013a,b]:

$$\sigma(k_1 \pm k_2, r_1 \pm r_2, l_1 \pm l_2) = B_1(k_1, r_1, l_1) \star B_2(k_2, r_2, l_2) \tag{1.12}$$

In conclusion, the quadratic relationship enables to predict which stress harmonics are created given a set of field harmonics, e.g. due to MMF, slotting, PWM, eccentricities, etc. In particular, pulsating forces (with $r = 0$) are obtained from two rotating field waves with different frequencies and opposite wavenumbers. Rotating stress harmonics with low wavenumbers result from two rotating fields with close wavenumbers [Yang, 1981; Gieras et al., 2006].

Furthermore, the quadratic relationship (1.12) can be inversed by using the convolution approach [Rothe et al., 2010]. This approach enables to compute every couple of field waves from which a specific stress harmonic originates. It is consequently a powerful tool to diagnose the harmonic content of Maxwell stress distribution and determine the physical origins of each stress harmonic [La Delfa et al., 2016]. The convolution approach available in MANATEE software is detailed in Appendix A.9, and is illustrated in Chapter 5 for the SPMSM $12s10p$ design.

1.4 Interaction between Maxwell stress and structure

1.4.1 Contribution of radial, circumferential, and axial stress harmonics

The interaction between the Maxwell stress harmonics and the structure has been studied since the early 50's and the work of Alger [1953] on the noise and vibrations of IM. Radial, circumferential and axial stress harmonics have different NVH generation paths which are detailed in this subsection.

In electrical machines, radial vibrations of the external structure (e.g. the stator and frame for internal rotor topologies) are most likely to radiate airborne noise [Alger, 1953]. In the simple experiment 1.1.2, these radial vibrations are created by a radial stress harmonic of circumferential wavenumber $r = 2$. In real electrical machines, radial stress harmonics generate a radial deflection of structure teeth and thus of the external yoke. In classical references [Alger, 1953; Timar, 1989; Gieras et al., 2006], only radial stress harmonics are considered as potential source of noise and vibrations. In fact, the circumferential field is neglected in the radial stress computation, and the contribution of

circumferential stress on radial vibrations is neglected, compared to the contribution of radial stress [Zhu, 1991]. This modeling assumptions enables to simplify the magnetic computation, since only the radial flux is required, but is not accurate for all topologies electrical machines.

In fact, circumferential stress harmonics applied on a cylindrical structure generate radial yoke deflection, which might be emphasized due to tooth bending motion (or tooth rocking), especially in machines with large tooth height to yoke thickness ratio [Garvey and Le Flem, 1999]. Therefore, circumferential stress contribution on radial vibration level should not be neglected in synchronous machines [Garvey and Le Flem, 1999; Boesing, 2013]. Circumferential stress represented at tooth tips is actually the normal stress applying on tooth sides. Radial yoke deflection due to tooth bending from a circumferential stress harmonic of wavenumber $r = 2$ is illustrated in Figure 1.16.

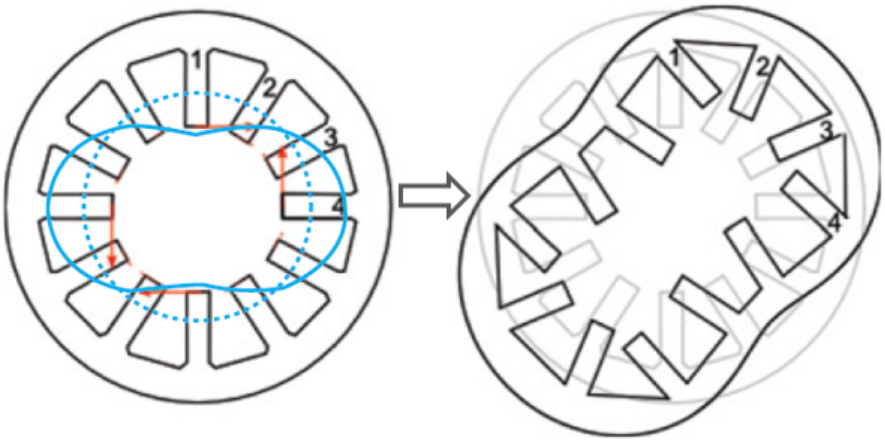

Figure 1.16 – Radial yoke deflection generated by circumferential forces of wavenumber $r = 2$ in SPMSM $12s10p$ (from Le Besnerais et al. [2013b])

The contribution of circumferential stress to radial vibrations in slotted structure is still actively investigated. In Boesing [2013]; Roivainen [2009]; Le Besnerais [2015b], circumferential stress harmonics do not create new frequency content but they interact with radial stress harmonics which have the same triplet (k, r, l). In conclusion, they modulate radial vibrations depending on their phase and may have an influence on the emitted noise level.

As illustrated in Figure 1.17, torque ripple (and also cogging torque in PMSMs), which originates from rotor circumferential vibrations, is also source of structure-borne noise [Gieras et al., 2006; Yoshida et al., 1998; De Madinabeitia, 2016]. Rotor vibrations may also propagate to the machine external structure through the bearings, and create mechanical noise in gears [Humbert et al., 2012]. In case of asymmetrical mounting with low stiffness, torque ripple may result in remarkable lateral motion able to radiate acoustic noise [Zou et al., 2017].

Finally, axial UMFs can apply on rotor and stator structures, hence create vibrations and structure-borne noise in bearings and end-shields [Kang et al., 2017].

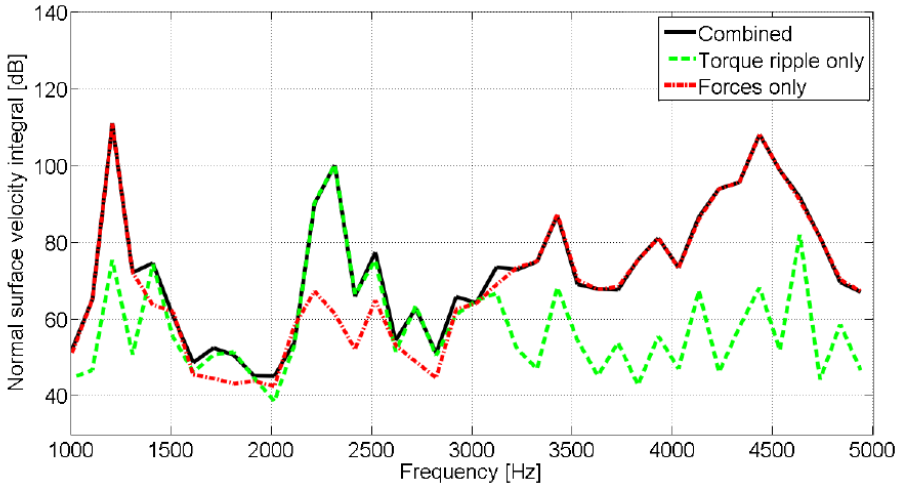

Figure 1.17 – Contributions of Maxwell stress harmonics and torque ripple to the stator vibrations of a loaded SCIM (from De Madinabeitia [2016])

1.4.2 Forced and resonant responses

Therefore, radial and circumferential excitations generate radial deflection and vibrations of the external structure. As shown in the simple experiment 1.1.2 in Figure 1.2a, the mechanical response follows the Maxwell stress excitation in terms of frequency and wavenumber, according to the structural linear properties regarding small displacements. In this case, the mechanical response is called forced response. The forced response is sometimes responsible for the major part of noise and vibrations level, especially in high-speed machines [Gilson et al., 2017].

In cylindrical structures, the deflection wave $\mathbf{u}$ of the external surface is a rotating wave having the same waveform as the exciting stress harmonic:

$$\mathbf{u}_x(t,\theta,z) = \mathrm{U}_x^{krl} \cos\left(2\pi k f_s t - r\theta + \pi l \frac{z}{\mathrm{L}_s} + \varphi_x^{krl}\right)\mathbf{e}_x \propto \sigma_x \tag{1.13}$$

where $x \in \{\rho;\theta;z\}$, $\mathrm{L_S}$ is the stator axial length, and φ_x^{krl} is the phase angle of deflection wave which may be different from the stress harmonic phase angle ϕ_x^{krl}. The mechanical behavior of slotted stator with a large number of teeth can be assimilated to a equivalent cylindrical structure, thus stator deflection has nearly the same shape as the excitation waveform. However, in case of slotted stator with few teeth, a stress harmonic of wavenumber $r = 2$ for example creates two deflection shapes of wavenumber $r = 2,4$ due to the presence of teeth [Braunisch et al., 2013]. Besides, deflection and excitation waveforms may also differ due to slotting modulation effect, as developed in Subsection 1.4.4.

Then, the vibration wave $\mathbf{v}$, also called velocity wave, is obtained by deriving the deflection $\mathbf{u}$ over time:

$$\mathbf{v}_x(t,\theta,z) = \frac{\partial \mathbf{u}_x}{\partial t} \tag{1.14}$$

Moreover, Maxwell stress harmonics can also excite structural modes of the electrical machine [Alger, 1953]. In this case, the stress harmonic resonates with the structure, and its mechanical response becomes resonant response as developed in the next Subsection 1.4.3.

1.4.3 Characterization of structural modes

The resonance between a structural mode and a stress harmonic strongly amplifies the noise and vibrations level caused by this stress harmonic, compared with forced response [Alger, 1953]. The set of structural modes is called modal basis. Structural modes of finite-length cylindrical shells can be characterized based on the following criteria:

— The direction of the modal shape: either radial, circumferential or axial direction.

— The triplet (f_{mn}, m, n), where f_{mn} is the natural frequency, m is the circumferential order and n is the axial order of the modal shape. Mode spatial order and stress harmonic wavenumber have different notations to prevent from any confusion between excitation and modal shape.

— The damping ratio ξ_{mn}, which quantifies energy dissipation. ξ_{mn} can only be obtained by Experimental Modal Analysis (EMA). In Yang [1981], damping ratio values are experimentally established between 1% and 4%, and set at 2% for SCIM studies in Timar [1989].

The modal basis strongly depends on the boundary conditions of the structure. The boundary conditions can be free (i.e. no constraint on displacement), clamped (i.e. no displacement) or simply supported (displacement is constrained only in one direction). Boundary conditions change the modal shape and the natural frequency of each mode [Soedel, 1993]. Mathematically speaking, the modal shape $\mathbf{d}$ associated to structural mode (f_{mn}, m, n) in free-free conditions is a standing wave:

$$\mathbf{d}_x(t,\theta,z) = \cos\left(2\pi f_{mn} t + \phi_f\right)\cos\left(m\theta + \phi_m\right)\cos\left(\pi n \frac{z}{\mathrm{L}_s} + \phi_n\right)\mathbf{e}_x \tag{1.15}$$

where $x \in \{\rho;\theta;z\}$, and ϕ_f, ϕ_m, ϕ_n are respectively the circumferential and axial phase angles, with $\phi_f = \phi_m = \phi_n = 0$ in free-free conditions. If the cylindrical structure is subject to other boundary conditions, the $z-$dependent term is no longer a cosine function and is called "beam function" [Lam and Loy, 1995].

Radial, circumferential and axial modal shapes are illustrated in Figure 1.18 for cylinders in free-free conditions. In e-NVH studies, the following modes are usually highlighted:

— Breathing mode for $(f_{00}, 0, 0)$ (Figure 1.18a).

— Bending mode for $(f_{10}, 1, 0)$ (Figure 1.18b).

— Ovalization mode for $(f_{20}, 2, 0)$ (Figure 1.18c).

Radial modes with non-zero axial wavenumber n are commonly called longitudinal modes [Zhu, 1991].

On Figure 1.18, the cylinder stands for the external surface which generates acoustic noise. Of course, the real structure is generally more complex than a cylinder, and a fortiori than the steel tube used in the simple experiment 1.1.2. In fact, the external structure is often composed of a slotted laminated stack containing electromagnetic sources (windings or magnets). To maintain these parts together, the structure is sometimes impregnated with resin and generally protected by a frame [Millithaler, 2013]. All of these parameters have a strong influence on natural frequencies and damping ratio [Millithaler, 2013]. Besides, new structural modes appear with the presence of teeth, such as tooth modes and coupled yoke/teeth modes. Finally, rotor and coupled stator/rotor modes can also be studied.

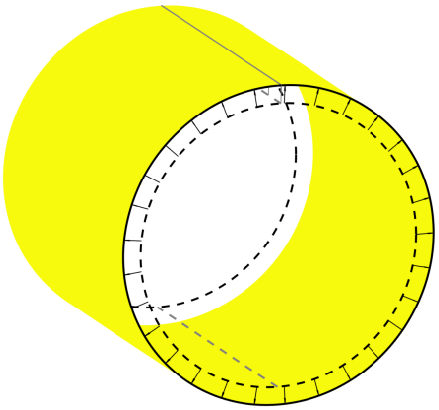

(a) Breathing mode ($f_{00}, 0, 0$)

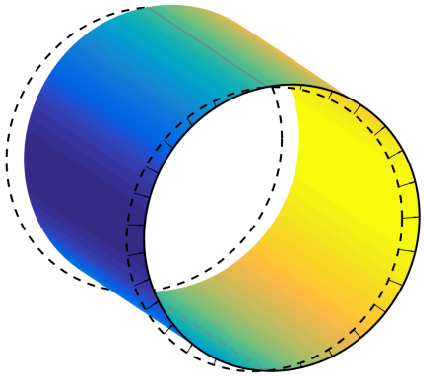

(b) Bending mode ($f_{10}, 1, 0$)

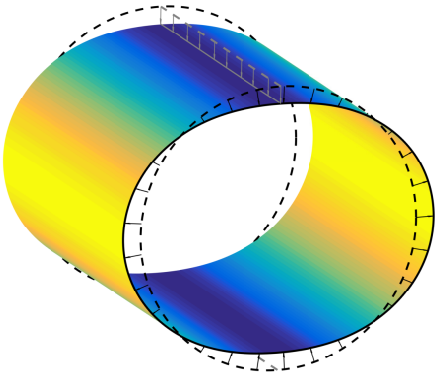

(c) Ovalization mode ($f_{20}, 2, 0$)

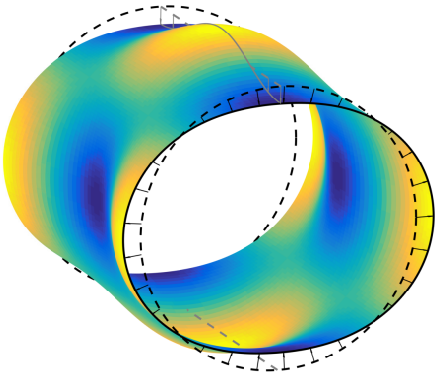

(d) Ovalization mode ($f_{21}, 2, 1$)

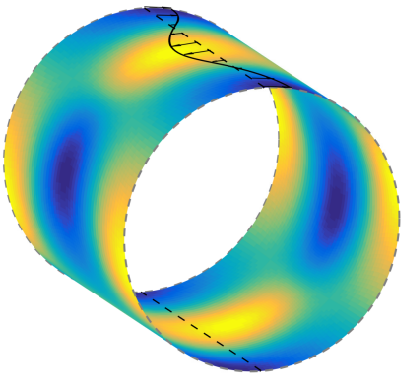

(e) Circumferential mode ($f_{21}, 2, 1$)

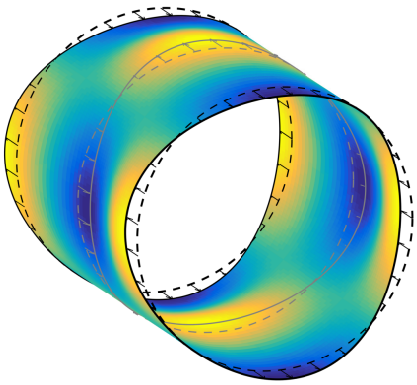

(f) Axial mode ($f_{21}, 2, 1$)

Figure 1.18 – Deflection shape of cylinder structural modes with free-free boundary conditions (obtained from Equation (1.15)).

1.4.4 Resonance condition in cylindrical structures

In vibroacoustic references based on a structural cyrlindrical modal of the stator structure [Jordan, 1950; Alger, 1953; Timar, 1989; Gieras et al., 2006], the resonance occurs if two conditions are fulfilled :

1. The rotating frequency kf of the stress harmonic is close to the natural frequency f_m of the cylindrical structural mode.
2. The circumferential wavenumber r of the stress harmonic is equal to the circumferential mode order m.
3. The stress harmonic magnitude is high enough.

meaning:

$$kf \approx f_m \quad \& \quad |r| = m \tag{1.16}$$

At resonance, the deflection shape $\mathbf{u}$ of the external structure should be a rotating wave following the stress harmonic excitation [Le Besnerais, 2008], as in Equation (1.13). However, due to the non-linear vibrational behavior of cylindrical structures [Amabili et al., 2016], the deflection shape $\mathbf{u}$ may also follow the modal shape given by Equation (1.15). The two possible deflection shapes due to the resonance of a stress harmonic at $(k,2,0)$ with the ovalization mode $(f_{20} = kf_s, 2, 0)$ are illustrated in Figure 1.19. In the NVH literature, this non-linear phenomenon is not clearly identified and little investigated.

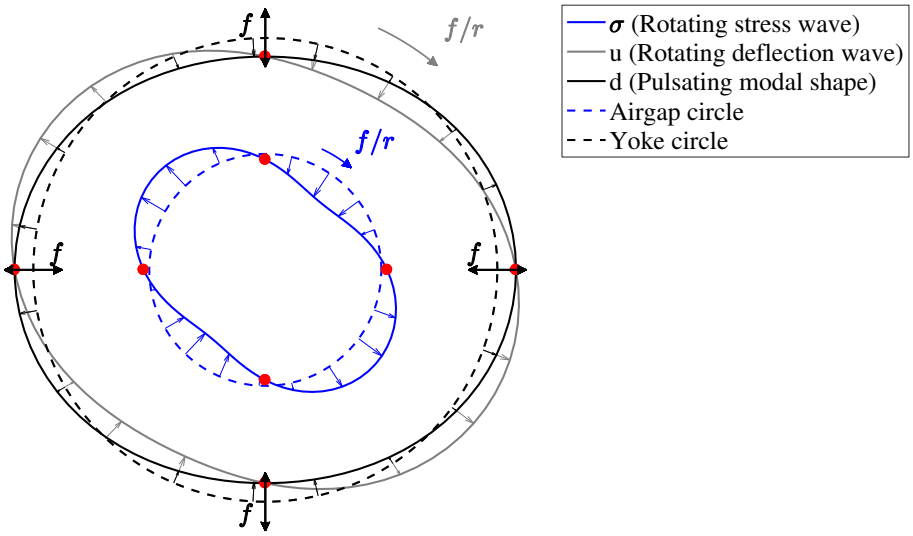

Figure 1.19 – Resonance between a stress harmonic of wavenumber $r = 2$ and ovalization mode (obtained from Equations (1.9), (1.13), (1.13), (1.15), and (1.16)).

Furthermore, the validity of resonance condition (1.16) in slotted structures can be questioned in presence of spatial aliasing, as recently investigated in Fang et al. [2018]. Teeth channel airgap flux density and Maxwell stress is concentrated at the interface between teeth and air. From a mathematical point of view, the stator teeth sample the airgap stress waves. Figure 1.20 illustrates the slotting modulation effect for the SPMSM $12s10p$ prototype. Two stress waves of wavenumber $r = -2$ (in purple, the minus sign is because this stress harmonic rotates in clockwise direction) and $r = 10$ (in blue) are seen by the slotted stator, which contains twelve teeth. The stress harmonic with $r =$

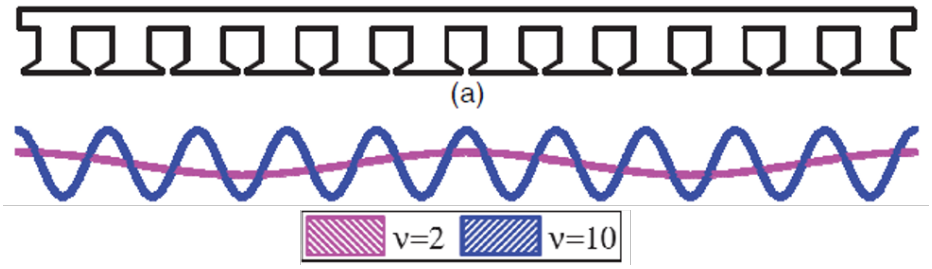

Figure 1.20 – Slotting modulation effect on stress harmonics of wavenumber $|r| \leq Z_s/2$ in PMSM $12s10p$ [Fang et al., 2018].

$10 = 2p$ is mainly created by the interaction of rotor and stator fundamental waves. The stress harmonic with $r = -2$ is mainly due to the first stator slotting harmonic at $Z_s - p$ interacting with rotor fundamental at p, meaning $r = Zs - 2p = 2$ for SPMSM $12s10p$ [Dajaku and Gerling, 2009].

From Shannon sampling theorem, spatial aliasing occurs when the circumferential wavenumber of the exciting harmonic is greater than half the number of teeth, i.e. $|r| \leq Z_s/2$. It means that a slotted structure can only see stress harmonics of circumferential wavenumber lesser than half the number of teeth. Furthermore, any harmonics whose wavenumber is higher than Shannon criteria is modulated by twice the maximum frequency, which is the stator tooth number in the present case. Aliasing effect appears for instance in PMSMs with close number of stator teeth and poles. Concerning SPMSM $12s10p$ topology, the stress harmonic with $r = -2$ excites the ovalization mode, from the classical resonance condition (1.16). However, the stress wave with $r = 10$ is modulated by the stator teeth and is seen from the stator structure as a stress wave of wavenumber $r = -2$ [Fang et al., 2018]. Therefore, the stress wave with $r = 10$ rather excites the ovalization mode than the radial mode of order $m = 10$.

In conclusion, the main consequence of slotting modulation effect is the ability to excite low mode orders by stress harmonics with high wavenumber, thus contradicting the resonance condition "$|r| = m$". In the new resonance condition, r is now the wavenumber seen by the slotted structure and not the wavenumber of the Maxwell stress harmonic.

1.4.5 Modal contribution in electrical machines

The excitation of radial modes is the most likely to generate noise and vibrations by causing radial deflection of the external structure [Alger, 1953]. Radial modes are mainly excited by radial stress harmonics but they can also resonate with circumferential harmonics in slotted machines [Boesing, 2013], since the latter may generate radial deflection (cf. Subsection 1.4.1).

Based on analytical modal analysis of equivalent cylinders, radial modes with “low” circumferential orders generally have the most influence on noise and vibrations, in particular breathing mode, bending mode and ovalization mode. In fact, maximal displacement magnitude in function of circumferential wavenumber decreases such as [Jordan, 1950]:

$$U_x^{rl} \propto \frac{1}{(r^2-1)^2} \tag{1.17}$$

Generally, the greater are the orders m and n, the lower is the resonance peak and the higher is the natural frequency f_{mn}, except for $m = 0$ and $m = 1$ [Jordan, 1950]. This is

due to structure stiffness regarding deformation as a whole (for $m = 0$ and $m = 1$) or deformation with a large number of nodes. However, higher modes may have an influence on noise and vibrations of large diameter machines. For example, radial mode contribution $(f_{18,0}, 18, 0)$ is observable in the case of a large WRSM used as hydropower generator [Traxler-Samek et al., 2012], while it is clearly negligible in some HEVs traction machines [Yang et al., 2013b; Hofmann et al., 2014].

In presence of electromagnetic field asymmetries such as eccentricities, new structural modes can be potentially excited, which could generate much more noise and vibrations. In particular, UMP and UMF may potentially excite the stator and rotor bending modes [Ede et al., 2002], and overload bearings [Tenhunen, 2003]. Therefore, the most problematic radial modes in NVH studies are breathing modes for $(f_{0n}, 0, n \geq 0)$, bending modes for $(f_{1n}, 0, n \geq 0)$ and ovalization modes for $(f_{2n}, 0, n \geq 0)$.

Besides, circumferential modes are excited by circumferential excitations (including torque ripple) which mainly generate yoke torsion, and very few radial vibrations. They might contribute to rotor circumferential vibrations (i.e. speed ripple) increase and amplify structure-borne due to torque ripple [Valavi et al., 2018].

Resonances with axial modes are likely to generate noise and vibrations by axially exciting bearings and end-shields. 3D effects result in harmonics with non-zero axial wavenumbers $l > 0$ that may excite axial structural modes or radial modes with non-zero axial order n [Blum et al., 2014; Kang et al., 2017].

1.4.6 Scientific challenges addressed in this thesis about the interaction of stress harmonics and slotted structures

There are many remaining challenges in the study of interaction between stress harmonics and slotted structures, as developed in the previous subsections. Among them, two challenges are particularly retained for the following of this thesis:

1. The first challenge concerns the contribution of circumferential stress harmonics to the radial vibrations of slotted structures, as presented in Subsection 1.4.1. This aspect is investigated in Devillers et al. [2017b] based on simulation results of a SCIMs $36s28r6p$ used in traction application, and in Chapter 5 based on simulation and experimental results on the SPMSM $12s10p$ prototype.
2. The second challenge addresses the slotting modulation effect which transforms high wavenumbers of stress harmonics into low wavenumbers, and can resonate with low-order structural modes.

The resonance effect is also investigated in Chapter 5, especially the fact that the deflection shape follows the exciting stress wave in forced response and follows the modal shape in resonant response, which is therefore a non-linear mechanical behavior and might change the emitted noise level.

1.5 Acoustic noise generation

The acoustic noise generation process is not investigated in this thesis, hence the present subsection only aims at defining the different quantities used to evaluate the acoustic properties of electrical machines. Acoustic noise results from the traveling of coupled pressure/velocity waves in the air. These pressure waves originate from the local velocity (or vibration) of air particles in contact with the machine structure, which

is subject to external excitations, in particular magnetic stress excitations. Physically speaking, the emitted acoustic power from the product of the local velocity wave **v** and pressure wave p. By averaging this product over the wave period $T = 1/f$, the acoustic intensity I is obtained:

$$\mathbf{I} = < p\mathbf{v} >_T \tag{1.18}$$

Acoustic intensity is a vector collinear with velocity vector field. Its magnitude decreases with distance ρ from source, as spherical vibration waves decay in $1/\rho$. In free field, i.e. no sound reflections, and far away from the acoustic source, velocity v and pressure p are proportional and linked to sound speed in the air, noted c_0 and air density ρ_0, such as $p \propto \rho_0 c_0 |\mathbf{v}|$. Therefore, acoustic intensity is quadratically proportional to pressure or vibration level [Fahy and Gardonio, 2007]:

$$I = |\mathbf{I}| \propto < \rho_0 c_0 |\mathbf{v}|^2 >_T \propto < \frac{p^2}{\rho_0 c_0} >_T \tag{1.19}$$

From acoustic intensity, noise level is physically represented by two quantities: Sound Pressure Level (SPL) and Sound Power Level (SWL) [Yang, 1981]. Such as acoustic intensity, SPL quantifies the sound level perceived at specific position regarding the acoustic source, and therefore decreases with distance from source. This is the physical quantity perceived by human ear. SPL, noted L_p, is expressed in dB as a logarithmic function of the acoustic intensity, such as:

$$L_p = 10\log_{10}\left(\frac{I}{I_0}\right) = 20\log_{10}\left(\frac{p_{rms}}{p_0}\right) \tag{1.20}$$

where $I_0 = 10^{-12}$ W/m^2 is the reference intensity, p_{rms} is the RMS value of the acoustic pressure wave, and $p_0 = 2.10^{-5}$ Pa is the reference pressure [Ellison and Moore, 1968].

SWL quantifies the overall sound power level radiated by the acoustic source in the whole space. SWL is independent from the position and characterizes the intrinsic noise level of the source. It enables to compare the NVH performances of different electrical machines, regardless of the context. SWL, noted L_w, is also expressed in dB as a logarithmic function of the acoustic power:

$$L_w = 10\log_{10}\left(\frac{W}{W_0}\right) \tag{1.21}$$

where W is the acoustic power value, and $W_0 = 10^{-12}$ W is the reference acoustic power. The acoustic power is obtained by integrating the acoustic intensity on any surface S enclosing the electrical machine [Yang, 1981]:

$$W = \int_S \mathbf{I}.\mathbf{dS} \tag{1.22}$$

From logarithmic properties, two noisy machines with same SWL increases by 3 dB the overall SWL. Likewise, dividing by two the acoustic power reduces by 3 dB the SWL. Besides, pressure is proportional to vibrations, which is also proportional to excitations (cf. Subsection 1.4). Therefore, SPL and SWL are also logarithmic functions of vibrations, and excitations in forced response:

$$L_w \propto 20\log_{10}\left(\frac{v_{rms}}{v_0}\right) \propto 20\log_{10}\left(\frac{F_{rms}}{F_0}\right) \tag{1.23}$$

The use of logarithmic scale is explained by human audition physiology, which has a logarithmic behavior in magnitude. The physical value of SPL can be corrected to account for human's ear sensitivity limited to [20,20000] Hz. The most used weighting curve is the A-weighting curve [IEC61672-1, 2013]. The resulting A-weighting SPL is expressed in dBA. For example, 100 dB at 100 Hz equals to 80 dBA at human's ear damps low frequencies. The maximum ear sensitivity is around 2500 Hz. Therefore, worse noise issues occur when structural modes of the electric motors or forced electromagnetic excitations are close to 2500 Hz.

Finally, the emitted noise is also influenced by the radiation factor of the external surface, depending on the structural mode [Gieras et al., 2006]. In particular, the higher the circumferential wavenumber, the higher the cut-off frequency is. Maxwell stress excitations with high-wavenumbers may be filtered by both structural and acoustic behaviors, hence the dominance of low-wavenumber stress harmonics in the e-NVH generation process.

1.6 Low-noise design rules and noise reduction techniques

In Section 1.6, the main noise and vibration reduction techniques are presented, so as to include them in the electrical machine design process, and also to compare them in the benchmark project developed on the test rig designed during this thesis (cf. Subsection 5.1.2.1).

1.6.1 e-NVH design stages of electrical machines used in EVs/HEVs

In EVs/HEVs applications, the e-NVH design of electrical machines generally require three stages:

1. A quick NVH ranking of several machine topologies by estimating the relative SWL between these topologies [Boisson et al., 2014], when machine housing is not designed yet.
2. A detailed NVH calculation giving the absolute SWL of the electrical machines in its housing [Schlensok et al., 2008], eventually including its interactions with gearbox.
3. A realistic NVH calculation giving the absolute SPL heard by the driver in the vehicle, which is called auralization [van der Giet, 2011], or outside the vehicle (passing-by noise).

For the first design phase, it is necessary to establish design rules for low-noise machines [Le Besnerais, 2008; van der Giet, 2011] and run fast e-NVH studies. Specific algorithms such as Electromagnetic Vibration Synthesis (EVS) proposed in MANATEE software enables to speed up computation time. Different topologies are relatively compared based on fast and accurate magnetic noise models presented in Sections 2.3-2.4. The second and third phases require highly detailed numerical models, based on Finite-Element Analysis (FEA) [Pellerey, 2012; Tan-Kim et al., 2015], and are out of this thesis scope.

1.6.2 Low-noise design rules

Low-noise design rules can be deduced from the knowledge of Maxwell stress harmonics origins, and of their interaction with the structure, as presented in Subsections 1.2-

1.5.

During the first design step, the priority is to avoid slot and pole combinations that are most likely to create airborne noise [Kron, 1931], as well as torque ripple [Heller and Jokl, 1969] which can create structure-borne noise. The aim is also to prevent from creating low-wavenumbers in the Maxwell stress harmonic content that may excite low structural modes [Yang, 1981; Le Besnerais, 2008]. For example, changing the number of rotor bars by only one or two might increase noise and vibration level of IM up to ±20 dB [Le Besnerais et al., 2009a]. [Zhu et al., 2013] investigate several combinations of slot and pole numbers in concentrated windings PMSM regarding UMP. Therefore, an optimal combination can be found to meet both vibroacoustic and electromagnetic requirements.

In variable-speed machines, converter and machine should be designed simultaneously, to limit as much as possible the interaction between excitation and structure. In particular, PWM switching frequency should be far from the natural frequencies of breathing modes [Le Besnerais et al., 2010a; Valavi et al., 2018]. It is easier to design low-noise fixed-speed machines and to ensure that excitation harmonics do not match with structural modes for the given synchronous frequency f_s [Valavi et al., 2018].

The risk of exciting a structural mode increases in case of operation at variable speed as the rotating frequency of each stress wave generally depends on the operating speed. This phenomenon is illustrated on the theoretical spectrogram of Figure 1.21 for the HEV Toyota Prius 2004 machine. There are two potential resonance points with breathing mode $m = 0$ at around $5kHz$ and 3200 and 6400RPM. The resonance at 3200RPM, respectively 6400RPM, is due to the stress harmonic of triplet $(24f_s, 0, 0)$, respectively $(12f_s, 0, 0)$.

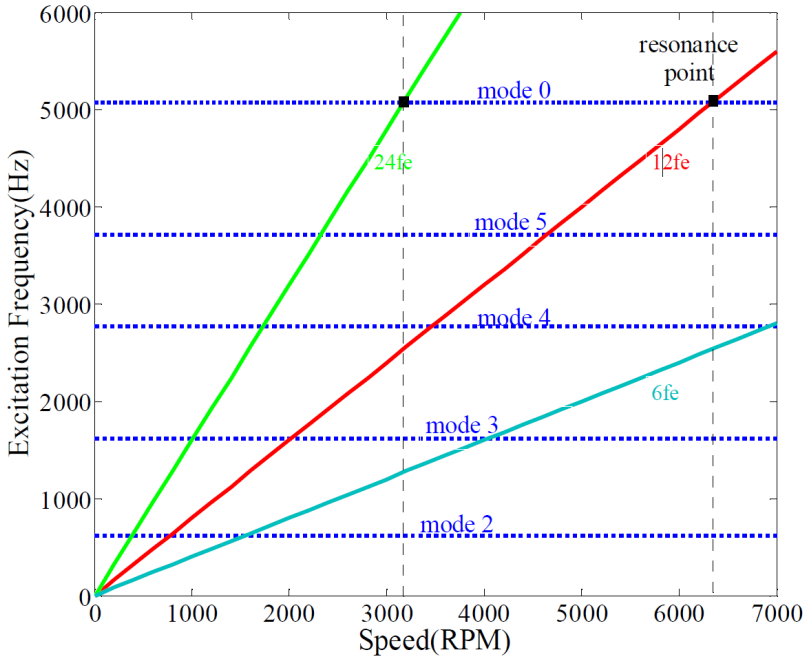

Figure 1.21 – Spectrogram showing the risk of vibration resonance at variable speed for the Toyota Prius 2004 IPMSM (from Yang et al. [2013b]).

From Hofmann et al. [2014], the risk of exciting breathing mode is actually the main issue of variable speed traction machines used in EVs/HEVs. It results from the fact that pulsating radial force harmonics (or radial force ripple) always exist, especially when using PWM to vary speed (cf. Figure 1.10), and may cross breathing modes natural fre-

quencies due to the wide supply frequency f_s range. Besides, most of the synchronous machines used for traction in EVs/HEVs have distributed windings, for which the lowest stress wavenumber r_{min} is given by $r_{min} = \gcd(Z_s, 2p) = 2p$. As most of the traction machines have more than three pole pairs ($p = 3$), the lowest stress wavenumber r_{min} is greater than 6, meaning that stress harmonics (except pulsating radial force harmonics) have generally too high wavenumbers to create noise.

If the structural resonance is not avoidable, reduction techniques are applied to damp the excitation and/or the mechanical response. Reduction techniques are commonly divided into passive and active techniques, both potentially acting on the excitation, mechanical and acoustic responses [Vér and Beranek, 2005]. Subsections 1.6.3 and 1.6.4 propose a short review of noise mitigation techniques available in the literature.

1.6.3 Passive reduction techniques

Passive reduction techniques stand for noise mitigation solutions which are not power supplied. They are usually considered during the machine design, as most of them influence the topology. For existing noisy machines, they can be applied when remanufacturing some parts (for example, rotor or stator laminations, winding pattern etc.). In particular, pole and slot reshaping can lead to noise and vibration reduction without compromising the electromagnetic performances [Le Besnerais et al., 2009c; Putri et al., 2016]. More complex passive strategies can be further investigated to reduce MMF and slotting harmonics.

1.6.3.1 Rotor and/or stator skewing

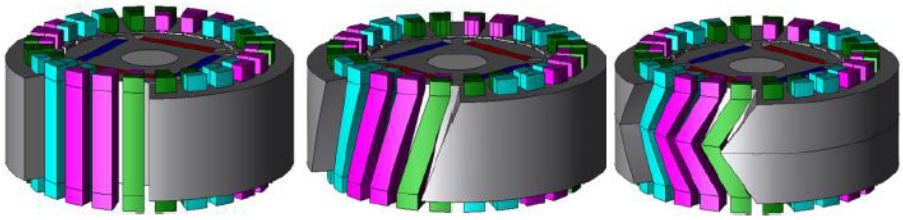

Figure 1.22 – Examples of stator slot skewing for IPMSMs (from Park et al. [2016]).

Skewing is generally used to reduce torque pulsation (meaning pulsating circumferential force) due to MMF and slotting harmonics. However, it can also reduce other harmonics of radial stress [Yang et al., 2013a; Blum et al., 2014; Kang et al., 2017]. In Park et al. [2016], a V-skew technique illustrated in Figure 1.22 is adopted to compensate axial UMF due to conventional skew, however torque ripple reduction is less effective. It raises the general question of finding a compromise between reducing rotor vibrations originating from torque ripple and structure-borne noise due to parasitic excitations. The use of skewing to mitigate exciting stress harmonics is limited by:

— The reduction of machine efficiency.

— The introduction of axial UMF and axially-varying radial stress distribution, which can increase noise and vibrations level at certain speeds due to new resonances [Blum et al., 2014]. On Figure 1.23b, breathing modes with different axial wavenumbers are excited in function of the skewing pattern;

— The difficulty to find the best skew angle to reduce the interaction with the principal modes of vibrations [Mikina, 1935]. Optimal skew angle might also depends on load operation [Azar et al., 2012].

— The difficulty to manufacture the rotor and/or stator with perfect skew, knowing that imperfect skew may increase noise and vibrations [Despret et al., 2016].

— The fact that topologies with integer number of slots per pole and per phase may benefit more from skewing than fractional-slot topologies [Sizov et al., 2012].

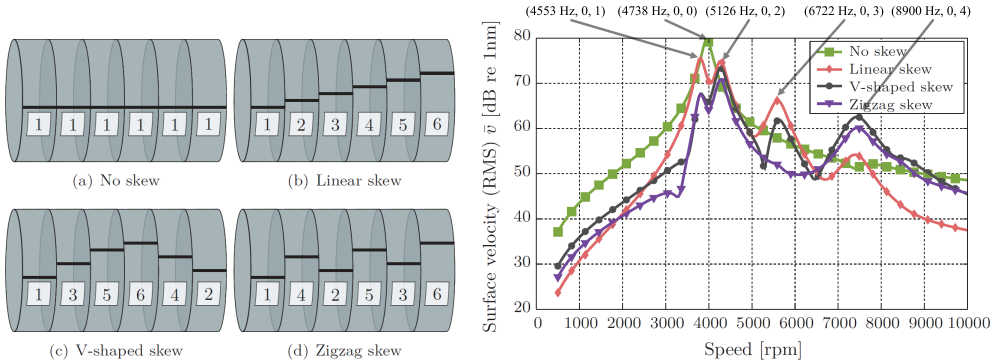

(a) Magnet skewing strategies. (b) Vibration level.

Figure 1.23 – Vibration level in function of rotor magnet skewing strategy (adapted from Blum et al. [2014]).

1.6.3.2 Notches, or dummy slots

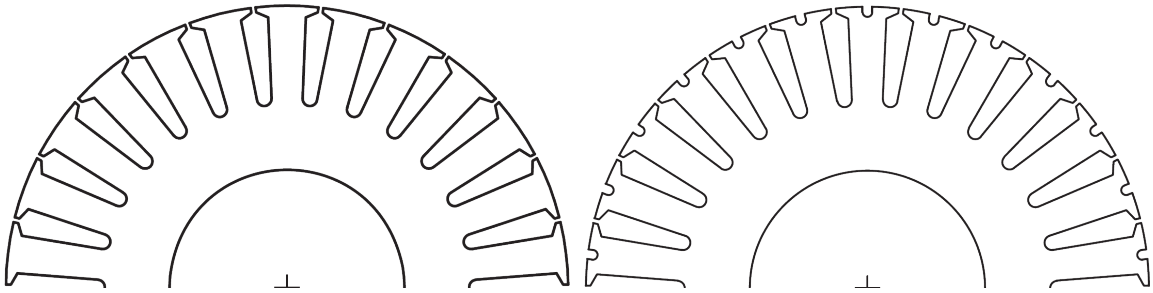

(a) Conventional squirrel cage rotor (b) Same rotor with notches

Figure 1.24 – Squirrel cage rotor with notches from Zhou and Shen [2017]

Notches, also called dummy slots, are empty slots which are added in the rotor and/or stator teeth. The aim is to increase the circumferential wavenumbers of slotting harmonics to avoid exciting low mode orders [Zhou and Shen, 2017; Lan et al., 2017]. However, notch geometry should be close to slot geometry to get the expected effect, hence it is not suited to large open slot topologies. Besides, it increases saturation at tooth tip which can alter electromagnetic performances through slot leakage inductance increase.

1.6.3.3 Magnetic wedges

The aim of this technique is to reduce slotting effect by adding magnetic wedges (wedge with magnetic relative permeability from 2 to 10) at slot openings [Delaere et al.,

2003]. Besides, magnetic wedge have two side-effect on supply current: it reduces magnetizing current but increases slot leakage current. Therefore, even if slotting harmonics are reduced, the current level might be higher and compensate more noise and vibration reduction [Le Besnerais and Souron, 2016].

1.6.3.4 Other passive techniques

Other passive mitigation techniques can be considered:

— In case of PWM, the main mitigation technique to reduce PWM harmonics is the use of random switching frequency to spread the harmonic content.

— Flux barriers in the stator core enable to reduce the low spatial harmonics of the stator MMF in concentrated winding machines [Dajaku and Gerling, 2012]. However, it also reduces the structure stiffness and potentially increases the risk of resonance.

— It is possible to cancel a specific harmonic by adding a secondary winding in the stator slots (called damper winding) in series with a capacitor [Bauw et al., 2017]. Flux density harmonics are filtered by the RLC circuit created by the secondary winding and the capacitor. The capacitor value is chosen such as the RLC resonance frequency matches with the frequency of the disturbing flux harmonic.

— Passive reduction techniques can be also applied on the mechanical properties, such as the choice of resin for windings impregnation [Millithaler et al., 2017].

In conclusion, several passive reduction techniques can be considered and even implemented on a same machine. For example in Zou et al. [2017], a sensitivity study is performed on pole shaping, stator slot angular width, and stator notching to achieve significant reduction of torque and force ripple.

1.6.4 Active reduction techniques

Active techniques are necessarily used once the machine is operating, and therefore adequate to existing noisy machine which cannot be remanufactured. During the design, they are generally not considered except if passive techniques cannot be applied.

1.6.4.1 Current injection

A first active strategy is the injection of stator current harmonics to create a counter stress harmonic at the desired frequency, as proposed in Cassoret et al. [2003]; Franck et al. [2011] for IMs and in Pellerey et al. [2012]; Boesing [2013] for SMs. Current injection requires an adequate inverter and a close loop control to adapt phase and amplitude in real time. If the harmonic phase is not controlled, the injected stress harmonics may generate more noise. The current harmonic is generally injected in the stator winding. The circumferential wavenumbers of the main injected stress harmonics are consequently 0 or $2p$. In conclusion, current injection in the stator winding may not be effective to mitigate stress harmonics with another wavenumber than 0 or $2p$.

If the main noise issue originates from PWM harmonics, random modulation in converter enables to spread the stress harmonic content [Bolognani, 1999], and decrease discomfort due to the tonal and high frequency airborne noise due to PWM excitations.

1.6.4.2 Compromise between torque and stress harmonics

Another strategy is to find a compromise between the operating torque and the generation of noisy stress harmonics [Bekemans, 2006]. As explained in Subsection 1.2.1, the load state has a modulation effect on stress harmonics as it sets the interaction between stator and rotor fields. Particularly in SM, the load state is given by the load angle between i_d and i_q, where i_d and i_q are respectively the direct and quadrature currents obtained with Park transform. Zhu et al. [2005] show that radial and circumferential excitations (including torque) can be characterized in function of i_d and i_q. In Pellerey et al. [2010], it is shown that load angle has mostly an influence on time harmonics rather than spatial harmonics. Radial stress harmonics can reach local maxima in function of load angle an could increase radiated noise. It is therefore possible to find an optimum between torque and a specific stress harmonic which is responsible for noise and vibrations emission [Kurihara et al., 2015].

1.6.4.3 Other active techniques

Other active mitigation techniques can be considered:

— In Shahaj and Garvey [2011], the authors propose an active reduction technique in large electrical machines based on the destructive interference of magnetostriction and Maxwell stress harmonics.

— In Mininger [2005], piezoelectric actuators are set on a SRM stator to actively damp stator vibrations due to resonance with low-order radial modes.

1.7 Conclusion

Chapter 1 develops the physical process of e-NVH generation in electrical machines. The electromagnetic excitations are Maxwell stress harmonics (or waves) located at the interface between the airgap and the external structure. These stress harmonics excite and deform the structure, and potentially resonate with its structural modes according to the resonance condition (see Subsection 1.4.4). However, scientific challenges remain on the physical understanding of the interaction between Maxwell stress harmonics and slotted structures, including the contribution of circumferential stress harmonics to radial vibrations due to tooth bending, and the excitation of low-order structural modes by high-wavenumber stress harmonics due to slotting modulation effect. The test rig and the SPMSM designed during this thesis aims at experimentally illustrating and investigating those questions, as developed in Chapter 5.

Besides, Chapter 1 also shows the necessity of building a multi-physics model to predict the noise and vibration level and include it in the machine design. In particular, the e-NVH models has to compute Maxwell stress excitations and the structural response, accounting for the interaction with structural modes. Besides, the main noise and vibration reduction techniques have been presented in Subsection 1.6, so as to consider them in the multi-physics modeling and in the design process. The different multi-physics models used for e-NVH simulation in electrical machines are presented in Chapter 2.

Chapter 2

Simulation and modeling of e-NVH in electrical machines

Contents

2.1 Introduction

2.1.1 Multi-physics modeling

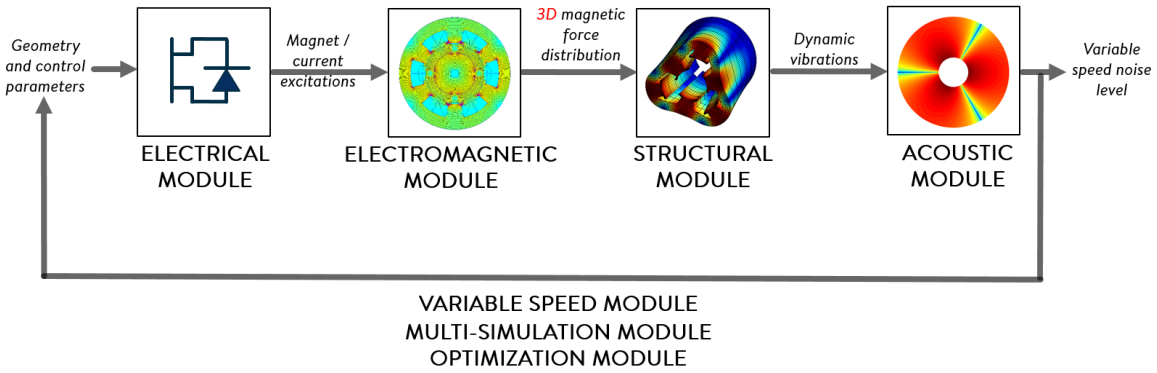

Figure 2.1 – e-NVH simulation workflow following the causal path from magnetic excitation to audible noise [MANATEE, 2018]

The vibroacoustic study of an electrical machines requires a multi-physics approach which reproduces the actual generation path of noise and vibrations due to magnetic stress, as shown in Figure 2.1. First, the knowledge of machine topology and supply enables to compute the electromagnetic field and resulting Maxwell stress harmonics applying on the structure. A structural mechanical study gives the machine vibrations response subject to the exciting stress harmonics. This vibration response accounts for potential resonances between structural modes and stress harmonics. Finally, vibrations of the outer structure generate acoustic waves of sound pressure which may create noise in the audible frequencies.

Therefore, the multi-physics approach generally includes the following modules [Boesing, 2013]:

1. An electric module which computes the electromagnetic sources depending on the control strategy.
2. An electromagnetic and mechanical module which first aims at computing the electromagnetic field and flux density, then at deducing Maxwell stress distribution and finally project them on machine structure.
3. A structural mechanical module which computes the vibration response resulting from all the stress harmonics.
4. An acoustic module which computes the sound pressure field radiated by the outer surface of the machine.

"Module" term should be carefully distinguished from "model" and "method" terms. A "module" is one physical part of the multi-physics study, which may be solved using "models" with different granularity levels. The "model" is the formulation of the physical problem, including assumptions, physical laws etc. The "method" refers to the model resolution process in order to solve the problem, e.g. obtain the physical quantities. However, model and method are commonly interchangeable in the literature.

2.1.2 Context and Outlines

Developing several models for each module enables to have several e-NVH simulation workflows, and adapt both granularity level and computation time to the design stage requirements, as explained in Section 2.2. The simulation workflow of MANATEE in detailed e-NVH design stage is the Electromagnetic Vibration Synthesis (EVS) synthesis defined in Subsection 2.2.2, and which is used for the SPMSM $12s10p$ design in Chapter 5. Besides, the numerical aspects intrinsic to e-NVH modeling are developed in Subsection 2.2.4 to establish some comparison criteria and classify the different models.

The magnetic models available in MANATEE at the beginning of the thesis [MANATEE, 2015], the analytical Permeance/MagnetoMotive Force method (PMMF) enables to compute Maxwell stress distribution in SCIMs, and the SubDomain Method (SDM) is implemented for SPMSMs topologies. MANATEE is also coupled with FEMM [FEMM, 2018] to perform Finite-Element Analysis (FEA) of various topologies. The thesis objective in terms of magnetic model development is to extend or implement a fast and accurate magnetic model in MANATEE, in order to have a complementary set of models which is applicable to a large variety of electrical machines (SM and IM), and dedicated to the early electromagnetic design stages. Therefore, Section 2.3 proposes a qualitative comparison of the main existing magnetic models through a non-exhaustive state of the art. Each model is investigated regarding the granularity levels and performances criterion established in Subsection 2.2.3 for e-NVH simulation purpose, which leads to the choice of extending the semi-analytical SDM.

Finally, Section 2.4 focuses on the main mechanical models used in vibroacoustic studies, in particular the computation of airgap stress distribution using Maxwell Stress Tensor (MST), and the vibration level prediction based on EVS. The EVS relies on the computation of Frequency Response Functions (FRFs), which represent the structure mechanical response subject to a stress harmonic associated to a particular frequency and wavenumber. As for the magnetic models, FRFs can be computed using simple analytical models based on equivalent cylinders assumptions or numerical Finite-Element (FE) structural models.

2.2 e-NVH simulation workflow and numerical challenges

2.2.1 Coupling between modules

The e-NVH multi-physics modeling complexity lies in the complexity inside each module, and also in the coupling in-between [Imhoff et al., 1990; Hameyer et al., 1999]. The type of coupling is a part in the global modeling assumptions set and granularity level. In reality, the coupling is strong, meaning that all modules are intrinsically coupled in both directions. On the contrary, a weak coupling assumes that each module are sequentially considered and that the next module has no effect on the previous one.

A strong coupling between two or more modules is sometimes necessary for the electromagnetic and vibroacoustic modeling. For instance, all modules are strongly coupled to account for the temperature effect on physical properties [Bracikowski, 2012], such as variation of remanent flux density or natural frequencies. In this case, the multi-physics approach also includes a heat transfer module.

Incidentally, a strong coupling between the electric circuit and the electromagnetic model enables to include new currents induced by airgap electromagnetic field, which counteract existing field and stress harmonics due to Lenz's law [dos Santos et al., 2014].

In particular, strong electromagnetic to electric circuit coupling is recommended to capture frequency harmonics due to back-Electromotive Force (EMF) in SMs (e.g. at $5f_s, 7f_s$), which impact on pulsating forces at $6f_s, 12f_s$. Regarding IMs, the strong coupling enables to catch Rotor Slot Harmonics (RSHs) (cf. Section 4.4) which interfere with the exiting stress harmonics. However, strongly coupled modules imply iterative evaluations of each module which may increase simulation duration in the time domain. Relying on frequency-based Electric Equivalent Circuit (EEC) as proposed in MANATEE might be less accurate than a strong coupling but enable to speed up computation time.

2.2.2 Electromagnetic Vibration Synthesis (EVS)

The Electromagnetic Vibration Synthesis (EVS) enables an efficient computation of NVH level in electrical machines [Roivainen, 2009; van der Giet, 2011; Boesing, 2013]. EVS simulation workflow is illustrated in Figure 2.2 and is identical to the causal path [Boesing, 2013]. EVS consists in computing separately the operational electromagnetic excitation (i.e. Maxwell stress distribution in the airgap) and the structural response characterization. The structural characterization can be performed with rotating wave excitation [Roivainen, 2009; Boesing, 2013] or tooth excitation [Torregrossa et al., 2012; Régniez et al., 2016]. The Maxwell stress distribution is formulated as a superposition of rotating stress waves (i.e. harmonics) in the airgap. The coupling between each physics is weak, as there is generally no significant feedback from the mechanical response to the Maxwell stress distribution, and from the acoustic response to the mechanical one [Boesing, 2013]. EVS methodology is further detailed in Subsection 2.4.2.1. Furthermore, EVS can be extended to acoustic stage using linearity property of the full vibroacoustic model, and becomes Electromagnetic Noise Synthesis (ENS) [McCulloch et al., 2002; Müller-Trapet et al., 2010].

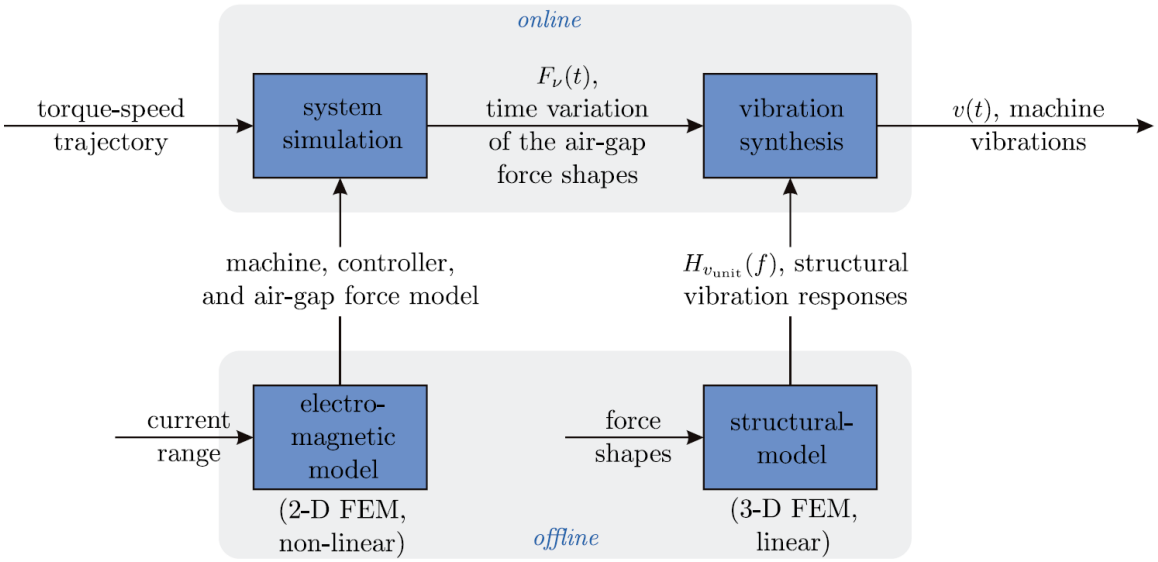

Figure 2.2 – e-NVH modeling using EVS [Boesing, 2013]

EVS is naturally computational efficient if the models used to predict stress harmonics and structural response are fast and accurate [Boesing, 2013], and is particularly relevant for e-NVH simulation in detailed design stages, to perform the structural characterization including housing. Furthermore, this method is implemented in MANATEE software and is used for the SPMSM $12s10p$ design in Chapter 5. Model choice for

each physics regarding design stages and numerical aspects is discussed in next Subsection 2.2.3.

2.2.3 Choice of model granularity regarding e-NVH design stages

Any model relies on simplifying assumptions regarding the complexity of the real phenomenon. These assumptions are required by the method to solve the model. The granularity level characterizes the simplification level of the model compared to the real phenomenon. A high-level model or coarse model, respectively a low-level model or fine model, relies on a large number of assumptions, respectively on a low number of assumptions.

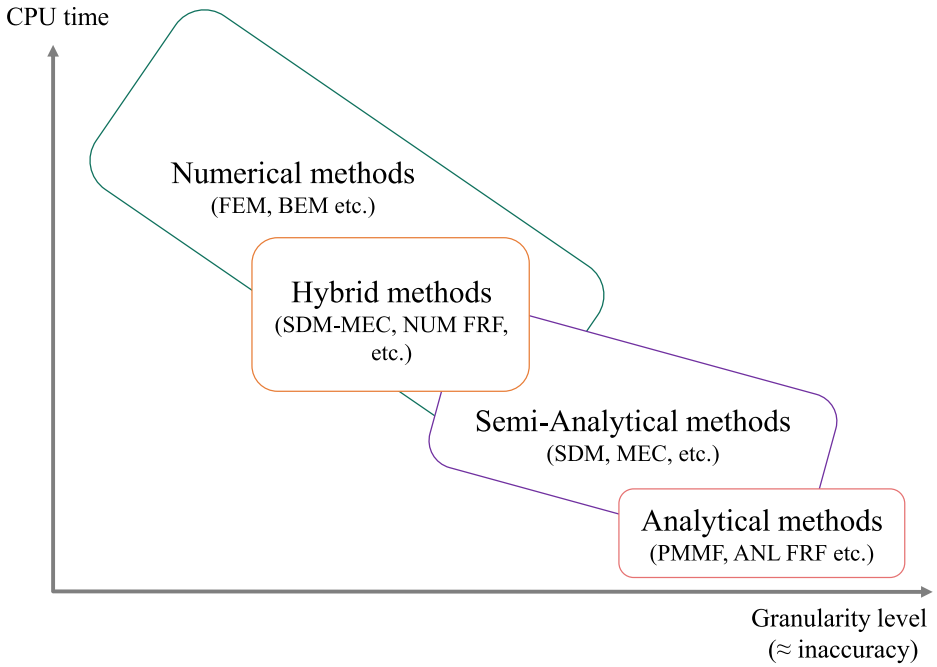

Figure 2.3 – Computation time in function of granularity level

The choice of the model depends on the design stage (see Subsection 1.6.1) and the required granularity level. Granularity is intrinsically linked to the method which is used for the model resolution. From the literature, methods can be classified in four categories (cf. Figure 2.3):

— Analytical methods: the solution is explicit (mathematical expression) and does not require to solve a system of equations. The resolution is instantaneous. Analytical methods are generally used in high-level models.

— Semi-analytical methods: the solution is explicit and requires to numerically solve a system of equations. Semi-analytical methods may offer an interesting compromise between granularity and computation time.

— Numerical methods: the solution is implicit and requires to solve a system of equations. The granularity level can be high or low. The lower is the granularity level, the more essential are the numerical methods, in spite of the computation time.

— Hybrid methods: a combination of the above.

For high level models, analytical and semi-analytical methods should theoretically provide results faster than numerical methods with comparable accuracy. Therefore,

having several models with different granularities is a very powerful tool to optimize the NVH and electromagnetic design. In particular, the early topology exploration relies on high-level models (step 1 in Subsection 1.6.1) while the final validation is made with low-level coupled models (steps 2 and 3). Besides, passive and active reduction techniques can be efficiently embedded in an optimal design process using fast analytical magnetic and structural models. Finally, the use of several granularity models enable speed-up optimization process using space-mapping between coarse and fine models [Encica et al., 2007].

2.2.4 Numerical challenges in e-NVH simulations

2.2.4.1 Time versus harmonic resolution in e-NVH simulations

In transient analysis, electromagnetic and mechanical models are necessary solved in time domains [Tang et al., 2005; Climente-Alarcon et al., 2018]. In steady-state analysis, electromagnetic and mechanical models can be solved both in time and harmonic domains using analytical and numerical models. Depending on the model assumptions and the time and space harmonic content of magnetic field and stress, the resolution may be faster in one domain than the other.

However, the electromagnetic harmonic resolution is much more complex in case of magnetic saturation. If saturation is neglected, a multi-harmonic resolution can be considered [Hannon et al., 2015]. Due to rotor motion, injecting a mono-frequency current in stator windings creates multi time and space harmonics at rotor side [Lubin et al., 2011b].

In case of magnetic saturation, flux harmonics cannot be considered separately (cf Subsection 1.2.1). The recent harmonic-balance technique introduces saturation in the numerical resolution of inductor [Giust, 2016]. However, it has not been applied to electrical machines, which contains much more harmonics than an inductor. Time resolution is generally performed for non-linear magnetic problems.

In mechanical analysis, the simulation is generally performed in the harmonic domain [Roivainen, 2009; Boesing, 2013]. Historically, the first mechanical models to understand the interaction between stress harmonics and structures are analytical, and based on an time and space harmonic formulation [Alger, 1953; Jordan, 1950]. The mechanical response has the same harmonic content as the stress distribution, due to linear elastic deformation. Displacement and vibration distributions are consequently much sparser in harmonic domain than in time and space domains. The overall vibration response is obtained by summing the mechanical response of each stress harmonic (see EVS in Subsection 2.4.2.1). In acoustic models, SPL and SWL are generally simulated in harmonic domain [Roivainen, 2009; Gieras et al., 2006].

Finally, the vibration response can also be obtained by solving the mechanical equations in the time domain [Tang et al., 2005; Martinez et al., 2016], and it is possible to mix time, space and harmonic formulation in electromagnetic models. For example, analytical models based on the Analytical Resolution of Maxwell Equations (ARME) often rely on time-stepping and spatial harmonic formulation [Gysen et al., 2010]. In any case, sound quality metrics are only based on time signals which means that the virtual prototyping of sound quality requires to go back to time domain.

2.2.4.2 Time/frequency discretization

In time domain, the magnetic field must be sampled in a discrete set of times steps. The number of time-steps Δt is given by Shannon sampling frequency, which depends on the maximum frequency of the excitation f_{max}, such as:

$$\Delta t < \frac{1}{2 f_{max}} \tag{2.1}$$

If the Shannon criterion is not fulfilled, non-physical time harmonics appear due to aliasing. Maximum frequency can be rather especially in presence of high frequency phenomena such as PWM. Therefore, time-step value is small and the number of time steps required to simulate an operating period is increased, such as computation time [Le Besnerais, 2016]. This is especially challenging when trying to capture both low frequency content (e.g. mechanical vibrations linked to rotor speed) and high frequency content (e.g. due to PWM harmonics) within the same e-NVH simulation model.

In presence of synchronous and asynchronous frequencies, for example due to mechanical slip in loaded SCIMs, or asynchronous PWM, it is often not possible to compute each electromagnetic field waves on an integer period number. In fact, for a random mechanical slip value, synchronous and asynchronous harmonics cannot be both periodic on the simulating period. The non-periodicity introduces spectral leakage, i.e. non-physical harmonics in the stress harmonic content. Spectral leakage occurs for example in the e-NVH simulation of SCIMs [Rainer et al., 2010]. Spectral leakage can generate non-physical harmonics which are amplified by resonance with structural modes. Therefore, these numerical artifacts strongly pollute simulated noise and vibrations level, and techniques have been developed to reduce spectral leakage based on the prior knowledge of harmonic content from analytical study and on FFT windowing strategies.

In transient simulations, the numerical transient is mainly responsible for simulation time increase [Sprangers et al., 2014b], and may also introduce numerical artifacts in stress spectrum if steady state is not exactly reached.

2.2.4.3 Spatial discretization (meshing)

In space domain, the magnetic problem is decomposed in a discrete set of nodes, such as in Finite-Element Method (FEM) or Magnetic Equivalent Circuit (MEC). As shown by the quadratic relationship (1.12), two field harmonics with high and close wavenumbers can contribute to generate airgap stress harmonics with low wavenumber. To accurately predict stress harmonics, the number of nodes N in the airgap must be greater than twice the highest wavenumbers r_{max} present in field spectrum:

$$\mathrm{N} > 2 r_{max} \tag{2.2}$$

Besides, an irregular and random airgap mesh can introduce numerical errors in the magnetic field solution [Hallal, 2014]. As shown in Figure 2.4, the blue peaks around 10 kHz and 18 kHz on the acceleration spectrum are numerical artifacts. Hallal [2014] recommends to use a uniform airgap mesh, and to set the rotor angular step $\Delta\theta$ (i.e. rotor motion between two time-steps) to be equal or a multiple of the distance d between two nodes. However, this technique called "blocked step technique" links time discretization and mesh fineness, such as a fine time discretization necessarily imposes a fine mesh. Moreover, blocked step technique implies that at low-speed, a higher number of nodes

are required to reach the same maximum frequency. As a consequence, it is not possible to simulate PWM noise near 0 RPM and a part of the spectrum is missing at low speed [Pellerey, 2012].

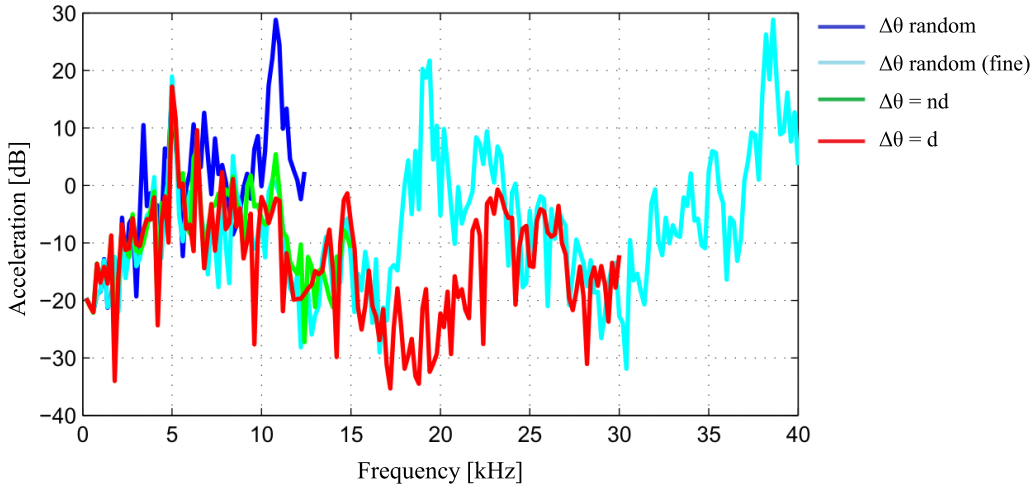

Figure 2.4 – Acceleration spectrum obtained with different airgap meshes (adapted from Hallal [2014]).

To reduce the computational effort in 3D electromagnetic simulations, it is possible to use the multi-slices technique [Piriou and Razek, 1990]. Multi-slicing includes 3D effects such as skewing with several 1D or 2D magnetic simulations. In a multi-slices model, the machine is divided into a discrete number of slices in the axial direction. In each slice, flux density is assumed to be axially invariant. Therefore, the multi-slicing approach enables to include the variation of radial and circumferential flux densities in the axial direction. However, the axial flux density component is undetermined. A multi-slices 2D model is sometimes called quasi-3D or 2.5D model. By extension, a multi-slices 1D model is referred as 1.5D. The number of slices should be sufficient to observe the desired axial wavenumbers and avoid aliasing effect [Weilharter et al., 2011]:

$$N_{slices} > 2 l_{max} \tag{2.3}$$

Similarly to techniques correcting spectral leakage in time domain based on a prior study of the flux density harmonic content, it is possible to undersample the axial field distribution as also shown in Weilharter et al. [2011].

2.2.4.4 Spatial harmonic discretization

Magnetic field generally contains a discrete set of space harmonics, as its distribution along the airgap is periodic. Besides, harmonic magnitude converges to zero for high frequency orders and wavenumbers. Therefore, in harmonic models such as magnetic models based on the ARME, the harmonic content can be truncated to a finite harmonic number [Gysen et al., 2010], which depends on Shannon criterion (cf. Equation (2.2)). For these reasons, the magnetic field distribution is generally much sparser in harmonic domain than in spatial domain.

When using a small number of harmonics such as Shannon criterion (2.2) is not fulfilled, the resulting magnetic field is oscillatory, as illustrated in Figure 2.5. It can be seen on the FFT Figure 2.5b that the harmonic content of the flux density computed below

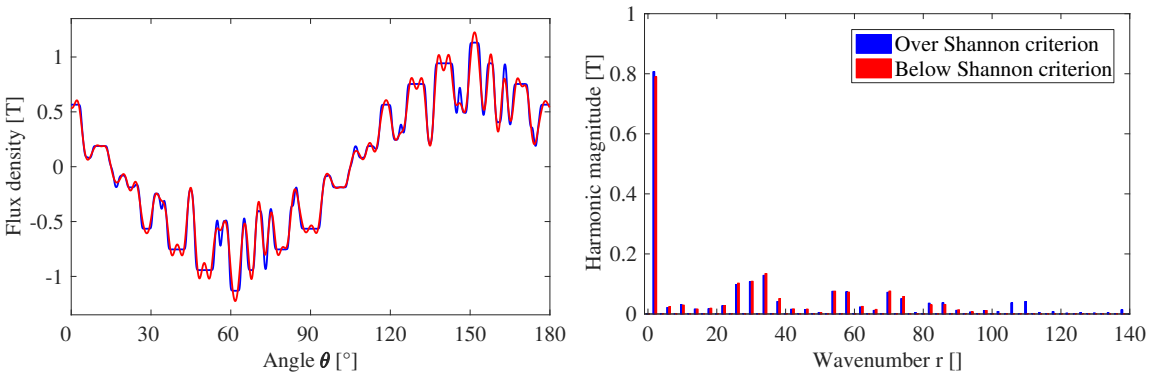

(a) Radial airgap flux density

(b) Spatial FFT

Figure 2.5 – Radial airgap flux density and spatial FFT with high and low spatial harmonic discretizations obtained with SDM (adapted from Boughrara et al. [2015]).

Shanon criterion is truncated from $r = 100$, as only 100 airgap harmonics have actually been considered in the SDM resolution (see Subsection 4.2.3.2). However, since the number of unknowns is reduced, the numerical resolution is much faster and the model is for example accurate enough to compute the fundamental flux density and deduce EEC parameters [Boughrara et al., 2015].

Besides, spatial harmonic formulation may also introduce Gibbs phenomenon in case of magnetic field discontinuities, for example in slots, teeth or magnet corners. Gibbs phenomenon is illustrated in Figure 2.6. In fact, airgap tangential flux density should be zero at the interface with rotor teeth, but is oscillatory due to the slope break (meaning discontinuous derivative) at teeth and slot corners. Gibbs phenomenon is an intrinsic limit of Fourier series and is not removed by increasing the number of spatial harmonics [Lubin et al., 2010]. It occurs for example when computing the MST on the tooth contour from the flux density obtained with SDM, as illustrated in Subsection 4.3.3.1. However, Gibbs phenomenon is only limiting when considering maximum values and not Root Mean Square (RMS) values.

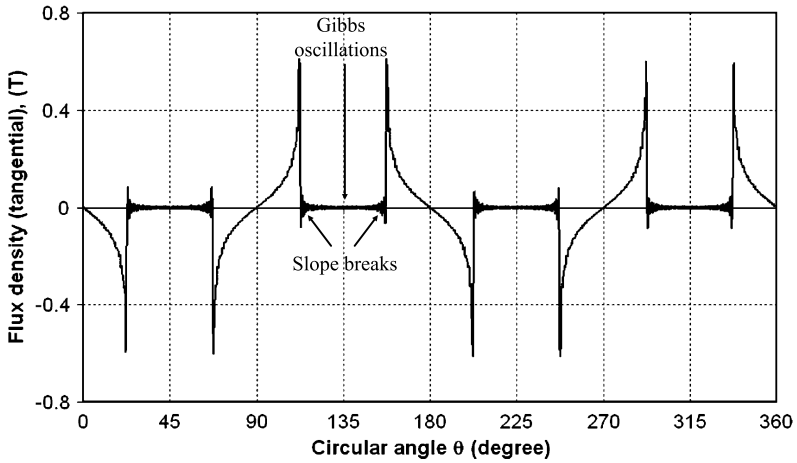

Figure 2.6 – Gibbs phenomenon due to discontinuous derivatives (adapted from Lubin et al. [2010]).

2.2.4.5 Speed discretization

In variable speed studies, the e-NVH behavior should be determined for every speed in the speed range. Therefore, it is necessary to discretize the speed curve, knowing that speed discretization should be fine enough to catch maximum resonance peaks with structural modes [Le Besnerais, 2016] while not increasing too much the simulation time. The lower the modal damping and the higher the natural frequency, the lower must be the speed step. Taking the SPMSM $12s10p$ example on the speed range 0-1300 RPM, a resonance occurs at 850 RPM between the ovalization mode measured at $f_2 = 720$ Hz with damping ratio $\xi_2 = 0.004$, and the exciting stress harmonic of frequency $10f_s$ and wavenumber $r = 2$ (see Subsection 5.3.3). To catch this resonance in the e-NVH simulation, the speed step ΔN should be defined such as:

$$\Delta \text{N} \ll \frac{60\xi_2 f_2}{10p} \approx 3.5 \text{ RPM} \tag{2.4}$$

The simulated SWL at variable speed obtained from EVS with a fine speed step is illustrated in Figure 5.11b for SPMSM $12s10p$.

2.2.4.6 Direct coupling between multi-physics models

The electromagnetic and mechanical direct coupling still requires lots of computational effort and are still under investigation [Wang, 2013]. Numerical complexity mostly lies in projecting the electromagnetic solution, obtained for the electromagnetic mesh, on the structural mesh [Hameyer et al., 1999; Martinez et al., 2016].

2.3 Magnetic modeling for vibroacoustic study

2.3.1 Comparison criteria between electromagnetic models

Based on Chapter 1, the electromagnetic model should feature:

— At least radial and circumferential stress harmonics, and axial ones if necessary (see Subsection 1.4).

— The different sources of flux density harmonics: slotting, MMF, control supply, faults, saturation, 3D effects, etc. (see Subsection 1.2).

— The possibility to implement noise reduction techniques: skewing, current injection etc. (see Subsection 1.6).

Of course, a single electromagnetic model cannot account for every effect. Besides, it is not relevant to systematically account for every harmonic source even if it is available in the model. As said in Subsection 2.2.4, accounting for all these parameters requires a highly detailed 3D electromagnetic model which is really time consuming. The granularity level must be chosen accordingly to the design stage (cf. Subsection 1.6.1). Therefore, the different electromagnetic models can be compared regarding the following criteria:

— Granularity level, involving:

1. Model dimensions (1D/1.5D/2D/2.5D/3D).
2. Modeling of harmonics sources.
3. Modeling of various machine topologies.
4. Modeling of e-NVH reduction techniques.

— Performances: mostly computation time versus accuracy of the resolution method. Of course, performances can only be compared for models with the same granularity level.

In the following, a non-exhaustive state of the art of analytical (Subsection 2.3.2), semi-analytical (Subsection 2.3.3), numerical (Subsection 2.3.4) and hybrid methods (Subsection 2.3.5) is presented.

2.3.2 Analytical methods

Analytical models provide a fast estimation of the flux density spectrum but they often rely on strong assumptions. Magnetic materials are generally supposed to be linear, isotropic and homogeneous. In this Subsection 2.3.2, analytical methods which account for slotting effects are either 1D or 1.5D using multi-slicing method.

2.3.2.1 1D Permeance/MagnetoMotive Force method (PMMF)

Principle

PMMF is an analytical method which gives the radial component of the flux density in the middle of the airgap. Stator and rotor iron cores are assumed to be infinitely permeable, meaning their reluctance is null. The flux density results from the product of the airgap permeance function Λ with the MMF [Doherty and Nickle, 1926; Brudny, 1997; Gaussens et al., 2012]:

$$B_\rho(t,\theta) = \Lambda(t,\theta)\mathrm{MMF}(t,\theta) \tag{2.5}$$

The airgap permeance function includes the harmonic content of any source of airgap length variations, as illustrated by Figure 2.7) for doubly slotted topologies such as SCIMs.

The MMF represents the magnetic sources distribution along the airgap, and includes current harmonics.

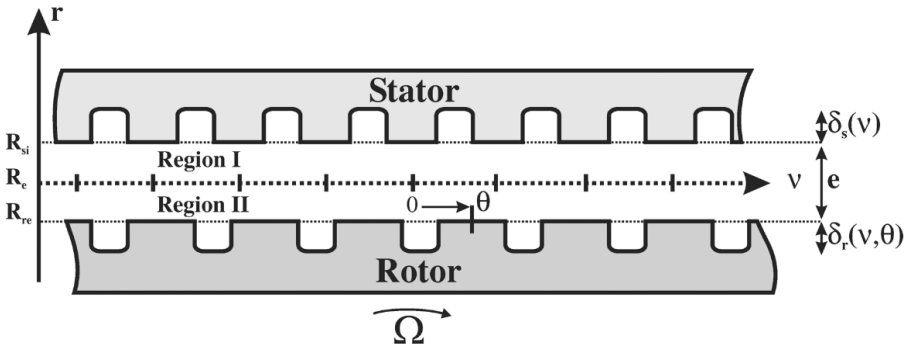

Figure 2.7 – Airgap length variations in doubly slotted structure (from Gaussens et al. [2012]).

Granularity level and existing topologies

PMMF enables to separate time and spatial information in both MMF and permeance quantities. It is also possible to separate time and spatial harmonic contents of stator and rotor slotting effects in the permeance function [Brudny, 1997].

Furthermore, time and space separation in MMF and permeance enables to include many types of harmonic sources. Eccentricities can be added to the airgap permeance expression [Al-Nuaim and Toliyat, 1998]. Nandi [2004] models magnetic saturation as an average airgap length increase and an additional a saturation wave in the permeance function.

Besides, PWM and any current harmonics, including rotor induced currents, can be added in the MMF, for example by using a EEC extended to time and space harmonics [Hubert, 2001]. Thanks to an electrical coupling, it is possible to include secondary induced harmonics in stator and rotor current spectra [Toliyat and Lipo, 1995].

The variation of radial stress distribution over axial direction can be directly accounted for using a 2D PMMF model in radial and axial directions [Bossio et al., 2004; Martinez et al., 2015], or using the multi-slices method (i.e. a PMMF 1.5D model).

The PMMF is very relevant to identify physical origins of stress harmonics. The main limitation of PMMF is the restriction to radial flux density component [Serrano-Iribarnegaray et al., 2013]. It is particularly suited to machines with small airgap such as IMs or SRMs [Gaussens et al., 2012], in which flux lines are quasi-radial in the airgap. Besides, it can also be adapted to WRSMs topologies as developed in Misir et al. [2016]. However, PMMF may be inaccurate for large airgap machines where flux lines are not radial and circumferential stress harmonics cannot be systematically neglected [Serrano-Iribarnegaray et al., 2013].

2.3.2.2 ARME in an equivalent slotless airgap

Principle

The Analytical Resolution of Maxwell Equations (ARME) consists in directly solving the magnetic governing equation in a physical domain. The governing equation is obtained from Maxwell equations [Doherty and Nickle, 1926; Hague, 1929]. The governing equation is a Laplace/Poisson/diffusion equation, expressed in electromagnetic field $\mathbf{H}$, Magnetic Scalar Potential (MSP), or Magnetic Vector Potential (MVP).

Magnetic Scalar Potential (MSP) is applicable only if the problem is current free (e.g. in open-circuit PMSM [Zhu et al., 2010b]). Magnetic Vector Potential (MVP) is applicable to any magnetic problem formulation, and directly gives the magnetic flux which eases the computation of electromagnetic flux lines, stress distribution and electrical parameters. Regarding the analytical complexity, both MSP and MVP are scalar fields in 2D problems, while $\mathbf{H}$ is a 2D-vector field. However, in 3D problems, MVP and electromagnetic field have two components to determine (the third one is obtained from divergence theorem) against only one for MSP [Meessen, 2012].

In conclusion, MVP is more adapted to 2D problems [Gysen et al., 2010; Dubas and Espanet, 2009; Lubin et al., 2010], while MSP is dedicated to 3D current free problems [De La Barrière et al., 2012; Meessen, 2012; Youmssi, 2006]. For 3D problems including currents, the governing equation can be expressed in MVP [Gerling and Dajaku, 2003], or directly expressed in electromagnetic field as MVP brings no simplification [Lubin and Rezzoug, 2015].

MSP, noted Φ, and MVP, noted $\mathbf{A}$, are expressed as:

$$\mathbf{H} = -\nabla\Phi \tag{2.6}$$

$$\mathbf{B} = \nabla \times \mathbf{A} \tag{2.7}$$

Poisson equation is solved for domains with magnetic field sources (e.g. surface magnets, slots with current density). Poisson equations for MSP and MVP are:

$$\nabla^2\Phi = \frac{1}{\mu_r}\nabla.\mathbf{M} \tag{2.8}$$

$$\nabla^2\mathbf{A} = -\mu_0\mu_r\mathbf{J} - \mu_0\nabla\wedge\mathbf{M} \tag{2.9}$$

where $\mathbf{M}$ is magnetization, $\mathbf{J}$ is current density, μ_0 is the void magnetic permeability, and μ_r is the relative permeability of the domain.

Laplace equation is the Poisson equation without magnetic sources and is solved in the airgap, and in rotor and stator yokes. The diffusion equation can also be solved for domains with electromagnetic diffusion (e.g. solid rotor of Solid Rotor Induction Machines (SRIMs)), necessary using the MVP or electromagnetic field formulations to account for current presence [Gerling and Dajaku, 2003; Lubin and Rezzoug, 2015].

The potential/field solution is directly expressed in Fourier series. For this reason, ARME is often referred as Fourier analysis or harmonic modeling in many references [Gysen et al., 2010; Sprangers et al., 2016].

However, the ARME is only possible under certain simplifying assumptions. Each physical domain must have the same periodicity (generally 2π) and a simple geometry, expressed in Cartesian/cylindrical coordinates, with homogeneous and linear material. A fortiori, local saturation is neglected but the iron relative permeability can be either finite or infinite [Nogarede et al., 1990]. For radial flux machines, both cylindrical and Cartesian coordinate systems can be considered depending on the real geometry [Gysen et al., 2010].

Granularity level and existing topologies

In slotless machines, the analytical field solution is explicit, and directly expressed in function of the source terms [Nogarede et al., 1990]. ARME includes the time and space harmonics of the rotor and stator MMF [Zhu, 1991]. In case of slotted machines, the airgap can be smoothed into an equivalent slotless airgap by considering an equivalent current sheet distribution. However, slotting harmonics are not included in the flux density spectrum [Zhu, 1991].

Doherty and Nickle [1926]; Hague [1929] seem to be the first developing the ARME in the airgap of electrical machines. This method has been applied to the 2D analysis of SPMSM, which have been industrially used since the early 80's [Boules, 1984]. A SPMSM model based on ARME is illustrated in Figure 2.8, which enables to compute the flux distribution presented in the simple experiment 1.1.2 in Figure 1.2b. A comprehensive review of 2D models of SPMSM based on ARME can be found in [Pfister and Perriard, 2011]. ARME has also been used to model slotless SRIMs in Bolte [1979]; Gerling and Dajaku [2003].

Moreover, the ARME can directly give the 3D magnetic flux density distribution in slotless machines [Gerling and Dajaku, 2003; Youmssi, 2006; De La Barrière et al., 2012], and therefore include 3D effects such as skewing [Jumayev et al., 2016]. The multi-slicing technique can also be used with ARME.

Therefore, the ARME is very fast to compute the airgap flux density distribution. It computes design parameters such as electromagnetic torque, EMF, inductances, etc. [Nogarede et al., 1990]. The analytical formulation in Fourier series makes the ARME

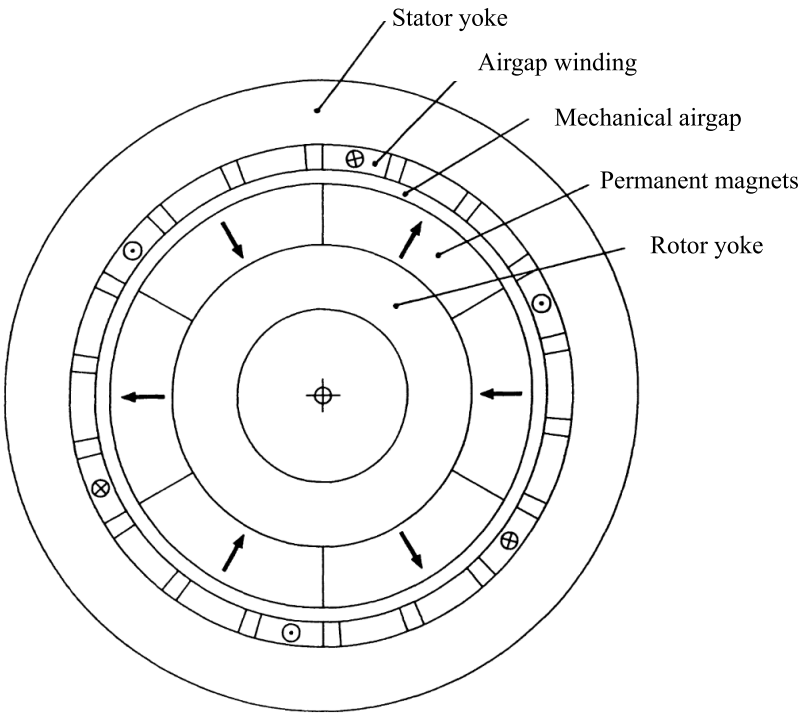

Figure 2.8 – ARME in a slotless SPMSM with airgap windings (translated from Nogarede et al. [1990]).

very suitable for fast electromagnetic and vibroacoustic design of slotless machines, or machines with negligible slotting effects.

2.3.2.3 ARME and 1D relative permeance

In ARME, the main difficulty lies in directly accounting for slotting effects. Zhu [1991] proposes a methodology to include stator slotting effect a posteriori in SPMSM, using a 1D relative permeance function.

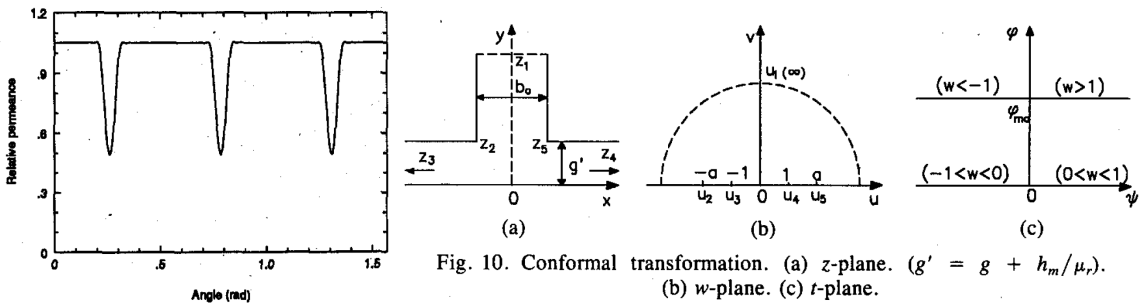

Fig. 10. Conformal transformation. (a) z-plane. ($g' = g + h_m/\mu_r$). (b) w-plane. (c) t-plane.

(a) Stator 1D relative permeance (b) Conformal Transformation (CT).

Figure 2.9 – Stator 1D relative permeance obtained with Conformal Transformation (CT) (from Zhu and Howe [1993])

First, rotor and stator airgap flux densities are computed using the ARME in an equivalent slotless machine. Then, a relative permeance function modulates the airgap radial flux density, such as [Zhu, 1991]:

$$B_\rho(t,\theta) = \Lambda_{S,rel}(\theta) B_\rho^{slotless}(t,\theta) \tag{2.10}$$

where $\Lambda_{S,rel}$ is the relative permeance function and $\hat{B}_\rho$ is the radial flux density computed in the equivalent slotless airgap. $\hat{B}_\rho$ can be also seen as a relative MMF. The 1D relative permeance function is illustrated in Figure 2.9a.

The relative permeance function is analytically computed using the tooth contour method and Conformal Transformation (CT), as did [Carter, 1926] to compute Carter coefficient. A simple model composed of the airgap and a single rectangular slot is considered. In this model, a unitary magnetic potential is located at the boundary between the airgap and the rectangular slot. Then, both airgap and rectangular slot are mapped into a half polar plane in which the slot magnetic potential is resolvable. The slot potential solution is mapped back in the original rectangular domain using the inverse CT. Finally, the airgap potential is computed and contains the slotting effect. The radial relative permeance is obtained by deriving potential as shown by Equation (2.6). The successive conformal mappings are illustrated in Figure 2.9b.

In conclusion, the ARME combined with 1D relative permeance includes both MMF and slotting harmonics [Zhu, 1991] in radial flux density. This is the equivalent of PMMF for SPMSMs. The main drawback is the missing circumferential flux component, although it should not be neglected in SPMSMs with larger airgap and tooth width, especially in case of concentrated windings with low number of teeth.

2.3.3 Semi-analytical methods

In more recent studies, the ARME is generally used along with semi-analytical methods to include slotting effects on both radial and circumferential flux densities, such as SubDomain Method (SDM) or Complex Permeance (CP).

As said in Subsection 2.2.3, semi-analytical methods differ from purely analytical methods by relying on a numerical resolution because there are too many unknowns. They generally have a lower level modeling but some assumptions used in the analytical section remain the same. In particular, magnetic materials are supposed to be linear, isotropic and homogeneous. Geometry is also simplified into an equivalent cylindrical or Cartesian geometry.

The present state of the art deals with the main semi-analytical methods which are used to compute the flux density in electrical machines. Each semi-analytical method include radial and circumferential flux densities. The numerical resolution may introduce numerical problems which are also discussed.

2.3.3.1 ARME and 2D Complex Permeance (CP)

Principle

The Analytical Resolution of Maxwell Equations (ARME) with the 2D Complex Permeance (CP) is the extension of the ARME with 1D relative permeance to the circumferential component. Similarly to 1D relative permeance, the 2D slotless airgap flux density is computed, then modulated by the 2D airgap complex permeance function [Žarko et al., 2006]:

$$\underline{B}(t,\theta) = \underline{\Lambda}^*(\theta)\underline{B}^{slotless}(t,\theta) \tag{2.11}$$

where $\underline{B}$ is the complex flux density, $\underline{B}^{slotless}$ is the complex slotless flux density, and $\underline{\Lambda}^*$ is the complex permeance conjugate such as:

$$\underline{B} = B_\rho + jB_\theta \tag{2.12}$$

$$\underline{\Lambda} = \Lambda_\rho + j\Lambda_\theta \tag{2.13}$$

$$\underline{B}^{slotless} = B_\rho^{slotless} + jB_\theta^{slotless} \tag{2.14}$$

It means that the real part contains the radial information while imaginary part contains circumferential information. $\hat{\underline{B}}$ can be also seen as relative complex MMFs. Radial and tangential permeances are illustrated in Figure 2.10.

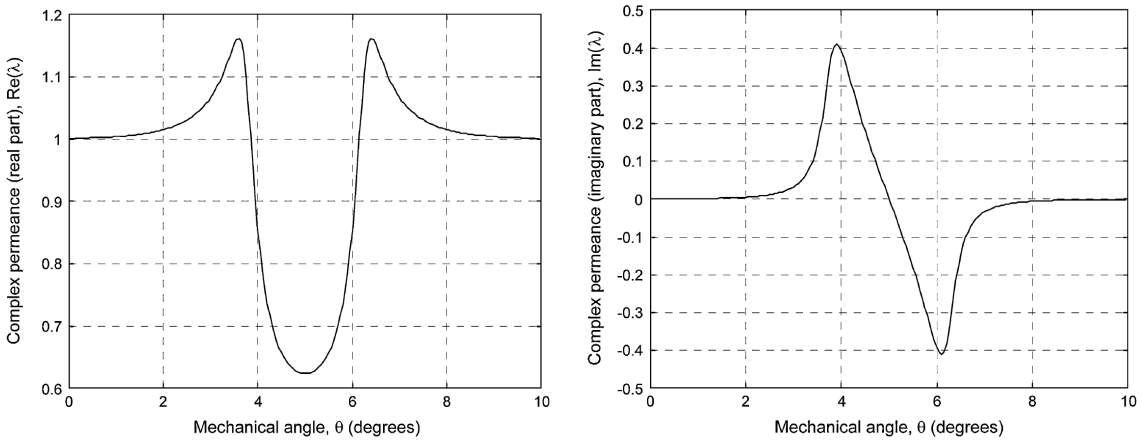

(a) Stator radial permeance

(b) Stator circumferential permeance

Figure 2.10 – Stator 2D complex permeance obtained with Conformal Transformation (CT) (from Žarko et al. [2006]).

Complex Permeance (CP) is obtained using the numerical Schwarz-Christoffel Conformal Transformation (CT), which is a complex function by nature [Žarko et al., 2006]. In fact, mapping the potential solution back to the initial plane requires iterative numerical integrations, hence the semi-analytical designation. In the 1D relative permeance developed in Zhu [1991], the imaginary part of the CT is ignored especially because of the additional computational effort.

Existing topologies

The first models aim at including slotting effect in cogging and electromagnetic torque calculation in SPMSM [Žarko et al., 2006, 2009; Boughrara et al., 2009]. More recently, Alam and Abbaszadeh [2016] include eccentricity in the complex permeance computation.

CP has also been extended to SCIM topologies in O'Connell [2008]. The CP model is strongly coupled with an electric circuit. It gives accurate results for rotor current harmonics, as well as mean radial and circumferential forces. However, there are few results on flux density distribution computation, hence on Maxwell stress distribution.

Numerical aspects and conclusion

The numerical integrations may imply an ill-conditioned system due to singular points, especially at tooth tips [Žarko et al., 2006].

Žarko et al. [2009]; Boughrara et al. [2009] concluded that CP method gives satisfying results for on-load flux density and electromagnetic torque computation. However, there is a non-negligible error in the cogging torque computation compared with FEA [Žarko et al., 2009]. In Zhu et al. [2010c], stress harmonics are computed in a SPMSM and show good agreement with FEA. However, radial and circumferential flux density distributions as well as stress harmonics are only validated for the initial rotor position and not for any rotor position Žarko et al. [2009]; Zhu et al. [2010c].

In O'Connell [2008], electromagnetic quantities are computed for numerous rotor position. However, it is said that computing CT at each position requires most of the computational effort. Although CP method enables to account for radial and circumferential flux density component, no reference except Fakam et al. [2015] has been found to clearly illustrate its relevancy in the fast electromagnetic and vibroacoustic prediction. It is difficult to conclude on the CP applicability to the e-NVH study of electrical machines.

2.3.3.2 ARME and SubDomain Method (SDM)

Principle

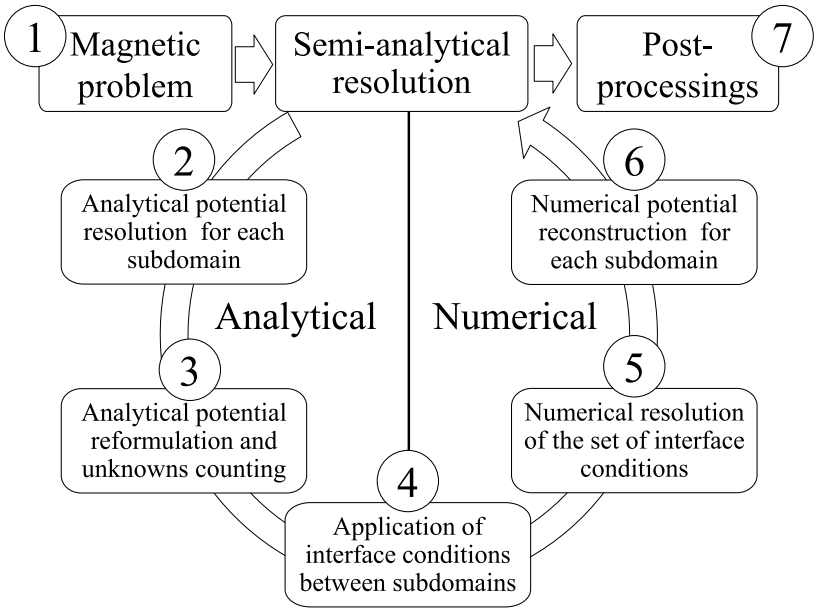

Figure 2.11 – SubDomain Method (SDM) principle.

The SubDomain Method (SDM) based on the ARME directly takes into account slotting effects in the magnetic field solution, contrary to the ARME and 1D relative permeance or 2D CP. The main processing steps to obtain the magnetic field are presented in Figure 2.11.

SDM consists in dividing the problem into physical regions named subdomains in which the ARME is mathematically possible (step ① in Figure 2.11). Figure 2.12a illustrates a subdomain division of a SPMSM, including surface Permanent Magnet (PM) I, the airgap II, stator slot openings i, and stator slots j. Depending on its Boundary Conditions (BCs) and source terms, each subdomain has a specific solution, as it is detailed in Chapter 3. In the example of Figure 2.12a, rotor and stator iron cores are assumed to be infinitely permeable, hence they are external boundaries of the subdomain model. How-

ever, the infinite permeability assumption is no longer compulsory since recent SDM improvements [Dubas and Boughrara, 2017].

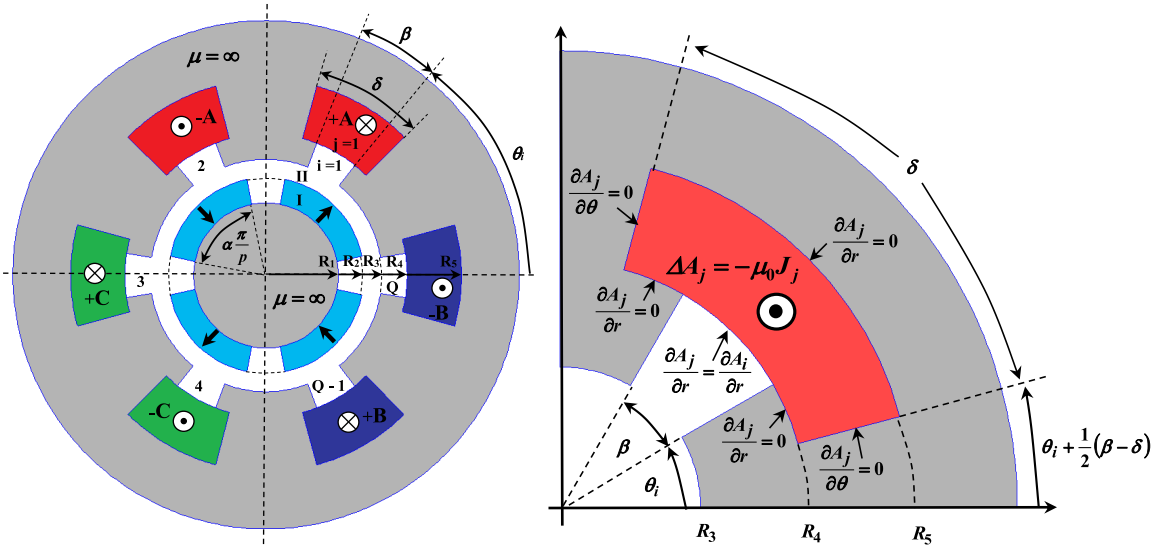

(a) SPMSM 6*s*4*p* subdomains (I, II, i, j) (b) BCs of stator slot subdomain.

Figure 2.12 – Subdomain model of a SPMSM 6*s*4*p* (from Lubin et al. [2011a])

Steps ② to ④ consist in performing the ARME presented in Subsection 2.3.2.2, in addition to potential reformulations specific to the SDM. In each subdomain, the governing equation can be expressed in either Magnetic Scalar Potential (MSP) or Magnetic Vector Potential (MVP). As said in Subsection 2.3.2.2, they should be formulated in Magnetic Vector Potential (MVP) in case of 2D problem. Subdomains must also fulfill the ARME assumptions, such as cylindrical or Cartesian geometry, uniform and linear properties etc [Gysen et al., 2010].

Subdomain model is generally 2D or 2.5D using multi-slicing. 3D models have already been investigated for radial flux structures in Meessen [2012], but the analytical formulation is much more complex and the numerical resolution is much longer than 2.5D models. This is due to the 2D Fourier projections between adjacent surfaces when applying interface continuity at step ④ [Meessen, 2012].

The ARME gives in each subdomain the magnetic potential expressed in Fourier series, each harmonic depending on several unknown constants. In step ③, each potential expression is reformulated to obtain dimensionless expressions. In several publications, potential is also reformulated to facilitate the application of Interface Conditions (ICs) between subdomains (step ④ [Lubin et al., 2010]).

ICs ensure potential and field continuity at each interface between two subdomains. They result in a set of independent equations which enables to find the unknown constants (step ④). If potential solutions of two adjacent subdomains are expressed in a different Fourier basis (e.g. between slots and airgap), it is necessary to project one Fourier basis on the other. This Fourier projection between subdomains is how SDM can account for slotting effects [Zhu et al., 2010b; Lubin et al., 2010]. Furthermore, a finite number of Fourier harmonics is chosen in each subdomains to enable the numerical resolution [Gysen, 2011].

The equation set generally contains too many equations to be analytically solved. Therefore, the linear system of equations is put into matrix form and solved numerically

(step ⑤) [Liu and Li, 2007]:

$$\mathbb{M}\mathbf{X} = \mathbf{S} \tag{2.15}$$

where $\mathbb{M}$ is called topological matrix, $\mathbf{X}$ is the vector of unknown integration constants, and $\mathbf{S}$ is referred as source vector.

Once the unknown constants $\mathbf{X}$ are determined, time and space distribution of magnetic flux density can be computed in each subdomain (step ⑥), especially in the airgap. Then, magnetic stress and torque, flux linkage, Back-Electromotive Force (BEMF), inductances, and iron, magnets and windings losses can be computed from potential and flux density distribution [Pfister et al., 2016; Prieto et al., 2015; Gaussens et al., 2013b]. Because both analytical and numerical resolutions are successively accomplished, the SDM based on the ARME is called semi-analytical method.

Origins

Origins of SDM are intrinsically linked to the ARME evolution towards the estimation of slotting effect, through the development of analytical methods based on ARME and presented in the previous sections. In Bolte [1984], Fourier projections are developed between airgap and stator slots of SCIM, in Cartesian coordinates. In Ackermann and Sottek [1995], the subdomain methodology is developed for a SPMSM with inner/outer rotor in both cylindrical and Cartesian coordinates. However, no numerical validation is given as the conclusion states that model complexity exceeds the computation capabilities.

A simplified SDM with numerical validation appears in the late 2000's, for the modeling of SPMSM in: Cartesian coordinates [Liu and Li, 2007], 2D cylindrical coordinates [Gysen et al., 2008], and polar coordinates [Bellara et al., 2009; Dubas and Espanet, 2009]. However, these models rely on the "One slot per pole approximation" in the IC between stator slots and airgap, which neglects the interaction effect between adjacent slots as noted in Zhu et al. [2010b]; Lubin et al. [2010]. In fact, the model is a superposition of Z_s models where a single stator slot is considered.

The exact SDM applied to SPMSM without simplification is found in three major articles which were almost published simultaneously [Gysen et al., 2010; Zhu et al., 2010b; Lubin et al., 2010]. Lubin et al. [2010] develop an elementary model to provide a better understanding of slotting effect in SDMs. Zhu et al. [2010b] include periodicities in the subdomain model, reformulate the set of interface conditions to reduce the computation time, and consider internal and external rotor topologies. In Gysen et al. [2010], subdomain methodology is unified to any type of 2D coordinate systems and numerical resolution aspects are further discussed, such as the use of dimensionless expressions.

Based on these publications and those published afterwards, the method is generally named SDM but is also referred as "exact analytical model", "harmonic model" or "Fourier-based Model". This multi-designation has been accounted for in the state of the art.

Existing topologies

SDM has mainly be applied to model SM, especially PMSM, due to their popularity in the past decades. A few reference models are cited here, but there are many others featuring various modeling levels. SPMSMs with semi-closed slots, stator and rotor fields,

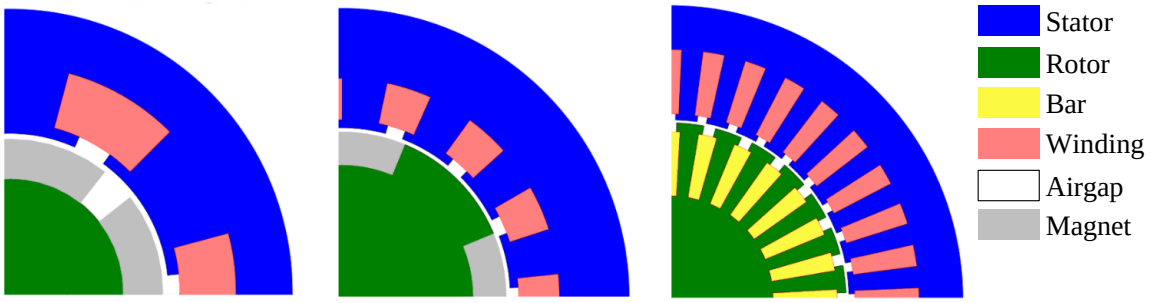

SPMSM *6s4p*
Lubin et al. [2011a]

Inset PMSM *15s4p*
Lubin et al. [2012]

SCIM *36s28r4p*
Boughrara et al. [2015]

Figure 2.13 – Topology examples of subdomain models.

and assuming infinite permeability are modeled in Wu et al. [2011]; Lubin et al. [2011a]. Surface-inset PMSM models with same features can be found in Rahideh and Korakianitis [2012]; Lubin et al. [2012]. IPMSMs are more complex to model due to rotor saturation bridges, however a few models exist for open-circuit V-shape IPMSMs [Shin et al., 2017], spoke-type IPMSMs with infinite permeability [Boughrara et al., 2012] and with finite permeability [Roubache et al., 2018a].

Besides PMSM topologies, other SMs have been modeled using SDM, such as WRSM [Bali et al., 2010], SRM with infinite and finite permeability [Gaussens et al., 2013b; Djelloul-Khedda et al., 2017], SynRM with finite permeability [Sprangers et al., 2015], Flux-Switching Machine (FSM) [Boughrara et al., 2013], PMSMs with embedded magnetic gear [Penzkofer and Atallah, 2015]. Gysen [2011] proposes a framework for the SDM assuming iron infinite permeability that can be applied to various topologies of SMs.

SDM has also been applied to several topologies of IMs, even if there are fewer references on the topic. For SCIMs in particular, the complexity lies in accounting for the double slotting effect, the asynchronous rotor motion and rotor induced current.

In Lubin et al. [2011b], the subdomain model computes eddy-currents in rotor bars generated with a current sheet located at the slotless stator bore. These bar currents are computed by solving the Helmholtz equation in the rotor slots subdomains for each space harmonic of the stator MMF. This enables to get the rotor reaction field directly in the airgap flux density.

In Boughrara et al. [2015], the subdomain model computes the global performances of SCIM, with both current and voltage inputs by using a EEC. Furthermore, this model enables to directly account for space harmonics due to both stator slotting and MMF, by including stator slots subdomains with current density. Rotor bar currents are also obtained by solving the Helmholtz equation. In the stator subdomains and in the airgap, the electromagnetic quantities are assumed to vary at the supply frequency, while they vary at the slip frequency in the rotor subdomains. Current harmonics in rotor bars due to the space harmonics of the stator mmf are therefore neglected. Besides, the method to account for rotor motion and especially to get the time harmonics in the airgap flux density due to rotor slotting is not specified.

In Sprangers et al. [2014a], the subdomain model also includes both rotor and stator slots subdomains. The problem is first solved without considering that the rotor bars are conductive to compute the EMF in each bar. Eddy-currents are deduced by solving the EEC, whose parameters are computed using the analytical expressions of resistance and inductances detailed in [Pyrhönen et al., 2008]. Rotor currents are then injected in

a second simulation to get the rotor reaction field in the airgap flux density. Sprangers et al. [2014b] extends this model by coupling subdomains and EEC equations. These equations are solved simultaneously with a transient time-stepping method to directly get the rotor reaction field in the airgap. This second method provides accurate results in comparison with FEM regarding torque ripple and harmonics of induced rotor currents. However, this subdomain model requires to compute a numerical transient first to reach steady state and rotor induced currents are less accurate than those directly obtained with Helmholtz equation.

Other topologies are modeled by SDM, such as Solid Rotor Induction Machines (SRIMs) in Boughrara et al. [2014], Doubly-Fed Induction Machines (DFIMs) using a coupling with MEC to include saturation [Wang et al., 2016], and dual rotor (squirrel-cage and PM rotors) topologies in Dalal et al. [2016].

No paper dealing with subdomain models of brushed DCMs has been found in the literature, but there is apparently no SDM intrinsic limitation to the modeling of such machine.

Granularity level

SDM can model both magnet and current sources. It accounts for any magnetization shapes such as radial, parallel or Hallbach magnetization. Magnets have an isotropic and uniform relative permeability and a linear $\mathbf{B}(\mathbf{H})$ curve.

Concerning the armature reaction fields, the windings can have (non)-overlapping single/double layer and are usually described by a connection matrix. It is possible to include current harmonics, such as PWM or induced stator harmonics due to rotor slotting and MMF with a EEC coupling [Hannon et al., 2015]. For IM, induced currents can be directly solved with Helmholtz equation or included with a circuit coupling, as said previously. Assuming linear permeability, it is possible to solve stator and rotor fields at once or separately. For example, Figure 1.9 represents stator and rotor airgap fields computed with the SDM. As said in Subsection 1.3.3, the stator/rotor fields separation enables to diagnose stress harmonics origins.

In most of subdomain models, iron is assumed to have infinite relative permeability in order to obtain an analytical solution in slots [Lubin et al., 2010; Gysen et al., 2010; Zhu et al., 2010b]. In fact, infinite permeability ensures that the tangential field to any iron interface is zero. In this case, iron parts are external boundary conditions of the subdomain problem and the potential inside iron is unknown. However, three recent analytical formulations enable to solve potential equation in iron:

— In Sprangers et al. [2016], slots and teeth are in the same subdomain, in which a stepwise relative permeability function is introduced. The MVP equation is then reformulated including the non-uniform permeability, leading to a new analytical solution.

— In Roubache et al. [2017], a non-periodic analytical solution is introduced in teeth and slots. Interface conditions between slots and teeth are solved using iterative Taylor polynomial expansions.

— In Dubas and Boughrara [2017], teeth and slots potential are solved by superposing two eigenvalue problems, the first in the circumferential direction (classic problem) and the second in the radial direction (new problem).

This last formulation has been simultaneously developed during this thesis and is further explained in Chapter 3 and Section 4.3. Besides, Figure 1.6 shows the flux density distribution obtained with this finite permeability SDM.

Finally, it is possible to mesh the machine topology in elementary subdomains (as in MEC) and potentially account for local saturation [Roubache et al., 2018b].

These methods enable to include global or local saturation, but the computation time is hugely increased, due to the fact that integration constants in iron parts must be also solved numerically. The numerical implementation of SDM with finite permeability should therefore be optimized in order to compete with non-linear FEA in terms of performances [Roubache et al., 2018b].

SDM enables to compute UMP due to asymmetric windings Zhu et al. [2013], or magnet manufacturing tolerances. SDM includes several fault and dysfunctions modeling, such as eccentricity using a first order perturbation method [Fu and Zhu, 2012] or superposition method in Li et al. [2015]. Manufacturing tolerances such as pole shifting or uneven magnetization in PMSMs can be further investigated [Pina et al., 2016]. It is also possible to simulate defective/broken bars and open phases in stator and/or rotor windings [Roubache et al., 2016].

Reduction techniques such as rotor and stator skewing can be investigated using 2.5D multi-slices subdomain models [Xia et al., 2015]. It is also possible to add notches [Oner et al., 2016] or magnetic wedges in slot openings. Besides, current injection and load impacts can be investigated with SDM, as it enables to compute torque and estimate losses.

Numerical aspects and conclusion

Numerical problems are frequently pointed out in the SDM literature and are addressed in particular in Gysen [2011]; Tiegna et al. [2013]. The first numerical challenge of the SDM is to find the best harmonics number in each subdomain as a compromise between accuracy and computation time. Choosing a low number of harmonics gives inaccurate and oscillatory solutions, but choosing a too large number of harmonics may cause the topological matrix to be ill-conditioned. Such problem can be avoided with the potential reformulation under dimensionless expressions [Gysen, 2011].

As explained in Subsection 2.2.4.4, SDM is subject to Gibbs phenomenon in singular points, such as teeth and slot corners. However, the solution is always smoother in the middle of subdomains, which is in favor of the computation of electromagnetic field and stress in the middle of the airgap [Lubin et al., 2011a].

The SDM is a very powerful tool for the fast magnetic computation of various topologies of electrical machines. The method accounts for many harmonic sources and enables to implement various reduction techniques. Another main advantage is the formulation in Fourier series which enables to directly investigate the harmonic content of the magnetic stress distribution. Compared with FEM and MEC, SDM does not rely on a mesh formulation and prevents from introducing mesh artifacts in the flux density spectrum which is a major advantage for vibroacoustic study.

For the same granularity level, SDM is generally much faster than FEM for PMSM [Lubin et al., 2011a; Sprangers et al., 2014b]. Moreover, SDM computation time can be optimized using techniques discussed in Subsection 4.2.3. For these reasons, SDM has

already been used in vibroacoustic studies especially for topological optimization [Boisson, 2014; Verez, 2014]. For example, in Boisson [2014], the proposed subdomain model is used to investigate the influence of geometrical parameters on torque and noise level, at variable speed, over 10000 simulated topologies.

The main limits are the difficulties to include saturation and 3D-effects, although finite-permeability subdomains have been recently introduced to partially overcome these difficulties [Sprangers et al., 2016; Dubas and Boughrara, 2017].

2.3.3.3 Magnetic Equivalent Circuit (MEC) method

Principle

The Magnetic Equivalent Circuit (MEC) is the magnetic analogy of the electric circuit modeling. Considering an elementary magnetic circuit, the magnetic Ohm's law, called Hopkinson's law, becomes:

$$\mathscr{F} = \mathscr{R}\Phi \tag{2.16}$$

where $\mathscr{F}$ is the Magnetic Scalar Potential (MSP) (in Ampere), $\mathscr{R}$ is the circuit reluctance and Φ is the magnetic flux (in Weber) flowing in the circuit. The MEC method consists in discretizing the magnetic problem into a reluctance network fed by the different MMF and/or flux sources [Ostović, 1989]. MEC is also referred as reluctance network or lumped magnetic model.

MEC methodology is naturally similar to electric circuit methodology. First, reluctances values are computed based on the flux paths in the machine. Then, MMFs are evaluated with Ampere's theorem and disposed either in the teeth or in the yoke. Problem unknowns are therefore MSP values at each node and flux values in each branch. The solution is obtained by applying Kirchhoff's circuit laws. This results in a linear matrix system under the form [Benlamine et al., 2016]:

$$\mathbf{S} = \mathbb{R}(\mathbf{X})\mathbf{X} \tag{2.17}$$

where $\mathbf{S}$ is the vector of magnetic sources, e.g. containing MMFs and remanent fluxes, $\mathbb{R}$ the reluctance matrix, $\mathbf{X}$ the vector containing unknown potentials and fluxes. $\mathbb{R}$ naturally depends on flux values in non-linear materials to account for saturation, implying an iterative non-linear resolution [Benlamine et al., 2016].

Existing topologies

Thanks to its generic formulation, the MEC method established itself as a powerful semi-analytical model of electrical machines, especially to account for local saturation [Ostović, 1989]. The MEC method provides a fast and accurate estimation of radial and circumferential flux densities in PMSM [Bracikowski et al., 2012]. In particular, the ability to compute local saturation makes it very relevant to model flux barriers in IPMSM and SynRM [Kemmetmuller et al., 2014; Tessarolo et al., 2014] and pole saturation in WRSM and SRM [Utegenova et al., 2018; Peng and Gyselinck, 2016].

It is also used for the modeling of induction machines [Vandevelde and Melkebeek, 1997; Sudhoff et al., 2007]. In particular, Vandevelde and Melkebeek [1997] apply MEC to the computation of radial magnetic stress harmonics and show good results in comparison with FEA and experiments.

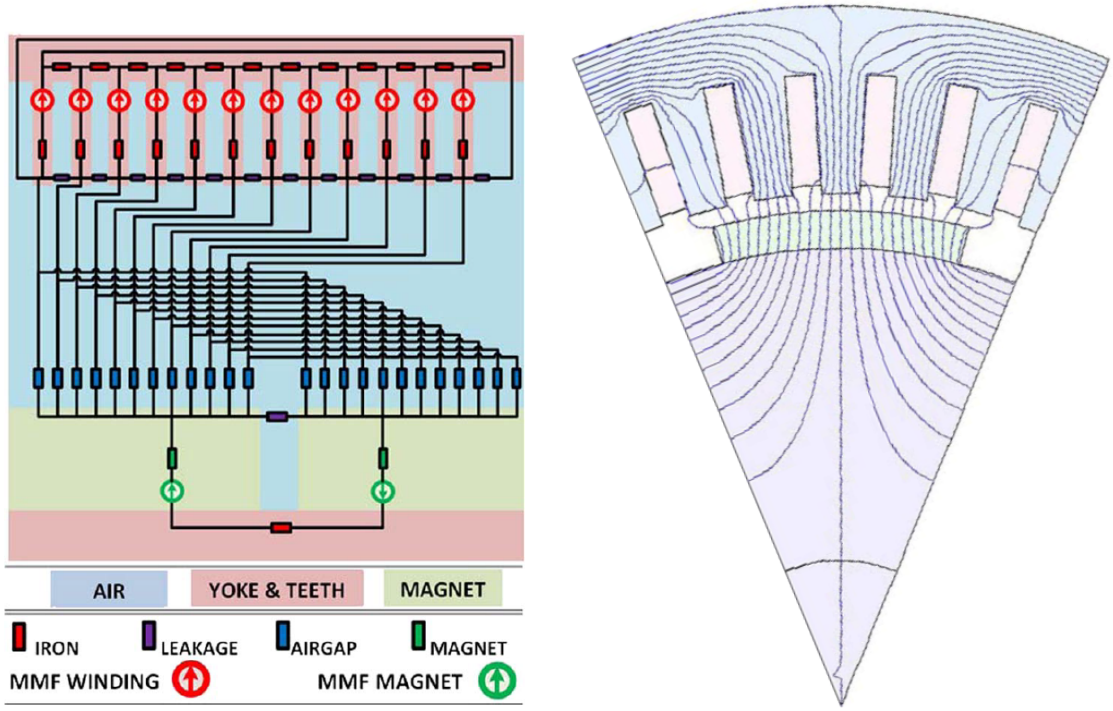

(a) Magnetic Equivalent Circuit (MEC) (b) Open-circuit flux paths computed with FEA

Figure 2.14 – Example of SPMSM Magnetic Equivalent Circuit (MEC) (from Bracikowski et al. [2012]).

Granularity level

Furthermore, MEC can account for 3D effects by adding a magnetic circuit in the axial direction [Hoang et al., 2014; Faiz and Ghasemi-Bijan, 2015]. Compared with previous analytical models, the 3D MEC computes the axial flux density and may consequently include all the axial effects. However, computation time is logically much more important.

Finally MEC enables heat transfer, electric, magnetic and vibroacoustic coupling using multi-physics lumped models [Bracikowski et al., 2012].

Numerical aspects and conclusion

For small MECs, the mesh contains a few loops and then the solution can be found analytically [Zhu et al., 2009]. However, such MEC is not accurate enough to be used in vibroacoustic studies. In fact, the main difficulty is to mesh the airgap in order to accurately model the flux paths when poles pass in front of teeth, for each rotor position. Most of the reluctances are therefore concentrated in the airgap to account for slotting effects and local saturation at tooth tip [Bracikowski et al., 2012].

Due to the large number of unknowns and the non-linear resolution, most of MECs are consequently solved with numerical methods. In fact, the reluctance matrix is very close to those obtained with the FEM with non-zero terms only on diagonal and few subdiagonals. Numerical resolution relies on the same algorithms dedicated to sparse matrices. Besides, non-linear algorithms (mostly fixed-point and Newton-Raphson algorithms) are also transposed to MEC resolution [Benlamine et al., 2016; Utegenova et al., 2018].

The main drawback of MEC is the prior study of flux paths to build the reluctance net-

work for each rotor position. A few Finite-Element Analysis (FEA) snapshots along with interpolation can provide this information [Bracikowski et al., 2012; Zhu et al., 2009]. The flux paths can also be analytically asserted to speed up calculations [Gyselinck and Sabariego, 2013]. Besides, the moving band technique is adapted from FEM to prevent from recomputing reluctances for each time step [Sadowski et al., 1992b; Utegenova et al., 2018]. Finally, the analytical estimation of reluctances also require mesh elements with simple geometric shapes (rectangular or cylindrical), which may imply geometry simplification.

Building a fine MEC for vibroacoustic prediction may be a tedious task, regarding numerical challenges in Subsection 2.2.4. In particular, MEC discretizes time and space domains and is therefore mesh-sensitive. It may be inaccurate to assert high time and spatial harmonics of flux density. However, the main advantages are local saturation estimation and the ability to include axial effects with 2.5D and 3D models.

2.3.4 Numerical methods

There are many numerical methods for the electromagnetic problem resolution. The main numerical method is the Finite-Element Method (FEM). Among the other methods, one can cite the Boundary-Element Method (BEM) [O'Connell, 2008], the Finite Differences Method (FDM), the Finite Integration Method (FIM) [Korecki, 2009], and the Spectral Element Method (SEM) [Curti et al., 2017]. However, all of these methods remain very marginal compared with FEM.

FEM has certainly the lowest granularity level, as it enables to include any phenomenon required in e-NVH design. It accounts for 3D complex geometries [Tan-Kim et al., 2015], non-linearities such as saturation, non-linear circuit coupling, hysteresis, non-homogeneous and anisotropic materials [Ma et al., 2015], faults and dysfunctions etc. Therefore, FEM is applied to any machine topologies and can further investigate passive and active reduction techniques.

Thanks to its versatility, FEM could be used as a black box for the electromagnetic and vibroacoustic design of electrical machines. However, vibroacoustic simulations require a high time and space discretization, which makes FEM computation time rather long at best, prohibitive at worst and not suitable to early design stages (cf. Subsection 1.6.1). In addition to the computational effort, FEM may also introduce numerical errors in the solution due to time and space discretizations (see Subsection 2.2.4).

For these reasons, many works have intended to reduce the computational effort of FEM and erase mesh inaccuracies. For example, the sliding band techniques enables to use the same rotor and stator meshes for each time step, and keep the same mesh pattern in the airgap. In Boesing [2013], saturation is computed for one time-step and extrapolated to the others. Computation time can also be reduced with Model Order Reduction techniques [Henneron and Clenet, 2014].

2.3.5 Hybrid methods

An hybrid method consists in combining several (semi-)analytical and/or numerical methods to obtain a better compromise between granularity level and computation effort. Hybridization can be sequential, meaning the different models are successively

run, or intrinsic, meaning the different model unknowns are coupled and solved altogether. Historically, hybrid methods firstly aimed at include global/local saturation in analytical models. The following combinations can be found in the literature:

— Magnetic Equivalent Circuit (MEC) and SubDomain Method (SDM): intrinsic hybrid method whose aim is to model ferromagnetic parts with MEC to include local saturation and model linear parts with SDM [Ghoizad et al., 2007; Ouagued et al., 2015]. This hybridization enables to extend SDM to DCMs in Bazhar et al. [2017] and open-circuit IPMSMs in Zhang et al. [2017].

— Finite-Element Method (FEM) and SDM: also includes local saturation and complex geometries using FEA [Lee et al., 1991].

— MEC and Complex Permeance (CP): intrinsic hybrid method to include local saturation in complex permeance function [Hanic et al., 2016]. This hybridization enables to extend complex permeance to SynRM topologies [Tessarolo, 2015].

— Finite-Element Method (FEM) and CP: sequential hybrid method which consists in computing numerical complex permeance using FEA. In Fakam et al. [2013], this hybridization is used to include the effect of magnetic wedge in the complex permeance function.

— SDM and CP: sequential hybrid coupling which consists in computing the complex/relative permeance using SDM [Zhu et al., 2010a; Gaussens et al., 2013a]. The advantage is to compute complex permeance without Conformal Transformation (CT), and include for example eccentricity in CP which is much simpler than including eccentricity in the original subdomain model.

— Analytical Resolution of Maxwell Equations (ARME) and Permeance/MagnetoMotive Force method (PMMF): sequential hybrid coupling which consists in computing rotor and stator MMF and permeances using ARME [Doherty and Nickle, 1926; Boules, 1984], and injecting it in the fast PMMF model. This hybrid coupling is similar to ARME with 1D relative permeance.

— Permeance/MagnetoMotive Force method (PMMF) and Finite-Element Method (FEM): sequential hybrid coupling which consists in computing rotor and stator permeances using FEM and injecting it in the fast PMMF model, as it can be done in MANATEE [2018].

2.3.6 Choice of the electromagnetic method

The main conclusion is that currently no magnetic model comes out on top for all the retained e-NVH criteria, and a choice is necessary made depending on the studied topology and the required granularity level. A synthesis of the state of the art is proposed in Table 2.1, with a qualitative comparison of the discussed magnetic models regarding the main e-NVH criteria. The comparison is made regarding the models before 2016, i.e. for example before the possibility to include global saturation in the SDM as done in this thesis and thanks to the parallel work of Sprangers et al. [2016]; Dubas and Boughrara [2017]. Besides, the 1D relative permeance is not represented in Table 2.1, but it has exactly the same qualities as PMMF except it is dedicated to SPMSMs modeling.

The choice finally lies in between the semi-analytical SDM and MEC to complement PMMF and FEA which are already available in MANATEE. The main drawback of the SDM is the lack of saturation, but it is faster and more accurate to compute Maxwell stress harmonic, since it relies on a harmonic formulation while MEC relies on spatial

	PMMF	CP	SDM	MEC	FEM
Existing topologies	- - (SCIM)	- (SPMSM SCIM)	+ (All except IPMSM)	+ (All)	++ (All)
Dimension	1D	2D	2D	3D	3D
Computation time versus discretization	++	+	+	- -	- -
Saturation	Global	No	No	Local	Local
Geometry simplification	- (Only airgap)	- (Only airgap)	+ (Cart./Cyl. subdomains)	+ (Cart./Cyl. reluctances)	++ (No simplifications)
3D effects	-	-	-	+	+

Table 2.1 – Qualitative comparison of magnetic models used to compute Maxwell stress regarding e-NVH performances criteria (before 2016).

mesh discretization. The choice is finally made to extend the SDM in MANATEE to the other topologies of synchronous and induction machines, and focus on the subdomain modeling of on-load SCIMs and IPMSMs, and on the possibility to account for saturation. Besides, it is possible to couple SDM with both MEC and FEM to take benefits of the airgap harmonic formulation provided by SDM and of local saturation in iron cores provided by MEC.

2.4 Mechanical and acoustic modeling for vibroacoustic study

2.4.1 Computation of magnetic stress distribution

There are several methods to compute stress harmonics acting on the external structure of electrical machines Sadowski et al. [1992a]; Barre [2003]. Based on literature, the main methods are the Maxwell Stress Tensor (MST) which adapts to any electromagnetic model, and Virtual Work Principle (VWP) mostly for numerical FEM [Coulomb and Meunier, 1984; Bossavit, 2011]. Other stress computation methods such as equivalent currents and equivalent magnetic masses could be applied, however without any added value for electrical machines as explained in Barre [2003].

2.4.1.1 2D MST computed in the airgap

The Maxwell Stress Tensor (MST) is recall in Appendix A.2. From Equation (A.1), MST components can be seen as a magnetic stress (in Newton per square-meter [N/m^2]) which locally applies on both rotor and stator surfaces [Henrotte and Hameyer, 2004; Bossavit, 2011]:

$$\sigma_\rho(t,\theta) = \frac{{B_\rho}^2 - {B_\theta}^2}{2\mu_0} \tag{2.18}$$

$$\sigma_\theta(t,\theta) = \frac{B_\rho B_\theta}{\mu_0} \tag{2.19}$$

where σ_ρ and σ_θ are respectively the radial and circumferential components of the airgap magnetic stress, such as:

$$\sigma(t,\theta,z) = \sigma_\rho \mathbf{e}_\rho + \sigma_\theta \mathbf{e}_\theta \tag{2.20}$$

Even if MST has a radial component, its components do not depend on ρ-coordinate due to the fact that MST has been computed in the middle of the airgap.

If radial flux density is computed from 1D magnetic model, such as PMMF and ARME with 1D relative permeance, the MST must be simplified into:

$$\sigma_\rho(t,\theta) \approx \frac{{B_\rho}^2}{2\mu_0} \tag{2.21}$$

This further implies that the effect of circumferential flux density on radial stress and the effect of circumferential stress on radial vibrations through tooth bending motion are neglected.

In case of multi-slices model (defined in Subsection 2.2.4.3), the simplified MST expressions (2.18)-(2.21) can be applied for each slice. Therefore, the multi-slicing approach enables to include the variation of radial and circumferential stresses in the axial direction, which is for example due to skewing.

However, the multi-slicing approach along with 2D MST does not include the axial flux density, and therefore the axial stress. The axial component should be included with 3D MST in case axial stress cannot be neglected.

The time and space harmonic content of the magnetic stress is obtained by performing a complex 2D Fourier Transform (FT) on the MST:

$$\sigma_x(t,\theta) = \mathrm{Re}\left[\sum_{k=0}^{k=+\infty}\sum_{r=-\infty}^{r=+\infty} \underline{\sigma}_x^{kr} e^{j\left(2\pi k f_s t - r\theta\right)}\right] \tag{2.22}$$

with $x \in \rho,\theta$ and where $\underline{\sigma}_x^{kr}$ is the complex magnitude of the stress wave, such as $\underline{\sigma}_x^{kr} = \sigma_x^{kr} e^{j\phi_x^{kr}}$, taking the notation used to define rotating stress waves in Subsection 1.3.2. In 2D, each stress harmonic is described through its couple (k,r), assuming zero axial order $l = 0$ due to the axial invariance. The fact that MST has been computed at a specific radius explains why MST spectrum has only circumferential and axial wavenumbers.

2.4.1.2 MST projection on slotted structures

As explained in Subsection 1.4, the airgap magnetic flux density does not continuously apply on a slotted structure. In fact, they are concentrated at the interface between airgap and teeth [Boesing, 2013]. From MST and continuity equations between two medias, magnetic stress at this interface is necessary normal [Le Besnerais, 2008]. Therefore, radial stress is due to the normal stress component applying on tooth tip and circumferential stress results from the normal stress component applying on tooth sides. As magnetic saturation has an impact on the airgap flux density near the saturating tooth, it is globally included in the MST [Pile et al., 2018].

Based on MST, there are three main approaches to get the Maxwell stress distribution directly applying on the ferromagnetic parts. First, the stress distribution computed with the MST on the airgap cylinder can be directly reported on the slotted structure as a first approximation, which assumes that teeth do not exist in the mechanical model and

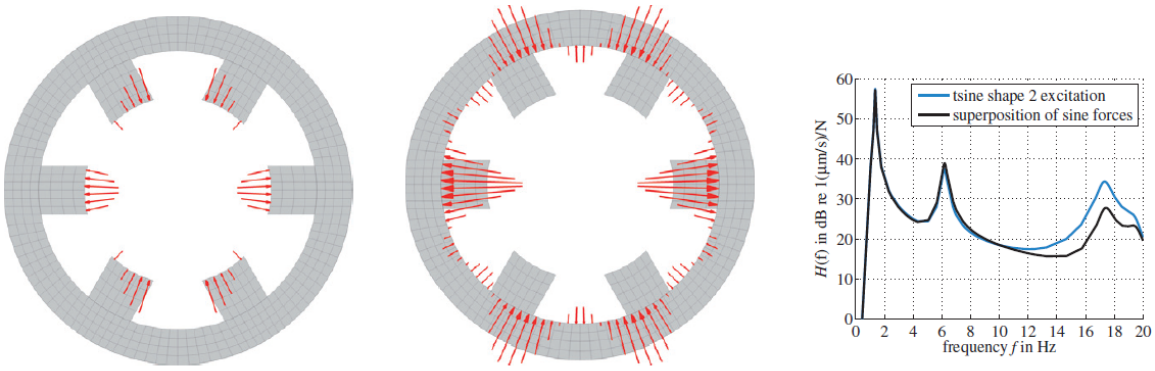

(a) Tsine force

(b) Sine force approximation of tsine force

(c) Response comparison

Figure 2.15 – Continuous stress distribution ("sine force") versus tooth resultant force distribution ("tsine force") [Boesing, 2013].

that the airgap flux density is the same in the airgap middle or at the interface with the structure.

This is the first and most common method in e-NVH literature and in the historical references [Alger, 1953; Jordan, 1950; Timar, 1989], for mainly two reasons. First, it only requires to determine the airgap flux density, at least the radial component to estimate the radial stress, which can be computed using fast 1D analytical electromagnetic models. Secondly, the MST computed in the airgap is also convenient to carry Fourier Transforms (FTs) and get the stress harmonic content. However, this approach has not been rigorously validated for any electrical machines.

The second approach consists in computing the local stress applying on each tooth Boesing [2013]. Either the stress distribution comes from the MST which is computed along a path enclosing the tooth, as shown in Figure 2.16b, or it comes from the airgap stress projection on each tooth Boesing [2013]. The first and second methods are illustrated in Figure 2.15. It is shown that structural responses are almost identical up to 10 kHz, independently of the excitation shape [Boesing, 2013].

The third approach consists in modeling the magnetic excitation at each tooth tip with lumped forces, including radial and circumferential forces, as well as resultant moment [Sizov et al., 2012]. Lumped forces are computed by integrating the MST on the same kind of paths used for the second approach. The second and third methods are illustrated in Figure 2.16a, where the red dots indicate the lumped radial force value. It is shown that both approaches give an airgap excitation waveform which is dominated by the wavenumber $r = 2$. However, the difference in structural response due to lumped force loading or stress loading is not investigated in [Sizov et al., 2012].

In Boesing [2013], it is concluded that lumped forces and stress formulations should be ideally equivalent. However, the physical meaning of local force density obtained from MST, meaning the mathematical validity of deducing Equations (2.18)-(2.19) from Equations (A.3)-(A.4), is still being debated. In comparison with Virtual Work Principle (VWP), Pile et al. [2018] show that the MST should be used with lumped forces rather than stress distribution at tooth tip. Besides, the local saturation effect may not be correctly included in the local MST formulation. Including saturation is still a research area [Pile et al., 2018].

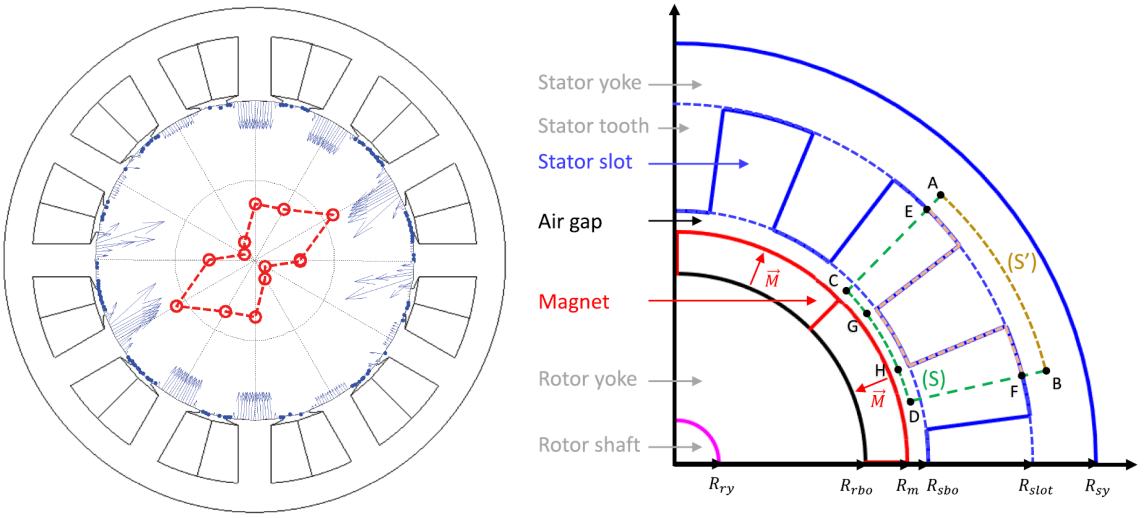

(a) Lumped forces vs. tooth tip stress distributions in a PMSM $12s10p$ [Sizov et al., 2012]

(b) Tooth contour paths in dotted lines [Pile et al., 2018]

Figure 2.16 – Lumped forces versus stress distributions obtained with MST for several integration paths enclosing stator teeth.

2.4.1.3 Virtual Work Principle (VWP) inside the structure

The VWP has been developed to compute the Maxwell stress distribution in FEM by Coulomb and Meunier [1984]. It computes the elementary force applied at each node of the studied domain, including local saturation phenomenon. The force distribution obtained with VWP, also called nodal force, is illustrated in Figure 2.17 for linear and saturated cases. In non-saturated case (cf. Figure 2.17a), the nodal forces are exactly located at the tooth tip and zero elsewhere. It is shown in Figure 2.17b that nodal forces appears inside stator tooth in presence of magnetic saturation. If needed, resulting forces and moments applied on each tooth can be computed by integrating nodal forces [Coulomb and Meunier, 1984].

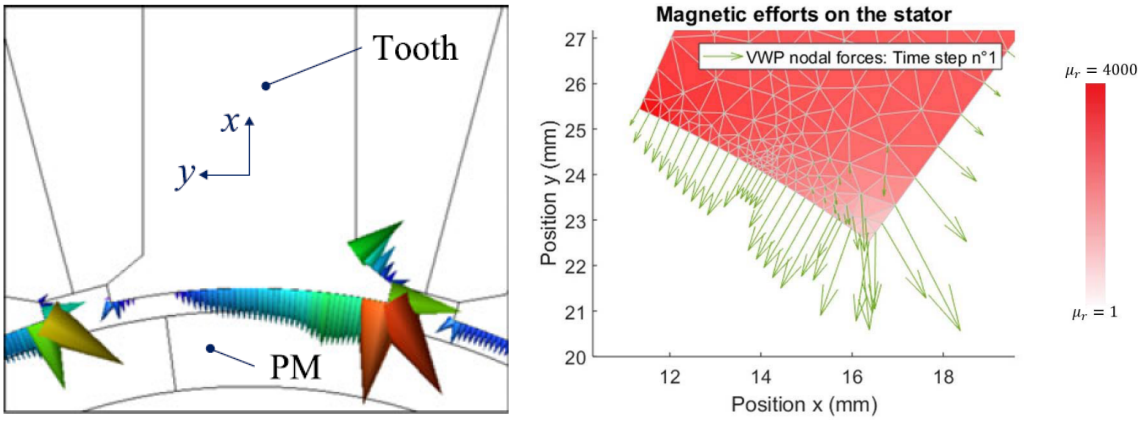

(a) Linear case [Zou et al., 2017]

(b) Saturated case [Pile et al., 2018]

Figure 2.17 – Nodal force distribution obtained with VWP in linear and saturated cases.

The main advantage of the VWP is to directly compute force distribution inside the structure, which can be converted in stress distribution by dividing with each elementary surface area. Contrary to the local MST based on a mathematical tensor development, the VWP formulation is based on local physical formulation of magnetic stress [Bossavit,

2011]. It is more accurate but logically more costly in terms of numerical efforts as it requires a transient analysis [Sizov et al., 2012] and fine time and space discretizations [Zou et al., 2017; Pile et al., 2018].

2.4.2 Mechanical and acoustic models

2.4.2.1 Electromagnetic Vibration Synthesis (EVS)

As said in Subsection 1.4.1, e-NVH mainly results from the radial vibrations of the external structure of the electrical machine.

In the Electromagnetic Vibration Synthesis (EVS) technique (cf. Subsection 2.2.2), the overall displacement response of the external structure is obtained by summing all the displacement harmonics defined by Equation (1.13), which results in computing the complex 2D FT of radial displacement Boesing [2013]; Roivainen [2009]; van der Giet [2011]:

$$u_\rho(t,\theta) = \mathrm{Re}\left[\sum_{k=0}^{k=+\infty}\sum_{r=-\infty}^{r=+\infty} \underline{\mathrm{U}}_\rho^{kr}\, e^{j\left(2\pi k f_s t - r\theta\right)}\right] \tag{2.23}$$

where $\underline{\mathrm{U}}_\rho^{kr}$ is the complex magnitude of the displacement harmonic at (kf_s, r), such as $\underline{\mathrm{U}}_\rho^{kr} = \mathrm{U}_\rho^{kr} e^{j\varphi_\rho^{kr}}$. The complex 2D FTs of radial vibrations is also introduced:

$$v_\rho(t,\theta) = \mathrm{Re}\left[\sum_{k=0}^{k=+\infty}\sum_{r=-\infty}^{r=+\infty} \underline{\mathrm{V}}_\rho^{kr}\, e^{j\left(2\pi k f_s t - r\theta\right)}\right] \tag{2.24}$$

where $\underline{\mathrm{V}}_\rho^{kr}$ is the vibration complex magnitude, which is expressed from displacement complex magnitude such as:

$$\underline{\mathrm{V}}_\rho^{kr} = j2\pi k f_s \underline{\mathrm{U}}_\rho^{kr} \tag{2.25}$$

due to the derivative relationship (1.14) between displacement and vibrations.

As the mechanical structure is linear (cf. Subsection 1.4.1), the complex magnitudes of displacement and stress harmonics with same couple (kf_s, r) can be linked by a transfer function, which is called Frequency Response Function (FRF), or unit-wave response function [Roivainen, 2009]. From Subsection 1.4.1, radial displacement is only due to radial and circumferential stress harmonics, such as [van der Giet, 2011]:

$$\underline{\mathrm{U}}_\rho^{kr} = \underline{\mathrm{FRF}}_{\rho,\rho}^{kr}\, \underline{\sigma}_\rho^{kr} + \underline{\mathrm{FRF}}_{\rho,\theta}^{kr}\, \underline{\sigma}_\theta^{kr} \tag{2.26}$$

where $\overline{\mathrm{FRF}}_{\rho,\rho}$, called radial FRF, is the FRF between radial displacement and the radial excitation harmonic and $\overline{\mathrm{FRF}}_{\rho,\theta}$, called circumferential FRF, is the FRF between radial displacement and the circumferential excitation harmonic [van der Giet, 2011]. The FRF notion can be actually defined as the complex displacement of the external structure subject to a unit-magnitude rotating stress wave of couple (kf_s, r), meaning such as $\underline{\mathbf{F}}^{kr} = 1$ [Roivainen, 2009].

FRFs especially account for potential resonances between stress harmonics and structural modes. In addition to modal parameters, the FRF strongly depend on the boundary conditions of the structure, which are defined in Subsection 1.4.3. In Subsections 2.4.2.2 and 2.4.2.3, FRFs are computed with fast analytical models under certain assumptions, and numerical models using FEA. FRFs can also be measured by EMA, using a hammer

shock or a vibrating pot, or by Operational Modal Analysis (OMA), using the real machine excitation during operation.

2.4.2.2 Analytical FRF based on equivalent cylinders

In analytical models, FRFs are generally limited to the radial component and do not account for the axial wavenumber l [Gieras et al., 2006]. Besides, the excitation frequency is a continuous quantity, noted f, such as $f = kf_s$ with f_s arbitrary varying. Therefore, displacement and stress complex magnitudes are noted $\underline{U}^{fr}$ and $\underline{F}^{fr}$.

Assimilating the structure to an equivalent isotropic and homogeneous cylinder, the analytical FRF is a second order transfer function depending on the natural frequency f_{mn} and damping ratio ξ [Gieras et al., 2006]:

$$\underline{\mathrm{FRF}}^{fr}_{\rho,\rho} = \frac{\underline{U}^{fr}_s}{1-\left(\frac{f}{f_m}\right)^2 + j2\xi_m\frac{f}{f_m}} \tag{2.27}$$

where $\underline{U}^{fr}_s$ is the static displacement due to a unit stress wave $\underline{F}^{fr} = 1$, and f_m and ξ_m are the natural frequency and modal damping of structural mode (f_m, m), with $m = r$. Analytical FRFs are illustrated in Figure 2.18 for the SPMSM $12s10p$ prototype.

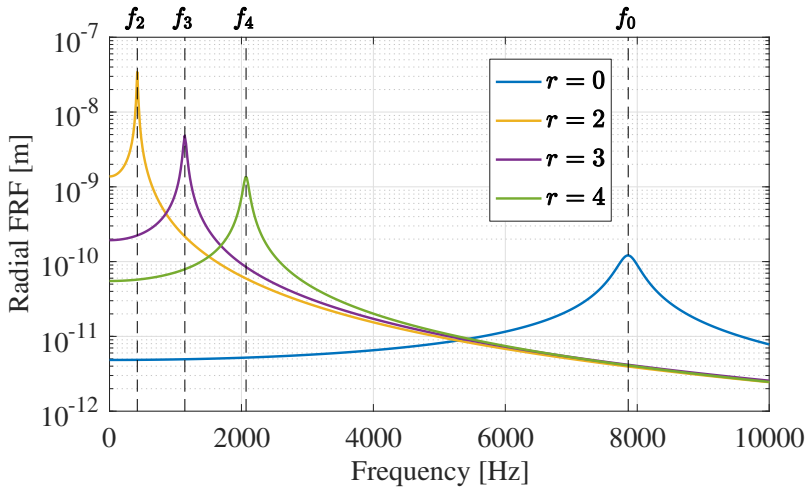

Figure 2.18 – Analytical radial FRFs of SPMSM $12s10p$ prototype computed from Equations (2.27), (A.6)-(A.11) and with $\xi_m = 2\%$.

Therefore, the modal basis must be determined before computing the analytical FRF. The modal analysis can be performed analytically based on equivalent cylinders and shell theories [Soedel, 1993; Gieras et al., 2006]. There are many references giving analytical expressions of natural frequencies, depending on the structure homogeneity and orthotropy. The influence of boundary conditions, teeth, and windings on modal basis have also been deeply investigated [Gieras et al., 2006; Verez and Espanet, 2015]. Finally analytical expressions have been developed for longitudinal modes [Gieras et al., 2006]. However, it may be necessary to compute the modal basis with FEA or measure it with EMA to include more complex physical aspects, such as realistic boundary conditions, composite materials, etc. [Millithaler, 2013].

Besides, Roivainen [2009] proposes an analytical model based on tooth lumped force and moment to transform the circumferential stress at tooth tip into two resulting lumped radial forces applied on yoke (see Figure 2.19). Then, the equivalent radial forces are

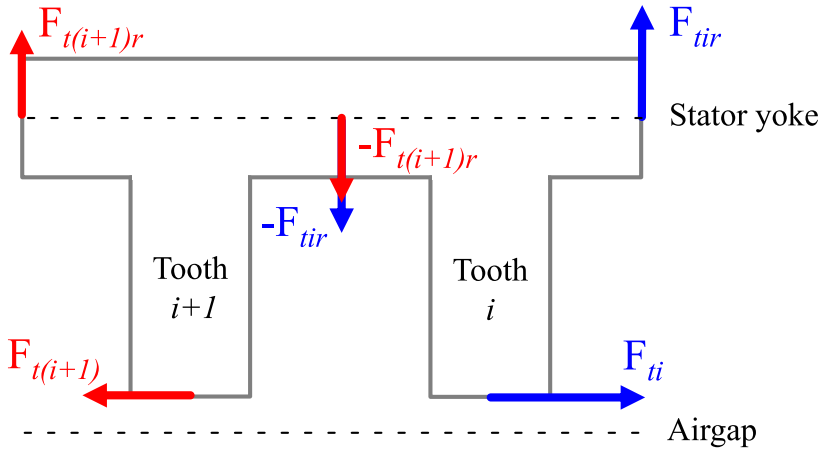

Figure 2.19 – Lumped circumferential force at tooth tip F_t transformed into lumped radial force applied on yoke F_{tr} (adapted from Roivainen [2009]).

combined with the radial FRF to obtain the radial displacement, which model that fact that circumferential stress harmonics can resonate with radial structural modes. This analytical model shows accurate results compared with numerical models based on unit-magnitude rotating waves. However, it has not been implemented and validated for any other electrical machines yet.

2.4.2.3 Numerical FRF based on time-harmonic FEA

Radial and circumferential FRFs introduced in Equation 2.26 can be computed using 2D/3D FE structural models [Boesing, 2013], based on the unit-magnitude rotating stress wave technique [Roivainen, 2009]. The unit-magnitude rotating stress wave is transformed into an equivalent unit-magnitude force wave applying on each tooth tip node, as illustrated in Figure 2.20 for a stress wave of triplet $(f,2,0)$. The FRF complex value is the absolute or RMS displacement value of all the nodes constituting the external surface [van der Giet, 2011; Roivainen, 2009; Boesing, 2013].

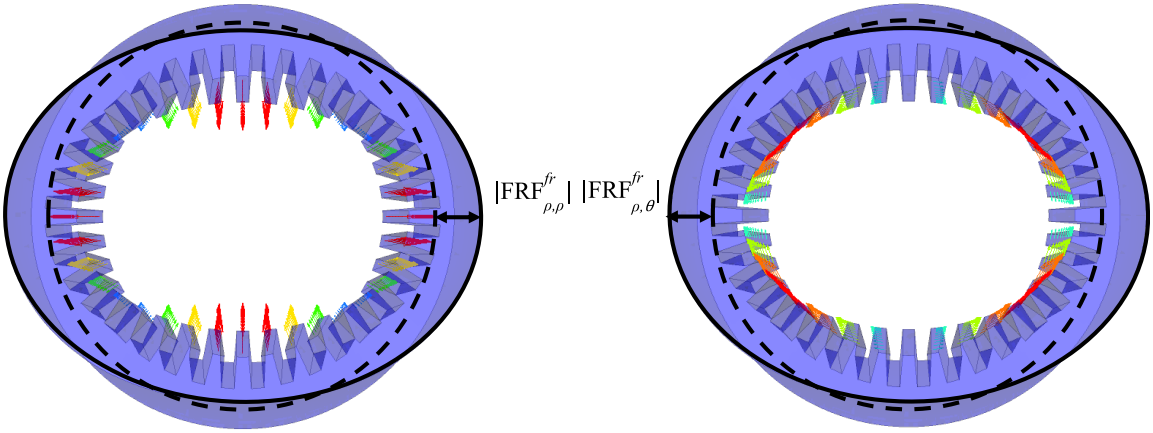

(a) Radial $(f,2,0)$ (b) Circumferential $(f,2,0)$

Figure 2.20 – Unit-magnitude rotating stress waves of triplet $(f,2,0)$ with clamped-free boundary conditions.

Stress waves are successively applied in radial and circumferential directions to obtain radial and circumferential FRFs. Furthermore, the FEA is performed for positive

and negative wavenumbers, and for many frequency values f to get the FRFs on the whole frequency range of the electromagnetic excitation. Therefore, this may require a large number of time-harmonic FEAs and is more dedicated to the second design stage (see Subsection 1.6.1). Besides, a previous computation of the modal basis is not required, since modal parameters are already included in the numerical FRFs. However, a prior numerical modal analysis enables to establish the frequency range of the unit-magnitude rotating stress waves, reducing the computational effort and ensuring that they do excite their structural modes.

In Boesing [2013]; Roivainen [2009], numerical FRFs method enable to account for the circumferential stress contribution in the NVH simulation of SMs. Radial and circumferential FRFs are illustrated in Figure 2.21 for the particular case of a SRM $6s4p$ [Boesing, 2013], using a 2D FEA structural model. It is shown that circumferential stress harmonics do excite radial modes with comparable magnitude, as explained in Subsection 1.4.1, except for breathing mode of order $m = 0$ which cannot be excited with circumferential harmonics [Boesing, 2013].

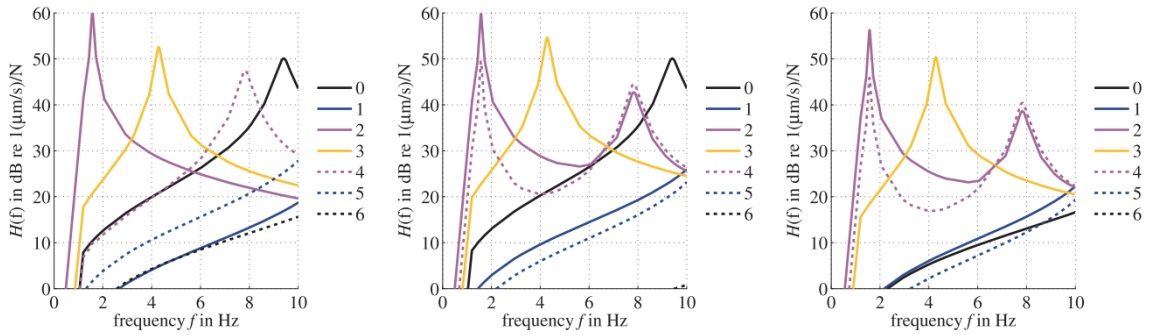

(a) Sine forces, radial. (b) Tsine forces, radial. (c) Tsine force, tangential.

Figure 2.21 – Numerical radial and circumferential FRFs with 2D FE structural model using two MST projections (from Boesing [2013]).

As illustrated in Figure 2.21 (b) and (c), the unit-magnitude stress wave of wavenumber $r = 4$ in dotted purple line excites the ovalization mode $m = 2$ around 1600 Hz, meaning there may be a coupling between FRFs of radial modes which is not included in the analytical approach.

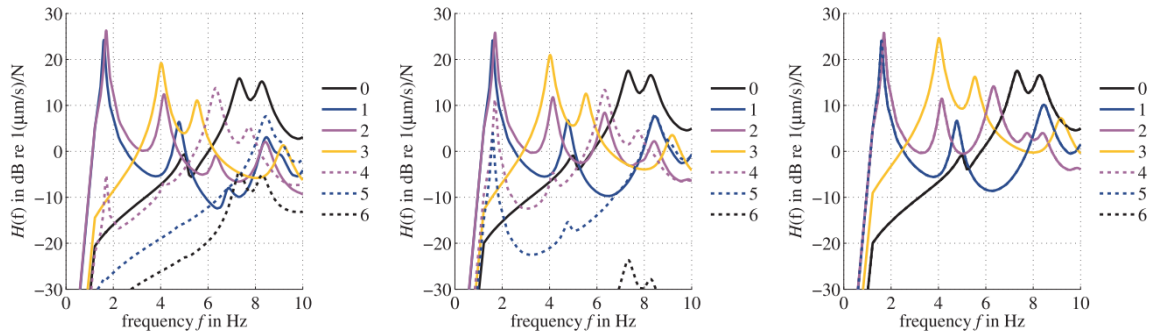

(a) Sine force, radial. (b) Tsine force, radial. (c) Tooth force, radial.

Figure 2.22 – Numerical radial FRFs with 3D FE structural model using three MST projections (from Boesing [2013]).

Finally, it can be seen in Figure 2.22 that FRFs for each unit-magnitude stress wave

have several resonance peaks, whereas the resonance condition 1.16 gives only one resonance for $r = m$. This comes from the fact that FEAs have been performed using a 3D structural models, with a uniform load distributed stator tooth tips or bore, depending on the loading type: "Sine", "Tsine" or "Tooth force" (cf. Figure 2.22) [Boesing, 2013]. Therefore, the unit-magnitude stress waves are characterized by the triplet $(f, r, l = 0)$. They locally resonate with longitudinal modes of triplet $(f_{mn}, m = r, n \geq 0)$, meaning that the harmonic excitation waveform must not necessarily match everywhere with the modal shape to resonate. However, maximum deflection is stronger for the ovalization mode $(f_{20}, 2, 0)$, because it perfectly matches circumferential and axial wavenumbers of the stress harmonic $(k, 2, 0)$. In conclusion, a coupling exist between longitudinal modes with same circumferential order m [Boesing et al., 2016], and this coupling is also illustrated on the numerical FRFs obtained for SPMSM $12s10p$ in Chapter 5. One remaining challenge is to account for this longitudinal coupling in the analytical FRFs model.

2.4.3 Acoustic models

The sound power level can be directly computed using the numerical Boundary-Element Method (BEM) [Roivainen, 2009; van der Giet, 2011] or with (semi)-analytical methods based on infinite/finite cylindrical shells or spherical shells [Wang and Lai, 2001; Gieras et al., 2006]. The acoustic power $\mathrm{W}_m(f)$ radiated by a vibration wave of complex magnitude $\underline{\mathrm{V}}_\rho^{kr}$, with $f = kf_s$, $r = m$, is given by [Le Besnerais, 2008]:

$$\mathrm{W}_m(f) = \frac{1}{2}\rho_0 c_0 \mathrm{S}_c \sigma_m(f) < \left(\underline{\mathrm{V}}_\rho^{kf,r}\right)^2 > \tag{2.28}$$

where S_c is the structure outer surface, ρ_0 the air density, c_0 the sound speed in the air and $\sigma_m(f)$ the modal radiation efficiency, also called radiation factor. This radiation factor depends on the machine geometry and accounts for acoustic resonances. It can be compute analytically assuming that the emitting structure is an infinite/finite cylindrical shell or a spherical shell [Wang and Lai, 2001; Gieras et al., 2006].

Then, the SWL at a frequency f is [Yang, 1981]:

$$\mathrm{L}_w(f) = 10\log_{10}\left(\sum_m \frac{\mathrm{W}_m(f)}{\mathrm{W}_0}\right), \quad \mathrm{W}_0 = 10^{-12}\mathrm{W} \tag{2.29}$$

The A-weighted SWL is given by:

$$\mathrm{L}_{w\mathrm{A}} = 10\log_{10}\left(\sum_f 10^{0.1\left[\mathrm{L}_w(f)+\Delta\mathrm{L}_\mathrm{A}(f)\right]}\right) \tag{2.30}$$

where $\Delta\mathrm{L}_\mathrm{A}(f)$ is the A-weighting function.

2.5 Conclusion

Chapter 2 proposes a state of the art on the e-NVH simulation techniques, which involves a multi-physics coupling between electromagnetic, structural mechanics, and acoustic models. Different simulation workflows exists, such as the EVS which is used in MANATEE and computes the vibration level by summing the contribution of each Maxwell stress harmonic based on FRFs. Besides, developing several models for each physical module enables to adapt both granularity level and computation time to the e-NVH design stage requirements. For this purpose, the main magnetic modeling technique which enable to compute the Maxwell stress distribution are investigated and

compared, in order to implement in MANATEE a magnetic model which is complementary with the already available PMMF method and FEA. The SDM is finally chosen, and the thesis aims at extending it to other topologies of synchronous and induction machines, especially focusing on the subdomain modeling of SCIMs and IPMSMs, and on the possibility to account for saturation. Furthermore, the two following chapters deals with the SDM theory and methodology, in particular with the ARME in physical subdomains of electrical machines (cf. Chapter 3) and the application of magnetic continuity conditions between these subdomains (cf. Chapter 4).

Chapter 2 gives also a short overview of Maxwell stress computation methods and mechanical models used in e-NVH studies. In analytical models, the Maxwell stress distribution is generally computed with the MST applied in the middle of the airgap and reported on the stator structure. However, this technique may be inaccurate as discussed in Subsection 2.4.1, especially in presence of large teeth such in the SPMSM $12s10p$. Therefore, the modeling overview presented in Chapter 2 is useful in the intent of comparing the different models with measurements performed on the SPMSM $12s10p$ prototype, as developed in Chapter 5.

Chapter 3

2D polar analytical solution of Magnetic Vector Potential in physical regions of electrical machines

Contents

3.1 Introduction

3.1.1 Outlines

Chapter 3 develops the Analytical Resolution of Maxwell Equations (ARME) theory for the subdomain modeling of radial flux electrical machines. In this thesis, the ARME is used to directly solve the magnetic governing equation formulated in Magnetic Vector Potential (MVP) inside a physical region, called subdomain. ARME main advantage is to compute radial and circumferential flux densities with a good compromise between computation time and accuracy, without introducing meshing errors. As illustrated in Figure 2.11, the ARME is performed after dividing the magnetic problem into several subdomains (e.g. the airgap, stator and rotor slots and teeth, magnets, stator and rotor yoke etc.) and before the numerical resolution of interface continuity conditions between theses subdomains. The ARME can be decomposed into three steps:

First of all, the magnetic governing equation in each subdomain is derived from Maxwell equations, material constitutive laws and MVP formulation, considering the modeling assumptions listed in Subsection 3.1.3. In terms of maths, the governing equation is a 2^{nd}-order Partial Differential Equations (PDEs) over time and space for the MVP, as detailed in Subsection 3.2.

The general mathematical problem, referred as subdomain problem, is then formulated in Subsection 3.3. In order to be analytically solved, the subdomain MVP PDE is associated to a set of mathematical Boundary Conditions (BCs) applying on the subdomain edges. The BCs are given by the physical continuity equations of the magnetic field and flux density crossing the interface between two medias, which are given in Subsection 3.2.3.4. Mathematically speaking, the subdomain problem can be generally expressed as the superposition of two eigenvalue problems in radial and circumferential directions, as defined in Subsection 3.3.4.

Finally, the general resolution methodology of the eigenvalue problems is detailed in Subsections 3.4 and 3.5. Using the Separation of Variables (SoV) method, the PDE is transformed into two independent 2^{nd}-order Ordinary Differential Equations (ODEs) which are solved for different eigenvalue problems that can be found in the subdomain modeling of electrical machines. The aim is to extend the ARME to the largest variety of electrical machine topologies.

3.1.2 Contributions

The developed approach is based on the Sturm-Liouville theory [Liouville, 1836], which uses functional analysis to solve the PDE in each subdomain, depending on the nature of source terms and ICs. This mathematical overlay may add complexity in the analytical developments, but is essential to understand which subdomain problems can be analytically solved or not, and how to perform the resolution. Besides, the mathematical considerations aims at developing a unified ARME theory for subdomain models of SMs and IMs.

The first main originality of Chapter 3 is to develop the eigenvalue problem in radial direction, which enables to account for iron finite permeability in teeth subdomains using superposition principle, thus potentially include global saturation among the SDM capabilities. Furthermore, it is shown that the subdomain problem formulation which enables to perform the ARME is not unique. The choice of the formulation has an impact on the subdomain model resolution, as later discussed in Section 4.3.

Besides, two other contributions are proposed. The first one consists in accounting for the presence of interior (or buried) PMs to compute the open-circuit airgap flux density of IPMSMs, which is briefly presented in Subsection 3.5.1.1 and further explained in Devillers et al. [2017a]). This technique is also extended to WRSMs topologies as implemented in MANATEE during this thesis. The second one is the development of a new analytical formulation for the particular solution of shorted pitch double layer windings (see Subsection 3.5.2.4), which reduces the number of slot subdomains by two in comparison with the formulation proposed in Boughrara et al. [2014].

Therefore, the present work can be used as a framework for future researchers who would like to understand the mathematical fundamentals of the ARME, especially to build new subdomain models including iron finite permeability.

3.1.3 Modeling assumptions in subdomains

In this thesis, the following list of physical subdomains can be considered:

— airgap;

— surface Permanent Magnets (PMs);

— rotor and stator slots with either windings, bars, or inset PMs;

— rotor and stator slot openings (including magnetic wedges with $\mu_r > 1$);

— rotor and stator teeth;

— rotor and stator yokes;

— solid rotor for SRIMs

— airgap windings;

— empty slots, e.g. for notches or pockets in SynRMs;

These subdomains enable to build a large variety of electrical machine topologies, and also to investigate acoustic noise reduction techniques (cf. Section 1.6).

In all of these subdomains, the ARME is performed considering the following assumptions:

1. The geometry is 2D and expressed in polar coordinates. As shown in Figure 3.1, each subdomain is an annular part defined by its inner and outer radii R_1 and R_2, and its minimum and maximum angles Θ_1 and Θ_2. The angular width is $a = \Theta_2 - \Theta_1$.
2. Magnetic problem formulation is in Magnetic Vector Potential (MVP), as explained in Subsection 2.3.3.2.
3. Physical properties are constant, uniform and isotropic. Therefore, relative magnetic permeability μ_r and electrical conductivity σ are constant values. The iron magnetic permeability can be finite or infinite.
4. Problem is stationary: supply frequency f_s and rotor motion Ω are constant, induced currents are established. The problem is solved for each simulation instant t_0, which corresponds to a specific rotor position associated to a specific magnetic source distribution.

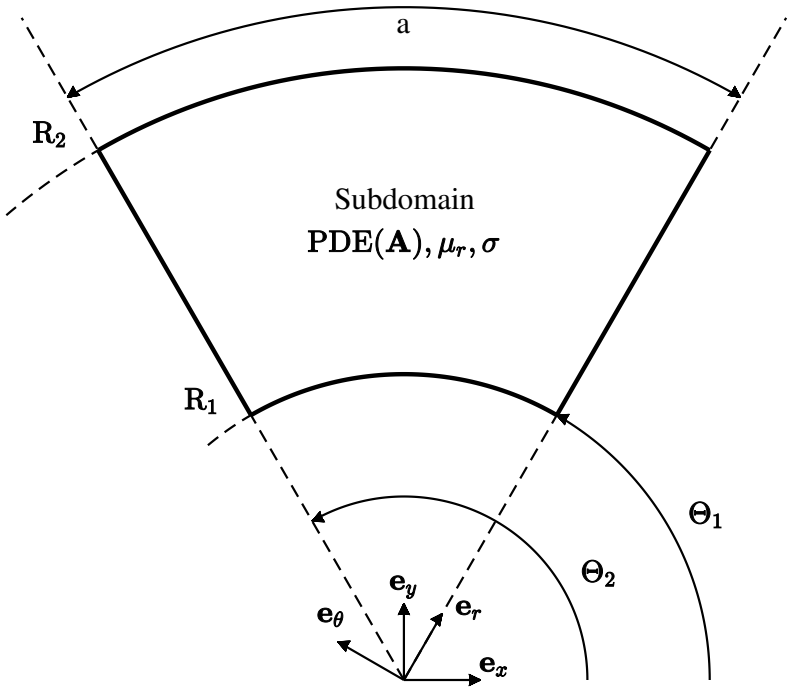

Figure 3.1 – Subdomain with annular part geometry and uniform electromagnetic properties.

3.2 Maxwell equations and MVP formulation

3.2.1 Maxwell equations

Maxwell equations are:

$$\nabla.\mathbf{B} = 0 \tag{3.1}$$

$$\nabla \times \mathbf{H} = \mathbf{j} + \frac{\partial \mathbf{D}}{\partial t} = \mathbf{j} + \mathbf{j_d} \tag{3.2}$$

$$\nabla \times \mathbf{E} = -\frac{\partial \mathbf{B}}{\partial t} \tag{3.3}$$

$$\nabla.\mathbf{D} = \rho \tag{3.4}$$

where $\mathbf{B}$ is the magnetic flux density, $\mathbf{H}$ is the magnetic field, $\mathbf{E}$ is the electric field, $\mathbf{D}$ is the displacement field, $\mathbf{j}$ is the current density, $\mathbf{j_d}$ is the displacement current density, ρ is the electric charge density, "$\nabla.$" is the divergence operator, and "$\nabla\times$" is the curl operator.

Maxwell-Gauss's law (3.4) is not considered, as there is no electric charge density in the considered subdomains of electrical machines. Moreover, Maxwell-Ampere's law (3.2) can be simplified because displacement current density $\mathbf{j_d}$ is generally negligible compared to current density $\mathbf{j}$ in low frequency electromagnetic devices, meaning:

$$\mathbf{j_d} = \frac{\partial \mathbf{D}}{\partial t} \ll \mathbf{j} \tag{3.5}$$

Maxwell-Ampere's law becomes:

$$\nabla \times \mathbf{H} = \mathbf{j} \tag{3.6}$$

3.2.2 Constitutive laws in electromagnetic materials

In ferromagnetic materials, the relation between $\mathbf{B}$ and $\mathbf{H}$ is not linear and is called $\mathbf{B}(\mathbf{H})$ curve. In a linear material media, the relation between magnetic flux density and

field is:

$$\mathbf{B} = \mu_0 \mu_r \mathbf{H} + \mu_0 \mathbf{M} \tag{3.7}$$

where $\mathbf{M}$ is the magnetization field, μ_0 is the void magnetic permeability, and μ_r is the magnetic relative permeability. In paramagnetic materials (such as air, copper, aluminum etc.) flux density and magnetic field are always linearly proportional.

Besides, in a moving electric conductor, the current density inside the conductor is expressed by the local Ohm's law:

$$\mathbf{j} = \sigma(\mathbf{E} + \mathbf{v} \times \mathbf{B}) + \mathbf{j_{ext}} \tag{3.8}$$

where σ is the electric conductivity, $\mathbf{v}$ is the conductor speed in the static referential, "$\times$" is the vector product, and $\mathbf{j_{ext}}$ is the external current density.

At the interface between two medias, two magnetic continuity conditions apply:

1. Continuity of the magnetic flux density component which is normal to the interface (edge in 2D, surface in 3D);
2. Continuity of the magnetic field component which is tangential to the interface (contained in the interface);

The normal flux density continuity equation derives from Maxwell-Thomson's Equation (3.1), and is mathematically expressed as:

$$n_{12}.(\mathbf{B}_2 - \mathbf{B}_1) = \mathrm{B}_{n2} - \mathrm{B}_{n1} = 0 \tag{3.9}$$

where indexes $_1$ and $_2$ refer to the two medias at the interface, n_{12} is the normal vector to interface and oriented from $_1$ to $_2$, and "." is the scalar product.

The tangential field interface condition is obtained from the Maxwell-Ampere's Equation (3.2):

$$\big(n_{12} \times (\mathbf{H}_2 - \mathbf{H}_1)\big).\mathbf{e}_z = \mathrm{H}_{t2} - \mathrm{H}_{t1} = j_s \tag{3.10}$$

where j_s is the linear current density located at the interface. Such linear current density does not really exist in electrical machines, but it can be used in electromagnetic models of electrical machines to represent the current density in slotted windings by an equivalent current sheet located at stator bore radius, as used in the SCIM subdomain model developed in Section 4.4.

3.2.3 2D Magnetic Vector Potential (MVP) formulation

3.2.3.1 General magnetodynamic MVP PDE

From Maxwell-Thomson's law (3.1), the flux density divergence is always zero. Then, flux density derives from the Magnetic Vector Potential (MVP) $\mathbf{A}$ such as:

$$\mathbf{B} = \nabla \times \mathbf{A} \tag{3.11}$$

Then, substituting Equation (3.11) in Maxwell-Faraday's law (3.3) yields:

$$\mathbf{E} = -\frac{\partial \mathbf{A}}{\partial t} \tag{3.12}$$

From Maxwell equations, constitutive laws and MVP definition, the general magnetodynamic Partial Differential Equation (PDE) for the MVP can be obtained:

$$\nabla^2 \mathbf{A} - \mu_0 \mu_r \sigma \left[\frac{\partial \mathbf{A}}{\partial t} - \mathbf{v} \times (\nabla \times \mathbf{A}) \right] = -\mu_0 \mu_r \mathbf{j_{ext}} - \mu_0 \nabla \times \mathbf{M} \tag{3.13}$$

where "∇^2" is Laplacian vector operator. MVP governing equation is therefore a second order PDE over time and space variables, and including magnetization and current density source terms in the second member.

3.2.3.2 Magnetodynamic MVP PDE expressed in 2D polar coordinates

In this thesis, the magnetodynamic PDE is not solved in presence of external magnetic sources, even if analytical solutions can be found for example to model induced current in windings or magnets and estimate losses. Without source terms, the magnetodynamic PDE is called diffusion equation, which enables for instance to compute the induced current in a rotor squirrel cage, or in a solid rotor, due to stator MMF harmonics. In 2D polar coordinates, the diffusion equation yields:

$$\frac{\partial^2 \mathrm{A}_z}{\partial r^2} + \frac{1}{r}\frac{\partial \mathrm{A}_z}{\partial r} + \frac{1}{r^2}\frac{\partial^2 \mathrm{A}_z}{\partial \theta^2} - \mu_0 \mu_r \sigma \left[\frac{\partial \mathrm{A}_z}{\partial t} + \Omega \frac{\partial \mathrm{A}_z}{\partial \theta} \right] = 0 \tag{3.14}$$

where Ω is the rotor angular speed. However, the diffusion equation can be analytically solved only if it is expressed as the following Helmholtz equation:

$$\frac{\partial^2 \underline{\mathrm{A}}_z}{\partial r^2} + \frac{1}{r}\frac{\partial \underline{\mathrm{A}}_z}{\partial r} + \frac{1}{r^2}\frac{\partial^2 \underline{\mathrm{A}}_z}{\partial \theta^2} - \underline{\alpha}^2 \underline{\mathrm{A}}_z = 0 \tag{3.15}$$

where $\underline{\alpha}$ is the complex diffusion coefficient, which implies that MVP is complex too. The link between Equations (3.14) and (3.15) is not straight forward, and requires to assume that MVP has a unique pulsation ω_{rm} in solid rotor and rotor bar subdomains [Lubin et al., 2011b]:

$$\underline{\mathrm{A}}_z(t, r, \theta) = \underline{\mathrm{A}}_z(r, \theta) e^{j\omega_{rm} t} \tag{3.16}$$

where ω_{rm} accounts for the relative motion (hence "$_{rm}$") between the rotor subdomain and the stator MMF harmonic, which is:

$$\omega_{rm} = 2\pi k f_s - n\Omega \tag{3.17}$$

with kf_s the frequency and n the wavenumber of the stator MMF harmonic (not to confuse with r, which stands for the radial coordinate in Chapters 3 and 4), such as:

$$\mu_0 \mu_r \sigma \left[\frac{\partial \mathrm{A}_z}{\partial t} + \Omega \frac{\partial \mathrm{A}_z}{\partial \theta} \right] = j \mu_0 \mu_r \sigma \omega_{rm} \underline{\mathrm{A}}_z \tag{3.18}$$

Therefore, the diffusion coefficient can be expressed as:

$$\underline{\alpha} = \sqrt{j \mu_0 \mu_r \sigma \omega_{rm}} \tag{3.19}$$

Then, the diffusion in rotor subdomains is assumed to be established (cf. Subsection 3.1.3), meaning the induced current pulsation ω_{rm} is steady. Helmholtz equation (3.15)

is solved for each rotor position and stator current distribution associated to the simulation instant t_0, in order to account for rotor slotting effect as in magnetostatic cases.

Therefore, it is worth mentioning that the simulation instant t_0 and the diffusion coefficient $\underline{\alpha}$ in rotor subdomains are independent parameters. Even if time is implicitly included in the diffusion coefficient, this is not a magnetoharmonic resolution which gives the airgap flux density distribution over time and space. The magnetoharmonic resolution only gives the proper diffusion effect in rotor subdomains given a stator MMF harmonic.

In conclusion, each stator MMF harmonic (f, n) must be taken separately to account for the proper diffusion coefficient $\underline{\alpha}$ in the rotor subdomain and validate the present approach [Lubin et al., 2011b].

3.2.3.3 Magnetostatic MVP PDE expressed in 2D polar coordinates

The PDE in subdomains without magnetic sources nor diffusion is the magnetostatic Laplace equation:

$$\frac{\partial^2 A_z}{\partial r^2} + \frac{1}{r}\frac{\partial A_z}{\partial r} + \frac{1}{r^2}\frac{\partial^2 A_z}{\partial \theta^2} = 0 \tag{3.20}$$

The PDE in subdomains with current sources is a magnetostatic Poisson equation:

$$\frac{\partial^2 A_z}{\partial r^2} + \frac{1}{r}\frac{\partial A_z}{\partial r} + \frac{1}{r^2}\frac{\partial^2 A_z}{\partial \theta^2} = -\mu_0 \mu_r J_z(t_0) \tag{3.21}$$

where J_z is the axial component of the external current density distribution, which depends on the simulation instant t_0.

The PDE in subdomains with magnet sources is also a magnetostatic Poisson equation:

$$\frac{\partial^2 A_z}{\partial r^2} + \frac{1}{r}\frac{\partial A_z}{\partial r} + \frac{1}{r^2}\frac{\partial^2 A_z}{\partial \theta^2} = -\mu_0 \frac{1}{r}\left(\frac{\partial}{\partial r} - \frac{\partial M_r}{\partial \theta}\right) \tag{3.22}$$

where M_r and M_θ are radial and circumferential components of the magnetization distribution, which depends on the magnets position at the simulation instant t_0.

3.2.3.4 Magnetic continuity equations formulated in 2D polar coordinates

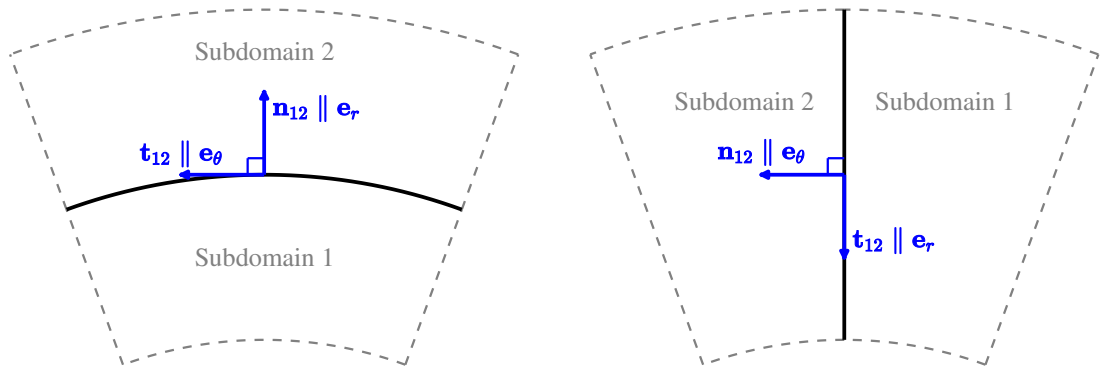

(a) Interface on circumferential edge.

(b) Interface on radial edge.

Figure 3.2 – Continuity equations in polar coordinates.

Continuity equations (3.9) and (3.10) are formulation in the 2D polar coordinate system. As shown in Figure 3.2, each subdomain interface, i.e. an edge in 2D, is either a line segment in the radial direction or an arc segment in the circumferential direction. Therefore, n_{12} is collinear to $\mathbf{e}_r$ on an arc segment (i.e. $n_{12} \parallel \mathbf{e}_r$) and n_{12} is collinear to $\mathbf{e}_\theta$ on a line segment (i.e. $n_{12} \parallel \mathbf{e}_\theta$). Moreover, continuity equations are reformulated in function of MVP to obtain the BCs for the PDE.

It comes by derivation that normal flux density continuity (3.9) is necessary ensured if the MVP is also continuous:

$$\mathrm{A}_{z2} - \mathrm{A}_{z1} = 0 \quad \Rightarrow \quad \mathrm{B}_{n2} - \mathrm{B}_{n1} = 0 \tag{3.23}$$

Using Equations (3.7) and (3.11), tangential field continuity (3.10) yields:

$$-\frac{1}{\mu_0}\left(\frac{1}{\mu_{r2}}\frac{\partial \mathrm{A}_{z2}}{\partial r} - \frac{1}{\mu_{r1}}\frac{\partial \mathrm{A}_{z1}}{\partial r}\right) - \left(\frac{\mathrm{M}_{\theta 2}}{\mu_{r2}} - \frac{\mathrm{M}_{\theta 1}}{\mu_{r1}}\right) = j_s, \quad n_{12} \parallel \mathbf{e}_r \tag{3.24}$$

$$\frac{1}{\mu_0 r}\left(\frac{1}{\mu_{r2}}\frac{\partial \mathrm{A}_{z2}}{\partial \theta} - \frac{1}{\mu_{r1}}\frac{\partial \mathrm{A}_{z1}}{\partial \theta}\right) - \left(\frac{\mathrm{M}_{r2}}{\mu_{r2}} - \frac{\mathrm{M}_{r1}}{\mu_{r1}}\right) = j_s, \quad n_{12} \parallel \mathbf{e}_\theta \tag{3.25}$$

3.3 Subdomain problem formulation using the superposition of two eigenvalue problems

3.3.1 Illustration for stator slots and teeth subdomains assuming or not infinitely permeable iron

The type of mathematical problem that is solved in this section can be illustrated by the example of stator teeth and slots subdomains assuming or not iron infinite permeability.

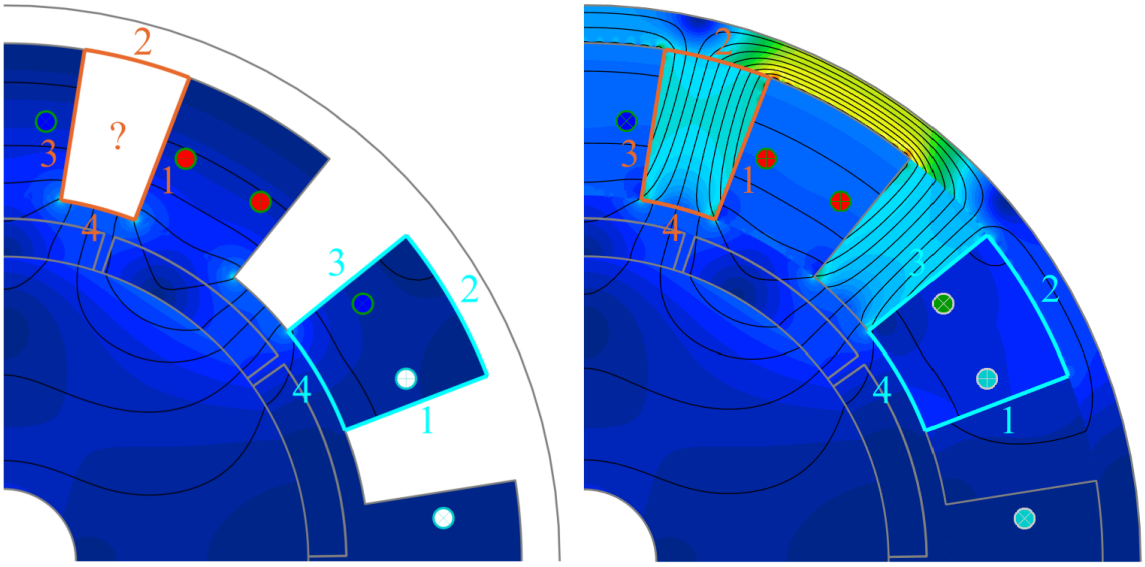

(a) Stator infinite permeability case: MVP unknown in stator teeth.

(b) Stator finite permeability case: MVP computed in stator teeth.

Figure 3.3 – Illustration of stator tooth (in orange) and stator slot (in cyan) subdomain problems.

Concerning the SPMSM $12s10p$, the classic subdomain method assumes infinite permeability in stator teeth and yoke (cf. Figure 2.12) and computes MVP and flux density

only in rotor yoke, surface PMs, airgap and stator slots subdomains, as represented in Figure 3.3a. In the stator slot subdomain colored in cyan, the MVP computation requires to solve the subdomain Poisson PDE with current density (cf. Equation (3.21)), such as the flux density is perpendicular at each interface with infinitely permeable iron parts (edges n°1-3), and that tangential field and normal flux density are continuous at the airgap interface (edge n°4).

Using the subdomain method developed in this thesis, MVP and flux lines are also computed in iron subdomains, including rotor yoke, stator teeth, stator yoke as illustrated in Figures 1.6b and 1.6a. The MVP problem in stator slots under iron finite permeability assumption is now illustrated in cyan in Figure 3.3b. The MVP computation requires to solve the same Poisson PDE as in infinite permeability case, but it must also ensure the magnetic continuity equations with the four neighboring subdomains, i.e. stator slots on right edge n°1 and left edge n°3, stator yoke on top edge n°2, and airgap on bottom edge n°4. The same problem can be formulated for a stator tooth colored in orange in Figure 3.3b, except that the governing equation is now the Laplace PDE (3.20).

3.3.2 General PDE formulation in a subdomain with continuity conditions

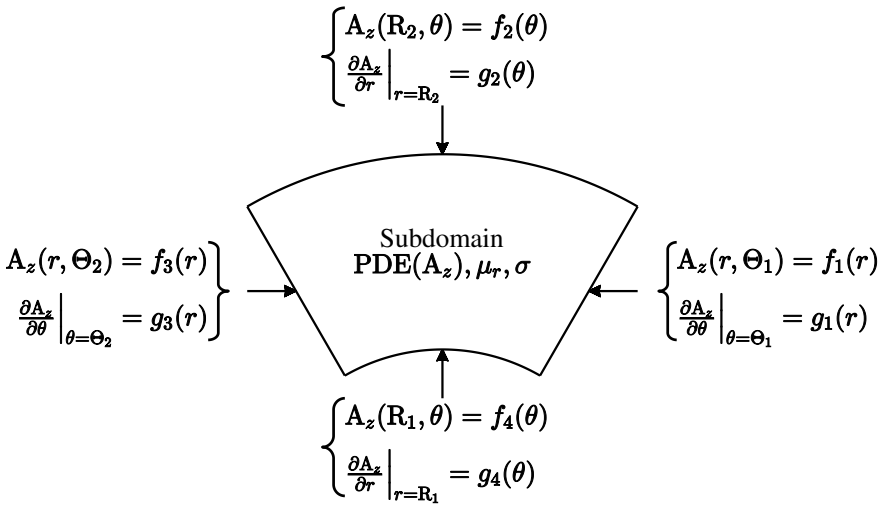

Figure 3.4 – General formulation for the ARME in a subdomain.

The general MVP problem to solve analytically in each subdomain is illustrated in Figure 3.4. The possible MVP PDEs are the magnetostatic Laplace and Poisson equations (3.20)-(3.22), and the magnetoharmonic Helmholtz equation (3.15) (see Subsection 3.2).

The functions $f_i, g_i, i \in [\![1,4]\!]$ defined in Figure 3.4 represent the normal flux density and tangential field continuity equations which have been developed in Subsection 3.2.3.4. In the SDM terminology, a continuity condition is either called Interface Condition (IC) if the condition applies on an edge shared with a neighboring subdomain, or Boundary Condition (BC) if the condition is imposed on a subdomain edge which is an external boundary of the subdomain problem. In terms of maths, ICs and BCs are exactly the same.

Furthermore, each subdomain is mathematically subject to only four continuity conditions, even if there are eight physical continuity equations applying on the four edges as represented in Figure 3.4. In fact, there are two continuity conditions per sharing edge, meaning one IC for each neighboring subdomain. The number of neighboring subdomains implies the number of ICs.

Edges without any IC are necessary subject to a BC. Mathematically speaking, BCs cannot be imposed for both MVP and its derivative along a same edge, meaning that there is at most one BC per edge. Therefore, the resulting set of four continuity conditions can be chosen among the eight following possibilities:

$$\Big\{(f_1 \text{ or } g_1) \text{ and } (f_2 \text{ or } g_2) \text{ and } (f_3 \text{ or } g_3) \text{ and } (f_4 \text{ or } g_4)\Big\} \tag{3.26}$$

where f_i and g_i can be ICs or BCs depending on the subdomain problem. This mathematical formulation is illustrated in Figure 3.5.

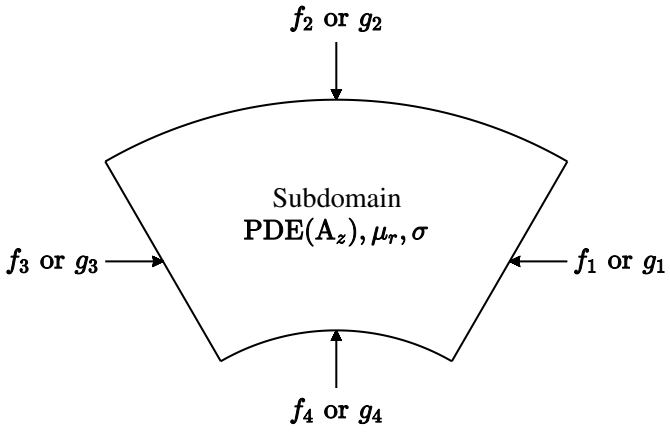

Figure 3.5 – Mathematical formulation of BCs and ICs on subdomain edges.

Although ICs and BCs do not differ in terms of maths, this distinction is quite relevant in the subdomain methodology. As shown in Section 3.4, BCs enable to find the MVP analytical solution in each subdomain. On the other hand, ICs enable to determine the unknown integration constants introduced by the analytical resolution and solve the whole subdomain problem (see Section 4.2). Therefore, BCs and ICs are complementary and applied at different stages of the subdomain methodology.

In next Subsection 3.3.3, the different kinds of BCs are detailed depending on the subdomain properties.

3.3.3 Definition of Boundary Conditions (BCs)

3.3.3.1 Non-homogeneous Boundary Condition (NBC)

A BC is non-homogeneous if its value varies along the edge, as represented by the functions f_i and g_i depending on r or θ. As said in previous Subsection 3.3.2, BCs and ICs are exactly the same in terms of maths. Therefore, ICs are necessary Non-homogeneous Boundary Conditions (NBCs) since potential and tangential fields arbitrary vary along the edge.

For example, Figure 3.3b illustrates a stator tooth subdmain in orange and a stator slot subdomain in cyan whose PDE is subject to four ICs/NBCs, due to the magnetic

continuity equations with airgap, stator yoke, and the two surrounding slots for the tooth subdomain or the two surrounding teeth for the slots subdomain.

3.3.3.2 Dirichlet Homogeneous Boundary Condition (HBC)

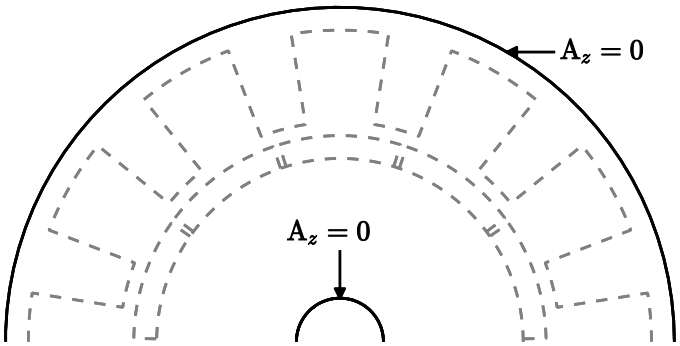

Figure 3.6 – Dirichlet HBCs applied on external boundaries of stator and rotor yokes, implying zero radial flux density at the interface.

A Dirichlet Homogeneous Boundary Condition (HBC) means that the MVP is imposed to be zero along the edge, i.e. $f_i = 0$ with $i \in [\![1,4]\!]$, or more explicitly:

$$A_z(R_x, \theta) = 0, \qquad n_{12} \parallel \mathbf{e}_r \tag{3.27}$$

$$A_z(r, \Theta_x) = 0, \qquad n_{12} \parallel \mathbf{e}_\theta \tag{3.28}$$

where $R_x \in \{R_1, R_2\}$ and $\Theta_x \in \{\Theta_1, \Theta_2\}$.

This is mainly used to delimit the domain study of the subdomain problem, by saying that the MVP is zero on the external boundaries, as illustrated in Figure 3.6. For internal rotor topologies, Dirichlet HBCs apply on rotor yoke inner radius and stator yoke outer radius if stator and rotor yoke are including in the subdomain problem. The flux lines are forced to be tangential to the external boundaries. The Dirichlet HBCs can also be used to apply symmetry conditions.

3.3.3.3 Neumann Homogeneous Boundary Condition (HBC)

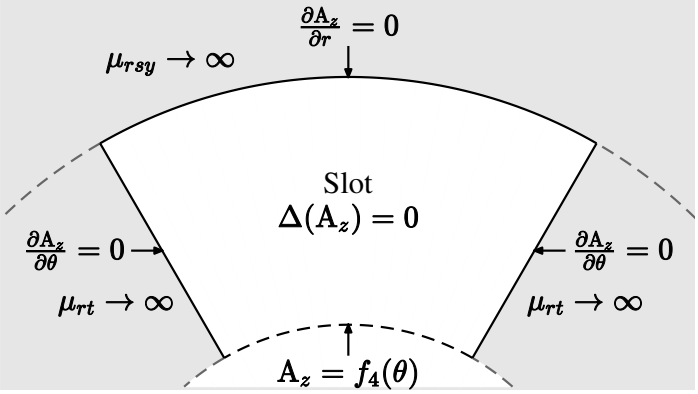

Figure 3.7 – Neumann HBCs applied on stator slot interfaces with infinitely permeable stator yoke and teeth, enforcing zero tangential field at the interface.

A Neumann HBC means that the derivative of the MVP along the edge is imposed to be zero, i.e. $g_i = 0$ with $i \in [1,4]$. Neumann HBCs can be obtained using the infinite permeability assumption, which simplifies the continuity equations (3.24) and (3.25).

Assuming that:

— Media 2 is infinitely permeable, i.e. $\mu_{r2} \to \infty$.

— Medias 1 and 2 have no magnet sources, i.e. $\mathbf{M}_1 = \mathbf{M}_2 = 0$.

— There is no linear current density at the interface between 1 and 2, i.e. $j_s = 0$.

The tangential field continuity equations (3.24) and (3.25) result in the following Neumann HBCs:

$$\left.\frac{\partial \mathrm{A}_{z1}}{\partial r}\right|_{r=\mathrm{R}_x,\theta} = 0, \qquad n_{12} \parallel \mathbf{e}_r \tag{3.29}$$

$$\left.\frac{\partial \mathrm{A}_{z1}}{\partial \theta}\right|_{r,\theta=\Theta_x} = 0, \qquad n_{12} \parallel \mathbf{e}_\theta \tag{3.30}$$

where $\mathrm{R}_x \in \{\mathrm{R}_1, \mathrm{R}_2\}$ and $\Theta_x \in \{\Theta_1, \Theta_2\}$.

Neumann HBCs obtained from infinite permeability assumption are illustrated in Figure 3.7, e.g. for a stator or rotor slot surrounded by non-saturated electrical steel. Physically speaking, the infinite permeability assumption imposes the magnetic field to cross perpendicularly the interface with the infinitely permeable media.

3.3.3.4 Periodic Boundary Condition (PBC)

A Periodic Boundary Condition (PBC) means that the MVP is periodic on opposite edges, i.e. $f_1 = f_3$, or $g_1 = g_3$, or $f_2 = f_4$, or $g_2 = g_4$. For annular subdomains with angular width $a = 2\pi$, such as airgap, surface PMs, yokes, the MVP solution is 2π-periodic which yields the following PBC:

$$\forall\, \theta \in [0, 2\pi], \quad \mathrm{A}_z(r,\theta) = \mathrm{A}_z\Big(r, \theta + 2\pi\Big) \tag{3.31}$$

$$\forall\, \theta \in [0, 2\pi], \quad \left.\frac{\partial \mathrm{A}_z}{\partial \theta}\right|_{r,\theta} = \left.\frac{\partial \mathrm{A}_z}{\partial \theta}\right|_{r,\theta+2\pi} \tag{3.32}$$

In subdomain problems subject to PBC, an additional Anti-periodic Boundary Condition (ABC) can apply if the MVP is π-anti-periodic, such as:

$$\forall\, \theta \in [0, 2\pi], \quad \mathrm{A}_z(t,r,\theta) = -\mathrm{A}_z\Big(t, r, \theta + \pi\Big) \tag{3.33}$$

$$\forall\, \theta \in [0, 2\pi], \quad \left.\frac{\partial \mathrm{A}_z}{\partial \theta}\right|_{r,\theta} = -\left.\frac{\partial \mathrm{A}_z}{\partial \theta}\right|_{r,\theta+\pi} \tag{3.34}$$

The ABC can be for example applied in electrical machines with even number of slots.

3.3.4 Definitions of eigenvalue problems and superposition principle

From Sturm-Liouville theory [Herman, 2013], a Partial Differential Equation (PDE) can be analytically solved using the eigenvalue problem decomposition, which is possible only if there are one or two Non-homogeneous Boundary Conditions (NBCs) (i.e.

Interface Conditions (ICs) with other subdomains) applying on opposite edges, while the two or three other edges have Homogeneous Boundary Conditions (HBCs) or Periodic Boundary Conditions (PBCs).

If the one or two ICs are on circumferential edges, the PDE is called an eigenvalue problem in circumferential direction (θ-direction). This type of eigenvalue problems is classic in the subdomain modeling of electrical machines. For example, the stator slot case assuming iron infinite permeability in Figure 3.7 is an eigenvalue problem in θ-direction.

Otherwise, if the one or two ICs are on radial edges, the PDE is an eigenvalue problem in radial direction (r-direction). This type of problem is for example solved when applying the magnetic continuity equations on a radial edge between a slot and a tooth, which enables to account for tooth finite permeability as illustrated in Figure 3.3b. This development is a personal and original contribution to the subdomain modeling of electrical machines, although it has also been developed in parallel by Dubas and Boughrara [2017].

If there are both ICs on circumferential and radial edges, the PDE can be solved using the superposition principle, which consists in dividing the general problem into two eigenvalue subproblems in circumferential and radial directions, such as:

— PDE(A_z^C) is the eigenvalue subproblem in circumferential direction, meaning it is subject to NBCs on one or two circumferential edges, and HBCs on the two or three other edges. In this thesis, eigenvalue problems in circumferential direction are solved for Laplace PDE in Subsection 3.4.2 and Helmholtz PDE in Subsection 3.4.5.

— PDE(A_z^R) is the eigenvalue subproblem in radial direction, meaning it is subject to NBCs on one or two radial edges, and HBCs on the two or three other edges. In this thesis, eigenvalue problems in radial direction are only solved for Laplace PDE in Subsection 3.4.3.

As each PDE can be analytically and independently solved, the MVP, noted A_z, is solution of the general problem such as:

$$A_z = A_z^C + A_z^R \tag{3.35}$$

where A_z^C is the solution of the eigenvalue problem in θ-direction, and A_z^R is the solution of the eigenvalue problem in r-direction.

Therefore, the superposition principle is necessary used to solve the MVP PDE in slots and teeth subdomain problems when considering tooth finite permeability, because there are both ICs in cicumferential direction (with airgap and yoke) and radial directions (with the two adjacent teeth). However, there are several possible formulations to define the eigenvalue problems in circumferential and radial directions, among the eight combinations of continuity conditions given in Equation (3.26).

The main superposition principle formulation developed in this thesis is illustrated in Figure 3.8 and can be applied to slots and teeth subdomains assuming finite permeability of teeth and yoke. This formulation has been developed in parallel in Dubas and Boughrara [2017]. The eigenvalue problem in circumferential direction has Neumann HBCs on radial edges (see the solution in Subsection 3.4.2.2), while the eigenvalue problem in radial direction has Dirichlet HBCs on circumferential edges (see the solution in Subsection 3.4.3.1). This formulation is for example used to obtain Figures 1.6b, 1.6a and 3.3b. In particular, the respective contribution of A_z^C and A_z^R which results in the

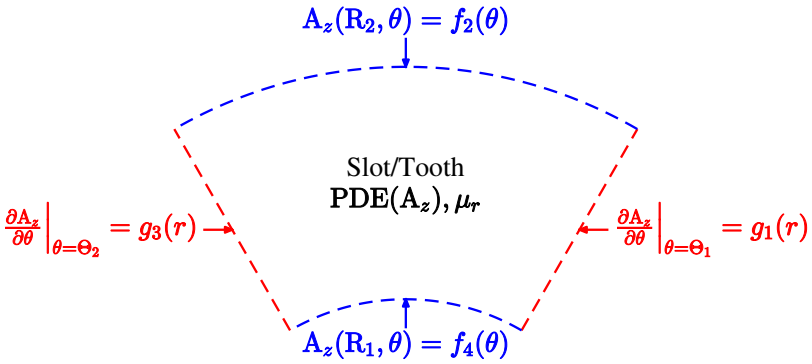

(a) Slot/Tooth subdomain problem with four ICs/NBCs.

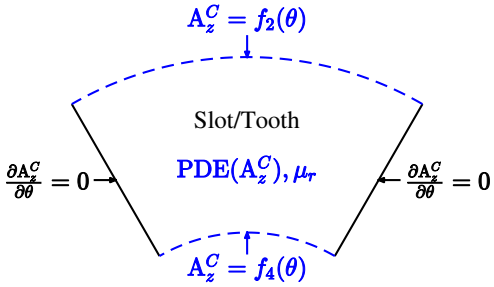

(b) Eigenvalue problem in θ-direction.

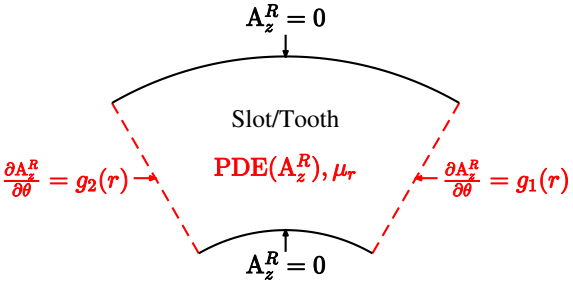

(c) Eigenvalue problem in r-direction.

Figure 3.8 – Superposition principle (1^{st} formulation noted F_1) applied on MVP PDE in slots and teeth subdomains assuming iron finite permeability.

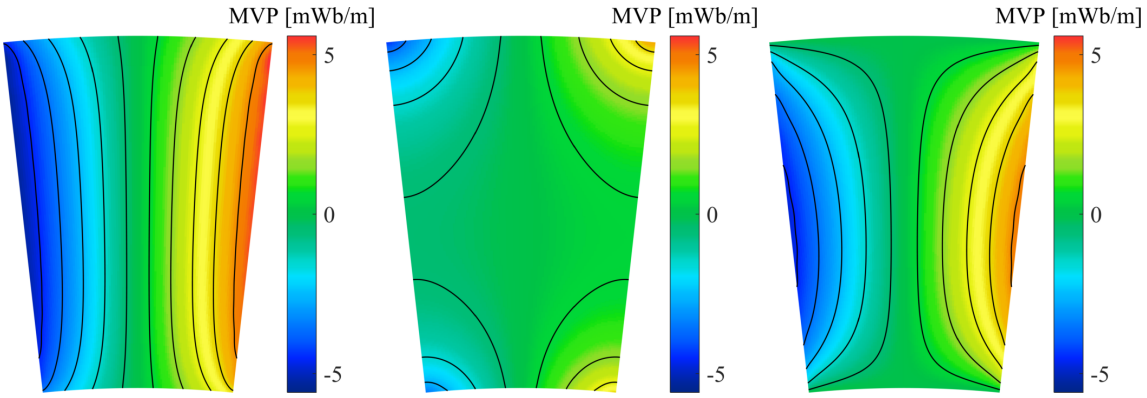

(a) A_z (General solution) (b) A_z^C (Circ. solution) (c) A_z^R (Radial solution)

Figure 3.9 – Contribution of the two eigenvalue problems in circumferential and radial directions to the general MVP solution.

orange tooth MVP illustrated in Figure 3.3b are given in Figure 3.9. Two other formulations are developed in Chapter 4 to solve the MVP in teeth and slots subdomains infinite permeability of yoke. These two formulations are compared in Subsection 4.3 regarding numerical aspects.

3.3.5 Definition of homogeneous and particular solutions

In terms of maths, the general MVP solution of the eigenvalue problem is the sum of the homogeneous solution A_{zh} and a particular solution A_{zp}:

$$A_z = A_{zh} + A_{zp} \tag{3.36}$$

The homogeneous solution A_{zh} is a solution of the homogeneous PDE, which is the PDE without any source terms in the second member. The homogeneous PDEs is the Laplace equation (3.20) in every magnetostatic case and the Helmholtz equation (3.15) in the magnetoharmonic case. The homogeneous solution gives the eigenvalues and eigenfunctions depending on the problem direction and on the nature of the BCs, and are given in Section 3.4.

The particular solution A_{zp} is the solution of the general Poisson PDE only accounting for the magnetization or current density source term. The particular solution is obtained by expanding the magnetic source distribution in the eigenfunctions basis and solving the Poisson PDE. Particular solutions for PMs and windings are given in Section 3.5.

If the superposition principle is used, Equations (3.35) and (3.36) merge together:

$$A_z = A_{zh}^C + A_{zh}^R + A_{zp}^C + A_{zp}^R \tag{3.37}$$

3.3.6 Separation of Variables (SoV) technique

3.3.6.1 Separation of Variables principle

To enable the analytical resolution, the homogeneous PDE is decomposed into several Ordinary Differential Equations (ODEs) using the Separation of Variables (SoV) technique. The MVP is written as a product of two mono-variables functions R and Θ :

$$A_z(t_0, r, \theta) = R(t_0, r)\Theta(t_0, \theta) \tag{3.38}$$

where t_0 is the simulation instant parameter, on which sets the rotor position (hence, for example, the PM distribution) and the stator and rotor current distributions.

For compactness, instant parameter t_0 is implicit in the following developments, except in the expression of magnetic sources to specify that they are considered for the specific distribution of the simulated instant. Besides, 1^{st} and 2^{nd} derivative operators are respectively noted " $'$ " and " $''$ ".

3.3.6.2 SoV in homogeneous Laplace PDE

Injecting Equation (3.38) in (3.20) yields:

$$r^2\frac{\mathrm{R}''}{\mathrm{R}}+r\frac{\mathrm{R}'}{\mathrm{R}}=-\frac{\Theta''}{\Theta} \tag{3.39}$$

which is a two variables differential equation, where r-dependent terms are isolated in the left member and θ-dependent terms are in the right member. Therefore, right and left members are necessary equal to a constant real term, noted λ and called eigenvalue. The Laplace PDE results in two ODEs linked by the eigenvalue λ, such as:

$$\begin{cases} r^2\mathrm{R}''+r\mathrm{R}'-\lambda\mathrm{R}=0 & (3.40)\\ \Theta''+\lambda\Theta=0 & (3.41)\end{cases}$$

3.3.6.3 SoV in homogeneous Helmholtz PDE

From Equation (3.15), the MVP has complex values, hence the Separation of Variables (SoV) is expressed as a product of two complex functions:

$$\underline{\mathrm{A}_z}(r,\theta)=\underline{\mathrm{R}}(r)\underline{\Theta}(\theta) \tag{3.42}$$

Injecting Equation (3.38) in (3.15) yields:

$$r^2\frac{\underline{\mathrm{R}}''}{\mathrm{R}}+r\frac{\underline{\mathrm{R}}'}{\mathrm{R}}-(\underline{\alpha}r)^2=-\frac{\underline{\Theta}''}{\underline{\Theta}} \tag{3.43}$$

Once again, r and θ dependent terms are isolated in left and right members. The eigenvalue λ is introduced. λ could be complex regarding the complex nature of the MVP because of the complex diffusion coefficient $\underline{\alpha}$. However, the Sturm-Liouville theory shows that eigenvalues are real for any eigenvalue problems treated afterwards [Herman, 2013]. Therefore, the Helmholtz PDE gives the two following ODEs:

$$\begin{cases} r^2\underline{\mathrm{R}}''+r\underline{\mathrm{R}}'-\left[(\underline{\alpha}r)^2+\lambda\right]\underline{\mathrm{R}}=0 & (3.44)\\ \Theta''+\lambda\Theta=0 & (3.45)\end{cases}$$

Besides, the function Θ is also real as it is a solution of ODE (3.45) which is independent from $\underline{\alpha}$, and is the same equation as in Laplace case. Therefore, only the r-dependent ODE differs between Helmholtz and Laplace problems.

3.3.6.4 MVP solution with separated variables

The MVP solution is obtained by summing the solution for each eigenvalue:

$$\mathrm{A}_z(r,\theta)=\sum_{\lambda}\mathrm{R}_\lambda(r)\Theta_\lambda(\theta) \tag{3.46}$$

with R_λ is a solution of Equations (3.40) or (3.44), which is complex only in Helmholtz case, and Θ_λ is a solution of Equations (3.41) or (3.45).

R_λ is called eigenfunction in eigenvalue problems on r-direction, while Θ_λ is the eigenfunction in those on θ-direction. The Sturm-Liouville theory ensures that eigenfunctions with distinct eigenvalues are orthogonal regarding the scalar product defined in Appendix A.5, and used for the application of ICs between subdomains in Section 4.2.2.

3.3.7 Application of BCs to the MVP solution with separated variables

3.3.7.1 HBCs expressions after SoV

HBCs which apply on MVP either apply on R or Θ function depending on if the edge is a line or an arc segment, such as:

$$\text{Dirichlet HBC (3.27)} : \quad n_{12} \parallel \mathbf{e}_r, \quad A_z(R_x,\theta) = 0 \quad \Rightarrow \quad R(R_x) = 0 \tag{3.47}$$

$$\text{Dirichlet HBC (3.28)} : \quad n_{12} \parallel \mathbf{e}_\theta, \quad A_z(r,\Theta_x) = 0 \quad \Rightarrow \quad \Theta(\Theta_x) = 0 \tag{3.48}$$

$$\text{Neumann HBC (3.29)} : \quad n_{12} \parallel \mathbf{e}_r, \quad \left.\frac{\partial A_z}{\partial r}\right|_{r=R_x,\theta} = 0 \quad \Rightarrow \quad R'(R_x) = 0 \tag{3.49}$$

$$\text{Neumann HBC (3.30)} : \quad n_{12} \parallel \mathbf{e}_\theta, \quad \left.\frac{\partial A_z}{\partial \theta}\right|_{r,\theta=\Theta_x} = 0 \quad \Rightarrow \quad \Theta'(\Theta_x) = 0 \tag{3.50}$$

where $R_x \in \{R_1, R_2\}$ and $\Theta_x \in \{\Theta_1, \Theta_2\}$.

3.3.7.2 BCs for eigenvalue problems in θ-direction

For eigenvalue problems in circumferential direction, HBCs apply on the eigenfunction Θ. The four possible sets of HBC are:

$$\left(\left[\Theta(\Theta_1) \text{ or } \Theta'(\Theta_1)\right] = 0\right) \quad \text{and} \quad \left(\left[\Theta(\Theta_2) \text{ or } \Theta'(\Theta_2)\right] = 0\right) \tag{3.51}$$

The sets used in this thesis are:

$$\begin{cases} & \Theta(\Theta_1) = \Theta(\Theta_2) = 0 & (3.52) \\ \text{or} & \Theta'(\Theta_1) = \Theta'(\Theta_2) = 0 & (3.53) \end{cases}$$

where Equation (3.52) describes for example the Dirichlet HBCs used in the superposition principle formulation illustrated in Figure 4.15, and Equation (3.53) describes the Neumann HBCs used in slot subdomains assuming infinite permeability (cf Figure 3.7), or in formulations of superposition principle illustrated in Figures 3.9, 4.9 and 4.10.

The mixed Dirichlet and Neumann HBCs $\left[\Theta(\Theta_x) = 0 \quad \text{and} \quad \Theta'(\Theta_y) = 0\right]$, with $x, y \in \{1,2\}$, are not used in subdomain models of common electrical machines.

Furthermore, the PBC (3.31) becomes for $\theta = \Theta_1$:

$$\Theta(\Theta_1) = \Theta(\Theta_1 + 2\pi) \quad \text{and} \quad \Theta'(\Theta_1) = \Theta'(\Theta_1 + 2\pi) \tag{3.54}$$

3.3.7.3 BCs for eigenvalue problems in r-direction

For eigenvalue problems in r-direction, HBCs apply on the eigenfunction R. The four possible sets are:

$$\left(\left[R(R_1) \text{ or } R'(R_1)\right] = 0\right) \quad \text{and} \quad \left(\left[R(R_2) \text{ or } R'(R_2)\right] = 0\right) \tag{3.55}$$

The sets used in this thesis are:

$$\begin{cases} & R(R_1) = R(R_2) = 0 & (3.56) \\ \text{or} & R(R_1) = R'(R_2) = 0 & (3.57) \end{cases}$$

where Equation (3.56) describes the Dirichlet HBCs used in the superposition principle formulation illustrated in Figure 3.8c, and Equation (3.57) describes the mixed

Dirichlet and Neumann HBCs used in the superposition principle formulations illustrated in Figures 4.9, 4.10 and 4.15.

The Neumann HBCs and the PBC are not used for eigenvalue problems in radial direction in this thesis.

3.4 Analytical solutions of homogeneous ODEs

3.4.1 General solution of Laplace ODEs

3.4.1.1 Resolution of Laplace ODEs

Solutions of Laplace ODEs (3.40) and (3.41) depend on the sign of the eigenvalue λ:

— If $\lambda = 0$:

$$\begin{cases} R_0(r) = C_{10} + C_{20}\ln(r) & (3.58) \\ \Theta_0(\theta) = C_{30} + C_{40}\theta & (3.59) \end{cases}$$

where C_{10}, C_{20}, C_{30} and C_{40} are real integration constants.

— If $\lambda > 0$:

$$\begin{cases} R_\nu(r) = C_{1\nu} r^\nu + C_{2\nu} r^{-\nu} & (3.60) \\ \Theta_\nu(\theta) = C_{3\nu}\cos(\nu\theta) + C_{4\nu}\sin(\nu\theta) & (3.61) \end{cases}$$

where $\nu = \sqrt{\lambda}$, and $C_{1\nu}, C_{2\nu}, C_{3\nu}$ and $C_{4\nu}$ are real integration constants.

— If $\lambda < 0$:

$$\begin{cases} R_\upsilon(r) = C_{1\upsilon}\cos\left[\upsilon\ln(r)\right] + C_{2\upsilon}\sin\left[\upsilon\ln(r)\right] & (3.62) \\ \Theta_\upsilon(\theta) = C_{3\upsilon}e^{\upsilon\theta} + C_{4\upsilon}e^{-\upsilon\theta} & (3.63) \end{cases}$$

where $\upsilon = \sqrt{-\lambda}$, and $C_{1\upsilon}, C_{2\upsilon}, C_{3\upsilon}$ and $C_{4\upsilon}$ are real integration constants.

The case $\lambda \geq 0$ is the solution of Laplace eigenvalue problems in θ-direction, which are classic in the subdomain modeling technique.

The case $\lambda \leq 0$ is the solution of Laplace eigenvalue problems in r-direction, which is used in MVP solution of slots and teeth subdomains accounting for finite permeability. The relative permeability does not seem to be accounted for as it does not appear in the Laplace MVP solutions above. This is due to the fact that the relative permeability is uniform in the subdomain, and only appears when applying the tangential field continuity condition with the adjacent subdomains (cf. Equations (3.24) and (3.25)).

3.4.1.2 Reformulation based on numerical considerations

In Equations (3.58) and (3.62), absolute value in logarithmic functions is not necessary since $r > 0$. r may be zero, for example in the rotor yoke subdomain if there is no shaft. In this case, $R_0(r) = C_{10}$ and $R_\nu(r) = C_{1\nu} r^\nu$, and $R_\upsilon(0) = 0$ so that MVP has finite values.

The expressions in $r^{\pm\nu}$ in Equations (3.58) and (3.60) diverge for any values of r when $\nu \to \infty$, which make them hardly exploitable in the subdomain methodology. To reduce this numerical aspect, these equations are reformulated using dimensionless expressions:

$$\text{If} \quad \nu = 0: \quad \mathrm{R}_0(r) = \mathrm{C}_{10} + \mathrm{C}_{20}\ln\left(\frac{r}{\mathrm{R}_2}\right) \tag{3.64}$$

$$\text{If} \quad \nu > 0: \quad \mathrm{R}_\nu(r) = \mathrm{C}_{1\nu}\left(\frac{r}{\mathrm{R}_2}\right)^\nu + \mathrm{C}_{2\nu}\left(\frac{\mathrm{R}_1}{r}\right)^\nu \tag{3.65}$$

by renaming: $\mathrm{C}_{10} := \mathrm{C}_{10} - \mathrm{C}_{20}\ln(\mathrm{R}_2)$, $\mathrm{C}_{1\nu} := \mathrm{C}_{1\nu}\mathrm{R}_2^{-\nu}$, and $\mathrm{C}_{2\nu} := \mathrm{C}_{2\nu}\mathrm{R}_1^{\nu}$.

However, it is not possible to find a dimensionless expression for Equation (3.63), although terms in $e^{\pm\upsilon\theta}$ also diverge for any values of θ when $\upsilon \to \infty$. Besides, for all of the eigenvalue problems developed afterwards, it can be shown that $\mathrm{C}_{40} = 0$, yielding:

$$\text{If} \quad \lambda = 0: \quad \Theta_0(\theta) = \mathrm{C}_{30} \tag{3.66}$$

3.4.1.3 General MVP solution formulated in series

From Equations (3.46), (3.61), and (3.64)-(3.66), the homogeneous MVP solution for Laplace eigenvalue problems in θ-direction, i.e. for $\lambda = \nu^2 \geq 0$, can be written under series form such as:

$$\begin{aligned}\mathrm{A}^{\mathrm{C}}_{zh}(r,\theta) = a_0 + b_0\ln\left(\frac{r}{\mathrm{R}_2}\right) \\ + \sum_{\nu>0}\left[a_\nu\left(\frac{r}{\mathrm{R}_2}\right)^\nu + b_\nu\left(\frac{\mathrm{R}_1}{r}\right)^\nu\right]\cos(\nu\theta) + \left[c_\nu\left(\frac{r}{\mathrm{R}_2}\right)^\nu + d_\nu\left(\frac{\mathrm{R}_1}{r}\right)^\nu\right]\sin(\nu\theta)\end{aligned} \tag{3.67}$$

where a_0, b_0, a_ν, b_ν, c_ν, and d_ν are the unknown integration constants with $\forall \nu \geq 0$, $a_\nu = \mathrm{C}_{1\nu}\mathrm{C}_{3\nu}$, $b_\nu = \mathrm{C}_{2\nu}\mathrm{C}_{3\nu}$, $c_\nu = \mathrm{C}_{1\nu}\mathrm{C}_{4\nu}$, and $d_\nu = \mathrm{C}_{2\nu}\mathrm{C}_{4\nu}$.

From Equations (3.46), (3.62)-(3.63), (3.64) and (3.66), the homogeneous MVP solution for Laplace eigenvalue problems in r-direction, i.e. for $\lambda = -\upsilon^2 \leq 0$, can be written under series form such as:

$$\begin{aligned}\mathrm{A}^{\mathrm{R}}_{zh}(r,\theta) = a_0 + b_0\ln\left(\frac{r}{\mathrm{R}_2}\right) \\ + \sum_{\upsilon>0}\left(a_\upsilon e^{\upsilon\theta} + b_\upsilon e^{-\upsilon\theta}\right)\cos\left[\upsilon\ln(r)\right] + \left(c_\upsilon e^{\upsilon\theta} + d_\upsilon e^{-\upsilon\theta}\right)\sin\left[\upsilon\ln(r)\right]\end{aligned} \tag{3.68}$$

where a_0, b_0, a_υ, b_υ, c_υ, and d_υ are the unknown integration constants with $\forall \upsilon \geq 0$, $a_\upsilon = \mathrm{C}_{1\upsilon}\mathrm{C}_{3\upsilon}$, $b_\upsilon = \mathrm{C}_{2\upsilon}\mathrm{C}_{3\upsilon}$, $c_\upsilon = \mathrm{C}_{1\upsilon}\mathrm{C}_{4\upsilon}$, and $d_\upsilon = \mathrm{C}_{2\upsilon}\mathrm{C}_{4\upsilon}$.

3.4.1.4 Reformulation to account for Interface Conditions (ICs)

Therefore, there are six analytical integrations constants per eigenvalue problem to find, although there are only two BCs/ICs applying on each edge in the eigenvalue problem direction, i.e. on circumferential edges ($r = \mathrm{R}_1$ and $r = \mathrm{R}_2$) for circumferential problems, and on radial edges ($\theta = \Theta_1$ and $\theta = \Theta_2$) for radial problems. From Sturm-Liouville theory, it is shown that eigenfunctions with distinct eigenvalues are orthogonal, regarding the scalar product defined in Appendix A.5. This scalar product also shows that cosine and sine terms are orthogonal for a same eigenvalue. The orthogonal eigenfunction basis $\mathscr{B}_\nu$, $\mathscr{B}_\upsilon$ of circumferential and radial eigenvalue problems can be defined as:

$$\mathscr{B}_\nu(\theta) = \begin{bmatrix} 1 & \cos(\nu\theta) & \sin(\nu\theta) \end{bmatrix}_{\nu>0} \tag{3.69}$$

$$\mathscr{B}_\upsilon(r) = \begin{bmatrix} 1 & \cos\left[\upsilon\ln(r)\right] & \sin\left[\upsilon\ln(r)\right]_{\upsilon>0} \end{bmatrix} \tag{3.70}$$

To determine the six unknown integration constants, three scalar products can be applied on each edge to ensure the constant, cosine and sine components continuity of the MVP or of the tangential field with the adjacent subdomains. This results in six unknown integration constants for six continuity equations, so the eigenvalue problem can be solved.

As it is generally done in Sturm-Liouville problems, the MVP solution is reformulated to facilitate the application of ICs. Contrary to the dimensionless reformulation performed in Subsection 3.4.1.2, this reformulation is not necessary for the numerical resolution of ICs but it provides simpler and more physical relations between the unknown integration constants of each subdomain as illustrated in Subsection 4.2.1. Therefore, four new integration constants which represent cosine and sine components on the two edges in the eigenvalue problem direction are introduced. For circumferential problems, the reformulation yields:

$$\begin{aligned} \mathrm{A}^{\mathrm{C}}_{zh}(r,\theta) = a_0 + b_0 \ln\left(\frac{r}{\mathrm{R}_2}\right) \\ + \sum_{\nu>0} \Big[\Big(\mathrm{A}_\nu \mathrm{F}_{1\nu}(r) + \mathrm{B}_\nu \mathrm{F}_{2\nu}(r)\Big) \cos(\nu\theta) \\ + \quad \Big(\mathrm{C}_\nu \mathrm{F}_{1\nu}(r) + \mathrm{D}_\nu \mathrm{F}_{2\nu}(r)\Big) \sin(\nu\theta) \Big] \end{aligned} \tag{3.71}$$

where A_ν, B_ν, C_ν, and D_ν are the new unknown integration constants, and $\mathrm{F}_{1\nu}$, $\mathrm{F}_{2\nu}$ are two functions such as:

$$\mathrm{F}_{1\nu}(\mathrm{R}_1) = 1, \quad \mathrm{F}_{2\nu}(\mathrm{R}_1) = 0, \quad \mathrm{F}_{1\nu}(\mathrm{R}_2) = 0, \quad \mathrm{F}_{2\nu}(\mathrm{R}_2) = 1 \quad \text{for MVP continuity} \tag{3.72}$$

$$\mathrm{F}'_{1\nu}(\mathrm{R}_1) = 1, \quad \mathrm{F}'_{2\nu}(\mathrm{R}_1) = 0, \quad \mathrm{F}'_{1\nu}(\mathrm{R}_2) = 0, \quad \mathrm{F}'_{2\nu}(\mathrm{R}_2) = 1 \quad \text{for field continuity} \tag{3.73}$$

Expressions of $\mathrm{F}_{1\nu}$, $\mathrm{F}_{2\nu}$ are given all along Chapter 4 for various sets of ICs applying on circumferential edges. They are based on geometrical polynoms defined in Appendix A.6.1.

The same reformulation is performed for radial eigenvalue problems:

$$\begin{aligned} \mathrm{A}^{\mathrm{R}}_{zh}(r,\theta) = a_0 + b_0 \ln\left(\frac{r}{\mathrm{R}_2}\right) \\ + \sum_{\upsilon>0} \Big[\Big(\mathrm{A}_\upsilon \mathrm{G}_{1\upsilon}(\theta) + \mathrm{B}_\upsilon \mathrm{G}_{2\upsilon}(\theta)\Big) \cos\left[\upsilon\ln(r)\right] \\ + \quad \Big(\mathrm{C}_\upsilon \mathrm{G}_{1\upsilon}(\theta) + \mathrm{D}_\upsilon \mathrm{G}_{2\upsilon}(\theta)\Big) \sin\left[\upsilon\ln(r)\right] \Big] \end{aligned} \tag{3.74}$$

where A_υ, B_υ, C_υ, and D_υ are the new unknown integration constants, and $\mathrm{G}_{1\upsilon}$, $\mathrm{G}_{2\upsilon}$ are two functions such as:

$$\mathrm{G}_{1\upsilon}(\Theta_1) = 1 \quad \mathrm{G}_{2\upsilon}(\Theta_1) = 0 \quad \mathrm{G}_{1\upsilon}(\Theta_2) = 0 \quad \mathrm{G}_{2\upsilon}(\Theta_2) = 1 \quad \text{for MVP continuity} \tag{3.75}$$

$$\mathrm{G}'_{1\upsilon}(\Theta_1) = 1 \quad \mathrm{G}'_{2\upsilon}(\Theta_1) = 0 \quad \mathrm{G}'_{1\upsilon}(\Theta_2) = 0 \quad \mathrm{G}'_{2\upsilon}(\Theta_2) = 1 \quad \text{for field continuity} \tag{3.76}$$

Expressions of G_{1v}, G_{2v} are given in Section 4.3 for various sets of ICs applying on radial edges. They are based on hyperbolic functions cosh and sinh.

In Subsections 3.4.2.1-3.4.3.2, MVP solutions are developed for five Laplace eigenvalue problems in circumferential and radial directions.

3.4.2 Solution of Laplace ODEs for eigenvalue problems in θ-direction

3.4.2.1 Eigenvalue problem in θ-direction with PBC

The Laplace eigenvalue problem in θ-direction with PBC is for example solved in airgap (see Subsection 4.2.1.4), surface PM (see Subsection 4.2.1.3), airgap windings, stator and rotor yoke subdomains.

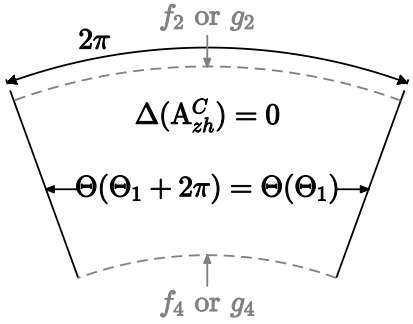

Figure 3.10 – Laplace eigenvalue problem in θ-direction with PBC.

Applying the PBC (3.54) as illustrated in Figure 3.10, the following eigenvalues ν, eigenfunction basis $\mathscr{B}_n$, and integration constants $\mathscr{C}_n$ are obtained:

$$\begin{cases} \nu = n, \quad n \in \mathbb{N} & (3.77) \\ \mathscr{B}_\nu(\theta) := \mathscr{B}_n(\theta) = \begin{bmatrix} 1 & \cos(n\theta) & \sin(n\theta) \end{bmatrix} & (3.78) \\ \mathscr{C}_\nu := \mathscr{C}_n = \begin{bmatrix} a_0 & b_0 & A_n & B_n & C_n & D_n \end{bmatrix} & (3.79) \end{cases}$$

with $a_0, b_0, A_n, B_n, C_n, D_n$ the subdomain integration constants as defined in Subsection 3.4.1.4.

From Equations (3.71) and (3.77), the MVP solution of Laplace eigenvalue problems in θ-direction subject to PBC is:

$$\begin{aligned} A_{zh}^C(r,\theta) = a_0 + b_0 \ln\left(\frac{r}{R_2}\right) \\ + \sum_{n=1}^{N\to\infty} \Big[\Big(A_n F_{1n}(r) + B_n F_{2n}(r)\Big)\cos(n\theta) \\ + \Big(C_n F_{1n}(r) + D_n F_{2n}(r)\Big)\sin(n\theta) \Big] \end{aligned} \tag{3.80}$$

which introduces the highest harmonic order N, which is theoretically infinite, but is chosen at a certain value for the numerical resolution of ICs set (see an example in Subsection 4.2.3.2), and the functions F_{1n}, F_{2n} defined by Equations (3.72)-(3.73). F_{1n} and F_{2n} depend on the nature of the BCs/ICs applying on both circumferential edges (i.e. for

$r = \mathrm{R}_1$ and $r = \mathrm{R}_2$), represented by the functions f_2, g_2, f_4, g_4 in Figure 3.10.

The MVP solution in 2π-periodic problems is therefore the MVP 1D Fourier series, which explains why both ARME and SDM are often referred as "Fourier-based model" or "harmonic modeling". It is shown here that the use of Fourier series is actually a consequence of the more general Sturm-Liouville theory. From this observation, the eigenfunction basis is classically referred as Fourier basis.

3.4.2.2 Eigenvalue problem in θ-direction with Neumann HBCs

The Laplace eigenvalue problem in θ-direction with Neumann HBCs is for example solved in slot (see Subsection 4.2.1.5 for stator slot case), slot opening, magnetic wedge, and notch subdomains assuming infinite permeability (cf. Figure 3.7). This eigenvalue problem is also solved in slot and tooth subdomains assuming tooth finite permeability, using the first formulation of superposition principle (cf. Figure 3.8b).

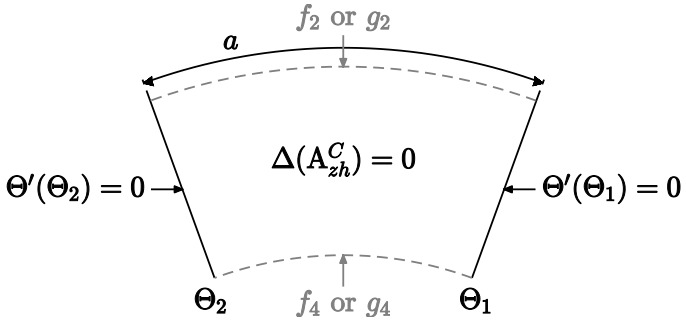

Figure 3.11 – Laplace eigenvalue problem in θ-direction with Neumann HBCs.

Applying Neumann HBCs (3.53) illustrated in Figure 3.11, the following eigenvalues ν, Fourier basis $\mathscr{B}_\nu$, and integration constants $\mathscr{C}_\nu$ are obtained:

$$\begin{cases} \nu := \nu_m = \frac{m\pi}{a}, \quad m \in \mathbb{N} & (3.81) \\ \mathscr{B}_\nu(\theta) := \mathscr{B}_m(\theta) = \begin{bmatrix} 1 & \cos\left[\nu_m(\theta - \Theta_1)\right] \end{bmatrix} & (3.82) \\ \mathscr{C}_\nu := \mathscr{C}_m = \begin{bmatrix} a_0 & b_0 & \mathrm{A}_m & \mathrm{B}_m \end{bmatrix} & (3.83) \end{cases}$$

with $a_0, b_0, \mathrm{A}_m, \mathrm{B}_m$ the new subdomain integration constants.

From Equations (3.71) and (3.81)-(3.83), the MVP solution of Laplace eigenvalue problems in θ-direction subject to Neumann HBCs is:

$$\mathrm{A}_{zh}^{\mathrm{C}}(r,\theta) = a_0 + b_0 \ln\left(\frac{r}{\mathrm{R}_2}\right) + \sum_{m=1}^{\mathrm{M}\to\infty} \left[\mathrm{A}_m \mathrm{F}_{1m}(r) + \mathrm{B}_m \mathrm{F}_{2m}(r)\right] \cos\left[\nu_m(\theta - \Theta_1)\right] \tag{3.84}$$

where M is the highest harmonic order for numerical resolution (infinite in theory), and functions F_{1m}, F_{2m} are defined by Equations (3.72)-(3.73), depending on the nature of each BC/IC applying on both circumferential edges (i.e. for $r = \mathrm{R}_1$ and $r = \mathrm{R}_2$) which are represented by the functions f_2, g_2, f_4, g_4 in Figure 3.11.

3.4.2.3 Eigenvalue problem in θ-direction with Dirichlet HBCs

The Laplace eigenvalue problem in θ-direction with Dirichlet HBCs is only solved for tooth subdomain assuming finite permeability using the second superposition principle formulation illustrated in Figure 4.15. As shown by Subsection 4.3.3.1, the eigenvalue problem with Neumann HBCs developed in previous Subsection 3.4.2.2 should be preferred.

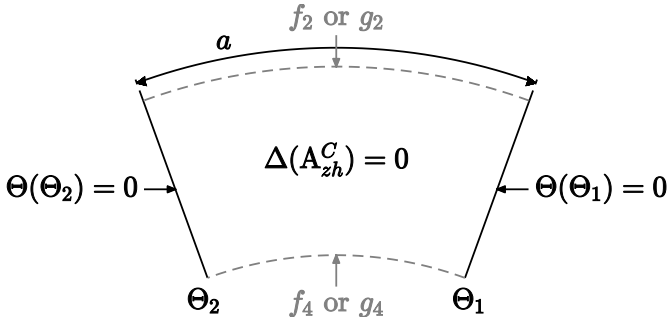

Figure 3.12 – Laplace eigenvalue problem in θ-direction with Dirichlet HBCs.

Applying Dirichlet HBCs (3.52) as illustrated in Figure 3.12, the following eigenvalues ν, Fourier basis $\mathscr{B}_\nu$, and integration constants $\mathscr{C}_\nu$ are obtained:

$$\begin{cases} \nu := \nu_m = \frac{m\pi}{a}, \quad m \in \mathbb{N} & (3.85) \\ \mathscr{B}_\nu(\theta) := \mathscr{B}_m(\theta) = \sin\left[\nu_m(\theta - \Theta_1)\right] & (3.86) \\ \mathscr{C}_\nu := \mathscr{C}_m = \begin{bmatrix} A_m & B_m \end{bmatrix} & (3.87) \end{cases}$$

with A_m, B_m the new subdomain integration constants.

From Equations (3.71) and (3.85)-(3.87), the MVP solution of Laplace eigenvalue problems in θ-direction subject to Dirichlet HBCs is:

$$A_{zh}^C(r,\theta) = \sum_{m=1}^{M\to\infty} \left[A_m F_{1m}(r) + B_m F_{2m}(r)\right] \sin\left[\nu_m(\theta - \Theta_1)\right] \tag{3.88}$$

where M is the highest harmonic order for numerical resolution (infinite in theory), and functions F_{1m}, F_{2m} are defined by Equations (3.72)-(3.73), depending on the nature of each BC/IC applying on both circumferential edges (i.e. for $r = R_1$ and $r = R_2$) which are represented by the functions f_2, g_2, f_4, g_4 in Figure 3.11.

3.4.3 Solution of Laplace ODEs for eigenvalue problems in r-direction

3.4.3.1 Eigenvalue problem in r-direction with Dirichlet HBCs

The Laplace eigenvalue problem in r-direction with Dirichlet HBCs is solved for slot and tooth subdomains assuming finite permeability using the superposition principle formulation illustrated in Figure 3.8c.

Applying Dirichlet HBCs (3.56) as illustrated in Figure 3.13, the following eigenvalues υ, Fourier basis $\mathscr{B}_\upsilon$, and integration constants $\mathscr{C}_\upsilon$ are obtained:

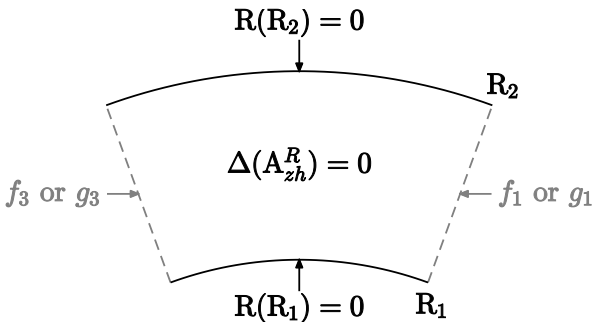

Figure 3.13 – Laplace eigenvalue problem in r-direction with Dirichlet HBCs.

$$\begin{cases} \upsilon := \upsilon_m = \dfrac{m\pi}{\ln\left(\frac{\mathrm{R}_2}{\mathrm{R}_1}\right)}, \quad m \in \mathbb{N} & (3.89) \\ \mathscr{B}_\upsilon(r) := \mathscr{B}_m(r) = \sin\left[\upsilon_m \ln\left(\frac{r}{\mathrm{R}_1}\right)\right] & (3.90) \\ \mathscr{C}_\upsilon := \mathscr{C}_m = \begin{bmatrix} \mathrm{A}_m & \mathrm{B}_m \end{bmatrix} & (3.91) \end{cases}$$

with $\mathrm{A}_m, \mathrm{B}_m$ the new subdomain integration constants. It can be noticed that the Fourier basis (3.90) has now dimensionless expressions of r.

From Equations (3.74) and (3.89)-(3.91), the MVP solution of Laplace eigenvalue problems in r-direction subject to Dirichlet HBCs is:

$$\mathrm{A}^{\mathrm{R}}_{zh}(r,\theta) = \sum_{m=1}^{\mathrm{M}\to\infty} \left[\mathrm{A}_m \mathrm{G}_{1m}(\theta) + \mathrm{B}_m \mathrm{G}_{2m}(\theta)\right] \sin\left[\upsilon_m \ln\left(\frac{r}{\mathrm{R}_1}\right)\right] \tag{3.92}$$

where M is the highest harmonic order for numerical resolution (infinite in theory), and functions G_{1m}, G_{2m} are defined by Equations (3.75)-(3.76), depending on the nature of each BC/IC applying on both radial edges (i.e. for $\theta = \Theta_1$ and $\theta = \Theta_2$), represented by the functions f_1, g_1, f_3, g_3 in Figure 3.13.

3.4.3.2 Eigenvalue problem in r-direction with mixed HBCs

The Laplace eigenvalue problem in r-direction with mixed HBCs is solved for slot and tooth subdomains with finite permeability while assuming infinite permeability of stator yoke, using the superposition principle formulations illustrated in Figures 4.9, 4.10 and 4.15.

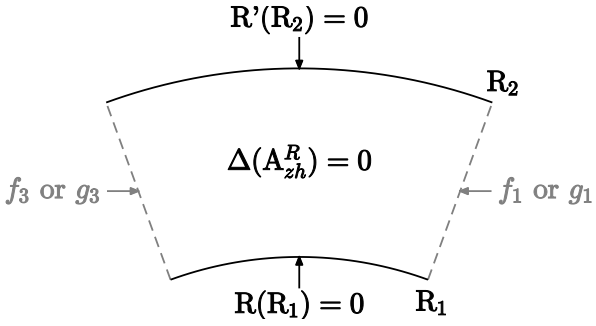

Figure 3.14 – Laplace eigenvalue problem in r-direction with mixed HBCs.

Applying mixed Dirichlet and Neumann HBCs (3.57) as illustrated in Figure 3.14, the following eigenvalues υ, Fourier basis $\mathscr{B}_\upsilon$, and integration constants $\mathscr{C}_\upsilon$ are obtained:

$$\begin{cases} \upsilon := \upsilon_m = \dfrac{m\pi}{\ln\left(\frac{R_2}{R_1}\right)}, \quad m = 2k+1, \quad k \in \mathbb{N} & (3.93) \\ \mathscr{B}_\upsilon(r) := \mathscr{B}_m(r) = \sin\left[\upsilon_m \ln\left(\frac{r}{R_1}\right)\right] & (3.94) \\ \mathscr{C}_\upsilon := \mathscr{C}_m = \begin{bmatrix} A_m & B_m \end{bmatrix} & (3.95) \end{cases}$$

which is the same as the Dirichlet HBCs case (cf. Subsection 3.4.3.1) except that m takes odd integer values only.

From Equations (3.74) and (3.93)-(3.95), the MVP solution of Laplace eigenvalue problems in r-direction subject to mixed Dirichlet and Neumann HBCs is:

$$A^R_{zh}(r,\theta) = \sum_{m=1,3,5...}^{M\to\infty} \left[A_m G_{1m}(\theta) + B_m G_{2m}(\theta)\right] \sin\left[\upsilon_m \ln\left(\frac{r}{R_1}\right)\right] \tag{3.96}$$

where M is the highest harmonic order for numerical resolution (infinite in theory), and functions G_{1m}, G_{2m} are defined by Equations (3.75)-(3.76), depending on the nature of each BC/IC applying on both radial edges (i.e. for $\theta = \Theta_1$ and $\theta = \Theta_2$), represented by the functions f_1, g_1, f_3, g_3 in Figure 3.13.

3.4.4 General solution of Helmholtz ODEs formulated in series

In this thesis, Helmholtz ODEs (3.44) and (3.45) are only solved for eigenvalue problems in θ-direction. Therefore, the eigenvalue λ is either positive or zero (cf. Subsection 3.4.1). Besides, the solution of ODE (3.45) is the same as for Laplace case. The solution of Helmholtz ODE (3.44) is:

— If $\lambda = 0$:

$$R_0(r) = \underline{C}_{10} I_0(\underline{\alpha} r) + \underline{C}_{20} K_0(\underline{\alpha} r) \tag{3.97}$$

where $\underline{C}_{10}$ and $\underline{C}_{20}$ are complex integration constants, I_0 is the modified Bessel function of first kind and 0^{th} order, K_0 is the modified Bessel function of second kind and 0^{th} order, and $\underline{\alpha}$ is the diffusion coefficient (cf. Equation (3.19)).

— If $\lambda > 0$:

$$R_\nu(r) = \underline{C}_{1\nu} I_\nu(\underline{\alpha} r) + \underline{C}_{2\nu} K_\nu(\underline{\alpha} r) \tag{3.98}$$

where $\nu = \sqrt{\lambda}$, $\underline{C}_{1\nu}$ and $\underline{C}_{2\nu}$ are complex integration constants, I_ν is the modified Bessel function of first kind and ν^{th} order, and K_ν is the modified Bessel function of second kind and ν^{th} order.

It is not possible to get dimensionless expressions in r inside Bessel functions. Besides, it can be noticed that modified Bessel functions I and K are used rather than Bessel functions J and Y. J and Y are also solutions of Helmholtz equation (3.44) but they are oscillatory in nature. Therefore, I and K are more suitable in the SDM methodology regarding numerical computation [Gerling and Dajaku, 2003].

From Equations (3.46), (3.61), (3.66), and (3.97)-(3.98), the homogeneous MVP solution for Helmholtz eigenvalue problems in θ-direction, i.e. for $\lambda = \nu^2 \geq 0$, can be written under series form such as:

$$\begin{aligned} \mathrm{A}_{zh}^{\mathrm{C}}(r,\theta) &= \underline{a}_0 \mathrm{I}_0(\underline{\alpha} r) + \underline{b}_0 \mathrm{K}_0(\underline{\alpha} r) \\ &+ \sum_{\nu>0} \Big[\underline{a}_\nu \mathrm{I}_\nu(\underline{\alpha} r) + \underline{b}_\nu \mathrm{K}_\nu(\underline{\alpha} r)\Big] \cos(\nu\theta) + \Big[\underline{c}_\nu \mathrm{I}_\nu(\underline{\alpha} r) + \underline{d}_\nu \mathrm{K}_\nu(\underline{\alpha} r)\Big] \sin(\nu\theta) \end{aligned} \tag{3.99}$$

where $\underline{a}_0$, $\underline{b}_0$, $\underline{a}_\nu$, $\underline{b}_\nu$, $\underline{c}_\nu$, and $\underline{d}_\nu$ are the unknown complex integration constants with $\forall \nu \geq 0$, $\underline{a}_\nu = \underline{\mathrm{C}}_{1\nu}\mathrm{C}_{3\nu}$, $\underline{b}_\nu = \underline{\mathrm{C}}_{2\nu}\mathrm{C}_{3\nu}$, $\underline{c}_\nu = \underline{\mathrm{C}}_{1\nu}\mathrm{C}_{4\nu}$, and $\underline{d}_\nu = \underline{\mathrm{C}}_{2\nu}\mathrm{C}_{4\nu}$.

As for Laplace solution, the Helmholtz MVP solution of eigenvalue in θ-direction is also reformulated to facilitate the application of ICs. The reformulation results in the same MVP expressions as Equations (3.71)-(3.73), except that the new integration constants $\underline{\mathrm{A}}_0$, $\underline{\mathrm{B}}_0$, $\underline{\mathrm{A}}_\nu$, $\underline{\mathrm{B}}_\nu$, $\underline{\mathrm{C}}_\nu$, and $\underline{\mathrm{D}}_\nu$ are complex, and the functions $\underline{\mathrm{F}}_{1\nu}$, $\underline{\mathrm{F}}_{2\nu}$ are complex and defined for $\nu = 0$. Besides, $\underline{\mathrm{F}}_{1\nu}$ and $\underline{\mathrm{F}}_{2\nu}$ are expressed in function of M and N (defined in Appendix A.6.2) which are combinations of the modified Bessel functions I and K.

In Subsections 3.4.5.1-3.4.5.2, MVP solutions are developed for two Helmholtz eigenvalue problems in circumferential direction using both matrix and series formulations.

3.4.5 Solution of Helmholtz ODEs for eigenvalue problems in θ-direction

3.4.5.1 Eigenvalue problem in θ-direction with PBC

The Helmholtz eigenvalue problem in θ-direction with PBC is solved for rotor yoke subdomain with induced current associated to the diffusion coefficient $\underline{\alpha}$ (cf. Equation (3.19)). This eigenvalue problem is used for example in subdomain models of SRIMs (cf. Subsection 3.2.3.2).

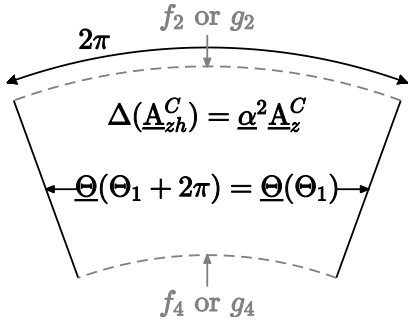

Figure 3.15 – Helmholtz eigenvalue problem in θ-direction with PBC.

Applying the PBC (3.54) as illustrated in Figure 3.15, the eigenvalues $\nu = n$ and Fourier basis $\mathscr{B}_n$ are respectively given by Equations (3.77) and (3.78). The complex integration constants $\underline{\mathscr{C}}_n$ are:

$$\underline{\mathscr{C}}_n = \begin{bmatrix} \underline{\mathrm{A}}_0 & \underline{\mathrm{B}}_0 & \underline{\mathrm{A}}_n & \underline{\mathrm{B}}_n & \underline{\mathrm{C}}_n & \underline{\mathrm{D}}_n \end{bmatrix} \tag{3.100}$$

From Equations (3.77), (3.71), and Subsection 3.4.4, the MVP solution of Helmholtz eigenvalue problems in θ-direction subject to PBC is:

$$\begin{aligned} \mathrm{A}_{zh}^{\mathrm{C}}(r,\theta) = {} & \underline{\mathrm{A}}_0\underline{\mathrm{F}}_{10}(r) + \underline{\mathrm{B}}_0\underline{\mathrm{F}}_{20}(r) \\ & + \sum_{n=1}^{\mathrm{N}\to\infty} \Big[\big(\underline{\mathrm{A}}_n\underline{\mathrm{F}}_{1n}(r) + \underline{\mathrm{B}}_n\underline{\mathrm{F}}_{2n}(r)\big)\cos(n\theta) \\ & + \big(\underline{\mathrm{C}}_n\underline{\mathrm{F}}_{1n}(r) + \underline{\mathrm{D}}_n\underline{\mathrm{F}}_{2n}(r)\big)\sin(n\theta) \Big] \end{aligned} \tag{3.101}$$

where N is the highest harmonic order for numerical resolution (infinite in theory), and functions $\underline{\mathrm{F}}_{1n}$ and $\underline{\mathrm{F}}_{2n}$ depend on the nature of the BCs/ICs applying on both circumferential edges (i.e. for $r = \mathrm{R}_1$ and $r = \mathrm{R}_2$), represented by the functions f_2, g_2, f_4, g_4 in Figure 3.15.

3.4.5.2 Eigenvalue problem in θ-direction with Neumann HBCs

The Helmholtz eigenvalue problem in θ-direction with Neumann HBCs is solved for rotor bar subdomains with induced current associated to the diffusion coefficient $\underline{\alpha}$ (cf. Equation (3.19)), and assuming rotor yoke infinite permeability. This eigenvalue problem is used for example in subdomain models of SCIMs (cf. Subsection 3.2.3.2).

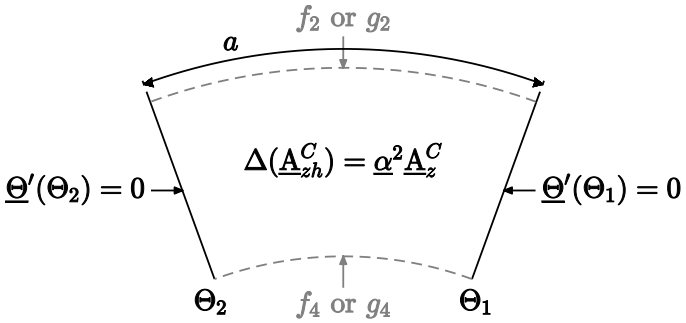

Figure 3.16 – Helmholtz eigenvalue problem in θ-direction with Neumann HBCs.

Applying Neumann HBCs (3.53) as illustrated in Figure 3.15, the eigenvalues $\nu = \nu_m$ and Fourier basis $\mathscr{B}_m$ are respectively given by Equations (3.81) and (3.82). The complex integration constants $\underline{\mathscr{C}}_m$ become:

$$\underline{\mathscr{C}}_m = \begin{bmatrix} \underline{\mathrm{A}}_0 & \underline{\mathrm{B}}_0 & \underline{\mathrm{A}}_m & \underline{\mathrm{B}}_m \end{bmatrix} \tag{3.102}$$

with $\underline{\mathrm{A}}_0, \underline{\mathrm{B}}_0, \underline{\mathrm{A}}_m, \underline{\mathrm{B}}_m$ the new complex subdomain integration constants.

From Equations (3.81), (3.71), and Subsection 3.4.4, the MVP solution of Helmholtz eigenvalue problems in θ-direction subject to Neumann HBCs is:

$$\mathrm{A}_{zh}^{\mathrm{C}}(r,\theta) = \underline{\mathrm{A}}_0\underline{\mathrm{F}}_{10}(r) + \underline{\mathrm{B}}_0\underline{\mathrm{F}}_{20}(r) + \sum_{m=1}^{\mathrm{M}\to\infty} \big[\underline{\mathrm{A}}_m\underline{\mathrm{F}}_{1m}(r) + \underline{\mathrm{B}}_m\underline{\mathrm{F}}_{2m}(r)\big]\cos\big[\nu_m(\theta - \Theta_1)\big] \tag{3.103}$$

where M is the highest harmonic order for numerical resolution (infinite in theory), and functions $\underline{\mathrm{F}}_{1m}$ and $\underline{\mathrm{F}}_{2m}$ are defined in Subsection 3.4.4, depending on the nature of each BC/IC applying on both circumferential edges (i.e. for $r = \mathrm{R}_1$ and $r = \mathrm{R}_2$), represented by the functions f_2, g_2, f_4, g_4 in Figure 3.16.

3.5 Analytical particular solutions of Poisson ODEs

3.5.1 Particular solutions for Permanent Magnets (PMs)

3.5.1.1 PMs modeling assumptions

In electrical machines, PMs can be mounted on the yoke surface or inset in slots as in SPMSMs, or completely buried in the lamination as in IPMSMs. In the following, only particular solutions of surface and inset cases are developed in Subsections 3.5.1.2 and 3.5.1.3.

In fact, the buried (or interior) case is theoretically far beyond the ARME assumptions, due to non-polar rotor topologies (e.g. V-shape or spoke shape) and the presence of saturation in rotor bridges. However, a new method has been developed during this thesis to compute the airgap flux density in open-circuit conditions (i.e. only due to rotor magnetization) for IPMSMs with V-shaped magnets [Devillers et al., 2017a]. First, the interior PMs magnetization distribution is computed by non-linear FEA for a single rotor position and without the stator slots. Then, an equivalent SPMSM subdomain model fed with the interior PMs magnetization distribution is computed to include the stator slotting effect in the open-circuit airgap flux density. This method is very fast and accurate in comparison with full FEA simulation but is not suited to full-load simulations [Devillers et al., 2017a].

For surface and inset PMs, the magnetization distribution in a PM can be both in radial and circumferential directions, as well as r and θ-dependent. In this thesis, as in classic SDM references, the magnetization is assumed to be only θ-dependent, in both radial and circumferential directions, such as:

$$\mathbf{M}(\psi,\theta) = \mathrm{M}_r(\psi,\theta)\mathbf{e}_r + \mathrm{M}_\theta(\psi,\theta)\mathbf{e}_\theta \tag{3.104}$$

where ψ is the position of the first PM. Parallel, radial and Hallbach magnetization patterns can be considered as illustrated in Figure 3.17, where B_{rem} is the remanent flux density.

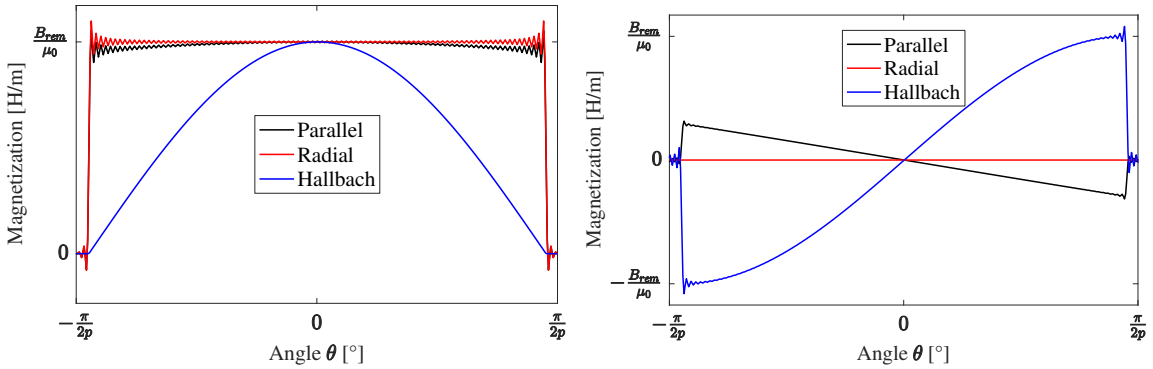

(a) Radial component $\mathrm{M}_r(\psi = 0,\theta)$.

(b) Circumferential component $\mathrm{M}_\theta(\psi = 0,\theta)$.

Figure 3.17 – Parallel, radial and Hallbach magnetization patterns of a north pole for SPMSM $12s10p$ prototype.

Both radial and circumferential magnetizations can be expressed as a 1D Fourier series:

$$\mathrm{M}_r(\psi,\theta) = \sum_{k=1,3,5...}^{\infty} \mathrm{M}_{rk} \cos\left[kp(\theta-\psi)\right] \tag{3.105}$$

$$\mathrm{M}_\theta(\psi,\theta) = \sum_{k=1,3,5...}^{\infty} \mathrm{M}_{\theta k} \sin\left[kp(\theta-\psi)\right] \tag{3.106}$$

where p is the pole pairs number. Expressions of Fourier coefficients M_{rk} and $\mathrm{M}_{\theta k}$ depend on the magnetization pattern, e.g. radial, parallel, Hallbach etc., and can be found in Rahideh and Korakianitis [2012].

Besides, the PM modeled in this thesis are assumed to have a constant relative permeability μ_r, with $\mu_r \approx 1$ for NdFeB, SmCo and ferrite PM types, which represent most of the PMs used in PMSMs.

In case of surface PMs, a relative permeability close to 1 enables to consider the whole set of PMs as a single subdomain, which thus includes the small airgap between north and south poles (cf. Figure 3.18). If the relative permeability is greater than 1 for a specific PM type, each surface PM should be treated as a single subdomain with NBCs on both radial edges, and the MVP solution would be similar to that of slots and teeth assuming finite permeability obtained from superposition principle (cf. Subsection 3.3.4).

In case of inset PMs, the relative permeability has no effect on the subdomain formulation since each PM is necessary modeled by a subdomain due to the ICs with iron teeth on both radial edges (cf. Figure 3.19).

As the magnetization is only θ-dependent, the eigenvalue problem in PM subdomains is in the circumferential direction. The Fourier basis is given by the resolution of the homogeneous Laplace ODE (cf. Subsection 3.4.2). Then, the magnetization is expressed in the Fourier basis. A MVP particular solution is obtained by injecting this new magnetization expression in the Poisson equation (3.22).

The particular solutions given in the following Subsections 3.5.1.2-3.5.1.3 are both suitable to teeth infinite or finite permeability assumption. However, they do not account for additional HBCs on circumferential edges, for example in case of rotor yoke infinite permeability assumption (at $r = \mathrm{R}_1$ for internal rotor topologies) as illustrated in Subsection A.6.3.

3.5.1.2 Particular solution in surface PMs with PBC in θ-direction

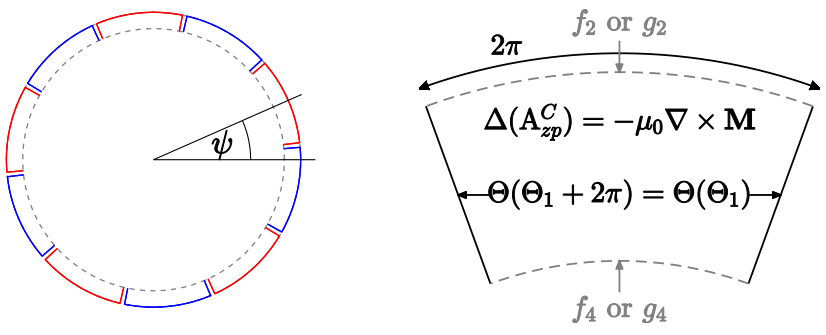

(a) Surface PMs distribution (b) Poisson PDE subject to PBC

Figure 3.18 – Surface PM subdomain problem.

As explained in Subsection 3.5.1.1 and illustrated in Figure 3.18a, surface PMs can be modeled as a single subdomain with a variable magnetization pattern $\mathbf{M}(\psi,\theta)$, which is 2π-periodic over circumferential direction and account for airgaps between north and south poles.

The position ψ of the first magnet is:

$$\psi(t_0) = \Omega t_0 + \psi_0 \tag{3.107}$$

with the rotating speed Ω constant over time, t_0 the specific instant of the magnetostatic simulation (cf. Subsection 3.2.3.3), and ψ_0 the initial position of the first surface PM.

Radial and circumferential magnetization components are expressed in the Fourier basis of periodic boundary problems in θ-direction (cf. Subsection 3.4.2.1):

$$\mathrm{M}_r(\psi,\theta) = \sum_{n=kp=p,3p...}^{\infty} \mathrm{M}_{rn}\cos(n\psi)\cos(n\theta) + \mathrm{M}_{rn}\sin(n\psi)\sin(n\theta) \tag{3.108}$$

$$\mathrm{M}_\theta(\psi,\theta) = \sum_{n=kp=p,3p...}^{\infty} -\mathrm{M}_{\theta n}\sin(n\psi)\cos(n\theta) + \mathrm{M}_{\theta n}\cos(n\psi)\sin(n\theta) \tag{3.109}$$

where M_{rn} and $\mathrm{M}_{\theta n}$ are the Fourier coefficients of radial and circumferential magnetizations for $\psi = 0$, which are non-zero only for multiple of pole pairs number p.

As illustrated in Figure 3.18b, the MVP particular solution $\mathrm{A}^{\mathrm{C}}_{zp}$ is also expressed in the Fourier basis:

$$\mathrm{A}^{\mathrm{C}}_{zp}(\psi,r,\theta) = \mu_0 \sum_{n=kp=p,3p...}^{\infty} \mathrm{R}_{cn}(\psi,r)\cos(n\theta) + \mathrm{R}_{sn}(\psi,r)\sin(n\theta) \tag{3.110}$$

where R_{cn} and R_{sn} are unknown functions, which are determined by injecting Equations (3.108)-(3.110) in Poisson equation (3.22). The two resulting ODEs in function of r and the eigenvalue $\lambda = n^2 = (kp)^2 > 0$ are:

$$r^2\mathrm{R}''_{cn} + r\mathrm{R}'_{cn} - n^2\mathrm{R}_{cn} = \quad (n\mathrm{M}_{rn} + \mathrm{M}_{\theta n})\sin(n\psi)r \tag{3.111}$$

$$r^2\mathrm{R}''_{sn} + r\mathrm{R}'_{sn} - n^2\mathrm{R}_{sn} = -(n\mathrm{M}_{rn} + \mathrm{M}_{\theta n})\cos(n\psi)r \tag{3.112}$$

whose particular solutions R_{cn} and R_{sn} are:

$$\mathrm{R}_{cn}(\psi,r) = -(n\mathrm{M}_{rn} + \mathrm{M}_{\theta n})\sin(n\psi)\mathrm{R}_{spm,n}(r) \tag{3.113}$$

$$\mathrm{R}_{sn}(\psi,r) = \quad (n\mathrm{M}_{rn} + \mathrm{M}_{\theta n})\cos(n\psi)\mathrm{R}_{spm,n}(r) \tag{3.114}$$

with $\mathrm{R}_{spm,n}(r)$ can be expressed as:

— If $n = p = 1$: $\mathrm{R}_{spm,1}(r) = \dfrac{1}{2} r\ln(r)$ (3.115)

— If $n > 1$: $\mathrm{R}_{spm,n}(r) = \dfrac{r}{n^2-1}$ (3.116)

3.5.1.3 Particular solution for inset PMs with Neumann HBCs in θ-direction

As explained in Subsection 3.5.1.1 and illustrated in Figure 3.19a, each inset PM can be modeled by a subdomain with a variable magnetization pattern $\mathbf{M}(\psi,\theta)$, where a is the subdomain angular width and b is the inset PM angular width, such as $a \geq b$.

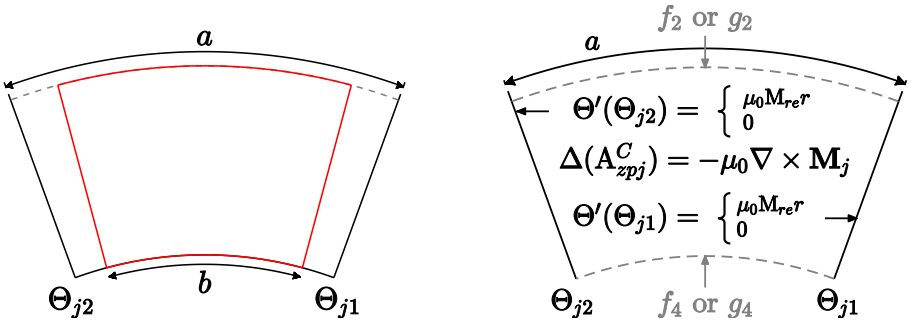

(a) Inset PMs distribution

(b) Poisson PDE subject to Neumann HBCs in θ-direction

Figure 3.19 – Inset PM subdomain problem.

The position of the j^{th} inset PM subdomain can be defined by its minimum angle Θ_{j1}, such as:

$$\Theta_{j1}(t_0) = \psi - \frac{a}{2} = \Omega t_0 + \Theta_{j10} + \frac{\pi}{p}(j-1) \tag{3.117}$$

where Ω is the rotating speed constant over time, t_0 is the specific instant of the magnetostatic simulation (cf. Subsection 3.2.3.3), Θ_{j10} is the initial position of the first inset PM subdomain, p is the pole pairs number, and $1 \leq j \leq 2p$.

Radial and circumferential magnetization components are expressed in the Fourier basis of Neumann homogeneous problems in θ-direction (see Subsection 3.4.2.2):

$$\mathrm{M}_{rj}(t_0,\theta) = (-1)^{(j-1)} \sum_{m=1}^{\infty} \mathrm{M}_{r\nu_m} \sin\left[\nu_m\big(\theta - \Theta_{j1}(t_0)\big)\right] \tag{3.118}$$

$$\mathrm{M}_{\theta j}(t_0,\theta) = (-1)^{(j-1)} \sum_{m=1}^{\infty} \mathrm{M}_{\theta\nu_m} \cos\left[\nu_m\big(\theta - \Theta_{j1}(t_0)\big)\right] \tag{3.119}$$

where $\mathrm{M}_{r\nu_m}$ and $\mathrm{M}_{\theta\nu_m}$ are the new Fourier coefficients of radial and circumferential magnetizations in the Fourier basis, and ν_m is defined in Equation (3.81).

As illustrated in Figure 3.19b, the particular MVP solution is also expressed in the Fourier basis:

$$\mathrm{A}^{\mathrm{C}}_{zpj}(t_0,r,\theta) = (-1)^{(j-1)}\mu_0 \sum_m (\nu_m \mathrm{M}_{r\nu_m} - \mathrm{M}_{\theta\nu_m})\mathrm{R}_{ipm,\nu_m}(r) \cos\left[\nu_m\big(\theta - \Theta_{j1}(t_0)\big)\right] \tag{3.120}$$

where R_{ipm,ν_m} is an unknown function which is determined by injecting Equations (3.118)-(3.120) in Poisson equation (3.22). The resulting ODE in function of r and the eigenvalue $\lambda = \nu_m^2$ is:

$$r^2 \mathrm{R}''_{ipm,\nu_m} + r\mathrm{R}'_{ipm,\nu_m} - \nu_m^2 \mathrm{R}_{ipm,\nu_m} = r \tag{3.121}$$

whose particular solution R_{ipm,ν_m} is the same as $\mathrm{R}_{spm,n}$, given by Equations (3.115)-(3.116) for $n = \nu_m$.

There is a particular case assuming infinite permeability of adjacent teeth, and if inset magnets are in contact with teeth edges, meaning $a = b$. In fact, both BCs on radial edges are non-homogeneous due to the tangential field continuity condition (3.25), which introduces the radial magnetization [Lubin et al., 2012]:

$$\left.\frac{\partial A_z}{\partial \theta}\right|_{r,\theta=\Theta_1} = \left.\frac{\partial A_z}{\partial \theta}\right|_{r,\theta=\Theta_2} = \mu_0 M_{re} r \tag{3.122}$$

where M_{re} is the magnetization radial component on magnet edges. As explained in Lubin et al. [2012], the particular solution can be found using the superposition principle to satisfy both NBCs.

In case of iron finite permeability and $a = b$, the non-homogeneous BCs are treated as Interface Conditions (ICs) with adjacent tooth subdomains.

3.5.2 Particular solution for AC/DC windings

3.5.2.1 Windings modeling assumptions

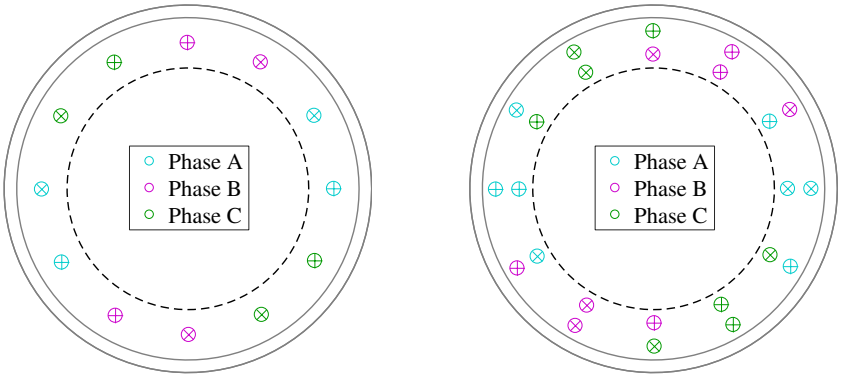

(a) Single layer (b) Radial double layer

Figure 3.20 – Airgap windings configurations.

In the general case, the current density distribution is expressed as:

$$\mathbf{j_{ext}}(t_0, r, \theta) = J_z(t_0, r, \theta)\mathbf{e}_z \tag{3.123}$$

where t_0 is the specific instant of the magnetostatic simulation (cf. Subsection 3.2.3.3).

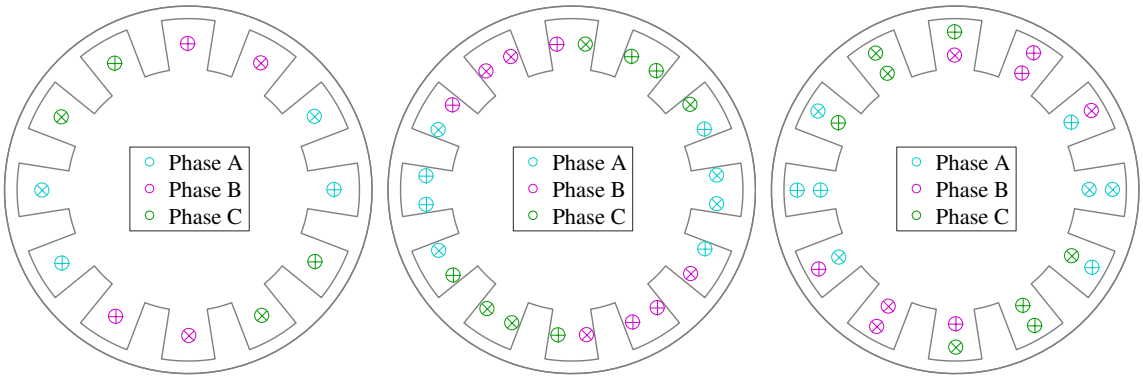

(a) Single layer (b) Circ. double layer (c) Radial double layer

Figure 3.21 – Slotted windings configurations.

Windings can be fed by DC or AC with no constraint on the number of phases. Windings can be distributed into slots or in the airgap, and their material is assumed to be

non-magnetic, i.e. with unitary relative permeability μ_r, such as in copper or aluminum.

In this thesis, three winding configurations are considered:

— Single layer winding (cf. Figures 3.21a and 3.20a).

— Double layer winding in circumferential direction (cf. Figure 3.21b), only for slotted windings as it is not relevant for airgap windings.

— Double layer winding in radial direction (cf. Figures 3.21c and 3.20b).

In case of slotted windings, there are Z_s or Z_r subdomains with current density, with i the subdomain index. In case of airgap winding, there is one subdomain for single layer an two subdomains for double layer windings in r-direction, subject to PBC in the circumferential direction.

Then, the current density distribution is expressed in the Fourier basis obtained from the resolution of Laplace ODEs (cf. Subsection 3.4). The Fourier basis depends on the windings configuration and on if windings are inside slots or in the airgap. Finally, the MVP particular solution is obtained by injecting this new current density expression in the Poisson equation (3.21).

The case of double layer slotted windings in r-direction is an original contribution which naturally results from the resolution of eigenvalue problems in radial direction. In previous references such as in Boughrara et al. [2014], double layer windings in r-direction are accounted for using two distinct subdomains, which increases the size of the subdomain model.

The particular solutions given in the following Subsections 3.5.2.2-3.5.2.5 are both suitable to teeth infinite or finite permeability assumption. However, they do not account for additional HBCs on circumferential edges, for example in case of stator yoke infinite permeability assumption (at $r = R_2$ for internal rotor topologies) as illustrated in Subsection A.6.5.

3.5.2.2 Particular solution for slotted windings with single layer

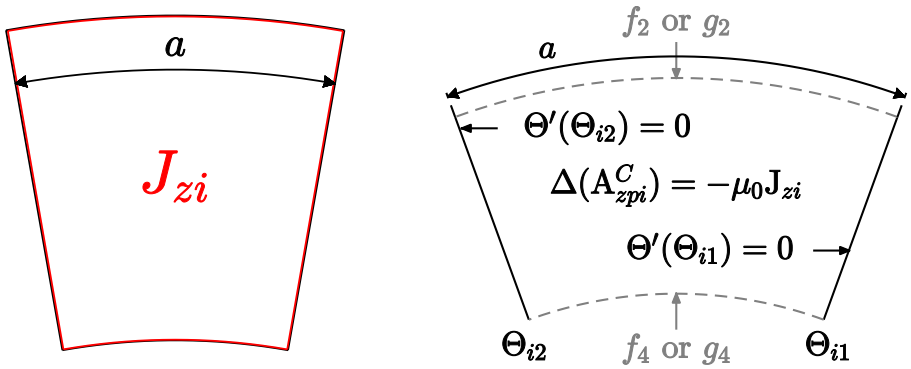

(a) Uniform current density distribution

(b) Poisson PDE subject to Neumann HBCs in θ-direction

Figure 3.22 – Single layer slotted windings subdomain problem.

For single layer windings, the current density in the i^{th} slot is uniform and noted $J_{zi}(t_0)$, as illustrated in Figure 3.22, where a is the slot angular width.

As the current density is uniform inside the slot subdomain, the particular solution is non-zero only for the eigenvalue $\lambda = 0$, which yields:

$$\mathrm{A}^{\mathrm{C}}_{zpi}(t_0, r, \theta) = \mu_0 \mathrm{J}_{zi}(t_0)\mathrm{R}_{sl}(r) \tag{3.124}$$

The particular solution R_{sl} is obtained by injecting Equation (3.124) in Poisson equation (3.21). The resulting ODE in function of r is:

$$r^2 \mathrm{R}''_{sl} + r\mathrm{R}'_{sl} = -r^2 \tag{3.125}$$

whose particular solution R_{sl} is:

$$\mathrm{R}_{sl}(r) = -\frac{r^2}{4} \tag{3.126}$$

3.5.2.3 Particular solution for slotted windings with double layer in θ-direction

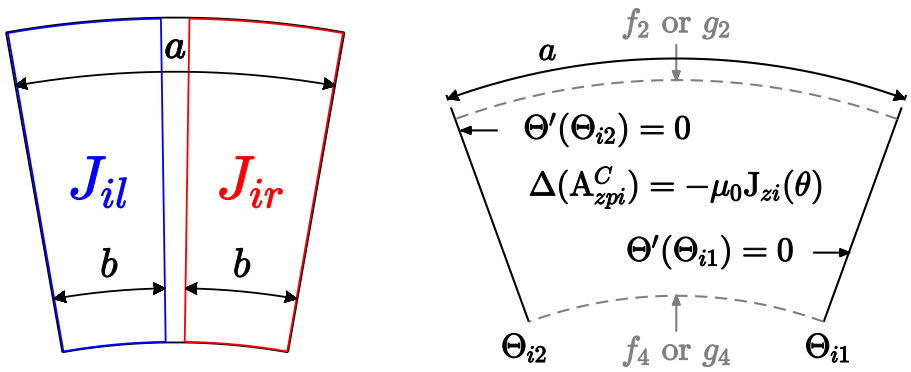

(a) Current density distribution

(b) Poisson PDE subject to Neumann HBCs in θ-direction

Figure 3.23 – Subdomain problem for slotted windings with double layer in θ-direction.

For double layer windings in θ-direction, the current density distribution is illustrated in Figure 3.23a, where a is the slot angular width and b is the angular width of right and left coils, whose current density are respectively J_{ir} and J_{il}. The current density distribution is expressed in the Fourier basis of Neumann boundary problems in θ-direction (cf. Subsection 3.4.2.2):

$$\mathrm{J}_{zi}(t_0, \theta) = \mathrm{J}_{i0}(t_0) + \sum_{m=1}^{\infty} \mathrm{J}_{i\nu_m}(t_0) \cos\left[\nu_m\big(\theta - \Theta_{i1}(t_0)\big)\right] \tag{3.127}$$

where $\mathrm{J}_{i0} = (\mathrm{J}_{ir}+\mathrm{J}_{il})/2$ is the slot average current density, $\mathrm{J}_{i\nu_m}$ is the Fourier coefficients of the current density distribution which depends on angular widths a and b (see Boughrara et al. [2014]), ν_m is defined in Equation (3.81), and $\Theta_{i1}(t_0)$ is:

$$\Theta_{i1}(t_0) = \begin{cases} \Theta_{i10} + \frac{2\pi}{\mathrm{Z}_s}(i-1) & \text{at stator side.} \quad (3.128) \\ \Omega t_0 + \Theta_{i10} + \frac{2\pi}{\mathrm{Z}_r}(i-1) & \text{at rotor side.} \quad (3.129) \end{cases}$$

where Θ_{i10} is the initial angular position of the subdomain.

As shown in Figure 3.23b, the particular MVP solution is also expressed in the Fourier basis of Neumann boundary problems in θ-direction:

$$\mathrm{A}^{\mathrm{C}}_{zpi}(t_0,r,\theta) = \mu_0 \mathrm{J}_{i0}(t_0)\mathrm{R}_{dlc,0}(r) + \mu_0 \sum_{m=1}^{\infty} \mathrm{J}_{i\nu_m}(t_0)\mathrm{R}_{dlc,\nu_m}(r)\cos\left[\nu_m\left(\theta - \Theta_{i1}(t_0)\right)\right] \quad (3.130)$$

where R_{dlc,ν_m} is an unknown function which is obtained by injecting Equations (3.127) and (3.120) in Poisson equation (3.21). The resulting ODE in function of r and the eigenvalue $\lambda = \nu_m^2$ is:

$$r^2\mathrm{R}''_{dlc,\nu_m} + r\mathrm{R}'_{dlc,\nu_m} - \nu_m^2\mathrm{R}_{dlc,\nu_m} = -r^2 \quad (3.131)$$

whose particular solution R_{dlc,ν_m} can be expressed as:

— If $\nu_m = 0$: $\mathrm{R}_{dlc,0}(r) = -\dfrac{r^2}{4}$ (3.132)

— If $\nu_m = 1$ or $\nu_m > 2$: $\mathrm{R}_{dlc,\nu_m}(r) = \dfrac{r^2}{\nu_m^2 - 4}$ (3.133)

— If $\nu_m = 2$: $\mathrm{R}_{dlc,2}(r) = -\dfrac{r^2\ln(r)}{4}$ (3.134)

It can be noticed that the case with $\nu_m = 0$ is the same as considering a single layer winding, i.e. $\mathrm{R}_{dlc,0}(r) = \mathrm{R}_{sl}(r)$, which is logical as $\nu_m = 0$ concerns the average current density J_{i0} in the slot.

3.5.2.4 Particular solution for slotted windings with double layer in r-direction

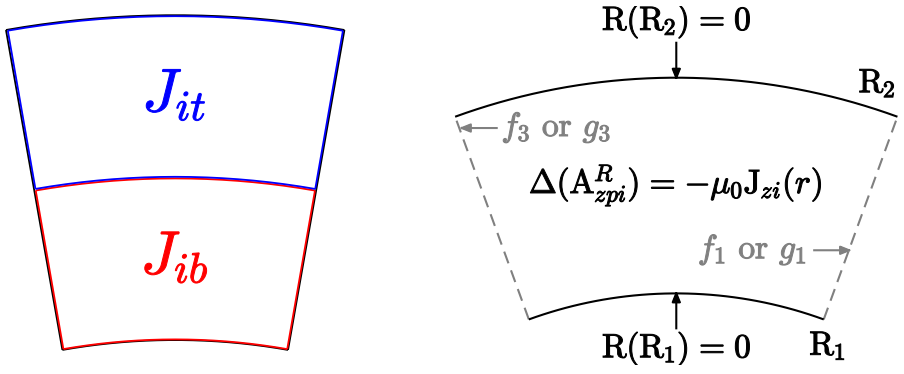

(a) Current density distribution $\mathrm{J}_{zi}(r)$

(b) Poisson PDE subject to Dirichlet HBCs in r-direction

Figure 3.24 – Subdomain with double layer windings in r-direction subject to Dirichlet HBCs.

For double layer windings in radial direction, the current density distribution is illustrated in Figure 3.24a, where J_{ib} and J_{it} are the current densities in bottom and top coils. The current density distribution is expressed in the Fourier basis of Dirichlet boundary problems in r-direction (see Subsection 3.4.3.1):

$$\mathrm{J}_{zi}(t_0,r) = \mathrm{J}_{i0}(t_0) + \sum_{m=1}^{\infty} \mathrm{J}_{i\upsilon_m}(t_0)\sin\left[\upsilon_m \ln\left(\frac{r}{\mathrm{R}_1}\right)\right] \quad (3.135)$$

where $J_{i0} = (J_{ib}+J_{it})/2$ is the slot average current density, v_m is defined in Equation (3.89), and J_{iv_m} is the Fourier coefficients of the two radial layers distribution:

$$J_{iv_m} = \frac{J_{it}-J_{ib}}{2v_m}\left(2\cos\left[v_m \ln\left(\frac{R_2+R_1}{2R_1}\right)\right]-1-(-1)^m\right) \tag{3.136}$$

As shown in Figure 3.24b, the particular MVP solution is also expressed in the Fourier basis of Dirichlet boundary problems in r-direction:

$$A^R_{zpi}(t_0,r,\theta) = \mu_0 J_{i0}(t_0) R_{sl}(r) + \mu_0 \sum_{m=1}^{\infty} J_{iv_m}(t_0) R_{dlr,v_m}(\theta) \sin\left[v_m \ln\left(\frac{r}{R_1}\right)\right] \tag{3.137}$$

where R_{dlr,v_m} is an unknown function which is obtained by injecting Equations (3.135) and (3.137) in Poisson equation (3.21). The resulting ODE in function of θ and the eigenvalue $\lambda = -v_m^2 < 0$ is:

$$R''_{dlr,v_m} + v_m^2 R_{dlr,v_m} = r^2 \tag{3.138}$$

whose particular solution R_{dlr,v_m} is:

$$\forall v_m > 0, \quad R_{dlr,v_m}(\theta) = \frac{r^2}{v_m^2} \tag{3.139}$$

It can be noticed that R_{dlr,v_m} is r-dependent, and not θ-dependent as it has been assumed before the resolution, which is logical regarding the current distribution invariance in θ-direction.

3.5.2.5 Particular solution for airgap windings

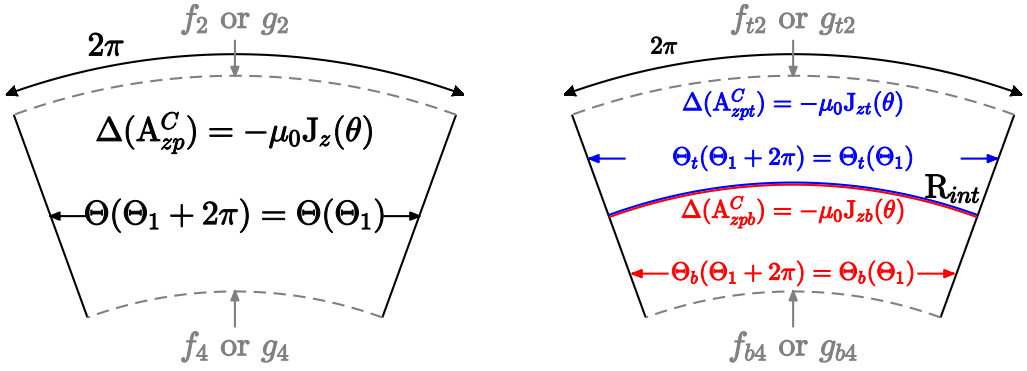

(a) Single layer winding

(b) Double layer winding in r-dir.

Figure 3.25 – Airgap winding subdomain(s) problem subject to PBC.

For airgap windings, the current density distribution is expressed in the Fourier basis of periodic boundary problems (see Subsection 3.4.2.1):

$$J_z(t_0,\theta) = \sum_{n=0}^{\infty} J_{cn}(t_0)\cos(n\theta) + J_{sn}(t_0)\sin(n\theta) \tag{3.140}$$

As illustrated in Figure 3.25, the particular MVP solution is also expressed in the Fourier basis:

$$A_{zp}^{C}(r,\theta) = \mu_0 \sum_n J_{cn}(t_0) R_{aw,n}(r)\cos(n\theta) + J_{sn}(t_0) R_{aw,n}(r)\sin(n\theta) \tag{3.141}$$

where $R_{aw,n}$ is an unknown functions which is determined by injecting Equations (3.140) and (3.141) in Poisson equation (3.21). The resulting ODE in function of r and the eigenvalue $\lambda = n^2$ is:

$$r^2 R''_{aw,n} + r R'_{aw,n} - n^2 R_{aw,n} = -r^2 \tag{3.142}$$

whose particular solution $R_{aw,n}$ is the same as R_{dlc,ν_m}, given by Equations (3.132)-(3.134) and for $\nu_m = n$.

In case of double layer winding in radial direction, the particular solution is computed for each layer and the magnetic continuity equations (cf. Subsection 3.2.3.4) are applied at the interface between both subdomains, for $r = R_{int}$ (cf. Figure 3.25b). This model can be further improved by considering only one airgap subdomain whose current density distribution depends on both r and θ, and can be expressed in two Fourier basis in r and θ-directions, as it has been done for slotted windings with double layer in Subsections 3.5.2.3 and 3.5.2.4.

3.6 Conclusion

Chapter 3 details the physical and mathematical developments based on functional analysis in order to solve the Magnetic Vector Potential (MVP) in regions of electrical machines. This can be used as a framework dedicated to the subdomain modeling of a large variety of electrical machines. The main contribution of this chapter is the superposition principle formulation to perform the analytical resolution in slots and teeth subdomains, in order to account for tooth finite permeability in the subdomain modeling technique. This framework is used in Chapter 4 to build subdomain models of SPMSMs and SCIMs and compute airgap flux density and magnetic stress, in the objective of fast and accurate e-NVH studies. It has also been used to develop subdomain models of IPMSMs and WRSMs in MANATEE software (not developed in this report).

Chapter 4

Semi-analytical electromagnetic SubDomain Method applied to radial flux machines

Contents

4.1 Introduction

4.1.1 Outlines

In Chapter 3, a general and flexible approach of the Analytical Resolution of Maxwell Equations (ARME) has been developed to find the Magnetic Vector Potential (MVP) solution given set of Boundary Conditions (BCs), a magnetic source, which is either a magnetization source or a current density source, and including induced currents or not. Based on these expressions, the MVP solution in typical subdomains of electrical machines, e.g. airgap, surface Permanent Magnets (PMs), stator and rotor slots, slot openings, rotor bars etc., can be obtained. However, the MVP solution still depends on unknown integration constants, which have been introduced when integrating the governing MVP Partial Differential Equations (PDEs) (cf. Subsection 3.4). These integration constants are the unknowns of the subdomain model, and the next step of the subdomain method is to compute these integration constants and obtained the MVP and the flux density in the different subdomains, as developed in Chapter 4.

Following the SubDomain Method (SDM) state of the art made in Subsection 2.3.3.2, Section 4.2 further details and illustrates the subdomain methodology, using the theoretical developments of Chapter 3 and based on the subdomain model example of the SPMSM $12s10p$ prototype assuming iron infinite permeability. It first consists in applying the Interface Conditions (ICs) between adjacent subdomains, which ensure normal flux density and tangential field continuities at the interface. An additional reformulation of MVP solution is performed to facilitate the application of ICs between subdomains. Then, the resulting set of ICs is numerically solved, which enables to compute MVP and flux density distributions in the different subdomains, in particular the airgap flux density and the resulting Maxwell stress. Finally, several techniques are introduced to optimize the computational efficiency of the SDM.

Based on the developed methodology, a new subdomain model of SPMSMs is developed in Section 4.3, assuming iron finite permeability in stator teeth and yoke. The MVP solution in stator slots and teeth is found using the superposition principle of two eigenvalue problems in circumferential and radial directions, detailed in Chapter 3. In particular, two formulations of superposition principle which are both applicable to stator teeth in theory are discussed. This subdomain model enables to account for saturation at stator side in both open-circuit and load conditions. Results are validated using Finite-Element Analysis (FEA) in this chapter and experimental results from the SPMSM $12s10p$ in Chapter 5.

In Section 4.4, a new subdomain method is proposed for the modeling of SCIM to compute the 2D airgap flux density including time and space harmonics due to stator/rotor slotting and MMF. Airgap flux density and bar current harmonic content are validated using transient FEA under both no-load and load operation. Furthermore, the assumptions of the developed model are deeply discussed, as well as its relevancy inside e-NVH simulation, in comparison with FEA and the 1D PMMF approach.

4.1.2 Contributions

A first contribution is the investigation and the synthesis of SDM optimization techniques based on various subdomain models found in the literature and implemented in MANATEE software, as discussed in 4.2.3 and Devillers et al. [2016]. The main techniques are the application of periodicity conditions, the prior selection of airgap har-

monics order based on a pre-analytical study, and the analytical substitutions to reduce the number of unknown integration constants and ICs to solve numerically.

A second contribution is the application of the ARME methodology developed in Chapter 3 to the subdomain modeling of SPMSMs assuming finite permeability, and comparing two formulations of superposition principle for stator teeth MVP solution. It is shown that the second formulation, although analytically correct, leads to considerable inaccuracies in the numerical resolution near tooth boundaries.

Finally, a third contribution concerns the subdomain modeling of SCIMs developed in Section 4.4, which is actually a synthesis of the two main existing references [Lubin et al., 2011b; Boughrara et al., 2015] and previously studied in the SDM state of the art (see Subsection 2.3.3.2). The originality resides in the computation of rotor bar induced currents due to each stator MMF harmonic accounting for the proper skin effect, and in the computation of RSHs in the airgap flux density time harmonic content [Devillers et al., 2018c]. Furthermore, the developed SCIM subdomain model is implemented in MANATEE to investigate the effect of circumferential stress on radial vibrations [Devillers et al., 2017b], and to compare stress harmonics computed from 2D SDM and 1D PMMF with radial vibrations obtained from experimental measurements [Devillers et al., 2018a].

4.2 Subdomain methodology

4.2.1 Subdomain model formulation based on SPMSM assuming infinite permeability

4.2.1.1 Presentation of the subdomain model

The objective of Section 4.2 is to detail and illustrate the resolution methodology of a subdomain model. The developments are based on the classic subdomain model of SPMSM assuming infinite permeability of stator and iron cores, and with all teeth wound concentrated windings. This enables to reduce the number of subdomains, hence the number of ICs to treat, and focus on how to solve them by applying the scalar products between the MVP solution of adjacent subdomains.

Assuming iron infinite permeability, the SPMSM subdomain model contains (cf. Figure 4.1):

— The surface PMs subdomain (one subdomain for all PMs as explained in Subsection 3.5.1.1).

— The airgap subdomain.

— Z_s stator slots subdomains, of index $i \in [\![1, Z_s]\!]$.

There are consequently Z_s+2 subdomains in the model. Stator teeth, stator yoke and rotor yoke are external boundaries of the subdomain model. The MVP is not solved inside stator teeth, stator yoke and rotor yoke, as illustrated in Figure 3.3a. The geometric parameters are specified in Figure 4.1, where R_r is the rotor bore radius, R_m is the top radius of surface PMs, R_s is the stator bore radius, R_y is the stator slot bottom radius and a is the stator slot angular width. The surface PMs have parallel magnetization pattern (cf. Figure 3.17). The magnetic relative permeability is noted μ_{rm} in the surface PMs subdomain, and is unitary everywhere else. Stator windings have two layers in circumferential direction and are tooth concentrated.

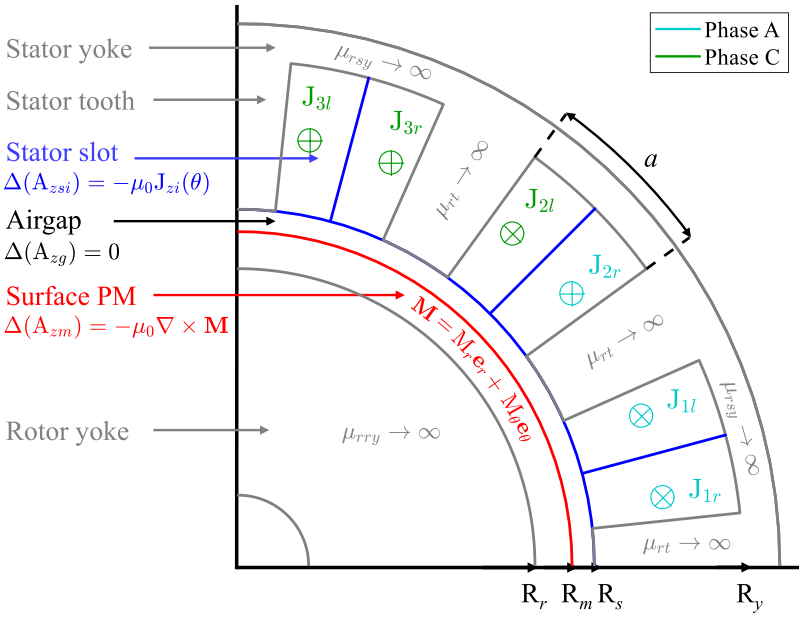

Figure 4.1 – Subdomain model of SPMSM $12s10p$ prototype.

In order to numerically solve the ICs, a finite number of harmonics is chosen to express the MVP in the Fourier basis of each subdomain: N for surface PMs and airgap subdomains, and K for stator slots subdomains.

4.2.1.2 Formulation of Interface Conditions (ICs)

There are only two interfaces in the considered SPMSM subdomain model:

— The first one is between surface PMs and airgap subdomains.

— The second one is between airgap and stator slots subdomains.

The interface between airgap and surface PMs subdomains is the circle of radius R_m. From Equations (3.24) and (3.23), normal flux density and tangential field ICs yields:

$$A_{zm}(R_m,\theta) = A_{zg}(R_m,\theta), \qquad \theta \in [0,2\pi] \tag{4.1}$$

$$\frac{\partial A_{zg}}{\partial r}\Big|_{R_m,\theta} = \frac{1}{\mu_{rm}} \frac{\partial A_{zm}}{\partial r}\Big|_{R_m,\theta} + \frac{M_\theta(\theta)}{\mu_{rm}}, \qquad \theta \in [0,2\pi] \tag{4.2}$$

In this subdomain model, the normal flux density condition (which actually applies on the MVP as explained in Subsection 3.2.3.4) is chosen to be included in the surface PMs subdomain problem while tangential field condition is included in airgap one. From Chapter 3, it only means that the airgap MVP is expressed in the Fourier basis of the surface PMs subdomain, while surface PMs tangential field is expressed in the Fourier basis of the airgap subdomain. Therefore, the normal flux density condition could have been perfectly included in the airgap problem, and the tangential field continuity in the surface PMs problem. Here, this consideration has a little impact since both airgap and surface PMs subdomains have the same Fourier basis of 2π-periodic boundary problems.

The interface between the airgap and stator slot subdomains is the circle of radius R_s. Normal flux density and tangential field ICs result in:

$$\forall i \in [\![1, Z_s]\!], \quad A_{zsi}(R_s, \theta) = A_{zg}(R_s, \theta), \quad \theta \in [\Theta_{si1}, \Theta_{si2}] \tag{4.3}$$

$$\left.\frac{\partial A_{zg}}{\partial r}\right|_{R_s,\theta} = g_{2g}(\theta), \qquad \theta \in [0, 2\pi] \tag{4.4}$$

where:

$$g_{2g}(\theta) = \begin{cases} \left.\frac{\partial A_{zsi}}{\partial r}\right|_{R_s,\theta}, & \theta \in [\Theta_{si1}, \Theta_{si2}], \quad i \in [\![1, Z_s]\!] \quad (4.5) \\ 0, & \theta \in [\Theta_{s(i-1)2}, \Theta_{si1}], \quad i \in [\![1, Z_s]\!] \quad (4.6) \end{cases}$$

The definition of g_{2g} comes from the fact that tangential field is zero at the interface between airgap and stator teeth, i.e for $\theta \in [\Theta_{s(i-1)2}, \Theta_{si1}]$, due to iron infinite permeability assumption.

Unlike the ICs between surface PMs and airgap subdomains (cf. Equations (4.1)-(4.2)), it is not possible to switch the order of airgap and stator slots in the second interface conditions (cf. Equations (4.3)-(4.4)). In fact, if the normal flux condition is included in the airgap problem, then the interface condition must also ensure the MVP continuity with the stator teeth. However, this is not possible since MVP in stator teeth is unknown due to the infinite permeability assumption.

The MVP solution in each subdomain is given in the next Subsections 4.2.1.3-4.2.1.5, accounting for the additional reformulation based on the functions F_{1v} and F_{2v} introduced in Subsection 3.4.1.4 to facilitate the application of ICs [Lubin et al., 2010; Ackermann and Sottek, 1995]. As a recall, contrary to the dimensionless reformulation performed in Subsection 3.4.1.2, this reformulation is not compulsory to numerically solve the ICs but it provides simpler and more physical relations between the unknown integration constants of each subdomain. Besides, these MVP reformulations are not unique, others may suit as well to simplify the application of ICs. For sake of clarity, the mathematical developments which have led to the reformulation for each subdomain are given in Appendix A.6.

4.2.1.3 Surface PM solution

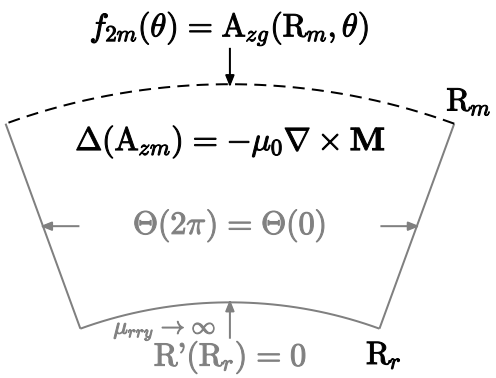

Figure 4.2 – Surface PM subdomain problem.

The surface PMs subdomain is a Poisson eigenvalue problem in θ-direction subject to PBC which is illustrated in Figure 4.2. The MVP solution A_{zm} is the sum of the homogeneous solution obtained in Subsection 3.4.2.1 and of the particular solution obtained in Subsection (3.5.1.2) which accounts for the radial and circumferential magnetization distributions $\mathrm{M}_r(\theta)$ and $\mathrm{M}_\theta(\theta)$. In Appendix A.6.3, the MVP solution A_{zm} is reformulated to include the rotor yoke infinite permeability assumption and the MVP continuity condition (4.1) with the airgap subdomain at $r = \mathrm{R}_m$.

Finally, the general MVP solution A_{zm} can be expressed as:

$$\begin{aligned}\mathrm{A}_{zm}(\psi, r, \theta) = a_{m0} \\ + \sum_{n=1}^{\mathrm{N}} \Bigg[\Big(\mathrm{A}_{mn} \frac{\mathrm{P}_n(\mathrm{R}_r, r)}{\mathrm{P}_n(\mathrm{R}_r, \mathrm{R}_m)} - \mu_0 \big[\mathrm{M}_{rn} \mathrm{X}_{mn}(r) + \mathrm{M}_{\theta n} \mathrm{Y}_{mn}(r) \big] \sin\big(n\psi\big) \Big) \cos(n\theta) \\ + \quad \Big(\mathrm{B}_{mn} \frac{\mathrm{P}_n(\mathrm{R}_r, r)}{\mathrm{P}_n(\mathrm{R}_r, \mathrm{R}_m)} + \mu_0 \big[\mathrm{M}_{rn} \mathrm{X}_{mn}(r) + \mathrm{M}_{\theta n} \mathrm{Y}_{mn}(r) \big] \cos\big(n\psi\big) \Big) \sin(n\theta) \Bigg]\end{aligned} \tag{4.7}$$

where:

— ψ is the position of the first surface PM, which depends on the time parameter t_0 as defined by Equation (3.107).

— a_{m0}, A_{mn}, B_{mn} are the new integration constants which represent the constant, cosine and sine components of the surface PMs MVP at the interface $r = \mathrm{R}_m$ with the airgap subdomain.

— P_n is a geometrical polynom defined in Appendix A.6.1.

— X_{mn} and Y_{mn} are the new particular solutions associated to the Fourier components M_{rn}, $\mathrm{M}_{\theta n}$ of the magnetization distribution, and are defined in Appendix A.6.3.

Besides, $\mathscr{B}_n(\theta) = \begin{bmatrix} 1 & \cos(n\theta) & \sin(n\theta) \end{bmatrix}$ is the surface PMs Fourier basis (same as airgap subdomain's).

Therefore, the analytical expression of the MVP in surface PMs subdomain at $r = \mathrm{R}_m$ results in:

$$\mathrm{A}_{zm}(\psi, \mathrm{R}_m, \theta) = a_{m0} + \sum_{n=1}^{\mathrm{N}} \mathrm{A}_{mn} \cos(n\theta) + \mathrm{B}_{mn} \sin(n\theta) \tag{4.8}$$

4.2.1.4 Airgap MVP solution

The airgap subdomain problem is a Laplace eigenvalue problem in θ-direction subject to PBC, as illustrated in Figure 4.3. The MVP solution A_{zg} in the airgap subdomain is the Laplace homogeneous solution obtained in Subsection 3.4.2.1. In Appendix A.6.4, the MVP solution A_{zg} is reformulated to include the tangential field continuity conditions (4.2)-(4.4) at the interface with surface PMs subdomain (for $r = \mathrm{R}_m$) and stator slots subdomains (for $r = \mathrm{R}_s$).

Finally, the general MVP solution A_{zg} can be expressed as:

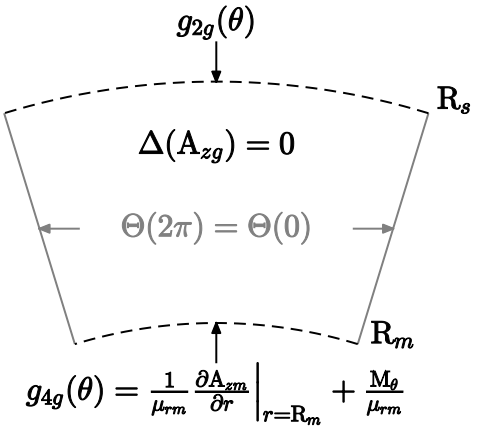

Figure 4.3 – Airgap subdomain problem, with g_{2g} defined in Equations (4.5)-(4.6).

$$\begin{aligned} A_{zg}(r,\theta) = a_{g0} \\ + \sum_{n=1}^{N} \Bigg[\Big(A_{gn} \frac{R_m}{n} \frac{P_n(r,R_s)}{E_n(R_m,R_s)} - \Big(B_{gn} \frac{R_s}{n} \frac{P_n(R_m,r)}{E_n(R_m,R_s)} \Big) \cos(n\theta) \\ + \Big(C_{gn} \frac{R_m}{n} \frac{P_n(r,R_s)}{E_n(R_m,R_s)} - \Big(D_{gn} \frac{R_s}{n} \frac{P_n(R_m,r)}{E_n(R_m,R_s)} \Big) \sin(n\theta) \Bigg] \end{aligned} \tag{4.9}$$

where :

— a_{g0}, A_{gn}, B_{gn}, C_{gn}, D_{gn} are the new integration constants which represent the cosine and sine components of the MVP derivative at the interfaces $r = R_m$ and $r = R_s$.

— P_n and E_n are the geometrical polynoms defined in Appendix A.6.1.

Besides, $\mathscr{B}_n(\theta) = \begin{bmatrix} 1 & \cos(n\theta) & \sin(n\theta) \end{bmatrix}$ is the airgap Fourier basis (same as surface PMs subdomain's).

Therefore, the analytical expression of the tangential field H_{tg} at the interfaces with the surface PMs and stator slots subdomains yields:

$$H_{tg}(R_m,\theta) = -\frac{1}{\mu_0} \Big[\sum_{n=1}^{N} A_{gn} \cos(n\theta) + C_{gn} \sin(n\theta) \Big] \tag{4.10}$$

$$H_{tg}(R_s,\theta) = -\frac{1}{\mu_0} \Big[\sum_{n=1}^{N} B_{gn} \cos(n\theta) + D_{gn} \sin(n\theta) \Big] \tag{4.11}$$

4.2.1.5 Stator slots MVP solution

Stator slots subdomains with current density distribution are Poisson eigenvalue problems in θ-direction subject to Neumann HBC, as illustrated in Figure 4.4. The MVP solution A_{zsi} in the i^{th} stator slot is the sum of the homogeneous solution obtained in Subsection 3.4.2.2 and of the particular solution obtained in Subsection (3.5.2.3) which accounts for the current density distribution $J_{zi}(\theta)$. In Appendix A.6.5, the MVP solution A_{zsi} is reformulated to simplify the MVP continuity condition (4.3) with the airgap subdomain at $r = R_s$.

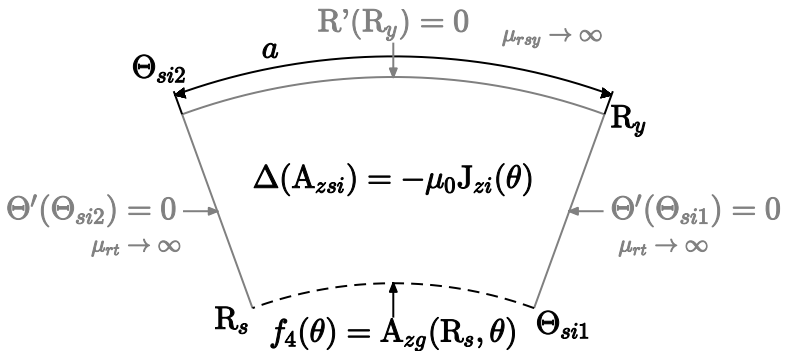

Figure 4.4 – Stator slots subdomain problem.

Finally, the general MVP solution A_{zsi} can be expressed as:

$$\begin{aligned} A_{zsi}(t_0,r,\theta) &= A_{si0} + \mu_0 J_{i0}(t_0) X_{si0}(r) \\ &+ \sum_{k=1}^{K} \left[A_{sik} \frac{P_{\nu_k}(r,R_y)}{P_{\nu_k}(R_s,R_y)} + \mu_0 J_{i\nu_k}(t_0) X_{sik}(r) \right] \cos\left[\nu_k(\theta-\Theta_{si1})\right] \end{aligned} \tag{4.12}$$

where:

— t_0 is the simulation instant at which the current density distribution is considered.

— A_{si0}, A_{sik} are the new integration constants which represent the constant and cosine components of the i^{th} stator slot subdomain MVP at the interface $r = R_s$ with the airgap subdomain.

— P_{ν_k} is a geometrical polynom defined in Appendix A.6.1.

— X_{si0} and X_{sik} are the new particular solutions associated to the constant and cosine Fourier components J_{i0}, $J_{i\nu_k}$ of the current density distribution for slotted double layer windings in θ-direction, and are defined in Appendix A.6.5.

Besides, $\mathscr{B}_{ik}(\theta) = \left[1 \quad \cos\left[\nu_k(\theta-\Theta_{si1})\right]\right]$ is the Fourier basis of the i^{th} stator slot.

Therefore, the analytical expression of the MVP A_{zsi} of stator slot subdomains at the interface $r = R_s$ with the airgap subdomain results in:

$$A_{zsi}(t_0,R_s,\theta) = A_{si0} + \sum_{k=1}^{K} A_{sik} \cos\left[\nu_k(\theta-\Theta_{si1})\right] \tag{4.13}$$

4.2.2 Application and resolution of Interface Conditions (ICs)

4.2.2.1 Interface Conditions (ICs) between surface PMS and airgap subdomains

From Subsections 4.2.1.3-4.2.1.5, the surface PM, airgap and stator slots subdomains have respectively $2N+1$, $4N+1$ and $(K+1)Z_s$ unknown integration constants. Therefore, $6N+(K+1)Z_s+2$ equations are required to solve the subdomain model. They are obtained by projecting the potential and tangential field continuity conditions on the corresponding Fourier bases chosen in Subsection 4.2.1.2.

The MVP continuity between surface PMs and airgap subdomains at $r = R_m$ (cf. Equation (4.1)) is projected in the Fourier basis $\mathscr{B}_n$ of the surface PMs subdomain:

$$\langle \mathrm{A}_{zm}(\mathrm{R}_m,\theta),1\rangle = \langle \mathrm{A}_{zg}(\mathrm{R}_m,\theta),1\rangle, \quad \theta\in[0,2\pi] \tag{4.14}$$
$$\langle \mathrm{A}_{zm}(\mathrm{R}_m,\theta),\cos(n\theta)\rangle = \langle \mathrm{A}_{zg}(\mathrm{R}_m,\theta),\cos(n\theta)\rangle, \quad \theta\in[0,2\pi] \tag{4.15}$$
$$\langle \mathrm{A}_{zm}(\mathrm{R}_m,\theta),\sin(n\theta)\rangle = \langle \mathrm{A}_{zg}(\mathrm{R}_m,\theta),\sin(n\theta)\rangle, \quad \theta\in[0,2\pi] \tag{4.16}$$

The tangential field continuity between airgap and surface PMs subdomains at $r = \mathrm{R}_m$ (cf. Equation (4.2)) is projected in the Fourier basis $\mathscr{B}_n$ of the airgap subdomain:

$$\langle \frac{\partial \mathrm{A}_{zg}}{\partial r}\Big|_{\mathrm{R}_m,\theta},1\rangle = \langle \frac{\partial \mathrm{A}_{zm}}{\partial r}\Big|_{\mathrm{R}_m,\theta},1\rangle, \quad \theta\in[0,2\pi] \tag{4.17}$$
$$\langle \frac{\partial \mathrm{A}_{zg}}{\partial r}\Big|_{\mathrm{R}_m,\theta},\cos(n\theta)\rangle = \langle \frac{\partial \mathrm{A}_{zm}}{\partial r}\Big|_{\mathrm{R}_m,\theta},\cos(n\theta)\rangle, \quad \theta\in[0,2\pi] \tag{4.18}$$
$$\langle \frac{\partial \mathrm{A}_{zg}}{\partial r}\Big|_{\mathrm{R}_m,\theta},\sin(n\theta)\rangle = \langle \frac{\partial \mathrm{A}_{zm}}{\partial r}\Big|_{\mathrm{R}_m,\theta},\sin(n\theta)\rangle, \quad \theta\in[0,2\pi] \tag{4.19}$$

The application of ICs between surface PMs subdomain and airgap subdomain is straight forward. Since they have the same Fourier basis $\mathscr{B}_n$ associated to 2π-periodic problems, the scalar product results in directly equalizing constant, cosine and sine components. Besides, surface PMs and airgap MVP have been reformulated in Subsection 4.2.1 to reduce the left hand side to an unknown integration constants, such as:

$$a_{m0} = a_{g0} \tag{4.20}$$
$$\mathrm{A}_{mn} = \mathrm{A}_{gn}\frac{\mathrm{R}_m}{n}\frac{\mathrm{P}_n(\mathrm{R}_m,\mathrm{R}_s)}{\mathrm{E}_n(\mathrm{R}_m,\mathrm{R}_s)} - \mathrm{B}_{gn}\frac{\mathrm{R}_s}{n}\frac{2}{\mathrm{E}_n(\mathrm{R}_m,\mathrm{R}_s)} \tag{4.21}$$
$$\mathrm{B}_{mn} = \mathrm{C}_{gn}\frac{\mathrm{R}_m}{n}\frac{\mathrm{P}_n(\mathrm{R}_m,\mathrm{R}_s)}{\mathrm{E}_n(\mathrm{R}_m,\mathrm{R}_s)} - \mathrm{D}_{gn}\frac{\mathrm{R}_s}{n}\frac{2}{\mathrm{E}_n(\mathrm{R}_m,\mathrm{R}_s)} \tag{4.22}$$
$$\mathrm{A}_{gn} = -\frac{1}{\mu_{rm}}\left[\mathrm{A}_{mn}\frac{\mathrm{E}_n(\mathrm{R}_r,\mathrm{R}_m)}{\mathrm{P}_n(\mathrm{R}_r,\mathrm{R}_m)} - \mu_0\left[\mathrm{X}'_{mn}(\mathrm{R}_m)\mathrm{M}_{rn} + (\mathrm{Y}'_{mn}(\mathrm{R}_m)-1)\mathrm{M}_{\theta n}\right]\sin\left(n\psi\right)\right] \tag{4.23}$$
$$\mathrm{C}_{gn} = -\frac{1}{\mu_{rm}}\left[\mathrm{C}_{mn}\frac{\mathrm{E}_n(\mathrm{R}_r,\mathrm{R}_m)}{\mathrm{P}_n(\mathrm{R}_r,\mathrm{R}_m)} + \mu_0\left[\mathrm{X}'_{mn}(\mathrm{R}_m)\mathrm{M}_{rn} + (\mathrm{Y}'_{mn}(\mathrm{R}_m)-1)\mathrm{M}_{\theta n}\right]\cos\left(n\psi\right)\right] \tag{4.24}$$

Noticing that Equation (4.17) yields $0 = 0$, ICs between surface PMs and airgap subdomains give $4\mathrm{N}+1$ equations. The others are obtained by applying the ICs between the airgap and stator slot subdomains.

4.2.2.2 Interface Conditions (ICs) between airgap and stator slots subdomains

The tangential field continuity between airgap and stator slots subdomains at $r = \mathrm{R}_s$ (cf. Equations (4.4)) is projected in the airgap subdomain Fourier basis $\mathscr{B}_n$:

$$\langle \frac{\partial \mathrm{A}_{zg}}{\partial r}\Big|_{\mathrm{R}_s,\theta},1\rangle = \langle g_{2g}(\theta),1\rangle, \quad \theta\in[0,2\pi] \tag{4.25}$$
$$\langle \frac{\partial \mathrm{A}_{zg}}{\partial r}\Big|_{\mathrm{R}_s,\theta},\cos(n\theta)\rangle = \langle g_{2g}(\theta),\cos(n\theta)\rangle, \quad \theta\in[0,2\pi] \tag{4.26}$$
$$\langle \frac{\partial \mathrm{A}_{zg}}{\partial r}\Big|_{\mathrm{R}_s,\theta},\sin(n\theta)\rangle = \langle g_{2g}(\theta),\sin(n\theta)\rangle, \quad \theta\in[0,2\pi] \tag{4.27}$$

with g_{2g} defined in Equation (4.5)-(4.6).

The MVP continuity between stator slots and airgap subdomains at $r = \mathrm{R}_s$ (cf. Equation (4.3)) is projected in the stator slot subdomains Fourier basis $\mathscr{B}_{ik}$:

$$\langle \mathrm{A}_{zsi}(\mathrm{R}_s,\theta),1\rangle = \langle \mathrm{A}_{zg}(\mathrm{R}_s,\theta),1\rangle, \quad \theta \in [\Theta_{si1},\Theta_{si2}] \tag{4.28}$$

$$\langle \mathrm{A}_{zsi}(\mathrm{R}_s,\theta),\cos\left[\nu_k(\theta-\Theta_{si1})\right]\rangle = \langle \mathrm{A}_{zg}(\mathrm{R}_s,\theta),\cos\left[\nu_k(\theta-\Theta_{si1})\right]\rangle, \quad \theta \in [\Theta_{si1},\Theta_{si2}] \tag{4.29}$$

In this case, the application of ICs between airgap and stator slots subdomain requires to compute the scalar products between the airgap and stator slots Fourier bases $\mathscr{B}_n$ and $\mathscr{B}_{ik}$. The scalar products result in the following equations:

$$\sum_{i=1}^{\mathrm{Z}_s} \mathrm{J}_{i0}(t_0) = 0 \tag{4.30}$$

$$\begin{aligned}\mathrm{B}_{gn} &= \frac{1}{\pi}\sum_{i=1}^{\mathrm{Z}_s}\mu_0 \mathrm{J}_{i0}(t_0)\mathrm{X}'_{si0}(\mathrm{R}_s)\mathrm{I}_1(i,n)\\ &+\frac{1}{\pi}\sum_{\substack{1\le i\le \mathrm{Z}_s\\ 1\le k\le \mathrm{K}}}\left(\mathrm{A}_{sik}\frac{\nu_k \mathrm{E}_{\nu_k}(\mathrm{R}_s,\mathrm{R}_y)}{\mathrm{R}_s\mathrm{P}_{\nu_k}(\mathrm{R}_s,\mathrm{R}_y)}+\mu_0\mathrm{J}_{i\nu_k}(t_0)\mathrm{X}'_{sik}(\mathrm{R}_s)\right)\mathrm{I}_3(i,k,n)\end{aligned} \tag{4.31}$$

$$\begin{aligned}\mathrm{D}_{gn} &= \frac{1}{\pi}\sum_{i=1}^{\mathrm{Z}_s}\mu_0 \mathrm{J}_{i0}(t_0)\mathrm{X}'_{si0}(\mathrm{R}_s)\mathrm{I}_2(i,n)\\ &+\frac{1}{\pi}\sum_{\substack{1\le i\le \mathrm{Z}_s\\ 1\le k\le \mathrm{K}}}\left(\mathrm{A}_{sik}\frac{\nu_k \mathrm{E}_{\nu_k}(\mathrm{R}_s,\mathrm{R}_y)}{\mathrm{R}_s\mathrm{P}_{\nu_k}(\mathrm{R}_s,\mathrm{R}_y)}+\mu_0\mathrm{J}_{i\nu_k}(t_0)\mathrm{X}'_{sik}(\mathrm{R}_s)\right)\mathrm{I}_4(i,k,n)\end{aligned} \tag{4.32}$$

$$\begin{aligned}\mathrm{A}_{si0} &= \mathrm{A}_{g0}+\frac{1}{a}\sum_{n=1}^{\mathrm{N}}\left(\mathrm{A}_{gn}\frac{2\mathrm{R}_m}{n\mathrm{E}_n(\mathrm{R}_m,\mathrm{R}_s)}-\mathrm{B}_{gn}\frac{\mathrm{R}_s\mathrm{P}_n(\mathrm{R}_m,\mathrm{R}_s)}{n\mathrm{E}_n(\mathrm{R}_m,\mathrm{R}_s)}\right)\mathrm{I}_1(i,n)\\ &+\left(\mathrm{C}_{gn}\frac{2\mathrm{R}_m}{n\mathrm{E}_n(\mathrm{R}_m,\mathrm{R}_s)}-\mathrm{D}_{gn}\frac{\mathrm{R}_s\mathrm{P}_n(\mathrm{R}_m,\mathrm{R}_s)}{n\mathrm{E}_n(\mathrm{R}_m,\mathrm{R}_s)}\right)\mathrm{I}_2(i,n)\end{aligned} \tag{4.33}$$

$$\begin{aligned}\mathrm{A}_{sik} &= \frac{2}{a}\sum_{n=1}^{\mathrm{N}}\left(\mathrm{A}_{gn}\frac{2\mathrm{R}_m}{n\mathrm{E}_n(\mathrm{R}_m,\mathrm{R}_s)}-\mathrm{B}_{gn}\frac{\mathrm{R}_s\mathrm{P}_n(\mathrm{R}_m,\mathrm{R}_s)}{n\mathrm{E}_n(\mathrm{R}_m,\mathrm{R}_s)}\right)\mathrm{I}_3(i,n)\\ &+\left(\mathrm{C}_{gn}\frac{2\mathrm{R}_m}{n\mathrm{E}_n(\mathrm{R}_m,\mathrm{R}_s)}-\mathrm{D}_{gn}\frac{\mathrm{R}_s\mathrm{P}_n(\mathrm{R}_m,\mathrm{R}_s)}{n\mathrm{E}_n(\mathrm{R}_m,\mathrm{R}_s)}\right)\mathrm{I}_4(i,n)\end{aligned} \tag{4.34}$$

where I_1, I_2, I_3 and I_4 are integrals of trigonometric functions defined in Appendix A.7. Equation (4.30) is not useful for the integration constants resolution, hence the scalar products result in $2\mathrm{N}+(\mathrm{K}+1)\mathrm{Z}_s$ equations.

4.2.2.3 Numerical resolution of Interface Conditions (ICs)

From Subsections 4.2.2.1-4.2.2.2, the ICs give $6\mathrm{N}+(\mathrm{K}+1)\mathrm{Z}_s+1$ equations to find $6\mathrm{N}+(\mathrm{K}+1)\mathrm{Z}_s+2$ integration constants. Hence, one equation is missing. One MVP constant component can be set to 0 as potential reference, e.g. the airgap constant a_{g0}. This also implies $a_{m0}=0$ from Equation (4.20). Therefore, there are $6\mathrm{N}+(\mathrm{K}+1)\mathrm{Z}_s$ equations for $6\mathrm{N}+(\mathrm{K}+1)\mathrm{Z}_s$ integration constants. The linear system of equations can be put into matrix form and solved numerically:

$$\mathbb{M}\mathbf{C}(t_0) = \mathbf{S}(t_0) \tag{4.35}$$

where $\mathbb{M}$ is the topological matrix, $\mathbf{C}$ is the vector of unknown integration constants, and $\mathbf{S}$ is the source term vector. The size of the subdomain model is the total number of unknown integration constants and is noted N_{sdm}. The topological matrix contains geometrical polynoms and scalar products between integration constants, i.e. terms related

to the homogeneous solutions, while **S** contains the current density and magnetization, i.e. terms related to the particular solutions.

For single slotted machines, only the source vector is time-dependent. For example, in the SPMSM subdomain model developed in Subsections 4.2.1-4.2.2, the surface PMs subdomain does not actually move. The rotation is included by updating the magnetization distribution for each t_0, i.e. for the specific rotor position at t_0. In presence of moving subdomains such as rotor slots, the topological matrix is also time-dependent, and the linear system becomes:

$$\mathbb{M}(t_0)\mathbf{C}(t_0) = \mathbf{S}(t_0) \tag{4.36}$$

4.2.2.4 Post-processings of electromagnetic quantities

Once integration constants are determined, it enables to compute the MVP and flux density distribution in every subdomain, such as:

$$\mathrm{B}_r(t_0, r, \theta) = \frac{1}{r}\frac{\partial \mathrm{A}_z}{\partial \theta}\Big|_{t_0,r,\theta} \tag{4.37}$$

$$\mathrm{B}_\theta(t_0, r, \theta) = -\frac{\partial \mathrm{A}_z}{\partial r}\Big|_{t_0,r,\theta} \tag{4.38}$$

The MVP contours give the flux lines in the subdomain model.

Airgap magnetic stress and electromagnetic torque can be computed using the MST (cf. Subsection 2.4.1.1 and Appendix A.2). MST can be applied for any radius is the airgap, especially to get the stress at the interface with stator iron. However, MST gives more accurate results if it is computed in the middle of the airgap, where the solution is smoother due to lower Gibbs phenomenon (cf. Subsection 2.2.4.4) [Lubin et al., 2010].

Flux linkage in stator phases can be computed using the Stoke theorem applying on the MVP in stator slots containing windings. The flux ϕ_i in the i^{th} stator slot is expressed as:

$$\phi_i(t_0) = \frac{\mathrm{L}_s}{\mathrm{S}_{slot}} \int_{\Theta_{si2}}^{\Theta_{si2}} \int_{\mathrm{R}_s}^{\mathrm{R}_y} \mathrm{A}_{zsi}(t_0, r, \theta) r\, dr\, d\theta \tag{4.39}$$

where $\mathrm{L_S}$ is the axial length of the stator stack and S_{slot} is the stator slot surface area. EMF is then the time derivative of flux linkage. The electromagnetic torque can also be obtained by summing the product of stator current and stator back-EMF (i.e. computed from flux linkage without stator current density) over the stator phases.

The induced current density j_{ind} is computed by applying the local Ohm's law (cf. Equations (3.8)) in function of the MVP time derivative (cf. Equations (3.12)), such as:

$$j_{ind}(t_0) = -\sigma \frac{\partial \mathrm{A}_z}{\partial t_0}\Big|_{t_0,r,\theta} \tag{4.40}$$

Equation (4.40) enables to estimate eddy-current losses in PMs subdomains under the resistance limited assumption (i.e. neglecting skin effect). In rotor bars and solid rotor subdomains, where induced current have been included in the Helmholtz MVP PDE resolution, the induced current density can be expressed in complex such as:

$$j_{ind}(t_0, r, \theta) = -\mathrm{Re}\left[j\sigma\omega_{rm}\underline{\mathrm{A}}_z(t_0, r, \theta) \right] \tag{4.41}$$

where ω_{rm} is assumed to be the only pulsation in the rotor subdomain (cf. Subsection 3.2.3.2).

The MVP can also be computed in the infinite permeable subdomains as a post-processing by applying the MVP continuity conditions on the contour, as explained in Subsection 4.3.3.2. This enables for example to estimate iron losses.

4.2.3 Optimization of the resolution

4.2.3.1 Difference between single and doubly slotted machines

Using the magnetostatic formulation developed in Section 3.2, the subdomain models can be divided in two categories regarding the numerical resolution: single slotted (e.g. SPMSMs, Solid Rotor Induction Machines (SRIMs) etc.) and doubly slotted machines (e.g. SCIMs, inset PMSMs, DFIMs, WRSMs etc.). In single slotted machines, the topological matrix is not time-dependent (cf. Equation 4.35) meaning that matrix inversion is performed for all simulation instants t_0 at once, by considering a source matrix of size $\mathrm{N}_{sdm} \times \mathrm{N}_t$ which contains the source vector for each instant. For doubly slotted machines, both source vector and topological matrix depend on t_0 (cf. Equation 4.36) and the numerical resolution is performed N_t times. The topological matrix is time-dependent because the airgap subdomain ICs depends on the rotor slots position, which depends on t_0.

The numerical resolution is much faster for single slotted machines, as the topological matrix is only computed once, so as the Cramer system resolution which can be factorized for each instant t_0. For doubly slotted machines, both topological matrix construction and Cramer system resolution are performed N_t times. However, the topological matrix construction can be optimized by recomputing only t_0-dependent submatrices, i.e. submatrices which account for the ICs between rotor slots and airgap subdomains, and updating the topological matrix at each t_0 as implemented in MANATEE software during this thesis.

Machine	FEA		SDM	
	Nodes	Elements	N_{sdm}	N_{max}
SCIM $36s28r4p$	10914	21432	1158	400
SPMSM $36s4p$	10613	20900	1050	400

Table 4.1 – FE mesh properties and SDM harmonic numbers.

Figure 4.6 illustrates the computation time evolution in function of N_t for one single slotted machine (a SPMSM $36s4p$ from Lubin et al. [2011a]) and a doubly slotted machine (a SCIM $36s28r4p$ from Boughrara et al. [2015]). The computation time evolution is also given in comparison with FEA performed on FEMM software assuming infinite permeability of rotor and stator yokes. The computation time accounts for building and solving the finite-element model (i.e. build the geometry, mesh and solve) or the subdomain model (i.e. build topological matrix and source vector, and solve). Both topologies are illustrated in Figure 4.5, and FE mesh and subdomain harmonics properties are given in Table 4.1. Figure 4.6 shows that computation time is much lower for SDM than FEM, regarding both topologies. Besides, it is noticed that computation time varies linearly

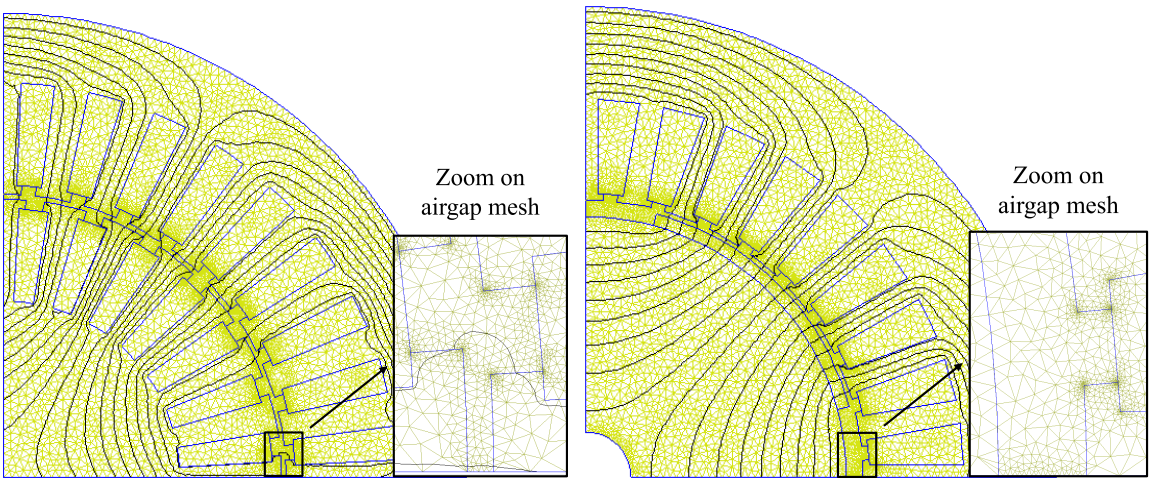

(a) SCIM $36s28r4p$ (b) SPMSM $36s4p$

Figure 4.5 – Single and doubly slotted machines, meshed on FEMM.

with the instants number N_t except for the single slotted topology (SPMSM $36s4p$) using SDM, due to the fact numerical resolution is performed for all instants at once. In particular, simulating the SPMSM $36s4p$ for 1000 instants lasts around 0.2 s, and around 50 s for SCIM $36s28r4p$.

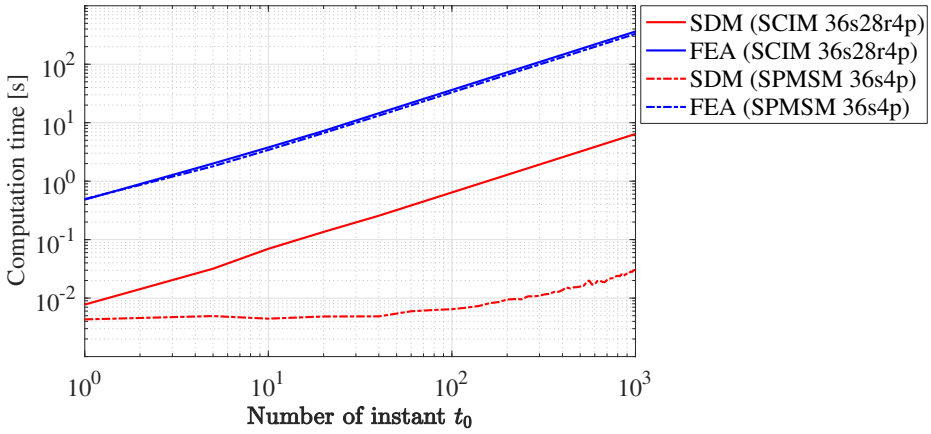

Figure 4.6 – Evolution of computation time in function of the instants number N_t comparing one single slotted topology (SPMSM) and one doubly slotted topology (SCIM), using SDM and FEM.

4.2.3.2 Choice of harmonic orders in each subdomain

The choice of harmonic orders is a key parameter to optimize computation time regarding accuracy. In fact, the exact MVP solution has theoretically an infinite number of harmonics. As harmonics magnitude tends to zero when the harmonic order tends to infinite, the harmonics set is truncated after a chosen highest harmonic order, i.e. N and K in the example developed in Subsections 4.2.1-4.2.2. Then, the choice of harmonic orders sets the total number of unknowns, thus the size of the linear system to solve and the required time to solve it.

The choice of harmonic orders in the airgap subdomain can be efficiently made thanks to a pre-analytical determination of the spatial harmonic content of the airgap flux density, depending on the studied topology, as also proposed by [Hannon et al.,

2016]. In the case of the SPMSM $12s10p$ in open-circuit condition, the spatial harmonics orders are all combination of p and Z_s, i.e all multiples of $\gcd(Z_s, p)$. This removes a certain number of harmonic orders in the airgap subdomain MVP, and reduces the problem size.

However, this prior study does not give insight on the highest harmonic order in the airgap, noted N_{max}, which is theoretically infinite but practically finite. The question is: at which multiple of p and Z_s does the magnitude of flux density harmonics become negligible regarding the electromagnetic quantities of interest (e.g. radial and circumferential flux density and stress harmonics, average torque, torque ripple, etc.) ? The answer can be given by a first simulation for a large number of spatial harmonics at a single instant, for example $N_{max} = 20Z_s$ in the case of the SPMSM $12s10p$. This prior simulation sets the highest harmonic order considered, i.e. the spatial Shannon criterion (2.2) in practice, to correctly estimate the harmonic content of stress harmonics.

Otherwise, the highest harmonic order can be chosen by directly assuming the maximal limit of stator permeance and rotor MMF harmonics order which can be observed. Taking the SPMSM $12s10p$ example, the stress harmonic of frequency $10f_s$ and wavenumber $r = 2$ is mainly due to the interaction of the 11^{th} harmonic of rotor MMF at $(11f_s, 11p)$ with the 4^{th} harmonic of stator slots at $(f_s, 4Z_s + p)$ as shown in Subsection 5.2.2.2. Therefore, the highest harmonic rank in the airgap N_{max} must be larger than $11p$ and $4Z_s$, and can be for example equal to $10Z_s + p$. In fact, this value ensures to observe up to the 10^{th} harmonic of the stator permeance combined with the fundamental rotor MMF, and up to around the $(10Z_s/p + 1)^{th}$ harmonic of rotor MMF combined with the mean stator permeance. In conclusion, the airgap harmonic orders n for the particular case of SPMSM in open-circuit condition can be written:

$$n = n_0 \gcd(Z_s, p) \leq N_{max}, \quad n_0 \in \mathbb{N}, \quad n_0 = 1 \ldots N \tag{4.42}$$

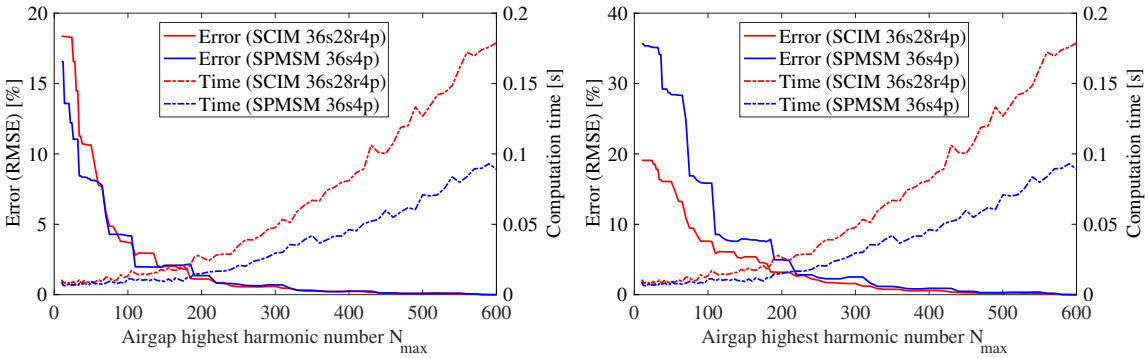

(a) Radial airgap flux density

(b) Circumferential airgap flux density

Figure 4.7 – Impact of the highest harmonic order N_{max} on Root Mean Square Error (RMSE) and computation time.

Then, the choice of the highest order in the airgap naturally sets the highest harmonic order in the other subdomains for the eigenvalue problem in circumferential direction. In the surface PMs subdomain, the periodicity is the same as in the airgap and the highest order is consequently N_{max} too. In the stator slots subdomains, the highest harmonic order K_{max} can set using the criterion proposed by Gysen [2011]:

$$K_{max} = \frac{\tau}{2\pi} N_{max} \tag{4.43}$$

where τ is twice the stator slot angular width (i.e. $\tau = 2a$ following Subsection 4.2.1.1 notation). This equation can be obtained from the Fourier basis projection between the periodic airgap subdomain and the non-periodic stator slots subdomains by computing integrals (A.84)-(A.85). For stator teeth and slots with same angular width, τ is equal to the stator pitch $2\pi/Z_s$ and then the criterion becomes

$$K_{max} = \frac{N_{max}}{Z_s} \tag{4.44}$$

which is therefore around 10, to match with the assumption of reaching the 10^{th} harmonic of stator permeance. If K_{max} is chosen below the Shannon criterion, i.e. K_{max} is lower than 10, e.g. $K_{max} = 5$, then airgap flux density harmonics whose order is higher than $5Z_s + p$ are due to the combination of stator permeance harmonics lower than 6 with higher rotor MMF harmonics, meaning that the stator slotting may be inaccurately estimated.

Therefore, choosing the highest harmonic rank in each subdomain at the practical Shannon criterion should lead to the better compromise between computation time and accuracy. Choosing it below Shannon criterion means that accuracy is decreased to the detriment of computation time, which can also be useful depending on the required granularity level for the electromagnetic simulation (cf. Subsection 2.2.3). Figures 4.7a-4.7b illustrates the impact of N_{max} value on the RMSE of radial and circumferential airgap flux densities and on the computation time. x-axis represents the value of N_{max}, while RMSE and computation time are respectively represented on left and right y-axes. RMSE is computed regarding the radial and circumferential airgap flux densities obtained with the highest order $N_{max} = 400$. Harmonics in surface PMs and stator slot subdomains are respectively N_{max} and $K_{max} = \text{round}(N_{max}/Z_s)$.

Figures 4.7a and 4.7b show that RMSE converges inversely proportional to the N_{max} for radial and circumferential cases. For the SPMSM $6s4p$, the RMSE (i.e. the line in red) reaches 0 at around $N_{max} = 150$, meaning that the practical Shannon criterion is also around 150. Besides, the circumferential case converges slower than the radial case, due to the fact that slotting harmonics have relatively a larger impact on the circumferential flux density than on the radial component for high spatial orders.

Finally, the pre-selection of harmonic orders in non-periodic subdomains such as stator slots, especially in presence of current density or magnetization source terms remains, such as the choice of harmonic orders for eigenvalue problems in radial direction, which can be addressed in future works.

4.2.3.3 Accounting for periodicity and anti-periodic conditions

If the electrical machine has a spatial periodicity lesser than 2π, for example the SCIM $36s28r4p$ with integer number of slots per pole and per phase illustrated in Figure 4.5a, the size of the subdomain model can be reduced by including this periodic BC in the analytical resolution of the concerned subdomains, i.e. only the airgap subdomain for the SCIM $36s28r4p$. Assuming that the spatial periodicity is equal to $2\pi/c$, where c is the spatial periodicity factor, the PBC, initially given by Equation (3.31), becomes:

$$\forall\, \theta \in \left[\Theta_1, \Theta_1 + \frac{2\pi}{c}\right], \quad \mathrm{A}_z(r,\theta) = \mathrm{A}_z\left(r, \theta + \frac{2\pi}{c}\right) \tag{4.45}$$

$$\forall\, \theta \in \left[\Theta_1, \Theta_1 + \frac{2\pi}{c}\right], \quad \left.\frac{\partial \mathrm{A}_z}{\partial \theta}\right|_{r,\theta} = \left.\frac{\partial \mathrm{A}_z}{\partial \theta}\right|_{r,\theta+\frac{2\pi}{c}} \tag{4.46}$$

The non-zero harmonic orders in the airgap MVP solution are [Zhu et al., 2010b; Hannon et al., 2018]:

$$n = kc, \quad k \in \mathbb{N} \tag{4.47}$$

and the number of rotor and stator slots can be also divided by c, meaning the rotor slots number Z_r becomes $\mathrm{Z}_{r0} = \mathrm{Z}_r/c$ and the stator slots number Z_s becomes $\mathrm{Z}_{s0} = \mathrm{Z}_s/c$. Furthermore, if the number of stator and rotor slots is even, the ABC can be applied such as:

$$\forall\, \theta \in \left[\Theta_1, \Theta_1 + \frac{\pi}{c}\right], \quad \mathrm{A}_z(t,r,\theta) = -\mathrm{A}_z\left(t, r, \theta + \frac{\pi}{c}\right) \tag{4.48}$$

$$\forall\, \theta \in \left[\Theta_1, \Theta_1 + \frac{\pi}{c}\right], \quad \left.\frac{\partial \mathrm{A}_z}{\partial \theta}\right|_{r,\theta} = -\left.\frac{\partial \mathrm{A}_z}{\partial \theta}\right|_{r,\theta+\frac{\pi}{c}} \tag{4.49}$$

The non-zero harmonic orders in the airgap MVP solution become:

$$n = 2kc, \quad k \in \mathbb{N} \tag{4.50}$$

In conclusion, the size of the subdomain model can be reduced by $2c$ accounting for both ABC and PBC. In theory, this globally reduces the computation time of the numerical resolution by a factor $(2c)^2$.

4.2.3.4 Reduce the number of integration constants in the numerical resolution

The size of the subdomain model can also be reduced by removing some integration constants and their associated ICs from the numerical resolution. This can be done by analytically reformulating the set of ICs. The aim is to substitute the ICs which contain few unknown integration constants in the other ICs which are solved numerically [Zhu et al., 2010b]. This technique can be applied to the SPMSM subdomain model developed in Subsections 4.2.1-4.2.2 to reduce the number of ICs from nine to two. In fact, surface PMs integration constants expressions (Equations (4.21)-(4.22)) are injected into airgap integration constants expressions (Equations (4.23)-(4.24)-(4.31)-(4.32)), which is easily done since they are expressed in the same Fourier basis. Then, the obtained equations are injected in the stator slots ones (Equations (4.33)-(4.33)). The obtained topological matrix is much smaller since its size is now $(\mathrm{K}+1)\mathrm{Z}_s$, hence faster to solve, but the matrix coefficients are quite tedious to express analytically, and longer to compute numerically since each matrix coefficient is now a series of N terms due to the introduction of airgap integration constants. Besides, the other subdomains integration constants have to be computed as a post-processing. Finally, this technique is much more complex if every subdomain has a different periodicity, such as in subdomain models of SCIMs, because the substitution is not straight forward.

Another technique to reduce the number of integration constants is to simplify the subdomain model complexity. For example, in presence of slot openings, slot and slot

opening subdomains can be merged into an equivalent subdomain whose depth is equal to the overall depth, whose angular width is equal to slot opening width, and whose magnetic source term (magnetization or current density) is corrected by the ratio of real and virtual surfaces. This technique is used in the developed SCIM subdomain model (see Section 4.4), and has also been suggested by Hannon et al. [2018]. However, the resulting MVP distribution in stator slots is not representative of the real MVP distribution since the stator slot geometry is simplified. If the real MVP distribution in stator slots is required, e.g. to compute EMF, another subdomain model including the actual slot geometry has to be solved, as developed in Subsection 4.4.1. However, this additional subdomain model is much faster than the first one since it only accounts for stator subdomains, i.e. there is no rotor motion and the topological matrix is time-independent.

4.3 Contribution to the subdomain modeling assuming finite permeability

4.3.1 Presentation of Surface PMSM subdomain model assuming finite permeability

4.3.1.1 Subdomain model description and assumptions

The objective of Section 4.3 is to detail and illustrate the ARME methodology developed in Chapter 3, in particular to solve the MVP in stator teeth and slots subdomains assuming finite permeability of stator teeth. Therefore, the developments involve the resolution of eigenvalue problems in both radial and circumferential directions using superposition principle. They are also based on the subdomain model of SPMSM to compare both subdomains with and without tooth infinite permeability assumptions. Although the stator yoke can be included in the subdomain model, it is assumed to have infinite permeability to reduce the number of subdomains and ICs to treat. Besides, contrary to the previous section, the analytical developments of ICs are not detailed, for the sake of compactness and clarity, as there are many more equations due to the introduction of a second eigenvalue problem in radial direction.

Assuming stator teeth finite permeability and stator yoke infinite permeability, the SPMSM subdomain model contains (cf. Figure 4.8):

— The surface PM subdomain.

— The airgap subdomain.

— Z_s stator slots subdomains, of index $i \in [\![1, \mathrm{Z}_s]\!]$.

— Z_s stator teeth subdomains, of index $i \in [\![1, \mathrm{Z}_s]\!]$.

There are consequently $2\mathrm{Z}_s + 2$ subdomains in the model. Stator yoke and rotor yoke are external boundaries of the subdomain model. The geometric parameters are specified in Figure 4.8, where R_r is the rotor bore radius, R_m is the top radius of surface PMs, R_s is the stator bore radius, R_y is the stator slot bottom radius and a is the stator slot angular width. The stator teeth angular width is $b = {}^{2\pi}/_{\mathrm{Z}_s} - a$. The surface PMs have parallel magnetization pattern (cf. Figure 3.17). The magnetic relative permeability is noted μ_{rm} in the surface PMs subdomain, μ_{rti} in the stator teeth subdomains, and is unitary in airgap and stator slots subdomains. Stator windings have two layers in circumferential direction and are tooth concentrated.

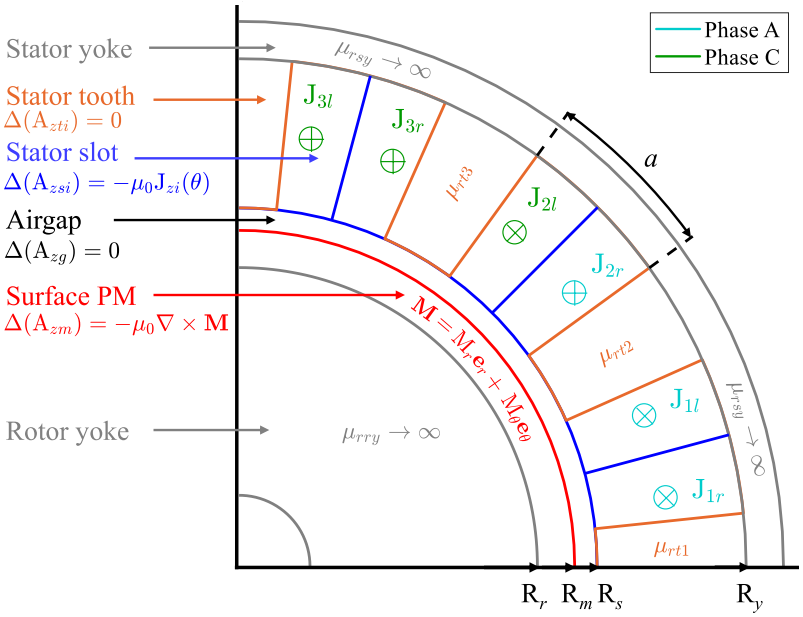

Figure 4.8 – Subdomain model of SPMSM $12s10p$ prototype with finite permeable teeth.

In order to numerically solve the ICs, a finite number of harmonics is chosen to express the MVP in the Fourier basis of each subdomain: N for surface PMs and airgap subdomains, K for the stator slots subdomains solution in circumferential direction, M for the stator teeth subdomains solution in circumferential direction, and L for stator slots and teeth solutions in radial direction.

4.3.1.2 Formulation of Interface Conditions (ICs)

There are three interfaces in the considered SPMSM subdomain model:

— The first one is between surface PMs and airgap subdomains, and is the same as in Subsection 4.2.1.2.

— The second one is between the airgap subdomain and stator slots and teeth subdomains.

— The third one is between adjacent stator slots and teeth subdomains.

The interface between airgap, stator slot and stator teeth subdomains is the circle of radius R_s. Normal flux density and tangential field ICs result in:

$$\forall i \in [\![1, Z_s]\!], \quad A_{zsi}(R_s, \theta) = A_{zg}(R_s, \theta), \quad \theta \in [\Theta_{si1}, \Theta_{si2}] \tag{4.51}$$

$$\forall i \in [\![1, Z_s]\!], \quad A_{zti}(R_s, \theta) = A_{zg}(R_s, \theta), \quad \theta \in [\Theta_{ti1}, \Theta_{ti2}] \tag{4.52}$$

$$\frac{\partial A_{zg}}{\partial r}\Big|_{R_s,\theta} = g_{2g}(\theta), \quad \theta \in [0, 2\pi] \tag{4.53}$$

where:

$$g_{2g}(\theta) = \begin{cases} \frac{\partial A_{zsi}}{\partial r}\Big|_{R_s,\theta}, & \theta \in [\Theta_{si1}, \Theta_{si2}], \quad i \in [\![1, Z_s]\!] \\ \frac{1}{\mu_{rti}} \frac{\partial A_{zti}}{\partial r}\Big|_{R_s,\theta}, & \theta \in [\Theta_{ti2}, \Theta_{ti2}], \quad i \in [\![1, Z_s]\!] \end{cases} \tag{4.54, 4.55}$$

The treatment of ICs (4.51)-(4.53) is quite similar to the infinite permeability case for the circumferential eigenvalue problem of stator slots and teeth subdomains. However,

the scalar products introduce a new type of integrals since radial eigenvalue problem introduces θ-dependent hyperbolic functions.

Interfaces between stator slot and stator teeth subdomains are radial edges at $\theta = \Theta_{ti1} = \Theta_{s(i-1)2}$ and $\theta = \Theta_{ti2} = \Theta_{si1}$. Normal flux density and tangential field ICs result in:

$$\forall i \in [\![1, Z_s]\!], \quad A_{zti}(r, \Theta_{ti1}) = A_{zsi}(r, \Theta_{s(i-1)2}), \qquad r \in [R_s, R_y] \tag{4.56}$$

$$\forall i \in [\![1, Z_s]\!], \quad A_{zti}(r, \Theta_{ti2}) = A_{zsi}(r, \Theta_{si1}), \qquad r \in [R_s, R_y] \tag{4.57}$$

$$\forall i \in [\![1, Z_s]\!], \quad \frac{\partial A_{zsi}}{\partial \theta}\Big|_{r,\Theta_{si1}} = \frac{1}{\mu_{rti}} \frac{\partial A_{zti}}{\partial \theta}\Big|_{r,\Theta_{ti2}}, \qquad r \in [R_s, R_y] \tag{4.58}$$

$$\forall i \in [\![1, Z_s]\!], \quad \frac{\partial A_{zsi}}{\partial \theta}\Big|_{r,\Theta_{si2}} = \frac{1}{\mu_{rt(i+1)}} \frac{\partial A_{zt(i+1)}}{\partial \theta}\Big|_{r,\Theta_{t(i+1)1}}, \qquad r \in [R_s, R_y] \tag{4.59}$$

Regarding the developed methodology, the ICs formulation (4.56)-(4.59) means that the normal flux density condition is chosen to be included in the stator teeth PMs subdomain problem while tangential field condition is included in stator slot one. In fact, this consideration does not matter, since slots and teeth subdomains have the same periodicity in the radial direction. The Fourier components of the radial solution can be directly equalized without change of Fourier basis, such as for ICs between surface PMs and airgap subdomains. However, the geometrical polynoms of the circumferential solution as well as the r-dependent particular solutions have to be projected on the radial Fourier basis using the scalar product defined in Appendix A.5.

Furthermore, if the normal flux density condition is included in stator teeth subdomains, it leads to convergence problems and numerical inaccuracies on teeth boundaries, as explained in Subsection 4.3.3.1. In the next Subsection 4.3.1.3, the MVP solution is given in stator teeth and slots subdomains, accounting for an additional reformulation which includes the tangential field continuity condition.

4.3.1.3 MVP expression in the different subdomains

MVP in surface PM and airgap subdomains is the same as in Subsection 4.2.1, and are respectively given by Equations (4.7) and (4.9).

The MVP solution in stator teeth and slots subdomains is obtained by applying the superposition principle, i.e. by summing both solutions of circumferential and radial eigenvalue problems, as defined in Subsection 3.3.4. The problem in stator teeth subdomains is a Laplace PDE whose circumferential and radial eigenvalues problems are represented on Figures 4.9a-4.9b. The eigenvalue problem in circumferential direction has Neumann HBCs on radial edges, whose solution A^C_{zti} is given in Subsection 3.4.2.3), before the reformulation to account for potential continuity with the airgap on the circumferential edge at $r = R_s$, and for the Neumann HBC at $r = R_y$ due to stator yoke infinite permeability. After reformulation, A^C_{zti} can be written:

$$A^C_{zti}(r, \theta) = A_{ti0} + \sum_{m=1}^{M} A_{tim} \frac{P_{\nu_m}(r, R_y)}{P_{\nu_m}(R_s, R_y)} \cos(\nu_m(\theta - \Theta_{ti1})) \tag{4.60}$$

where A_{ti0}, A_{tim} are the unknown integration constants, and the eigenvalue ν_m is given by Equation (3.81). It can be noticed that it is the same homogeneous solution as for the stator slot subdomain in the infinite permeability case (cf. Subsection 4.2.1.5).

The stator tooth subdomain problem in r-direction has mixed HBCs on circumferential edges: Dirichlet HBC at $r = R_s$ and Neumann HBC from yoke infinite permeability

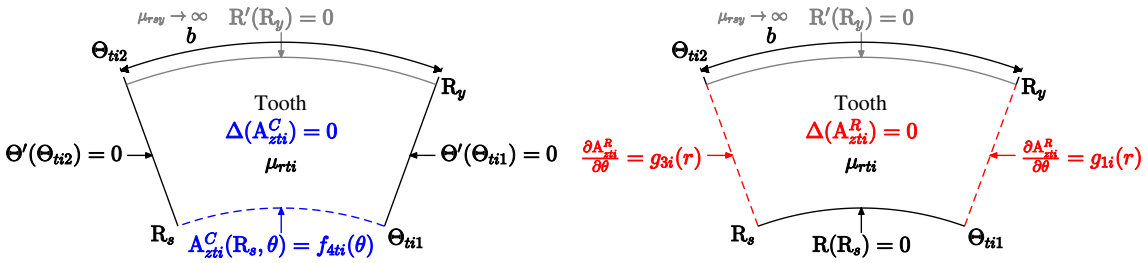

(a) Eigenvalue problem in θ-direction with Neumann HBCs, where f_{4ti} is given by Equation (4.52).

(b) Eigenvalue problem in r-direction with Neumann HBCs, where g_{1i}, g_{3i} is given by Equations (4.58)-(4.59).

Figure 4.9 – Superposition principle for MVP PDE in stator teeth subdomains assuming teeth finite permeability and yoke infinite permeability (first formulation F_1).

at $r = R_y$. The MVP solution A^R_{zti} is given in Subsection 3.4.3.2) before the reformulation to account for tangential field continuity with the adjacent stator slots subdomains on the radial edges at $\theta = \Theta_{si1}$ and $\theta = \Theta_{si2}$. After reformulation, A^R_{zti} can be written:

$$A^R_{zti}(r,\theta) = \sum_{l=1,3,5...}^{2L-1} \left[-A_{til} \frac{1}{\upsilon_l} \frac{\cosh(\upsilon_l(\theta - \Theta_{ti2}))}{\sinh(\upsilon_l(\Theta_{ti2} - \Theta_{ti1}))} + B_{til} \frac{1}{\upsilon_l} \frac{\cosh(\upsilon_l(\theta - \Theta_{ti1}))}{\sinh(\upsilon_l(\Theta_{ti2} - \Theta_{ti1}))} \right] \sin\left(\upsilon_l \ln\left(\frac{r}{R_s}\right)\right) \tag{4.61}$$

where A_{til}, B_{til} are the unknown integration constants, and the eigenvalue υ_l is given by Equation (3.93).

The stator slot subdomain problem is a Poisson PDE with current density source whose circumferential and radial eigenvalues problems are represented on Figures 4.10a-4.10b. The homogeneous problem is a Laplace PDE, and since the superposition principle is the same for both stator teeth and slots subdomains, homogeneous solutions of circumferential and radial eigenvalues problem are the same as for stator teeth. Besides, the particular solution accounting for current density is the same as for the infinite permeability case solution, and A^C_{zsi} is:

$$A^C_{zsi}(t_0,r,\theta) = A_{si0} + \mu_0 J_{i0}(t_0) X_{si0}(R_s) + \sum_{k=1}^{K} \left(A_{sik} \frac{P_{\nu_k}(r,R_y)}{P_{\nu_k}(R_s,R_y)} + \mu_0 J_{i\nu_k}(t_0) X_{sik}(R_s) \right) \cos(\nu_k(\theta - \Theta_{si1})) \tag{4.62}$$

where A_{si0}, A_{sik} are the unknown integration constants, J_{i0}, $J_{i\nu_k}$ are the constant and cosine Fourier components of the current density distribution for slotted double layer windings in θ-direction, X_{si0}, X_{sik} are the particular solutions defined in Appendix A.6.5, and the eigenvalue ν_k is given by Equation (3.81).

The general solution A^R_{zsi} can be written:

$$A^R_{zsi}(r,\theta) = \sum_{l=1,3,5...}^{2L-1} \left[-A_{sil} \frac{1}{\upsilon_l} \frac{\cosh(\upsilon_l(\theta - \Theta_{si2}))}{\sinh(\upsilon_l(\Theta_{si2} - \Theta_{si1}))} + B_{sil} \frac{1}{\upsilon_l} \frac{\cosh(\upsilon_l(\theta - \Theta_{si1}))}{\sinh(\upsilon_l(\Theta_{si2} - \Theta_{si1}))} \right] \sin\left(\upsilon_l \ln\left(\frac{r}{R_s}\right)\right) \tag{4.63}$$

where A_{sil}, B_{sil} are the unknown integration constants, and the eigenvalue υ_l is given by Equation (3.93) (same as for teeth subdomains).

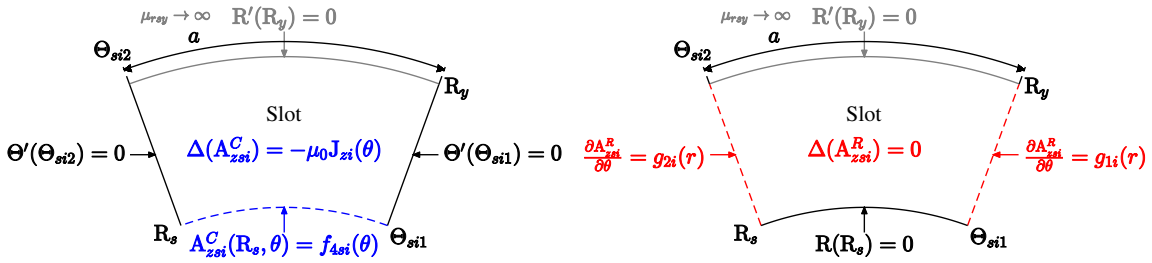

(a) Eigenvalue problem in θ-direction with Neumann HBCs, where f_{4si} is given by Equation (4.51).

(b) Eigenvalue problem in r-direction with mixed HBCs, where g_{1i}, g_{3i} is given by Equations (4.58)-(4.59).

Figure 4.10 – Superposition principle for MVP PDE in stator slots subdomains assuming teeth finite permeability and yoke infinite permeability.

Thanks to this reformulation, the tangential field continuity equations (4.58)-(4.59) give the following relations between the unknown integration constants:

$$\forall i \in [\![1, Z_s]\!], \quad A_{sil} = \frac{B_{til}}{\mu_{rti}} \tag{4.64}$$

$$\forall i \in [\![1, Z_s]\!], \quad B_{sil} = \frac{A_{t(i+1)l}}{\mu_{rt(i+1)}} \tag{4.65}$$

These simple relations enable to substitute two integration constants in the other ICs and reduce the number of integration constants which has to be numerically solved (cf. Subsection 4.2.3.4). Without performing the aforementioned substitution, the total number of integration constants in the subdomain model is $6N + (K + M + 4L + 2)Z_s$, meaning $(M + 4L + 1)Z_s$ more than the infinite permeability case.

4.3.2 Simulation results and validation with FEA under open-circuit condition

4.3.2.1 Uniform finite permeability of stator teeth

The SPMSM subdomain model with stator teeth finite permeability is implemented in MANATEE software [MANATEE, 2018] for the e-NVH simulation of the SPMSM $12s10p$ designed in this thesis. The geometrical and magnetic parameters are given in Table 5.1. First, the tooth relative permeability is assumed to be $\mu_{rti} = 2500$. The MVP is solved under open-circuit condition, i.e. only with rotor surface PMs excitation. The flux density distribution and flux lines are illustrated in Figure 4.11, and fully validated with FEA [Ansys, 2018] with $\mu_{rti} = 2500$. Radial and circumferential airgap flux densities are obviously similar to those obtained with the infinite permeability case, as shown in Figure 4.12.

The different harmonic numbers in the subdomain are detailed in Table 4.2, and corresponds to a high accuracy. The size of the subdomain model, i.e. the total number of unknowns is $N_{sdm} = 3864$. For a single instant t_0, the computation time is almost twice higher to build the topological matrix and the source vector than solving the ICs (0.5 s versus 0.3 s). However, the subdomain model does not account for periodicities or airgap harmonic pre-selection and the computation time does not reflect the possible computational efficiency of the method.

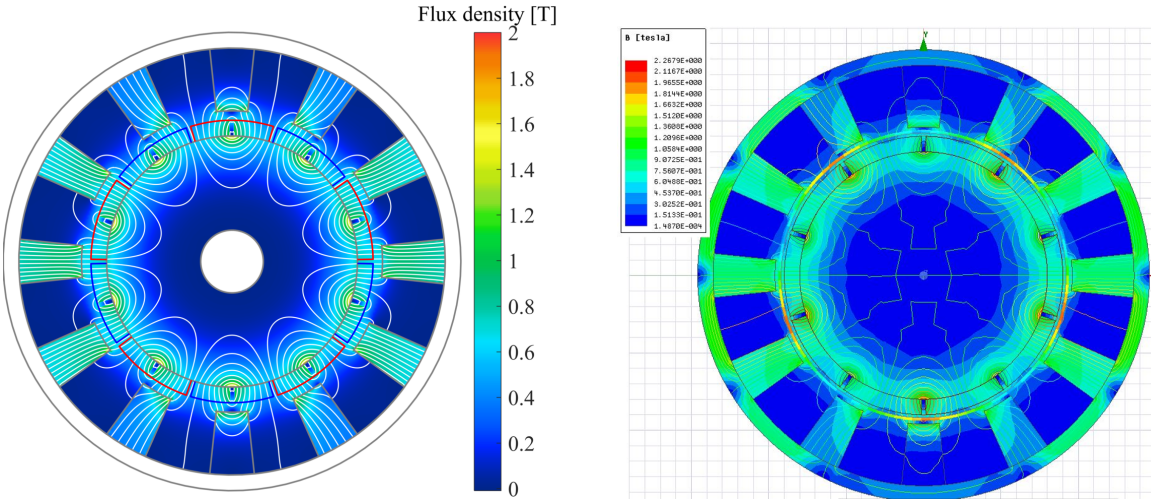

(a) SDM (b) FEA

Figure 4.11 – Flux lines comparison between SDM and FEA for $\mu_r = 2500$.

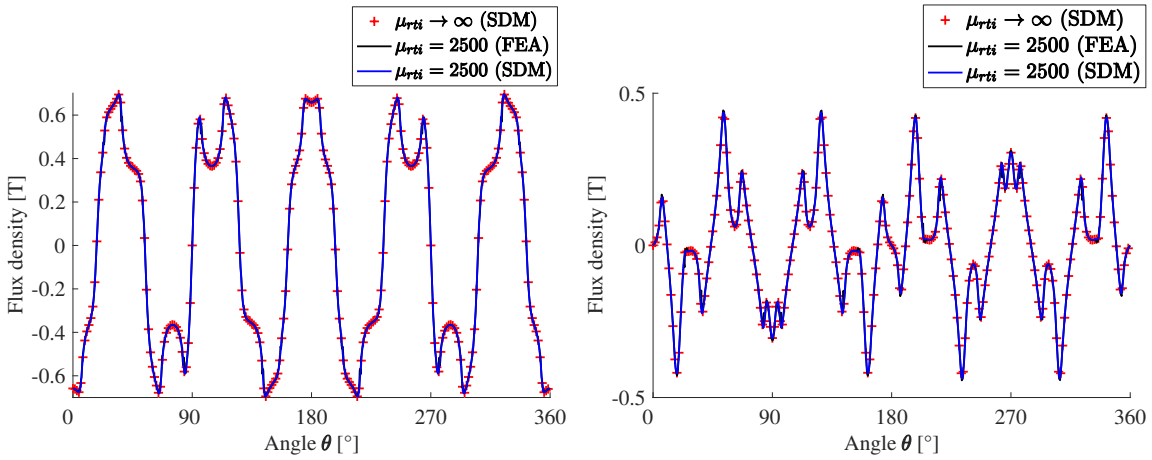

(a) Radial airgap flux density (b) Circumferential airgap flux density

Figure 4.12 – Airgap flux comparison between SDM and FEA for $\mu_r = 2500$.

	Airgap & Surface PMs	Stator slots (circumferential)	Stator tooth (circumferential)	Stator slot & tooth (radial)
Harmonic number	N	K	M	L
Value	500	20	15	20

Table 4.2 – Harmonic numbers in subdomains.

4.3.2.2 Uniform finite permeability except in one tooth

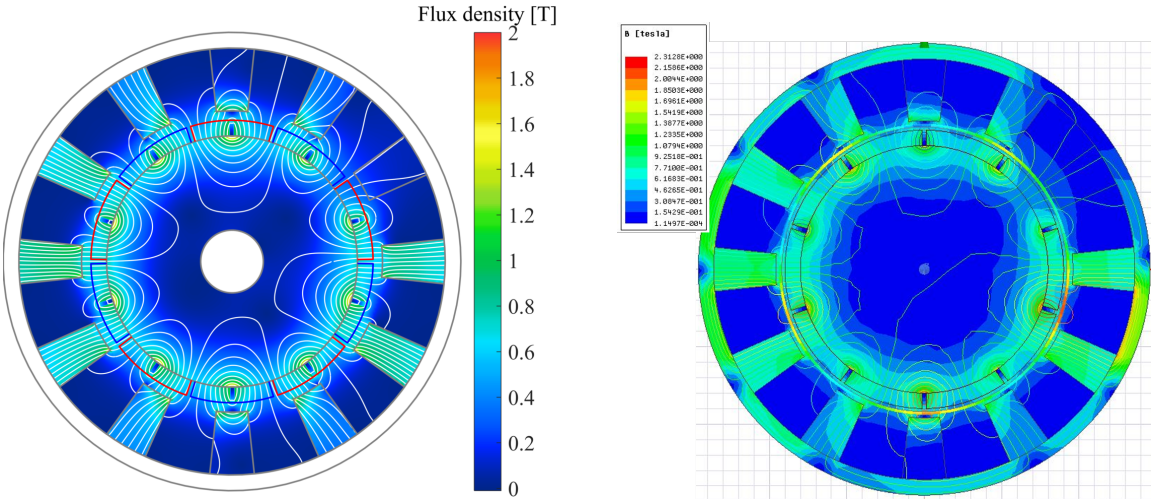

(a) SDM (b) FEA

Figure 4.13 – Comparison between SDM and FEA for $\mu_r = 2500$ except in the 2^{nd} tooth.

On a second phase, the tooth relative permeability is still assumed to be $\mu_{rti} = 2500$ in every tooth except in the 2^{nd} one, which is assimilated to air, i.e. with $\mu_{rt2} = 1$. The flux density distribution and flux lines are illustrated on Figures 4.13 and 4.14, and validated with FEA [Ansys, 2018]. It can be seen in Figure 4.14 that the flux density drops in the airgap in front of the non magnetic tooth, in comparison with the finite permeability case. The model has also been validated for other relative permeability values, such as $\mu_{rti} = 1$ to check the limit cases.

Therefore, it may be possible to include a global saturation by updating the relative permeability in each tooth depending on the B(H) curve of the ferromagnetic material and on the magnetic excitation, as investigated in Subsection 4.3.3.3.

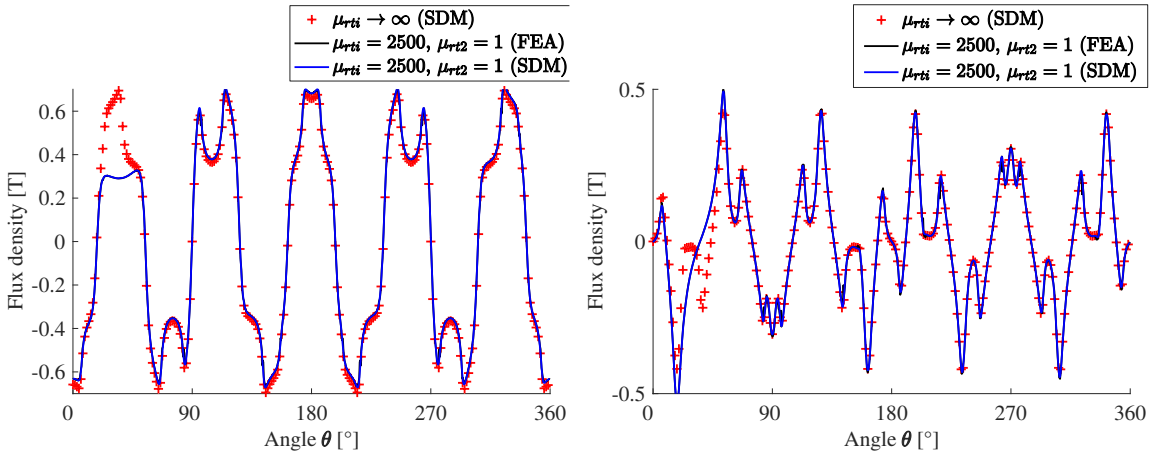

(a) Radial airgap flux density (b) Circumferential airgap flux density

Figure 4.14 – Airgap flux comparison between SDM and FEA for $\mu_r = 2500$ except in the 2^{nd} tooth.

4.3.3 Discussions

4.3.3.1 On the choice of the superposition principle formulation

The initial superposition principle formulation used during this thesis to solve the stator tooth subdomain MVP, noted F_2, is illustrated in Figure 4.15. Formulation F_2 slightly differs from the formulation presented in Figure 4.9, referred as F_1 in the present subsection. The only difference with F_1 is the eigenvalue problem in circumferential direction, which has Dirichlet HBCs on radial edges and not Neumann HBCs. These Dirichlet HBCs enable to directly account for the MVP continuity at the interface with adjacent slots, while the slots subdomain MVP account for the tangential field continuity with F_1. In theory, there is no reason to chose F_1 rather than F_2 for the stator tooth, but since it is a semi-analytical method, the numerical considerations are also relevant to classify the analytical formulations.

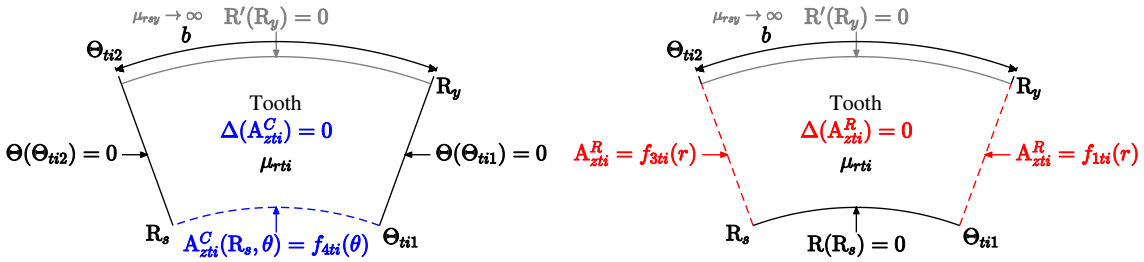

(a) Eigenvalue problem in θ-direction with Dirichlet HBCs.

(b) Eigenvalue problem in r-direction with mixed HBCs.

Figure 4.15 – Superposition principle for MVP PDE in stator teeth subdomains assuming teeth finite permeability and yoke infinite permeability (second formulation F_2).

Considering the Laplace problem in θ-direction subject to Dirichlet HBCs, the MVP solution is expressed in the Fourier basis of sine functions to fulfill the Dirichlet HBCs (see Subsection 3.4.2.3). On the other hand, the Laplace problem in radial direction is also subject to Dirichlet HBCs and expressed with sine functions as well. By superposition, this formulation enforces the general MVP solution to be zero at the corners, and therefore to be discontinuous with the MVP in the adjacent subdomains.

Tooth MVP and flux density distributions are illustrated for F_1 and F_2 in Figure 4.16, with a low pixel definition to clearly see the zero pixel at right and left hand bottom corners of the MVP distribution on in Figure 4.16b obtained with F_2. Concerning the flux density distribution, strong oscillations can be observed on the tooth boundaries. It comes from the fact that the radial flux density derives from the MVP, which is singular in the corners and makes the derivative diverging. Besides, the MVP in teeth has generally a non-zero constant value, which is approximated by the series of sine functions introduced by the Dirichlet HBCs in F_2, and is source of oscillations due to Gibbs phenomenon (see Subsection 2.2.4.4). The MVP constant value is better accounted in F_1 thanks to the integrations constants A_{ti0}, B_{ti0} introduced by the Neumann HBCs.

This oscillatory phenomenon is illustrated in Figure 4.17, when comparing the ICs at $r = R_s$ (Equations (4.51)-(4.53)) from both airgap and tooth sides. The radial flux density computed with F_2 is truncated in order to see the comparison with F_1 and the airgap side, but it is worth mentioning that unrealistic values around 50 Tesla are reached in the corners. The comparison of F_1 and F_2 regarding the application of ICs $r = R_s$ between the third tooth and the airgap is zoomed in in Figure 4.18.

The oscillatory phenomenon is also illustrated in Figure 4.19 when comparing the

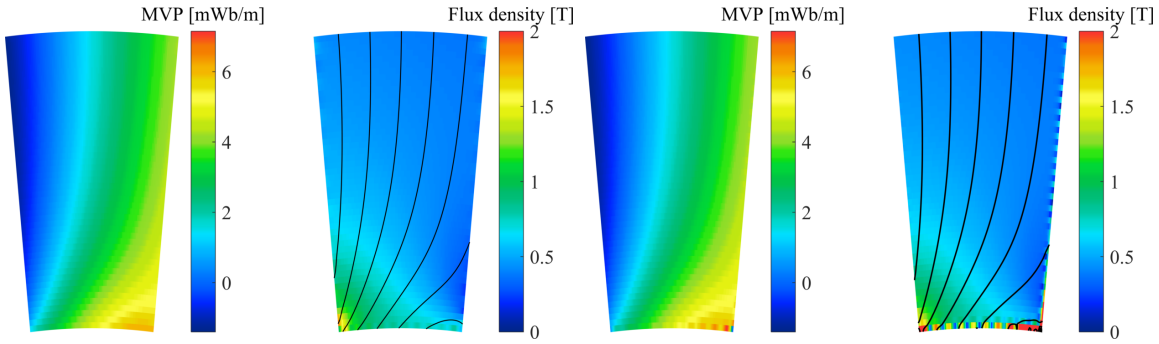

(a) 1^{st} formulation (F_1) (b) 2^{nd} formulation (F_2)

Figure 4.16 – Comparison of the two superposition principle formulations regarding MVP and flux density distribution in the 3^{rd} tooth at no-load case.

ICs on the radial edge between the 3^{rd} tooth and the 2^{nd} slot at $\theta = \Theta_{t31} = \Theta_{s22}$. Therefore, the first formulation F_1 is clearly preferable for the slot and tooth MVP solutions accounting for finite permeability. Besides, F_1 only requires to solve $2Z_s$ more integration constants than F_2 since A_{ti0}, B_{ti0} are the only new integration constants, and therefore F_1 is almost as fast as F_2.

Concerning F_1, the superposition principle formulation enforces the radial flux density to be zero at the corners, which has less impact on the flux density distribution. However, slight oscillations can still be seen on Figures 4.16a and 4.17. Therefore, these oscillations are also observable on magnetic stress if the latter is computed strictly on the interface between airgap and teeth. It may be recommended to compute lumped magnetic forces experiences by teeth using a MST contour further away from tooth surface, knowing that oscillations should drastically mitigate near the interface. Finally, if the proposed SDM is used for iron loss estimation, potential numerical error can be made due to these high frequency oscillations.

4.3.3.2 On the possibility to compute MVP and flux density as a post-processing of the infinite permeability model

The superposition principle formulation also enables to solve the MVP and the flux density iron cores as a post-processing of the subdomain model assuming infinite permeability, as shown in this subsection. Considering the SPMSM example, the aim is to find the MVP solution in rotor yoke, stator yoke and stator teeth subdomains, e.g. for iron loss calculation.

The rotor yoke subdomain problem is a 2π-periodic Laplace eigenvalue problem, hence its solution is the same as the airgap solution except that a Dirichlet HBC applies on the internal boundary at $r = R_i$ (cf. Subsection 3.3.3.2), yielding:

$$A_{zry}(r,\theta) = \sum_{n=1}^{N} \left(A_{ryn} \frac{E_n(R_i, r)}{E_n(R_i, R_r)} \cos(n\theta) + \left(B_{ryn} \frac{E_n(R_i, r)}{E_n(R_i, R_r)} \sin(n\theta) \right] \right. \tag{4.66}$$

where A_{ryn} and B_{ryn} are the rotor yoke integration constants are computed straight forward by applying the MVP continuity condition at the interface $r = R_r$ with surface PMs subdomain, whose solution is already known from the infinite permeability case. This post-processing is for example applied to show rotor yoke flux density distribution in Figure 4.11a and 4.13a, since the rotor yoke is assumed to be infinitely permeable in

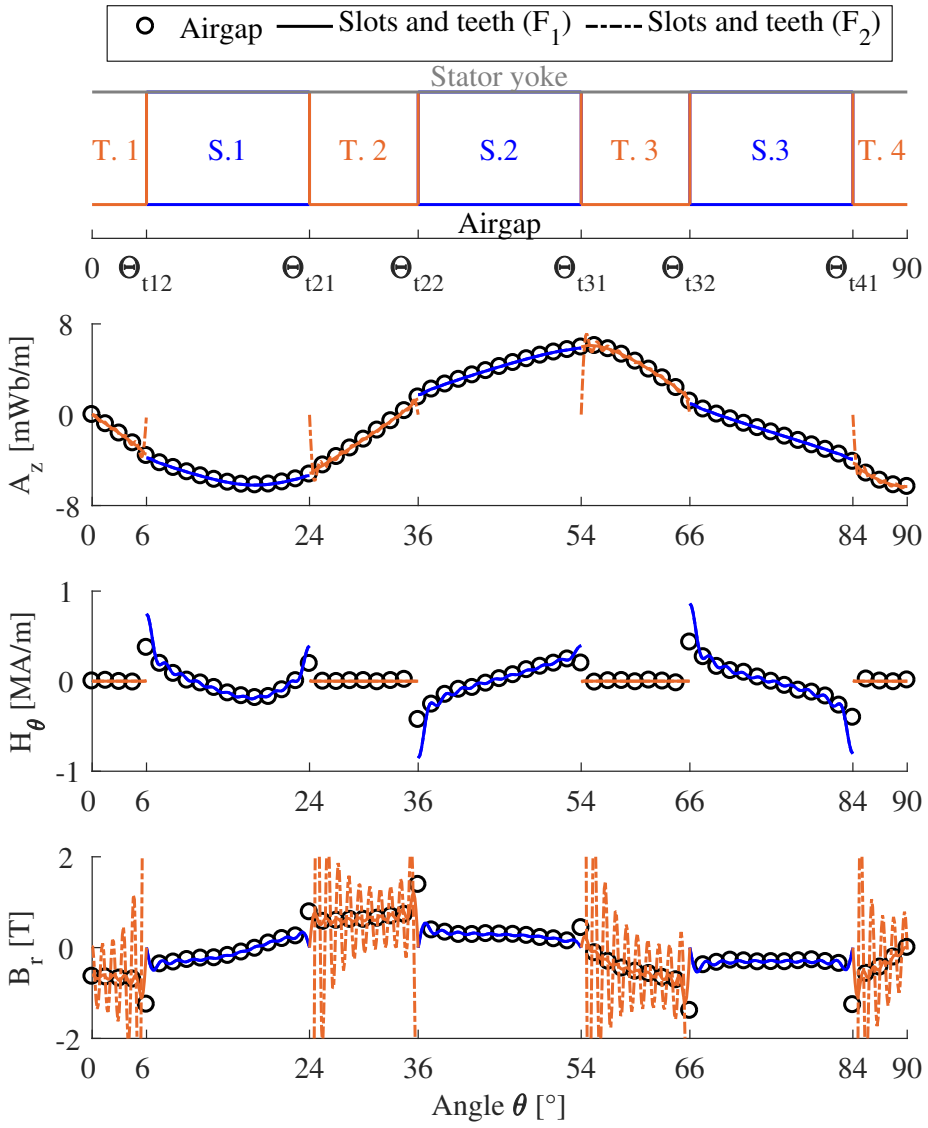

Figure 4.17 – Comparison of the two superposition principle formulations F_1 (in plain line) and F_2 (in dashed line) at the interface between airgap and stator teeth and slots ($r = R_s$).

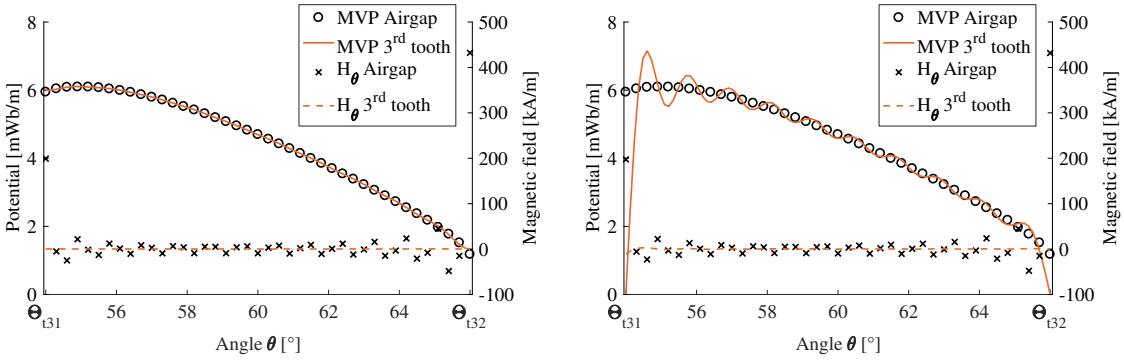

(a) 1^{st} formulation (F_1)

(b) 2^{nd} formulation (F_2)

Figure 4.18 – Zoom on MVP and tangential field continuity between 3^{rd} tooth and airgap (at $r = R_s$) for each superposition principle formulation.

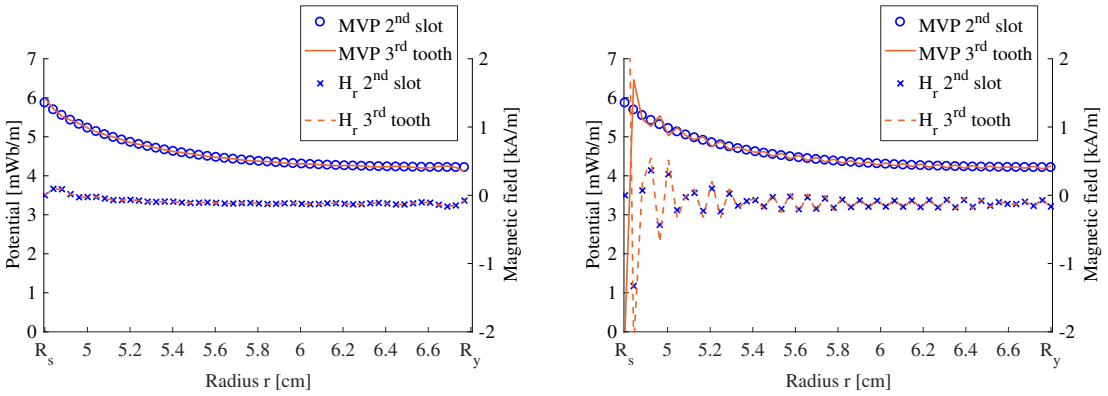

(a) 1^{st} formulation (F_1) (b) 2^{nd} formulation (F_2)

Figure 4.19 – MVP and tangential field continuity between 3^{rd} tooth and 2^{nd} slot (at $\theta = \Theta_{t31} = \Theta_{s22}$) for each superposition principle formulation.

Subsection 4.3.2.

Concerning stator core, the MVP computation requires to solve an additional subdomain model which only contains a stator yoke subdomain and Z_s stator teeth subdomains, which are assumed to have infinite permeability (i.e. $\mu_{rti}, \mu_{rsy} \to \infty$). The stator yoke MVP solution A_{zsy} is a 2π-periodic Laplace eigenvalue problem, hence its solution is the same as the airgap solution, except that a Dirichlet HBC applies on the external boundary at $r = R_e$ (cf. Subsection 3.3.3.2), yielding:

$$A_{zsy}(r,\theta) = \sum_{n=1}^{N} \left(A_{syn} \frac{R_y}{n} \frac{E_n(r,R_e)}{P_n(R_y,R_e)} \cos(n\theta) + \left(B_{syn} \frac{R_y}{n} \frac{E_n(r,R_e)}{P_n(R_y,R_e)} \sin(n\theta) \right] \right. \tag{4.67}$$

where A_{syn} and B_{syn} are the stator yoke integration constants, which are determined by applying the ICs with the stator slots subdomains, whose solution is already known from the infinite permeability simulation, and stator teeth subdomains whose MVP solution is given in Subsection 4.3.1.3. As said before, the stator tooth subdomain problem is a Laplace eigenvalue problems in radial and circumferential directions. The MVP solution in the radial direction is given by Equation (4.61). The stator tooth integration constants for the radial solution A_{til}, B_{til} are determined by applying the MVP continuity with the stator slots MVP solution on radial edges (cf. Equations (4.56)-(4.57)). The MVP solution in the circumferential direction is given by Equation (4.60). The stator tooth integration constants for the circumferential solution A_{ti0}, A_{tim} and B_{tim} are determined by applying the MVP continuity (cf. Equation 4.52) with the airgap MVPs computed previously.

4.3.3.3 On the possibility to account for global saturation assuming finite stator yoke permeability

The possibility to account for global saturation is investigated based on the SPMSM $12s10p$ under load condition. To increase the degrees of freedom of the subdomain model, the stator yoke is also assumed to have a finite relative permeability μ_{rsy} and is added in the subdomain model. The stator yoke MVP solution is thus given by Equation 4.67. Then, the MVP solution in stator slots and teeth is modified to account for the ICs with the stator yoke at $r = R_y$. The resulting superposition principle formulation is illustrated in Figure 3.8. The Laplace eigenvalue problem in radial direction is now subject

to Dirichlet HBCs and not mixed HBC anymore. The radial solutions for stator teeth and slots slightly differ from Equations (4.61) and (4.63), since the harmonic order l takes any integer values and the eigenvalue υ_l is given by Equation (3.89) (cf. Subsection 3.4.3.1). Furthermore, the circumferential MVP solution for stator teeth becomes:

$$\begin{aligned} A^{C}_{zti}(r,\theta) &= A_{ti0} + B_{ti0}\ln(r) \\ &+ \sum_{m=1}^{M}\left(A_{tim}\frac{E_{\nu_m}(r,R_y)}{E_{\nu_m}(R_s,R_y)} + B_{tim}\frac{E_{\nu_m}(R_s,r)}{E_{\nu_m}(R_s,R_y)}\right)\cos\left(\nu_m(\theta-\Theta_{ti1})\right) \end{aligned} \tag{4.68}$$

where A_{ti0}, B_{ti0}, A_{tim}, B_{tim} are the i^{th} stator tooth integration constants for the circumferential solution, which are determined by applying the MVP continuity with airgap and stator yoke MVPs.

The circumferential solution for stator slots becomes:

$$\begin{aligned} A^{C}_{zsi}(t_0,r,\theta) &= A_{si0} + B_{si0}\log(r) + \mu_0 J_{i0}(t_0)R_{dlc,0}(R_s) + \sum_{k=1}^{K}\Bigg[A_{sik}\frac{E_{\nu_k}(r,R_y)}{E_{\nu_k}(R_s,R_y)} \\ &+ B_{sik}\frac{E_{\nu_k}(R_s,r)}{E_{\nu_k}(R_s,R_y)} + \mu_0 J_{i\nu_k}(t_0)R_{dlc,\nu_k}(R_s)\Bigg]\cos\left(\nu_k(\theta-\Theta_{si1})\right) \end{aligned} \tag{4.69}$$

where A_{si0}, B_{si0}, A_{sik}, B_{sik} are the i^{th} stator slots integration constants for the circumferential solution, which are determined by applying the MVP continuity with airgap and stator yoke MVPs, J_{i0}, $J_{i\nu_k}$ are the constant and cosine Fourier components of the current density distribution for slotted double layer windings in θ-direction, and $R_{dlc,0}$, R_{dlc,ν_k} are the particular solutions given by Equations (3.132)-(3.134).

Therefore, the SPMSM subdomain model accounting for stator teeth and yoke with finite permeability contains:

— The surface PMs subdomain.

— The airgap subdomain.

— Z_s stator slot subdomains, of index $i \in [\![1, Z_s]\!]$.

— Z_s stator tooth subdomains, of index $i \in [\![1, Z_s]\!]$.

— The stator yoke subdomain.

There are consequently $2Z_s + 3$ subdomains in the model, and the size of the subdomain model is $8N + (2K + 2M + 4L + 4)Z_s$, i.e. $2N + (K + M + 2)Z_s$ more than the case with infinitely permeable stator yoke.

The subdomain model is simulated at load case, with a stator slot current density varying from 0 to 20 A/mm^2 and $\phi_0 = 90°$ (electrical degrees). The operating point at 20 A/mm^2 should not be reached in reality but it enables to highly saturate the stator yoke and validate the proposed method. The obtained torque versus current density curve is illustrated in Figure 4.20, alongside the considered B(H) curve of the stator lamination (M400-50A).

SDM results are compared with non-linear FEA (MANATEE coupling with FEMM [FEMM, 2018]). Radial and tangential flux densities are illustrated in Figure 4.21 for the maximum stator slot current density. It can be seen that the fundamental flux density

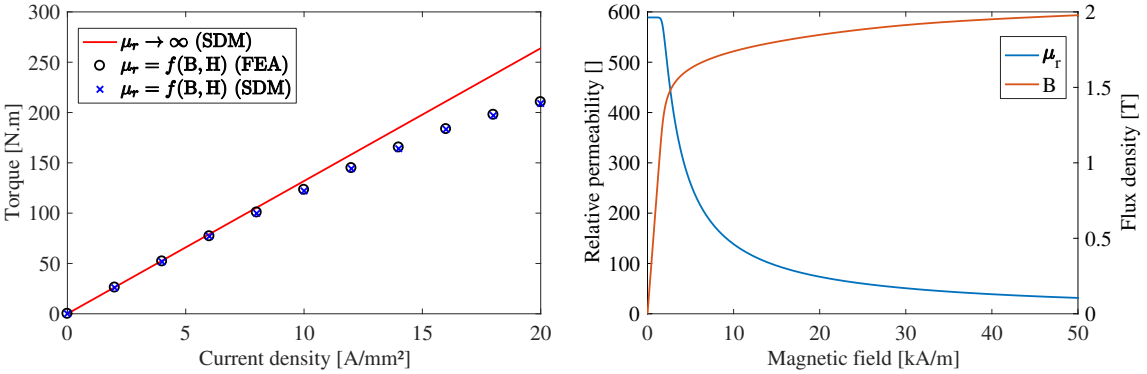

(a) Torque versus stator slot current density.

(b) B(H) curve (electric steel M400-50 A).

Figure 4.20 – Electromagnetic torque versus stator slot current density and B(H) curve of stator lamination for SPMSM $12s10p$.

is well estimated, which further validates this model including global saturation. The spatial harmonic content is also much closer to the FEA simulation than the infinite permeability case. In particular, the saturation harmonic which affects first stator slotting harmonic at $Z_s - p$ is well estimated. Besides, the harmonic with wavenumber 1, which originates from the concentrated windings distribution, has also significantly decreased due to saturation in stator yoke subdomain, but is still 50% higher than the one obtained with FEA since stator yoke relative permeability is assumed to be uniform.

The obtained flux density distribution for the maximum stator slot current density is illustrated in Figure 4.22, in comparison with non-linear FEA, and using the FEMM colormap for the flux density distribution obtained with SDM. It can be seen that both maps are quite similar. Relative permeabilities in stator teeth are found by applying an iterative fixed-point method which requires 5 iterations, i.e. 5 more computation time. The lowest permeability is reached in the third tooth ($\mu_{rt3} \approx 20$) and the highest is in the fifth tooth ($\mu_{rt3} \approx 336$). Of course, the flux density distribution is roughly estimated in the stator yoke subdomain, in particular the maximum value, since a uniform relative permeability is considered for the entire subdomain. Besides, slope breaks are clearly visible between yoke and teeth subdomains, due to the non-physical discontinuous relative permeability at the interface.

Furthermore, since the relative permeability is uniform inside the tooth, the corners do not saturate more than the rest of the tooth, as it should in case of local saturation, which may imply that saturation harmonics with higher orders than $Z_s \pm p$ could not be accurately estimated. In conclusion, this method is suitable to the present SPMSM which has large open slots, but should also be validated on electrical machines with a large number of teeth and tooth tips, to validate or not the estimation of saturation harmonics with higher wavenumbers than $Z_s \pm p$.

4.3.4 Conclusion on the finite-permeability model relevancy in e-NVH studies

The SDM including iron finite permeability based on superposition principle is validated for the SPMSM $12s10p$ subdomain model. Two superposition principle formulations for the tooth MVP solution have been investigated in Subsection 4.3.3.1, and the first formulation relying on Neumann HBCs for the circumferential problem is recommended to avoid numerical problems. The MVP solutions resulting from the first super-

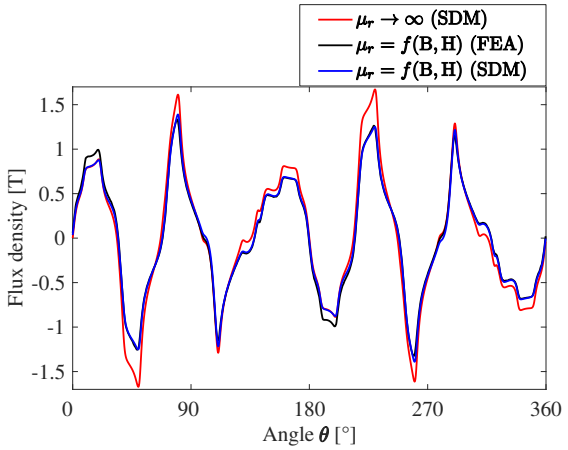

(a) Radial airgap flux density

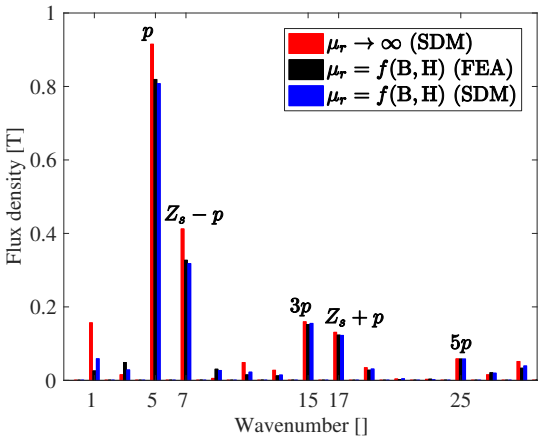

(b) Radial FFT over space

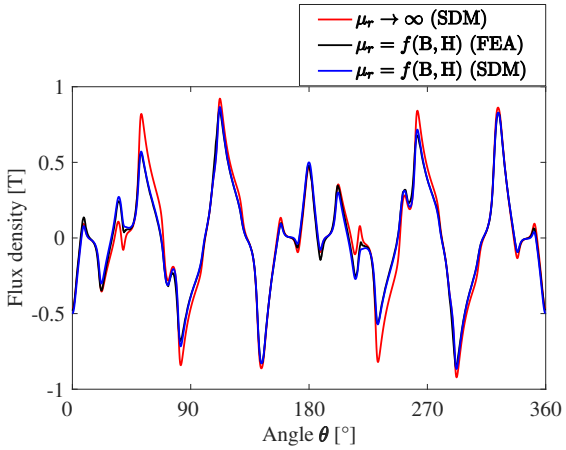

(c) Circumferential airgap flux density

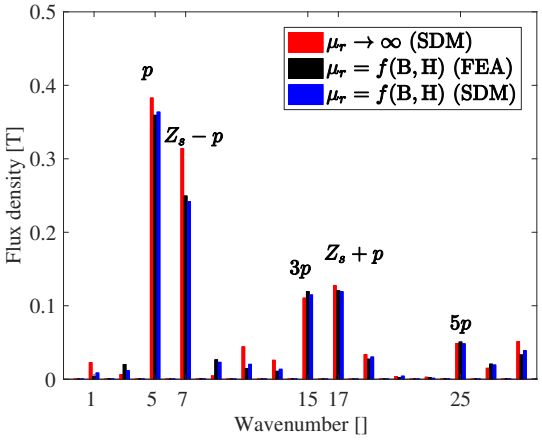

(d) Circumferential FFT over space

Figure 4.21 – Airgap flux density comparison between SDM and non-linear FEA accounting for stator core saturation.

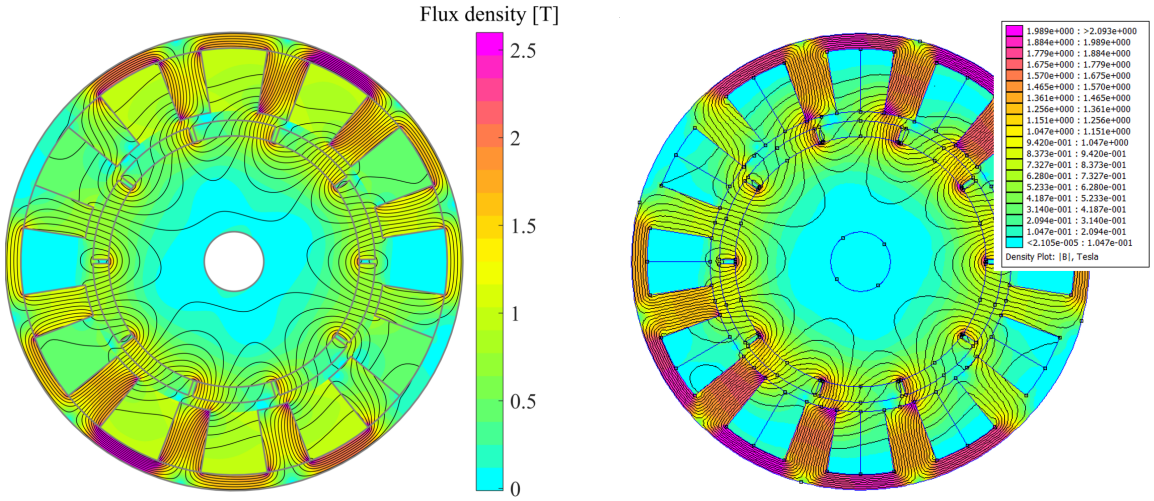

(a) SDM including global saturation

(b) FEA including local saturation

Figure 4.22 – Flux lines comparison between SDM and non-linear FEA accounting for stator core saturation.

position principle formulation are given in Subsection 4.3.1.3 with stator yoke infinite permeability assumption, and in Subsections 4.3.3.2-4.3.3.3 without.

Compared with the infinite permeability model, the finite permeability model enables to account for global saturation in the spatial harmonic content by setting the relative permeability of stator teeth and yoke subdomains in function of the magnetic excitation and the B(H) curve. However, the relative permeability is time-dependent, meaning that the stator topological matrix also becomes time-dependent, and the numerical resolution requires one resolution per time step, as discussed in 4.3.4. Besides, the non-linear resolution necessary increases calculation time hence non-linear SDM faces the same problem as non-linear FEA or MEC. As the saturation is global in each subdomain and is intrinsically linked to the fundamental flux density, a possible strategy to avoid the non-linear iteration process could consist in evaluating the relative permeability distribution for one instant t_0, and then modulate it by the stator supply frequency f_s.

Regarding e-NVH simulation requirements, the fact that flux density can be computed in iron parts does not mean it must be systematically done. In fact, the infinite permeability assumption can also be seen as an advantage as it reduces the number of subdomains and results in a faster model to compute the magnetic stress in early electromagnetic design phase. Besides, the developed methodology based on superposition principle also enables to compute the MVP in infinitely permeable iron cores as a post-processing, as shown in Subsection 4.3.3.2.

In conclusion, the developed methodology certainly extends the SDM capabilities by including saturation harmonics in the flux density harmonic content, but it also introduces an additional complexity in both analytical and numerical aspects, which globally increases the computation duration (by a factor 5 for the considered SPMSM), the difficulty to implement the method, and is a non-negligible factor of numerical inaccuracies.

4.4 Contribution to Squirrel Cage Induction Machines (SCIMs) subdomain modeling

4.4.1 Presentation of the SCIM subdomain model

4.4.1.1 Subdomain model description and assumptions

Section 4.4 deals with a subdomain model development of SCIMs, including the harmonic content due to MMF and slotting effects, under both no-load and load conditions. The development and implementation in MANATEE of the SCIM subdomain model is based on two previous subdomain modeling approaches [Lubin et al., 2011b; Boughrara et al., 2015] which have already been discussed in the SDM state of the art (see Subsection 2.3.3.2). The topology used for the validation is a SCIM $36s28r4p$ (i.e. 36 stator slots, 28 rotor bars and 4 poles ($p = 2$)) with single layer distributed windings (three slots per pole and per phase $q = 3$) taken from Boughrara et al. [2015], and illustrated in Figure 4.23. This section mainly focuses on validating and discussing the modeling assumptions behind the proposed SCIM model, as the analytical developments, such as the MVP solution in each subdomain and the application of ICs between adjacent subdomains which results in a large amount of equations, can be found in Devillers et al. [2018c].

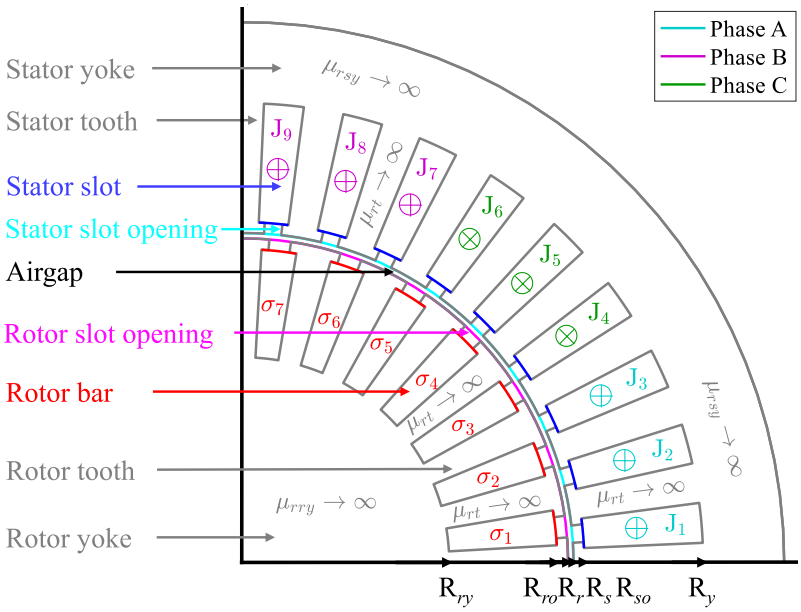

Figure 4.23 – SCIM $36s28r4p$ studied topology and assumptions

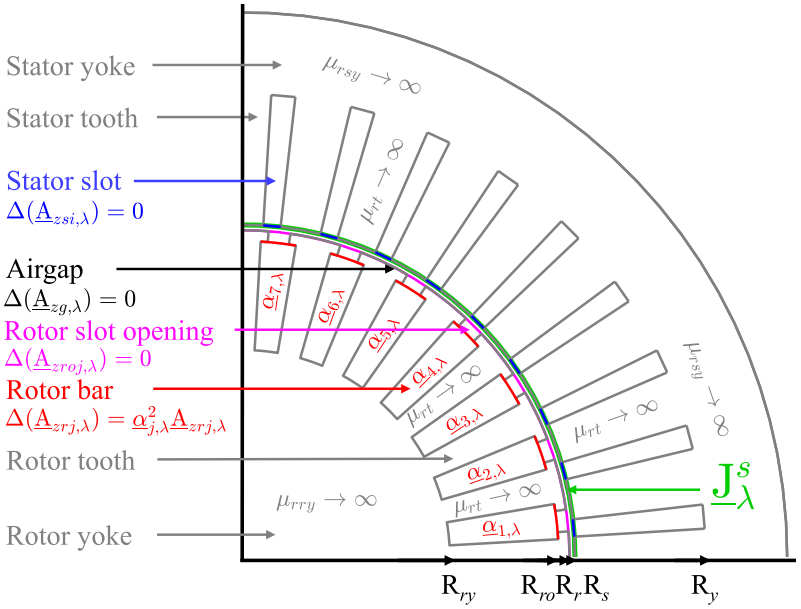

Figure 4.24 – 1^{st} subdomain model to compute MVP in airgap and rotor subdomains (performed N_λ times).

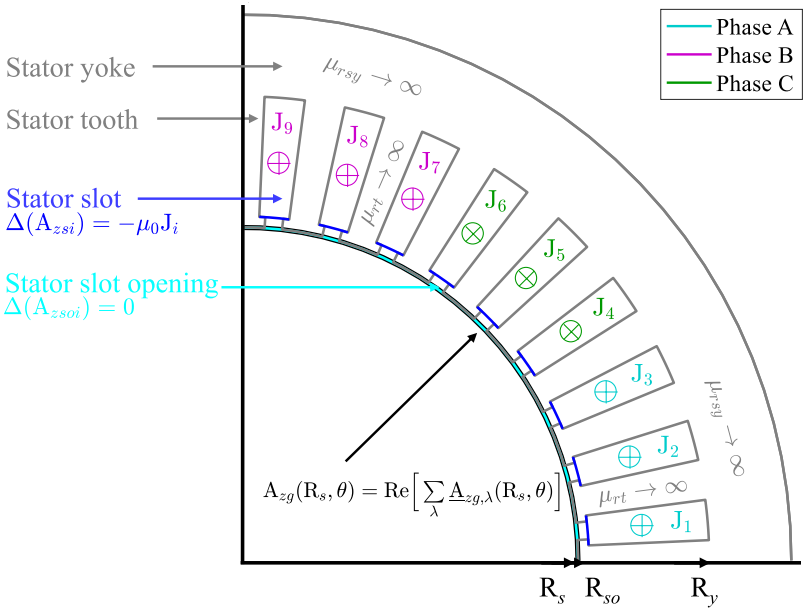

Figure 4.25 – 2^{nd} subdomain model to compute MVP in stator subdomains (performed one time).

The new subdomain modeling approach is actually composed of two distinct subdomain models, illustrated on Figures 4.24 and 4.25. First, the subdomain model represented in Figure 4.24 enables to compute the airgap flux density including time and space harmonics due to stator and rotor MMFs and slots. This first subdomain model is composed of:

— Z_r rotor bars subdomains, of index $j \in [\![1, Z_r]\!]$ and with uniform electrical conductivity σ_j.

— Z_r rotor slot openings subdomains.

— The airgap subdomain.

— Z_s simplified stator slots subdomains, of index $i \in [\![1, Z_s]\!]$ to avoid modeling slot openings and to reduce the number of integration constants (see Subsection 4.2.3.4).

— The current sheet distribution $\underline{J}^s_{k,\lambda}$ at the stator bore.

Both stator and rotor slots subdomains are naturally modeled (such as in Boughrara et al. [2015])) to account for both slotting effects in the spatial harmonic content. Stator and rotor cores are assumed to be infinitely permeable. The model is solved for each rotor position (associated to the simulation instant t_0) to include the stator MMF harmonics in the rotor bar currents and the RSHs in the airgap and stator flux density harmonic contents.

As explained in Subsections 3.2.3.2 and 3.2.3.2, the analytical computation of induced current in rotor bars requires to solve the Helmholtz eigenvalue problem, which relies on the assumption that there is a unique current pulsation ω_{rm} in the rotor bar subdomain. This condition is fulfilled if the root cause of rotor-induced harmonics, i.e. time and space harmonics of the stator MMF, are considered separately in the subdomain model. Therefore, the stator MMF distribution at the instant t_0 is expressed in Fourier series as an infinite superposition of stator MMF harmonics, associated to their electrical frequency kf_s and wavenumber $r = \lambda p$. Each stator MMF harmonic is then modeled by an equivalent current sheet $\underline{J}^s_{k,\lambda}$ located at the stator bore (such as in Lubin et al. [2011b]), which is associated to the proper diffusion coefficient $\underline{\alpha}_{j,\lambda}$ in each rotor bar. It is worth mentioning that all the subdomain model quantities become complex

since the Helmholtz eigenvalue problem yields complex MVP solutions. The equivalent current sheet $\underline{J}^s_{k,\lambda}$ located at the stator bore is expressed as:

$$\underline{J}^s_{k,\lambda}(t_0,\theta) = \underline{J}_{k,\lambda} e^{i(2k\pi f_s t_0 - \lambda p\theta)} \tag{4.70}$$

where $\underline{J}_{k,\lambda}$ is the current sheet complex magnitude and $i = \sqrt{-1}$. Besides, the values taken by λ in case of distributed windings with an integer number of slots per pole and per phase is given by:

$$\begin{aligned} &\lambda = 1 \pm 2q\eta \quad \eta \in \mathbb{N} \\ \text{i.e.} \quad &\lambda = 1, -5, 7, -11, 13, \ldots \end{aligned} \tag{4.71}$$

In the rotor bars referential, the induced current pulsation due to the equivalent current sheet $\underline{J}^s_{k,\lambda}$ is then:

$$\omega_{rm,k,\lambda} = 2\pi f_{r,k,\lambda} = 2\pi\big[k - \lambda(1-s)\big] f_s \tag{4.72}$$

where $f_{r,k,\lambda}$ is the associated rotor current frequency and s is the fundamental slip. Finally, the resulting diffusion coefficient $\underline{\alpha}_{j,k,\lambda}$ used in the Helmholtz eigenvalue problem for the j^{th} rotor bar subdomain is given by:

$$\underline{\alpha}_{j,k,\lambda} = \sqrt{i\mu_0\sigma_j\omega_{rm,k,\lambda}} \tag{4.73}$$

The possibility to assign a different electrical conductivity σ_j to each rotor bar subdomain enables for example to simulate the effect of broken bar on the airgap flux density harmonic content [Boughrara et al., 2015]. Besides, only the stator current fundamental (i.e. $k = 1$) is considered in this section, hence diffusion coefficient is noted $\underline{\alpha}_{j,\lambda}$ and rotor current frequency is noted $f_{r,\lambda}$.

Since stator slots are current free, it is no longer necessary to model the real stator slots geometry, in particular stator slot openings. Stator slots and slot openings can be modeled by an equivalent slot to reduce the number of subdomains hence the number of ICs to solve numerically, as proposed in Subsection 4.2.3.4. The equivalent slot has the same depth as the real slot and the same angular width as the slot opening which is responsible for the slotting harmonics.

Therefore, this first subdomain model enables to accurately compute the rotor bar induced currents due to each time and space harmonic of the stator MMF harmonic, and includes stator and rotor slotting effects, in particular RSHs by accounting for rotor motion, in the airgap magnetic stress computation. However, the MVP computed in the stator slots is not physical, since stator current is distributed at stator bore, and the slot geometry is also not real. Furthermore, the second subdomain model illustrated in Figure 4.25 enables to reconstruct the MVP and flux density distributions inside the actual stator slots, accounting for the proper current density distribution J_i, the real slot shape and the presence of slot opening if any. The second subdomain model is composed of:

— Z_s stator slot openings subdomains, of index $i \in [\![1, Z_s]\!]$.

— Z_s stator slot subdomains, of index $i \in [\![1, Z_s]\!]$, with uniform current density J_i.

— The airgap flux density distribution $A_{zg}(R_s,\theta) = \mathrm{Re}[\sum_\lambda \underline{A}_{zg,\lambda}(R_s,\theta)]$, located at stator bore and computed from the first subdomain model.

Once stator slot MVP solution is obtained, flux linkage and EMF can be computed as detailed in Subsection 4.2.2.4. The second subdomain model is very fast to solve since they are only stator slots and no need to account for rotor motion (cf. Subsection 4.2.3.1). The developed subdomain methodology is validated in Subsections 4.4.2 and 4.4.3 for the simulation of SCIM $36s28r4p$ at both no-load and load cases.

4.4.1.2 Determination of the required number of current sheet models

The exact airgap flux density prediction requires to solve the first subdomain model as many times as the number of stator MMF harmonics (infinite in theory), and then sum the contribution of each harmonic. The number of spatial harmonics is necessarily truncated to the same harmonic number N_{max} as for the airgap subdomain, since they are both expressed in the 2π-periodic Fourier basis (cf. the method to compute the current sheet $\underline{J}^s_{k,\lambda}$ detailed in Devillers et al. [2018c]). A certain number of simulations, noted N_λ, is still required for each instant t_0, i.e. for each stator current distribution and rotor position, such as:

$$|1 \pm 6N_\lambda| p \leq N_{max} \tag{4.74}$$

In the case of SCIM $36s28r4p$, assuming that the airgap harmonic number N_{max} is for example chosen to include up to the 10^{th} stator slotting harmonic order, i.e. $N_{max} = 10Z_s + p$, the first subdomain model has to be solved $N_\lambda = 30$ times for each t_0, which results in a thirty times longer model. N_λ can be reduced by noticing that the skin effect (proportional to the inverse of diffusion coefficient) converges when $|\lambda|$ increases. Therefore, the same diffusion coefficient $\underline{\alpha}_{j,\lambda}$ can be considered for all stator MMF harmonics from a certain order $\lambda = 1 \pm 6N_\lambda$. In the presented model, the first $\eta \leq N_\lambda - 1$ simulations account for the proper diffusion coefficient in rotor bars, which is expressed as $\underline{\alpha}_{j,\lambda}$. The last simulation includes all the higher stator MMF harmonics (such as $|\lambda| \geq |1 \pm 6N_\lambda|$) in the current sheet, associated to the same diffusion coefficient $\underline{\alpha}_{j,1\pm6N_\lambda}$.

Therefore, bar current harmonics induced by the higher space harmonics (such as $|\lambda \geq 1 \pm 6N_\lambda|$) have a lower skin effect than in theory, but the error generated by this assumption is negligible if N_λ is chosen so that the skin effect has already converged for $\underline{\alpha}_{j,1\pm6N_\lambda}$. However, it is worth mentioning that any bar current harmonic has its own frequency $f_{r,\lambda}$ since it only depends on the relative motion between the rotor bars and the current sheet.

The current sheet superposition modeling is illustrated in Figure 4.26, which represents the airgap MVP solution $\mathrm{Re}[\underline{A}_{zg}(R_g,\theta)]$ for $N_\lambda = 1$ (red curve), meaning all the space harmonics have the same diffusion coefficient as the fundamental ($\lambda = 1$), and for $N_\lambda = 5$ (dark blue curve), meaning the four first space harmonics ($\lambda = 1, -5, 7, -11$) have their proper diffusion coefficient and higher harmonics ($|\lambda| \geq 13$) have the same diffusion coefficient as the fifth harmonic ($\lambda = 13$). There is a slight difference between the MVP solution obtained with $N_\lambda = 1$ and $N_\lambda = 5$, due to the fact that the skin effect actually converges from $N_\lambda = 5$ for the SCIM $36s28r4p$ topology. Concerning the airgap MVP solution with $N_\lambda = 5$, the intermediate solutions ($\mathrm{Re}[\underline{A}_{zg,\lambda}(R_g,\theta)]$) for $\lambda = 1, -5, 7, -11$ and $|\lambda| \geq 13$ are also represented to illustrate the summation over λ of any electromagnetic quantities in the model.

4.4.1.3 Simulation setup

In the following, the proposed subdomain model is applied to the SCIM $36s28r4p$ of Figure 4.23 for both assumptions $N_\lambda = 1$ and $N_\lambda = 5$, and validated with transient

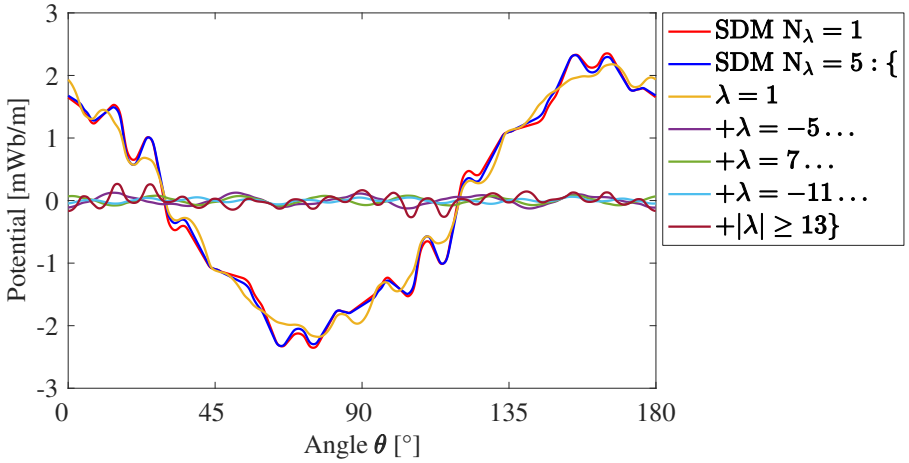

Figure 4.26 – Airgap MVP solution resulting from both assumptions $N_\lambda = 1$ and $N_\lambda = 5$ for the SCIM $36s28r4p$.

FEA [Ansys, 2018] assuming infinite iron permeability. The geometrical and electrical parameters of SCIM $36s28r4p$ are given in Boughrara et al. [2015]. The SCIM is simulated at no-load operation in Subsection 4.4.2, and load operation in Subsection 4.4.3. The validation is performed regarding time and spatial harmonic content of radial and circumferential airgap flux densities, spatial distribution of rotor bar currents, and frequency content of rotor bar currents, electromagnetic torque and EMF.

	Rotor bars	Rotor slot openings	Airgap	Stator slot openings	Stator slots	Total
Harmonic number	4	2	100 ($N_{max} = 400$)	2	4	748

Table 4.3 – Harmonic numbers in the different subdomains.

The harmonic numbers in the different subdomains are given in 4.3. The subdomain model accounts for periodicity, where the periodicity factor $c = \gcd(Z_s, Z_r, p) = 2$ enables to reduce the number of rotor and stator subdomains by $2c = 4$ (cf. Subsection 4.2.3.3). Moreover, the airgap harmonic number is four times less than the highest harmonic order, i.e. $N = N_{max}/4$. This harmonic selection results in a subdomain model size of 548 unknowns instead of 2296, which is 16 times faster in theory.

At no-load state, slip is strictly zero ($s = 0\%$) as if the rotor were driven by an external machine at synchronous speed. The simulation duration is equal to a rotor mechanical period $p/(1-s)f_s = 0.04$ s, where $f_s = 50$ Hz, and the time step between two instant t_0 is $\Delta t = 0.0001$ s. Under load condition, slip is equal to $s = 10\%$, which is quite high in reality but this value enables to reduce the computation time of the transient FEA and limit spectral leakage due to the presence of asynchronous frequencies (cf Subsection 2.2.4.2). The simulation duration is equal to a rotor electrical period $1/sf_s = 0.2$ s and time step is $\Delta t = 0.0001$ s as well. In both cases, time step is very small in order to catch high frequencies in the flux density and to compute accurately the harmonic content of the airgap magnetic stress. Besides, the stator is fed with sinusoidal three-phase currents (i.e. $k = 1$) with star coupling, and with RMS phase current $I_{rms} = 15$ A. Therefore, rotor bar current harmonics are only due to the space harmonics of the MMF, and RSHs are observed in the stator EMF and not in stator currents.

4.4.2 Simulation results and validation with FEA for slip s=0%

4.4.2.1 Airgap flux density

The resulting radial and circumferential flux densities distributions for zero slip are shown in Figure A.4, and the flux lines in the subdomain model are illustrated in Figure A.3a at $t_0 = 0$ s. Then, Figure 4.27 illustrates both components over space and their spatial harmonic content for $t_0 = 0$ s, while Figure 4.28 illustrates the time distribution and harmonic content at $\theta = 0°$ for the radial flux density, and $\theta = 4°$ for the circumferential flux density, where θ is the airgap angle. The angle $\theta = 4°$ is chosen to observe the circumferential flux density in front of a stator slot since the circumferential flux density is always zero in front of a stator tooth, except if there is a rotor bar in front of the stator tooth.

The subdomain model with $N_\lambda = 5$ is in great accordance with transient FEA, while the subdomain model with $N_\lambda = 1$ shows slight discrepancies since rotor-induced currents due to the space harmonics of stator MMF (for $|\lambda > 1|$), and therefore harmonics of rotor MMF, are not computed in the model (see the explanation in Subsection 4.4.2.2 which deals with bar current computation).

The highest peak in radial FFTs is naturally the fundamental of the radial flux density at $(f_s, p) = (50\text{ Hz}, 2)$. Spatial harmonics at $r = \{34;38\} = Z_s \pm p$ are due to stator MMF and slotting harmonics, while spatial harmonics at $r = \{26;30\} = Z_r \pm p$ are due to rotor slotting harmonics, plus MMF harmonics for $N_\lambda = 5$.

Besides, the RSHs can be observed in the flux density harmonic content at the following frequencies [Nandi, 2004]:

$$f_{rsh}^{\kappa\pm} = \left(\kappa \frac{Z_r}{p}(1-s) \pm 1\right) f_s, \quad \kappa \in \mathbb{N} \tag{4.75}$$

The first RSHs are given for $\kappa = 1$ at $f_{rsh}^{1\pm} = \{650\text{ Hz}; 750\text{ Hz}\}$ as shown in Figure 4.28.

4.4.2.2 Rotor bar currents

The rotor bar induced currents are computed by deriving the rotor bar MVP over time t_0 for each λ, as given by Equation (4.41). The time and spatial distribution of rotor bar current for $s = 0\%$ is shown in Figure 4.29a. Figures 4.29b and 4.30a respectively give the spatial current distribution at $t_0 = 0$ s and time waveform in the first rotor bar. Rotor current harmonics are illustrated in Figure 4.30b, and are induced at the frequencies $f_{r,\lambda}$ given by Equation (4.72) in the rotor reference frame. Results given by the SDM with $N_\lambda = 5$ are very close to those obtained with FEA. The fundamental of the rotor current (i.e. for $\lambda = 1$) is null because the relative speed $\omega_{rm,\lambda}$ between the stator MMF fundamental and the rotor is null, which results in $\underline{\alpha}_{j,1} = 0$ (cf. Equation (4.73)). The first rotor current harmonics are at $f_{r,-5} = f_{r,7} = 300$ Hz and are therefore overlapped in the time FFT in Figure 4.30b. Naturally, the SDM with $N_\lambda = 1$ finds null rotor bar currents since $N_\lambda = 1$ means that all the space harmonics of stator MMF have the diffusion coefficient of the rotor current fundamental, i.e. $\underline{\alpha}_{j,1} = 0$.

4.4.2.3 Electromagnetic torque and Electromotive Force (EMF)

The instantaneous electromagnetic torque is computed with the MST method (cf. Equation (A.5)). The instantaneous torque and its FFT over time are shown in Figure 4.31. For $s = 0\%$, the average electromagnetic torque is zero, although a small constant component is present in the FEA, probably due to the fact that numerical steady state

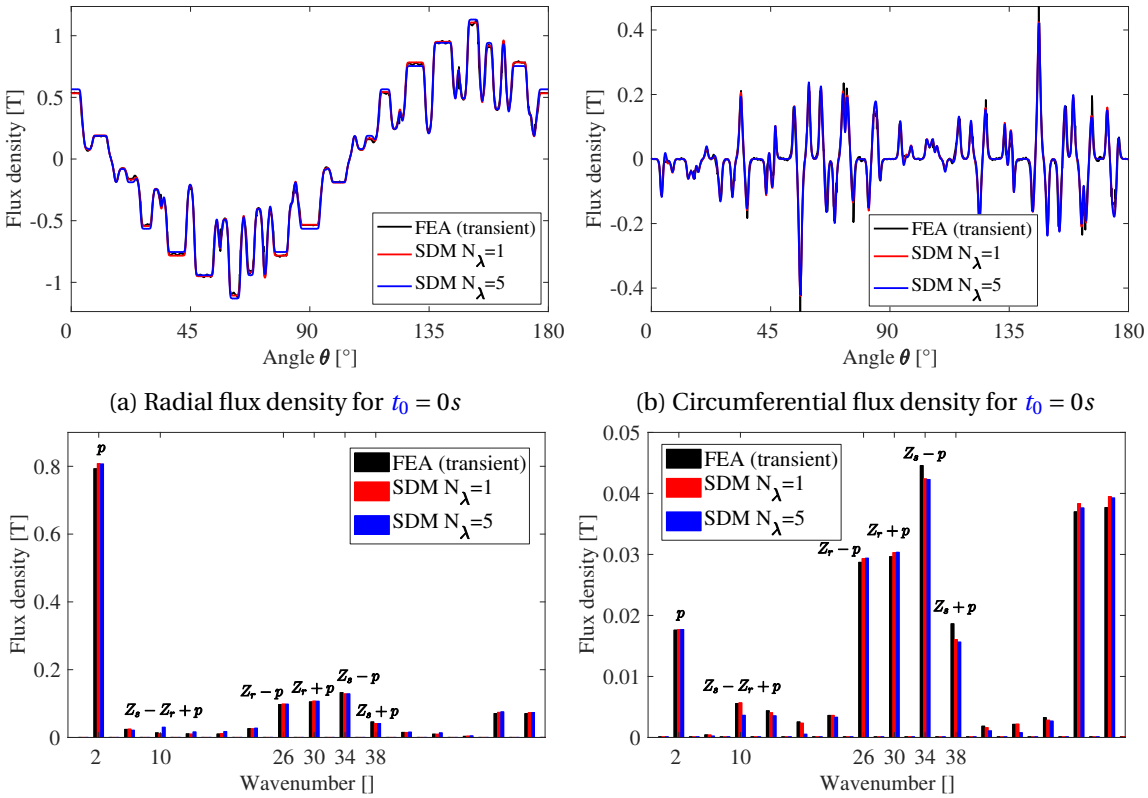

(a) Radial flux density for $t_0 = 0s$

(b) Circumferential flux density for $t_0 = 0s$

(c) Radial FFT over space for $t_0 = 0s$

(d) Circumferential FFT over space for $t_0 = 0s$

Figure 4.27 – Airgap flux density over space and FFT for slip $s = 0\%$.

has not been fully reached. As said in Subsection 1.3.2), a zero average torque means that the average value of the circumferential airgap stress over time and space at $(f, r) = (0\,\text{Hz}, 0)$ is zero. Besides, torque ripple harmonics are in fact pulsating harmonics of circumferential stress given by $(f > 0, r = 0)$. In particular, it can be seen on the FFT that the first and main torque ripple harmonic at 600 Hz is better estimated with $\text{N}_\lambda = 5$ than with $\text{N}_\lambda = 1$. It shows that the rotor current harmonics computed with $\text{N}_\lambda = 5$ do not generate new harmonic content but they modulate both magnitude and phase of the existing harmonics. Using the convolution approach, each harmonic of magnetic stress can be decomposed into a product of two flux density harmonics [Rothe et al., 2010]. In this particular case, the main torque ripple harmonic (600 Hz,0) comes from the combination of two flux density harmonics due to rotor slotting and MMF such as:

$$(600\,\text{Hz}, 0) = \left(\left[\frac{\text{Z}_r}{p}(1-s) \pm 1\right] f_s - f_s, \text{Z}_r - p - (\text{Z}_r + p)\right) \tag{4.76}$$

The EMF is computed from flux linkage by integrating stator slots MVP, as said in Subsection 4.2.2.4. EMF in phase A and its FFT over time are illustrated in Figure 4.32 for $s = 0\%$. Time harmonics induced in the stator windings are due to the RSHs given by Equation (4.75, at $f_{rsh}^{1\pm} = \{650\,\text{Hz}; 750\,\text{Hz}\}$ in the present case. EMF fundamental is well estimated by both SDM with $\text{N}_\lambda = 1$ and $\text{N}_\lambda = 5$, but harmonic content is more accurate with $\text{N}_\lambda = 5$ in terms of magnitude and phase.

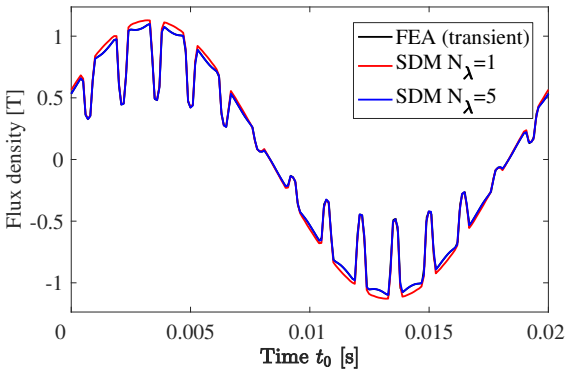

(a) Radial flux density over one stator electrical period for $\theta = 0°$

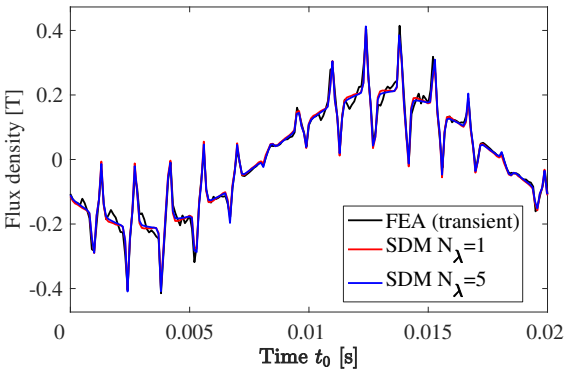

(b) Circumferential flux density over one stator electrical period for $\theta = 4°$

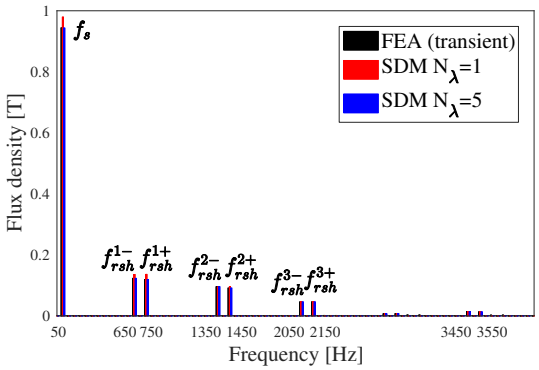

(c) Radial FFT over one mechanical period for $\theta = 0°$

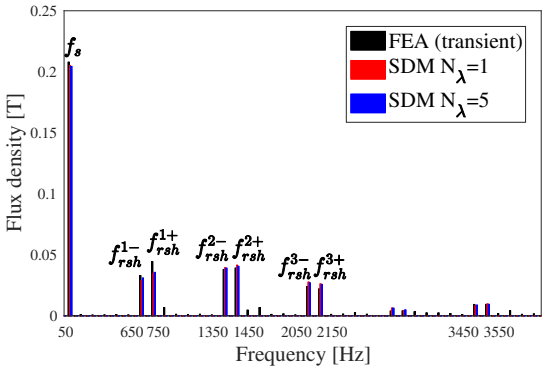

(d) Circumferential FFT over one mechanical period for $\theta = 4°$

Figure 4.28 – Airgap flux density over time and FFT for slip $s = 0\%$.

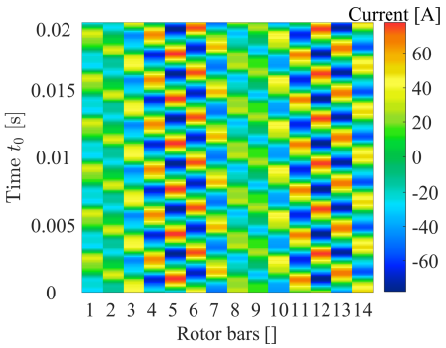

(a) For all rotor bars over a stator electrical period (SDM)

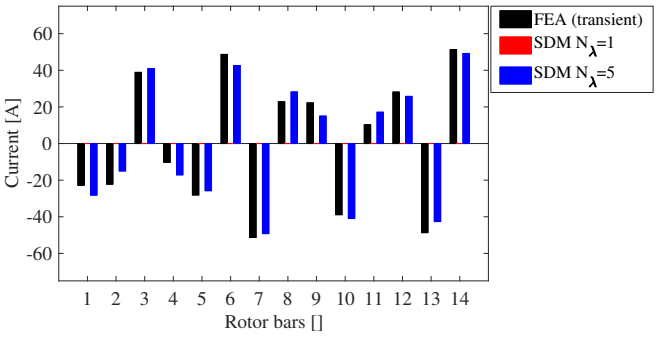

(b) For all rotor bars, at $t_0 = 0s$

Figure 4.29 – Current distribution in rotor bars over time for slip $s = 0\%$.

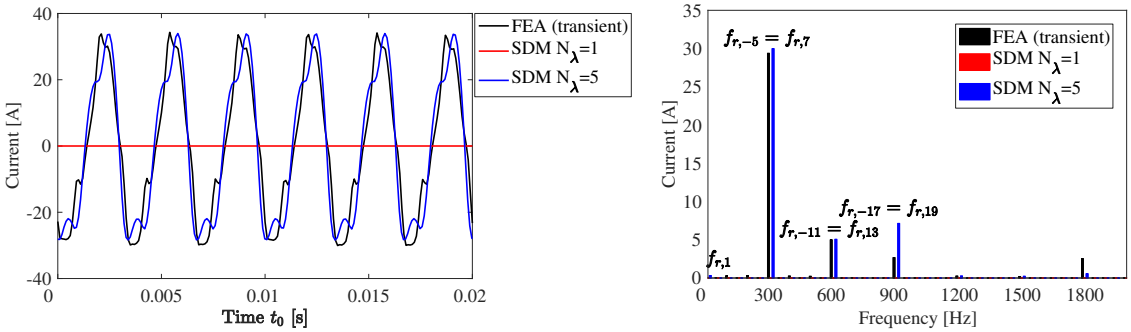

(a) Current versus time over a stator electrical period (b) Current FFT over a mechanical period

Figure 4.30 – Current in the first rotor bar versus time and FFT for slip s = 0%.

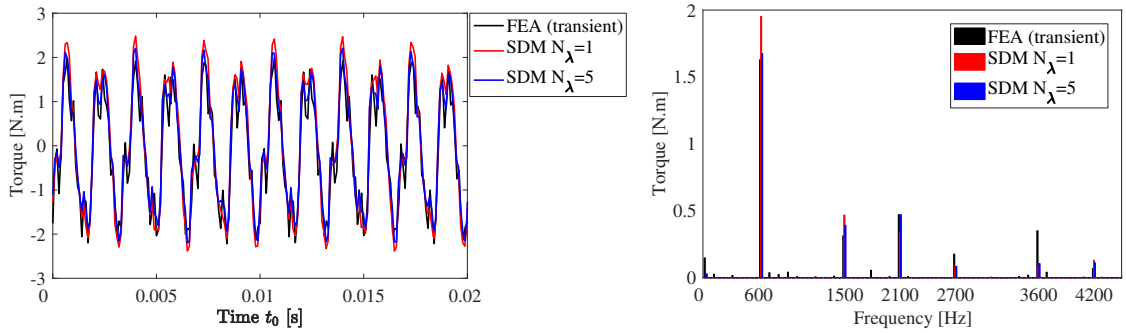

(a) Torque over a stator electrical period (b) FFT over a mechanical period

Figure 4.31 – Electromagnetic torque versus time and FFT for slip s = 0%.

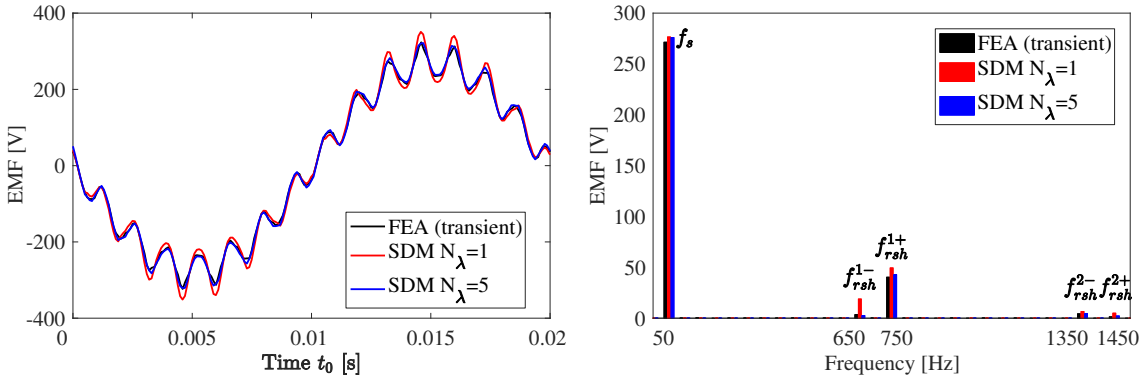

(a) EMF versus time over a stator electrical period (b) FFT over a mechanical period

Figure 4.32 – EMF versus time and FFT for slip s = 0%.

4.4.3 Simulation results and validation with FEA for slip s=10%

4.4.3.1 Airgap flux density

The resulting radial and circumferential flux densities distributions for slip $s = 10\%$ are shown in Figure A.5, and the flux lines in the subdomain model are illustrated in Figure A.3b at $t_0 = 0$ s. Then, Figure 4.33 illustrates both components over space and their spatial harmonic content for $t_0 = 0$ s, while Figure 4.34 illustrates the time distribution and harmonic content at $\theta = 0°$ for the radial flux density, and $\theta = 4°$ for the circumferential flux density.

The air gap flux density has considerably decreased due to the induced rotor MMF which almost cancels the fundamental of the stator MMF for $s = 10\%$. The spatial FFT in Figure 4.33c shows that the harmonic of wavenumber $r = Z_s - (Z_r - p) = 10$ in the radial flux density is wrongly estimated by the SDM with $N_\lambda = 1$. In fact, this harmonic is due to the interaction of the fundamental of stator and rotor MMFs at $r = p$ with the first harmonic of rotor and stator slotting interaction at $r = Z_s - Z_r$. Because of a wrong assumption on the diffusion coefficients for $\lambda = 1, -5, 7, -11$, an error is made on the rotor bar currents computation and consequently on the rotor MMF. This directly affects spatial harmonic $r = 10$ of the flux density and furthermore every magnetic stress harmonic produced by this flux harmonic. Besides, the first RSHs are given for $k = 1$ at $f_{rsh}^{1\pm} = \{580\text{ Hz}; 680\text{ Hz}\}$ as shown in Figure 4.34.

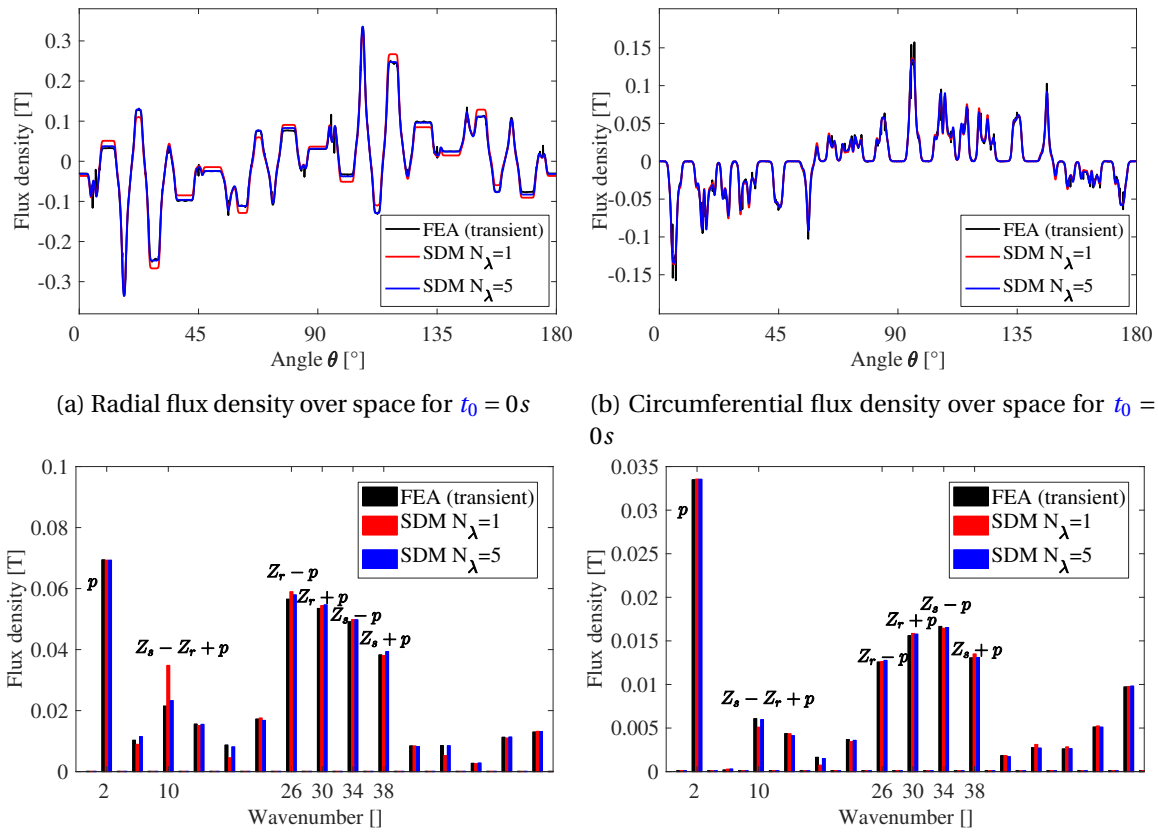

(a) Radial flux density over space for $t_0 = 0s$

(b) Circumferential flux density over space for $t_0 = 0s$

(c) Radial FFT over space for $t_0 = 0s$

(d) Circumferential FFT over space for $t_0 = 0s$

Figure 4.33 – Airgap flux density over space and FFT for slip $s = 10\%$.

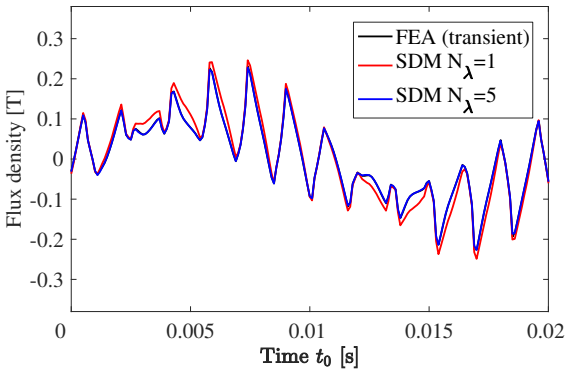

(a) Radial flux density over one stator electrical period for $\theta = 0°$

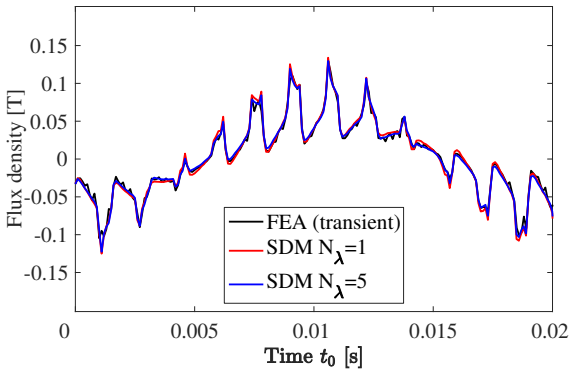

(b) Circumferential flux density over one stator electrical period for $\theta = 4°$

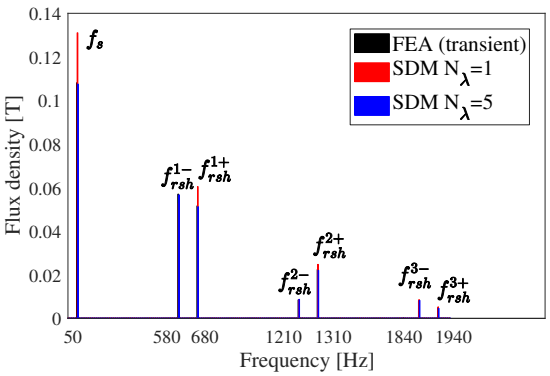

(c) Radial FFT over one rotor electrical period for $\theta = 0°$

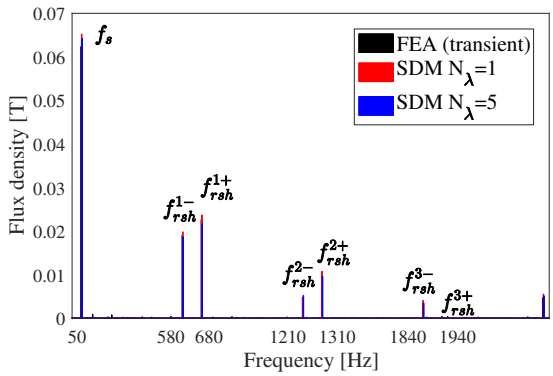

(d) Circumferential FFT over one rotor electrical period for $\theta = 4°$

Figure 4.34 – Time distribution of airgap flux density and FFT for slip $s = 10\%$.

4.4.3.2 Rotor bar currents

The time and spatial distribution of rotor bar current for $s = 10\%$ is shown in Figure 4.35a. Figures 4.35b and 4.36a respectively give the spatial current distribution at $t_0 = 0$ s and time waveform in the first rotor bar. Rotor current harmonics are illustrated in Figure 4.36b. The current fundamental frequency is at $f_{r,1} = sf_s = 5$ Hz and the first rotor current harmonics are at $f_{r,-5} = 275$ Hz and $f_{r,7} = 265$ Hz in the rotor referential. In the stator referential, the frequency of these two rotor current harmonics is the same as the frequency of the first RSHs, for $f_{rsh}^{1\pm} = \{580\text{ Hz}; 680\text{ Hz}\}$. In fact, rotor slotting and rotor MMF produce harmonics with the same frequency and wavenumbers [Joksimović et al., 1999]. From Figure 4.36b, it is shown that the bar current fundamental is accurately estimated by both $N_\lambda = 1$ and $N_\lambda = 5$, but once again the harmonic content is more accurate for the SDM with $N_\lambda = 5$.

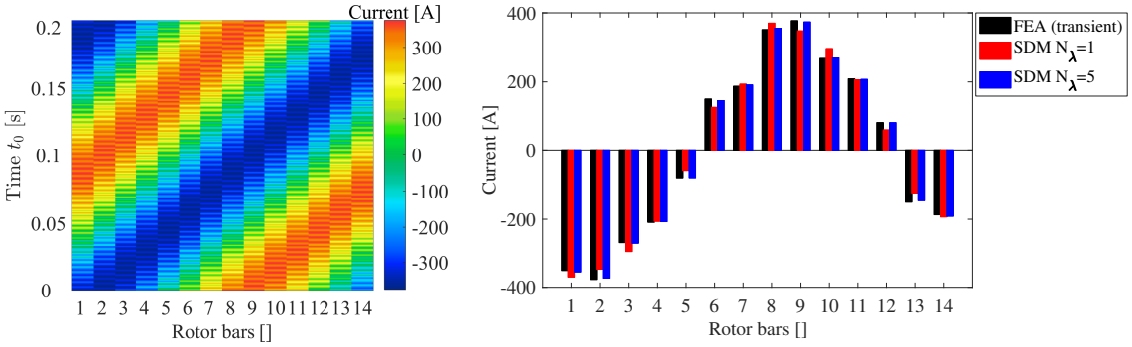

(a) For all rotor bars over one rotor electrical period

(b) For all rotor bars, at $t_0 = 0$

Figure 4.35 – Current distribution in rotor bars over time for slip $s = 10\%$.

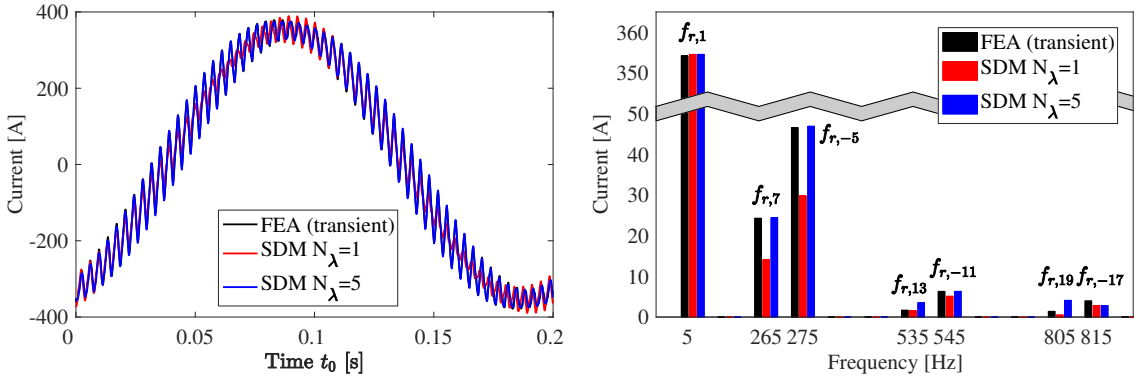

(a) Current over one rotor electrical period

(b) Current FFT over one rotor electrical period

Figure 4.36 – Current versus time in the first rotor bar and FFT for slip $s = 10\%$.

4.4.3.3 Electromagnetic torque and Electromotive Force (EMF)

The instantaneous electromagnetic torque and its FFT over time are shown in Figure 4.37 for $s = 10\%$. The average electromagnetic torque is around 3.5 N.m., and the first torque ripple harmonic is at 530 Hz as given by Equation (4.76) for $s = 10\%$. Contrary to SMs, the presence of both stator and rotor fields does not add new harmonic content in the electromagnetic torque. As in no-load case, torque ripple harmonics due to rotor

MMF harmonics only interfere with torque ripple harmonics due to slotting harmonics. In terms of magnitude, torque ripple harmonics represent around 60% of the average torque, which is quite consequent. This is mainly due to the fact that rotor bars are not skewed to remove the first torque ripple harmonic (cf. Subsection 1.6.3.1).

Besides, the torque versus slip (or speed) curve can be obtained from SDM simulations including parasitic torques due to stator MMF harmonics if their proper diffusion coefficient is accounted for (i.e. $|\lambda| \leq 1 \pm 2q\eta$), as shown in Lubin et al. [2011b].

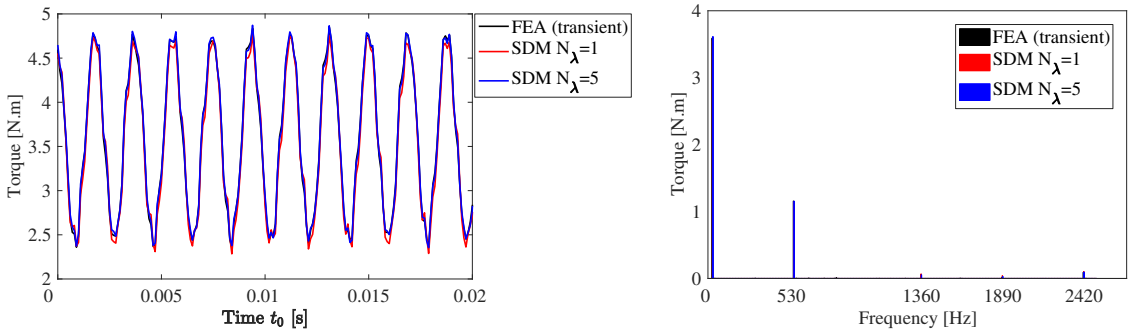

(a) Torque over one stator electrical period

(b) Torque FFT over one rotor electrical period

Figure 4.37 – Electromagnetic torque over time and FFT for slip $s = 10\%$.

EMF in phase A and its FFT over time are illustrated in Figure 4.32 for $s = 10\%$. Time harmonics induced in the stator windings are due to the RSHs given by Equation (4.75), at $f_{rsh}^{1\pm} = \{580\text{ Hz}; 680\text{ Hz}\}$ in the loaded case. The EMF magnitude drops by around 250 V due to the fact that the stator supply is a current source, and the back-EMF created by the rotor currents is in phase opposition with the EMF created by the stator currents.

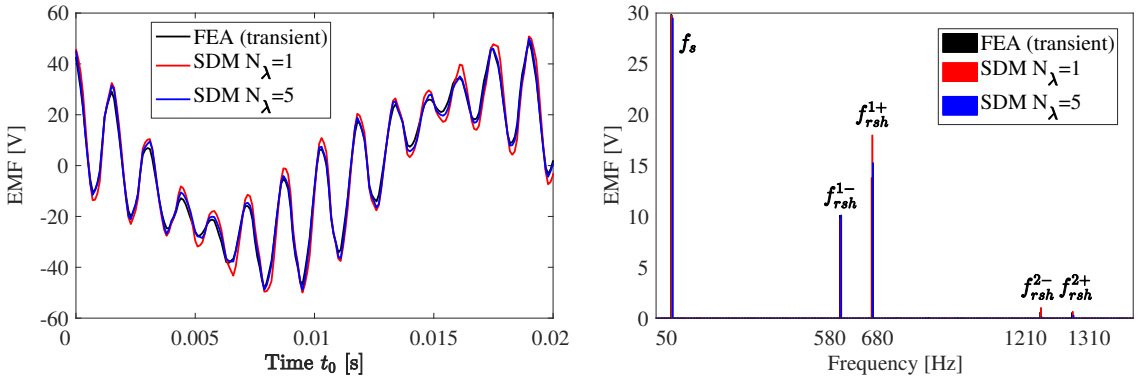

(a) EMF over one stator electrical period

(b) EMF FFT over one rotor electrical period

Figure 4.38 – EMF in Phase A over time and FFT for slip $s = 10\%$.

4.4.4 Discussions

4.4.4.1 On the 2D SDM SCIM models performances in comparison with transient FEA

As shown in Subsections 4.4.2-4.4.3, the SDM with $N_\lambda = 5$ matches perfectly with transient FEA [Ansys, 2018] for the studied machine. It validates the approach of current sheet superposition assuming infinite permeability, and justifies the approximation of

Method	Transient		Steady state		Total	
	$s = 0\%$	$s = 10\%$	$s = 0\%$	$s = 10\%$	$s = 0\%$	$s = 10\%$
Transient FEA	2 h	46 h	40 mn	3 h 20	2 h 40 mn	49 h
SDM ($N_\lambda = 1$)	-	-	10 s	1 mn 40 s	10s	1 mn 40 s
SDM ($N_\lambda = 5$)	-	-	1 mn 30 s	8 mn 20 s	1 mn 30 s	8 mn 20 s

Table 4.4 – Computation time comparison between transient FEA and the two subdomain models with $N_\lambda = 1$ and $N_\lambda = 5$.

constant skin effect for space harmonics higher than the fifth one, i.e. for $|\lambda| \geq 17$. For each electromagnetic quantity, both SDMs with $N_\lambda = 1$ and $N_\lambda = 5$ predict the same harmonic content, as rotor bars and current sheet harmonics rotate at the speed whether $N_\lambda = 1$ or $N_\lambda = 5$. Furthermore, the SDM with $N_\lambda = 5$ systematically gives better results in terms of magnitude and phase, because the proper diffusion coefficient is set in the rotor bars for the main harmonics of stator MMF.

However, using the SDM with $N_\lambda = 5$ increases the computation time by five for $s = 10\%$, as shown in Table 4.4 which compares the overall computation time for transient FEA and the two subdomain models with $N_\lambda = 1$ and $N_\lambda = 5$. Concerning the FE model, most of the computation time is dedicated to achieve the numerical transient and reach steady state, which amounts to around 1200 time steps (0.12 s) at no-load case and 28000 time steps (2.8 s) for the load case. The computation time per time step is around 6 s during the numerical transient, and is a bit longer when recording the steady state due to data storage. Then, an additional and non-negligible amount of time is required to post-processed mesh data, and compute radial and tangential airgap flux densities, and induced current in rotor bars. The total number of triangle elements is 13294, and the airgap is finely meshed to ensure around 40 nodes per tooth and 4 elements along airgap thickness. Of course, periodicity is included to reduce the size of the FE model.

For the SDM, solving the first subdomain model for a given λ and t_0 takes less than 50 ms of computation time in presence of induced currents, and less than 25 ms if no induced currents are computed since the numerical system is real. The computation time for a given t_0 is therefore multiplied by the number of space harmonics N_λ which are simulated separately. Besides, the post-processing time required to compute the electromagnetic quantities from the integration constants, including running the second subdomain model to compute stator phase EMF, is negligible compared with the resolution time in itself, as it lasts only a few seconds for all t_0. Therefore, the developed subdomain model with $N_\lambda = 5$ shows very good performances as it reduces the computation time up to a factor 350 for the load case.

4.4.4.2 On the added value regarding previous 2D SDM SCIM models

As said before, the developed SCIM SDM is inspired from two previous existing subdomain model [Lubin et al., 2011b; Boughrara et al., 2015]. As said in the SDM state of the art (see Subsection 2.3.3.2), the first model developed in Lubin et al. [2011b] enables to compute the airgap flux density accounting for rotor induced currents, but without stator slotting harmonics since stator slots are not represented in the subdomain model. Besides, the airgap flux density in computed in the rotor referential and must be transformed into the stator referential to compute the magnetic stress. Finally, the proper skin effect for each stator MMF harmonic is accounted for using current sheet superposition. In Boughrara et al. [2015], the model (referred here as "Slotted harm.") accounts

for rotor and stator slotting harmonics but only in the space domain since rotor is not moving. Moreover, it does not account at all for the time harmonic content in any of the electromagnetic quantities, in particular in the airgap flux density, and the rotor induced currents are computed for all the stator MMF harmonics at the same time, with the diffusion coefficient of the rotor current fundamental ($\underline{\alpha}_{j,1} = \sqrt{i2\pi\mu_0\sigma_j s f_s}$). Therefore, the added value of the proposed model resides in the computation of rotor bar induced with proper skin effect while including both time and space harmonic contents.

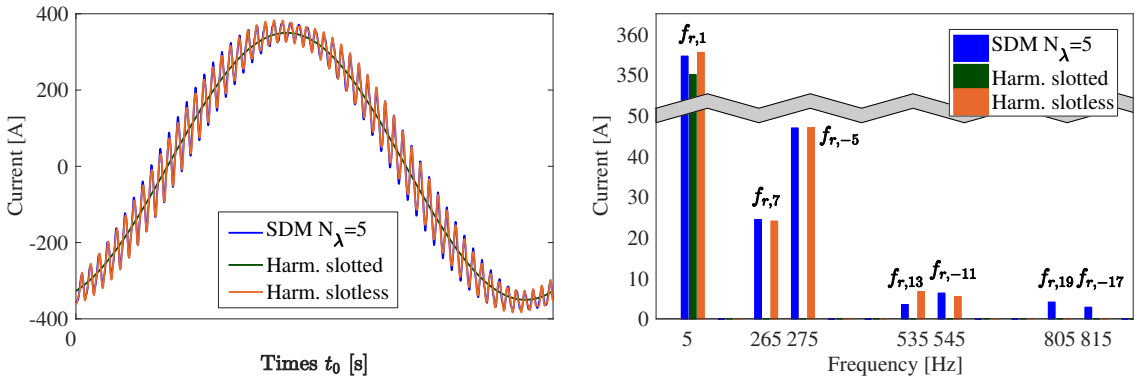

(a) Current over one rotor electrical period

(b) Current FFT over one rotor electrical period

Figure 4.39 – Comparison between two previous models and the proposed model regarding current in the first rotor bar for SCIM $36s28r4p$ at slip $s = 10\%$.

Figure 4.39 illustrated the instantaneous current in the first bar obtained with the developed SDM approach ($N_\lambda = 5$), compared to the two previous approaches, "Harm. slotless" refers to the model implemented from Lubin et al. [2011b], also including five current sheet models, and "Harm. slotted" refers to the model implemented from Boughrara et al. [2015]. First, it can be seen that the current harmonic content is well predicted by "Harm. slotless". The slight difference is due to the non-modeling of stator slots, as stator slotting harmonics are also source of induced currents (in a negligible amount for this topology, cf. Subsection 4.4.4.3). However, since only five current sheets have been considered, the rotor bar current contains five time harmonics and the airgap flux density contains five time and space harmonics. Finally, "Harm. slotted" only gives insight on the rotor current fundamental, which is less accurately estimated. First, the fundamental magnitude depends on the "relative" initial position of the rotor bars regarding stator slots, since rotor is not physically moving. Besides, the rotor current fundamental is induced by all the stator MMF harmonics at once.

4.4.4.3 On the assumption of single pulsation ω_{rm} in rotor bars

In Subsection 3.2.3.2, the Helmholtz problem is solve in rotor bars assuming the presence of a unique pulsation, which has been ensured in the subdomain by taking separately each harmonic of the stator MMF. However, as stator slots are represented in the first subdomain model, they are also source of induced current harmonics in the rotor bars, for the same reasons as stator MMF harmonics, which interfere with the latter. The current in the first bar which is induced only by the stator MMF fundamental (i.e. for $\lambda = 1$) is represented in Figure 4.40. On the time FFT, new current harmonics can be observe for $\lambda = -17$ and $\lambda = 19$, due to the first stator slotting harmonics of wavenumber $Z_s \pm p = \{34, 38\}$. Therefore, the rotor induced currents due to stator slotting harmonics are indeed included in the frequency content, however they are overestimated since

the associated diffusion coefficient is not $\underline{\alpha}_{j,-17}$ and $\underline{\alpha}_{j,19}$, but the diffusion coefficient of the stator MMF $\underline{\alpha}_{j,1}$. Noticing the magnitude ratio between rotor current harmonics induced by stator slotting harmonics and those induced by stator MMF harmonics, this approximation has a very little impact on the overall modeling accuracy.

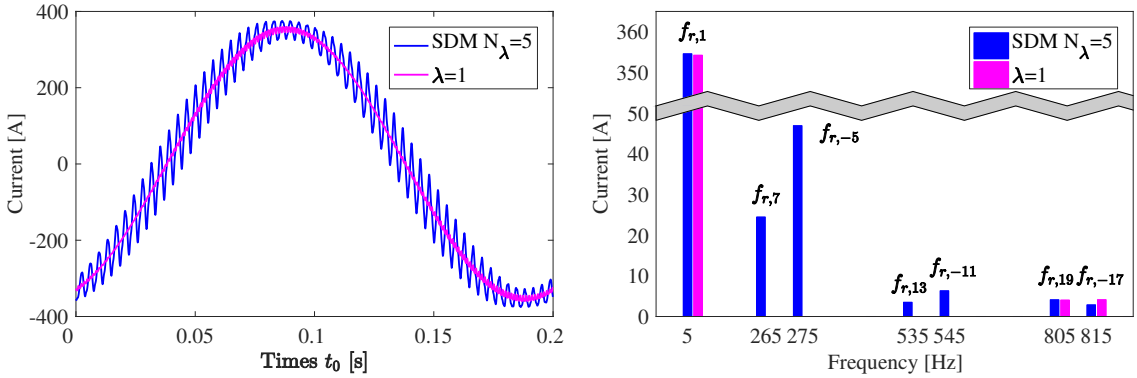

(a) Current over one rotor electrical period

(b) Current FFT over one rotor electrical period

Figure 4.40 – Stator slotting effects on the current fundamental ($\lambda = 1$) in the first rotor bar for SCIM $36s28r4p$ at slip $s = 10\%$. Validation of the single pulsation assumption in rotor bars.

4.4.4.4 On the infinite permeability assumption

The developed SCIM subdomain model is based on infinite permeability assumption in stator and rotor cores, as it is generally assumed in analytical models such as PMMF. However, this assumption is particularly strong in SCIMs, where rotor and stator permeances cannot be systematically neglected compared with airgap permeance. In fact, the airgap length is generally very small in SCIMs, and as the number of poles is generally quite low, the flux lines travel in stator and rotor cores is also much longer. This results in a MMF drop that is not predicted by the present model, but is clearly observable in Figure 4.41 when accounting for finite permeability of stator core ($\mu_{rs} = 2500$) or for magnetic saturation (with the B(H) curve defined in Figure 4.20a). The rotor core is still assumed to be infinitely permeable so as to only quantify the stator permeability impact.

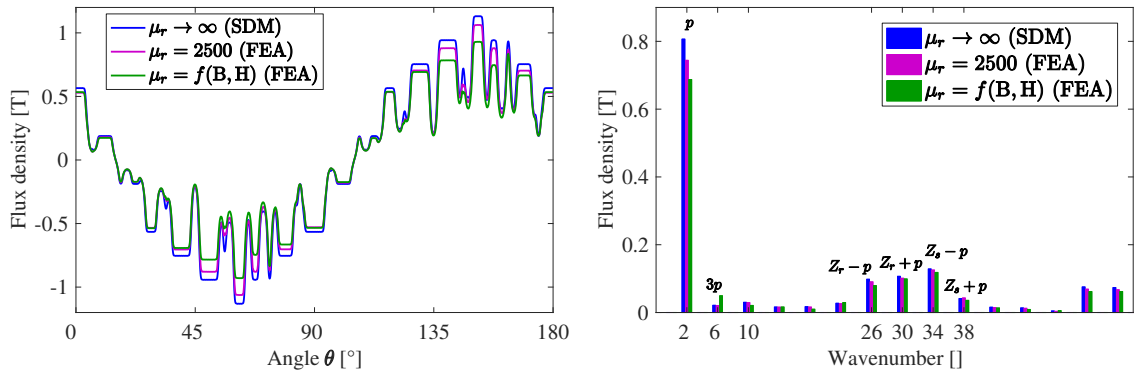

(a) Radial flux density for $t_0 = 0s$

(b) Radial FFT over space for $t_0 = 0s$

Figure 4.41 – Airgap flux density over space and FFT for SCIM $36s28r4p$ at slip $s = 0\%$. Comparison between SDM with infinitely permeable iron, and FEA (MANATEE coupling with FEMM [FEMM, 2018]) for finite permeability and non-linear permeability cases.

However, accounting for finite permeability mainly decreases the flux density fundamental and can be globally including by multiplying the flux obtained with infinite permeability by a saturation permeance factor, such as it is done in PMMF. Besides, the subdomain model accounting for finite permeability developed in this thesis can also be used, but it results in a huge amount of interface conditions to solve between airgap, slots, slot openings, teeth, teeth isthmus etc., hence a much longer model from e-NVH viewpoint. Moreover, the Helmholtz eigenvalue problem in radial direction can be analytically solved, but then the treatment of ICs with adjacent teeth requires to integrate Bessel functions multiplied by sine of logarithm functions, which represents an analytical challenge. Another modeling solution is to compute the induced currents apart with the slotless harmonic model developed in Lubin et al. [2011b], and inject them in a doubly slotted subdomain model to get all of the harmonic content due to rotor motion. Finally, the developed SCIM model is clearly not suitable to account for magnetic saturation as modeled in Subsection 4.3.3.3 since it relies on linear superposition of independent current sheet models.

4.4.5 Conclusion on the relevancy of 2D SCIM subdomain models compared to 1D PMMF model for e-NVH studies

For fast e-NVH simulation of SCIMs, the choice of the magnetic model lies in between the classic 1D PMMF model and the developed 2D subdomain model. For all the SCIMs simulated or tested during this thesis, the PMMF model is always faster and as accurate as the SDM to estimate the harmonic content of the radial Maxwell stress at no-load, and also under load operation providing rotor induced currents can be estimated (for example with an Electric Equivalent Circuit (EEC) or by the harmonic subdomain model developed in Lubin et al. [2011b]). In Devillers et al. [2018a], both SDM and PMMF methods enable to predict the main harmonic content of measured vibrations generated by a SCIM $48s30r4p$ under both load ($s = 5.3\%$) and no-load operations. For load case ($s = 5\%$ is chosen for the simulation, and not 5.3% to prevent from introducing spectral leakage which distorts the real magnitude of stress harmonics), only the rotor current fundamental is included in the PMMF, and is previously computed with an EEC to have a very fast method. This explains the differences between 1D PMMF and 2D transient FEA and SDM (with $N_\lambda = 3$) observed on the radial flux density comparison given in Figure 4.42.

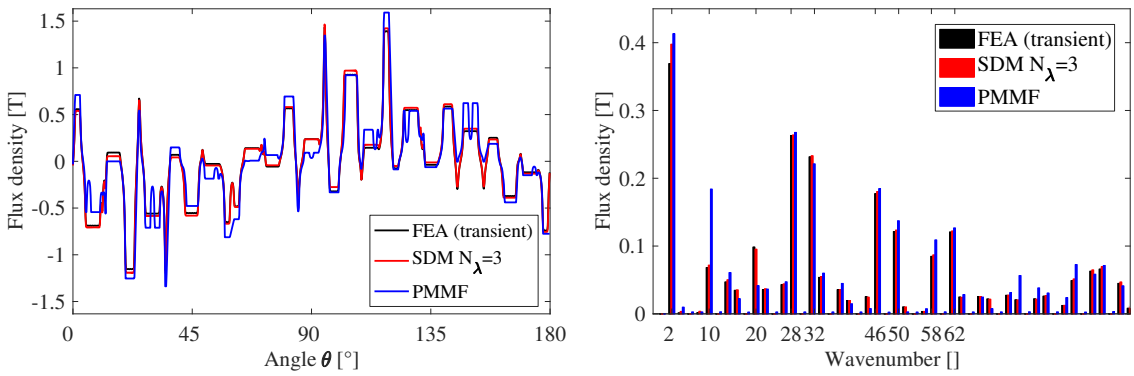

(a) Radial flux density for $t_0 = 0s$

(b) Radial FFT over space for $t_0 = 0s$

Figure 4.42 – Airgap flux density over space and FFT at slip $s = 5\%$. Comparison between 2D transient FEA, 2D SDM, and 1D PMMF for SCIM $48s30r4p$ [Devillers et al., 2018a].

The vibrations spectrum measured for $s = 5.3\%$ is illustrated in Figure 4.43. The air-gap stress harmonics responsible for the main vibration peaks around 610 Hz, 810 Hz and 2230 Hz are well predicted by the three methods. They are due to the RSHs of low wavenumbers ($r = \pm 2$) given by Equation (4.75), especially for $\left(Z_r(1-s)/p-2\right)f_s = 612.5$ Hz, $\left(Z_r(1-s)/p+2\right)f_s = 812.5$ Hz, and $\left(3Z_r(1-s)/p-2\right)f_s = 2237.5$ Hz. Other peaks are not predicted by any of the three methods, especially around 1100 Hz, and could also result from mechanical excitations.

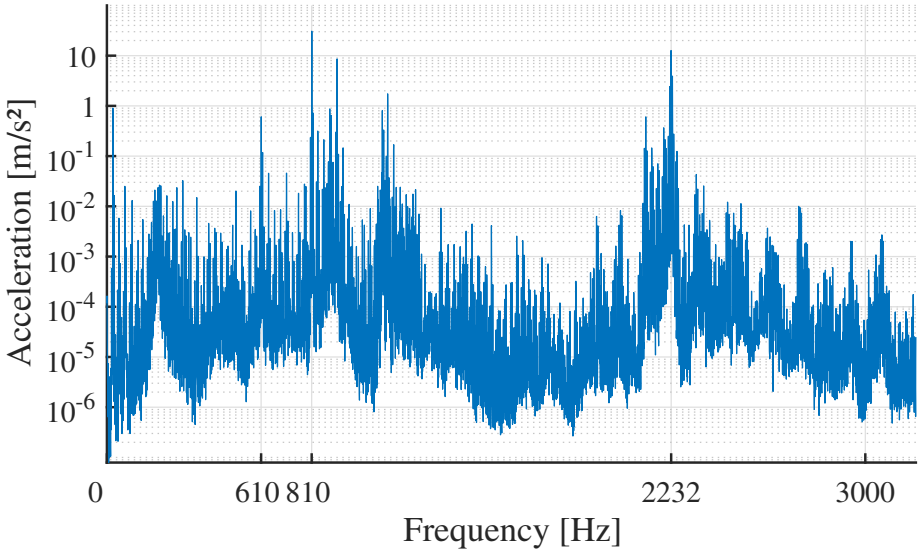

Figure 4.43 – Vibrations spectrum measured for SCIM $48s30r4p$ at $s = 5.3\%$, $f_s = 50$ Hz.

The magnitude of these stress harmonics is compared for the three methods in Table 4.5. The fundamental stress at $(2f_s, 2p) = (100\text{ Hz}, 4)$ is also included in the comparison although it has no effect on the vibration level, since it is strongly damped by the structure at 100 Hz which is far from the natural frequency of the fourth radial mode. The magnitude ratio between the different methods is lesser than 3 dB for all the considered stress harmonics, which validates both analytical approaches for the computation of radial stress harmonics.

Stress harmonic (kf_s, r)	Magnitude $10\log(\sigma_r)$ [dB Re. 1N/m^2]		
	PMMF	SDM	FEA
$(2f_s, 2p) = (100\text{ Hz}, 4)$	47.4	48.3	47.9
$(12.25f_s, 2) = (612.5\text{ Hz}, 2)$	38.8	35.2	37.4
$(16.25f_s, -2) = (812.5\text{ Hz}, -2)$	36.4	36.0	38.0
$(44.75f_s, -2) = (2237.5\text{ Hz}, -2)$	29.3	31.2	30.7

Table 4.5 – Comparison of the main harmonic stress magnitudes computed with 2D transient FEA, 2D SDM, and 1D PMMF, for SCIM $48s30r4p$ at $s = 5\%$, $f_s = 50$ Hz.

Of course, the PMMF cannot estimate the circumferential flux density, and therefore the influence of circumferential flux density on radial stress and the influence of circumferential stress on radial vibrations (see Subsection 2.4.1.1), but the assumption of neglecting circumferential effects in the MST computation may be generally accurate for SCIMs, as it is also shown in Devillers et al. [2017b] for a particular traction SCIM $36s28r6p$ used in railway applications.

4.5 Conclusion

Chapter 4 details the subdomain methodology and extends its capabilities for the modeling of SPMSMs and SCIMs, by accounting for global saturation in stator teeth subdomains, induced currents in rotor bars subdomains and rotor slotting harmonics in airgap and stator slots subdomains. Besides, the main optimization techniques to improve the computational efficiency are investigated and discussed. It is particularly shown that the SDM is very fast for the simulation of single slotted machines (such as SPMSMs), and less computationally efficient for doubly slotted machines (such as SCIMs). For the same granularity level and for all the studied topologies, the SDM is much faster and as accurate or more than FEA and is therefore relevant in fast e-NVH simulations. However, pushing the SDM limits such as it has been done to include global saturation might lead to much longer models and less accurate results compared to non-linear FEA including local saturation. Besides, the SDM does not systematically replace simpler analytical models in terms of computation time versus accuracy, such as for example the 1D PMMF for the e-NVH simulation of SCIMs.

Chapter 5

Design and experimental validation of a test rig for e-NVH study

Contents

5.1 Introduction

5.1.1 Outlines

The comprehensive understanding and modeling of the interaction between magnetic stress harmonics and slotted structures in electrical machines is still subject to several scientific questions, as developed in Chapter 1. In particular, the contribution of circumferential stress to radial vibrations and the resonance condition between stress harmonics and structural modes in slotted structures remain partly investigated and determined yet. Besides, the model choice for each multi-physics aspect among that large variety of existing models is quite complex in order to perform e-NVHs simulations, as shown in Chapter 2. Therefore, the last part of this thesis aims at building an experimental test rig to investigate the remaining scientific challenges, and also to validate and compare the different modeling techniques which already exist or will be developed. Chapter 5 deals with the test rig design and experimental validation, and slightly investigate the remaining challenges.

Section 5.2 focuses on the test rig design to achieve the benchmark purposes, i.e. building a noisy machine which can clearly illustrate the multi-physics complexity of e-NVH studies in electrical machines, regarding the main objectives and constraints given in Subsection 5.1.2. The design methodology follows a reverse engineering process based on the comprehensive understanding of e-NVH generation developed in Chapter 1, which can be applied to determine the best way to make an illustrative noisy machine. First, the vibroacoustics considerations suggest to produce noise by making stress harmonics resonate with structural modes in audible frequencies, in particular radial modes with low spatial orders. Then, the ideal stress harmonic content is deduced, as it must contain harmonics with low wavenumbers and whose electrical frequency can match with the corresponding natural frequency.

The adopted design is a Surface Permanent Magnet Synchronous Machine (SPMSM) with 12 stator slots and 10 poles ($12s10p$), which is first considered in open-circuit conditions (only rotor surface PM excitation) and is driven by another machine. All geometric and materials properties are detailed in Subsection 5.2.1.2. The SPMSM $12s10p$ design results from e-NVH simulations performed on MANATEE software [MANATEE, 2018] using Electromagnetic Vibration Synthesis (EVS) (cf. 5.2.4), based on the Maxwell airgap stress harmonics computed with the SubDomain Method (SDM) (cf. 5.2.2), and radial and circumferential Frequency Response Functions (FRFs) computed with FEA (MANATEE coupling with Altair [2018], see Subsection 5.2.4).

Section 5.3 presents the experimental validation of the test rig design. First, the flux density harmonics generated by the rotor magnetization is measured in the air and compared with 3D FEA. Then, several Experimental Modal Analyses (EMAs) are performed on the stator lamination stack, with different fixation conditions, in particular to observe the impact of endshields and stack pressure on the natural frequencies and modal shapes. Besides, rotor bending modes are also experimentally measured to check if they can potentially introduce dynamic eccentricity at certain frequencies. Finally, the acceleration level and Sound Pressure Level (SPL) are measured with a runup up to 1300 RPM to validate the first resonance between the ovalization mode and a stress harmonic resulting from the combination of flux density harmonics due to stator slotting and rotor MMF. Both acceleration spectrogram and SWL sonagram show that the rotor surface

PMs also excite bending mode, which can be explained by the presence of unbalance magnetization harmonics (as measured in Subsection 5.3.1.1), and likely a dynamic eccentricity.

The simulation models developed in the design process are fitted with the experimental results in Section 5.4, especially to:

— include the real magnetization harmonic content;

— excite the stator bending mode;

— better estimate the FRFs regarding the natural frequency and the damping of both ovalization and bending modes of the stator lamination stack.

The EVS is performed again with corrected stress harmonics and FRFs in Subsection 5.4.3 to get closer results on acceleration spectrogram.

Finally, Section 5.5 deals with the investigation of resonance phenomenon, circumferential effects and slotting modulation effect. First, several Operational Deflection Shapes (ODSs) are performed to observe the stator deflection shape far from resonance, close to resonance, and at the resonance between the ovalization mode and the stress harmonic due to stator slotting and rotor MMF harmonic content (cf. Subsection 5.5.1). Then, the contribution of circumferential stress harmonics to the radial acceleration level is estimated by measuring the radial and circumferential accelerations at tooth tips, and by comparing with the stator yoke radial vibrations in front of the tooth. The measurements are compared with the stator yoke acceleration level obtained from the EVS considering both radial and circumferential stress harmonics, and the EVS considering only radial stress harmonics (cf. Subsection 5.5.2). Finally, the slotting modulation effect is applied on the radial stress harmonic to investigate the impact of spatial aliasing on the SPMSM $12s10p$.

5.1.2 Test rig objectives and design constraints

5.1.2.1 Objectives

On the long term basis, the test rig designed during this thesis aims at building a benchmark project on vibroacoustics of electrical machines to improve the scientific comprehension on the topic, by sharing publicly all data (including design, materials etc.) and deeply discussing the results [Devillers et al., 2018b]. For this purpose (which is obviously larger than the test rig purpose in this thesis), the main objectives are:

1. Show that the main noise and vibration level emitted by the test rig comes from the electromagnetic excitation (see Subsection 5.3.3).
2. Clearly illustrate e-NVH generation process, in particular the contribution of forced and resonant responses, and focusing on the resonance condition (see Subsection 5.5.1).
3. Investigate the remaining scientific challenges in the e-NVH understanding, i.e. (cf. Chapter 1):
   — The contribution of circumferential flux density to radial stress harmonics (see Subsection 5.5.2).
   — The contribution of circumferential stress to radial vibrations (see Subsection 5.5.2).

- The contribution of slotting modulation effect to radial vibrations in presence of spatial aliasing (see Subsection 5.5.3).
- The contribution of magnetostriction to radial vibrations (not studied here).
- The contribution of torque pulsations to acoustic noise (not studied here).

4. Investigate noise and vibrations mitigation techniques (not studied here), which are detailed in Section 1.6:
   - Low-noise design rules, e.g. the GCD rule between teeth number and pole pairs number in PMSMs.
   - Passive techniques: skewing, notching, rewinding, magnetic wedges, etc.
   - Active techniques, in particular the current injection and the compromise between torque generation and stress harmonics which are likely to create noise.
5. Validate electromagnetic and vibroacoustic models and workflows used in e-NVH simulations (cf. Chapter 2), including:
   - The EVS using analytical, semi-analytical and numerical methods for each physical module (only SDM, analytical and numerical FRFs are studied in Sections 5.2 and 5.4).
   - A full numerical analysis to include as many physical aspects as possible (not studied here).
   - The coupling between the different physical modules, in particular the computation and the projection of Maxwell stress harmonics on a slotted structure (not studied here).
6. Develop and extend fast and accurate models from the experimental investigations to improve the e-NVH estimation at every design stage, implemented in MANATEE and Pyleecan [Pyleecan, 2018], which stands for "Python Library for Electrical Engineering Computational Analysis". Pyleecan is an open and non-commercial project launched in 2018 and initiated by EOMYS to gather, unify and coordinate current and future open-source initiatives in electrical machines and drives software development [Bonneel et al., 2018].
7. Produce simulation and experimental results in a normalized format that can be largely shared and reused by others for future research.

5.1.2.2 Design constraints

The main design constraint imposed to the test rig electrical machine is the ability to magnetically excite several modes of the external structure in the audible frequencies. The different modes should occur at distant natural frequencies so that each resonance phenomenon can be clearly isolated and identified. Following the same illustrative constraint, the machine topology is intentionally simplified to only tackle the intrinsic complexity of the interaction between stress harmonics and slotted structures. It should be easier to study circumferential and modulation effects if the magnetic stress harmonic content is finite, discrete, sparse and unambiguously identifiable.

Then, the setup of measurement sensors imposes a size constraint on the slots and the airgap. The slots must be sufficiently deep and large to place accelerometers on the teeth sides to measure the acceleration in both radial and circumferential directions.

This constraint agrees with the objective of observing circumferential effects, as long teeth should emphasize the yoke displacement due to the tooth bending induced by circumferential stress harmonics. Likewise, assuming large slots naturally limits the maximum number of slots hence increases the risk of spatial aliasing for a given number of poles. Besides, the airgap has to be large enough to insert a flux sensor and measure the time and space distribution of the airgap flux density. The airgap flux density measurement aims at estimating the stress harmonic content. The larger is the air gap, the more stress harmonics with high wavenumbers are filtered, but the lower is the magnitude of circumferential forces applying on teeth.

Finally, the chosen design must comply with the assumptions of the (semi-)analytical magnetic and vibroacoustic models used in the EVS and presented Chapter 2, in particular:

— The SDM for electromagnetic field computation, which implies polar geometry and magnetic linearity of ferromagnetic parts.

— The analytical computation of acoustic radiation factor of the stator structure, assuming cylindrical shape.

Concerning the structural modeling, investigating the interaction between Maxwell stress harmonics and slotted structures is obviously contradictory with validating the structural models based on slotless equivalent cylinders (see Subsection 2.4.2.2), and the radial and circumferential FRFs are computed using structural FEA.

5.1.3 Contributions

The main originality of Chapter 5 is the design of a particular noisy machine especially to illustrate and investigate the interaction between stress harmonics and slotted structures, in order to create a benchmark project dedicated to the validation and comparison of e-NVHs models. A second contribution consists in illustrating the ODS of the stator yoke in both forced and resonant responses, and shows the non-linear behavior of the stator structure at resonance, as it follows the modal shape and not the excitation waveform anymore. A third contribution is the coupled experimental and simulation to illustrate and investigate both circumferential effects and slotting modulation effect on noise and vibration emission. A last contribution is the design and manufacturing of an airgap flux sensor to measure the radial airgap flux density distribution and estimate the harmonic content of Maxwell stress.

5.2 Test rig design

5.2.1 Discussions on the test rig design

5.2.1.1 Choice of the topology for the machine prototype

From Section 1.4, the prototype should generate noise and vibrations due to the excitation of low-order structural modes, in order to increase the vibration level and have the lowest values of natural frequencies. The breathing mode associated to the circumferential order $m = 0$ is generally at high frequency and is not very interesting for the study of circumferential effects, since it cannot be excited by tooth bending motion due to circumferential stress harmonics. The bending mode associated to the circumferential order $m = 1$ can be excited in presence of Unbalanced Magnetic Pull (UMP), i.e

stress harmonics with wavenumber $r = 1$ induced by eccentricity, irregular magnetization, fractional winding etc. (cf. Section 1.2.2). However, exciting the bending mode should be avoided for the prototype because it creates mechanical eccentricity and lots of parasitic forces. In fact, the ovalization mode associated to the circumferential order $m = 2$ has the lowest natural frequency and is the easiest one to be excited for the benchmark purposes. Besides, its naturally frequency can be adjusted in the audible range by setting properly the stator dimensions.

Consequently, the aim is to find a topology which produces airgap stress harmonics of wavenumber $r = 2$ to excite the ovalization mode. The stress harmonics are created by the interaction of rotating magnetic field waves, as shown in Subsection 1.3. From the quadratic relationship (1.12), a stress harmonic of wavenumber $r = 2$ is obtained from the combination of two flux density harmonics whose wavenumber differ by two. This implies that the flux density spectrum is actually not sparse in the spatial domain since either each harmonic with odd wavenumber or each harmonic with even wavenumber potentially exists in the spatial harmonic content. Besides, force harmonics with odd wavenumbers only exist if there are both even and odd wavenumbers in the flux density spectrum. Therefore, the flux density spectrum should exclusively contain either even or odd wavenumbers to avoid exciting odd orders of structural mode, in particular $m = 1$.

The first decision consists in choosing between synchronous or induction machines. In induction machines, the mechanical slip generates asynchronous harmonics which coexists with synchronous ones and causes spectral leakage (cf. Subsection 2.2.4.2), except for particular values of slip. Besides, there are naturally more harmonics in induction machines than synchronous machines at variable speed due to RSHs and local saturation. Due to these drawbacks, induction machines are eliminated from the available topologies.

Therefore, the designed machine is a SM, and the next decision consists in choosing the rotor topology between surface PM, interior PM, wound, synchro-reluctant, and switched-reluctant rotor topologies. The main advantage of PM and wound rotors compared with synchro- and switched-reluctant topologies is the ability to excite the stator only with the rotor field, hence mechanically separate the magnetic excitation from the excited structure. Besides, it does not require PWM to generate a rotating field at variable frequency, which would add many airgap stress harmonics. This is also why a simple slotted stator with windings is not considered. However, the PMs rotor has to be driven by an external motor, which increases the cost and the technical complexity of the test rig, since the driving machine must be vibroacoustically isolated from the studied machine to prevent from any perturbations on measurements.

The surface PM rotor topology is finally retained as it is free from rotor slotting and saturation effects under open-circuit condition, which is not the case of interior PM and wound rotors. The main drawback of the surface PMs is the difficulty to avoid eccentricity due to imperfect PM sticking. Besides, the additional harmonic content in case of unbalance magnetization between the different PMs are directly transmitted to the harmonic content of the airgap flux density, i.e. not smoothed by rotor lamination as it is the case for interior PMs rotors.

Finally, the choice of the number of pole pairs p and stator slots Z_s of the SPMSM remains to produce stress harmonics of wavenumber $r = 2$ and excite the ovalization mode. In SPMSMs at no-load, the lowest non-zero wavenumber r_{min} is given by the

well-known Great Common Divisor (GCD) rule:

$$r_{min} = \text{gcd}(Z_s, 2p) = 2 \tag{5.1}$$

If Z_s is even and $p = 1$, $r_{min} = 2$ so the condition is fulfilled. However, it disagrees with the constraint of choosing a close number of poles and stator teeth in order to study spatial aliasing due to slotting modulation effect. Besides, increasing the number of poles enables to reduce the rotating speed of the driving machine and therefore the mechanical tolerances of the test bench. The SPMSM $12s10p$ topology is finally retained because it is used in the automotive sector and is known to be particularly noisy. Other topologies such as $6s4p$ or $12s14p$ could also be considered.

5.2.1.2 Final specifications of the designed SPMSM $12s10p$

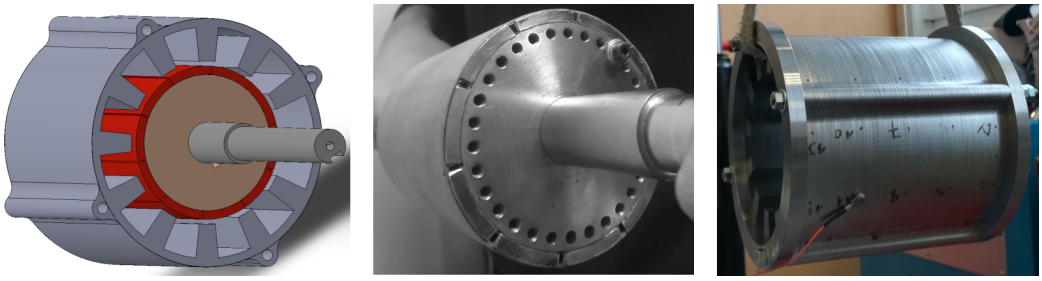

Figure 5.1 – Surface PM rotor and stator lamination stack.

The designed SPMSM $12s10p$ is illustrated in Figure 5.1. The geometrical and material properties are listed in Table 5.1. The geometry is polar, i.e. either composed of radial or circular edges to comply with the SDM assumption. The stator lamination stack is pressurized by four bolts which enable to vary the elastic Young modulus in the axial direction. The external surface of the stator lamination stack is therefore quasi cylindrical, which enables to observe cylindrical structural modes and comply with the acoustic model assumption. The stator slot width is 18°, i.e. around 1.5 cm to put accelerometers on stator teeth side, and the airgap length is 3 mm which is large enough to put the airgap sensor at stator bore radius (see Subsection 5.2.1.4 for the instrumentation setup). The rotor is balanced up to 5000 RPM, which is hence the maximum rotation speed, and is obviously sufficient to ensure that at least one stress harmonic of wavenumber $r = 2$ can excite the ovalization mode.

5.2.1.3 Choice of the frame, driving machine and coupling

The test bench including the SPMSM $12s10p$, the frame and the driving machine is illustrated in Figure 5.2. The aim is to design an experimental test rig which is robust to shaft eccentricity and misalignment between the two machines, and to vibrationally isolate the studied SPMSM from the driving machine. The driving machine is a DC machine for the easy variable speed command which only requires a programmable DC voltage supply. The DC machine can reach 3300 RPM without load, and 3000 RPM with a 10 N.m load. Therefore, this driving machine cannot reach the SPMSM maximum speed, but a runup to 3300 RPM is already enough to validate the SPMSM design, which is the main objective of Chapter 5. Another driving machine will be chosen once the SPMSM design is validated.

Parameter	Symbol	Value
Number of poles	p	10
Number of stator teeth	Z_s	12
Air gap length	g	2.5 [mm]
Rotation speed	N	0-5000 [RPM]
Stator lamination		M400 – 50A
Stator bore radius	R_s	48 [mm]
Stator yoke height	H_{sy}	5 [mm]
Stator tooth length	H_{tooth}	20 [mm]
Stator outer radius	R_{sy}	73 [mm]
Stator stack length	L_s	140 [mm]
Stator slot width	W_s	18 [°]
Permanent magnet		NdFeB(N42)
Remanent flux density	B_{rem}	1.28 [T]
Magnetic relative permeability	μ_{rm}	1.05
Magnetization direction		parallel
Maximum temperature	T_{max}	120 [°C]
Magnet width	W_m	36 [°]
Magnet top radius	R_m	45 [mm]
Magnet height	H_m	5 [mm]
Magnet length	L_m	70 [mm]
Magnet sleeve height		0.5 [mm]
Rotor steel		C22(XC18)
Rotor bore radius	R_r	40 [mm]
Rotor shaft radius	R_{ry}	20 [mm]
Rotor length	L_r	140 [mm]

Table 5.1 – Benchmark prototype parameters.

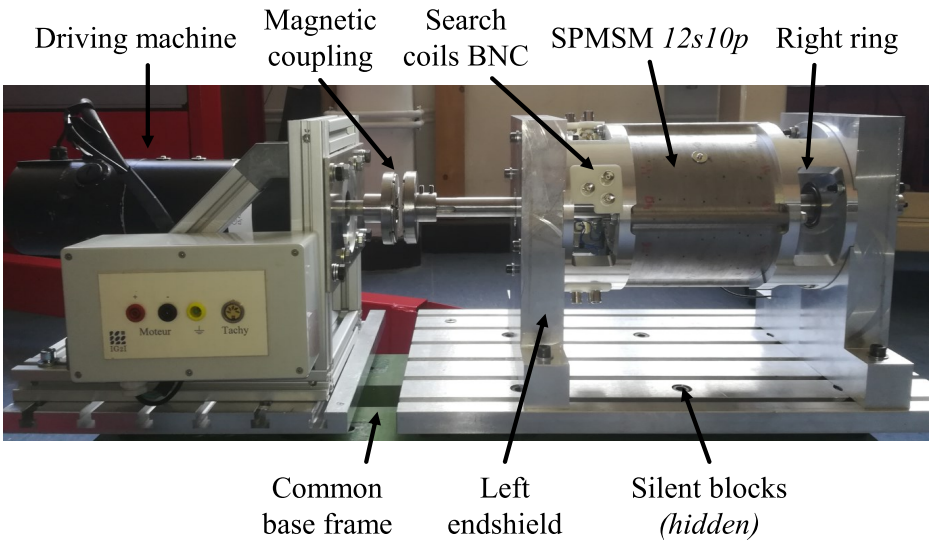

Figure 5.2 – Design test rig with the SPMSM $12s10p$ on the right and the driving machine on the left. Both are coupled with a radial flux magnetic coupling.

Concerning the frame of the SPMSM $12s10p$, the four bolts which pressurizes the stator lamination stack are screwed on two lateral rings, which are screwed to vertical endshields. Lateral rings and endshields are in aluminum to prevent from increasing leakage flux and from vibrating due to Maxwell stress. The lateral rings have holes to enable the passing of instruments wiring, e.g. for accelerometers, search coils etc. The stator lamination stack can be easily dismounted which enables to study different types of stator stacks, in particular impregnated stacks.

The SPMSM $12s10p$ and the driving machine are screwed on two independent T-slot tables, which are screwed on a common base frame using silent blocks to reduce the vibration transmission through the base frame. The T-slot tables are orthogonal to set the alignment of both machines in the two directions of the base frame plane. The third direction (vertical direction) can be also adjusted since the driving machine is mounted on a vertical rail in aluminum profile. Both machines can be coupled with a mechanical coupling (see Figure 5.26a) or a magnetic coupling (as shown in Figure 5.2) to limit the transmission of torque ripple and axial force ripple, and also limit the effect of shaft eccentricity. However, the magnetic coupling decreases the maximum transmitted torque and creates a constant axial force between both shaft which solicit the silent blocks and bend the driving machine. It also stresses the bearings in the axial direction and requires the use of conical bearings. Therefore, the measurements presented in the following are performed with the mechanical coupling, even if rotor vibrations of the driving machine may be directly transmitted to the surface PM rotor.

5.2.1.4 Instrumentation setup

The external surface of the stator yoke is entirely accessible to put accelerometers and measure both modal shapes and ODSs. The stator slots are sufficiently wide to stuck tri-axes accelerometers on teeth side (see Figure 5.31a) in order to measure radial and circumferential accelerations at tooth tips. The axial acceleration is negligible in theory since the SPMSM topology does not feature 3D effects such as skewing.

Besides, a search coil is wound around each tooth to measure the average flux per tooth. Each search coil is wired to a BNC plug placed in blocks of three in the left lateral ring (see Figure 5.2). Furthermore, the air gap measures 2.5 mm in order to setup the air gap flux density sensor on stator bore radius, which is a flexible electronic circuit illustrated in Figure 5.3a. The electronic circuit is composed of 120 independent coils separated of 0.2 mm, and is 0.15 mm thick. The airgap flux density measurement principle is described in Figure 5.3b. The objective is to simultaneously measure the induced voltage in each coil seeing the surface PMs rotating, and to obtain the local flux density value by integrating the voltage measurement over time.

The main difficulty is to simultaneously measure the 120 voltages, and to ensure that the airgap flux sensor is correctly disposed in the airgap, e.g. to avoid any eccentricity which could invalidate the flux density measurement. Besides, the number of coils sets the spatial resolution of the flux density measurement, and has been chosen thanks to electromagnetic simulations using the SDM. The expected flux density measurement is illustrated in Figure 5.4. Shannon sampling theorem gives an accuracy up to the 60^{th} wavenumber but some discrepancies can be observed from the 30^{th} wavenumber.

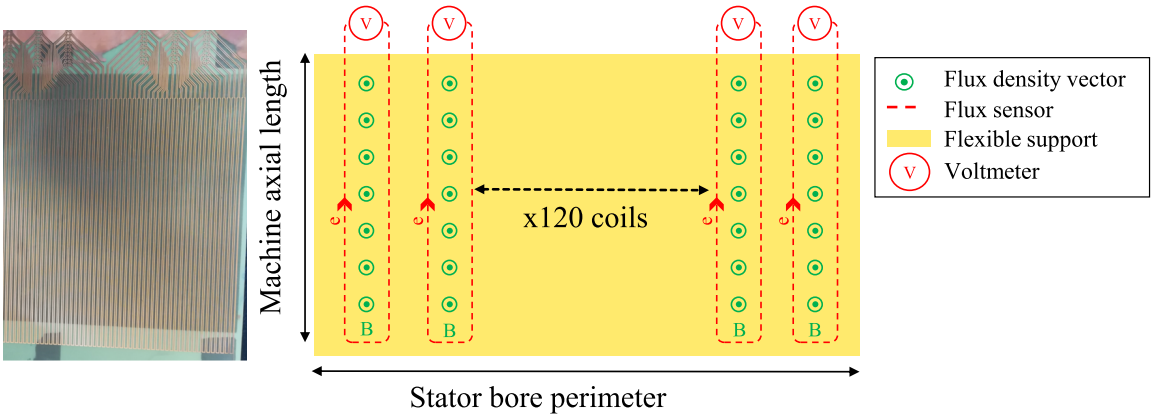

(a) Prototype (b) Airgap flux sensor principle

Figure 5.3 – Airgap flux sensor principle and prototype in flexible electronic circuit.

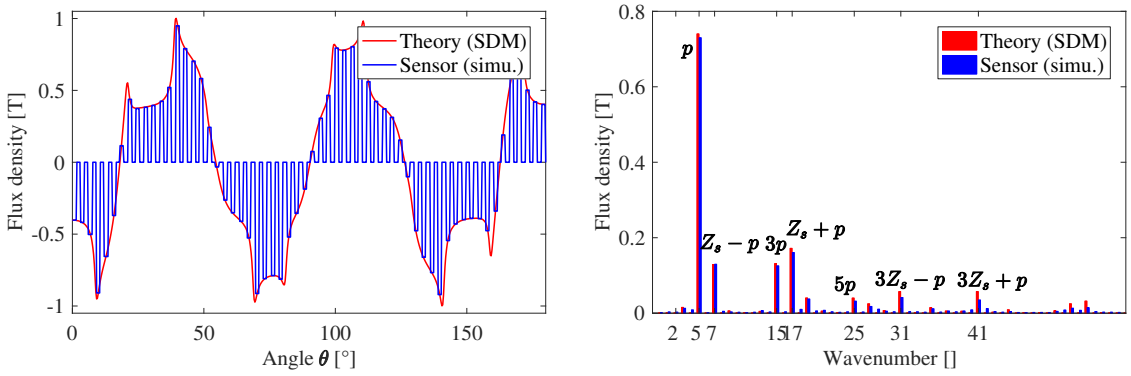

(a) Airgap flux density over space (b) Airgap flux density FFT over space

Figure 5.4 – Comparison between airgap flux density obtained from SDM and the airgap sensor simulation at stator bore radius ($r = R_s$).

5.2.2 Electromagnetic simulation of SPMSM $12s10p$

5.2.2.1 Airgap flux density harmonic content

The flux density is computed using the SDM including ferromagnetic parts with linear finite permeability, as developed in 4.3. The parameters of the rotor exciting magnetization are ideal and given in Table 5.1. The 2D harmonic content of the airgap flux density is illustrated in Figure 5.5. The fundamental flux density is colored in red at (f_s, $p = 5$). The harmonics colored in blue at (f_s, $Z_s \pm p = \{-7, 17\}$) are the first stator slotting harmonics and the harmonics colored in black are harmonics of rotor MMF at ($3f_s$, $3p = 15$) and ($5f_s$, $5p = 25$). It can be noticed that the 2D harmonic content of both radial and circumferential stress are exactly the same in terms of electrical orders and wavenumbers, as said in Section 1.2. Concerning the constraint on wavenumbers to generate stress harmonics of wavenumber $r = \pm 2$, all the flux density wavenumbers are odd and it can be easily seen that the constraint is fulfilled. As a recall, the sign before the wavenumber indicates the rotating direction of the flux density/stress wave. Both stress harmonics with wavenumber $r = \pm 2$ can resonate with the ovalization mode of circumferential order $m = 2$.

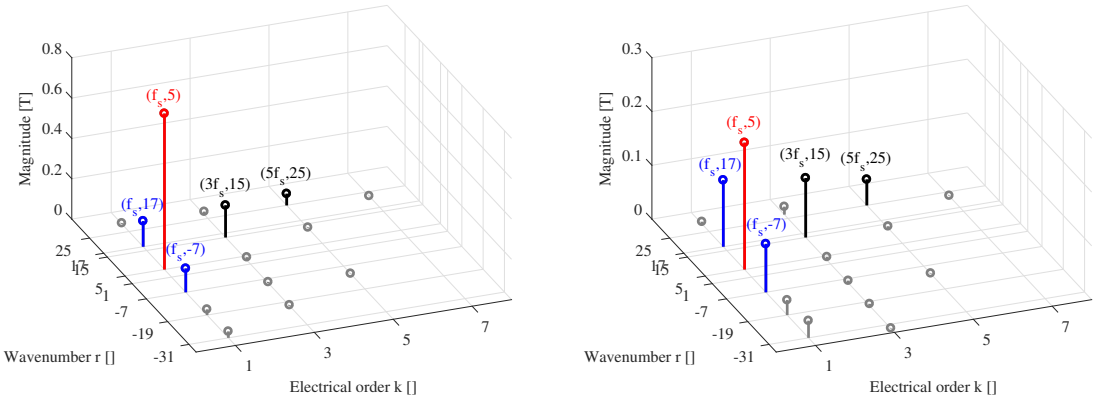

(a) 2D FFT of radial flux

(b) 2D FFT of circumferential flux

Figure 5.5 – Time and space harmonic content of radial and circumferential airgap flux densities for the SPMSM $12s10p$ under open-circuit condition (only rotor MMF).

5.2.2.2 Airgap stress harmonic content

The airgap stress is computed using the 2D MST in the middle of the airgap (cf. Subsection 2.4.1.1). The 2D harmonic content of radial and circumferential airgap stress distributions are illustrated in Figure 5.6. As for the flux density, a strong similarity is observed between the harmonic content of both components. The main difference is the presence of a constant component (i.e at ($k = 0$, $r = 0$)) in the radial stress, while there is no constant circumferential stress since the SPMSM is considered in open-circuit condition, and therefore average torque is null. Even with considering only rotor MMF and stator slotting harmonics, the airgap stress spectrum contains already 17 harmonics whose wavenumbers are lower than $|r| = 10$.

The highest magnitude stress harmonic of wavenumber $r = \pm 2$ is at $f = 2f_s$. This stress harmonic ($2f_s$, -2) mainly results from the combination of the fundamental of radial flux density (f_s, 5) and the first stator slotting harmonic (f_s, -7). However, this

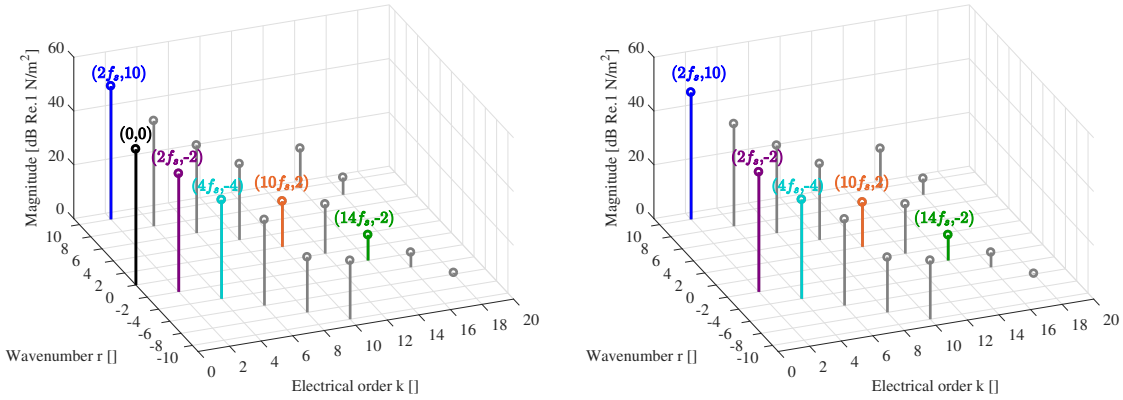

(a) 2D FFT of radial stress

(b) 2D FFT of circumferential stress

Figure 5.6 – Time and space harmonic content of radial and circumferential airgap stress for the SPMSM $12s10p$ under open-circuit condition (only rotor MMF).

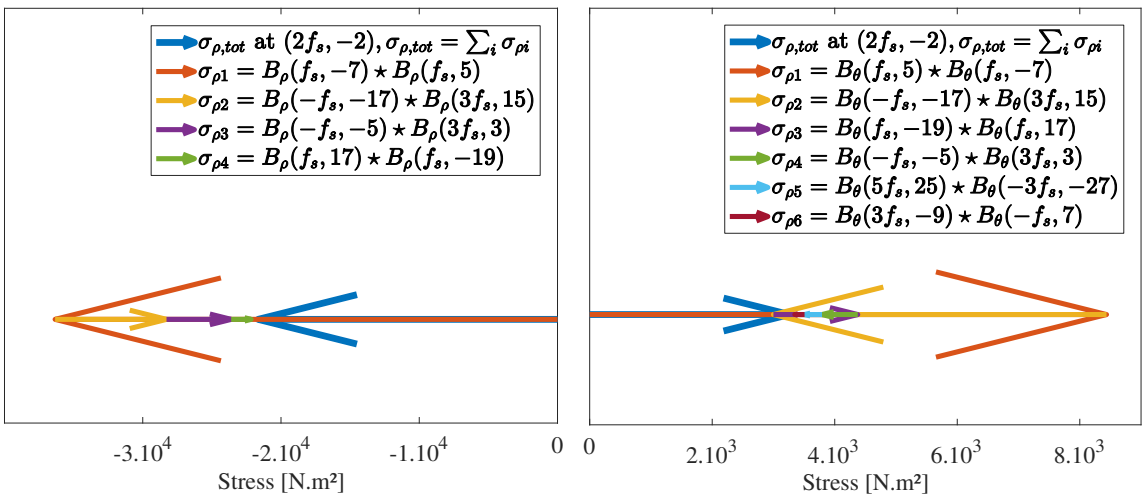

(a) B_ρ^2 radial stress combinations

(b) B_θ^2 radial stress combinations

Figure 5.7 – Decomposition of stress harmonic ($2f_s$, -2) into the combination of radial and flux density harmonics using the convolution approach.

stress harmonics also results from other couples of radial and circumferential flux density harmonics, which can be found using the convolution approach implemented in MANATEE during this thesis (see Appendix A.9 for further details on the convolution approach). The main combinations of radial and circumferential flux density harmonics obtained with the convolution approach are illustrated in Figure 5.7. In fact, the couple (f_s, 5)$\star$(f_s, -7) of radial flux density harmonics is almost twice larger than the magnitude of the stress harmonic ($2f_s$, -2), and is damped by the other contributions. By looking at all the existing combinations for a single stress harmonic, it may be ineffective to target only a few flux density harmonics (for example a particular magnetization harmonic) to mitigate e-NVH. In the present SPMSM case, a global PM shape optimization could be preferred to reduce the impact of the noisy stress harmonics.

Besides, the convolution approach is more relevant in load condition since both rotor and stator flux densities combine themselves, and the vector plot in Figure 5.7 gives insight on the magnitude and also the phase of each flux density couple. In open-circuit case, every phase is either 0 for constructive interaction or 180° for destructive interaction since rotor magnetization is ideal (parallel) and all the rotor MMF harmonics are in phase or in phase opposition (cf. the parallel magnetization pattern illustrated in Figure 3.17).

Furthermore, the second stress harmonic of interest is at ($10f_s$, 2) and is mainly due to the interaction of the 11^{th} harmonic of rotor MMF at ($11f_s$, $11p$) with the 4^{th} harmonic of stator slots at (f_s, $4Z_s + p$). The third stress harmonic of interest is at ($14f_s$, -2) and is mainly due to the interaction of the 15^{th} harmonic of rotor MMF at ($15f_s$, $15p$) with the 6^{th} harmonic of stator slots at (f_s, $6Z_s + p$). Finally, the main stress harmonic of wavenumber $r = -4$ at $f = 4f_s$ is mainly due to the combination of the 5^{th} harmonic of rotor MMF at ($5f_s$, $5p$) with the 2^{th} harmonic of stator slots at (f_s, $2Z_s + p$).

The magnitude of the stress harmonic at ($10f_s$, 2) is one hundred times lower than the main harmonic at ($2f_s$, -2) but it is enough to resonate with the ovalization mode, as shown in the following by simulations and experiments. Besides, as its frequency is five times higher, the rotor speed required to match with the natural frequency of the ovalization mode is five times lower. The rotation speed N at which the resonance with the ovalization mode occurs is given by:

$$\mathrm{N} = \frac{60 f_{20}}{kp} = \frac{12 f_{20}}{k} \tag{5.2}$$

where k is the electrical order of the stress harmonic (either $k = 2$, $k = 10$ or $k = 14$ here) and f_{20} is the natural frequency of the ovalization mode (of circumferential order $m = 2$). Therefore, the resonance with the stress harmonics at ($2f_s$, -2), ($10f_s$, 2) and ($14f_s$, -2) respectively occurs for $\mathrm{N} = 6f_{20}$, $\mathrm{N} = 1.2f_{20}$ and $\mathrm{N} \approx 0.86f_{20}$, meaning f_{20} should be inferior to 5000/6 to observe the resonance with the main stator slotting harmonic ($2f_s$, -2).

The variation of stress harmonic content in function of speed is represented in Figure 5.8. This is another representation of 2D FFT, where each stress harmonic are represented by a rectangle whose color depends on the stress harmonic magnitude. Natural frequencies of radial structural modes are represented by the red crosses and the values are obtained from the finite-element modal analysis (see next Subsection 5.2.3.1). Following the resonance conditions (1.16), a resonance may occur when a stress harmonic passes over a red cross. As the finite-element modal analysis yields f_{20} = 790 Hz, the ovalization mode $m = 2$ can be excited by both stress harmonics at ($2f_s$, -2) and ($10f_s$,

2) over the 0-5000 RPM speed range, specifically for N = 948 RPM and N = 4740 RPM, as illustrated in Figure 5.8. The resonance with the slotting harmonics at ($14f_s$, -2) occurs for N = 677 RPM.

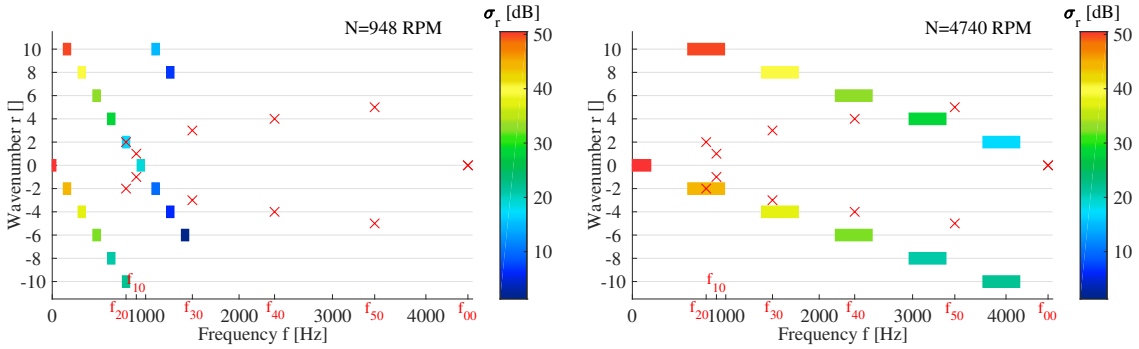

(a) Force spectrum at 948 RPM

(b) Force spectrum at 4740 RPM

Figure 5.8 – Evolution of force harmonic content in function of speed for machine prototype.

5.2.3 Structural mechanics simulation of SPMSM $12s10p$

5.2.3.1 Stator modal analysis

As said in Subsection 2.4.2, the modal analysis can be performed using analytical models based on equivalent cylinders, with a correcting factor to account for the presence of stator teeth. In the analytical model, the stator is assumed to have isotropic elastic properties given by the second line of Table 5.2, and free-free boundary conditions, since clamped-clamped boundary conditions is too strong regarding the lateral rings and endshields in aluminum. The modal analysis is also performed on Hypermesh/Optistruct [Altair, 2018], by modeling only the stator stack and both rings as illustrated in Figure 5.9. The stator stack has transversely isotropic elastic properties given in Table 5.2. The clamped boundary conditions are imposed on the four spots where the lateral rings are screwed to the endshields, represented by the light green triangles.

The comparison of stator natural frequencies between the analytical model (ANL) and the structural FEA is made in Table 5.3. Both models give approximatively the same natural frequencies for radial modes with $m = \{2;3;4\}$, however the natural frequency is really different for the breathing mode ($m = 0$). Besides, the bending mode ($m = 1$) in free-free conditions is physical since it is a solid body motion, as illustrated in Figure 1.18b. The bending mode appears in the FEA due to the fact that some nodes of each lateral ring are clamped, which is obviously more realistic. This phenomenon is further investigated in Subsection 5.3.2 by comparing the EMA of the stator stack in free-free conditions and the EMA of the stator stack pressurized by both lateral rings and endshields.

Young modulus [GPa]		Poisson ratio		Shear modulus [GPa]	
E_x	215	ν_{xy}	0.3	G_{xy}	9.6
E_y	215	ν_{yz}	0.3	G_{yz}	82.7
E_z	25	ν_{zx}	0.3	G_{zx}	82.7

Table 5.2 – Elastic properties of transversely isotropic stator lamination stack (electrical steel M400-50 A).

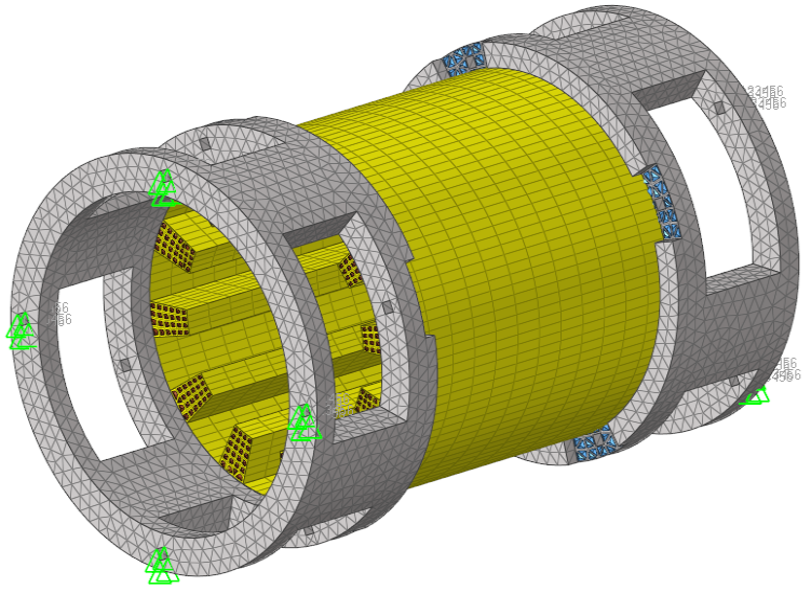

Figure 5.9 – FEA model (Hypermesh) of the stator stack and both stator rings with structural mesh and clamped boundary conditions represented by the light green triangles.

	Natural frequency f_{mn} [Hz]	
Mode (m,n)	ANL (Free-free, isotropic, no rings)	FEA (Transversely isotropic, both rings clamped at 4 points)
(0,0)	7863	4451
(1,0)	-	897 / 903
(2,0)	421	785 / 793
(3,0)	1142	1492 / 1499
(4,0)	2070	2371 / 2393

Table 5.3 – Comparison of stator natural frequencies between analytical model (ANL) and structural FEA.

5.2.3.2 Stator Frequency Response Functions (FRFs)

The analytical radial FRFs are illustrated in Figure 2.18, using the natural frequencies given by the analytical modal analysis performed in Subsection 5.2.3.1. Both radial and circumferential FRFs are also computed on Hypermesh/Optistruct using the unit-magnitude rotating stress wave detailed in Figure 2.15c, with one equivalent force per tooth. In both analytical and numerical FRFs and for each structural mode and stress wavenumber, the damping ratio is assumed to be $\xi = 2\%$ in the present simulation. Numerical radial and circumferential FRFs are illustrated in Figure 5.10 for stress wavenumbers $r = \{0;1;2;3;4\}$ and they have also been computed for $r = \{5;9;10;11\}$.

Radial and circumferential are very close for all wavenumbers except for $r = 0$, where the breathing mode (radial mode with $m = 0$) is around 4300 Hz and the circumferential mode with $m = 0$ (which is due to the synchronous bending motion of all the stator teeth) is around 1100 Hz. Contrary to analytical FRFs, several peaks can be observed on each numerical FRF, as said in Subsection 2.4.2.3. In fact, unit-magnitude stress waves mainly resonate with their corresponding structural mode but they also resonate with other structural modes, in particular longitudinal modes (i.e. with same circumferential wavenumber and non-zero axial wavenumber, cf. Subsection 1.4.3).

Since there is one equivalent force per tooth, stator teeth sample the unit-magnitude stress wave and create spatial aliasing effect since the considered wavenumbers are higher than half of the stator teeth number Z_s. Therefore, stress harmonics of wavenumber $r = \{9;10;11\}$ are respectively seen by the structure as stress harmonics of wavenumber $r = \{3;2;1\}$ (as it is illustrated in Figure 5.35 for the fundamental stress $r = 2p = 10$), which imply that FRFs associated to wavenumbers $r = \{9;10;11\}$ are respectively the same as FRFs for $r = \{3;2;1\}$.

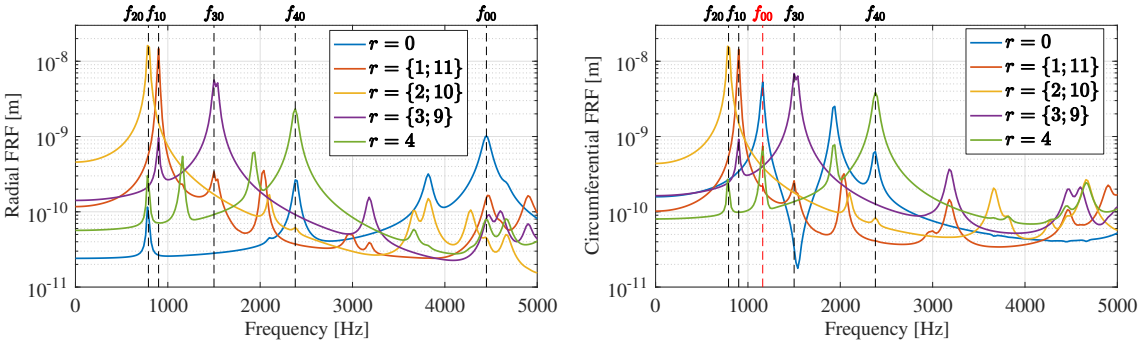

(a) Radial FRF

(b) Circumferential FRF

Figure 5.10 – Radial and circumferential FRFs obtained from FEA (MANATEE Optistruct).

5.2.4 Electromagnetic Vibration Synthesis (EVS) of SPMSM $12s10p$

The EVS is performed on MANATEE using the airgap stress harmonics obtained from the SDM in Subsection 5.2.2.2, associated to radial and circumferential FRFs obtained from FEA in Subsection 5.2.3.2. The EVS is performed on the whole speed range, from 0 – 5000 RPM. The Sound Power Level (SWL) is deduced from the vibration level using analytical radiation factors, as briefly detailed in Subsection 2.4.3.

The variable speed SWL sonagram is illustrated in Figure 5.11a, as well as the modal contribution to the overall SWLfor each speed in Figure 5.11b. Both figures show a main resonance between the ovalization mode and the first slotting harmonic at N = 4740

RPM, and lower resonances with the slotting harmonics of wavenumber $r = \pm 2$ appear at 677 RPM and 948 RPM, as predicted in Subsection 5.2.2.2. Besides, there is also a resonance with the main slotting harmonic of wavenumber $r = -4$ around 3650 RPM. Circumferential stress harmonics of wavenumber $r = 0$ also interact with the circumferential mode of order $m = 0$ at 1100 Hz and create two resonances around 1300 RPM and 1950 RPM. Those resonances are not predicted by the analytical model since they originate from the circumferential FRF associated to the circumferential unit-magnitude stress wave of wavenumber $r = 0$.

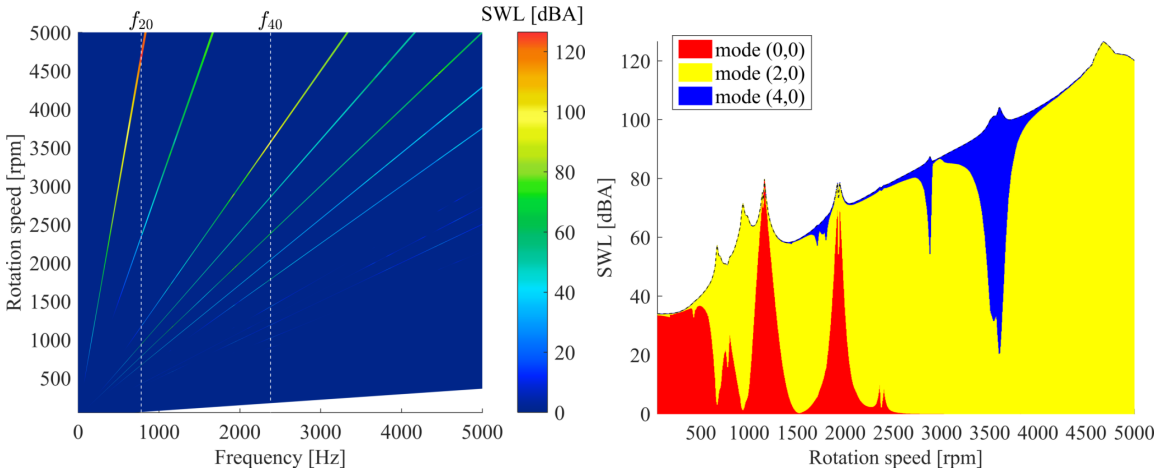

(a) Variable speed SWL sonagram.

(b) Variable speed SWL modal contribution.

Figure 5.11 – Variable speed SWL sonagram and modal contribution (obtained with MANATEE EVS).

As a conclusion, the SPMSM $12s10p$ design is validated regarding the objective of successively observing resonances with structural modes of different orders, including $m = \{0;2;4\}$. However, from the structural FEA accounting for partly clamped lateral rings, the main resonance with the ovalization mode is almost at the SPMSM maximum speed and is beyond the maximum speed of the driving machine. Therefore, in the next Section 5.3, the experimental measurements are performed between 0 and 1300 RPM to validate the first resonances between the ovalization mode and the two slotting harmonics of wavenumber $r = \pm 2$ at $(10f_s, 2)$ and $(14f_s, -2)$.

5.3 Experimental validation of the test rig design

5.3.1 Validation of the airgap stress harmonic content

5.3.1.1 Measurement of the surface PMs magnetization

In Subsection 5.3.1, the aim is to validate the harmonic content of the airgap stress simulated with the ideal rotor magnetization given in Section 5.2.2. First, the real distribution of the rotor magnetization is checked by measuring the flux density on all the rotor surface in the air using a Hall effect probe, as illustrated in Figure 5.12. The Hall effect probe is mounted on the rail of the T-slot table to measure the magnetization pattern for several axial positions and ensure the probe alignment between these different positions. The remanent flux density is higher near the rotor sides (for L = 0.005 m and L = 0.13 m) due to end-effects and quasi-constant for the other axial positions.

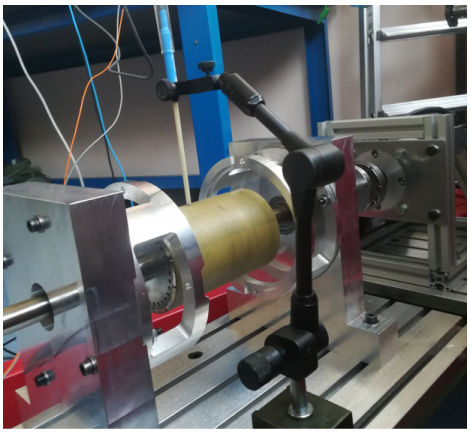

(a) Experimental setup

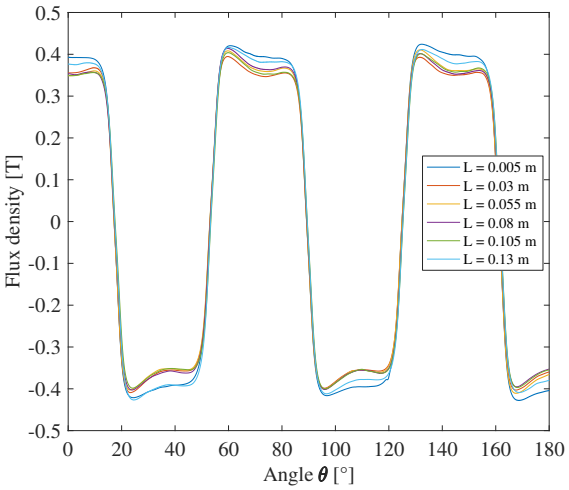

(b) Radial flux density measurement

Figure 5.12 – Radial magnetization measurement of the surface PM rotor in the air (R_g = 46.5 mm) with a Hall-effect probe for several axial positions.

The experimental results are compared with 3D FEA [Ansys, 2018] assuming ideal magnetization in Figure 5.13, for the axial position L = 0.07 m, i.e. in the middle of the rotor. Both magnetization patterns are quite similar but the harmonic content of the real magnetization is much richer due to asymmetries, which probably results from uneven magnetization between the tile PMs, and also for a potential eccentricity when sticking the PMs on the rotor surface. In the 3D FEA simulation, the same end-effect is observed, i.e. the remanent flux density is also higher near the rotor sides. In conclusion, the rotor magnetization measurement shows the existence of the rotor MMF harmonics expected to generate stress harmonics of wavenumber $r = \pm 2$, in particular $(11f_s, 11p)$ (cf. Subsection 5.2.2.2).

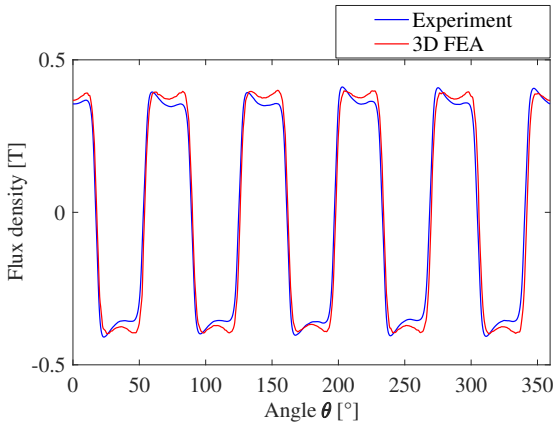

(a) Comparison over space

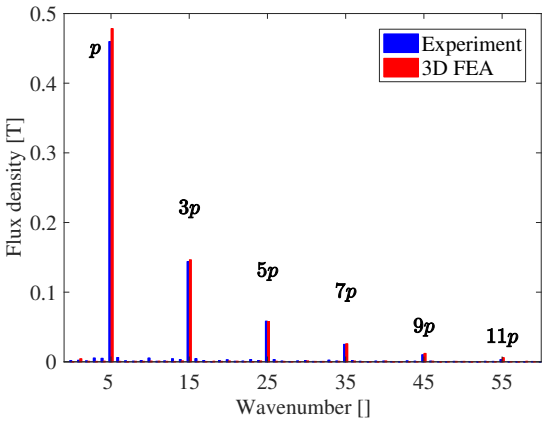

(b) FFT comparison over space

Figure 5.13 – Comparison of theoretical magnetization distribution computed with 3D FEA and measured magnetization with a Hall-effect probe, at the axial position L = 0.07 m.

5.3.1.2 Measurement of stator tooth flux

In the previous Subsection 5.3.1.1, the magnetization measurement has been performed without the stator lamination stack. To validate the real airgap flux density mag-

nitude and the stator slotting harmonics, the airgap flux density should be locally measured with the airgap flux sensor, but it is still under manufacturing. Therefore, only the induced voltage in the search coils wound around each tooth (cf. Subsection 5.2.1.4) is measured to check the fundamental and the harmonic content of the airgap flux density.

The comparison is shown in Figure 5.14 for the first tooth at 500 RPM and a good agreement is found between experiment and simulation for the voltage fundamental and the harmonics at $3f_s$ and $5f_s$. However, this experiment also shows the presence of smaller harmonics likely due to the unbalance magnetization and rotor surface PMs eccentricity, as explained in Subsection 5.3.1.1. This confirms the fact that odd wavenumbers probably exist in the airgap stress harmonic content, and that stator bending mode may potentially be excited.

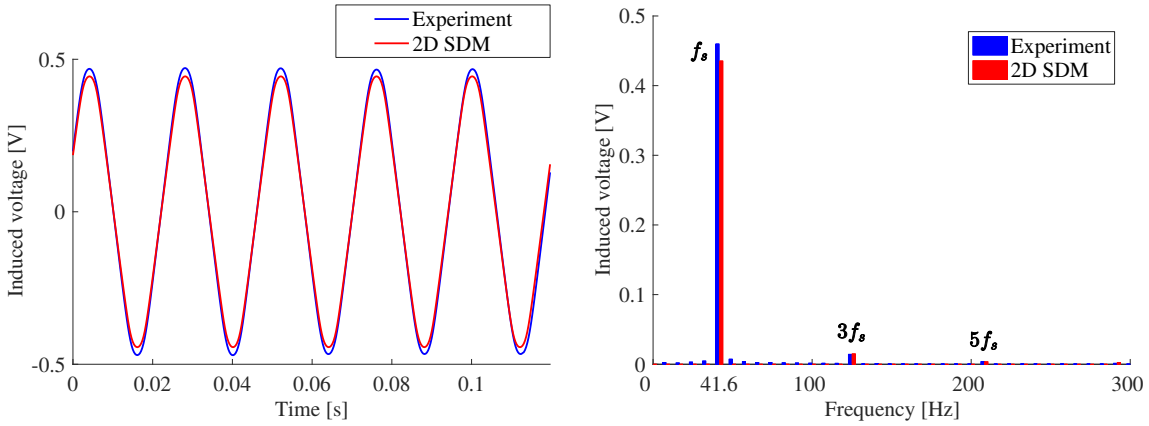

(a) Induced voltage over one rotor mechanical period

(b) Induced voltage FFT

Figure 5.14 – Induced voltage comparison between simulation (MANATEE SDM) and experimentation at 500 RPM ($f_s \approx 41.6$Hz).

5.3.2 Experimental Modal Analysis (EMA)

Mode (m,n)	Natural frequency f_{mn} [Hz]			
	T = 4.6 N.m No endshields No rotor	T = 4.6 N.m Both endshields No rotor	T = 7 N.m Both endshields No rotor	T = 7 N.m Both endshields With rotor
(0,0)	7526	7503	7525	7537
(1,0)	–	755 /772	843 / 863	850
(2,0)	638 / 777	708	715	720
(3,0)	1456	1459	1497	1495
(4,0)	2380	2390	2427	2424

Table 5.4 – Influence of the fixation conditions (tightening torque value T, and presence or not of both endshields and of the rotor) on the structural modes of the stator lamination stack.

The EMA using a roving shock hammer is performed on the stator lamination stack to measure the modal basis of the stator lamination stack. Besides, EMAs are performed for different fixation conditions to investigate their influence on the structural modes, and to conclude on the modal basis robustness regarding stator stack fixation. First, the

stator stack is pressurized by the four bolts and the lateral rings with a tightening torque T = 4.6 N.m and hung to a flexible string, to get close to free-free boundary conditions. Then, the stator stack and the lateral rings are put in the SPMSM frame between both endshields, but without the rotor inside. A second EMA is performed for the same tightening torque T = 4.6 N.m and a third EMA for T = 7 N.m. Finally, a fourth EMA is performed with the rotor inside the stator stack, which is the highest stiffness considered.

The natural frequency for each structural modes and fixation conditions are given in Table 5.4. It can be seen that the fixation conditions have mostly an impact on the bending mode (for $m = 1$) and the ovalization mode (for $m = 2$), with around a 10% gap between first and fourth EMA, and a very little impact on radial modes with $m = \{0;3;4\}$. Therefore, the modal basis is quite robust regarding stator stack fixations, and in particular to the influence of tightening torque, which is an interesting conclusion for the measurement repeatability since both stator stack and rotor can be dismounted (e.g. to setup or remove the airgap sensor or accelerometers on teeth side).

From Table 5.4, the bending mode is not reached by the first EMA in free-free conditions. However, two ovalization modes in phase quadrature are found at 638 Hz and 777 Hz, which may be explained by the presence of four blots to pressurize the stack. When putting the stator stack and the lateral rings between both endshields for the second EMA, only the first ovalization mode remains at 708 Hz. Moreover, the second ovalization mode turns into two bending modes at 755 Hz and 772 Hz, probably because the lateral rings pressure is not homogeneously distributed along the stator stack perimeter.

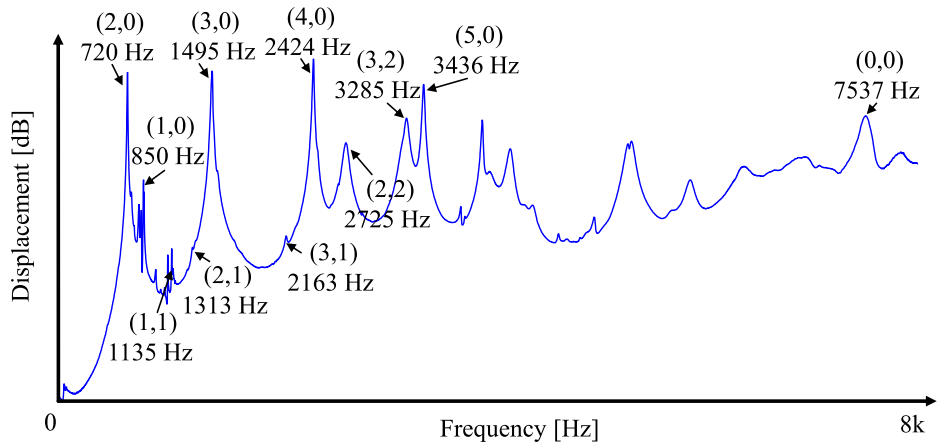

Figure 5.15 – Experimental radial FRF including all radial modes obtained from the EMA for the highest stiffness fixation condition, and performed with roving hammer excitation.

The experimental radial FRF including all structural modes is illustrated in Figure 5.15 for the highest stiffness, i.e. T = 7 N.m, with both endshields and with rotor. Natural frequencies of radial modes ($m = \{0;1;2;3;4\}, n = 0$) appear at the frequencies given by Table 5.4, i.e. respectively at f_{00} = 7537 Hz, f_{10} = 850 Hz, f_{20} = 720 Hz, f_{30} = 1495 Hz, f_{40} = 2424 Hz. Other peaks exist in the radial FRF due to the excitation of radial modes with higher circumferential orders (e.g. $m = 5$), and also the excitation of longitudinal modes such as ($m = 2, n = \{1;2\}$) and ($m = 3, n = \{1;2\}$). The radial FRF enables to measure the real damping ratios ξ_{mn} associated to each structural mode (f_{mn}, m, n).

Finally, an additional EMA is performed on the rotor and the shaft between both endshields, and obviously without the stator stack so as to hit at several points on both rotor and shaft with the hammer shock. The first rotor bending mode is at 233 Hz and the second bending mode is at 795 Hz, as illustrated in Figure 5.16. Therefore, the second rotor

bending mode is near the stator stack bending mode and may emphasize the dynamic eccentricity due to UMP.

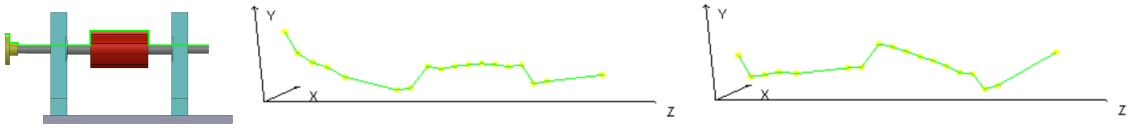

(a) EMA setup (b) First bending mode at 233 Hz (c) Second bending mode at 795 Hz

Figure 5.16 – EMA of rotor, shaft and magnetic coupling mounted in bearings and pressurized by both endshields.

5.3.3 Stator yoke acceleration and Sound Pressure Level (SPL) at variable speed (0-1300 RPM)

The stator yoke radial acceleration level and the SPL are measured at variable speed (0-1300 RPM) to check the existence of resonance with the ovalization mode, as predicted in Subsection 5.2.4. A 1-axis accelerometer is stuck on the stator yoke outer surface to measure the radial acceleration ($n°1$ in Figure 5.17a), and a close field microphone is placed at 20 centimeters above the stator surface to measure SPL ($n°2$ in Figure 5.17a). The acceleration spectrogram is illustrated in Figure 5.17b and the SPL sonagram is illustrated in Figure 5.17d.

It can be seen on the acceleration spectrogram that the main acceleration component between 0 and 1300 RPM is at $2f_s$ and is a forced excitation. In fact, it has been shown in the magnetic stress simulation study (cf. Subsection 5.2.2.2) that this acceleration component is mainly due to the superposition of the fundamental stress ($2f_s$,10) and of the first slotting stress harmonic ($2f_s$,-2), which is thus far from the natural frequency of the ovalization mode, measured at 720 Hz in Subsection 5.3.2.

Besides, the resonant response is also clearly visible on the acceleration spectrogram, especially due to many resonances with both ovalization and bending modes, characterized by the two yellow and red vertical bands around their natural frequencies at 720 Hz and 850 Hz. The specific resonance between the higher slotting harmonic ($10f_s$,2) and the ovalization mode is clearly observable at 720 Hz and 850 RPM, as predicted in Subsection 5.2.4.

Furthermore, the rotor magnetization and the tooth flux density measurements in Subsection5.3.1 have suggested the existence of parasitic UMPs in the airgap stress harmonic content, which is now demonstrated since the acceleration spectrogram shows that the stator bending mode at 850 Hz is considerably excited. Finally, a third structural mode is a little excited between 1050 Hz and 1150 Hz, which probably corresponds to the first longitudinal bending modes at ($f_{11} = \{1050\text{ Hz}, 1135\text{ Hz}\}, m = 1, n = 1$), which are in phase quadrature as illustrated in Figures 5.30c-5.30d. These longitudinal bending modes are also present in the radial FRF obtained from EMA and illustrated in Figure 5.15.

So as to better see the contribution of each exciting magnetic stress harmonics at a specific speed, the acceleration FFT at 700 RPM is given in Figure 5.17c. The acceleration FFT shows the huge amount of existing harmonics in the real spectrum, and highlight the magnitude predominance of the magnetic excitations which are theoretically predicted in Subsection 5.2.2.2.

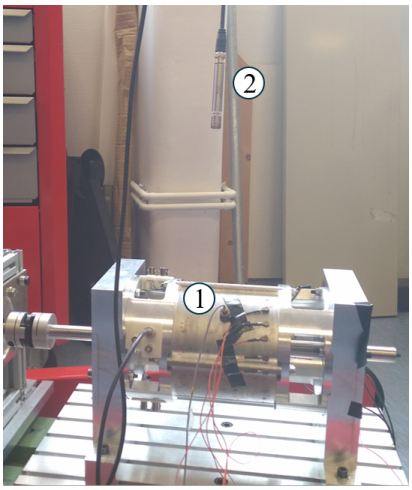

(a) Measurement setup

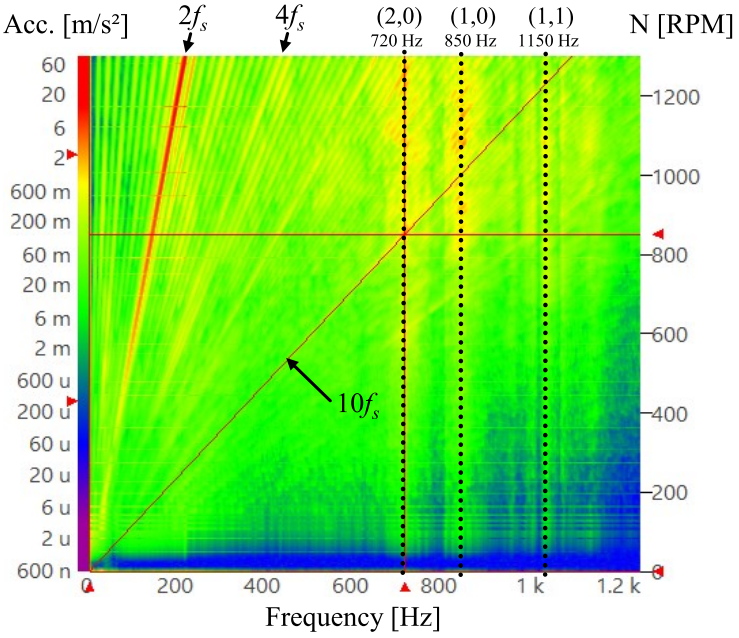

(b) Acceleration spectrogram (0-1300 RPM)

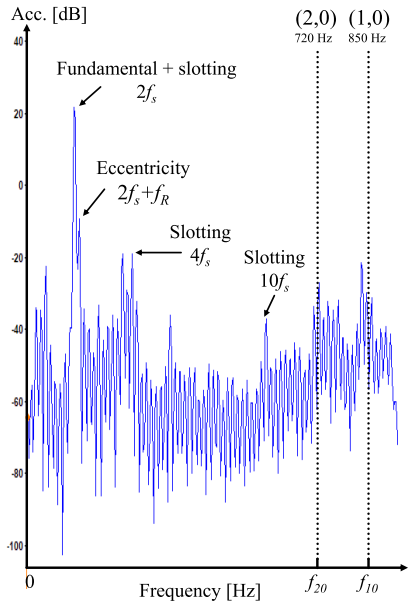

(c) Acceleration FFT at 700 RPM

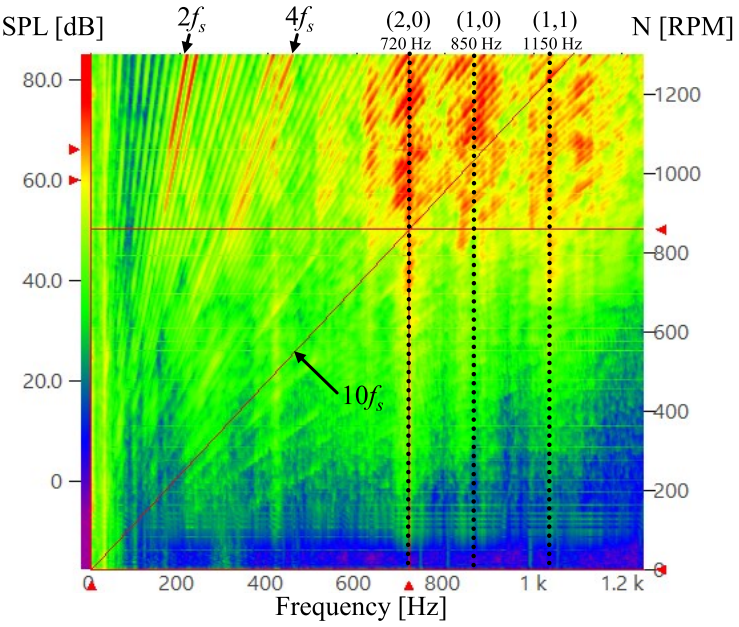

(d) SPL sonagram (0-1300 RPM)

Figure 5.17 – Measurement setup for acceleration and SPL measurement of the SPMSM $12s10p$ at variable speed (0-1300 RPM).

The SPL sonagram emphasizes the resonances with both ovalization and bending modes, as well as the forced excitations with stress harmonics at $2f_s$ and $4f_s$. The SPL sonagram also shows that many excitations coexist in the SPMSM $12s10p$, and confirms the dense harmonic content observed on the acceleration FFT at 700 RPM (cf. Figure 5.17c). The SPL sonagram is actually much richer than the sonagram predicted in Subsection 5.2.4. This is mostly explained by the presence of rotor eccentricity and the unbalance magnetization which modulate the theoretical stress harmonic content. In particular, the sideband at $2f_s + f_R$ near the main stress component at $2f_s$ is characteristic of a dynamic eccentricity, where $f_R = p\text{N}/60$ is the rotor mechanical frequency.

In Subsection 5.5.1, the assertions made in this paragraph concerning the resonances with the different structural modes are experimentally proved by performing the ODS of the stator stack.

5.3.4 Impact of the driving machine and end-shields on the vibroacoustic measurements

The impact of the driving machine on the vibroacoustic measurements is estimated by measuring the acceleration only due to the driving machine, for a runup between 0 and 3300 RPM. The acceleration spectrogram is illustrated in Figure 5.18a. Sharp resonances can be observed above 2200 RPM, and the main acceleration contribution is due to the resonance with the breathing mode which is also around 7500 Hz, as for the SPMSM $12s10p$. However, the radial acceleration magnitude of the driving machine is much lower than the one of the studied SPMSM regarding the speed range 0-1300 RPM, and therefore the driving machine should not generate major acceleration harmonics which may be transmitted to the SPMSM through the shaft and could disturb the acceleration measurement performed on the SPMSM.

An accelerometer is also put on the top of the left endshield to see if the endshield acceleration spectrum is correlated with the stator stack acceleration spectrum, and check the endshields influence on the stator stack acceleration spectrogram illustrated in Figure 5.17b. In comparison, the endshield spectrogram is illustrated in Figure 5.18b, with both horizontal and vertical red cursors to locate the the ovalization mode resonance at 720 Hz and 850 RPM.

First of all, a large resonance band between 500 Hz and 700 Hz is mainly responsible for the left endshield acceleration level, and corresponds to the excitation of a structural mode which does not appear in the stator stack radial FRF obtained from EMA (see Figure 5.15). Furthermore, the left endshield is subject to mechanical excitations at low frequency, whose frequency is proportional to the rotor mechanical frequency f_R. These mechanical excitations most likely originate from mechanical friction in bearings. Finally, it is difficult to conclude on the impact of the ovalization and bending mode of the stator stack around 720 Hz and 850 Hz. However, the resonance with the longitudinal bending modes 1050 Hz and 1135 Hz is clearly visible on the spectrogram, since this mode has an axial wavenumber $n = 1$ and excites left and right endshields in phase quadrature, which necessarily creates an acceleration perpendicularly to the axial direction (i.e. in the xy-plane) as illustrated by the ODS in Figures 5.30c-5.30d.

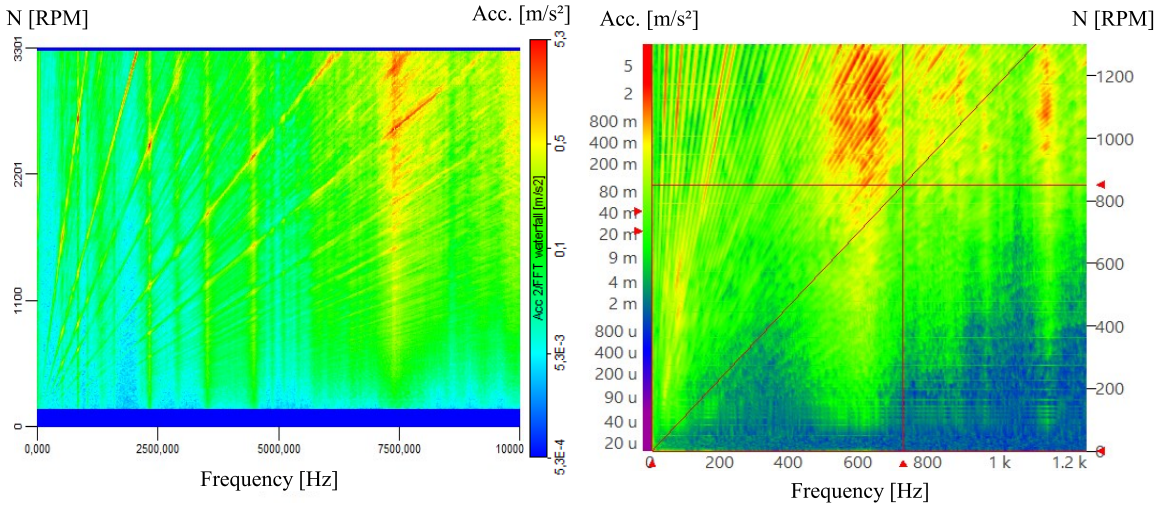

(a) Radial acceleration spectrogram of the driving machine.

(b) Acceleration spectrogram on the top of left endshield.

Figure 5.18 – Acceleration spectrograms to check the impact of driving machine and endshields on the stator stack acceleration measurement between 0 and 1300 RPM.

5.4 Validation of the EVS at variable speed (0-1300 RPM) with measured stress harmonic content and fitted FRFs

5.4.1 Electromagnetic simulation including real magnetization pattern

5.4.1.1 Airgap flux density harmonic content

The real magnetization pattern obtained by the experiment in Subsection 5.3.1.1 is injected in the subdomain model to include the parasitic harmonics due to unbalance magnetization of the PMs. Besides, a dynamic eccentricity of 5% is also simulated by modulating the airgap flux density distribution by a cosine function:

$$\mathrm{B}_{\rho}^{ecc}(t,\mathrm{R}_g,\theta) = \mathrm{B}_{\rho}(t,\mathrm{R}_g,\theta)\Big(1-0.05\cos(\Omega t-\theta)\Big) \tag{5.3}$$

$$\mathrm{B}_{\theta}^{ecc}(t,\mathrm{R}_g,\theta) = \mathrm{B}_{\theta}(t,\mathrm{R}_g,\theta)\Big(1-0.05\cos(\Omega t-\theta)\Big) \tag{5.4}$$

where R_g is the airgap middle radius, Ω is the rotation speed and B_{ρ}, B_{θ} are the airgap flux density components computed without eccentricity. This first order model of dynamic eccentricity enables to include the sidebands around the stress harmonics existing in the spectrum without eccentricity, as it is done in the PMMF method (see Subsection 2.3.2.1).

The radial airgap flux density including real magnetization and 5% dynamic eccentricity is compared with the ideal flux density in Figure 5.19. The real magnetization pattern has been scaled to obtain the same fundamental magnitude ($r = 5$) as for the ideal case. Besides, the 2D FFT of radial and circumferential flux densities is shown in Figure 5.20. The new parasitic harmonics are clearly visible between the main rotor MMF harmonics (f_s,5), ($3f_s$,15), ($5f_s$,25), etc.

5.4.1.2 Airgap stress harmonic content

The airgap stress harmonic content is computed with the MST in the middle of the airgap using the 2D airgap flux density computed in Subsection 5.4.1.1. The stress har-

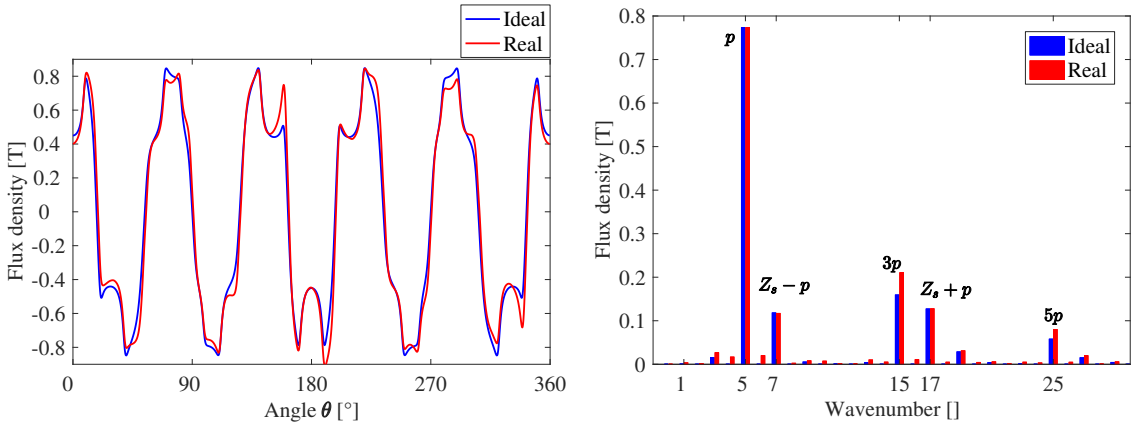

(a) Radial airgap flux density

(b) Radial FFT over space

Figure 5.19 – Comparison between radial airgap flux density created by the ideal (parallel) magnetization and by the measured magnetization plus 5% dynamic eccentricity (obtained from MANATEE SDM for $t_0 = 0$ s).

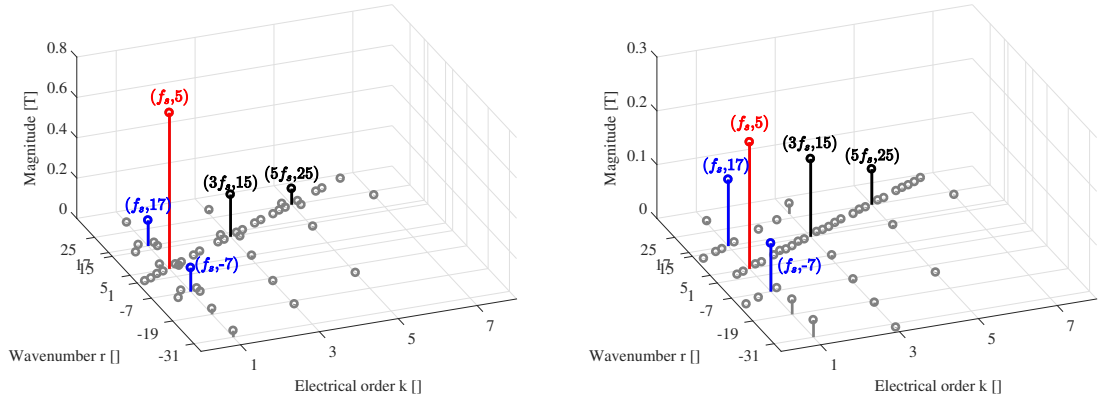

(a) Radial 2D FFT

(b) Circumferential 2D FFT

Figure 5.20 – Time and space harmonic content of radial and circumferential airgap flux densities under open-circuit condition, with the measured magnetization and 5% dynamic eccentricity.

monic content is represented in Figure 5.21, which can be directly compared with 5.8. The real magnetization is characterized by the parasitic harmonics which form diagonals (in green/cyan) between the main stress harmonics (in red/orange/yellow). The dynamic eccentricity is characterized by the horizontal sidebands around each excitation harmonic. In particular, the stress harmonic content now contains both even and odd wavenumbers and stress harmonics of wavenumber $r = 1$ can resonate with the stator bending modes as experimentally observed in Subsection 5.3.3. In conclusion, the stress harmonic content is much more dense and predicts many potential resonance with stator ovalization and bending modes at 720 Hz and 850 Hz.

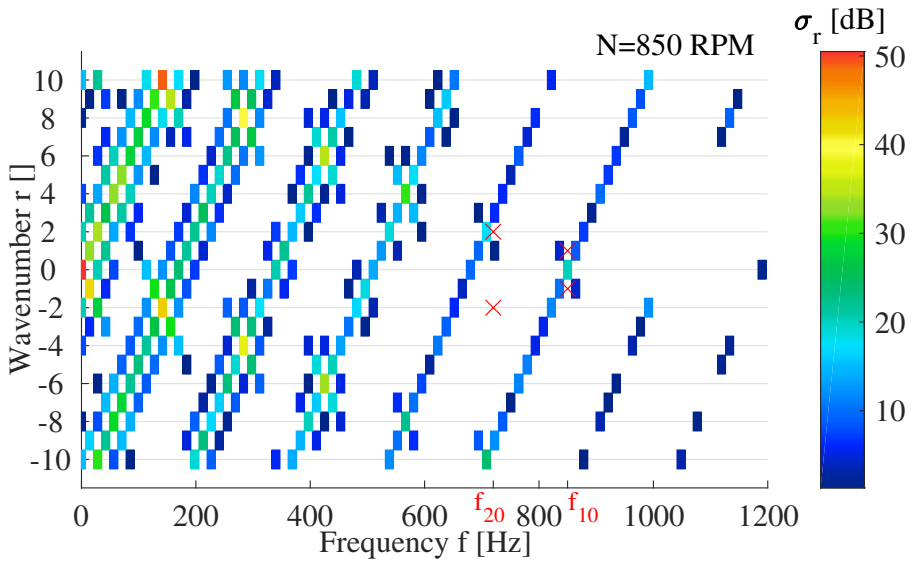

Figure 5.21 – Stress harmonic content at 850 RPM for SPMSM $12s10p$ with the measured magnetization and 5% dynamic eccentricity at open-circuit condition.

Furthermore, the convolution approach is applied to the stress harmonic ($2f_s$,-2) as shown in Figure 5.22, which can be compared with the ideal case illustrated in Figure 5.7. The rotor MMF harmonics obtained with the real magnetization pattern are phase shifted. Therefore, the elementary stress component resulting from the combination of flux density harmonics due to rotor MMF are also phase shifted. The phase angle of each elementary stress component is depicted on the vector plot in Figure 5.22. It can be seen that accounting for both real magnetization pattern and dynamic eccentric has not created new high magnitude components in the generation of the stress harmonic ($2f_s$,-2).

5.4.2 Structural mechanics simulation with fitted elastic properties

5.4.2.1 FE modal analysis with fitted elastic properties and comparison with analytical and EMA results

In Subsections 5.2.3.1 and 5.3.2, the structural modes of the stator stack lamination have been estimated with analytical and finite-element models, and measured with EMA. The aim of Subsection 5.4.2 is to fit the elastic properties of the stator lamination stack, originally given in Table 5.2, so that the structural finite-element model gets closer to the experimental FRF for the structural modes impacting the acceleration spectrogram between 0 and 1300 RPM, i.e. ovalization and bending modes at 720 Hz and 850 Hz.

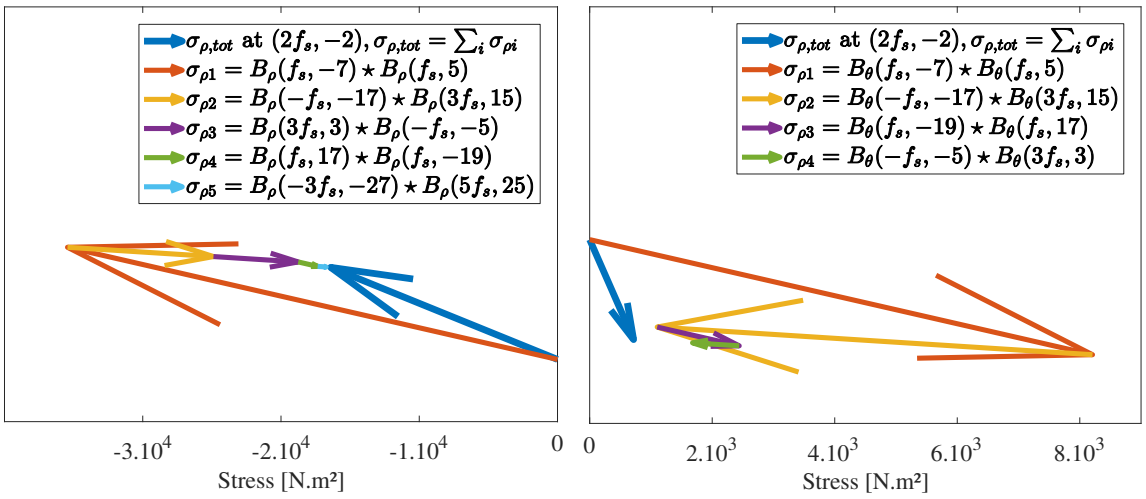

(a) B_ρ^2 radial stress combinations

(b) B_θ^2 radial stress combinations

Figure 5.22 – Decomposition of stress harmonic ($2f_s$, -2) for the real magnetization pattern using the convolution approach.

	Frequency f_{mn} [Hz]			
Mode (m,n)	ANL	Prior FEA	EMA	Fitted FEA
(0,0)	7863	4451	7537	3895
(1,0)	-	897 / 903	850	838 / 848
(2,0)	421	785 / 793	720	729 / 735
(3,0)	1142	1492 / 1499	1495	1357 / 1388
(4,0)	2070	2371 / 2393	2424	2116 / 2127

Table 5.5 – Comparison of stator natural frequencies between EMA and structural FEA with and without fitted parameters

Young modulus [GPa]		Poisson ratio		Shear modulus [GPa]	
E_x	170	ν_{xy}	0.3	G_{xy}	7.7
E_y	170	ν_{yz}	0.3	G_{yz}	65.4
E_z	20	ν_{zx}	0.3	G_{zx}	65.4

Table 5.6 – Fitted elastic properties to match with the natural frequency of both ovalization and bending modes obtained with EMA.

The natural frequency obtained with the analytical, FEA and EMA performed in the previous subsections are compared in Table 5.5. The FEA with partly clamped boundary conditions (cf. Figure 5.9) logically provides more accurate natural frequencies for radial modes $m = \{1;2\}$, i.e. for structural modes of interest, and also for $m = \{3;4\}$. However, the natural frequency of breathing mode ($m = 0$) is actually more accurate using the analytical model with free-free boundary conditions.

Furthermore, the elastic properties of the stator lamination stack are fitted in Hypermesh/Optistruct [Altair, 2018] to get the natural frequency of ovalization and bending modes closer to the experimental values, and the resulting properties are given in Table 5.6. The fitted FEA natural frequencies are given in the right column of Table 5.5. Both ovalization and bending modes are better estimated, to the detriment of the other radial modes $m = \{0;3;4\}$ but they are out of the validation scope since they are not excited on the speed range 0-1300 RPM. A new torsional mode for $m = 0$ appears at $f_{00} = 1108$ Hz, which does not exist in the EMA. Moreover, the longitudinal bending modes found by the EMA at 1050 Hz and 1135 Hz are not predicted by the structural FEA. These two differences probably comes from the assumption of clamping the lateral only on the four threaded holes, as illustrated in Figure 5.9. The modal shapes of ovalization, bending, and torsional modes at respectively 729 Hz, 838 Hz and 1108 Hz are illustrated in Figure 5.23. The impact of clamping the four threaded holes can be observed on each modal shape.

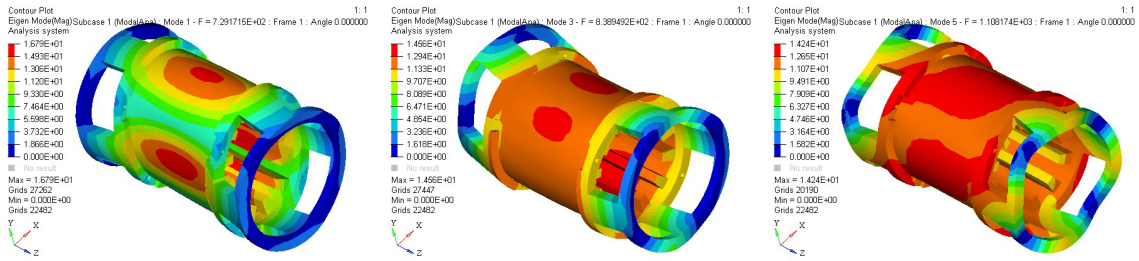

(a) Ovalization mode at ($f_{20} = 729$ Hz, 2, 0)

(b) Bending mode at ($f_{10} = 838$ Hz, 1, 0)

(c) Torsional mode at ($f_{00} = 1108$ Hz, 0, 0)

Figure 5.23 – Modal shapes of ovalization, bending and torsional modes computed with FEA considering fitted elastic properties (cf. Table 5.6).

5.4.2.2 Fitted Frequency Response Functions (FRFs)

The fitted numerical FRFs in both radial and circumferential directions are computed with Hypermesh/Optistruct, and are illustrated in Figure 5.24. The numerical FRF is extracted at the exact position of the reference accelerometer ($n°1$ in Figure 5.17a). The experimental values of damping ratios ξ_{mn} are extracted from the experimental radial FRF illustrated in Figure 5.15, yielding $\xi_{20} = 0.004$ and $\xi_{10} = 0.003$. However, the FRFs presented in Figure 5.24 do not include the experimental damping, which is kept as its default value of 2%.

5.4.3 EVS at variable speed (0-1300 RPM) using fitted FRFs and real magnetization

The EVS is performed on MANATEE [2018] software using fitted FRFs computed in last Subsection 5.4.2.2 and the airgap stress harmonic content accounting for real magnetization and dynamic eccentricity (cf. Subsection 5.4.1.2). The simulated acceleration

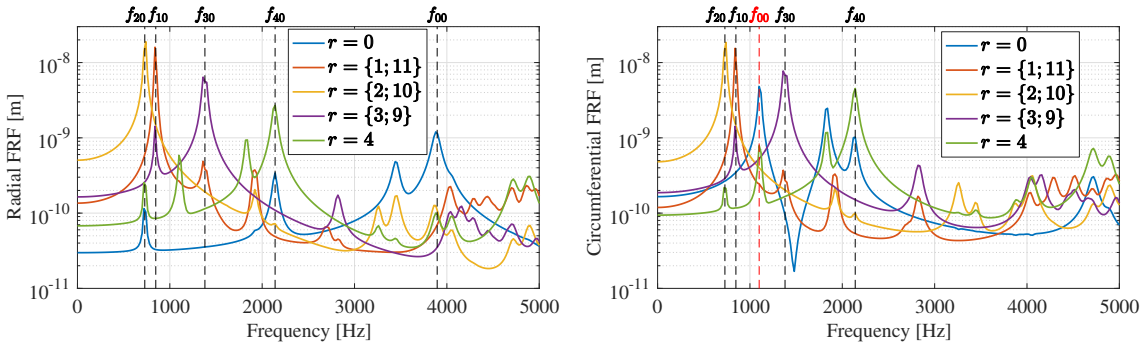

(a) Radial FRF (b) Circumferential FRF

Figure 5.24 – Radial and circumferential FRFs obtained from FEA (MANATEE Optistruct) with fitted elastic properties (cf. Table 5.6).

spectrogram is illustrated in Figure 5.25b and can be directly compared with the experimental spectrogram in Figure 5.17b. Besides, the acceleration spectrum at 700 RPM is represented in Figure 5.25a and can be compared with Figure 5.17c.

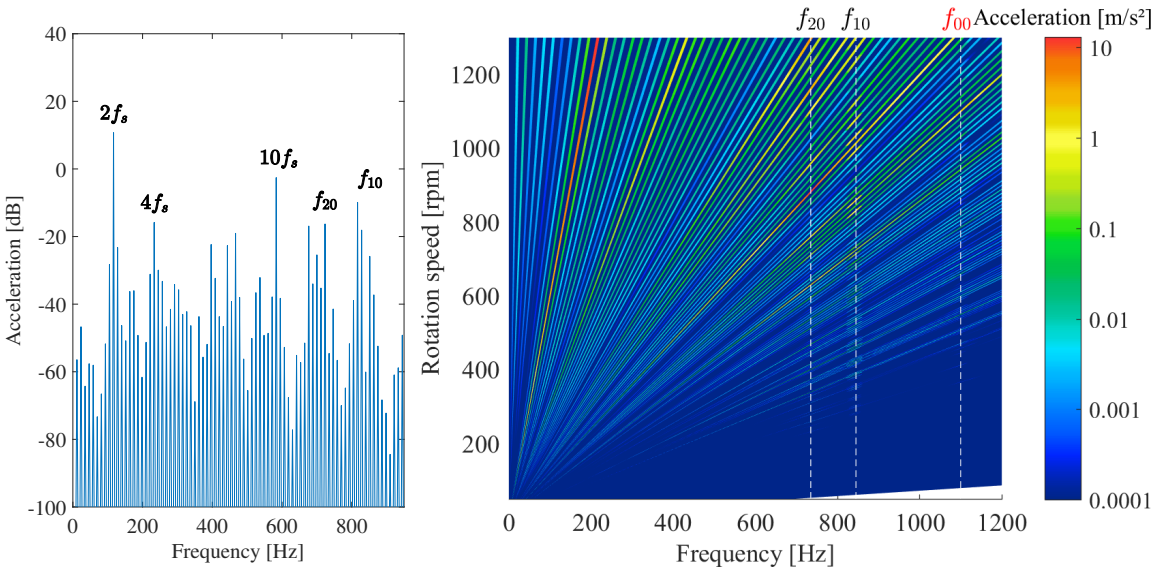

(a) Acceleration FFT at 700 RPM (b) Acceleration spectrogram up to 1300 RPM with fitted EVS

Figure 5.25 – Simulated acceleration at variable speed between 0 and 1300 RPM with fitted EVS (obtained with MANATEE).

As shown on the simulated spectrogram, the number of magnetic excitations has largely increased due to the introduction of uneven magnetization and dynamic eccentricity, in comparison with the number of magnetic excitations included in the simulated sonagram with ideal rotor MMF (cf. Figure 5.11a). The acceleration level is mainly due to the forced excitation of the fundamental stress and the first slotting stress harmonic at $2f_s$. Besides, the resonance between the ovalization mode and the slotting harmonic ($10f_s$,2) at 728 Hz and around 875 RPM is well estimated. The modal contribution of the bending mode (848 Hz,1,0) is also clearly visible, such as the torsional mode (1108 Hz,0,0) which is excited by the pulsating harmonics of circumferential stress. However, this resonance with torsional mode is naturally not present in the experimental spectrogram. Similarly, the resonances with the longitudinal bending modes measured between 1050 Hz and 1150 Hz are not predicted by the EVS with fitted FRFs.

5.5 Investigation of e-NVH scientific challenges

5.5.1 Analysis of Operational Deflection Shapes (ODS) in forced and resonant responses

5.5.1.1 Experimental setup

The Operational Deflection Shape (ODS) enables to measure the stator stack deflection shape for each frequency and given a rotation speed, and provides physical insight on the interaction between stress harmonics and the stator structure of the electrical machine. Therefore, the ODS is used to investigate the forced response of the SPMSM stator in both forced and resonant responses, respectively in Subsections 5.5.1.2 and 5.5.1.3. The ODS is further performed in Subsection 5.5.1.4 to highlight the presence of UMP in the stress harmonic content, exciting the first bending mode (f_{10} = 850 Hz,1,0) and the two longitudinal bending modes (f_{11} = {1050 Hz, 1135 Hz}, $m = 1, n = 1$).

The ODS measurement setup is illustrated in Figure 5.26. The stator yoke is discretized in 4 axial layers and 24 nodes per layer, meaning a total of 96 nodes. The ODS is performed with 6 roving mono-axis accelerometers, hence requires 16 successive measurements for one rotation speed. With this setup, the ODS may capture radial modes with circumferential wavenumbers up to 12 and axial wavenumbers up to 2, from Shannon sampling theorem. The aim is to observe the stator yoke deflection associated to the fundamental excitation of wavenumber $r = 2p = 10$.

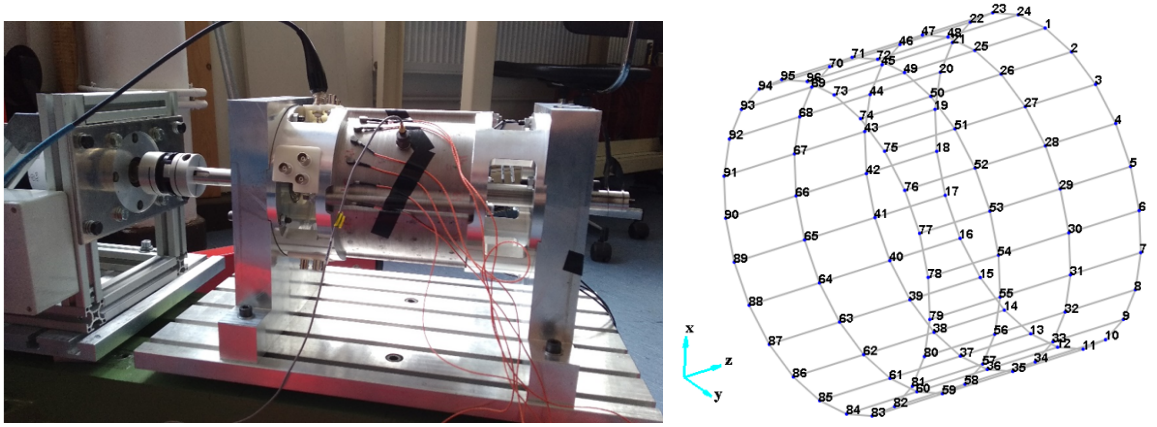

(a) Initial position of the 6 accelerometers

(b) Mesh with 4 axial layers and 24 nodes per layer

Figure 5.26 – ODS measurement setup with 6 roving accelerometers for a total of 96 nodes.

5.5.1.2 Deflection shape in forced response

The ODS is first performed at 550 RPM ($f_s \approx 45.8$ Hz), where there is no resonance from the acceleration spectrogram (cf. Figure 5.17b). Three forced excitations are illustrated in Figure 5.27 and are due to the stress harmonics ($2f_s$,-2), ($4f_s, -4$) and ($10f_s$,2) which are respectively represented in purple, cyan and orange in the airgap stress 2D FFT in Figure 5.22. The three deflections are rotating waves as expected, since the stator yoke response is forced due to the fact that exciting frequencies are far from the natural frequency of their corresponding structural mode. Besides, the rotation direction is respected for each excitation, since ($2f_s$,-2) and ($4f_s, -4$) rotates in the opposite direction compared with ($10f_s$,2). However, the deflection shape at $2f_s$ does not seem influenced

by the fundamental stress ($2f_s$,10) since the deflection shape wavenumber is $r = 2$, not $r = 2$ and $r = 10$. This can be due to the fact that the stator structure is too stiff to be deformed by a stress harmonic of wavenumber $r = 10$, and also to the fact that the stress harmonic of wavenumber $r = 10$ is modulated by the stator teeth, as discussed afterwards in Subsection 5.5.3.

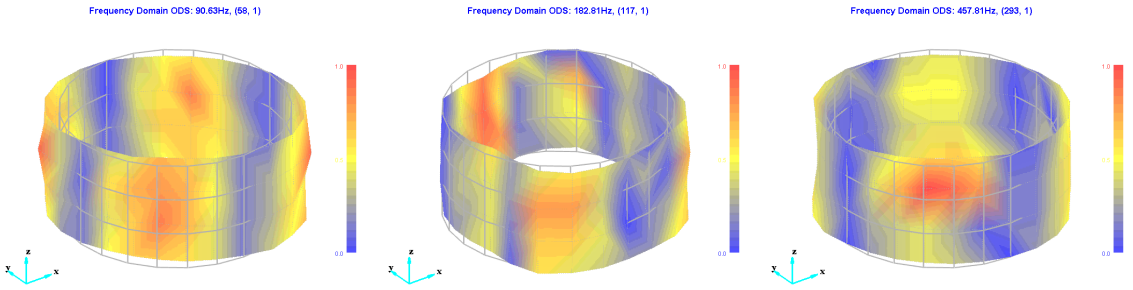

(a) Rotating deflection at ($2f_s$,-2) (b) Rotating deflection at ($4f_s, -4$) (c) Rotating deflection at ($10f_s, 2$)

Figure 5.27 – ODS of the stator yoke at 550 RPM for three forced excitations at ($2f_s, -2$), ($4f_s, -4$) and ($10f_s, 2$).

5.5.1.3 Deflection shape in resonant response

Subsection 5.5.1.3 aims at investigating the resonance effect on the stator stack deflection shape, in particular by tracking the deflection shape generated by the stress harmonic ($10f_s$,2) in both forced and resonant responses. For this purpose, the ODS is performed at three different speeds between 0 and 1300 RPM, as illustrated in Figure 5.28:

1. 550 RPM: far from resonance between ($10f_s$, 2) and ovalization mode at 720 Hz.
2. 700 RPM: close to resonance between ($10f_s$, 2) and ovalization mode at 720 Hz.
3. 550 RPM: at resonance between ($10f_s$, 2) and ovalization mode at 720 Hz.

The three ODSs for each speed are represented in Figure 5.29. It is shown that the forced rotating deflection far from resonance progressively becomes a pulsating deflection at resonance, which follows the modal shape. In fact, the oval deflection at 700 RPM is a mix of rotating and pulsating deflection. Therefore, the ODS confirms the non-linearity intrinsic to the resonance phenomenon, involving phase shifting and the apparition of a standing deflection wave.

For a cylindrical structure subject to free-free boundary conditions, the non-linearity can be explained by the trigonometric relationship between standing and rotating waves. By applying twice the trigonometric relationship (1.11), it can be shown that any standing wave (1.15) is the sum of four rotating waves with same frequency and wavenumbers but rotating in different directions, meaning:

$$\mathbf{d}_x(t,\theta,z) = \frac{1}{4}\sum_{1}^{4}\cos\left(2\pi f_{mn}t \pm m\theta \pm \pi n\frac{z}{L_s}\right)\mathbf{e}_x \tag{5.5}$$

where the four possibilities are: $(+m,+n)$, $(+m,-n)$, $(-m,-n)$, $(-m,+n)$, and $x \in \{\rho;\theta;z\}$. Therefore, the standing wave of the modal shape necessarily includes the rotating deflection wave given by Equation (1.13).

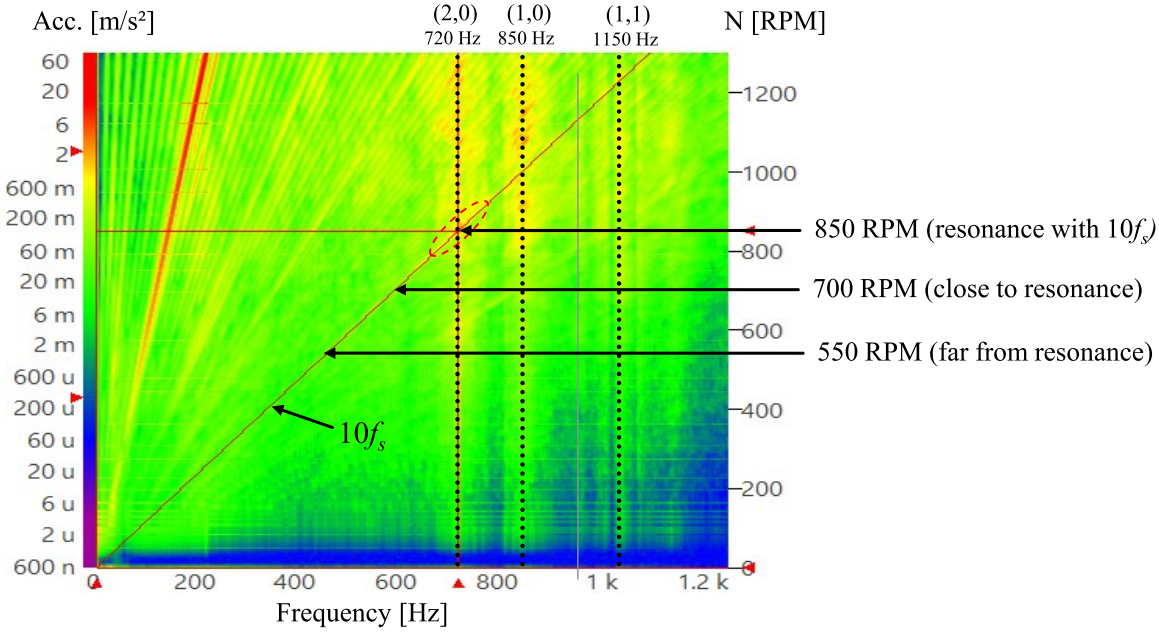

Figure 5.28 – Three ODS performed at 550, 700 and 850 RPM to observe the forced excitation and the resonance between the stress harmonic (10f_s,2) and the ovalization mode at 720 Hz.

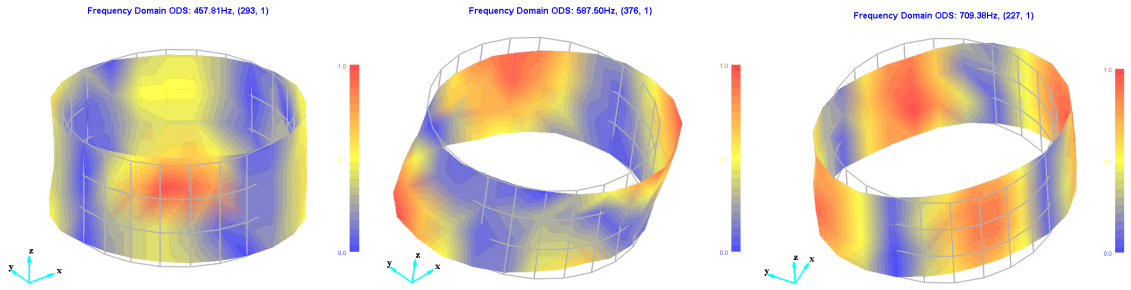

(a) Rotating deflection at 550 RPM (b) Pulsating and rotating deflection at 700 RPM (c) Pulsating deflection at 850 RPM

Figure 5.29 – ODS of the stator yoke far from resonance (550 RPM), close to resonance (700 RPM) and at resonance (850 RPM) between stress harmonic (10f_s,2) and ovalization mode (f_{20} = 720 Hz,2,0).

5.5.1.4 Deflection shape due to rotor eccentricity

The ODS also enables to check the presence of UMP in the stress harmonic content. As shown in Figure 5.21, the dynamic eccentricity modulates the first slotting stress harmonics ($2f_s$, -2) into two UMPs ($2f_s \pm f_R$, -1). Therefore, the deflection shape is measured at 850 RPM (i.e. $f_s \approx 70.8$ Hz) and $f = 2f_s + f_R$ and is illustrated in Figure 5.30a. The considered harmonic of UMP is far from the natural frequency of the bending so a forced response characterized by a rotating deflection is observed. Besides, the pulsating deflection in resonant response is represented for the first bending mode (f_{10} = 850 Hz,1,0) (cf. Figure 5.30b) and the two longitudinal bending modes (f_{11} = {1050 Hz, 1135 Hz}, m = 1, n = 1) (cf. Figures 5.30c-5.30d).

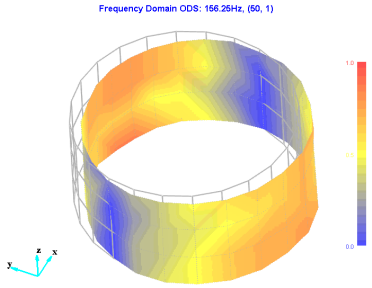

(a) Rotating deflection ($2f_s + f_R, -1, 0$) due to the modulation of the first slotting stress harmonic ($2f_s, -2$))

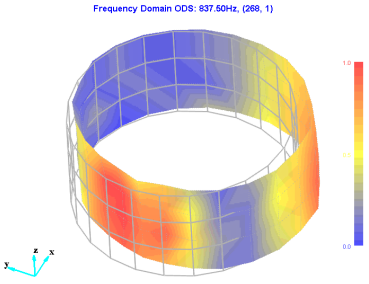

(b) Pulsating deflection due to bending mode (f_{10} = 850 Hz,1,0)

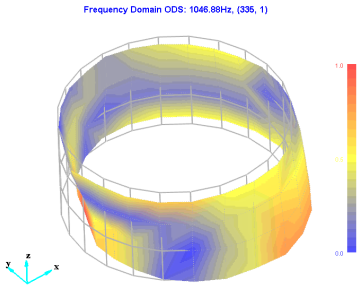

(c) Pulsating deflection due to longitudinal bending mode (f_{11} = 1050 Hz,1,1)

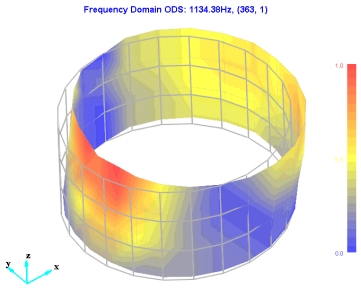

(d) Pulsating deflection due to longitudinal bending mode (f_{11} = 1135 Hz,1,1)

Figure 5.30 – ODS of the stator yoke at 850 RPM to see the rotor eccentricity effects in forced and resonant responses, with bending modes (f_{10} = 850 Hz,1,0), (f_{11} = 1050 Hz,1,1) and (f_{11} = 1135 Hz,1,1).

5.5.2 Analysis of circumferential effects

The influence of circumferential effects, i.e. the influence of circumferential flux density on radial stress and the influence of circumferential stress on radial vibrations cannot be directly measured in the SPMSM. In this subsection, circumferential effects are investigated based on an experiment with three stator teeth having a tri-axes accelerometer on their side (cf. Figure 5.31a) to measure radial and circumferential accelerations at tooth tip. Besides, three mono-axis accelerometers are put on the stator yoke external

surface in front of the stator teeth with a tri-axes accelerometer. Radial and circumferential accelerations at tooth tip are compared with the radial acceleration of the yoke in front of the tooth in Figure 5.31b, for N = 850 RPM. Regarding the acceleration components at $2f_s$, the magnitude of yoke radial acceleration is 7 m/s^2 while magnitudes of tooth radial and circumferential accelerations are respectively 5.7 m/s^2 and 5.2 m/s^2. Therefore, the magnitude difference between stator yoke and tooth tip radial acceleration is around 19% (i.e. ≈ -0.9 dB on acceleration level and ≈ -1.8 dB on SWL level), and can be explained by the circumferential acceleration at tooth tip which also contributes to yoke radial acceleration due to tooth bending motion. Besides, the ratio is naturally not the same for each acceleration harmonics as it depends on their phase shift angle, which yields constructive or destructive interferences.

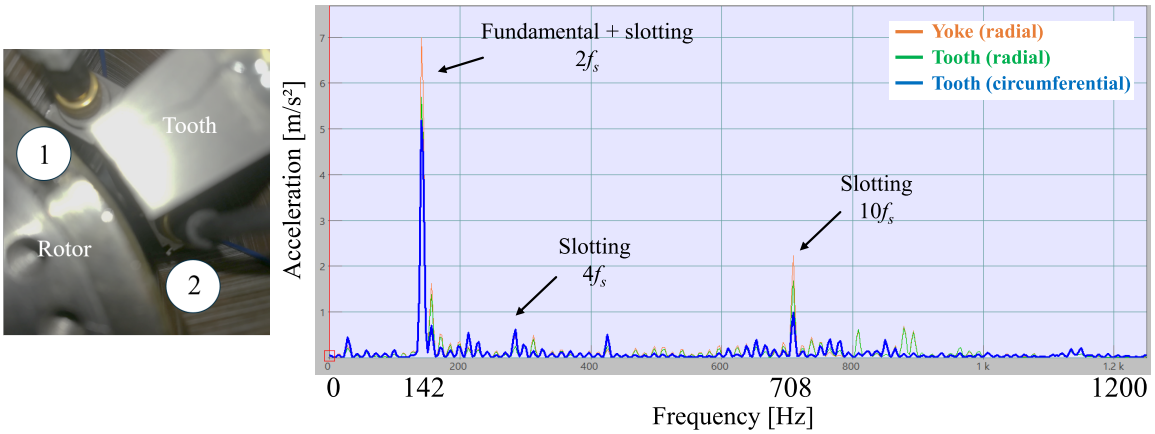

(a) Tri-axes positioned on tooth side

(b) Acceleration FFT at 850 RPM

Figure 5.31 – Experimental comparison between radial and circumferential accelerations at tooth tips and radial acceleration on stator yoke in front of each tri-axes.

To further investigate the contribution of circumferential stress to yoke radial acceleration, two additional EVSs are performed on MANATEE software at 850 RPM: one EVS only with radial stress harmonics associated to radial FRFs, and one EVS only with circumferential stress harmonics associated to circumferential FRFs. The obtained acceleration FFTs are compared in Figure 5.32 with the original EVS including both stress components. Regarding the acceleration components at $2f_s$, the magnitude of yoke radial acceleration is 5.1 m/s^2 with both stress components, 4 m/s^2 only with radial stress and 2.9 m/s^2 only with circumferential stress. Therefore, the stator yoke magnitude difference between EVS with both components and EVS only including radial stress is around 21% (i.e. ≈ -1.05 dB on acceleration level and ≈ -2.1 dB on SWL level), which is the same difference as experimentally observed between radial displacement of yoke and tooth tip. Of course, the present conclusion cannot be applied to the circumferential acceleration at tooth tip since it is not only due to circumferential magnetic stress. In fact, the same way as circumferential acceleration at tooth tip contributes to yoke radial acceleration due to tooth bending motion, yoke radial acceleration reciprocally contributes to tooth circumferential acceleration, in addition to circumferential magnetic stress harmonics.

Finally, the effect of circumferential flux density on radial stress harmonics is investigated based on a last EVS, which considers only radial stress harmonics computed with the MST neglecting the circumferential flux density component (cf. (Equation 2.21)), and associated to radial FRFs. The acceleration harmonics are twice lower than those obtained with the original EVS including both stress components, as illustrated by the

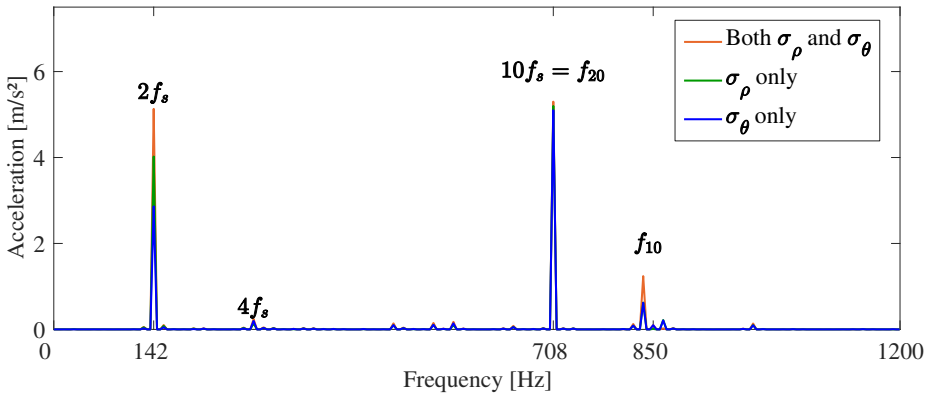

Figure 5.32 – Acceleration FFT at 850 RPM accounting for both stress components, only radial stress and only circumferential stress.

FFT comparison in Figure 5.33. It is concluded that neglecting both circumferential effects in the e-NVH study of SPMSM $12s10p$ leads to an error of -3 dB for the estimation of vibration level, and -6 dB for the estimation of SWL. In a future work, this simulation should be also validated thanks to the measurement of radial airgap flux density, which enables to deduce the radial magnetic stress, inject it in the EVS and compare the obtained acceleration FFT with the real acceleration FFT given in Figure 5.31b.

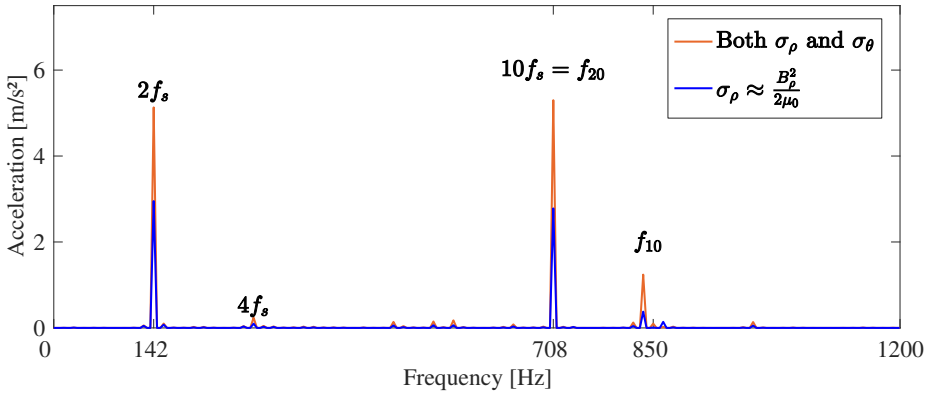

Figure 5.33 – Acceleration FFT at 850 RPM accounting for both stress components and only radial stress while neglecting circumferential flux density.

5.5.3 Analysis of slotting modulation effect

In SPMSM $12s10p$, spatial aliasing occurs for each stress harmonic whose circumferential wavenumber is greater than half the number of teeth, i.e. $|r| \geq 6$ (cf. Subsection 1.4.4). The harmonic content of radial airgap stress distribution accounting for slotting modulation effect is illustrated in Figure 5.34b, where all stress harmonics with $|r| > 6$ have been reported on stress harmonics with $|r| \leq 6$, from the slotting modulation coefficients given in Fang et al. [2018]. Stress harmonic magnitudes with and without slotting modulation effect are compared in Table 5.7.

In particular, it means that the fundamental stress harmonic $(2f_s, 10)$ is modulated by the stator teeth and is seen from the stator structure as a new stress harmonic $(2f_s, -2)$, i.e. with same frequency and wavenumber as the first slotting harmonic. Figure 5.35 represents the two original airgap stress harmonics $(2f_s, 10)$ (in dark blue) and $(2f_s, -2)$ (in dark purple), as it is also illustrated in Figure 1.20 from Fang et al. [2018]. Furthermore,

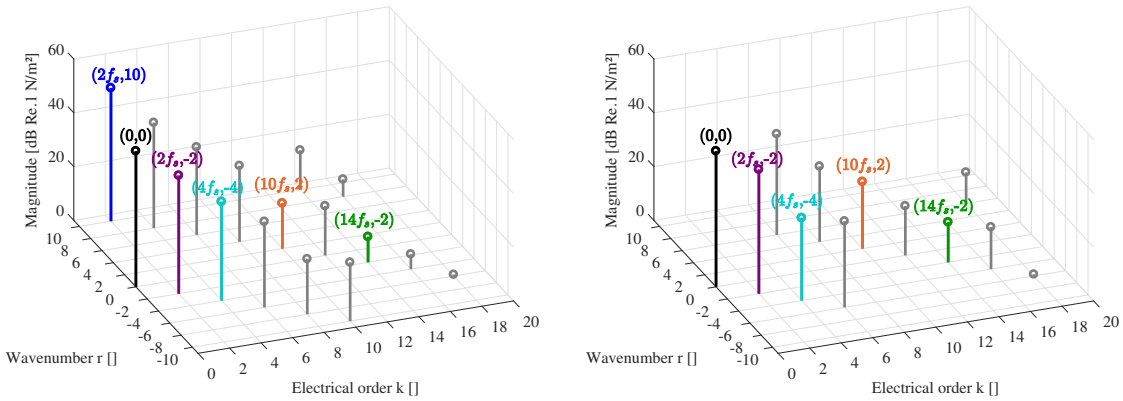

(a) Without modulation effect

(b) With modulation effect

Figure 5.34 – Time and space harmonic content of radial airgap stress with and without slotting modulation effect assuming ideal rotor magnetization.

Stress harmonic (kf_s, r)	Magnitude $10\log(\sigma_r)$ [dB Re. 1N/m^2]	
	Original	Modulated
$(2f_s, 10)$	49.5	–
$(2f_s, -2)$	43.9	46.2
$(4f_s, -4)$	36.8	30.8
$(10f_s, 2)$	16.9	24.9
$(14f_s, -2)$	9.5	15.0

Table 5.7 – Comparison of stress harmonics magnitude with and without slotting modulation effect.

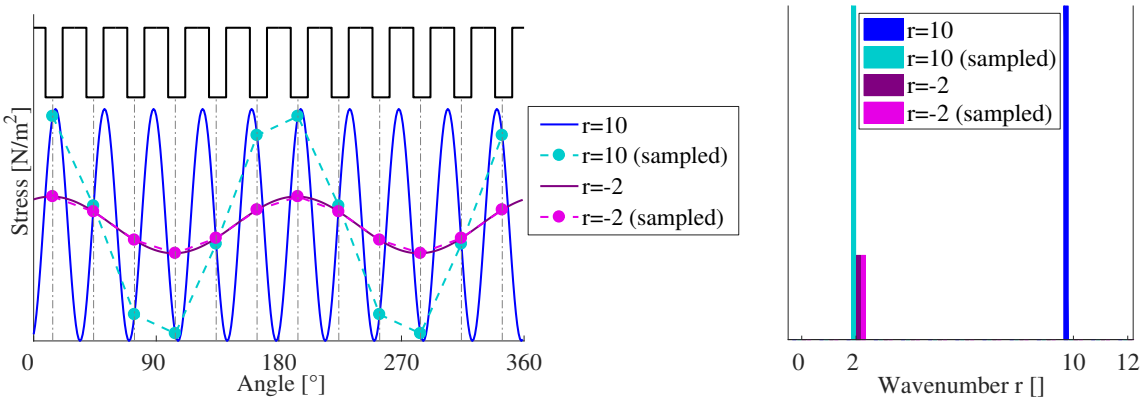

(a) Tooth sampling of stress harmonics (2f_s,-2) and (2f_s, 10)

(b) Spatial FFT

Figure 5.35 – Tooth sampling of stress harmonics (2f_s, 10) and (2f_s,-2), and spatial aliasing of (2f_s, 10) into (2f_s,-2) due to slotting modulation effect.

the airgap stress harmonics resulting from tooth sampling are represented in doted lines, respectively in light blue for sampled ($2f_s$, 10) and in magenta for ($2f_s$, -2). It can be seen that the sampled ($2f_s$, 10) has become a stress harmonic with two maxima and minima, and which rotates in the same direction as ($2f_s$, -2). Therefore, the sampled stress harmonic ($2f_s$, 10) has become a stress harmonic ($2f_s$, -2), which interferes (constructively in the present case) with the original stress slotting harmonic ($2f_s$, -2) whose magnitude increases by 2.3 dB as shown in Table 5.7, i.e. by almost 58.8%.

5.6 Conclusion

In Chapter 5, an experimental test rig has been designed to illustrate the interaction between magnetic stress harmonics and the structure of electrical machines. Practically speaking, the aim is to build a sort of noisy electrical machine whose stress harmonic origins and structural modes are well determined. The main scientific objectives are to clearly illustrate the forced and resonant responses, in particular the resonance effect with structural modes, and investigate circumferential effects, i.e. the effect of circumferential flux density on radial stress and the effect of circumferential stress on radial vibrations, and slotting modulation effects, i.e. the spatial aliasing due to teeth undersampling the magnetic stress harmonics.

The SPMSM $12s10p$ topology under open-circuit condition is particularly relevant for the test rig purpose since it creates magnetic stress harmonics due to stator slotting and rotor MMF harmonics, which are likely to excite the ovalization mode. Besides, circumferential effects are particularly strong due to the large airgap and the low number of teeth. The latter also enables to undersample the main stress harmonic due to the flux density fundamental. The SPMSM design has been performed using the Electromagnetic Vibration Synthesis (EVS) workflow in MANATEE software. The magnetic stress harmonics are computed using the semi-analytical SubDomain Method (SDM) developed in Chapter 3-4 and the Maxwell Stress Tensor (MST) in the middle of the airgap. The mechanical response is computed based on numerical Frequency Response Functions (FRFs) using structural FEA. The e-NVH design predicts at least three resonances with the ovalization mode, two at low speed (below 1000 RPM) and one at high speed (below 5000 RPM).

The design is validated with experimental measurements, including real rotor magnetization measurement, flux density in stator teeth, Experimental Modal Analysis (EMA) with roving hammer, stator yoke acceleration spectrogram and Sound Pressure Level (SPL) sonagram at variable speed (0-1300 RPM), and Operational Deflection Shapes (ODSs) of stator structure at different speeds. The experimental results show that the main acceleration harmonics and deflection shapes including the resonance with the ovalization mode under 1000 RPM are well predicted by the initial design. However, the stator bending mode is also strongly excited, due to unbalance magnetization of the Permanent Magnets (PMs) and rotor eccentricity. Furthermore, a new EVS is performed based on the experimental data, including measured magnetization, rotor eccentricity and FRFs fitted with EMA, which enables to accurately predict the overall harmonic content seen on the experimental acceleration spectrogram. Besides, the contribution of circumferential effects is measured at around 20% on the main acceleration harmonic at twice the supply frequency. The slotting modulation effect increases the magnitude of the main stress harmonic by around 58.8%, i.e. by 2.3 dB the acceleration magnitude, and by 4.6 dB the resulting SWL

In conclusion, this chapter also shows that it is very complex to build an electrical

machines only with stress harmonics predicted by the initial design. In fact, the magnetic stress harmonic content is generally much richer than expected, as least due to manufacturing tolerances. In the particular case of the designed SPMSM $12s10p$, the main stress harmonic content due to rotor MMF and stator slots can still be observed but it also contains parasitic stress harmonics due to unbalance magnetization and rotor eccentricity. The perspectives of this chapter is to build a benchmark project on e-NVH studies of electrical machines to improve the scientific comprehension on the topic, by sharing publicly all data and deeply discussing the results.

Conclusion

"Finir est souvent plus difficile que commencer."

Jack Beauregard

Synthesis

First of all, the physical process of electromagnetic noise and vibrations (e-NVH) generation in electrical machines has been deeply described and explained through a state of the art. As a consequence, a multi-physics model is required to predict the noise and vibration level of a specific topology and to include it in the design process. The multi-physics model involves a coupling between electromagnetic, structural mechanics, and acoustic models. In particular, the multi-physics model has to compute the Maxwell stress harmonics in the airgap and the structural response accounting for the interaction with structural modes. Besides, the design can also account for the main noise and vibration reduction techniques such as the optimization of pole and slot numbers and shape, skewing, current injection etc.

The main simulation complexities lies in finding the best compromise between computation time and accuracy, while including most of the stress harmonic sources in the electromagnetic simulation, and projecting the airgap stress harmonics on the mechanical structure. For these reasons, there are different simulation workflows to estimate the e-NVH of an electrical machine, such as the Electromagnetic Vibration Synthesis (EVS) used in MANATEE, the software developed by EOMYS ENGINEERING dedicated to the fast and accurate electromagnetic and vibroacoustic simulation of electrical machines [MANATEE, 2018].

The EVS computes the vibration level by summing the contribution of each Maxwell stress harmonic according to their respective mechanical Frequency Response Function (FRF). Maxwell stress harmonics are computed using the Maxwell Stress Tensor (MST) in the airgap of the machine, which requires the knowledge of the time and spatial distribution of the radial and circumferential flux densities. For this purpose, the main magnetic modeling techniques which enable to compute the airgap flux density distribution are investigated and compared.

The SubDomain Method (SDM) is chosen thanks to its general formulation in Magnetic Vector Potential (MVP), which provides a fast and accurate estimation of the flux density harmonic content in the different physical regions of the electrical machines, called "subdomains", especially in the airgap to compute the MST, but also in Permanent Magnets (PMs), slots with windings, teeth, rotor bars, yoke etc. The MVP is analytically solved based on the eigenvalue problem theory (related to functional analysis) and superposition principle, and the solution in each subdomain is obtained by solving the electromagnetic interface conditions between the different subdomains.

The developed theory can be used as a framework dedicated to the subdomain modeling of a large variety of electrical machines. Therefore, the SDM has been validated and implemented in MANATEE for various topologies including SPMSM and SCIM as illustrated in the thesis report, and also DFIM, IPMSM and WRSM (not shown in the thesis report). In particular, an original contribution is the possibility to account for finite permeability and therefore global saturation in teeth subdomains, which is validated for the particular SPMSM designed during this thesis. Another major contribution is the modeling of SCIMs accounting for induced currents in rotor bars subdomains and rotor slotting harmonics in airgap and stator slots subdomains.

Besides, the main optimization techniques to improve the computational efficiency are investigated and discussed. It is particularly shown that the SDM is very fast for the simulation of single slotted machines (such as SPMSMs), and less computationally efficient for doubly slotted machines (such as SCIMs). For the same granularity level and for all the studied topologies, the SDM is generally faster and as accurate than Finite-Element Analysis (FEA) and is therefore relevant in fast e-NVH simulations. However, pushing the SDM limits such as it has been done to include global saturation might lead to much longer models and less accurate results compared to non-linear FEA including local saturation. Besides, the SDM does not systematically replace simpler analytical models in terms of computation time versus accuracy for the estimation of Maxwell stress harmonics. A comparison example is given for the e-NVH simulation of a particular SCIM, which is as accurate and much faster performed using the 1D Permeance/MagnetoMotive Force method (PMMF) regarding experimental results. Perspectives of work concerning the SDM in general are discussed in the next section.

Finally, it has been shown in the state of the art that scientific challenges remain on the physical understanding of the interaction between Maxwell stress harmonics and slotted structures. Therefore, an experimental test rig including a particular topology of noisy machine (a SPMSM $12s10p$) and an electromagnetic and vibroacoustic instrumentation setup is designed. The test rig objectives consist in experimentally illustrating the interaction between magnetic stress harmonics and slotted structures of electrical machines, investigating the aforementioned open questions, and validating and comparing the multi-physics models used in e-NVH studies. The SPMSM $12s10p$ topology under open-circuit condition is particularly relevant for the test rig purpose since it creates magnetic stress harmonics likely to excite the ovalization mode, from the combinations of rotor MMF and stator slotting harmonics. Moreover, the circumferential effects are particularly strong and the fundamental stress is sampled by stator teeth.

The SPMSM design has been performed using MANATEE software [MANATEE, 2018], where the magnetic stress harmonics are computed using the SDM and the MST in the middle of the airgap, and the mechanical response is computed based on numerical FRFs using structural FEA. The design is validated with experimental measurements, including real rotor magnetization measurement, flux density in stator teeth, Experimental Modal Analysis (EMA), stator yoke acceleration and emitted Sound Pressure Level (SPL) at variable speed (0-1300 RPM), as well as Operational Deflection Shapes (ODSs) of stator structure at different speeds.

Experimental results show that the main acceleration harmonics and deflection shapes are well predicted by the initial design. Several ODSs have shown that the stator deflection follows the rotating excitation waveform far from resonance and follows the pulsating modal shape near and at resonance. Two questions concerning the forced and resonant responses of the machine structure have been further investigated:

1. The contribution of circumferential effects to e-NVH generation, including the contribution of the circumferential flux density on radial stress and the effect of circumferential stress on radial vibrations. The contribution of circumferential effects is measured at around 20% on the main acceleration harmonic at twice the supply frequency.
2. The resonance effects including the non-linear structural behavior at resonance and slotting modulation effect. The latter appears in slotted structures with a low number of teeth regarding the wavenumbers of the main stress harmonics. The teeth undersample these stress harmonics and create stress harmonics with low wavenumber due to spatial aliasing, which can excite structural modes with low circumferential order. The slotting modulation effect increases the magnitude of the main stress harmonic by around 58.8%, i.e. by 2.3 dB the acceleration magnitude, and by 4.6 dB the resulting SWL.

However, the magnetic stress harmonic content is much richer than expected, due to unbalance magnetization of the PMs and rotor eccentricity. This experimental study shows that it is very complex to build an electrical machine with few Maxwell stress harmonics. In the particular case of the designed SPMSM $12s10p$, the airgap stress harmonic content predicted by the SDM can still be observed but it is surrounded by parasitic harmonics due to manufacturing tolerances. Perspectives of work concerning the experimental test rig are discussed in the last section of the conclusion.

Perspectives for the subdomain modeling technique

The potential research axes concerning the subdomain modeling technique could consist in:

1. Better estimating magnetic saturation, for example by:
   - directly including it in the SDM resolution process (under investigation: Dubas and Boughrara [2017]; Roubache et al. [2018b]);
   - coupling the SDM with Magnetic Equivalent Circuit (MEC) (under investigation: Bazhar et al. [2017]; Zhang et al. [2017]);
   - coupling the SDM with FEA [Lee et al., 1991] ;
   - coupling the SDM with Complex Permeance (CP) and include saturation permeance thanks to MEC.

   and to further improve the computation of magnetic stress in presence of local saturation, in the continuity of Pile et al. [2018].
2. Solving 3D MVP or magnetic field in slotted airgap in extension of Meessen [2012] to include axial stress harmonics and better estimate skewing effects and end-effects without the multi-slice modeling assumption.
3. Solving 2D Poisson equation subject to a 2D current or magnetization distribution, i.e. depending on both radial and circumferential variables, for example to include complex winding distributions with several layers in both directions, or to consider PMs shaping in the design process.
4. Solving 2D Laplace and Poisson equations in subdomains with irregular geometry, i.e neither polar nor Cartesian geometry [Read, 1993], for example to include variable geometries of slots, teeth, pocket (in SynRMs) etc.
5. Reducing computation time in doubly slotted machines:

— by using 2D time and space complex Fourier series as it has been done for single slotted machines [Pfister et al., 2016; Hannon et al., 2014]. The 2D complex Fourier series would also enable to estimate the induced currents in the conductive subdomains without relying on the current sheet modeling technique.

— by coupling the SDM with CP, for example in SCIMs to compute stator and rotor complex permeances and multiply it with the slotless airgap flux density (as investigated during this thesis (not shown in the thesis report), and initially developed by Zhu et al. [2010a] for SPMSMs).

6. Validating other topologies such as concentrated winding IMs or brushless DFIMs where there are high e-NVH challenges, and by using the subdomain methodology developed in this thesis.
7. Automatically determining harmonic numbers depending on machine topology, as discussed in Subsection 4.2.3.2, and generalize it to eigenvalue problems in radial directions.
8. Extending the strong coupling with an Electric Equivalent Circuit (EEC) for SMs and IMs in the continuity of Sprangers et al. [2014b]; Hannon et al. [2015].

Perspectives for the test rig

The experimental measurements illustrated in the thesis report have been mainly focused on validating the SPMSM $12s10p$ design, in order to show that the test rig can illustrate and investigate the scientific challenges related to e-NVH studies. The main objective of the test rig consists in creating a benchmark project to improve the scientific comprehension on the topic, by sharing publicly all data and deeply discussing the results [Devillers et al., 2018b]. The benchmark project is based on a measurement and simulation campaign, which is detailed here according to the list of objectives given in Subsection 5.1.2.1:

1. Show that the main noise and vibration level emitted by the test rig comes from the electromagnetic excitation: Operational Transfer Path Analysis (OTPA) and acoustic intensimetry for the whole test rig in (semi-)anechoic chamber.
2. Clearly illustrate e-NVH generation process, in particular the contribution of forced and resonant responses, and focusing on the resonance condition: run-up on the full speed range 0-5000 RPM to resonate with the fundamental stress component, acceleration spectrogram, Sound Pressure Level (SPL) and Sound Power Level (SWL) sonagram, Operational Deflection Shape (ODS).
3. Investigate the remaining scientific challenges in the e-NVH understanding:
   — The contribution of circumferential flux density to radial stress harmonics: airgap radial flux density measurement using the airgap flux sensor.
   — The contribution of circumferential stress to radial vibrations: noise and vibration level on stator teeth and yoke in comparison with simulation, in the continuity of Subsection 5.5.2.
   — The contribution of slotting modulation effect to radial vibrations in presence of spatial aliasing: ODS, noise and vibration level comparison with simulation.
   — The contribution of magnetostriction to radial vibrations: not determined yet.

— The contribution of torque pulsations to structure-borne noise: torque and speed ripple measurement, OTPA.

4. Investigate noise and vibrations mitigation techniques, such as:
   — Low-noise design rules, e.g. the GCD rule between teeth number and pole pairs number in PMSMs: change both stator and rotor topologies and redo e-NVH measurements.
   — Passive techniques: replace stator and/or rotor by a stator and/or rotor with skew, notches, magnetic wedges, etc. and redo e-NVH measurements.
   — Active techniques, in particular harmonic current injection: wind the stator teeth and redo e-NVH measurements with a given injected current.

Both simulation and experimental results are produced in a normalized format that can be largely shared and reused by others for future research: several publications including a data publication to make data available to everyone. The webpage dedicated to the benchmark project can be found on EOMYS website [Eomys Engineering, 2018].

Bibliography

Ackermann, B. and Sottek, R. (1995). Analytical modeling of the cogging torque in permanent magnet motors. *Electrical Engineering*, 78(2):117–125. 62, 123

Al-Nuaim, N. A. and Toliyat, H. A. (1998). A novel method for modeling dynamic air-gap eccentricity in synchronous machines based on modified winding function theory. *IEEE Transactions on Energy Conversion*, 13(2):156–162. 55

Alam, F. R. and Abbaszadeh, K. (2016). Magnetic Field Analysis in Eccentric Surface-Mounted Permanent-Magnet Motors Using an Improved Conformal Mapping Method. *IEEE Transactions on Energy Conversion*, 31(1):333–344. 59

Alger, P. L. (1953). The Acoustic Behavior of Induction Motors. *Journal of the Acoustical Society of America*, 25(4). 8, 25, 28, 30, 31, 33, 34, 49, 72

Altair (2018). OptiStruct. *www.altairhyperworks.com/product/OptiStruct*. 171, 183, 197

Amabili, M., Balasubramanian, P., and Ferrari, G. (2016). Travelling wave and non-stationary response in nonlinear vibrations of water-filled circular cylindrical shells: Experiments and simulations. *Journal of Sound and Vibration*, 381:220–245. 33

Ansys (2018). Maxwell 2D v18. 139, 141, 154, 162, 187

Azar, Z., Zhu, Z. Q., and Ombach, G. (2012). Influence of Electric Loading and Magnetic Saturation on Cogging Torque, Back-EMF and Torque Ripple of PM Machines. *IEEE Transactions on Magnetics*, 48(10):2650–2658. 40

Bali, H., Amara, Y., Barakat, G., Ibtiouen, R., and Gabsi, M. (2010). Analytical Modeling of Open Circuit Magnetic Field in Wound Field and Series Double Excitation Synchronous Machines. *IEEE Transactions on Magnetics*, 46(10):3802–3815. 63

Barre, O. (2003). *Contribution à l'étude des formulations de calcul de la force magnétique en magnétostatique, approche numérique et validation expérimentale*. PhD thesis, Ecole Centrale de Lille et Université des Sciences et Technologies de Lille. 70

Bauw, G., Balavoine, F., Cassoret, B., Ninet, O., and Romary, R. (2017). Damper winding for noise and vibration reduction of PWM-fed induction machines. In *2017 IEEE International Electric Machines and Drives Conference (IEMDC)*, pages 1–6. IEEE. 41

Bazhar, S., Fontchastagner, J., Takorabet, N., and Labbe, N. (2017). Hybrid Analytical Model Coupling Laplace's Equation and Reluctance Network for Electrical Machines. *IEEE Transactions on Magnetics*, 53(6):1–4. 69, 210

Bekemans, M. (2006). *Modélisation des machines électriques en vue du contrôle des efforts radiaux*. PhD thesis, Université Catholique de Louvain. 24, 42, 229

Bellara, A., Amara, Y., Barakat, G., and Dakyo, B. (2009). Two-Dimensional exact analytical solution of armature reaction field in slotted surface mounted PM radial flux synchronous machines. *IEEE Transactions on Magnetics*, 45(10):4534–4538. 62

Benlamine, R., Hamiti, T., Vangraefschepe, F., Dubas, F., and Lhotellier, D. (2016). Modeling of a coaxial magnetic gear equipped with surface mounted PMs using nonlinear adaptive magnetic equivalent circuits. In *2016 XXII International Conference on Electrical Machines (ICEM)*, pages 1888–1894. IEEE. 66, 67

Blum, J., Merwerth, J., and Herzog, H.-G. (2014). Investigation of the segment order in step-skewed synchronous machines on noise and vibration. In *2014 4th International Electric Drives Production Conference (EDPC)*, pages 1–6. IEEE. 23, 35, 39, 40

Boesing, M. (2013). *Noise and Vibration Synthesis based on Force Response Superposition*. PhD thesis, Fakultät für Elektrotechnik und Informationstechnik der Rheinisch-Westfälischen Technischen Hochschule Aachen. 29, 34, 41, 45, 47, 49, 68, 71, 72, 74, 76, 77, 78

Boesing, M., Callan-Bartkiw, B., Kotter, P., Zirn, O., Berkemer, J., and Wegener, K. (2016). Noise-Vibration-Harshness simulation of ultralight vehicle traction drives based on a universal modelling approach. In *8th IET International Conference on Power Electronics, Machines and Drives (PEMD 2016)*, number 2, pages 6 .–6 . Institution of Engineering and Technology. 78

Boisson, J. (2014). *Modélisation analytique magnéto-accoustique des machines synchrones à commutation de flux à aimants permanents - optimisation du dimensionnement*. PhD thesis, ENS Cachan. 66

Boisson, J., Louf, F., Ojeda, J., Mininger, X., and Gabsi, M. (2014). Low Computational-cost determination of Vibrational Behavior: Application to Five-phase Flux-Switching Permanent-Magnet Motor. *IEEE Transactions on Magnetics*, PP(99):1–1. 37

Bolognani, S. (1999). Random modulation and acoustic noise reduction in IM drives: a case study. In *9th International Conference on Electrical Machines and Drives*, volume 1999, pages 137–141, Canterbury, UK. IEE. 41

Bolte, E. (1979). *Three-dimensional calculation of the asynchronous sector motor with solid iron rotor*. PhD thesis, University of Dortmund. 56

Bolte, E. (1984). Analytical calculation of the two-dimensional field in the air gap and the slots of electrical machines. *IEEE Transactions on Magnetics*, 20(5):1783–1785. 62

Bonneel, P., Le Besnerais, J., Pile, R., and Devillers, E. (2018). Pyleecan: An Open-Source Python Object-Oriented Software for the Multiphysic Design Optimization of Electrical Machines. *2018 XIII International Conference on Electrical Machines (ICEM)*, pages 948–954. 173

Bossavit, A. (2011). Virtual power principle and Maxwell's tensor: which comes first? *COMPEL - The international journal for computation and mathematics in electrical and electronic engineering*, 30(6):1804–1814. 70, 73

Bossio, G., DeAngelo, C., Solsona, J., Garcia, G., and Valla, M. (2004). A 2-D Model of the Induction Machine: An Extension of the Modified Winding Function Approach. *IEEE Transactions on Energy Conversion*, 19(1):144–150. 55

Boughrara, K., Chikouche, B. B. L., Ibtiouen, R., Zarko, D., and Touhami, O. (2009). Analytical Model of Slotted Air-Gap Surface Mounted Permanent-Magnet Synchronous Motor With Magnet Bars Magnetized in the Shifting Direction. *IEEE Transactions on Magnetics*, 45(2):747–758. 59, 60

Boughrara, K., Dubas, F., and Ibtiouen, R. (2014). 2-D Analytical Prediction of Eddy Currents, Circuit Model Parameters, and Steady-State Performances in Solid Rotor Induction Motors. *IEEE Transactions on Magnetics*, 50(12):1–14. 64, 83, 113, 114

Boughrara, K., Ibtiouen, R., and Lubin, T. (2012). Analytical prediction of magnetic field in parallel double excitation and spoke-type permanent-magnet machines accounting for tooth-tips and shape of polar pieces. *IEEE Transactions on Magnetics*, 48(7):2121–2137. 63

Boughrara, K., Lubin, T., and Ibtiouen, R. (2013). General Subdomain Model for Predicting Magnetic Field in Internal and External Rotor Multiphase Flux-Switching Machines Topologies. *IEEE Transactions on Magnetics*, 49(10):5310–5325. 63

Boughrara, K., Takorabet, N., Ibtiouen, R., Touhami, O., and Dubas, F. (2015). Analytical Analysis of Cage Rotor Induction Motors in Healthy, Defective, and Broken Bars Conditions. *IEEE Transactions on Magnetics*, 51(2):1–17. 52, 63, 121, 130, 149, 151, 152, 154, 163, 164

Boules, N. (1984). Two-Dimensional Field Analysis of Cylindrical Machines with Permanent Magnet Excitation. *IEEE Transactions on Industry Applications*, IA-20(5):1267–1277. 56, 69

Bracikowski, N. (2012). *Modélisation multi-physique par modèles à constantes localisées ; application à une machine synchrone à aimants permanents en vue de son dimensionnement.* PhD thesis, Ecole Centrale de Lille. 46

Bracikowski, N., Hecquet, M., Brochet, P., and Shirinskii, S. V. (2012). Multiphysics modeling of a permanent magnet synchronous machine by using lumped models. *IEEE Transactions on Industrial Electronics*, 59(6):2426–2437. 66, 67, 68

Braunisch, D., Ponick, B., and Bramerdorfer, G. (2013). Combined Analytical–Numerical Noise Calculation of Electrical Machines Considering Nonsinusoidal Mode Shapes. *IEEE Transactions on Magnetics*, 49(4):1407–1415. 30

Brudny, J. F. (1997). Modélisation de la denture des machines asynchrones : phénomènes de résonances. *Journal of Physics III*, 37(7):1009–1023. 54

Carter, F. (1926). The magnetic field of the dynamo-electric machine. *Journal of the Institution of Electrical Engineers*, 64(359):1115–1138. 58

Cassoret, B., Corton, R., Roger, D., and Brudny, J.-F. (2003). Magnetic noise reduction of induction machines. *IEEE Transactions on Power Electronics*, 18(2):570–579. 41

Climente-Alarcon, V., Arkkio, A., and Antonino-Daviu, J. (2018). 2-D Magnetomechanical Transient Study of a Motor Suffering a Bar Breakage. *IEEE Transactions on Industry Applications*, 9994(c):1–1. 49

Coulomb, J.-L. and Meunier, G. (1984). Finite element implementation of virtual work principle for magnetic or electric force and torque computation. *IEEE Transactions on Magnetics*, 20(5):1894–1896. 70, 73

Curti, M., Paulides, J. J. H., and Lomonova, E. A. (2017). Magnetic Modeling of a Linear Synchronous Machine with the Spectral Element Method. *IEEE Transactions on Magnetics*, 9464(c):1–1. 68

Dajaku, G. and Gerling, D. (2009). Magnetic Radial Force Density of the PM Machine with 12-teeth / 10-poles Winding Topolog y. *2009 IEEE International Electric Machines and Drives Conference, IEMDC '09*, pages 1715–1720. 20, 34

Dajaku, G. and Gerling, D. (2012). A novel 12-teeth/10-poles PM machine with flux barriers in stator yoke. In *2012 XXth International Conference on Electrical Machines*, pages 36–40. IEEE. 41

Dalal, A., Nekkalapu, S., and Kumar, P. (2016). 2-D Analytical Subdomain Model for Hybrid Dual-Rotor Motor. *IEEE Transactions on Magnetics*, 52(6). 64

De La Barrière, O., Hlioui, S., Ben Ahmed, H., Gabsi, M., and LoBue, M. (2012). 3-D formal resolution of maxwell equations for the computation of the no-load flux in an axial flux permanent-magnet synchronous machine. *IEEE Transactions on Magnetics*, 48(1):128–136. 55, 56

De Madinabeitia, I. G. (2016). *Analysis of Force and Torque Harmonic Spectrum in an Induction Machine for Automotive NVH Purposes.* PhD thesis, Chalmers University of Technology. 29, 30

Delaere, K., Belmans, R., and Hameyer, K. (2003). Influence of rotor slot wedges on stator currents and stator vibration spectrum of induction machines: A transient finite-element analysis. *IEEE Transactions on Magnetics*, 39(3 I):1492–1494. 40

Despret, G., Iamamura, B., Hecquet, M., Lanfranchi, V., and Randria, A. (2016). Imperfect skew impact on the vibration of the traction induction motor. *International Symposium on Electromagnetic Fields*, pages 3–8. 40

Devillers, E., Despret, G., Hecquet, M., Le Besnerais, J., Lubin, T., and Lecointe, J.-P. (2018a). Approche « sous-domaine vs perméance analytique » en vue d'estimer le contenu spatio-temporel des harmoniques de forces radiales d'une machine asynchrone. In *SGE 2018 Symposium de Génie Electrique*, Nancy. 121, 166, 252

Devillers, E., Hecquet, M., Cimetière, X., Lecointe, J.-P., Besnerais, J. L., and Lubin, T. (2018b). Experimental Benchmark for Magnetic Noise and Vibrations Analysis in Electrical Machines. In *2018 XIII International Conference on Electrical Machines (ICEM)*, pages 745–751, Alexandropolis. IEEE. 172, 211

Devillers, E., Hecquet, M., and Le Besnerais, J. (2017a). A new hybrid method for the fast computation of airgap flux and magnetic forces in IPMSM. In *2017 Twelfth International Conference on Ecological Vehicles and Renewable Energies (EVER)*, pages 1–8. 83, 108, 251

Devillers, E., Hecquet, M., Le Besnerais, J., and Régniez, M. (2017b). Tangential effects on magnetic vibrations and acoustic noise of induction machines using subdomain method and electromagnetic vibration synthesis. In *2017 IEEE International Electric Machines and Drives Conference (IEMDC)*, pages 1–8, Miami. IEEE. 35, 121, 167, 252

Devillers, E., Le Besnerais, J., Lubin, T., Hecquet, M., and Lecointe, J.-P. (2016). A review of subdomain modeling techniques in electrical machines: Performances and applications. In *2016 XXII International Conference on Electrical Machines (ICEM)*, pages 86–92, Lausanne. IEEE. 120

Devillers, E., Le Besnerais, J., Lubin, T., Hecquet, M., and Lecointe, J.-P. (2018c). An Improved 2-D Subdomain Model of Squirrel-Cage Induction Machine Including Winding and Slotting Harmonics at Steady State. *IEEE Transactions on Magnetics*, pages 1–12. 121, 149, 153, 252

Djelloul-Khedda, Z., Boughrara, K., Dubas, F., and Ibtiouen, R. (2017). Nonlinear Analytical Prediction of Magnetic Field and Electromagnetic Performances in Switched Reluctance Machines. *IEEE Transactions on Magnetics*, 53(7):1–11. 63

Doherty, R. E. and Nickle, C. A. (1926). Synchronous machines I-an extension of blondel's two-reaction theory. *Transactions of the American Institute of Electrical Engineers*, XLV:912–947. 54, 55, 56, 69

Dorrell, D. G. (2011). Sources and Characteristics of Unbalanced Magnetic Pull in Three-Phase Cage Induction Motors With Axial-Varying Rotor Eccentricity. *IEEE Transactions on Industry Applications*, 47(1):12–24. 23, 26

dos Santos, F. L. M., Anthonis, J., Naclerio, F., Gyselinck, J. J. C., Van der Auweraer, H., and Goes, L. C. S. (2014). Multiphysics NVH Modeling: Simulation of a Switched Reluctance Motor for an Electric Vehicle. *IEEE Transactions on Industrial Electronics*, 61(1):469–476. 21, 23, 46

Dubas, F. and Boughrara, K. (2017). New Scientific Contribution on the 2-D Subdomain Technique in Polar Coordinates: Taking into Account of Iron Parts. *Mathematical and Computational Applications*, 22(4):42. 61, 64, 66, 69, 93, 210

Dubas, F. and Espanet, C. (2009). Analytical Solution of the Magnetic Field in Permanent-Magnet Motors Taking Into Account Slotting Effect : No-Load Vector Potential and Flux Density Calculation. *IEEE Transactions on Magnetics*, 45(5):2097–2109. 55, 62

Ede, J., Zhu, Z., and Howe, D. (2002). Rotor resonances of high-speed permanent-magnet brushless machines. *IEEE Transactions on Industry Applications*, 38(6):1542–1548. 35

Eklund, P. and Eriksson, S. (2016). Air gap magnetic flux density variations due to manufacturing tolerances in a permanent magnet synchronous generator. In *2016 XXII International Conference on Electrical Machines (ICEM)*, pages 93–99. IEEE. 21

Ellison, A. J. and Moore, C. J. (1968). Acoustic noise and vibration of rotating electric machines. *Proceedings of the Institution of Electrical Engineers*, 115(11):1633–1640. 36

Encica, L., Echeverría, D., Lomonova, E. A., Vandenput, A. J. A., Hemker, P. W., and Lahaye, D. (2007). Efficient optimal design of electromagnetic actuators using space mapping. *Structural and Multidisciplinary Optimization*, 33(6):481–491. 49

Eomys Engineering (2017). Videos on electromagnetically-excited noise and vibrations. *https://eomys.com/e-nvh/article/videos-on-electromagnetically-excited-noise-and-vibrations?lang=en*. 14, 15

Eomys Engineering (2018). e-NVH benchmark. *https://www.eomys.com/recherche/article/e-nvh-benchmark*. 212

Fahy, F. and Gardonio, P. (2007). *Sound and Structural Vibration*. Elsevier. 36

Faiz, J. and Ghasemi-Bijan, M. (2015). Estimation of induction machine inductances using three-dimensional magnetic equivalent circuit. *IET Electric Power Applications*, 9(2):117–127. 67

Fakam, M., Hecquet, M., Lanfranchi, V., and Randria, A. (2013). Interaction between FE analysis and analytical approach in order to reduce the magnetic noise produced by a SPMSM. *International Symposium on Electromagnetic Fields*, (July). 69

Fakam, M., Hecquet, M., Lanfranchi, V., and Randria, A. (2015). Design and Magnetic Noise Reduction of the Surface Permanent Magnet Synchronous Machine Using Complex Air-Gap Permeance. *IEEE Transactions on Magnetics*, 51(4):1–9. 60

Fang, H., Li, D., Qu, R., and Yan, P. (2018). Modulation Effect of Slotted Structure on Vibration Response in Electrical Machines machine. *Transactions on Industrial Electronics*, PP(c):1–1. 33, 34, 204

FEMM (2018). David Meeker. *http://www.femm.info/wiki/HomePage*. 46, 146, 165

Franck, D., Van Der Giet, M., Hameyer, K., Giet, M. V. D., and Hameyer, K. (2011). Active reduction of audible noise exciting radial force-density waves in induction motors. *2011 IEEE International Electric Machines and Drives Conference (IEMDC)*, pages 1213–1218. 41

Frauman, P., Burakov, A., and Arkkio, A. (2007). Effects of the Slot Harmonics on the Unbalanced Magnetic Pull in an Induction Motor With an Eccentric Rotor. *IEEE Transactions on Magnetics*, 43(8):3441–3444. 21

Fu, J. and Zhu, C. (2012). Subdomain Model for Predicting Magnetic Field in Slotted Surface Mounted Permanent-Magnet Machines With Rotor Eccentricity. *IEEE Transactions on Magnetics*, 48(5):1906–1917. 65

Garvey, S. and Le Flem, G. D. (1999). Tangential forces matter. In *9th International Conference on Electrical Machines and Drives*, number 468, pages 174–178. 24, 29

Gaussens, B., Hoang, E., de la Barriere, O., Saint-Michel, J., Lécrivain, M., and Gabsi, M. (2012). Analytical Approach for Air-Gap Modeling of Field-Excited Flux-Switching Machine: No-Load Operation. *IEEE Transactions on Magnetics*, 48(9):2505–2517. 54, 55

Gaussens, B., Hoang, E., De La Barriére, O., Saint-Michel, J., Manfe, P., Lécrivain, M., and Gabsi, M. (2013a). Analytical armature reaction field prediction in field-excited flux-switching machines using an exact relative permeance function. *IEEE Transactions on Magnetics*, 49(1):628–641. 69

Gaussens, B., Hoang, E., de la Barriere, O., Saint-Michel, J., Manfe, P., Lécrivain, M., and Gabsi, M. (2013b). Uni- and Bidirectional Flux Variation Loci Method for Analytical Prediction of Iron Losses in Doubly-Salient Field-Excited Switched-Flux Machines. *IEEE Transactions on Magnetics*, 49(7):4100–4103. 62, 63

Gerling, D. and Dajaku, G. (2003). Three-dimensional analytical calculation of induction machines with multilayer rotor structure in cylindrical coordinates. *Electrical Engineering*, 86(4):199–211. 55, 56, 105

Ghoizad, H., Mirsalim, M., Mirzayee, M., and Cheng, W. (2007). Coupled magnetic equivalent circuits and the analytical solution in the air-gap of squirrel cage induction machines. *International Journal of Applied Electromagnetics and Mechanics*, 25(1-4):749–754. 69

Gieras, J. F., Wang, C., and Lai, J. C. (2006). *Noise of polyphase electric motors*. CRC Press. 8, 24, 28, 29, 33, 37, 49, 75, 78, 231

Gilson, A., Verez, G., Dubas, F., Depernet, D., and Espanet, C. (2017). Design of a high-speed permanent-magnet machine for electrically-assisted turbocharger applications with reduced noise emissions. In *2017 IEEE International Electric Machines and Drives Conference (IEMDC)*, pages 1–6. IEEE. 30

Giust, A. (2016). *The Harmonic Balance method for the solution of nonlinear circuit and field problems with harmonic sources and its integration with a commercial simulation software*. PhD thesis, University of Padova. 49

Guldemir, H. (1999). Illustration of rotor pole aliasing effect in induction motor line current spectrum. In *International Conference on Electrical and Electronics Engineering*. 23

Gyselinck, J. and Sabariego, R. V. (2013). Airgap reluctance identification for the magnetic equivalent circuit modelling of induction machines. pages 4–5. 68

Gysen, B. L. J. (2011). *Generalized harmonic modeling technique for 2D electromagnetic problems*. PhD thesis, TU Eindhoven. 61, 63, 65, 132

Gysen, B. L. J., Meessen, K. J., Paulides, J. J. H., and Lomonova, E. A. (2008). Semi-Analytical Calculation of the Armature Reaction in Slotted Tubular Permanent Magnet Actuators. *IEEE Transactions on Magnetics*, 44(11):3213–3216. 62

Gysen, B. L. J., Meessen, K. J., Paulides, J. J. H., and Lomonova, E. A. (2010). General Formulation of the Electromagnetic Field Distribution in Machines and Devices Using Fourier Analysis. *Magnetics, IEEE Transactions on*, 46(1):39–52. 49, 51, 55, 56, 61, 62, 64

Hague, B. (1929). *Electromagnetic Problems in Electrical Engineering*. Oxford University Press, London. 55, 56

Hallal, J. (2014). *Études Des Vibrations D'Origine Électromagnétique D'Une Machine Électrique : Conception Optimisée Et Variabilité Du Comportement Vibratoire*. PhD thesis, Université de Technologie de Compiègne (UTC). 50, 51

Hameyer, K., Driesen, J., Gersem, H. D., and Belmans, R. (1999). The classification of coupled field problems. *IEEE Transactions on Magnetics*, 35(3):1618–1621. 46, 53

Hanic, A., Zarko, D., and Hanic, Z. (2016). A Novel Method for No-Load Magnetic Field Analysis of Saturated Surface Permanent-Magnet Machines Using Conformal Mapping and Magnetic Equivalent Circuits. *IEEE Transactions on Energy Conversion*, 31(2):740–749. 69

Hannon, B., Sergeant, P., and Dupré, L. (2014). 2-D Analytical Subdomain Model of a Slotted PMSM With Shielding Cylinder. *IEEE Transactions on Magnetics*, 50(7):1–10. 211

Hannon, B., Sergeant, P., and Dupré, L. (2015). Voltage Sources in 2D Fourier-Based Analytical Models of Electric Machines. *Mathematical Problems in Engineering*, 2015:1–8. 49, 64, 211

Hannon, B., Sergeant, P., and Dupré, L. (2016). Time- and Spatial-Harmonic Content in Synchronous Electrical Machines. *IEEE Transactions on Magnetics*, 9464(c):1–1. 20, 131

Hannon, B., Sergeant, P., and Dupré, L. (2018). Computational-Time Reduction of Fourier-Based Analytical Models. *IEEE Transactions on Energy Conversion*, 33(1):281–289. 134, 135

Heller, B. and Jokl, A. (1969). Tangential Forces in Squirrel-Cage Induction Motors. *IEEE Transactions on Power Apparatus and Systems*, PAS-88(4):484–492. 38

Henneron, T. and Clenet, S. (2014). Model Order Reduction of Non-Linear Magnetostatic Problems Based on POD and DEI Methods. *IEEE Transactions on Magnetics*, 50(2):33–36. 68

Henrotte, F. and Hameyer, K. (2004). Computation of electromagnetic force densities: Maxwell stress tensor vs. virtual work principle. *Journal of Computational and Applied Mathematics*, 168(1-2):235–243. 70

Herman, R. L. (2013). *A Course in Mathematical Methods for Physicists*. CRC Press, 1st editio edition. 92, 96, 233

Hoang, K., Vido, L., Gabsi, M., and Gillon, F. (2014). 3D modeling of double excitation synchronous motor with reluctance network. In *2014 International Conference on Electrical Machines (ICEM)*, pages 2598–2604. IEEE. 67

Hofmann, A., Qi, F., Lange, T., and De Doncker, R. W. (2014). The breathing mode-shape 0: Is it the main acoustic issue in the PMSMs of today's electric vehicles? In *2014 17th International Conference on Electrical Machines and Systems (ICEMS)*, pages 3067–3073. IEEE. 35, 38

Hubert, A. (2001). *Contribution à l'étude des bruits acoustiques générés lors de l'association machines électriques-convertisseurs statiques de puissance. Application à la machine asynchrone*. PhD thesis, Université Technologique de Compiègne. 55

Humbert, L., Pellerey, P., and Cristaudo, S. (2012). Electromagnetic and Structural Coupled Simulation to Investigate NVH Behavior of an Electrical Automotive Powertrain. *SAE International Journal of Alternative Powertrains*, 1(2):2012–01–1523. 29

IEC61672-1 (2013). Electroacoustics - Sound level meters - Part 1: Specifications. 7, 37

Imhoff, J. F., Reyne, G., Foggia, A., and Sabonnadière, J. C. (1990). Modélisation des phénomènes électromagnétiques et mécaniques couples : application à l'analyse vibratoire des machines électriques. *Revue de Physique Appliquée*, 25(7):627–648. 46, 229

Joksimovic, G., Riger, J., Wolbank, T., Peric, N., and Vasak, M. (2011). Stator line current spectrum content of a healthy cage rotor induction machine. In *8th IEEE Symposium on Diagnostics for Electrical Machines, Power Electronics and Drives*, number October 2011, pages 113–118. IEEE. 23

Joksimović, G. M., Durovic, M. D., and Obradović, A. B. (1999). Skew and linear rise of MMF across slot modelling-winding function approach. *IEEE Transactions on Energy Conversion*, 14(3):315–320. 161

Jordan, H. (1950). *Electric motor silencer-formation and elimination of the noises in the electric motors*. W.Giradet-Essen. 8, 33, 34, 49, 72, 230

Jumayev, S., Boynov, K. O., Paulides, J. J., Lomonova, E. A., and Pyrhonen, J. (2016). Slotless PM Machines with Skewed Winding Shapes: 3-D Electromagnetic Semianalytical Model. *IEEE Transactions on Magnetics*, 52(11). 56

Kang, C. H., Kang, K. J., Song, J. Y., Cho, Y. J., and Jang, G. H. (2017). Axial Unbalanced Magnetic Force in a Permanent Magnet Motor due to a Skewed Magnet and Rotor Eccentricities. *IEEE Transactions on Magnetics*, 9464(c):1–1. 26, 29, 35, 39

Kemmetmuller, W., Faustner, D., and Kugi, A. (2014). Modeling of a permanent magnet synchronous machine with internal magnets using magnetic equivalent circuits. *IEEE Transactions on Magnetics*, 50(6):1–1. 66

Kim, J. Y., Sung, S. J., and Jang, G. H. (2012). Characterization and experimental verification of the axial unbalanced magnetic force in brushless DC motors. *IEEE Transactions on Magnetics*, 48(11):3001–3004. 26

Korecki, J. (2009). *Contribution à la modélisation 3D des systèmes életromagnétiques basse fréquence à l'aide de la méthode d'intégration finie (FIT)*. PhD thesis, Université de Lille 1. 68

Kron, G. (1931). Induction Motor Slot Combinations Rules to Predetermine Crawling, Vibration, Noise and Hooks in the Speed-Torque Curve. *Transactions of the American Institute of Electrical Engineers*, 50(2):757–767. 38

Kurihara, N., Chiba, A., Yamada, K., and Souda, A. (2015). A relationship of radial force sum and current waveforms in switched reluctance motor for noise reduction. In *2015 IEEE Energy Conversion Congress and Exposition (ECCE)*, pages 5560–5566. IEEE. 42

Kuroishi, M. and Saito, A. (2018). Effects of Magnetostriction on Electromagnetic Motor Vibration at Sideband Frequencies. *IEEE Transactions on Magnetics*, pages 1–8. 24

La Delfa, P., Fakam, M., Hecquet, M., and Gillon, F. (2016). Low Space Order Analysis of Radial Pressure in SPMSM With Analytical and Convolution Approaches. *IEEE Transactions on Magnetics*, 52(11):1–7. 28, 240

Låftman, L. (1998). Magnetostriction and its contribution to noise in a PWM inverter fed induction machine. *Le Journal de Physique IV*, 08(PR2):Pr2–567–Pr2–570. 24

Lam, K. and Loy, C. (1995). Effects of boundary conditions on frequencies of a multi-layered cylindrical shell. *Journal of Sound and Vibration*, 188(3):363–384. 31

Lan, H., Chen, Q., Zou, J., Xu, Y., Wang, M., and Liu, M. (2017). Influence of dummy slots on noise and vibration performance in permanent magnet synchronous machines. In *2017 IEEE Transportation Electrification Conference and Expo, Asia-Pacific (ITEC Asia-Pacific)*, pages 1–6. IEEE. 40

Le Besnerais, J. (2008). *Reduction of magnetic noise in PWM - supplied induction machines - low-noise design rules and multi-objective optimisation.* PhD thesis, Ecole Centrale de Lille. 33, 37, 38, 71, 78

Le Besnerais, J. (2015a). Effect of lamination asymmetries on magnetic vibrations and acoustic noise in synchronous machines. In *2015 18th International Conference on Electrical Machines and Systems (ICEMS)*, volume 48, pages 1729–1733. IEEE. 21

Le Besnerais, J. (2015b). Vibroacoustic Analysis of Radial and Tangential Air-Gap Magnetic Forces in Permanent Magnet Synchronous Machines. *IEEE Transactions on Magnetics*, 51(6):1–9. 26, 29

Le Besnerais, J. (2016). Fast prediction of variable-speed acoustic noise due to magnetic forces in electrical machines. In *2016 XXII International Conference on Electrical Machines (ICEM)*, pages 2259–2265, Lausanne. IEEE. 50, 53

Le Besnerais, J., Lanfranchi, V., Hecquet, M., and Brochet, P. (2009a). Optimal Slot Numbers for Magnetic Noise Reduction in Variable-Speed Induction Motors. *IEEE Transactions on Magnetics*, 45(8):3131–3136. 7, 38

Le Besnerais, J., Lanfranchi, V., Hecquet, M., and Brochet, P. (2010a). Characterization and Reduction of Audible Magnetic Noise Due to PWM Supply in Induction Machines. *IEEE Transactions on Industrial Electronics*, 57(4):1288–1295. 21, 38

Le Besnerais, J., Lanfranchi, V., Hecquet, M., and Brochet, P. (2013a). Bruit audible d'origine magnétique des machines asynchrones. *Techniques de l'Ingénieur*, D3580(2). 20, 28

Le Besnerais, J., Lanfranchi, V., Hecquet, M., Brochet, P., and Friedrich, G. (2010b). Prediction of Audible Magnetic Noise Radiated by Adjustable-Speed Drive Induction Machines. *IEEE Transactions on Industry Applications*, 46(4):1367–1373. 230

Le Besnerais, J., Lanfranchi, V., Hecquet, M., Lemaire, G., Augis, E., and Brochet, P. (2009b). Characterization and Reduction of Magnetic Noise Due to Saturation in Induction Machines. *IEEE Transactions on Magnetics*, 45(4):2003–2008. 21

Le Besnerais, J., Lanfranchi, V., Hecquet, M., Romary, R., and Brochet, P. (2009c). Optimal slot opening width for magnetic noise reduction in induction motors. *IEEE Trans. on En. Conv.*, 24(4):869–874. 39

Le Besnerais, J., Pellerey, P., Lanfranchi, V., and Hecquet, M. (2013b). Bruit audible d'origine magnétique dans les machines synchrones. *Techniques de l'Ingénieur*, D3581(1). 20, 28, 29

Le Besnerais, J. and Souron, Q. (2016). Effect of magnetic wedges on electromagnetically-induced acoustic noise and vibrations of electrical machines. In *2016 XXII International Conference on Electrical Machines (ICEM)*, pages 2217–2222. IEEE. 41

Lee, K., DeBortoli, M., Lee, M., and Salon, S. (1991). Coupling finite elements and analytical solution in the airgap of electric machines. *IEEE Transactions on Magnetics*, 27(5):3955–3957. 69, 210

Lefevre, Y., Lajoie-Mazenc, M., and Davat, B. (1988). Force Calculation in Electromagnetic Devices. In *Electromagnetic Fields in Electrical Engineering*, pages 231–235. Springer US, Boston, MA. 229

Li, Y., Lu, Q., Zhu, Z. Q., Wu, L. J., Li, G. J., and Wu, D. (2015). Analytical Synthesis of Air-Gap Field Distribution in Permanent Magnet Machines With Rotor Eccentricity by Superposition Method. *IEEE Transactions on Magnetics*, 51(11):1–4. 65

Lin, F., Zuo, S., Deng, W., and Wu, S. (2016). Modeling and Analysis of Electromagnetic Force, Vibration, and Noise in Permanent-Magnet Synchronous Motor Considering Current Harmonics. *IEEE Transactions on Industrial Electronics*, 63(12):7455–7466. 23

Liouville, J. (1836). Mémoire sur le développement des fonctions en parties de fonctions en séries dont les divers termes sont assujettis à satisfaire à une même équation différentielle du second ordre contenant un paramètre variable. *Journal de mathématiques pures et appliquées*, 1(1):255–265. 82

Liu, Z. J. and Li, J. T. (2007). Analytical Solution of Air-Gap Field in Permanent-Magnet Motors Taking Into Account the Effect of Pole Transition Over Slots. *IEEE Transactions on Magnetics*, 43(10):3872–3883. 62

Lubin, T., Mezani, S., and Rezzoug, A. (2010). Exact Analytical Method for Magnetic Field Computation in the Air Gap of Cylindrical Electrical Machines Considering Slotting Effects. *IEEE Transactions on Magnetics*, 46(4):1092–1099. 52, 55, 61, 62, 64, 123, 129

Lubin, T., Mezani, S., and Rezzoug, A. (2011a). 2-D Exact Analytical Model for Surface-Mounted Permanent-Magnet Motors With Semi-Closed Slots. *IEEE Transactions on Magnetics*, 47(2):479–492. 61, 63, 65, 130

Lubin, T., Mezani, S., and Rezzoug, A. (2011b). Analytic Calculation of Eddy Currents in the Slots of Electrical Machines: Application to Cage Rotor Induction Motors. *IEEE Transactions on Magnetics*, 47(11):4650–4659. 49, 63, 86, 87, 121, 149, 151, 162, 163, 164, 166

Lubin, T., Mezani, S., and Rezzoug, A. (2012). Two-dimensional analytical calculation of magnetic field and electromagnetic torque for surface-inset permanent-magnet motors. *IEEE Transactions on Magnetics*, 48(6):2080–2091. 63, 111, 112

Lubin, T. and Rezzoug, A. (2015). 3-D Analytical Model for Axial-Flux Eddy-Current Couplings and Brakes under Steady-State Conditions. *IEEE Transactions on Magnetics*, 51(10). 55, 56

Ma, J., Qu, R., and Li, J. (2015). Optimal design of an axial flux switched reluctance motor with grain oriented electrical steel. In *2015 18th International Conference on Electrical Machines and Systems (ICEMS)*, pages 2071–2077. IEEE. 68

MANATEE (2015). Eomys Engineering. *www.manatee-software.com, Build v1.05*. 46

MANATEE (2018). Eomys Engineering. *www.manatee-software.com, Build v1.07.02*. 8, 19, 20, 21, 22, 25, 45, 69, 139, 171, 197, 208, 209

Martinez, J., Belahcen, A., and Arkkio, A. (2015). 3D permeance model of induction machines taking into account saturation effects and its connection with stator current and shaft speed spectra. *IET Electric Power Applications*, 9(1):20–29. 55

Martinez, J., Belahcen, A., and Detoni, J. G. (2016). A 2D magnetic and 3D mechanical coupled finite element model for the study of the dynamic vibrations in the stator of induction motors. *Mechanical Systems and Signal Processing*, 66-67:640–656. 49, 53

McCulloch, C., Tournour, M., and Guisset, P. (2002). Modal Acoustic Transfer Vectors Make Acoustic Radiation Models Practical for Engines and Rotating Machinery. *LMS International*. 47

Meessen, K. J. (2012). *Electromagnetic Fields and Interactions in 3D Cylindrical Structures : Modeling and Application door*. PhD thesis, University of Eindhoven. 25, 55, 61, 210

Meessen, K. J., Paulides, J. J. H., and Lomonova, E. A. (2013). Force calculations in 3-D cylindrical structures using fourier analysis and the maxwell stress tensor. *IEEE Transactions on Magnetics*, 49(1):536–545. 229

Melkebeek, J., Hilgert, T., and Vandevelde, L. (2007). Numerical analysis of the contribution of magnetic forces and magnetostriction to the vibrations in induction machines. *IET Science, Measurement and Technology*, 1(1):21–24. 23, 24

Mikina, S. J. (1935). Effect of Skewing and Pole Spacing on Magnetic Noise in Electrical Machinery. *American Society of Mechanical Engineers*, 56(15):711–720. 40

Millithaler, P. (2013). *Dynamic behaviour of electric machine stators*. PhD thesis, Université de Franche-Comté. 26, 31, 75

Millithaler, P., Dupont, J.-B., Ouisse, M., Sadoulet-Reboul, E., and Bouhaddi, N. (2017). Viscoelastic property tuning for reducing noise radiated by switched-reluctance machines. *Journal of Sound and Vibration*, 407:191–208. 41

Mininger, X. (2005). *Réduction des vibrations des machines à réluctances variable à l'aide d'actionneurs piézoélectriques*. PhD thesis, ENS Cachan, France. 42

Misir, O., Dobbert, F., and Ponick, B. (2016). Analytical method for the air gap permeance calculation of salient pole synchronous machines. *e & i Elektrotechnik und Informationstechnik*, 133(2):103–111. 55

Müller-Trapet, M., Dietrich, P., van der Giet, M., Blum, J., Vorländer, M., and Hameyer, K. (2010). Simulated Transfer Functions for the Auralization of Electrical Machines. In *1st EAA EuroRegio 2010, Congress on Sound and Vibration*. 47

Nandi, S. (2004). A Detailed Model of Induction Machines With Saturation Extendable for Fault Analysis. *IEEE Transactions on Industry Applications*, 40(5):1302–1309. 21, 55, 155

Nandi, S., Toliyat, H. A., and Li, X. (2005). Condition Monitoring and Fault Diagnosis of Electrical Motors—A Review. *IEEE Transactions on Energy Conversion*, 20(4):719–729. 23

Nogarede, B., Lajoie-Mazenc, M., and Davat, B. (1990). Modélisation analytique des machines à aimants à induit sans encoches. *Revue de Physique Appliquée*, 25(7):707–720. 56, 57, 229

O'Connell, T. C. (2008). *An investigation of boundary-based field analysis methods for electric machines: the Schwarz-Christoffel and Boundary Element Methods*. PhD thesis, University of Illinois. 59, 60, 68

Oner, Y., Zhu, Z. Q., Wu, L. J., Ge, X., Zhan, H., and Chen, J. T. (2016). Analytical On-Load Subdomain Field Model of Permanent-Magnet Vernier Machines. *IEEE Transactions on Industrial Electronics*, 63(7):4105–4117. 65

Ostović, V. (1989). *Dynamics of Saturated Electric Machines*. Springer New York, New York, NY. 66

Ouagued, S., Aden Diriye, A., Amara, Y., and Barakat, G. (2015). A General Framework Based on a Hybrid Analytical Model for the Analysis and Design of Permanent Magnet Machines. *IEEE Transactions on Magnetics*, 51(11):1–4. 69

Park, G.-J., Kim, Y.-J., and Jung, S.-Y. (2016). Design of IPMSM Applying V-Shape Skew Considering Axial Force Distribution and Performance Characteristics According to the Rotating Direction. *IEEE Transactions on Applied Superconductivity*, 26(4):1–5. 39

Pellerey, P. (2012). *Étude Et Optimisation Du Comportement Vibro-Acoustique Des Machines Électriques : Application Au Domaine Automobile*. PhD thesis, Université Technologique de Compiègne. 37, 51

Pellerey, P., Favennec, G., Lanfranchi, V., and Friedrich, G. (2012). Active reduction of electrical machines magnetic noise by the control of low frequency current harmonics. In *IECON 2012 - 38th Annual Conference on IEEE Industrial Electronics Society*, pages 1654–1659. IEEE. 41

Pellerey, P., Lanfranchi, V., and Friedrich, G. (2010). Influence of the load angle on the magnetic pressure harmonic content of a WRSM. *IECON 2010 - 36th Annual Conference on IEEE Industrial Electronics Society*, pages 877–882. 19, 42

Peng, W. and Gyselinck, J. (2016). Magnetic-equivalent-circuit modelling of switched reluctance machines with mutual coupling effects. In *2016 XXII International Conference on Electrical Machines (ICEM)*, pages 426–432. IEEE. 66

Penzkofer, A. and Atallah, K. (2015). Analytical Modeling and Optimization of Pseudo-Direct Drive Permanent Magnet Machines for Large Wind Turbines. *IEEE Transactions on Magnetics*, 51(12):1–14. 63

Pfister, P. D. and Perriard, Y. (2011). Slotless permanent-magnet machines: General analytical magnetic field calculation. *IEEE Transactions on Magnetics*, 47(6):1739–1752. 56

Pfister, P.-D., Yin, X., and Fang, Y. (2016). Slotted Permanent-Magnet Machines: General Analytical Model of Magnetic Fields, Torque, Eddy Currents, and Permanent-Magnet Power Losses Including the Diffusion Effect. *IEEE Transactions on Magnetics*, 52(5):1–13. 62, 211

Pile, R., Devillers, E., and Le Besnerais, J. (2018). Comparison of Main Magnetic Force Computation Methods for Noise and Vibration Assessment in Electrical Machines. *IEEE Transactions on Magnetics*, 54(7):1–13. 71, 72, 73, 74, 210

Pina, A., Paul, S., Islam, R., and Xu, L. (2016). Analytical Model for Predicting Effects of Manufacturing Variations on Cogging Torque in Surface-Mounted Permanent Magnet Motors. *IEEE Transactions on Industry Applications*, 9994(c):1–1. 65

Piriou, F. and Razek, A. (1990). A model for coupled magnetic-electric circuits in electric machines with skewed slots. *IEEE Transactions on Magnetics*, 26(2):1096–1100. 51

Prieto, B., Martínez-Iturralde, M., Fontán, L., and Elosegui, I. (2015). Analytical Calculation of the Slot Leakage Inductance in Fractional-Slot Concentrated-Winding Machines. *IEEE Transactions on Industrial Electronics*, 62(5):2742–2752. 62

Putri, A. K., Rick, S., Franck, D., and Hameyer, K. (2016). Application of Sinusoidal Field Pole in a Permanent-Magnet Synchronous Machine to Improve the NVH Behavior Considering the MTPA and MTPV Operation Area. *IEEE Transactions on Industry Applications*, 52(3):2280–2288. 39

Pyleecan (2018). Eomys Engineering. *http://www.pyleecan.org*. 173

Pyrhönen, J., Jokinen, T., Hrabovcová, V., and Niemelä, H. (2008). *Design of Rotating Electrical Machines*. Wiley, Hoboken. 63

Rahideh, A. and Korakianitis, T. (2012). Analytical magnetic field calculation of slotted brushless permanent-magnet machines with surface inset magnets. *IEEE Transactions on Magnetics*, 48(10):2633–2649. 63, 109

Rainer, S., Bíró, O., Weilharter, B., and Stermecki, A. (2010). Weak coupling between electromagnetic and structural models for electrical machines. *IEEE Transactions on Magnetics*, 46(8):2807–2810. 50

Read, W. (1993). Series solutions for Laplace's equation with nonhomogeneous mixed boundary conditions and irregular boundaries. *Mathematical and Computer Modelling*, 17(12):9–19. 210

Régniez, M., Souron, Q., Bonneel, P., and Le Besnerais, J. (2016). Numerical simulation of structural-borne vibrations due to electromagnetic forces in electric machines – coupling between Altair Optistruct and Manatee software. *Researchgate, https://www.researchgate.net/publication/311102653_Numerical_simulation_of_structural-borne_vibrations_due_to_electromagnetic_forces_in_electric_machines_-_coupling_between_Altair_Optistruct_and_Manatee_software*. 47

Riley, C. M., Lin, B. K., Habetier, T. G., and Kliman, G. B. (1999). Stator current harmonics and their causal vibrations: a preliminary investigation of sensorless vibration monitoring applications. *IEEE Transactions on Industry Applications*, 35(1):94–99. 23

Roivainen, J. (2009). *Unit-wave response-based modeling of electromechanical noise and vibration of electrical machines*. PhD thesis, Helsinki University of Technology. 29, 47, 49, 74, 75, 76, 77, 78

Rothe, R., van der Giet, M., and Hameyer, K. (2010). Convolution approach for analysis of magnetic forces in electrical machines. *COMPEL - The international journal for computation and mathematics in electrical and electronic engineering*, 29(6):1542–1551. 28, 156, 239

Roubache, L., Boughrara, K., Dubas, F., and Ibtiouen, R. (2017). Semi-analytical modeling of spoke-type permanent-magnet machines considering the iron core relative permeability: subdomain technique and taylor polynomial. *Progress In Electromagnetics Research B*, 77(1):85–101. 64

Roubache, L., Boughrara, K., Dubas, F., and Ibtiouen, R. (2018a). New Subdomain Technique for Electromagnetic Performances Calculation in Radial-Flux Electrical Machines Considering Finite Soft-Magnetic Material Permeability. *IEEE Transactions on Magnetics*, 54(4):1–15. 63

Roubache, L., Boughrara, K., Dubas, F., and Ibtiouen, R. (2018b). Technique en Sous-Domaines Élémentaires dans les Machines Asynchrones à Cage d'Écureuil : Saturation Magnétique Locale et Courants de Foucault dans les Barres. In *Symposium De Genie Electrique*, Nancy. 65, 210

Roubache, L., Boughrara, K., and Ibtiouen, R. (2016). Analytical Electromagnetic Analysis of Multi-Phases Cage Rotor Induction Motors in Healthy, Broken Bars and Open Phases Conditions. *Progress In Electromagnetics Research B*, 70(October):113–130. 21, 65

Sadowski, N., Lefèvre, Y., Lajoie-Mazenc, M., and Bastos, J. P. A. (1992a). Sur le calcul des forces magnétiques. *Journal de Physique III*, 2(5):859–870. 70

Sadowski, N., Lefevre, Y., Lajoie-Mazenc, M., and Cros, J. (1992b). Finite Element Torque Calculation In Electrical Machines While Considering the Mouvement. *IEEE Transactions on Magnetics*, 28(March):1410–1413. 68

Schlensok, C., van der Giet, M., Herranz Gracia, M., van Riesen, D., and Hameyer, K. (2008). Structure-Dynamic Analysis of an Induction Machine Depending on Stator–Housing Coupling. *IEEE Transactions on Industry Applications*, 44(3):753–759. 37

Serrano-Iribarnegaray, L., Cruz-Romero, P., and Gomez-Exposito, A. (2013). Critical Review of the Modified Winding Function Theory. *Progress In Electromagnetics Research*, 133(November 2012):515–534. 55

Shahaj, A. and Garvey, S. D. (2011). A Possible Method for Magnetostrictive Reduction of Vibration in Large Electrical Machines. *IEEE Transactions on Magnetics*, 47(2):374–385. 24, 42

Shin, K.-H., Park, H.-I., Cho, H.-W., and Choi, J.-Y. (2017). Analytical prediction for electromagnetic performance of interior permanent magnet machines based on subdomain model. *AIP Advances*, 7(5):056669. 63

Sizov, G. Y., Zhang, P., Ionel, D. M., Demerdash, N., Brown, I. P., Smith, A., and Solveson, M. G. (2012). Modeling and analysis of effects of skew on torque ripple and stator tooth forces in permanent magnet AC machines. In *2012 IEEE Energy Conversion Congress and Exposition (ECCE)*, pages 3055–3061. IEEE. 40, 72, 73, 74

Soedel, W. (1993). *Vibrations of shells and plates*. Marcel Dekker. 31, 75

Sprangers, R. L. J., Gysen, B. L. J., Paulides, J. J. H., Waarma, J., and Lomonova, E. A. (2014a). Calculation of induced rotor current in induction motors using a slotted semi-analytical harmonic model. *Proceedings - 2014 International Conference on Electrical Machines, ICEM 2014*, 31(1):2709–2714. 63

Sprangers, R. L. J., Paulides, J. J. H., Gysen, B. L. J., and Lomonova, E. A. (2016). Magnetic Saturation in Semi-Analytical Harmonic Modeling for Electric Machine Analysis. *IEEE Transactions on Magnetics*, 52(2). 56, 64, 66, 69

Sprangers, R. L. J., Paulides, J. J. H., Gysen, B. L. J., Lomonova, E. A., and Waarma, J. (2014b). Electric circuit coupling of a slotted semi-analytical model for induction motors based on harmonic modeling. *2014 IEEE Energy Conversion Congress and Exposition (ECCE)*, pages 1301–1308. 50, 64, 65, 211

Sprangers, R. L. J., Paulides, J. J. H., Gysen, B. L. J., Waarma, J., and Lomonova, E. A. (2015). Semianalytical Framework for Synchronous Reluctance Motor Analysis Including Finite Soft-Magnetic Material Permeability. *IEEE Transactions on Magnetics*, 51(11):1–4. 63

Sudhoff, S. D., Kuhn, B. T., Corzine, K. A., and Branecky, B. T. (2007). Magnetic Equivalent Circuit Modeling of Induction Motors. *IEEE Transactions on Energy Conversion*, 22(2):259–270. 66

Tan-Kim, A., Lanfranchi, V., Vivier, S., Legranger, J., and Palleschi, F. (2015). Vibro-acoustic simulation and optimization of a claw-pole alternator. *IEEE Transactions on Industry Applications*, 52(99):5227–5232. 37, 68

Tang, Z., Pillay, P., Chen, Y., and Omekanda, A. (2005). Prediction of Electromagnetic Forces and Vibrations in SRMs Operating at Steady-State and Transient Speeds. *IEEE Transactions on Industry Applications*, 41(4):927–934. 49

Tenhunen, A. (2003). *Electromagnetic forces acting between the stator and eccentric cage rotor*. PhD thesis, Helsinki University of Technology. 22, 35

Tessarolo, A. (2015). Modeling and Analysis of Synchronous Reluctance Machines With Circular Flux Barriers Through Conformal Mapping. *IEEE Transactions on Magnetics*, 51(4):1–11. 69

Tessarolo, A., Degano, M., and Bianchi, N. (2014). On the analytical estimation of the airgap field in synchronous reluctance machine. In *2014 International Conference on Electrical Machines (ICEM)*, pages 239–244. IEEE. 66

Tiegna, H., Amara, Y., and Barakat, G. (2013). Overview of analytical models of permanent magnet electrical machines for analysis and design purposes. *Mathematics and Computers in Simulation*, 90:162–177. 65

Timar, P. L. (1989). *Noise and vibration of electrical machines*. Elsevier. 8, 24, 25, 28, 31, 33, 72

Toliyat, H. A. and Lipo, T. A. (1995). Transient analysis of cage induction machines under stator, rotor bar and end ring faults. *IEEE Transactions on Energy Conversion*, 10(2):241–247. 55

Torregrossa, D., Fahimi, B., Peyraut, F., and Miraoui, A. (2012). Fast Computation of Electromagnetic Vibrations in Electrical Machines via Field Reconstruction Method and Knowledge of Mechanical Impulse Response. *IEEE Transactions on Industrial Electronics*, 59(2):839–847. 47

Traxler-Samek, G., Lugand, T., and Uemori, M. (2012). Vibrational Forces in Salient Pole Synchronous Machines Considering Tooth Ripple Effects. *IEEE Transactions on Industrial Electronics*, 59(5):2258–2266. 35

Utegenova, S., Dubas, F., Jamot, M., Glises, R., Truffart, B., Mariotto, D., Lagonotte, P., and Desevaux, P. (2018). An Investigation Into the Coupling of Magnetic and Thermal Analysis for a Wound-Rotor Synchronous Machine. *IEEE Transactions on Industrial Electronics*, 65(4):3406–3416. 66, 67, 68

Valavi, M., Devillers, E., Le Besnerais, J., Nysveen, A., and Nilsen, R. (2018). Influence of Converter Topology and Carrier Frequency on Airgap Field Harmonics, Magnetic Forces, and Vibrations in Converter-Fed Hydropower Generator. *IEEE Transactions on Industry Applications*, 54(3):2202–2214. 22, 35, 38

Valavi, M., Nysveen, A., and Nilssen, R. (2015). Effects of Loading and Slot Harmonic on Radial Magnetic Forces in Low-Speed Permanent Magnet Machine With Concentrated Windings. *IEEE Transactions on Magnetics*, 51(6):1–10. 19

van der Giet, M. (2011). *Analysis of electromagnetic acoustic noise excitations: A contribution to low-noise design and to the auralization of electrical machines*. PhD thesis, Rheinisch-Westfalische Technische Hochschule Aachen. 37, 47, 74, 76, 78

Vandevelde, L. and Melkebeek, J. (1997). Calculation of radial magnetic forces for the analysis of noise and vibrations of squirrel-cage induction motors. In *Eighth International Conference on Electrical Machines and Drives*, volume 1997, pages 86–90. IEE. 66

Vér, I. and Beranek, L. (2005). *Noise and Vibration Control Engineering*. John Wiley and Sons, Inc., Hoboken, NJ, USA. 39

Verez, G. (2014). *Contribution à l'étude des émissions vibro-accoustiques des machines électriques. Cas des machines synchrones à aimants dans un contexte automobile*. PhD thesis, Université du Havre. 66

Verez, G. and Espanet, C. (2015). Natural frequencies analytical modeling of small industrial radial flux permanent magnet motors. In *2015 18th International Conference on Electrical Machines and Systems (ICEMS)*, pages 1963–1969. IEEE. 75

Wang, C. and Lai, J. (2001). The sound radiation efficiency of finite length circular cylindrical shells under mechanical excitation II: limitations of the infinite length model. *Journal of Sound and Vibration*, 241(5):825–838. 78

Wang, H., Yan, Y., Zhang, Z., and Xia, C. (2016). Analytical Field Calculation of Doubly Fed Induction Generator with Core Saturation Considered. In *8th IET International Conference on Power Electronics, Machines and Drives (PEMD 2016)*, pages 6 .–6 . Institution of Engineering and Technology. 64

Wang, Z. (2013). *Contribution to Finite Element Analysis of Magneto-Mechanical and Magneto-Thermal Phenomena*. PhD thesis, Université Lille 1. 53

Weilharter, B., Biro, O., Rainer, S., and Stermecki, A. (2011). Computation of Rotating Force Waves in Skewed Induction Machines Using Multi-Slice Models. *IEEE Transactions on Magnetics*, 47(5):1046–1049. 51, 240

Wu, L. J., Zhu, Z. Q., Chen, J. T., and Xia, Z. P. (2010). An Analytical Model of Unbalanced Magnetic Force in Fractional-Slot Surface-Mounted Permanent Magnet Machines. *IEEE Transactions on Magnetics*, 46(7):2686–2700. 26

Wu, L. J., Zhu, Z. Q., Staton, D., Popescu, M., and Hawkins, D. (2011). An Improved Subdomain Model for Predicting Magnetic Field of Surface-Mounted Permanent Magnet Machines Accounting for Tooth-Tips. *IEEE Transactions on Magnetics*, 47(6):1693–1704. 63

Wu, S., Tong, W., Sun, R., and Tang, R. (2018). A Generalized Method of Electromagnetic Vibration Analysis of Amorphous Alloy Permanent Magnet Synchronous Machines. *IEEE Transactions on Magnetics*, PP:1–5. 24

Xia, C., Zhang, Z., and Geng, Q. (2015). Analytical Modeling and Analysis of Surface Mounted Permanent Magnet Machines With Skewed Slots. *IEEE Transactions on Magnetics*, 51(5):1–8. 65

Yang, H.-Y., Lim, Y.-C., and Kim, H.-C. (2013a). Acoustic Noise/Vibration Reduction of a Single-Phase SRM Using Skewed Stator and Rotor. *IEEE Transactions on Industrial Electronics*, 60(10):4292–4300. 39

Yang, S. J. (1981). *Low noise electrical motors*. Oxford University Press, Oxford. 28, 31, 36, 38, 78

Yang, Z., Krishnamurthy, M., and Brown, I. P. (2013b). Electromagnetic and vibrational characteristic of IPM over full torque-speed range. In *2013 International Electric Machines and Drives Conference*, pages 295–302. IEEE. 35, 38

Yoshida, M., Murai, Y., and Takada, M. (1998). Noise reduction by torque ripple suppression in brushless DC motor. *PESC 98 Record. 29th Annual IEEE Power Electronics Specialists Conference (Cat. No.98CH36196)*, 2:1397–1401. 29

Youmssi, A. (2006). A Three-Dimensional Semi-Analytical Study of the Magnetic Field Excitation in a Radial Surface Permanent-Magnet Synchronous Motor. *IEEE Transactions on Magnetics*, 42(12):3832–3841. 55, 56

Žarko, D., Ban, D., and Lipo, T. A. (2006). Analytical Calculation of Magnetic Field Distribution in the Slotted Air Gap of a Surface Permanent-Magnet Motor Using Complex Relative Air-Gap Permeance. *IEEE Transactions on Magnetics*, 42(7):1828–1837. 58, 59

Žarko, D., Ban, D., and Lipo, T. A. (2009). Analytical Solution for Electromagnetic Torque in Surface Permanent-Magnet Motors Using Conformal Mapping. *IEEE Transactions on Magnetics*, 45(7):2943–2954. 59, 60

Zhang, Z., Xia, C., Yan, Y., Geng, Q., and Shi, T. (2017). A hybrid analytical model for open-circuit field calculation of multilayer interior permanent magnet machines. *Journal of Magnetism and Magnetic Materials*, 435:136–145. 69, 210

Zhou, G.-Y. and Shen, J.-X. (2017). Rotor Notching for Electromagnetic Noise Reduction of Induction Motors. *IEEE Transactions on Industry Applications*, 53(4):3361–3370. 40

Zhu, L., Jiang, S. Z., Zhu, Z. Q., and Chan, C. C. (2009). Analytical Modeling of Open-Circuit Air-Gap Field Distributions in Multisegment and Multilayer Interior Permanent-Magnet Machines. *IEEE Transactions on Magnetics*, 45(8):3121–3130. 67, 68

Zhu, W., Pekarek, S., and Fahimi, B. (2005). On the effect of stator excitation on radial and tangential flux and force densities in a permanent magnet synchronous machine. In *IEEE International Conference on Electric Machines and Drives, 2005.*, pages 346–353. IEEE. 19, 42

Zhu, Z., Popescu, M., Hawkins, D., Wu, L., and Staton, D. (2010a). Combined complex permeance and sub-domain model for analytical predicting electromagnetic performance of surface-mounted pm machines. In *5th IET International Conference on Power Electronics, Machines and Drives (PEMD 2010)*, pages 111–111. Institution of Engineering and Technology. 69, 211

Zhu, Z. Q. (1991). *The electromagnetic performance of brushless permanent magnet DC motors*. PhD thesis, University of Sheffield. 26, 29, 31, 56, 57, 58, 59

Zhu, Z. Q. and Howe, D. (1993). Instantaneous magnetic field distribution in brushless permanent magnet DC motors. III. Effect of stator slotting. *IEEE Transactions on Magnetics*, 29(1):143–151. 57

Zhu, Z. Q., Jamil, M. L. M., Wu, L. J., Mohd Jamil, M. L., and Wu, L. J. (2013). Influence of Slot and Pole Number Combinations on Unbalanced Magnetic Force in PM Machines With Diametrically Asymmetric Windings. *IEEE Transactions on Industry Applications*, 49(1):19–30. 38, 65

Zhu, Z. Q., Wu, L. J., and Xia, Z. P. (2010b). An Accurate Subdomain Model for Magnetic Field Computation in Slotted Surface-Mounted Permanent-Magnet Machines. *IEEE Transactions on Magnetics*, 46(4):1100–1115. 55, 61, 62, 64, 134

Zhu, Z. Q., Xia, Z. P., Wu, L. J., and Jewell, G. W. (2010c). Analytical Modeling and Finite-Element Computation of Radial Vibration Force in Fractional-Slot Permanent-Magnet Brushless Machines. *IEEE Transactions on Industry Applications*, 46(5):1908–1918. 60

Zou, J., Lan, H., Xu, Y., and Zhao, B. (2017). Analysis of Global and Local Force Harmonics and Their Effects on Vibration in Permanent Magnet Synchronous Machines. *IEEE Transactions on Energy Conversion*, 32(4):1523–1532. 20, 26, 29, 41, 73, 74

Appendix A

Appendices

A.1 Coordinate system for radial flux machines models

The cylindrical coordinate frame (ρ, θ, z) is illustrated on Figure A.1).

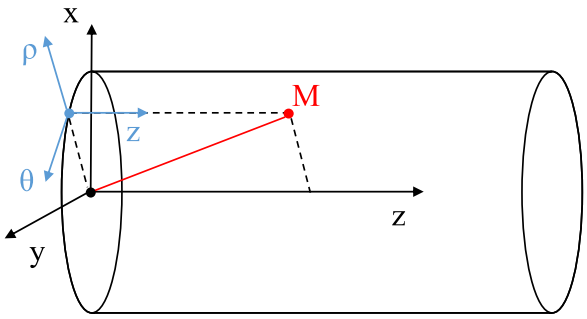

Figure A.1 – 3D cylindrical coordinate frame

It is worth mentioning that term "circumferential" should be preferred to "tangential" which is quite ambiguous in 3D problems. In 3D cylindrical problems, the circumferential direction is generated by the second vector of the orthonormal direct cylindrical basis. Circumferential direction is uniquely defined. Tangential direction means any directions which is orthogonal to normal direction, where normal direction is always uniquely defined from the context. Assuming that normal and radial directions are parallel, tangential direction is not unique as it can be any orthogonal direction to the radial one, then including both circumferential and axial directions.

Furthermore, cylindrical coordinates naturally refer to the triplet (ρ, θ, z) in 3D, but it also refers to the couple (ρ, z) in 2D. Polar coordinates refer to the couple (ρ, θ) in 2D. In the following, when dimension is not mentioned, cylindrical coordinates refer to 3D cylindrical coordinates.

A.2 Maxwell Stress Tensor (MST)

The electromagnetic forces **F** applying on a moving body can be computed using the MST, noted $\mathbb{T}$, such as [Lefevre et al., 1988; Imhoff et al., 1990]:

$$\mathbf{F} = \oint_S \mathbb{T}.\mathbf{n} dS \tag{A.1}$$

where S is any surface enclosing the moving body, and **n** in the vector normal to the surface and oriented towards the outside.

In cylindrical coordinate system (cf. Figure A.1), the MST is written [Lefevre et al., 1988; Imhoff et al., 1990]:

$$\mathbb{T} = \frac{1}{\mu_0} \begin{bmatrix} \frac{B_\rho^2 - B_\theta^2 - B_z^2}{2} & B_\rho B_\theta & B_\rho B_z \\ B_\theta B_\rho & \frac{B_\theta^2 - B_\rho^2 - B_z^2}{2} & B_\theta B_z \\ B_z B_\rho & B_z B_\theta & \frac{B_z^2 - B_\rho^2 - B_\theta^2}{2} \end{bmatrix} \tag{A.2}$$

The MST formulation comes from mathematical developments base on the introduction of Lorentz force in Maxwell equations [Bekemans, 2006; Meessen et al., 2013]. Therefore, the MST includes both Maxwell and Lorentz forces and is applicable in electrical machines working both with Maxwell and Lorentz forces [Nogarede et al., 1990].

In electrical machines, the 2D electromagnetic forces applying on stator and rotor structures are given by integrating the MST on the enclosing surfaces illustrated on Figure A.2. In both stator and rotor enclosing surfaces, only the airgap cylinder surface $S_{si} = S_{ro}$ remains, as flux density vector **B** is null (or clearly negligible) on stator outer surface S_{so} and rotor inner surface S_{ri}.

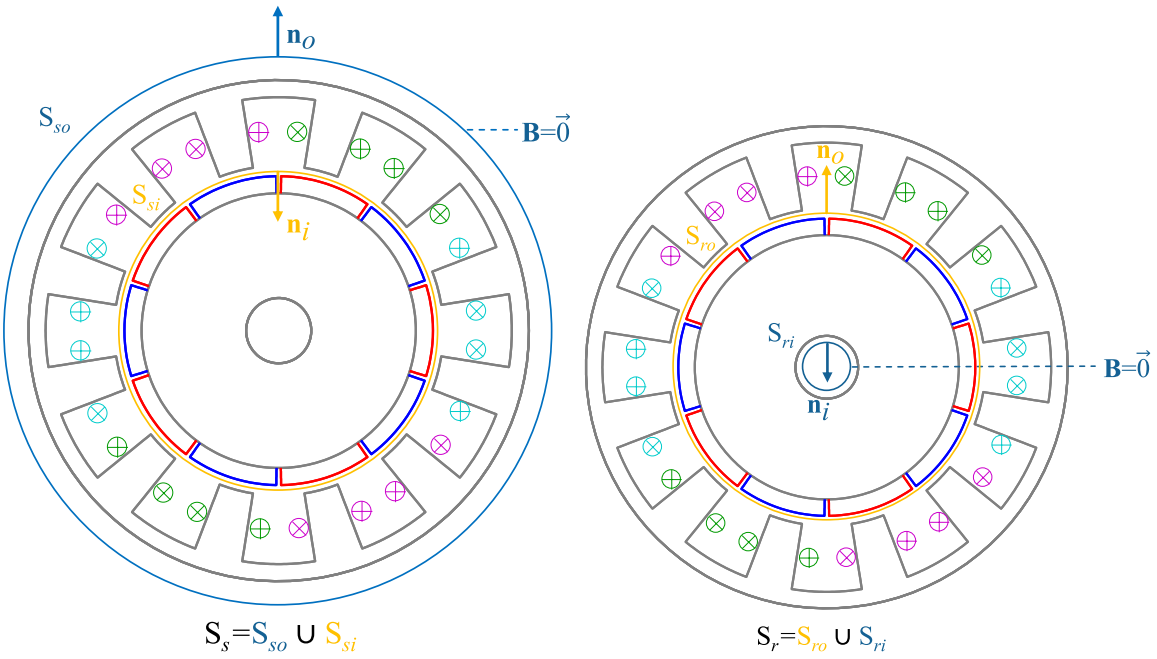

(a) Stator enclosing surface.

(b) Rotor enclosing surface.

Figure A.2 – Enclosing surfaces for electromagnetic force computation using MST.

Therefore, radial and circumferential forces applied on the stator are written:

$$F_{S,\rho} = \frac{L_S}{\mu_0} \int_0^{2\pi} \frac{B_\rho^2 - B_\theta^2}{2} \rho d\theta \tag{A.3}$$

$$F_{S,\theta} = \frac{L_S}{\mu_0} \int_0^{2\pi} B_\theta B_\rho \rho d\theta \tag{A.4}$$

where L_S is the stator axial length.

Radial and circumferential forces applied on the rotor are opposite to stator forces. For outer rotor topologies, the normal vectors are oppositely oriented so the sign of rotor and stator forces are also opposite.

Historically, the first use of MST is to compute the electromagnetic torque T_{em} in radial flux machines such as:

$$T_{em} = (R_g \mathbf{e}_\rho \times \mathbf{F}_R).\mathbf{e}_z = R_g F_{R,\theta} \tag{A.5}$$

where R_g is the middle airgap radius and $F_{R,\theta}$ is the circumferential force applied on the rotor.

A.3 Computation of analytical FRFs

From Jordan [1950]; Le Besnerais et al. [2010b], the static displacement $\underline{U}_s^{fr}$ due to unit stress harmonics is expressed as:

$$\underline{U}_s^{f0} = \frac{R_{sy}}{E_s}\left(\frac{R_{sy}}{h_{sy}} - 1\right) \tag{A.6}$$

$$\underline{U}_s^{f1} = \frac{12R_{sy}^2}{h_{sy}^2}\underline{U}_s^{f0} \tag{A.7}$$

$$\underline{U}_s^{fr} = \frac{R_{sy}^2}{h_{sy}^2}\frac{12}{\left(m^2-1\right)^2}\underline{U}_s^{f0}, \quad r = m \geq 2 \tag{A.8}$$

for inner rotor topologies, where R_{sy} is the cylinder outer radius, h_{sy} is the thickness, and E_s is the stator isotropic Young modulus. Equation A.8 shows the static displacement decrease at the power of four for high stress wavenumbers, as said in Subsection 1.4.5.

For an isotropic cylindrical structure, natural frequencies of radial modes are given by the analytical expressions [Gieras et al., 2006]:

$$f_0 = \frac{1}{2\pi h_{sy}\left(\frac{R_{sy}}{h_{sy}} - \frac{1}{2}\right)}\sqrt{\frac{E}{\rho\Delta_{wt}}} \tag{A.9}$$

$$f_1 = \sqrt{\frac{2}{1 + \frac{4}{3}\frac{h_{sy}^2}{R_{sy}^2}\frac{k_{mrot}}{k_{md}}}}f_0 \tag{A.10}$$

$$f_m = \frac{K_m}{2\sqrt{3}\left(\frac{R_{sy}}{h_{sy}} - \frac{1}{2}\right)}\frac{m(m^2-1)}{\sqrt{m^2+1}}f_0, \quad m \geq 2 \tag{A.11}$$

where ρ is the steel volumic mass, Δ_{wt} is the correction factor due to the additional winding and teeth mass, K_m is a corrective factor depending on the mechanical boundary conditions [Gieras et al., 2006], and k_{md} and k_{mrot} are mass addition factors for displacement and rotation [Gieras et al., 2006].

A.4 Obtention of MVP formulation from Maxwell equations

A.4.1 Mathematical developments based on vector analysis

Taking the curl of constitutive law (3.7) yields:

$$\nabla \times \mathbf{B} = \mu_0\mu_r \nabla \times \mathbf{H} + \mu_0 \nabla \times \mathbf{M} \tag{A.12}$$

where μ_r is constant and uniform and can be put out of the curl.

Simplified Maxwell-Ampere's law (3.6) and MVP expression (3.11) are inserted in the second member of Equation (A.12):

$$\nabla \times \nabla \times \mathbf{A} = \mu_0\mu_r \mathbf{j} + \mu_0 \nabla \times \mathbf{M} \tag{A.13}$$

From vector analysis, double curl is expressed as:

$$\nabla \times \nabla \times \mathbf{A} = \nabla(\nabla.\mathbf{A}) - \nabla^2\mathbf{A} \tag{A.14}$$

where "∇^2" is Laplacian vector operator.

To obtain potentials unity, the Coulomb's gauge is generally set in electromagnetic applied to electrical machines:

$$\nabla.\mathbf{A} = 0 \tag{A.15}$$

From Coulomb's gauge (A.15), divergence of MVP is null. The double curl is substituted in Equation (A.13):

$$-\nabla^2\mathbf{A} = \mu_0\mu_r\mathbf{j} + \mu_0\nabla\times\mathbf{M} \tag{A.16}$$

Then, the local Ohm's law (3.8) is inserted in Equation (A.16):

$$-\nabla^2\mathbf{A} = \mu_0\mu_r\sigma(\mathbf{E}+\mathbf{v}\times\mathbf{B}) + \mu_0\nabla\times\mathbf{M} \tag{A.17}$$

MVP and Electric Scalar Potential (ESP) expressions (3.11) and (3.12) are injected in Equation (A.17):

$$\nabla^2\mathbf{A} = \mu_0\mu_r\sigma\left[\frac{\partial\mathbf{A}}{\partial t} + \nabla(\mathrm{V}) - \mathbf{v}\times(\nabla\times\mathbf{A})\right] - \mu_0\nabla\times\mathbf{M} \tag{A.18}$$

A.4.2 Vector operators expressed in polar coordinates

The MVP PDE (3.13) is now expressed in the 2D polar coordinate system with orthonormal basis $(\mathbf{e}_r,\mathbf{e}_\theta)$ and coordinates (r,θ). As flux density is assumed to have two components in the polar plane $(\mathbf{e}_r,\mathbf{e}_\theta)$, MVP is along z-axis and is written:

$$\mathbf{A} = \mathrm{A}_z(t,r,\theta)\mathbf{e}_z \tag{A.19}$$

The Laplacian operator in polar coordinates is:

$$\nabla^2\mathbf{A} = \frac{\partial^2\mathbf{A}}{\partial r^2} + \frac{1}{r}\frac{\partial\mathbf{A}}{\partial r} + \frac{1}{r^2}\frac{\partial^2\mathbf{A}}{\partial\theta^2} \tag{A.20}$$

which simplifies into:

$$\nabla^2\mathbf{A} = \left(\frac{\partial^2\mathrm{A}_z}{\partial r^2} + \frac{1}{r}\frac{\partial\mathrm{A}_z}{\partial r} + \frac{1}{r^2}\frac{\partial^2\mathrm{A}_z}{\partial\theta^2}\right)\mathbf{e}_z \tag{A.21}$$

The MVP curl expression is:

$$\nabla\times\mathbf{A} = \left(\frac{1}{r}\frac{\partial\mathrm{A}_z}{\partial\theta} - \frac{\partial\mathrm{A}_\theta}{\partial z}\right)\mathbf{e}_r + \left(\frac{\partial\mathrm{A}_r}{\partial z} - \frac{\partial\mathrm{A}_z}{\partial r}\right)\mathbf{e}_\theta + \frac{1}{r}\left(\frac{\partial}{\partial r} - \frac{\partial\mathrm{A}_r}{\partial\theta}\right)\mathbf{e}_z = \frac{1}{r}\frac{\partial\mathrm{A}_z}{\partial\theta}\mathbf{e}_r - \frac{\partial\mathrm{A}_z}{\partial r}\mathbf{e}_\theta \tag{A.22}$$

The conductor speed $\mathbf{v}$ is non-null only for rotor conductors. It is assumed that $\mathbf{v}$ belongs the polar plane, and is in the circumferential direction:

$$\mathbf{v} = r\Omega\mathbf{e}_\theta \tag{A.23}$$

where Ω is the rotating speed. Then, from Equations (A.22) and (A.23):

$$\mathbf{v}\times(\nabla\times\mathbf{A}) = \left(r\Omega\mathbf{e}_\theta\right)\times\left(\frac{1}{r}\frac{\partial\mathrm{A}_z}{\partial\theta}\mathbf{e}_r - \frac{\partial\mathrm{A}_z}{\partial r}\mathbf{e}_\theta\right) = -\Omega\frac{\partial\mathrm{A}_z}{\partial\theta}\mathbf{e}_z \tag{A.24}$$

The external current density is assumed to be in the axial direction:

$$\mathbf{j_{ext}} = \mathrm{J}_z \mathbf{e}_z \tag{A.25}$$

Magnetization is assumed to be in radial and circumferential directions:

$$\mathbf{M} = \mathrm{M}_r(r,\theta)\mathbf{e}_r + \mathrm{M}_\theta(r,\theta)\mathbf{e}_\theta \tag{A.26}$$

Magnetization curl yields:

$$\nabla \times \mathbf{M} = \frac{1}{r}\Big(\frac{\partial}{\partial r} - \frac{\partial \mathrm{M}_r}{\partial \theta}\Big)\mathbf{e}_z \tag{A.27}$$

A.5 Orthogonality of eigenfunctions

From Sturm-Liouville theory, two eigenfunctions R_{λ_1} and R_{λ_2}, respectively Θ_{λ_1} and Θ_{λ_2}, corresponding to distinct eigenvalues λ_1 and λ_2 are orthogonal regarding the following scalar product, noted "$\langle .,. \rangle$":

$$\langle \mathrm{R}_{\lambda_1}, \mathrm{R}_{\lambda_2} \rangle = \int_{\mathrm{R}_1}^{\mathrm{R}_2} \mathrm{R}_{\lambda_1}(r)\mathrm{R}_{\lambda_2}(r)\, w_r(r)\, dr \quad = 0 \tag{A.28}$$

$$\langle \Theta_{\lambda_1}, \Theta_{\lambda_2} \rangle = \int_{\Theta_1}^{\Theta_2} \Theta_{\lambda_1}(\theta)\Theta_{\lambda_2}(\theta)\, w_\theta(\theta)\, d\theta = 0 \tag{A.29}$$

where w_r and w_θ are the weight functions of Sturm-Liouville operators for the ODEs in r and θ. In this thesis, weight functions values are [Herman, 2013]:

$$w_r(r) = \frac{1}{r} \tag{A.30}$$

$$w_\theta(\theta) = 1 \tag{A.31}$$

Therefore, eigenfunctions R_λ and Θ_λ form an orthogonal basis.

The scalar product is used to express a function in the eigenfunction basis. The projection of a r-dependent function h on radial edges is:

$$\langle h, \mathrm{R}_\lambda \rangle = \int_{\mathrm{R}_1}^{\mathrm{R}_2} \mathrm{R}_\lambda(r) h(r) \frac{1}{r} dr \tag{A.32}$$

associated to the norm N_R such as:

$$\mathrm{N}_\mathrm{R} = \langle \mathrm{R}_\lambda, \mathrm{R}_\lambda \rangle = \int_{\mathrm{R}_1}^{\mathrm{R}_2} \mathrm{R}_\lambda^2(r) \frac{1}{r} dr \tag{A.33}$$

The projection of a θ-dependent function h on circumferential edges is:

$$\langle h, \Theta_\lambda \rangle = \int_{\Theta_1}^{\Theta_2} \Theta_\lambda(\theta) h(\theta) d\theta \tag{A.34}$$

associated to the norm N_C such as:

$$\mathrm{N}_\mathrm{C} = \langle \Theta_\lambda, \Theta_\lambda \rangle = \int_{\Theta_1}^{\Theta_2} \Theta_\lambda^2(\theta) d\theta \tag{A.35}$$

The scalar product is used in Chapters 3 to reformulate the MVP expression depending on the ICs, and in Chapter 4 to express these ICs with the other subdomains, which require to have both MVP expressions in the same eigenfunction basis.

A.6 MVP reformulation in each subdomain

A.6.1 Geometrical polynoms

The reformulation performed to simplify the ICs in Subsection 4.2.1 introduces the two geometrical polynoms P and E defined as:

$$\mathrm{P}_z(x,y) = \left(\frac{x}{y}\right)^z + \left(\frac{x}{y}\right)^{-z} \tag{A.36}$$

$$\mathrm{E}_z(x,y) = \left(\frac{x}{y}\right)^z - \left(\frac{x}{y}\right)^{-z} \tag{A.37}$$

P and E have the following properties:

$$\mathrm{P}_z(x,x) = 2 \tag{A.38}$$

$$\mathrm{E}_z(x,x) = 0 \tag{A.39}$$

$$\mathrm{P}_z(x,y) = \mathrm{P}_z(y,x) \tag{A.40}$$

$$\mathrm{E}_z(x,y) = -\mathrm{E}_z(y,x) \tag{A.41}$$

$$\left.\frac{\partial \mathrm{P}_z}{\partial x}\right|_{x,y} = \frac{z}{x}\mathrm{E}_z(x,y) \tag{A.42}$$

$$\left.\frac{\partial \mathrm{E}_z}{\partial x}\right|_{x,y} = \frac{z}{x}\mathrm{P}_z(y,x) \tag{A.43}$$

A.6.2 Combinations of modified Bessel functions

$$\underline{\mathrm{N}}(m,n,x,y) = \mathrm{I}_m(x)\,\mathrm{K}_n(y) - \mathrm{K}_m(x)\,\mathrm{I}_n(y) \tag{A.44}$$

$$\underline{\mathrm{M}}(m,n,x,y) = \mathrm{I}_m(x)\,\mathrm{K}_n(y) + \mathrm{K}_m(x)\,\mathrm{I}_n(y) \tag{A.45}$$

A.6.3 Reformulation of Surface PM subdomain MVP

The surface PMs subdomain is a Poisson eigenvalue problem in θ-direction subject to PBC which is illustrated on Figure 4.2. The MVP solution A_{zm} in the surface PMs subdomain is the sum of the Laplace homogeneous solution (3.80) and of the particular solution (3.110). The homogeneous solution depends on six unknown integration constants a_{m0}, b_{m0}, a_{mn}, b_{mn}, c_{mn}, and d_{mn} and two unknown functions F_{1mn} and F_{2mn}, which account for the BCs/ICs on both circumferential edges at rotor bore radius $r = \mathrm{R}_r$ and top magnet radius $r = \mathrm{R}_m$. Due to the rotor yoke infinite permeability assumption, a Neumann HBC (3.29) applies on rotor bore radius R_r. Besides, the MVP expression is reformulated to account for the MVP continuity condition (4.1) with the airgap subdomain at R_m. The following scalar products are applied to determine F_{1mn} and F_{2mn} as defined in Equation (3.72):

$$\frac{1}{2\pi}\langle\frac{\partial \mathrm{A}_{zm}}{\partial r}\Big|_{\psi,r=\mathrm{R}_r,\theta}+\mathrm{M}_\theta(\theta),1\rangle=0 \quad\Rightarrow\quad b_0=0 \tag{A.46}$$

$$\frac{1}{\pi}\langle\frac{\partial \mathrm{A}_{zm}}{\partial r}\Big|_{\psi,r=\mathrm{R}_r,\theta}+\mathrm{M}_\theta(\theta),\cos(n\theta)\rangle=0 \tag{A.47}$$

$$\frac{1}{\pi}\langle\frac{\partial \mathrm{A}_{zm}}{\partial r}\Big|_{\psi,r=\mathrm{R}_r,\theta}+\mathrm{M}_\theta(\theta),\sin(n\theta)\rangle=0 \tag{A.48}$$

$$\frac{1}{2\pi}\langle \mathrm{A}_{zm}(\mathrm{R}_m,\theta),1\rangle=\mathrm{A}_{m0} \tag{A.49}$$

$$\frac{1}{\pi}\langle \mathrm{A}_{zm}(\mathrm{R}_m,\theta),\cos(n\theta)\rangle=\mathrm{A}_{mn} \tag{A.50}$$

$$\frac{1}{\pi}\langle \mathrm{A}_{zm}(\mathrm{R}_m,\theta),\sin(n\theta)\rangle=\mathrm{B}_{mn} \tag{A.51}$$

The first Neumann HBC directly yields $b_{g0}=0$. Two integration constants and one unknown functions will disappear after applying the Neumann HBC at $r=\mathrm{R}_r$. The old integration constant a_{m0} represents the constant component of the MVP Fourier series. Two new integration constants A_{mn} and B_{mn} are introduced to represent cosine and sine components at the interface between surface PMs and airgap subdomains. Therefore, the two new integration constants and the four old ones are linked by the developing the set of scalar products:

$$a_{mn}\frac{n}{\mathrm{R}_r}\Big(\frac{\mathrm{R}_r}{\mathrm{R}_m}\Big)^n-b_{mn}\frac{n}{\mathrm{R}_r}-\Big[n\mathrm{M}_{rn}\mathrm{R}'_{spm,n}(\mathrm{R}_r)+\mathrm{M}_{\theta n}\big(\mathrm{R}'_{spm,n}(\mathrm{R}_r)-1\big)\Big]\sin\big(n\psi\big)=0 \tag{A.52}$$

$$c_{mn}\frac{n}{\mathrm{R}_r}\Big(\frac{\mathrm{R}_r}{\mathrm{R}_m}\Big)^n-d_{mn}\frac{n}{\mathrm{R}_r}+\Big[n\mathrm{M}_{rn}\mathrm{R}'_{spm,n}(\mathrm{R}_r)+\mathrm{M}_{\theta n}\big(\mathrm{R}'_{spm,n}(\mathrm{R}_r)-1\big)\Big]\cos\big(n\psi\big)=0 \tag{A.53}$$

$$a_{mn}+b_{mn}\Big(\frac{\mathrm{R}_r}{\mathrm{R}_m}\Big)^n-(n\mathrm{M}_{rn}+\mathrm{M}_{\theta n})\sin\big(n\psi\big)\mathrm{R}_{spm,n}(\mathrm{R}_m)=\mathrm{A}_{mn} \tag{A.54}$$

$$c_{mn}+d_{mn}\Big(\frac{\mathrm{R}_r}{\mathrm{R}_m}\Big)^n+(n\mathrm{M}_{rn}+\mathrm{M}_{\theta n})\cos\big(n\psi\big)\mathrm{R}_{spm,n}(\mathrm{R}_m)=\mathrm{B}_{mn} \tag{A.55}$$

The expression of F_{1mn} is obtained by substituting the expression of the old integration constants in the MVP, such as:

$$\mathrm{F}_{1gn}(r)=\frac{\mathrm{P}_n(r,\mathrm{R}_m)}{\mathrm{P}_n(\mathrm{R}_r,\mathrm{R}_m)} \tag{A.56}$$

The new source terms X_{mn} and Y_{mn} can be written:

$$\mathrm{X}_{mn}(r)=n\mathrm{R}_{spm}(r)-\mathrm{R}_r\frac{\mathrm{E}_n(r,\mathrm{R}_m)}{\mathrm{P}_n(\mathrm{R}_r,\mathrm{R}_m)}\mathrm{R}'_{spm,n}(\mathrm{R}_r)-n\frac{\mathrm{P}_n(\mathrm{R}_r,r)}{\mathrm{P}_n(\mathrm{R}_r,\mathrm{R}_m)}\mathrm{R}_{spm,n}(\mathrm{R}_m) \tag{A.57}$$

$$\mathrm{Y}_{mn}(r)=\mathrm{X}_{mn}(r)-\frac{\mathrm{R}_r}{n}\frac{\mathrm{E}_n(r,\mathrm{R}_m)}{\mathrm{P}_n(\mathrm{R}_r,\mathrm{R}_m)} \tag{A.58}$$

E_n, P_n are defined in Appendix A.6.1 and $\mathrm{R}_{spm,n}$ is given by Equations (3.115)-(3.116).

A.6.4 Reformulation of airgap subdomain MVP

The airgap subdomain problem is a Laplace eigenvalue problem in θ-direction subject to PBC, as illustrated on Figure 4.3. The MVP solution A_{zg} in the airgap subdomain is the Laplace homogeneous solution (3.80), which depends on six integration constants

a_{g0}, b_{g0}, a_{gn}, b_{gn}, c_{gn}, and d_{gn} and two unknown functions F_{1gn} and F_{2gn}, accounting for the BCs/ICs on both circumferential edges at top magnet radius $r = R_m$ and stator bore radius $r = R_s$. The airgap MVP is subject to tangential field continuity conditions (4.2)-(4.4) with surface PMs and stator slots subdomains (at $r = R_m$ and $r = R_s$), with a Neumann HBC at $r = R_s$ in front of stator teeth due to iron infinite permeability. The following scalar products are applied to determine F_{1gn} and F_{2gn} as defined in Equation (3.73):

$$\frac{1}{2\pi}\langle A_{zg}(R_m,\theta),1\rangle = a_{g0} \tag{A.59}$$

$$\frac{1}{\pi}\langle \frac{\partial A_{zg}}{\partial r}\Big|_{R_m,\theta},\cos(n\theta)\rangle = A_{gn} \tag{A.60}$$

$$\frac{1}{\pi}\langle \frac{\partial A_{zg}}{\partial r}\Big|_{R_m,\theta},\sin(n\theta)\rangle = C_{gn} \tag{A.61}$$

$$\frac{1}{2\pi}\langle \frac{\partial A_{zg}}{\partial r}\Big|_{R_s,\theta},1\rangle = 0 \quad \Rightarrow \quad b_{g0} = 0 \tag{A.62}$$

$$\frac{1}{\pi}\langle \frac{\partial A_{zg}}{\partial r}\Big|_{R_s,\theta},\cos(n\theta)\rangle = B_{gn} \tag{A.63}$$

$$\frac{1}{\pi}\langle \frac{\partial A_{zg}}{\partial r}\Big|_{R_s,\theta},\sin(n\theta)\rangle = D_{gn} \tag{A.64}$$

where a_{g0} is the constant component of the MVP Fourier series, A_{gn} and B_{gn} are new integration constants which represent cosine and sine components of the circumferential flux density Fourier series at the same interface, and C_{gn} and D_{gn} are cosine and sine components at the interface between airgap and stator slots subdomains. Therefore, new and old integration constants are linked by developing the set of scalar products:

$$a_{gn}\frac{n}{R_m}\left(\frac{R_m}{R_s}\right)^n - b_{gn}\frac{n}{R_m} = A_{gn} \tag{A.65}$$

$$c_{gn}\frac{n}{R_m}\left(\frac{R_m}{R_s}\right)^n - d_{gn}\frac{n}{R_m} = C_{gn} \tag{A.66}$$

$$a_{gn}\frac{n}{R_s} - b_{gn}\frac{n}{R_s}\left(\frac{R_s}{R_m}\right)^{-n} = B_{gn} \tag{A.67}$$

$$c_{gn}\frac{n}{R_s} - d_{gn}\frac{n}{R_s}\left(\frac{R_s}{R_m}\right)^{-n} = D_{gn} \tag{A.68}$$

The expressions of F_{1gn} and F_{2gn} are obtained by substituting the expressions of the old integration constants in the MVP, such as:

$$F_{1gn}(r) = \frac{R_m}{n}\frac{P_n(r,R_s)}{E_n(R_m,R_s)} \tag{A.69}$$

$$F_{2gn}(r) = -\frac{R_s}{n}\frac{P_n(R_m,r)}{E_n(R_m,R_s)} \tag{A.70}$$

A.6.5 Reformulation of stator slots subdomains MVP

The stator slot subdomain is a Poisson eigenvalue problem in θ-direction subject to Neumann HBCs which is illustrated on Figure 4.4. The MVP solution A_{zsi} in the i^{th} stator slot subdomain is the sum of the Laplace homogeneous solution (3.84) and of the particular solution (3.130). The homogeneous solution depends on four integration constants a_{si0}, b_{si0}, a_{sik}, b_{sik} and two unknown functions F_{1ik} and F_{2ik}, accounting for

the BCs/ICs on both circumferential edges at stator bore radius $r = \mathrm{R}_s$ and stator internal yoke radius $r = \mathrm{R}_y$. Due to the stator yoke infinite permeability assumption, an additional Neumann HBC (3.29) applies on stator yoke radius R_y. Besides, the MVP expression is reformulated at $r = \mathrm{R}_s$ to account for the MVP continuity condition (4.4) with the airgap subdomain at $r = \mathrm{R}_s$.The following scalar products are applied to determine F_{1sik} and F_{2sik} as defined in Equation (3.72):

$$\frac{1}{a}\langle\frac{\partial \mathrm{A}_{zsi}}{\partial r}\Big|_{r=\mathrm{R}_y,\theta}, 1\rangle = 0 \tag{A.71}$$

$$\frac{1}{2a}\langle\frac{\partial \mathrm{A}_{zsi}}{\partial r}\Big|_{r=\mathrm{R}_y,\theta}, \cos\left[\nu_k(\theta-\Theta_{si1})\right]\rangle = 0 \tag{A.72}$$

$$\frac{1}{a}\langle \mathrm{A}_{zsi}(\mathrm{R}_s,\theta), 1\rangle = \mathrm{A}_{si0} \tag{A.73}$$

$$\frac{1}{2a}\langle \mathrm{A}_{zsi}(\mathrm{R}_s,\theta), \cos\left[\nu_k(\theta-\Theta_{si1})\right]\rangle = \mathrm{A}_{sik} \tag{A.74}$$

The integration constants b_{si0}, b_{sik} and one unknown functions will disappear after applying the Neumann HBC at $r = \mathrm{R}_r$. The integration constants A_{si0} and A_{sik} are introduced to represent the constant and cosine MVP components in the Fourier basis $\mathscr{B}_{ik}$ at the interface between the i^{th} stator slot and airgap subdomains. Therefore, the two new integration constants and the four old ones are linked by developing the set of scalar products:

$$\frac{b_{si0}}{\mathrm{R}_y} + \mathrm{J}_{i0}(t_0)\mathrm{R}'_{dlc,0}(\mathrm{R}_y) = 0 \tag{A.75}$$

$$a_{sik}\frac{\nu_k}{\mathrm{R}_y} - b_{sik}\left(\frac{\mathrm{R}_s}{\mathrm{R}_y}\right)^{\nu_k} + \mathrm{J}_{i\nu_k}(t_0)\mathrm{R}'_{dlc,\nu_k}(\mathrm{R}_y) = 0 \tag{A.76}$$

$$a_{si0} + b_{si0}\log\left(\frac{\mathrm{R}_s}{\mathrm{R}_y}\right) + \mathrm{J}_{i0}(t_0)\mathrm{R}_{dlc,0}(\mathrm{R}_s) = \mathrm{A}_{si0} \tag{A.77}$$

$$a_{sik}\left(\frac{\mathrm{R}_s}{\mathrm{R}_y}\right)^{\nu_k} + b_{sik} + \mathrm{J}_{i\nu_k}(t_0)\mathrm{R}_{dlc,\nu_k}(\mathrm{R}_s) = \mathrm{A}_{sik} \tag{A.78}$$

The expression of F_{1mn} is obtained by substituting the expression of the old integration constants in the MVP, such as:

$$\mathrm{F}_{1ik}(r) = \frac{\mathrm{P}_n(r,\mathrm{R}_y)}{\mathrm{P}_n(\mathrm{R}_s,\mathrm{R}_y)} \tag{A.79}$$

The new source terms X_{si0} and X_{sik} can be written:

$$\mathrm{X}_{si0}(r) = \mathrm{R}_{dlc,0}(r) - \mathrm{R}_{dlc,0}(\mathrm{R}_s) - \mathrm{R}_y\mathrm{R}'_{dlc,0}(\mathrm{R}_y)\ln\left(\frac{\mathrm{R}_s}{r}\right) \tag{A.80}$$

$$\mathrm{X}_{sik}(r) = \nu_k\mathrm{R}_{dlc,\nu_k}(r) + \mathrm{R}_y\frac{\mathrm{E}_{\nu_k}(\mathrm{R}_s,r)}{\mathrm{P}_{\nu_k}(\mathrm{R}_s,\mathrm{R}_y)}\mathrm{R}'_{dlc,\nu_k}(\mathrm{R}_y) - \nu_k\frac{\mathrm{P}_{\nu_k}(r,\mathrm{R}_y)}{\mathrm{P}_{\nu_k}(\mathrm{R}_s,\mathrm{R}_y)}\mathrm{R}_{dlc,\nu_k}(\mathrm{R}_s) \tag{A.81}$$

with E_{ν_k} defined in Appendix A.6.1, and R_{dlc,ν_k} given by Equations (3.132)-(3.134).

A.7 Scalar products

The change of Fourier basis between MVP solutions of eigenvalue problems in circumferential directions is illustrated taking the example of the application of ICs between airgap and stator slots subdomains in 4.2.2.2. The Fourier basis of the airgap subdomain is given by Equation (3.78) and the Fourier basis of stator slots subdomains is

given by Equation (3.82). The scalar products between the airgap and the i^{th} stator slot subdomains lead to the following integrals over θ:

$$\mathrm{I}_1(i,n) = \int_{\Theta_{i1}}^{\Theta_{i2}} \cos(n\theta)\, d\theta \tag{A.82}$$

$$\mathrm{I}_2(i,n) = \int_{\Theta_{i1}}^{\Theta_{i2}} \sin(n\theta)\, d\theta \tag{A.83}$$

$$\mathrm{I}_3(i,k,n) = \int_{\Theta_{i1}}^{\Theta_{i2}} \cos\left[\nu_k(\theta - \Theta_{i1})\right] \cos(n\theta)\, d\theta \tag{A.84}$$

$$\mathrm{I}_4(i,k,n) = \int_{\Theta_{i1}}^{\Theta_{i2}} \cos\left[\nu_k(\theta - \Theta_{i1})\right] \sin(n\theta)\, d\theta \tag{A.85}$$

A.8 Additional SCIM SDM simulation results

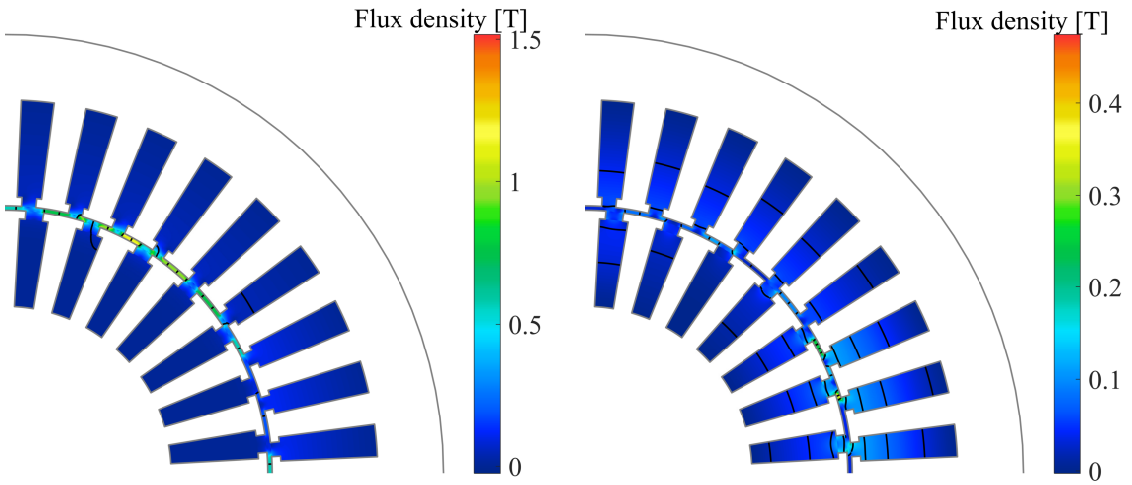

(a) Slip $s = 0\%$ (b) Slip $s = 10\%$

Figure A.3 – Flux lines obtained with the developed SDM ($\mathrm{N}_\lambda = 5$).

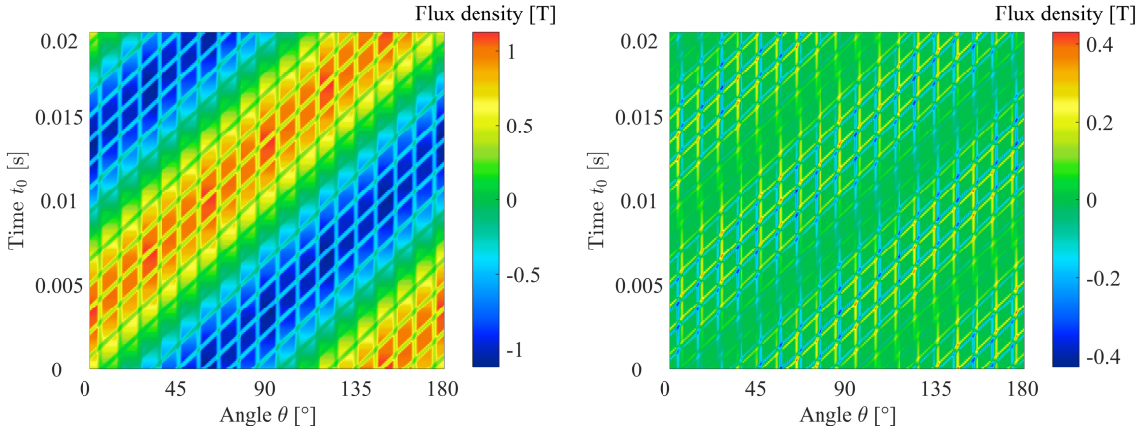

(a) Radial flux density (b) Circumferential flux density

Figure A.4 – Time and space distribution of airgap flux density over one stator electrical period for slip $s = 0\%$.

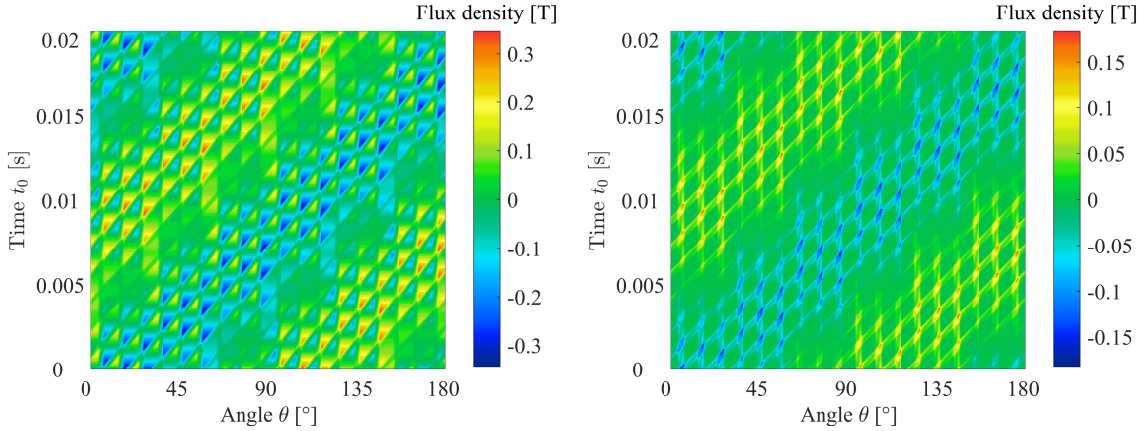

(a) Radial flux density

(b) Circumferential flux density

Figure A.5 – Time and space distribution of airgap flux density over one stator electrical period for slip $s = 10\%$.

A.9 Convolution approach

The harmonic content of magnetic force excitation or vibration can be quite rich in presence of sources detailed in Subsection 1.2). Identifying these sources in the excitation spectrum often requires to link the flux density harmonics with the exciting harmonics.

3D Fourier transform of radial, circumferential and axial components of flux density and forces are computed. The numerical computation of 3D Fourier transform requires to truncate series to a finite number of frequency and wavenumber values, respectively K, R and L. The product of two quantities in time and space domain is equal to the convolution product of their 2D Fourier transform. Therefore, the MST is reformulated using the convolution approach [Rothe et al., 2010]:

$$\bar{\mathrm{P}}_{\rho}^{kf,r,l} = \frac{\bar{\mathrm{B}}_{\rho}^{kf,r,l} * \bar{\mathrm{B}}_{\rho}^{kf,r,l} - \bar{\mathrm{B}}_{\theta}^{kf,r,l} * \bar{\mathrm{B}}_{\theta}^{kf,r,l} - \bar{\mathrm{B}}_{z}^{kf,r,l} * \bar{\mathrm{B}}_{z}^{kf,r,l}}{2\mu_0} \tag{A.86}$$

$$\bar{\mathrm{P}}_{\theta}^{kf,r,l} = \frac{\bar{\mathrm{B}}_{\rho}^{kf,r,l} * \bar{\mathrm{B}}_{\theta}^{kf,r,l}}{\mu_0} \tag{A.87}$$

$$\bar{\mathrm{P}}_{z}^{kf,r,l} = \frac{\bar{\mathrm{B}}_{\rho}^{kf,r,l} * \bar{\mathrm{B}}_{z}^{kf,r,l}}{\mu_0} \tag{A.88}$$

where $\bar{\mathrm{P}}_{\rho}^{kf,r,l}$, $\bar{\mathrm{P}}_{\theta}^{kf,r,l}$ and $\bar{\mathrm{P}}_{z}^{kf,r,l}$ are respectively the complex magnitude of the radial, circumferential and axial force harmonics; $\bar{\mathrm{B}}_{\rho}^{kf,r,l}$, $\bar{\mathrm{B}}_{\theta}^{kf,r,l}$ and $\bar{\mathrm{B}}_{z}^{kf,r,l}$ are respectively the complex magnitude of the radial, circumferential and axial flux density harmonics and $*$ is the 3D convolution product, also called Cauchy product. The convolution product links the force harmonic content with the harmonic content of the two flux density components q_1 and q_2 which created it, such as:

$$\bar{\mathrm{P}}^{kf,r,l} = \bar{\mathrm{Q}}_1^{kf,r,l} * \bar{\mathrm{Q}}_2^{kf,r,l} = \frac{1}{8\mathrm{NRL}} \sum_{k'=-\mathrm{K}}^{k'=\mathrm{K}} \sum_{r'=-\mathrm{R}}^{r'=\mathrm{R}} \sum_{l'=-\mathrm{L}}^{l'=\mathrm{L}} \bar{\mathrm{Q}}_1^{k'f,r',l'} * \bar{\mathrm{Q}}_2^{(k-k')f,r-r',l-l'} \tag{A.89}$$

where $\bar{\mathrm{P}}^{kf,r,l}$ is the 2D Fourier transform of any force component among (ρ, θ_S, z), and $\bar{\mathrm{Q}}_1^{kf,r,l}$ and $\bar{\mathrm{Q}}_2^{kf,r,l}$ are respectively the 3D Fourier transforms of the two flux density components.

In case of axially invariant magnetic quantities, the 2D convolution product is:

$$\bar{\mathrm{P}}^{kf,r} = \bar{\mathrm{Q}}_1^{kf,r} * \bar{\mathrm{Q}}_2^{kf,r} = \frac{1}{4\mathrm{NR}} \sum_{k'=-\mathrm{K}}^{k'=\mathrm{K}} \sum_{r'=-\mathrm{R}}^{r'=\mathrm{R}} \bar{\mathrm{Q}}_1^{k'f,r'} * \bar{\mathrm{Q}}_2^{(k-k')f,r-r'} \tag{A.90}$$

Equation (A.89) shows that a flux density harmonic either interacts with itself (if $q_1 = q_2$, $k' = k - k'$, $r' = r - r'$ and $l' = l - l'$) or it interacts with another harmonic of different frequency and wavenumber. It means that flux density harmonics from any type of sources (slotting, MMF, PWM, eccentricity etc.) combine themselves to create force harmonics. In fact, it can be shown from the 3D convolution product that KRL non-null harmonics of flux density create exactly $(2\mathrm{K}-1)(2\mathrm{R}-1)(2\mathrm{L}-1)$ components in the force spectrum. Therefore, reducing the harmonic content of the flux density reduces much more the harmonic content of the magnetic force.

Furthermore, the convolution approach provides valuable insight on the physical origins of force harmonics [La Delfa et al., 2016]. This tool also enables to analyze the contribution of stator and rotor field to a specific force harmonic.

As said before, the air gap flux density results from the sum of stator and rotor flux densities. Injecting Equation (1.7) in the quadratic relationship (1.1) yields:

$$\mathrm{F} \propto \mathrm{B}_\mathrm{S}^2 + \mathrm{B}_\mathrm{R}^2 + 2\mathrm{B}_\mathrm{S}\mathrm{B}_\mathrm{R} \tag{A.91}$$

Then, Equation (A.91) is reformulated under the convolution product form [Weilharter et al., 2011]:

$$\bar{\mathrm{P}}_\rho^{k,r} = \frac{\bar{\mathrm{B}}_{\mathrm{S},\rho}^{k,r} * \bar{\mathrm{B}}_{\mathrm{S},\rho}^{k,r} + \bar{\mathrm{B}}_{\mathrm{R},\rho}^{k,r} * \bar{\mathrm{B}}_{\mathrm{R},\rho}^{k,r} + \bar{\mathrm{B}}_{\mathrm{S},\rho}^{k,r} * \bar{\mathrm{B}}_{\mathrm{R},\rho}^{k,r} + \bar{\mathrm{B}}_{\mathrm{R},\rho}^{k,r} * \bar{\mathrm{B}}_{\mathrm{S},\rho}^{k,r}}{2\mu_0} \tag{A.92}$$

The equation above enables to differentiate stator and rotor flux density harmonics in force density spectrum. The simplified expressions of MST can be also formulated with the convolution approach. It is worth mentioning that the convolution product is not commutable, as opposed to the classical product.

The convolution approach has some limits, especially when it is not possible to isolate harmonic sources. For example, the harmonic signature of IPMSM due to stator MMF alone cannot be simulated. If the PM excitation is removed, then rotor flux barriers disappear and the obtained stator MMF is very far from the one obtained with rotor MMF. In fact, saturation harmonics cannot be isolated from the harmonic content of magnetic excitation as they are non-linearly dependent on the magnetic excitation. In this case, electromagnetic and vibro-acoustic simulations including one, all or several harmonic sources are required to determine the contribution of each source.

In conclusion, the convolution approach applied on MST enables to link the harmonic content of magnetic flux density and forces and helps to identify the origins of a specific force harmonic. This knowledge is primordial in the electromagnetic and vibro-acoustic design and to consider only the most relevant reduction techniques.

Appendix B

List of acronyms

ABC Anti-periodic Boundary Condition. 92, 134

AC Alternating Current. 20, 112

ARME Analytical Resolution of Maxwell Equations. 9, 49, 51, 55–58, 60–62, 69, 71, 79, 82, 83, 89, 102, 108, 120, 121, 135

BC Boundary Condition. 60, 61, 82, 88–90, 95, 99, 101–105, 107, 111, 112, 120, 133, 234, 236, 237

BEM Boundary-Element Method. 68, 78

BEMF Back-Electromotive Force. 62

BLDC BrushLess Direct Current. 20

CP Complex Permeance. 58–60, 69, 70, 210, 211

CT Conformal Transformation. 57–60, 69

DC Direct Current. 20, 112, 176

DCM Direct Current Machine. 17, 20, 64, 69

DFIM Doubly-Fed Induction Machine. 64, 130, 209, 211

EEC Electric Equivalent Circuit. 47, 52, 55, 63, 64, 166, 211

EMA Experimental Modal Analysis. 31, 74, 75, 171, 183, 188–190, 192, 195–197, 206, 209

EMF Electromotive Force. 47, 56, 63, 129, 135, 153, 154, 156, 158, 162, 163

e-NVH Electromagnetic Noise, Vibrations and Harshness. 6–10, 13, 24, 26, 31, 37, 42, 45–47, 50, 53, 60, 68–70, 72, 74, 78, 79, 117, 120, 139, 149, 166, 168, 171–174, 182, 204, 206–212

ESP Electric Scalar Potential. 232

EV Electric Vehicle. 9, 10, 37–39

EVS Electromagnetic Vibration Synthesis. 37, 46, 47, 49, 53, 74, 78, 171–174, 185, 186, 197, 198, 203, 204, 206, 208

FE Finite-Element. 46, 76, 77, 130, 163

FEA Finite-Element Analysis. 10, 37, 46, 60, 65–69, 74–79, 108, 119, 120, 130, 139–141, 146–149, 154, 155, 162, 163, 165–168, 171, 174, 183–187, 196–198, 206, 209, 210

FEM Finite-Element Method. 50, 64, 65, 67–70, 73, 130, 131

FRF Frequency Response Function. 46, 74–78, 171–174, 185, 186, 189, 190, 192, 195, 197, 198, 203, 206, 208, 209

FSM Flux-Switching Machine. 63

FT Fourier Transform. 71, 72, 74

HBC Homogeneous Boundary Condition. 91–93, 97, 98, 102–105, 107, 109, 111, 113–115, 125, 137–139, 142, 143, 145–147, 234–237

HEV Hybrid Electric Vehicle. 9, 10, 35, 37–39

IC Interface Condition. 61, 62, 82, 89, 90, 93, 94, 96, 99–107, 109, 112, 120–123, 127, 128, 130, 134–137, 139, 142, 143, 145, 149, 152, 166, 233, 234, 236, 237

IM Induction Machine. 17, 20, 28, 38, 41, 46, 47, 55, 63, 64, 82, 211

IPMSM Interior Permanent Magnet Synchronous Machine. 9, 18, 38, 39, 63, 66, 69, 70, 79, 83, 108, 117, 209, 240

MEC Magnetic Equivalent Circuit. 50, 64–70, 149, 210

MMF MagnetoMotive Force. 20–23, 28, 39, 41, 53–56, 58, 59, 63, 64, 66, 69, 86, 87, 120, 121, 132, 133, 149, 151–156, 159, 161–165, 171, 172, 180–182, 187, 193, 195, 198, 206, 207, 209, 240

MSP Magnetic Scalar Potential. 55, 56, 61, 66

MST Maxwell Stress Tensor. 25, 46, 52, 70–73, 77, 79, 129, 143, 155, 167, 180, 193, 203, 206, 208, 209, 229, 230, 239, 240

MVP Magnetic Vector Potential. 55, 56, 61, 64, 82, 83, 85, 86, 88–107, 109–111, 113, 115–117, 120–132, 134–139, 142–147, 149–156, 208, 210, 231–237

NBC Non-homogeneous Boundary Condition. 90, 92–94, 109, 112

NVH Noise, Vibrations, and Harshness. 6, 7, 28, 33, 35–37, 47, 49, 77

ODE Ordinary Differential Equation. 82, 95, 96, 98, 105, 109–111, 113–117, 233

ODS Operational Deflection Shape. 172, 174, 178, 192, 199–202, 206, 209, 211

OMA Operational Modal Analysis. 75

PBC Periodic Boundary Condition. 92, 93, 97, 98, 101, 106, 109, 113, 116, 124, 133, 134, 234, 235

PDE Partial Differential Equation. 82, 86–90, 92–96, 109, 111, 113–115, 120, 129, 137–139, 142, 232

PM Permanent Magnet. 60, 64, 83, 89, 92, 95, 101, 108–111, 120–127, 129, 132–137, 139, 143, 146, 171, 172, 175, 176, 178, 182, 187, 188, 193, 206, 208, 210, 234–236, 240

PMMF Permeance/MagnetoMotive Force method. 46, 54, 55, 58, 69–71, 79, 120, 121, 165–168, 193, 209

PMSM Permanent Magnet Synchronous Machine. 17, 20, 29, 34, 38, 55, 62, 63, 65, 66, 73, 109, 130, 173, 212

PWM Pulse Width Modulation. 21, 22, 28, 38, 41, 50, 51, 55, 64, 175, 240

RMS Root Mean Square. 36, 52, 76, 154

RMSE Root Mean Square Error. 132, 133

RSH Rotor Slot Harmonic. 47, 121, 151, 152, 154–156, 159, 161, 162, 167, 175

SCIM Squirrel Cage Induction Machine. 7, 9, 10, 18, 23, 30, 31, 35, 46, 50, 54, 59, 62, 63, 70, 79, 85, 107, 117, 120, 121, 130, 131, 133–135, 149, 150, 153, 154, 163–168, 209, 211

SDM SubDomain Method. 9, 10, 19–22, 25, 46, 52, 58, 60–65, 69, 70, 79, 82, 89, 102, 105, 108, 120, 121, 130, 131, 140, 141, 143, 146–149, 155–157, 159, 161–168, 171, 173, 174, 176, 178–180, 185, 188, 194, 206, 208–211, 238

SM Synchronous Machine. 20, 41, 42, 46, 47, 62, 63, 77, 82, 161, 175, 211

SoV Separation of Variables. 82, 95, 96

SPL Sound Pressure Level. 6, 36, 37, 49, 171, 190–192, 206, 209, 211

SPMSM Surface Permanent Magnet Synchronous Machine. 9, 10, 13, 17–22, 25, 28, 29, 33–35, 42, 46, 47, 53, 56–62, 67, 69, 70, 75, 78, 79, 88, 108, 117, 120–122, 129–136, 139, 143, 145–147, 149, 168, 171, 172, 175–178, 180–182, 186, 189, 191, 192, 195, 199, 202, 204, 206, 207, 209–211

SRIM Solid Rotor Induction Machine. 56, 64, 83, 106, 130

SRM Switched Reluctance Machine. 17, 42, 55, 63, 66, 77

SWL Sound Power Level. 7, 36, 37, 49, 53, 78, 171, 185, 186, 203, 204, 206, 210, 211

SynRM Synchro-Reluctant Machine. 17, 63, 66, 69, 83, 210

UMF Unbalanced Magnetic Force. 26, 29, 35, 39

UMP Unbalanced Magnetic Pull. 26, 35, 38, 65, 190, 199, 202

VWP Virtual Work Principle. 70, 72, 73

WRSM Wound Rotor Synchronous Machine. 17, 18, 20, 35, 55, 63, 66, 83, 117, 130, 209

Appendix C

List of symbols

$\underline{\alpha}$ Diffusion penetration coefficient [m^{-1}]. 86, 87, 96, 105–107

f_s Stator current electric frequency or synchronous frequency [Hz]. 24, 25, 39, 75, 83, 149, 164, 167

L_S Stator axial length [m]. 25, 26, 30, 129, 230

μ_0 Void magnetic permeability [H/m]. 56, 85

μ_r Magnetic relative (or recoil) permeability. 56, 83, 85, 109, 113, 140, 141, 231

Ω Rotor mechanical speed [rad/s]. 83, 86, 110, 111, 193, 232

ω_{rm} Induced current pulsation due to relative motion [rad/s]. 86, 130

p Number of pole pairs. 20, 39, 109–111, 132, 149

ψ Position of the first surface Permanent Magnet [rad]. 108, 124

q Number of stator phases. 20, 149

R_g Airgap middle radius [m]. 187, 193, 230

s Rotor mechanical slip. 152, 156–167, 238, 239

σ Electrical conductivity [S]. 83, 85

t_0 Simulation instant parameter [s]. 83, 87, 95, 110–112, 124, 126, 129, 130, 139, 149, 151, 153–157, 159, 161, 163, 165, 166, 194

Z_r Number of rotor slots. 20, 113, 151

Z_s Number of stator slots. 20, 39, 62, 113, 121, 132, 135, 146, 151, 152

Résumé étendu (Extended French abstract)

Introduction

Les machines électriques émettent généralement du bruit acoustique dans les fréquences audibles lorsqu'elles fonctionnent. Certaines peuvent être quasi silencieuses tandis que d'autres peuvent s'avérer potentiellement bruyantes. Malgré la présence grandissante des machines électriques dans notre environnement, le critère d'émission de bruit acoustique n'est pas systématiquement pris en compte lors de leur conception. Dans certains types d'applications, par exemple dans les secteurs domestique ou automobile où les problèmes de bruit sont plus généralement désignés par le terme « Bruit et Vibration (B&V) », ce critère est pris en compte avec l'utilisation d'outils informatiques, qui évoluent constamment pour s'adapter à l'usage croissant des machines électriques au sein d'applications de plus en plus variées.

Il y a principalement trois grandes familles de bruit acoustique dans les machines électriques :

1. le bruit d'origine aérodynamique, émis par exemple par les pâles des ventilateurs à la fréquence de passage des pâles ;
2. le bruit d'origine mécanique, dû par exemple aux frottements mécaniques dans les roulements et les engrenages du réducteur mécanique ;
3. le bruit d'origine électromagnétique, qui résulte de la présence de champs électromagnétiques variables à l'intérieur de la machine. Ces champs électromagnétiques interfèrent pour produire le couple électromagnétique nécessaire à la conversion électromécanique. Cependant, ils génèrent également des forces électromagnétiques parasites, par exemple à la fréquence de passage des pôles et des encoches, qui induisent des vibrations dans la structure qui peuvent à leur tour émettre du bruit acoustique dans les fréquences audibles.

En résumé, l'étude de la génération du bruit acoustique dans les machines électriques fait appel à plusieurs champs de la physique, dont l'acoustique, la mécanique et l'électromagnétique, et est souvent désignée par les termes « étude B&V » ou « étude vibroacoustique ». Cette thèse s'intéresse exclusivement aux bruits d'origine électromagnétique dans les machines à flux radial.

Le bruit acoustique d'origine électromagnétique est caractérisé par un contenu harmonique très prononcé et un son par conséquent très tonal. Par ailleurs, les forces d'excitation électromagnétiques peuvent résonner avec la structure de la machine si elles excitent ses fréquences naturelles. A la résonance, le niveau de B&V est considérablement amplifié et le bruit d'origine électromagnétique peut couvrir les autres sources de bruit. Ainsi, l'étude des B&V dus aux forces électromagnétiques est nécessaire étant données les raisons suivantes :

— le bruit est généralement source d'inconfort pour les personnes proches de la machine, dû au caractère tonal qui s'avère vite irritant ;

— le bruit peut provoquer des problèmes de santé dans les environnements industriels, où les employés travaillent chaque jour au contact de machines bruyantes;

— les vibrations induisent de la fatigue mécanique qui peut compromettre la sécurité des personnes et de la machine, réduit la durée de vie la machine, et augmente ses coûts de maintenance.

Ainsi, des normes internationales limitent le niveau de B&V émis par les machines électriques. Le défi dans la conception multi-physique d'une machine électrique consiste à trouver le design qui offre le meilleur compromis entre performances électromagnétiques et vibroacoustiques. Pour cela, la première phase de conception vise à explorer et classer les topologies susceptibles de répondre au cahier des charges, en se basant sur des modèles rapides et précis qui ne doivent pas ralentir le processus de conception classique. Par la suite, on effectue des simulations plus détaillées et potentiellement plus coûteuses en temps de calcul pour valider l'évolution du design. D'autres part, la modélisation des phénomènes électromagnétiques et vibroacoustiques permet d'inclure dès le début de la conception des techniques de réduction et de dissipation du bruit et des vibrations.

Cette thèse est une thèse CIFRE qui fait partie intégrante du programme de recherche interne d'EOMYS ENGINEERING, une société de conseil et de R&D spécialisée dans l'étude vibroacoustique des machines électriques. EOMYS développe et commercialise son propre logiciel MANATEE dédié à la simulation rapide et précise du bruit et des vibrations d'origine électromagnétique générés par les machines électriques.

La première étude scientifique qui décrit et explique les concepts clés du B&V d'origine électromagnétique, tels que le sujet est encore abordé actuellement, a été publiée au début des années 1950. Depuis cette date, de nombreuses études ont été réalisées dans le domaine, qui ont mené à une meilleure compréhension physique des phénomènes d'interaction entre forces électromagnétiques et structure. Toutefois, il subsiste un certain nombre de verrous scientifiques qui sont encore l'objet de recherches actives.

Premièrement, les contraintes environnementales ont mené au développement de nouveaux types de machines avec des meilleurs rendement énergétique et densité de puissance, et à la reconception des machines existantes de faible rendement. Ce progrès technologique a introduit de nouvelles topologies (par exemple les bobinages dentaires, les laminations avec concentration de flux etc.), de nouveaux matériaux (par exemple les aimants permanents, les tôles électriques à grains orientés etc.) et de nouvelles stratégies de commande grâce au développement de l'électronique de puissance. L'apparition de ces nouvelles technologies et la diminution des tailles de machines s'accompagne de nouveaux défis dans la conception électromagnétique et vibroacoustique. En particulier, l'usage massif de variateurs de vitesse électroniques a considérablement augmenté la contribution des forces électromagnétiques au niveau de bruit global des machines.

La prise en compte de ces nouvelles technologies nécessite de comprendre et modéliser de nouveaux phénomènes physiques. Cela remet aussi en cause certaines hypothèses de modélisation qui ne sont désormais plus valables. De plus, l'apparition de nouvelles applications, par exemple dans le secteur automobile, a durci les tolérances en termes de niveau de B&V tout en augmentant les plages de vitesse, la compacité etc. La course à la réduction du moindre décibel exige l'évaluation de toutes les sources potentielles de bruit, incluant par exemple les dysfonctionnements et les tolérances de fabrication, et donc complexifie le problème physique et les modélisations associées.

Par ailleurs, plusieurs verrous scientifiques relatifs à l'étude des interactions entre les forces électromagnétiques et la structure de la machine sont toujours d'actualités. La thèse s'intéresse plus spécifiquement à deux de ces verrous, qui sont :

1. déterminer la contribution de la composante circonférentielle (i.e. tangentielle en 2D) du champ magnétique aux forces radiales s'appliquant sur la structure, ainsi que la contribution des forces circonférentielles aux vibrations radiales de la struc-

ture ;

2. déterminer l'impact de l'effet de modulation des encoches, qui apparaît en particulier dans des topologies récentes de machines avec un nombre proche d'encoches et de dent. Cet effet de modulation implique que les harmoniques de force avec un nombre d'onde élevé peuvent résonner avec des modes structures de faible ordre spatial, dû au repliement spectral. Ce nouveau phénomène est naturellement peu documenté et ignoré dans la plupart des études B&V.

Enfin, les capacités de simulation B&V sont encore limitées par la puissance de calcul des ordinateurs actuels. En supposant qu'il soit possible d'inclure l'intégralité de la complexité physique au sein du modèle, la simulation prendrait des semaines même en l'exécutant sur un cluster de calcul. Ainsi, la simulation complète n'est clairement pas envisageable en termes de mémoire et de temps de calcul pour les premières phases d'exploration et de dimensionnement. Par conséquent, il existe une large palette de modèles électromagnétiques, mécaniques et acoustiques dédiés à la modélisation précise et rapide lors de ces premières phases de conception. Il peut être intéressant de créer un cas de référence (« benchmark ») pour comparer les différents modèles car il n'en existe pas encore dans la littérature.

La première contribution de cette thèse est le développement de la Méthode des Sous-Domaines (MSD) pour calculer la distribution des forces électromagnétiques dans de nombreuses topologies de machines, avec un bon compromis entre précision et temps de calcul. La deuxième contribution est la conception d'un banc d'essai dont le but est d'illustrer le phénomène général de B&V dus aux forces électromagnétiques pour une machine bruyante donnée, une Machine Synchrone à Aimants Permanents en Surface (MSAPS) $12s10p$, i.e. avec 12 encoches statoriques et 10 pôles. En outre, le banc d'essai vise à étudier la contribution des effets circonférentiels et de modulation des encoches.

Chapitre 1

Le Chapitre 1 porte sur les principaux aspects et challenges dans l'étude de la génération des B&V d'origine électromagnétiques dans les machines électriques, en particulier l'étude des origines des forces électromagnétiques et leur interaction avec la structure. Les topologies considérées sont essentiellement des machines à flux radial utilisés dans les applications automobiles (véhicules électriques et hybrides), telles que les Machines Asynchrones à Cage d'Ecureuil (MACE), les MSAP enterrés (MSAPE) et en surface (MSAPS).

Le principe de génération des forces électromagnétiques dans les machines électriques est illustré à partir d'une expérience simple, qui montre l'existence d'une relation quadratique dans le domaine spatio-temporel entre le champ et les forces électromagnétiques. En particulier, une seule onde tournante de champ électromagnétique génère une densité surfacique de force locale, qui se décompose en une densité de force (ou contrainte) statique et une onde de densité de force tournante, à deux fois la fréquence et le nombre d'onde de l'onde de champ. Dans la suite, la densité de force est plus simplement désignée par le terme force.

Dans le cas réel des machines électriques, le champ électromagnétique contient beaucoup d'harmoniques d'origines variées, qui se combinent pour créer des harmoniques de force magnétique d'après la relation quadratique entre champ et force. Les principales sources d'harmoniques de champ sont présentées, comme la discrétisation des

sources de champ électromagnétique dans les encoches au rotor et au stator (harmoniques de Force MagnétoMotrice (FMM) et d'encochage), l'utilisation de la Modulation de Largeur d'Impulsion (MLI), la présence de saturation magnétique, d'excentricités, de vrillage etc. Physiquement, les harmoniques de force proviennent des forces de Maxwell qui se concentrent à l'interface entre l'entrefer et le circuit magnétique.

Ces harmoniques de forces magnétiques excitent et déforment la structure, et résonnent potentiellement avec les modes de structure, par exemple les modes respirant, de flexion et ovalisant. La condition classique de résonance dans le cas d'une structure cylindrique stipule que la fréquence de l'harmonique de force doit être proche de la fréquence naturelle du mode, et que la forme d'onde de l'excitation et la déformée modale doivent avoir le même nombre de nœuds spatiaux. Cependant, un certain nombre de verrous scientifiques subsiste en ce qui concerne la compréhension physique de l'interaction entre harmonique de force et structures dentés, en particulier la contribution des forces circonférentiels aux vibrations radiales et l'excitation des modes de faible ordre spatial par des harmoniques de force avec un nombre d'onde élevé, qui contredit la condition classique de résonance pour les cylindres. La génération de bruit acoustique à partir des vibrations de la structure est aussi évoquée.

Enfin, connaissant les origines des harmoniques de forces, des techniques de réductions et de dissipation des bruits peuvent être envisager pour agir sur l'excitation et/ou la structure et réduire le niveau de B&V. Un court état de l'art des méthodes de réduction est proposé, dans le but de considérer ces techniques au sein des simulations électromagnétiques et vibroacoustiques, et dans le but ultérieur d'illustrer ces techniques grâce au banc d'essai conçu durant cette thèse. De manière générale, les techniques de réduction se divisent en deux catégories :

— des techniques passives considérant le choix du nombre d'encoches et de pôles ainsi que l'optimisation de leur forme, le vrillage, l'insertion d'encoches vides et de cales magnétiques etc ;

— des techniques actives avec l'injection d'harmoniques de courant, la dissipation active des vibrations etc.

Chapitre 2

Dans le Chapitre 1, on a montré la nécessité de construire des modèles multiphysiques pour prédire le niveau de B&V et le prendre en compte dans la phase de conception de la machine. En particulier, la simulation calcule les harmoniques de force magnétique et la réponse structurelle qui prend en compte la résonance avec les modes de structures. Le Chapitre 2 présente les principaux défis en termes de simulations électromagnétique et mécanique, suivi d'un état de l'art des principaux modèles utilisés dans les études vibroacoustiques. Certains de ces modèles sont ensuite utilisés dans le Chapitre 5 pour la conception de la MSAP $12s10p$.

Le principal défi dans le domaine de la simulation des B&V d'origine électromagnétique est de développer des modèles multiphysiques rapides et précis, en considérant les paramètres suivants :

— choisir le modèle approprié pour chaque physique et le couplage entre les modèles;

— définir la discrétisation temporelle ou fréquentielle de telle manière à capter les harmoniques de force à basse et haute fréquences ;

— définir la discrétisation spatiale (le maillage ou les harmoniques d'espaces) de telle manière à capter les harmoniques de force issus de la combinaison d'harmoniques de champ avec des nombres d'onde élevés ;

— définir la discrétisation en vitesse sur la plage de vitesse considérée (seulement pour les simulations à vitesse variable) pour capter les pics de B&V dus aux résonances avec les modes de structure.

Le fait de développer plusieurs modèles pour chaque physique permet de disposer de plusieurs processus pour simuler le niveau de B&V, et d'adapter ainsi la précision et le temps de calcul de la simulation aux exigences de chaque phase de conception. Le processus de simulation de MANATEE en phase de conception détaillée est la Synthèse Electromagnétique et Vibratoire (SEV), qui calcule indépendamment la distribution des forces magnétiques et la réponse vibratoire pour chaque harmonique de force magnétique. Le niveau de vibration global est la somme des contributions de chaque harmonique de force magnétique.

Les principaux modèles électromagnétiques sont ensuite qualitativement comparés à travers un état de l'art non-exhaustif. Les modèles en question sont la méthode de Perméance/Force MagnétoMotrice (PFMM), la Résolution Formelle des Equations de Maxwell (RFEM) associée aux perméances relative et complexe, la Méthode des Sous-Domaines (MSD), les réseaux de réluctances et la Méthode des Eléments Finis (MEF). Chaque modèle est évalué en fonction du niveau de granularité existant et des critères de performances dictés par la simulation B&V. Le modèle retenu est finalement la méthode semi-analytique des sous-domaines (MSD), dont le principal avantage est de calculer le champ radial et circonférentiel dans l'entrefer pour un certain nombre de topologies de machines, avec un bon compromis entre temps de calcul et précision, et sans introduire d'erreur de maillage numérique. En outre, cette thèse a pour but d'étendre la MSD à d'autres topologies de machines synchrones et asynchrones, et de se focaliser principalement sur la modélisation des MACE et des MSAPE, et sur la possibilité d'inclure la saturation magnétique.

Enfin, les principaux modèles pour calculer les harmoniques de force magnétique relatifs aux forces de Maxwell et la réponse mécanique de la structure sont développés. La distribution des forces magnétiques est généralement calculée par la méthode du Tenseur des Contraintes de Maxwell (TCM), pour lequel trois approches sont détaillées, et peut être aussi calculée avec le Principe des Travaux Virtuels. Le niveau de vibration est prédit par la méthode de SEV, qui nécessite le calcul des Fonctions de Réponse en Fréquence (FRF). Une FRF représente la réponse mécanique de la structure soumise à un harmonique de force magnétique pour une fréquence et un nombre d'onde donnés. Les FRF peuvent être calculés à partir de modèles analytiques simples basés sur un cylindre équivalent, ou sur un modèle numérique structurel de type éléments finis.

Chapitre 3

Le Chapitre 3 développe en profondeur la théorie mathématique et physique relative à la Méthode des Sous-Domaines (MSD), qui exploite la Résolution Formelle des Equations de Maxwell (RFEM) associée à de l'analyse fonctionnelle. Le but est de :

— construire une architecture complète pour la RFEM dédiée à la construction des modèles de sous-domaines ;

— étendre la MSD à un maximum de topologies ;

— calculer les composantes radiales et circonférentielles des forces magnétiques, dans l'objectif d'avoir un modèle rapide et précis.

Dans la méthodologie des sous-domaines, la RFEM intervient après avoir divisé le problème magnétique en différentes régions physiques appelées « sous-domaines » (par exemple l'entrefer, les encoches et les dents au rotor at au stator, les aimants permanents, les culasses etc.) et avant la résolution numérique des Conditions aux Interfaces (CI) entre les sous-domaines adjacents. La RFEM peut se décomposer en trois étapes successives : Premièrement, l'équation générale du comportement magnétique dans chaque sous-domaine est obtenue à partir des équations de Maxwell, des lois constitutives des matériaux, de la formulation en Potentiel Vecteur Magnétique (PVM), et après avoir formulé les hypothèses simplificatrices suivantes :

— la géométrie est polaire et 2D ;

— le problème est stationnaire : la vitesse du rotor et les fréquences des courants sont constantes, les courants induits sont établis ;

— les propriétés électromagnétiques (conductivité électrique, perméabilité magnétique etc.) uniformes et isotropes.

En termes mathématiques, l'équation du PVM est une Equation aux Dérivées Partielles (EDP) du second ordre en fonction du temps et de l'espace, qui s'appelle :

— l'EDP de Laplace pour les sous-domaines sans source de champ magnétique ;

— l'EDP de Poisson pour les sous-domaines avec source de courant et d'aimantation;

— l'EDP de Helmholtz pour les sous-domaines avec un matériau conducteur et des courants induits.

Ensuite, le problème mathématique général, appelé problème de sous-domaine, est formalisé. L'approche adoptée est basée sur la théorie de Sturm-Liouville, qui applique la théorie de l'analyse fonctionnelle pour résoudre l'EDP dans chaque sous-domaine, en fonction de la nature des termes sources (densité de courant ou aimantation) et des Conditions aux Interfaces (CI). Ces dernières sont données par les relations physiques de passage de l'induction et du champ magnétiques d'un milieu matériel à un autre. On montre que le problème de sous-domaine s'exprime mathématiquement et de manière plus générale comme la superposition de deux problèmes aux valeurs propres dans chacune des directions radiale et circonférentielle.

Enfin, la méthode générale de résolution des problèmes aux valeurs propres est détaillée. A partir de la méthode de séparation des variables, l'EDP est transformée en deux Equations Différentielles Ordinaires (EDO) indépendantes et du second ordre, qui sont résolues pour un grand nombre de sous-domaines rencontrés dans la modélisation des machines électriques.

La première originalité de ce Chapitre 3 est la formalisation et la résolution du problème aux valeurs propres dans la direction radiale, qui permet de prendre en compte une perméabilité magnétique finie dans les dents en utilisant le principe de superposition, et potentiellement d'inclure la saturation globale dans la MSD. De plus, on montre que la formulation du problème de sous-domaine qui mène à la RFEM n'est pas unique. Le choix de la formulation a un impact sur la résolution du modèle de sous-domaines, ce point étant étudié dans le Chapitre 4.

D'autres part, deux autres contributions sont apportées. La première n'est pas illustrée dans ce rapport mais est développée dans Devillers et al. [2017a]. Elle consiste à calculer la distribution spatio-temporelle du champ d'entrefer dans les MSAPE en circuit-ouvert à partir d'une seule simulation par éléments finis. Cette technique est étendue aux Machines Synchrones à Rotor Bobiné (MRSB) et a été implémentée dans MANATEE au cours de la thèse. La seconde contribution est la nouvelle formulation analytique de la solution particulière associée aux encoches avec bobinage distribué à double couche, qui réduit par deux le nombre d'inconnus à résoudre dans chaque sous-domaine d'encoche par rapport à la formulation proposée dans les publications précédentes.

Chapitre 4

La solution du Vecteur Potentiel Magnétique (VPM) dépend de constantes d'intégration inconnues introduites par la RFEM. Ces constantes d'intégration sont les inconnues du modèle de sous-domaines. L'étape suivante dans la méthodologie des sous-domaines et qui est développée dans ce Chapitre 4 consiste naturellement à calculer les constantes d'intégrations pour obtenir le VPM et le champ magnétique dans les différents sous-domaines.

De plus, un modèle de sous-domaines de la MSAPS avec l'hypothèse de perméabilité finie dans les dents et un modèle de sous-domaines de la MACE sont développés et intégrés à MANATEE. D'autres modèles de sous-domaines de MSAPE et MRSB ont aussi été implémentés (non montrés dans ce rapport). Les résultats de simulation sont validés par la Méthode des Eléments Finis (MEF), et la pertinence de la MSD en comparaison de la MEF et de la méthode de la Perméance/Force MagnétoMotrice (PFMM) pour la simulation électromagnétique et vibroacoustique est discutée.

La méthodologie des sous-domaines est détaillée et expliquée en se basant sur l'exemple de la MSAPS $12s10p$ avec l'hypothèse de perméabilité finie dans les dents. Cette dernière étape consiste à appliquer les Conditions aux Interfaces (CI) entre les différents sous-domaines. Une reformulation supplémentaire est effectuée pour faciliter l'application des CI. Ensuite, le système d'équations que constituent les CI et qui lie les constantes d'intégrations entre elles est numériquement résolu, ce qui permet de calculer le VPM et le champ magnétique dans les différents sous-domaines, en particulier dans l'entrefer pour déterminer les harmoniques de forces magnétiques qui s'appliquent sur la structure. Finalement, plusieurs techniques d'optimisation du temps de calcul de la MSD sont présentées. On montre également que la MSD est particulièrement rapide pour la simulation des machines à simple encochage (par exemple les MSAPS) et l'est moins pour les machines à double encochage (par exemple les MACE).

A partir de la méthodologie développée, un nouveau sous-domaine de MSAPS est créé avec l'hypothèse de perméabilité finie dans les dents et la culasse statoriques. La solution du VPM dans les dents et les encoches statoriques s'obtient à partir de la superposition des deux problèmes aux valeurs propres dans les directions radiale et circonférentielle, qui sont détaillés dans le Chapitre 3. En particulier, deux formulations du principe de superposition, en théorie toutes les deux applicables aux dents statoriques, sont comparées. Par ailleurs, ce modèle de sous-domaines permet potentiellement d'inclure la saturation magnétique dans le stator. Les résultats sont validés à partir de la méthode des éléments finis dans ce chapitre et également par des mesures expérimentales sur la MSAP $12s10p$ dans le Chapitre 5.

En outre, la MSD est appliquée à la modélisation des MACE pour calculer la distribution 2D du champ magnétique dans l'entrefer, incluant le contenu harmonique dû aux FMM et aux effets d'encochage statorique et rotorique. La méthode est validée à vide et en charge par deux simulations éléments finis en régime transitoire. Les hypothèses du modèle sont discutées en détail, ainsi que sa pertinence au sein de la simulation B&V par rapport au modèle de PFMM et à la MEF.

En résumé, pour le même niveau de modélisation et pour toutes les topologies étudiées, la MSD est beaucoup plus rapide et aussi précise (voire plus) que la MEF, et s'avère donc pertinente dans la simulation B&V rapide. Cependant, la prise en compte de la saturation dans la MSD ralentit considérablement la méthode et est moins précise par rapport à la MEF. D'autre part, la MSD ne remplace pas systématiquement les modèles analytiques simples, tels que la PFMM qui a un excellent compromis précision/temps de calcul pour l'estimation des harmoniques de forces radiales dans les MACE [Devillers et al., 2018a].

La première contribution du Chapitre 4 est l'étude et la synthèse des techniques d'optimisation basée sur de nombreux modèles de sous-domaines tirés de la littérature et implémentés dans MANATEE. Les principales techniques sont :

— l'application des conditions de périodicité ;
— la sélection en amont des rangs d'harmoniques spatiaux dans le sous-domaine d'entrefer grâce à une étude analytique ;
— la réduction du nombre de constantes d'intégrations et de CI à résoudre numériquement grâce à des substitutions analytiques.

La deuxième contribution est l'application de la théorie développée dans le Chapitre 3 pour calculer le VPM et le champ magnétique dans toute la machine en faisant l'hypothèse de perméabilité finie dans les dents et la culasse statoriques. Ce nouveau modèle de sous-domaines permet d'inclure la saturation magnétique. D'autres part, deux formulations du principe de superposition, a priori équivalentes, sont comparées et on montre que la deuxième formulation induit des erreurs numériques dans le calcul du champ aux abords du contour des dents.

Enfin, la troisième contribution concerne le nouveau modèle de sous-domaines pour la modélisation de la MACE [Devillers et al., 2018c]. L'originalité réside dans le fait que les harmoniques de courants induits dans les barres rotoriques dus aux harmoniques de la FMM statoriques sont calculés analytiquement avec le bon effet de peau, et que les harmoniques d'encochages rotoriques sont bien présents dans le contenu harmonique du champ d'entrefer. En outre, ce modèle est implémenté dans MANATEE pour étudier l'effet des forces circonférentielles sur les vibrations radiales (développé dans Devillers et al. [2017b]), et pour comparer les harmoniques de forces obtenus grâce à la PMMF 1D et la MSD 2D avec un spectre de vibrations radiales obtenu par mesures expérimentales.

Voici des potentiels axes de recherches pour la MSD :

— Mieux estimer la saturation magnétique, par exemple pour améliorer le calcul des forces locales qui s'appliquent sur la structure en présence de saturation dans les dents ;
— Résoudre le VPM ou le champ magnétique dans un modèle de sous-domaines 3D avec encoches pour inclure les harmoniques de force axiale et les effets de bord, et mieux estimer les effets du vrillage sans avoir recours à l'hypothèse du modèle multicouches ;

— Résoudre l'équation de Poisson 2D pour une distribution de densité de courant ou d'aimantation qui varie dans les deux directions, pour inclure par exemple des topologies de bobinage complexes, ou pour considérer des formes non-polaires d'aimant permanent ;

— Résoudre l'équation de Laplace ou de Poisson 2D dans des sous-domaines avec une géométrie irrégulière, c'est-à-dire ni polaire ni cartésienne, pour inclure n'importe quelle géométrie d'aimant, d'encoches ou de dents non polaires (par exemple les barrières de flux dans les Machines Synchro-Réluctantes) ;

— Réduire le temps de calcul dans les machines avec encoches au rotor et au stator ;

— Valider la MSD pour d'autres topologies en utilisant l'architecture développée dans cette thèse, telles que les machines asynchrones à bobinage fractionnaire/concentré, et les Machines Asynchrones à Double Alimentation qui sont sujettes aux problèmes de B&V, en particulier à cause de la commande électronique.

Chapitre 5

Le Chapitre 5 porte sur la réalisation du banc d'essai expérimental afin d'illustrer l'interaction des harmoniques de forces électromagnétiques avec la structure des machines électriques, et d'étudier certains des verrous scientifiques existants. La machine électrique du banc d'essai est conçue sur le logiciel de simulation MANATEE, puis le banc d'essai est réalisé et validé expérimentalement, de manière à étudier les effets circonférentiels et de modulation des encoches.

Premièrement, le choix de la machine bruyante est discuté et justifié. En termes pratiques, le but est de construire une machine électrique dont l'origine des forces électromagnétiques et les modes de structure sont bien connus. Cette machine doit clairement illustrer la complexité multiphysiques des études B&V, en particulier l'interaction entre les harmoniques de forces électromagnétiques et la structure en régime forcé et à la résonance. Un processus d'ingénierie inverse basé sur la compréhension des phénomènes physiques établie dans le Chapitre 1 permet de déduire une façon simple de faire une machine bruyante à des fins d'illustrations. Plus précisément, les considérations vibroacoustiques suggèrent de générer du bruit acoustique en faisant résonner les harmoniques de forces électromagnétiques avec les modes de structures de la machine qui sont dans les fréquences audibles, en particulier les modes radiaux de faible ordre spatial comme le mode ovalisant. On en déduit le contenu qualitatif des forces électromagnétiques qui doit être idéalement présent dans la machine de manière à exciter le mode ovalisant.

Le design final est une Machine Synchrone à Aimants Permanents en Surface (MSAPS) avec 12 encoches statoriques et 10 pôles ($12s10p$), que l'on considère en premier lieu en circuit ouvert (c'est-à-dire uniquement avec l'excitation des aimants permanents au rotor), et pilotée en vitesse par un moteur d'entraînement. La MSAPS $12s10p$ est particulièrement pertinente pour accomplir les objectifs du banc d'essai car :

— le mode ovalisant est susceptible d'être excité ;

— les effets circonférentiels sont particulièrement forts en raison de la longueur de l'entrefer et du faible nombre de dents ;

— le faible nombre de dents permet aussi de sous-échantillonner l'harmonique de force principale dû au fondamental du champ magnétique et ainsi d'observer l'effet de modulation des encoches.

Les dimensions de la MSAP $12s10p$ sont établies à partir de simulations électromagnétiques et vibroacoustiques sous MANATEE en utilisant la Synthèse Electromagnétique et Vibratoire (SEV), qui combine la distribution de force calculée par le Tenseur des Contraintes de Maxwell (TCM), et les Fonctions de Réponses en Fréquence (FRF) dans les directions radial et circonférentiel associées à chaque harmonique de force électromagnétique et calculées par la MEF. La simulation prédit au moins trois résonances avec le mode ovalisant, dont deux à faible vitesse (en dessous de 1000 tr/min) et une à haute vitesse (en dessous de 5000 tr/min). L'épaisseur d'entrefer est suffisante pour installer un capteur de flux dans l'entrefer au rayon d'alésage statorique dont le but est de mesurer la distribution spatio-temporelle de l'induction magnétique dans l'entrefer. D'autres part, les encoches sont suffisamment larges pour coller des accéléromètres tri-axes sur le côté des dents et mesurer les accélérations radiale et circonférentielle en bout de dent, afin d'investiguer les effets circonférentiels.

Ensuite, la conception du banc d'essai est validée par des mesures expérimentales. Les harmoniques de champ dus à l'aimantation du rotor sont mesurés dans l'air et comparés à une simulation par éléments finis en 3D. Cette première mesure montre la présence d'harmoniques parasites due à une aimantation différente des aimants, et d'une excentricité dynamique du rotor. Plusieurs Analyses Modales Expérimentales (AME) de la lamination statorique sont réalisées pour valider l'existence des modes de structure simulés et leur fréquence naturelle, et en considérant différentes conditions de fixation et de serrage afin d'en observer l'impact sur les fréquences naturelles et les déformées modales. D'autre part, les modes de flexion du rotor sont mesurés pour déterminer s'ils peuvent introduire de l'excentricité dynamique à certaines fréquences. Les spectres d'accélération de la culasse statorique et de pression acoustique sont mesurés entre 0 et 1300 tr/min, ce qui permet de valider la première résonance entre le mode ovalisant et un harmonique de force prédit par la MSD. Les résultats expérimentaux montrent que les principaux harmoniques de d'accélération de la culasse statorique et les déformées opérationnelles en dessous de 1000 tr/min sont bien estimés par le design initial. Cependant, le mode de flexion du stator est aussi considérablement excité en raison de l'excentricité dynamique du rotor et de l'irrégularité d'aimantation des différents aimants.

Les modèles de simulations électromagnétique et mécanique sont ensuite ajustés à partir des données expérimentales, notamment pour :

— inclure le contenu harmonique et l'excentricité dynamique grâce au profil d'aimantation mesuré ;

— exciter le mode de flexion du stator ;

— mieux estimer les FRF en se rapprochant des fréquences naturelles mesurées et en introduisant l'amortissement mesuré pour les modes ovalisant et de flexion du stator.

La SEV est effectuée une nouvelle fois avec les harmoniques d'excitations et les FRF corrigés, ce qui permet de retrouver par la simulation le contenu harmonique de l'accélération de la culasse statorique et de la pression acoustique mesurées.

Enfin, plusieurs déformées opérationnelles sont réalisées pour observer la déformation du stator loin de la résonance avec le mode ovalisant (régime forcé), proche de la résonance et à la résonance. La contribution des harmoniques de force circonférentielle aux vibrations radiales de la culasse est ensuite estimée en mesurant les accélérations radial et circonférentielle en bout de dent, et en comparant avec l'accélération radiale de la culasse statorique en face de la dent. La contribution circonférentielle mesurée est

d'environ 20% sur le principal harmonique d'accélération à deux fois la fréquence électrique fondamentale. Les mesures sont comparées avec l'accélération de la culasse statorique simulée par deux SEV, la première considérant les harmoniques de forces radiale et circonférentielle, la deuxième ne considérant que les harmoniques de force radiale. Les deux SEV donnent les mêmes ordres de grandeur, soit un écart en amplitude de 20% sur l'amplitude de l'harmonique principal d'accélération.

L'effet de modulation des encoches est appliqué sur le contenu harmonique de la force radiale, en particulier pour étudier l'impact du repliement spectral sur l'harmonique de force principal à deux fois la fréquence électrique fondamentale. La simulation montre que l'effet de modulation augmente l'amplitude de l'harmonique d'environ 58.8%, soit de 2.3 dB l'amplitude de l'accélération et de 4.6 dB le niveau de puissance acoustique.

En guise de conclusion, ce chapitre témoigne de la difficulté de réaliser une machine électrique contenant uniquement les harmoniques d'excitation prédits par le design initial. Le contenu harmonique des forces est généralement bien plus riche que prévu, par exemple à cause des contraintes de fabrications qui ne peuvent garantir une aimantation idéale et un alignement parfait du rotor, comme on a pu l'observer pour la MSAPS $12s10p$ conçue et réalisée durant cette thèse.

Les mesures expérimentales détaillées dans ce rapport ont eu principalement pour but de valider la conception de la MSAPS $12s10p$, afin de montrer que le banc d'essai permet d'illustrer l'interaction entre les forces électromagnétiques et la structure des machines électriques, et d'en approfondir la compréhension. A termes, le principal objectif du banc d'essai est de créer un cas de référence pour la comparaison des différents modèles électromagnétiques et vibroacoustiques, et de diffuser publiquement toutes les données relatives au cas de référence au sein de la communauté scientifique et industrielle. Voici en résumé les principaux objectifs du banc d'essai :

1. Montrer que la principale source de B&V émis par le banc d'essai provient bien de l'excitation électromagnétique à l'intérieur de la MSAPS $12s10p$.
2. Illustrer clairement le processus de génération des B&V d'origine électromagnétique, en particulier la contribution des réponses en régime forcé et à la résonance.
3. Investiguer les verrous scientifiques qui subsistent dans la compréhension du phénomène de B&V d'origine électromagnétique, à savoir déterminer :
   - — la contribution de la composante circonférentielle du champ magnétique aux forces radiales s'appliquant sur la structure ;
   - — la contribution des forces circonférentielles aux vibrations radiales de la structure ;
   - — l'impact de l'effet de modulation des encoches aux vibrations radiales, en présence de repliement spectral ;
   - — la contribution des harmoniques de couple électromagnétique au bruit acoustique.
4. Etudier les techniques de réduction et de dissipation des B&V telles que :
   - — les règles de conception silencieuse comme le choix du nombre de pôles et de dents au stator (et au rotor, en particulier pour les machines asynchrones);
   - — les techniques passives : vrillage, encoches vides, cales magnétiques etc. ;
   - — les techniques actives : injection de courant, contrôle des harmoniques de force et des vibrations.

Electromagnetic subdomain modeling technique for the fast prediction of radial and circumferential stress harmonics in electrical machines

Abstract The presence of magnetic stress harmonics inside the electrical machine is generally responsible for vibrations and acoustic noise generation. This phenomenon is called e-NVH (Noise, Vibrations and Harshness due to electromagnetic excitations) and has to be considered in the machine design to meet with NVH standard requirements, especially in automotive applications. The e-NVH assertion requires a multiphysics simulation including electromagnetic, mechanical and acoustic models, which must be fast and accurate especially for early design stages. This industrial PhD thesis takes part of the internal research program of EOMYS ENGINEERING company, which develops and commercializes MANATEE software, dedicated to the e-NVH simulation of electrical machines. In this modeling context, the present thesis investigates and extends the semi-analytical electromagnetic model, called Subdomain Method (SDM), for the computation of two-dimensional airgap magnetic stress harmonics in various topologies of electrical machines, mainly focusing on Surface Permanent Magnet Synchronous Machines (SPMSMs) and Squirrel Cage Induction Machines (SCIMs). The thesis also investigates two scientific open questions concerning the contribution of circumferential excitations to the overall vibration level and the slotting modulation effect, which appears in electrical machines with a close number of poles and teeth. For this purpose, an experimental test rig including a particular noisy machine (a SPMSM with 12 slots and 10 poles) and appropriate sensors has been designed and built. The test rig also aims at benchmarking the different multiphysics models currently used in e-NVH simulation workflow.

Keywords Electrical machines, Electromagnetic noise, Machines vibrations, Analytical models, Electromagnetic stress, Subdomain method, Experimental benchmark

Modélisation électromagnétique appliquée à la détermination des harmoniques de forces radiale et tangentielle dans les machines électriques en exploitant l'approche des sous-domaines

Résumé La présence d'harmoniques de forces électromagnétiques dans les machines électriques est généralement source de bruit acoustique et de vibrations (B&V). Ce phénomène doit être considéré dès les premières phases de conception pour respecter les normes en matière de B&V, en particulier dans le secteur automobile. Le niveau de B&V s'obtient à partir d'une simulation multi-physiques basée sur des modèles électromagnétiques, mécaniques et acoustiques, de préférence rapides et précis de manière à l'inclure le plus tôt possible dans la phase de conception. Cette thèse CIFRE est partie intégrante du programme de recherche interne de la société EOMYS ENGINEERING, qui développe et commercialise son logiciel MANATEE dédié à la simulation électromagnétique et vibroacoustique des machines électriques. Dans ce contexte de modélisation, cette thèse porte sur la méthode électromagnétique semi-analytique des sous-domaines pour le calcul des harmoniques de forces 2D dans l'entrefer d'une large variété de machines électriques, et se concentre particulièrement sur la Machine Synchrone à Aimant Permanents en Surface (MSAPS) et la machine asynchrone à cage d'écureuil. La thèse s'intéresse également à deux verrous scientifiques concernant la contribution des forces tangentielles au niveau de vibration global, et l'effet de modulation des dents qui apparaît dans les machines avec un nombre proche d'encoches et de pôles. A cet effet, un banc d'essai comprenant une machine bruyante particulière (une MSAPS avec 12 encoches et 10 pôles) et l'instrumentation nécessaire a été conçu et réalisé. Le banc d'essai vise enfin à comparer les différents modèles utilisés couramment dans les simulations B&V.

Mots-clefs Machines électriques, Bruit électromagnétique, Machines vibrations, Modèles mathématiques, Forces électromagnétiques, Méthode des sous-domaines, Cas de référence expérimental